The Petrology and Geochemistry of Igneous Dykes above the Temagami Anomaly (Ontario, Canada) and their Relationship to the 1.85 Ga Sudbury Impact

by

Alexander Kawohl

A dissertation submitted in fulfilment of the requirements for the degree

Doctor rerum naturalium (Dr. rer. nat.)

To the

Faculty of Philosophy

Julius-Maximilians-Universität Würzburg

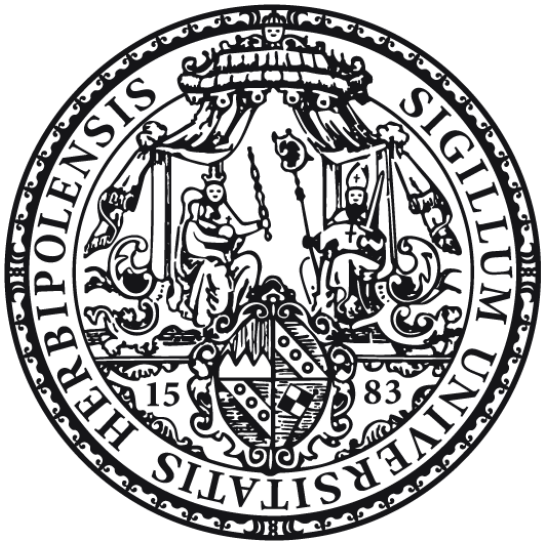

Würzburg, 2022

Author:	Alexander Kawohl ORCID 0000-0001-5582-1699

Title (English):	The Petrology and Geochemistry of Igneous Dykes above the Temagami Anomaly (Ontario, Canada) and their Relationship to the 1.85 Ga Sudbury Impact
Titel (Deutsch):	Die Petrologie und Geochemie magmatischer Gänge über der Temagami Anomaly (Ontario, Kanada) und ihre Beziehung zum 1,85 Ga Sudbury Impakt
Bibliographic data:	Doctoral dissertation Monograph 340 printed pages, plus digital appendix
Institution:	University of Würzburg Faculty of Philosophy Institute of Geography and Geology Department of Geodynamics and Geomaterials Research
Supervisors:	Univ. Prof. Dr. Hartwig E. Frimmel apl. Prof. Dr. Lutz Hecht apl. Prof. Dr. Thomas M. Will apl. Prof. Dr. Ulrich Schüßler Dr. Stefan Höhn
Day of enrolment:	24. October 2018
Day of submission:	08. December 2021
Day of defence:	05. July 2022

Recommended citation:

Kawohl, A. (2022). The Petrology and Geochemistry of Igneous Dykes above the Temagami Anomaly (Ontario, Canada) and their Relationship to the 1.85 Ga Sudbury Impact. Unpublished doctoral dissertation, University of Würzburg, Germany, 340 pp.

Abstract

The area northeast of Sudbury, Ontario, is known for one of the largest unexplained geophysical anomalies on the Canadian Shield, the 1,200 km^2 Temagami Anomaly. The geological cause of this regional magnetic, conductive and gravity feature has previously been modelled to be a mafic-ultramafic body at relatively great depth (2–15 km) of unknown age and origin, which may or may not be related to the meteorite impact-generated Sudbury Igneous Complex in its immediate vicinity. However, with a profound lack of outcrops and drill holes, the geological cause of the anomaly remains elusive, a genetic link to the 1.85 Ga Sudbury impact event purely speculative.

In search for any potential surface expression of the deep-seated cause of the Temagami Anomaly, this study provides a first, yet comprehensive petrological and geochemical assessment of exotic igneous dykes recently discovered in outcrops above, and drill cores into, the Temagami Anomaly. Based on cross-cutting field relations, petrographic studies, lithogeochemistry, whole-rock Nd-Sr-Pb isotope systematics, and U-Pb geochronology, it was possible to identify, and distinguish between, at least six different groups of igneous dykes: (i) Calc-alkaline quartz diorite dykes related to the 1.85 Ga Sudbury Igneous Complex (locally termed Offset Dykes); (ii) tholeiitic quartz diabase of the regional 2.22 Ga Nipissing Suite/Senneterre Dyke Swarm; (iii) calc-alkaline quartz diabase of the regional 2.17 Ga Biscotasing Dyke Swarm; (iv) alkaline ultrabasic dykes correlated with the 1.88–1.86 Ga Circum-Superior Large Igneous Province (LIP); and (v) aplitic dykes as well as (vi) a hornblende syenite, the latter two of more ambiguous age and stratigraphic position.

The findings presented in this study – the discovery of three new Offset Dykes in particular – offer some unexpected insights into the geology and economic potential of one of the least explored areas of the world-class Sudbury Mining Camp as well as into the nature and distribution of both allochthonous and autochthonous impactites within one of the oldest and largest impact structures known on Earth. Not only do the geometric patterns of dyke (and breccia) distribution reaffirm previous notions of the existence of discrete ring structures in the sense of a ~200-km multi-ring basin, but they provide critical constraints as to the pre-erosional thickness and extent of the impact melt sheet, thus helping to identity new areas for Ni-Cu-PGE exploration. Furthermore, this study provides important insights into the pre-impact stratigraphy and the magmatic evolution of the region in general, which reveals to be much more complex, compositionally divers, and protracted than initially assumed. Of note is the discovery of rocks related to the 2.17 Ga Biscotasing and the 1.88–1.86 Ga Circum-Superior magmatic events, as these were not previously known to occur on the southeast margin of the Superior Craton. Shortly predating the Sudbury impact and being contemporaneous with ore-forming events at Thompson (Manitoba) and Raglan (Cape Smith), these magmatic rocks could provide the missing link between unusual mafic, pre-enriched, crustal target rocks, and the unique metal endowment of the Sudbury Impact Structure.

The actual geological cause of the Temagami Anomaly remains open to debate and requires the downward extension of existing bore holes as well as more detailed geophysical investigations. The hypothesis of a genetic relationship between Sudbury impact event and Temagami Anomaly is neither borne out by any evidence nor particularly realistic, even in case of an oblique impact, and should thus be abandoned. It is instead proposed, based on circumstantial evidence, that the anomaly might be explained by an ultramafic complex of the 1.88–1.86 Ga Circum-Superior LIP.

Kurzfassung

Das Gebiet nordöstlich von Sudbury, Ontario, ist bekannt für eine der größten unerklärten geophysikalischen Anomalien auf dem Kanadischen Schild, die 1.200 km² große Temagami Anomalie. Die geologische Ursache dieser regionalen magnetischen, konduktiven und Schwere-Anomalie wurde bisweilen als ein mafisch-ultramafischer Körper in relativ großer Tiefe (2–15 km) unbekannten Alters und Ursprungs modelliert, der womöglich mit dem durch einen Impakt entstandenen Sudbury Igneous Complex in dessen unmittelbare Nachbarschaft verwandt sein könnte. Da es jedoch an Aufschlüssen und Tiefbohrungen grundlegend mangelt, bleibt die geologische Ursache dieser Anomalie unklar, eine genetische Beziehung zum 1,85 Ga Sudbury Impaktereignis rein spekulativ.

Auf der Suche nach einem potenziellen Oberflächenmanifestation der tiefliegenden Ursache der Temagami Anomalie liefert diese Studie eine erste und dennoch umfassende petrologische und geochemische Charakterisierung magmatischer Ganggesteine, die erst kürzlich in Aufschlüssen über der Temagami Anomalie, als auch in Bohrkernen, entdeckt wurden. Auf Grundlage von relativen geologischen Altersbeziehungen, petrographischen Untersuchungen, Lithogeochemie, Nd-Sr-Pb Isotopensystematiken sowie U-Pb Geochronologie war es möglich, mindestens sechs Gruppen von magmatischen Gesteinsgängen zu identifizieren und zu unterscheiden: (i) kalk-alkaline Quarz Diorit Gänge, die mit dem 1,85 Ga Sudbury Igneous Complex genetisch verwandt sind (lokal als Offset Dykes bezeichnet); (ii) tholeiitischer Quarz Dolerit der regionalen 2,22 Ga Nipissing Suite/Senneterre Gangschar (iii) kalk-alkaliner Quarz Dolerit der regionalen 2,17 Ga Biscotasing Gangschar; (iv) alkaline ultrabasische Gänge, die sich mit der 1,88–1,86 Ga Circum-Superior Large Igneous Province (LIP) korrelieren lassen; und (v) aplitische Gänge sowie ein (vi) Hornblende Syenit, beide von nach wie vor unklarem Alter und unklarer Zugehörigkeit.

Die in dieser Studie vorgestellten Ergebnisse – insbesondere die Entdeckung drei neuer Offset Dykes – bieten einige unerwartete Einblicke in die Geologie und das wirtschaftliche Potenzial eines der am wenigsten erforschten Gebiete des Sudbury Bergbaudistriktes sowie in die Beschaffenheit und Verteilung sowohl allochthoner als auch autochthoner Impaktgesteine innerhalb einer der größten und ältesten bekannten terrestrischen Impaktstrukturen. Die geometrischen Muster der Gang (und Brekzien-) Verteilung bestätigen nicht nur frühere Vorstellungen von der Existenz diskreter Ringstrukturen im Sinne eines ~200 km großen Multiringbeckens, sondern liefern auch Erkenntnisse über die ursprüngliche Mächtigkeit und Ausbreitung der Impaktschmelze, was unter anderem zur Identifizierung neuer potenzieller Gebiete für die Ni-Cu-PGE Exploration beiträgt. Darüber hinaus liefert diese Studie wichtige Einblicke in die Stratigraphie des Einschlagsgebietes und die magmatische Entwicklung der Region im Allgemeinen, welche sich als viel komplexer, in der Zusammensetzung vielfältiger, und zeitlich ausgedehnter erweist als ursprünglich angenommen. Hervorzuheben ist hierbei die Entdeckung von Gesteinen, die mit dem 2,17 Ga Biscotasing und dem 1,88–1,86 Circum-Superior Magmatismus in Verbindung stehen, da solche Gesteine bisher nicht am südöstlichen Rand des Superior Kratons bekannt waren. Diese Ereignisse, die kurz vor dem Sudbury Impakt und zeitgleich mit Erz-bildendem Magmatismus nahe Thompson (Manitoba) und Raglan (Cape Smith, Quebec) stattfanden, könnten das fehlende Bindeglied zwischen ungewöhnlich mafischen, vorangereicherten krustalen Zielgesteinen einerseits, und der einzigartigen Metallausstattung der Sudbury Impaktstruktur andererseits, darstellen.

Die tatsächliche geologische Ursache der Temagami Anomalie bleibt nach wie vor ungeklärt und erfordert letztlich die Erweiterung bestehender Bohrlöcher sowie detailliertere geophysikalische Untersuchungen. Die Hypothese eines genetischen Zusammenhangs zwischen Sudbury Impakt und Temagami Anomalie kann weder durch Beweise gestützt werden noch gilt sie als besonders realistisch, selbst im Falle eines obliquen Einschlags, und sollte daher verworfen werden. Stattdessen wird auf der Grundlage von Indizienbeweisen vorgeschlagen, dass die Temagami Anomalie durch einen ultramafischen Komplex der 1,88–1,86 Ga Circum-Superior LIP verursacht wird.

Acknowledgments

First and foremost, I'd like to express my sincerest gratitude to the geological staff of Inventus Mining, specifically Wayne, Wesley and Winston Whymark, Jacob VanderWal, Mark Hall, and Renan Silva, for their incredible work over the last years, for ongoing support, trust, and patience as well as for having provided access to claims, samples, and data. Their work builds the very foundation of the present thesis. I'm also deeply and forever indebted to my supervisor, Hartwig Frimmel, for having introduced me to this fascinating project, and for having raised the necessary funding. I'm incredibly grateful for his dedicated mentorship and friendship, and for him guiding me with such admirable optimism and patience through this journey. Thank you, Hartwig, for your always open door, for all the inspiration, encouragement, and constructive criticism, for allowing me to work with as much freedom as one could wish on this project, and for teaching me a lot about geology, scientific writing, English grammar, and the academic world in general.

Completing this piece of work took indeed a whole village. First, this project wouldn't have been possible without the enthusiasm and visionary mindset of Wayne Whymark, and the dedicated work of his son, Wesley Whymark. It is only through Wesley's extensive geological mapping and competent handling of all exploration activities that this project made such considerable progress. I sincerely thank Wes for his friendship, collaboration, and ongoing support, for openly sharing his plans, thoughts, and ideas on this project. My stays in Sudbury were a particularly pleasurable experience due to the company and able assistance of Winston Whymark, Jacob VanderWal, Renan Silva, and Nicolas Estrada; they were significantly engaged in the field work, sampling, and the logistical realisation of my trips, and always open for discussions. Special thanks and my greatest admiration to Andy Bite for sharing his life-long experience on the Sudbury geology. I extend my gratitude to Mark Hall, Joerg Kleinboeck and Julian Laferrière for participating in the mapping, sampling, core logging and core cutting, respectively. Gregg Snyder is thanked for access to the historic Falconbridge drill core. My warmest thanks goes to Peter Späthe for the preparation of thin sections; Stefan Höhn and Uli Schüßler for their technical expertise and for supervising the XRF, XRD and EMP measurements; Christel Tinguely and Petrus Le Roux as well as Sabrina Cauchies and Vinciane Debaille for performing the ICP-MS analyses; Wolfgang Dörr for providing access to mineral separation facilities; Axel Gerdes and Leo Millonig for conducting the LA-ICP-MS analyses; Tine Linge for navigating me through the administrational aspects of my employment; Fabienne Dietl and Christina Schäfer for the coordination of all post-graduate student affairs. This thesis benefited from insightful discussions with, and valuable advices from, Nikola Koglin, Martin Okrusch, Volker von Seckendorff, and Thomas Will; critical paper manuscript reviews by Jake Ciborowski, James Darling, Mike Easton, Reid Keays, Jennifer Smith, and Natasha Wodicka; fruitful discussions with my friends and office mates Felix Camenzuli, Wendell Fabricio-Silva, Matthias Gaar, and Katrin Hagen; countless correspondences with Jacob, Wes, and Hartwig, especially during the years of the pandemic, and their thorough comments on earlier drafts of this thesis. Last but not least, I'd like to thank Lutz Hecht for volunteering as an external examiner for this thesis.

Financial support for this study was generously provided by the German Research Foundation (project number 418960271, grant number FR 2183/12-1), Stefan Spears from Inventus Mining, Thomas Obradovich from Canadian Continental Exploration, and the Philosophical Faculty of the University of Würzburg, all of which is much appreciated.

Table of Content

Abbreviations

A list of abbreviations and acronyms frequently used in this work:

apfu	Atoms per formula unit
BIF	Banded iron formation
BMS	Base metal sulphide
BSE	Backscattered electron(s)
CHUR	Chondritic uniform reservoir
EDS-XRF	Energy-dispersive X-ray fluorescence
EMP	Electron microprobe
ERBB	East Range Breccia Belt
Fm	Formation
Ga	Giga anni (a billion years)
HFSE	High field strength elements (Hf, Zr, Ti, Nb, Ta)
HREE	Heavy rare earth elements (Tb, Dy, Ho, Er, Tm, Yb, Lu)
ICP-MS	Inductively coupled plasma mass spectrometry
IQD	Inclusion-bearing quartz diorite
LILE	Large ion lithophile elements (K, Rb, Sr, Cs, Ba, Th, U)
LIP	Large igneous province
LOI	Loss on ignition
LREE	Light rare earth elements (La, Ce, Pr, Nd, Sm, Eu, Gd)
Ma	Mega anni (a million years)
MSWD	Mean squared weighted deviation
OGS	Ontario Geological Survey
OIB	Ocean island basalt
MORB	Mid oceanic ridge basalt
PGE	Platinum group elements (Ru, Rh, Pd, Os, Ir, Pt)
PGM	Platinum group mineral(s)
PMM	Precious metal mineral(s)
ppb	Parts per billion
ppm	Parts per million
PTB	Pseudotachylitic breccia
QD	Quartz diorite
REE	Rare earth elements
RSD	Relative standard deviation
SCLM	Subcontinental lithospheric mantle
SE	Secondary electron(s)
SIC	Sudbury Igneous Complex
SUBX	Sudbury Breccia
TA	Temagami Anomaly
TABS	Te, As, Bi, Se, Sb
t_{DM}	Depleted mantle model age
UCC	Upper continental crust
vol%	Volume percent
WDS	Wave-length dispersive spectrometer
wt%	Weight percent
XRD	X-ray diffraction

Introduction

1.1 Temagami Anomaly

The Temagami Anomaly, near Sudbury, Ontario, is considered one of the largest unexplained geophysical anomalies on the Canadian Shield (e.g. Pilkington 1997). The anomaly was discovered by the geophysicist and prospector Norman B. Keevil in the late 1940s during one of the first civil applications of the airborne magnetometer (Keevil et al. 1948; Keevil 2017). Subsequent fieldwork led to the discovery of several mineral deposits within the surveyed area, however, the full potential of Keevil's initial discovery was not recognised until decades later, when regional geophysical coverage was made possible through the Geological Survey of Canada (e.g. Morley et al. 1968; McGrath et al. 1977) and the Earth Physics Branch of the former Department of Energy, Mines and Resources. By providing regional context, these studies shed completely new light on the Temagami Anomaly, which Coles et al. (1981, p. 659) described as follows:

> *"An exceptional, very intense anomaly* [that] *occurs about 50 km northeast of Sudbury, at about 46.9"N 80.4"W. The anomaly* […] *has an amplitude of at least 2500 nT and an extent along the flight track of some 25 km. The full extent of the anomaly can be seen in the low-level detailed Geological Survey of Canada maps, where a peak amplitude of about 9000 nT is found. A gravity anomaly is associated with the feature. Regional geological maps do not show rock units at the surface that can be associated directly with the magnetic anomaly, although mafic igneous rocks are mapped in the region. The dimensions and gradients associated with the anomaly suggest a body extending deep into the crust (of the order of 15 km)."* (Coles et al. 1981, p. 659).

Aside from its exceptional magnitude, and size corresponding to a surface area of some 1,200 km^2, another important aspect was revealed by these surveys (**Fig. 1.1**): The Temagami Anomaly mirrors the potential field anomaly that is associated with the *Sudbury Igneous Complex* in its immediate vicinity, which, following Dietz (1964), is now considered the product of an asteroid impact and is simultaneously one of the world's largest mining camps (Lightfoot 2016). The similarity is so striking that the anomaly has frequently been regarded as a possible twin of the Sudbury Igneous Complex, giving rise to wildest speculations about a genetic relationship. Since then, the anomaly has been the subject of a range of geophysical investigations. Card et al. (1984), for instance, recognised that the Temagami Anomaly has two components: A shorter wavelength-component corresponding to shallow Archaean iron formation, and another high-amplitude component of unknown origin extending deep into the crust (up to 18 km). They further noted that the magnetic anomaly coincides with a regional +20 mGal gravity feature, thus indicating not only the presence of magnetic, but also of relatively dense rocks (2.80–2.95 g/cm^3) at depth. Card et al. (1984) concluded that the anomaly is likely caused by a funnel-shaped magnetite-rich body (with a modelled magnetite content of 6–16.5 vol%) at depths greater than 2 km, which may be related to the Sudbury Igneous Complex. Card et al. (1984) hypothesised that a serpentinised ultramafic body would match the required magnetic susceptibility and gravity contrast. If correct, this would create a significant economic potential, considering the typical association of ultramafic intrusions, cratonic margins, and PGE-Cu-Ni-Co and Cr-Ti-V mineralisation (e.g. Maier 2005), irrespective of a potential link between the anomaly and the well-endowed Sudbury Igneous Complex.

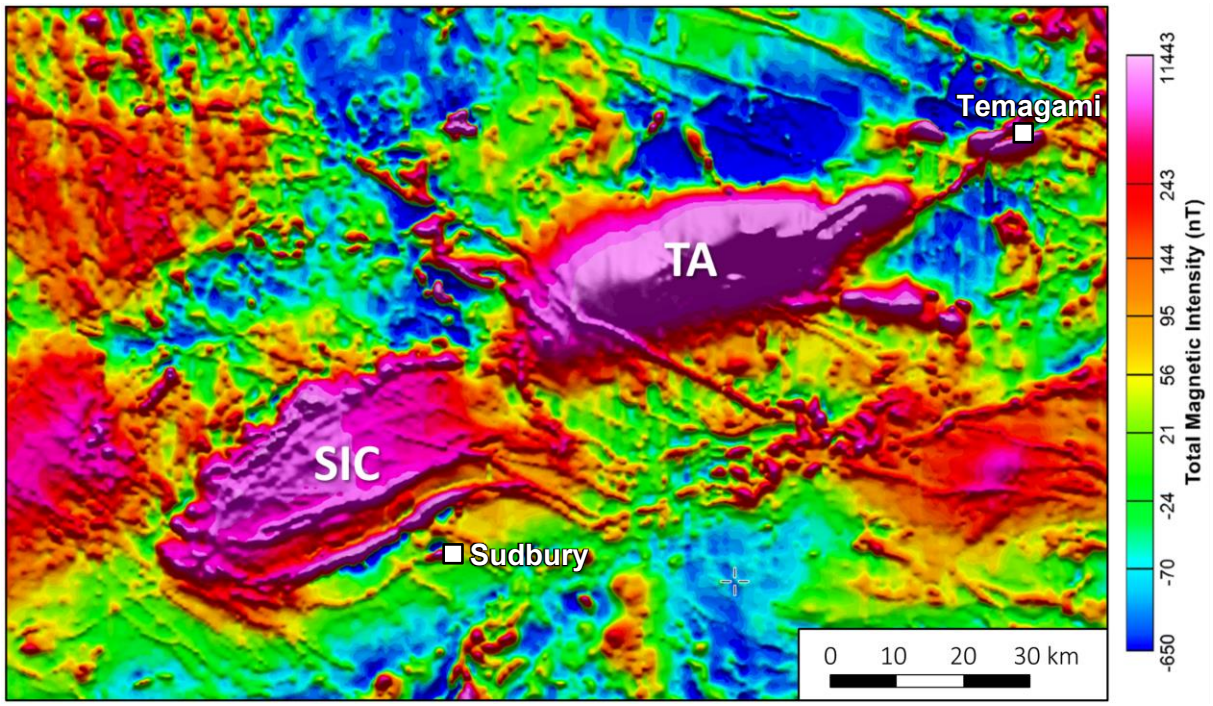

Figure 1.1 Total magnetic field map, showing the Temagami Anomaly (TA) and the Sudbury Igneous Complex (SIC); the former lacks any geological explanation, the latter constitutes one of the world's largest mining camps and is considered the remnant of one of the oldest, largest, and best-studied terrestrial impact structures; data source: Natural Resources Canada (2021a); with 200 m grid cell size, and with sun shading.

Milkereit & Wu (1996), based on vibroseismic profiles, claimed to have found evidence of a Palaeoproterozoic rift graben structure coincident with the Temagami Anomaly, covered by 3 to 4 km-thick sedimentary rocks, and bounded by steeply dipping faults. A seismically transparent zone below this presumed trench system was observed at depths below 6 km. According to Milkereit & Wu (1996), this zone of low reflectivity could be a larger intrabasement body, likely of intrusive origin, with a diameter of 15 km. Pilkington (1997) used 3D-inversion techniques to show that the causative body widens at depth and that it is more deep-seated in the west than it is in the east; he subsequently attributed the source of the Temagami Anomaly to an intrabasement feature (> 4 km). Craven et al. (1998) acquired magnetotelluric line profiles that revealed the presence of a shallow conductor interpreted as disseminated sulphide, and a deep-seated more resistive feature interpreted as (ultra-)mafic. Lately, Papapavlou et al. (2017) provided indirect constraints as to the relative age of the Temagami Anomaly. They found that the originally circular-shaped Sudbury Igneous Complex (e.g. Roest & Pilkington 1994) was deformed episodically at 1.75, 1.65 and again at 1.45 Ga into its present elliptical shape (**Fig. 1.1**). Thus, whatever the cause of the co-linear Temagami Anomaly, it was apparently deformed within the same tectonic regime, implying at least a Mesoproterozoic age of the anomaly, perhaps as old as the 1850 Ma Sudbury Igneous Complex itself (or older; Buchan & Ernst 1994). Most recently, Adetunji et al. (2021) employed 3D geophysical modelling and concluded that the anomaly is caused by a dense, magnetic, and conductive (likely ultramafic) body at depth. A similar conclusion was reached by Easton et al. (2020) in their qualitative interpretation of a recent high-resolution aeromagnetic survey covering, however, only parts of the Temagami Anomaly. Easton et al. (2020) additionally noted (i) that the anomaly consists of three segments, each slightly displaced by N-trending structures; (ii) that certain units of the sedimentary cover do show elevated magnetism; and (iii) the existence of linear features (presumably dykes) not previously recognised in geological maps.

1.2 Research Problem

Although the Temagami Anomaly has been known for quite some time and should – for reasons outlined above – be of outstanding economic and scientific interest, surprisingly little is known about the Temagami Anomaly, its potential causes and relationship to the Sudbury impact event, or even its surface geological makeup. The few previous attempts to drill into the anomaly (by Falconbridge Ltd. in 1991 and Wallbridge Mining Company Ltd. in 1999) ultimately proved unsuccessful as they were not able to penetrate the thick sedimentary cover, nor did they intersect any mineralisation or exotic lithology that would have justified a follow-up study. Previous field work was limited to reconnaissance-scale bedrock mapping conducted by the Ontario Geological Survey (Meyn 1977; Bennett 1978; Dressler 1982, 1986; Gates 1991) and by individual prospectors focusing on much smaller areas, most of which was done when the idea of the Sudbury Igneous Complex being the product of a meteorite impact (Dietz 1964) was not as widely accepted as it is today. Aside from these studies, large parts of the 1,200 km^2 Temagami Anomaly have not previously been mapped in detail, let alone systematically sampled and subjected to modern analytical techniques. In fact, three entire townships above the Temagami Anomaly, Armagh (90 km^2), Sheppard (100 km^2) and McCarthy (100 km^2), have not been geologically mapped at all. Three factors seem to have contributed to this significant gap of knowledge:

Unappealing geology. Early work (e.g. Lumbers & Card 1977) led to the impression that most of the area northeast of Sudbury is underlain by thick, monotonous, flat-lying, and barren sandstone and wacke (coining the term "Cobalt Plain"). The author can only surmise that this deflected the attention of corporations and the scientific community away from the Temagami Anomaly, towards areas of higher structural complexity, greater lithological diversity, or higher prospectivity (such as, the Sudbury Igneous Complex, the Grenville orogenic front, or the Archaean basement).

Lack of infrastructure. Field work, which is only possible in snow-free months anyways, is additionally hampered by a lack of proper infrastructure. Map coverage is, therefore, especially thin away from major highways and secondary gravel and logging roads. Also, some areas are only accessible by boat, float-equipped aircraft, or (in the winter months) by snowmobile; abundant muskegs, lakes, rivers, and dense vegetation make any field work a difficult endeavour.

Lack of outcrops. Much of the area is characterised by a low relief of < 100 m, in places thick quaternary overburden, and variable but overall poor outcrop conditions. Whereas outcrop can be abundant (10–20%) in areas underlain by sandstone, outcrop is rare (< 1%) in areas underlain by soft sedimentary rocks, especially in the northeastern part of the Temagami Anomaly.

In face of the rising global demand for Ni, Co, Cu, and platinum group metals, and the precipitous rise of metal prices in most recent years, yet another attempt was made in 2014/2015 by Canadian Continental Ltd. to drill into the Temagami Anomaly. Their bore hole AT-14-01 reached a final depth of 2,200 m and was the first to successfully penetrate the sedimentary cover, revealing intense alteration, brecciation, and various exotic lithotypes not exposed on surface (Kleinboeck 2015). This, together with an internal report documenting the existence of igneous units of unknown age and origin in this drill core, sparked renewed interest in the Temagami Anomaly, both on part of the mineral exploration industry and the scientific community. In the following years (2018–present), geologists of Inventus Mining, a Sudbury-based junior mining company, began to systematically explore the Temagami Anomaly and its potential causes. Their so-called "Sudbury

2.0" project (Whymark 2018) involves bedrock (re-)mapping, revisiting of known igneous rock exposures and mineral occurrences, outcrop stripping, and most recently, MT and IP surveys followed by additional drilling to target potential subsurface mineralisation. These ongoing efforts led to the discovery of multiple precious- and base metal occurrences, widespread presumably impact-related features, and multiple *igneous dykes* of unknown age and stratigraphic position.

The detailed characterisation of the above mentioned dykes, whether magmatic or impact-related, through field work, petrographic and mineralogical examination and in conjunction with geochemical, isotopic, and geochronological investigations, will be the focus of the present thesis.

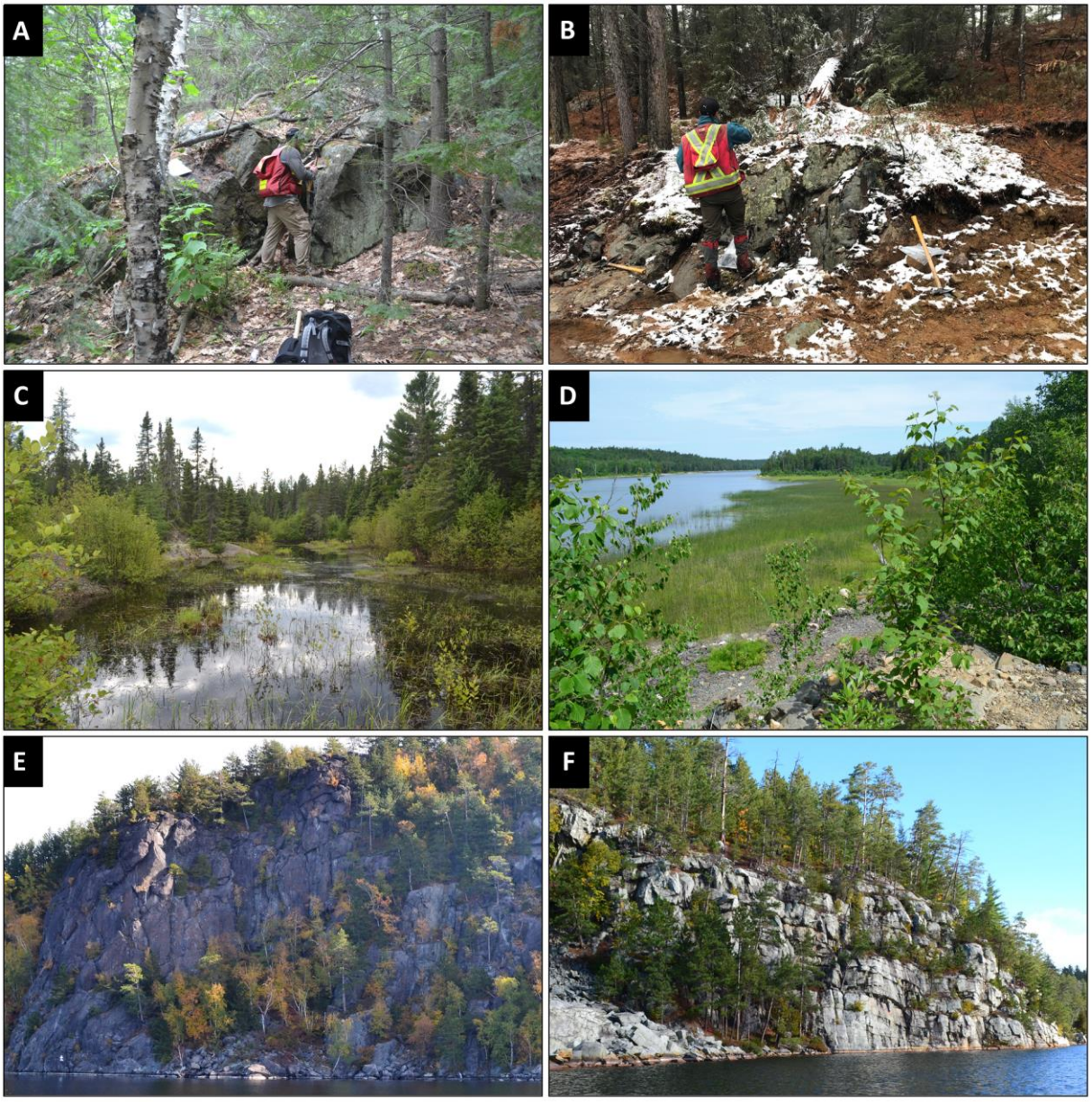

Figure 1.2 Representative field photographs providing an impression of the landscape and the natural outcrop conditions within the study area; **A:** outcrop of a mafic dyke, Rathbun Township; **B:** outcrop of another mafic dyke, Mackelcan Township; **C:** a swamp as it is typically found within structural lineaments and in areas underlain by relatively soft bedrock, Aylmer Township; **D:** view from the Rathbun Lake PGE-Cu-Ni mineral occurrence looking north, across Rathbun Lake, Rathbun Township; **E:** cliffs of massive Nipissing Suite gabbro, exposed along the east shore of Wanapitei Lake, Rathbun Township; **F:** steep cliffs resulting from weathering-resistant massive quartzite, Wolf Lake, Mackelcan Township.

1.3 Aims and Thesis Structure

This thesis, which is the result of a 3-year structured PhD program undertaken at the University of Würzburg, Germany, is primarily focused on the different igneous dykes that have recently and in the course of this project been discovered in outcrops above, and deep drill cores into, the Temagami Anomaly. Accordingly, the main objectives of this study were to:

- Provide a first and systematic lithological and lithogeochemical characterisation of the dykes.
- Test if and how the dykes are genetically related to the 1.85 Ga Sudbury impact event.
- Investigate whether the dykes can be correlated with known magmatic units/events within the immediate study area or within the wider region.
- Establish their petrogenesis, mode and timing of emplacement, and post-magmatic evolution.
- Test whether the dykes could be a surface manifestation of a deep-seated ultramafic complex.
- Reconstruct their mineralisation history (if applicable) / evaluate their economic potential.
- Gain a better understanding of the geology and magmatic evolution of the area in general.

Although it is not expected that this study can provide definite answers as to the deep-seated (2–15 km) and thus inaccessible geological cause of the Temagami Anomaly, it is hoped that, by addressing the above points, it will be beneficial in guiding the direction of future research and exploration in the area. Below follows a brief outline on how this thesis has been organised.

Chapter 1 serves as an introduction and literature review on the research topic and on foregoing studies, and it defines the motivation, the goals, and the structure of the thesis.

Chapter 2 is designed to provide the reader with the necessary theoretical framework trough a comprehensive review of relevant literature as it pertains to regional geology, Proterozoic magmatism (specifically dyke swarms), and the Sudbury Impact Structure. The chapter also defines the terminology that will be used throughout the thesis, and it describes the analytical methods.

Chapter 3,4 and 5 deal with the geology, petrology, geochemistry, and the emplacement of three impact melt dykes (i.e., Offset Dykes) that have been identified as such during this study. Each chapter begins with a brief geological overview of the study area, followed by the presentation of the results (from macro- to microscale), and eventually, the interpretation of the obtained data. Chapter 5 additionally includes an extensive characterisation and genetic interpretation of the PGE-Cu-Ni sulphide mineralisation that was found to be hosted by one of these Offset Dykes.

Chapter 6, 7 and 8 deal with hitherto unknown mafic (diabase) dykes genetically unrelated to the Sudbury impact event. Each chapter is structured in a similar way, beginning with a local geological overview, followed by the description of field observations, the description of microscopic findings, the presentation of geochemical, isotopic, and geochronological data, and eventually, their interpretation in light of the objectives raised above.

Chapter 9 addresses the nature and possible origin of felsic dykes (aplite, syenite). As these were discovered very recently, and as field work by the author was significantly compromised due to international travel restrictions since, this chapter is rather preliminary in scope and character.

Chapter 10 is a synthesis that discusses the above observations and their implications in a much broader context. The chapter concludes with a summary and offers an outlook on certain aspects that could not be addresses in this thesis thus outlining topics for future research.

Theoretical Background

2.1 Geological Context

The study area is situated in Northern Ontario, Canada, 65 km northeast of the City of Sudbury, 370 km north of Toronto, 190 km south of Timmins, and close to the provincial border between Ontario and Quebec; the Great Lakes and the border to the United States of America occur far to the south (**Fig. 2.1**). The closest towns nearby are Temagami, River Valley and Markstay. In terms of physical geography, the study area lies at the transition to the Boreal Forest region, amidst smooth hills and countless lakes, with a relief strongly influenced by the last glaciation. The climate is humid continental, characterised by hot summers and cold snow-rich winters. From a geological perspective, the Temagami Anomaly occurs at the rifted margin of the Superior Craton, and at the junction of three structural provinces (**Fig. 2.1**), namely:

- the Archaean *Superior Province* (locally represented by the Neoarchaean Abitibi Subprovince);
- the Palaeoproterozoic *Southern Province* (locally represented by the Huronian Basin); and
- the Meso- to Neoproterozoic *Grenville Province*.

A brief literature-based review on each of these is given below, noting that the stratigraphy, metallogeny and tectonometamorphic history of the region has been lengthily discussed elsewhere (e.g. Bennett 1978; Card 1978; Dressler 1982; Pye et al. 1984; Bennett et al. 1991; Jackson & Fyon 1991; Easton 1992; Lightfoot & Naldrett 1996a; Young et al. 2001; Long 2004; Rousell & Brown 2009; Easton et al. 2010; Ciborowski 2013; Lightfoot 2016; Bleeker et al. 2015; Davey et al. 2019).

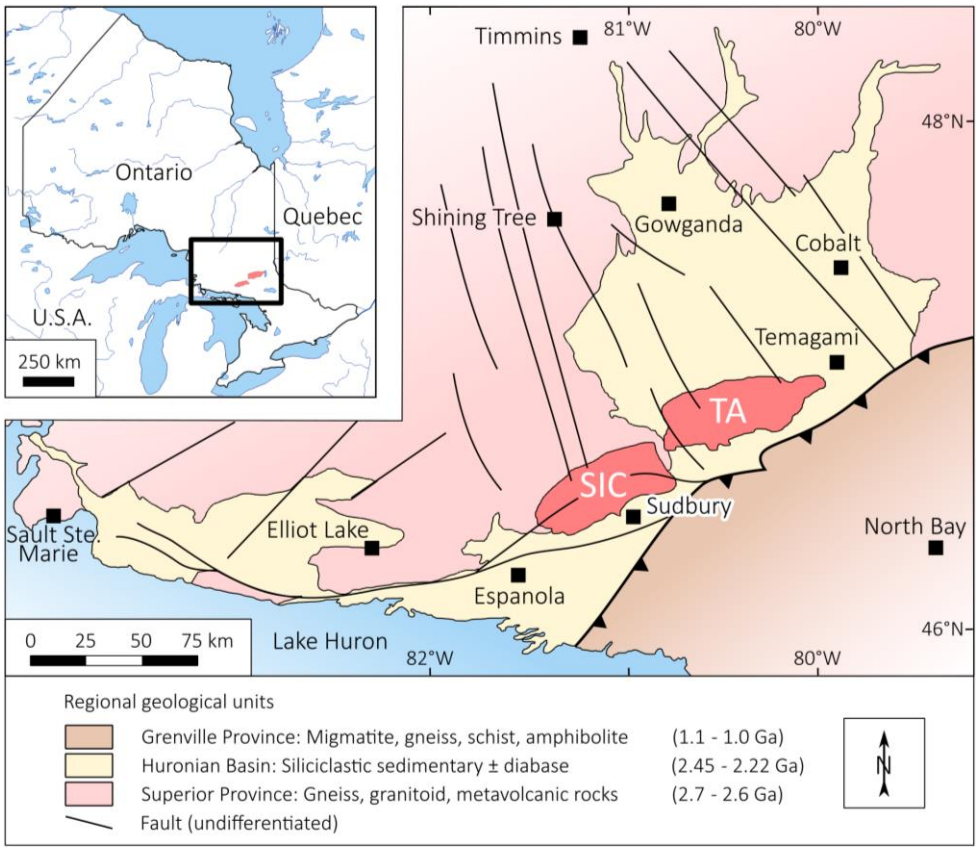

Figure 2.1 Regional setting of the Temagami Anomaly (TA) and the Sudbury Igneous Complex (SIC).

2.1.1 Neoarchaean basement

The oldest rocks in the region belong the Abitibi Subprovince of the Superior Province – a Neoarchaean granite-greenstone terrane composed of metavolcanic and metasedimentary rocks and tonalite-trondjhemite-granitoid (TTGs) batholites. These rocks mainly occur to the north and northwest of the study area, where they are uncomformably overlain by younger (Palaeoproterozoic) sedimentary rocks of the Huronian Supergroup (**Chapter 2.1.2**) and truncated by the Sudbury Impact Structure (**Chapter 2.1.4**). Directly north of Sudbury, the basement rocks consist of deeply exhumed 2.75–2.65 Ga retrogressed granulite-facies migmatitic gneiss (Levack Gneiss) (Krogh et al. 1984; Prevec et al. 2005; Petrus et al. 2016); and a post-tectonic 2623 ± 1 Ma granitoid batholith that is part of the extensive Ramsey-Algoma Suite (Card 1979; Meldrum et al. 1997).

Outliers of the southeast Abitibi Subprovince are locally exposed as erosive windows within the Huronian Basin, including the area of the Temagami Anomaly. These appear preferentially developed along N-striking faults and horst structures beneath a relatively thin Palaeoproterozoic sedimentary cover and include, from east to west, the Temagami, Emerald Lake, Turner and Parkin greenstone belts (Bennett 1978; Meyn 1970, 1977). Smaller and unnamed enclaves occur to their north and south (e.g. in the Pardo and Vogt townships). The rocks in these greenstone belts have been dated at ~2.75 Ga (e.g. Bowins & Heaman 1991; Ayer et al. 2006; Viehmann et al. 2014) and chiefly comprise a series of mafic and intermediate volcanic, mafic to felsic intrusive, and both clastic and chemical sedimentary rocks. They were formed by a complex interplay between plume magmatism, rifting, subduction, and volcanic arc accretion (e.g. Jackson & Fyon 1991; Jackson & Cruden 1995; Wyman et al. 2002; Mole et al. 2021). Volcanic rocks comprise tholeiitic to calc-alkaline basalt, andesite, dacite and subordinate rhyolite, and range in their mode of occurrence from massive flows (± pillowed, porphyric), to pyroclastic and volcaniclastic deposits, and hypabyssal equivalents (Meyn 1977; Bennett 1978). Komatiite sensu stricto is absent from this part of the Abitibi Subprovince, although a thin and laterally extensive unit of an ultrabasic fragmental rock has been described within the Temagami Greenstone Belt (Bennett 1978). This unit could be a komatiitic volcanic rock (John Ayer, pers. comm. 2019), similar to pyroclastic komatiites known from the Timmins area (Card 1990), and it is perhaps syngenetic with local pyroxenite dykes (Bennett 1978) and a small (~1 km^2) ultramafic layered complex (James & Hawke 1984). The by far dominant type of intrusions within the greenstone belts are, however, syn- to post volcanic intermediate to felsic batholiths, sills, and dykes, including feldspar-quartz porphyric diorite and rhyolite (Meyn 1977; Bennett 1978; Jackson & Fyon 1991). Dyklets of ultramafic lamprophyre cut the entire Archaean stratigraphy near Temagami (e.g. Bennett 1978). Sedimentary rocks are intercalated with the volcanic sequence and include pyritic black shale, wacke, conglomerate, limestone, and banded iron formation (BIF) of the Algoma type locally referred to as the Temagami Iron Formation (Bennett 1978; Gross 1980; Bowins & Crocket 1994; Thurston et al. 2012).

The aforementioned greenstone belts have been deformed into E-W-striking synclines, and regionally metamorphosed under greenschist- to lower amphibolite-facies conditions during the ~2.7 Ga Kenoran Orogeny (e.g. Stockwell 1982; Meldrum et al. 1997). The intensity of related deformation and the degree of metamorphism tend to increase from east (Temagami) to west (Parkin, Benny). In addition, these Archaean rocks have been locally affected by syn-depositional subseafloor alteration and VMS-type mineralisation, intrusion-related metasomatism, and later hydrothermal veining (Meyn 1970, 1977; Bennett 1978; Fyon & Crocket 1986; Card & Innes 1991).

2.1.2 Huronian Basin

The Huronian Supergroup was deposited between 2.45 Ga (Krogh et al. 1984; Ketchum et al. 2013; Bleeker et al. 2015) and ca. 2.31 Ga (Rasmussen et al. 2013; Hill et al. 2018; Hill 2019), and comprises siliciclastic sedimentary rocks, minor carbonates, and subordinate volcanic rocks. The Huronian Basin fill, although tectonically deformed and metamorphosed to some degree, is one of the largest, best preserved, and most extensively studied Palaeoproterozoic sedimentary successions in the world. It covers an area of ca. 20,000 km^2 (**Fig. 2.1**) and preserves a maximum thickness of 12 km south of Sudbury as it gradually thins to the north (Young et al. 2001). Deposition of the basin fill coincided with two major environmental changes, the Great Oxidation Event (e.g. Roscoe 1973; Holland 2002; Bekker et al. 2005), and the global Huronian Glaciation (e.g. Coleman 1908; Young 1970; Melezhik et al. 2013; Tang & Chen 2013), and it was locally accompanied by syn-depositional Witwatersrand-type U-Au mineralisation (e.g. Whymark & Frimmel 2018).

The Huronian Supergroup has been historically subdivided into four (unofficially five; Long 2009) groups. These are, in stratigraphic order, and separated by local to regional unconformities, the Elliot Lake, Hough Lake, Quirke Lake, Cobalt, and the Flack Lake groups (Robertson et al. 1969; Long 2009; **Fig. 2.2**). The Elliot Lake Group is 2–3 km thick and comprises the volcano sedimentary Thessalon, Elsie Mountain, Stobie, and Copper Cliff formations as well as the siliciclastic Matinenda and McKim formations (e.g. Bennett et al. 1991). Pillow structures and turbiditic interlayers indicate that the group was, at least in part, deposited in a deep-water setting (e.g. Long 2009). The overlying Hough Lake, Quirke Lake and Cobalt groups are similar insofar as they represent three macro-sedimentary cycles. Each cycle involved the deposition of unsorted matrix-supported conglomerate (diamictite) as sub-glacial till, followed by pro-deltaic siltstone and mudstone, and eventually, fluviatile mature and cross-bedded sandstone (Long 2004, 2009). It is widely accepted that these cycles reflect different stages of an ancient glaciation possibly accompanied by eustatic sea level changes (e.g. Young et al. 2001; Young 2018, 2019). A distinctive unit of laminated limestone, calcareous siltstone and ± stromatolithic dolostone occurs in the Quirke Lake Group (Hofmann et al. 1980; Bernstein & Young 1990). This unit is known as the Espanola Formation, and its origin in relation to the Huronian Glaciation remains debated (Bekker et al. 2005; Young 2013). The Cobalt Group is by far the most extensive group and covers an almost undeformed area northeast of Sudbury, the so-called *Cobalt Embayment* or *Cobalt Plain*. The Cobalt Group is 0–4 km thick and, in many places, directly overlies the Archaean basement, or truncating older groups (e.g. Long 2009). It has been divided into the diamictite- and siltstone-dominated Gowganda Formation, and the sandstone-dominated Lorrain Formation; further subdivisions for the Gowganda Formation have been proposed (e.g. Rainbird & Donaldson 1988; and **Fig. 2.2**). The unofficial post-glacial Flack Lake Group (Long 2009) is the youngest group of the Huronian Basin, but it is of limited extent or preservation. It comprises the Gordon Lake and the Bar River formations. The Flack Lake Group is predominantly siliciclastic, contains minor evaporite minerals, soft sediment deformation features, and evidence of microbial activity, which led some workers to suggest a coastal, more or less tidal influenced, depositional setting (e.g. Hill 2019).

The evolution of the Huronian Basin is best understood and summarised in the context of a Wilson Cycle (Wilson 1968; Young et al. 2001), beginning with local fault-controlled subsidence and rift-related intraplate volcanism, followed by rift-drift transition towards an epicontinental basin and accompanied by regional subsidence, and final basin closure during continent-continent collision.

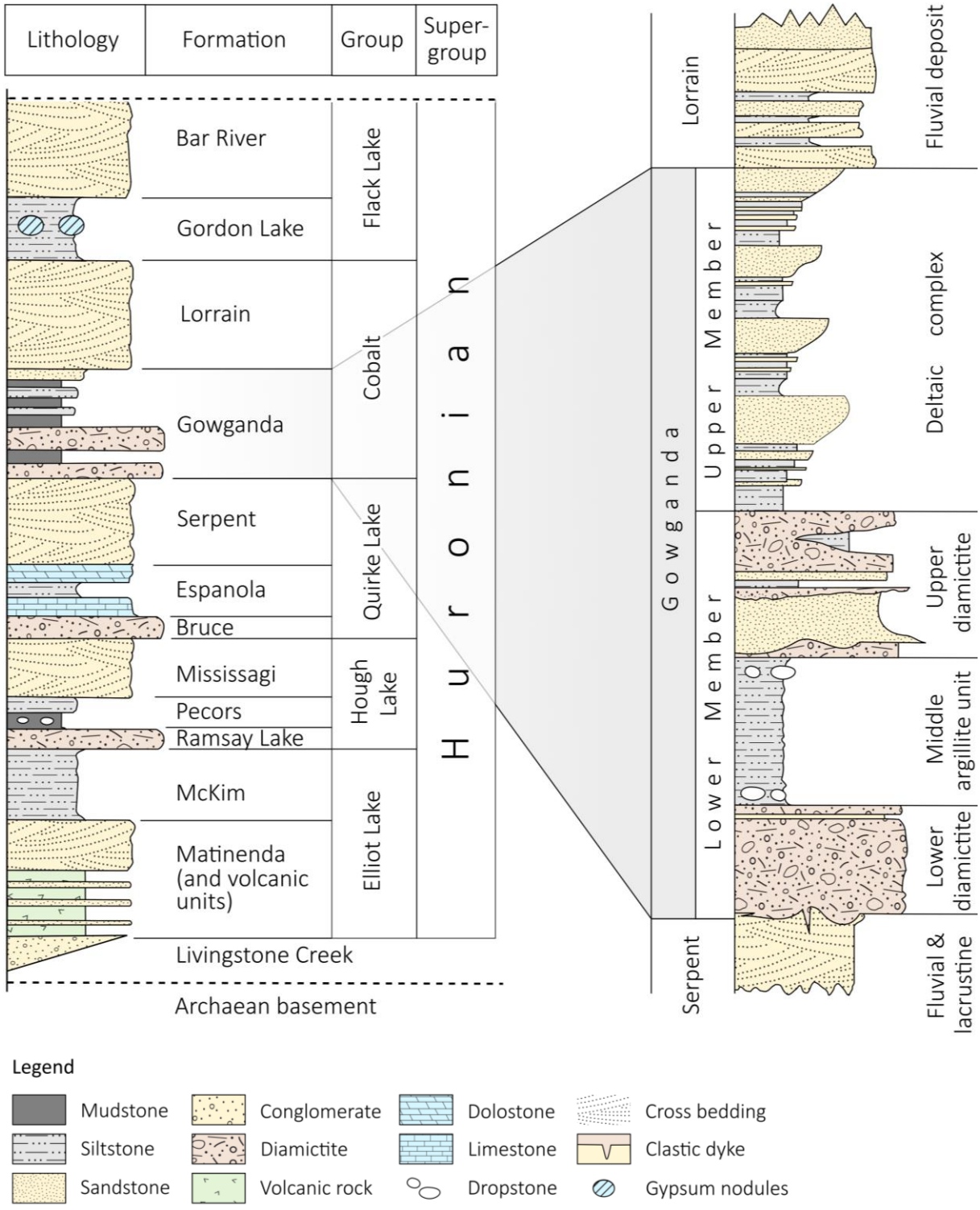

Figure 2.2 Stratigraphic section through the Huronian Supergroup (left) and the Gowganda Formation (right); after Long (2004, 2009), Melezhik et al. (2013) and Young (2018). The Elliot Lake, Hough Lake and Quirke Lake groups have been collectively, though informally, labelled the "lower Huronian"; the Cobalt and Flack Lake groups as the "upper Huronian" (e.g. Young et al. 2001, p. 235).

2.1.3 Proterozoic magmatism

Matachewan Dyke Swarm

The giant Matachewan Dyke Swarm comprises many N/NW-striking mafic dykes that span across an area of some 300,000 km² across the Canadian Shield. The dykes have been dated at 2446 ± 3 Ma and 2473 +16/-9 Ma (Heaman 1997), 2459 ± 5 Ma (Halls et al. 2005) and 2476 ± 7 Ma (Bleeker et al. 2015). Matachewan Dykes are common in the Neoarchaean basement north of Sudbury (**Fig. 2.3A**), where they can be traced for tens of kilometres in outcrop (Phinney & Halls 2001) and even further in aeromagnetic maps (West & Ernst 1991; **Fig. 2.3B,C**). In contrast, no Matachewan Dykes are found cutting the Huronian Supergroup, evidently because their emplacement predated the basin formation by ~10 Ma. Individual dykes are subvertical and may be up to 60 m wide but are typically as narrow as 10–20 m. Principal rock forming minerals are plagioclase, pyroxene, Fe-Ti-oxides, and quartz; textures range from equigranular, subophitic to plagioclase-glomerophyric (Bates & Halls 1991; Nelson et al. 1990; Ciborowski 2013), and plagioclase megacrysts of up to 20 cm in length have been reported by some (e.g. Halls 1991; Lightfoot 2016, p. 88). The dykes are characterised by a very uniform geochemical composition and exhibit a quite remarkable geochemical consistency along strike and between different dykes, which, together with a tight age range, supports their emplacement within a single magmatic event. All the dykes are quartz normative and classified as tholeiitic to boninitic basalt. Arc-like trace element patterns and a wide range in initial εNd (–4 to +4) testify to severe crustal contamination of the parental magma and/or its interaction with or deviation from the subcontinental lithospheric mantle (Ciborowski et al. 2015). The Matachewan Dykes are interpreted as a radiating dyke swarm with a point of convergence just southeast of Sudbury, and it has been suggested that the dykes were associated with the breakup of the Archaean supercontinent Kenorland and the subsidence of the Huronian Basin (e.g. Bleeker & Ernst 2006). A genetic link to the East Bull Lake Suite (see below) and the volcanic rocks at the base of the Huronian Supergroup has also been proposed (e.g. Ciborowski et al. 2015). No known mineralisation is associated with the Matachewan Dyke Swarm.

East Bull Lake Suite

The East Bull Lake Suite comprises a series of mafic-ultramafic intrusions that are exposed as a discontinuous NE-trending belt along the Archaean-Huronian contact and along the Grenville orogenic front. The three largest members of the suite are the East Bull Lake, Agnew, and River Valley intrusions dated at 2480 +10/-5 Ma, 2491 ± 5 Ma and 2476 +2/-1 Ma, respectively (Krogh et al. 1984; Easton et al. 2010), and each with a suboutcrop of 50–200 km² and a minimum stratigraphic thickness of 1–2 km (James et al. 2002). Smaller members (< 5 km²) include the Wisner, Falconbridge, Chicago Mine, Drury, Norduna and May anorthosites/gabbros (e.g. Prevec & Baadsgaard 2005), the Fraser wehrlite (Lightfoot 2016), and the Frood (2421 ± 32 Ma; Keays & Lightfoot 2020) and Street amphibolites (2475 +25/-10 Ma; Corfu & Easton 2001). Most of the intrusions show textural, modal, and cryptic layering at different scales, and a superimposed fractionation trend of (from bottom to top) anorthosite, troctolite, (olivine-)gabbronorite, gabbro, ferro syenite, and alkali feldspar granite. The East Bull Lake Suite and the Matachewan Dyke Swarm were apparently formed by the same parental (boninitic to tholeiitic) magma possibly related to a mantle plume southeast of Sudbury (Vogel et al. 1998a,b, 1999; Ciborowski et al. 2015). Some of the intrusions (e.g. River Valley) produce large and intense aeromagnetic anomalies and host sub-economic contact-style Cu-Pd-Pt sulphide mineralisation (e.g. Peck et al. 2001; Holwell et al. 2014).

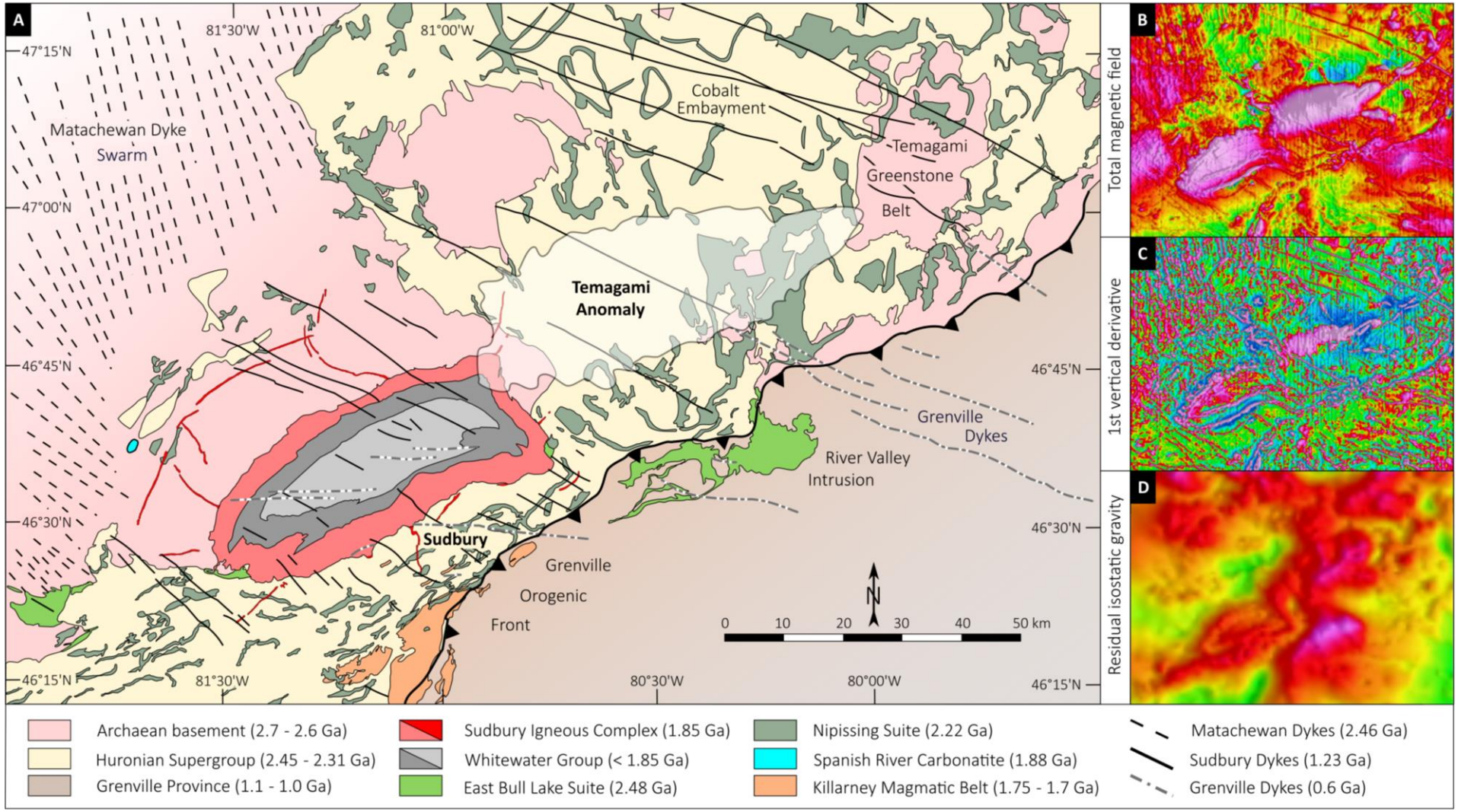

Figure 2.3 The Temagami Anomaly and its geological and geophysical environment; **A:** geological map highlighting the distribution of the various igneous rocks in the vicinity of the Temagami Anomaly; compiled after Lumbers & Card (1977), Dressler (1981a,b), Ames et al. (2005), the Ontario Geological Survey (2011), Olaniyan et al. (2013), Bleeker et al. (2015), Halls et al. (2015), Lightfoot (2016); **B:** map of the total magnetic field (same field of view as in Figure 2.3A); **C:** first vertical derivative of the total magnetic field; data source: Natural Resources Canada (2021a); **D:** isostatic residual gravity map; data source: Natural Resources Canada (2021a).

Nipissing Suite

Mafic intrusions of the Nipping Suite are certainly the most important magmatic rocks in the wider region, both in terms of volume (> 10^5 km^3) and economic significance. Geochronological studies constrain the emplacement of the Nipissing Suite to one single, short-lived magmatic event between 2220 and 2210 Ma (Corfu & Andrews 1986; Conrod 1989; Noble & Lightfoot 1992; Bleeker et al. 2015; Gordon 2016; Davey et al. 2019; Keays & Lightfoot 2020), despite paleomagnetic data suggesting otherwise (e.g. Buchan et al. 1989). Most of the intrusions occur as weakly to non-magnetic, undulating, up to 1 km thick sills; a few examples of cone sheets and lopoliths are also known (e.g. Hriskevich 1968; Palmer et al. 2007; Easton et al. 2020) as well as narrow dykes interpreted as magmatic feeders (Lightfoot et al. 1993; Lightfoot & Naldrett 1996a). Intrusions of the Nipissing Suite rarely cut the Neoarchaean basement rocks north of Sudbury, but they are very abundant throughout the Huronian Basin, where they account for ~20% of the mapped bedrock (**Fig. 2.3A**). In the Cobalt Embayment, the intrusions are well differentiated and largely unaffected by regional deformation and metamorphism. This differentiation has led to the development of a type stratigraphy for Nipissing Suite (e.g. Hriskevich 1968; Jambor 1971; Lightfoot & Naldrett 1989, 1996a): A confining unit of quartz diabase is always present, regardless of the intrusion shape or thickness, and it is interpreted as the chilled margin along the footwall and hangingwall. Up-sequence, quartz diabase grades into massive to crudely layered orthopyroxene gabbro, leucogabbro, and variable-textured gabbro. Irregular patches of pegmatoidal gabbro, with cm-sized hornblende or augite crystals, characterise the latter unit. Granophyric quartz gabbro, quartz diorite and aplite are typically found near the roof zone, together with rafts of metasomised or hornfelsed country rock. According to Lightfoot & Naldrett (1989, 1996a) and Jobin-Bevans (2004), all the lithological and textural diversity can be explained by a combination of fractional crystallisation, stoping, and in situ assimilation. Lightfoot et al. (1993) and Lightfoot & Naldrett (1996a) noticed that the composition of the chilled margins and of the confining quartz diabase varies little across the entire 300 km magmatic province. In accord with geochronological data, this led to the suggestion that the Nipissing Suite was fed by one uniform parental magma. This phenocryst-poor magma was characterised by 49–51.5 wt% SiO_2, 8–9 wt% MgO, a negative εNd, and an affinity transitional between tholeiitic and calc-alkaline (e.g. Lightfoot & Naldrett 1996a). Based on these features, Lightfoot et al. (1993) and Lightfoot & Naldrett (1996a) surmised a subduction-modified lithospheric mantle source. The data above, together with a low Mg#, < 150 ppm Ni, and the conspicuous absence of olivine from most of the intrusions, indicate that the parental magma underwent significant fractionation prior to its emplacement, perhaps along the crust-mantle boundary or within staging cambers that are not exposed at the current level of erosion. On a regional scale, the Nipissing Suite has been interpreted as the distal expression of the 2.22 Ga Ungava LIP centred around northern Quebec and linked with the NE-striking Senneterre Dyke Swarm in the Grenville Province (Buchan et al. 1998, 2007; Ernst & Bleeker 2010; Davey et al. 2019).

The Nipissing Suite has long been recognised as a principal host of base- and precious metals, including hydrothermal vein-type Cu-Co-Ag-Au, and disseminated to patchy net textured Cu-PGE-Ni sulphide mineralisation (e.g. Card & Pattison 1973). Although most workers agree upon a magmatic origin of the locally observed Cu-PGE-Ni mineralisation (Lightfoot & Naldrett 1996a; Sproule et al. 2007; Jobin-Bevans 2009; Lightfoot 2016), its exact spatial and genetic controls are still not particularly well understood, and despite numerous such occurrences being known (e.g. Davey et al. 2019), only one deposit has ever been discovered and mined for a short while in the 2000s (the Shakespeare Cu-Ni-Deposit 70 km west of Sudbury; Sproule et al. 2007; Dasti 2014).

Spanish River Carbonatite

A small and isolated alkaline complex occurs along the Spanish River, 55 km northwest of Sudbury and near the community of Cartier (**Fig. 2.3A**). The complex measures ca. 300 m in diameter and was emplaced into Neoarchaean quartz monzonite. In aeromagnetic maps it is clearly visible as a positive oval-shaped feature plunging north, which could indicate that the complex was emplaced within one of the many N-striking structures of the regional Onaping Fault System. The country rock has been extensively brecciated and fenitised at the intrusive contact. The alkaline complex itself appears of composite nature, with a core of sövite, and an outer zone of cancrinite syenite, ijolite, pyroxenite and glimmerite (Sage 1987). The sövite has been dated at 1880.6 ± 2.4 Ma via U-Pb on baddeleyite (Rukhlov & Bell 2010) and so far, it remains the only magmatic event of this age in the wider region. The Spanish River Carbonatite has in the past been prospected for vermiculite and Nb (pyrochlore), and its regolith has apparently been mined for a short while in an open cast for fertiliser (P, Ca, K). When the author visited the complex in 2016, mining operations had already ceased and the pit had been refilled, with little bedrock exposure remaining.

Killarney Magmatic Belt

A NE-trending belt of magmatic rocks cuts across the Huronian Supergroup just 10 km south of Sudbury and extends for 80 km as far as Lake Huron, parallel to the Grenville orogenic front, and well into the Grenville Province. The suite comprises predominantly (and variably metamorphosed) high-level granitoid plutons and related volcanic rocks (e.g. Davidson 1986), a small gabbronorite complex (Prevec 1995), and a few diabase and porphyric felsic dykes (Bleeker et al. 2015). Radiometric dating suggests that this magmatic activity was prolonged, ca. 1750–1700 Ma (van Breemen & Davidson 1988; Davidson et al. 1992; Sullivan & Davidson 1993; Prevec 1995; Bleeker et al. 2015), and contemporaneous with compressional deformation of the southern Huronian Basin (e.g. Piercey et al. 2007; Bleeker et al. 2015). The Killarney Magmatic Belt is extensive enough (> 250 km^2) to be associated with a regional negative gravity and a strongly positive magnetic anomaly (e.g. Easton 1992). Mineral resources have yet to be identified in this magmatic belt.

Chieflakian Event

Another group of granitoid plutons intruded the Huronian Supergroup and the older Killarney granitoids ca. 100 km southwest of Sudbury. The largest and most prominent example of the suite is the Croker Island Batholith, a 10 km composite complex of porphyric granite, syenite, diorite and gabbro, and of calc-alkaline affinity (Card 1965). The complex is associated with a very distinct circular, strongly magnetic anomaly, and it has been dated at 1475 ± 50 Ma via Rb-Sr (Van Schmus 1965). Other (non-magnetic) members include the 1446 +2/-1 Ma Chief Lake Complex (Davidson & Van Breemen 1994), the 1471 ± 3 Ma Bell Lake Pluton (Van Breemen & Davidson 1988; Fueten & Redmond 1997), and the 1500 ± 20 Ma Manitoulin Island Pluton (Van Schmus et al. 1975). Synchronous with this plutonism was the intrusion of lamprophyre dykes (minette) southwest of Espanola, dated at 1415 ± 40 Ma via Rb-Sr and K-Ar (Van Schmus 1971). Both the Killarney and Chieflakian rocks have been correlated with widespread anorogenic Geon 17 and Geon 14 magmatism across midcontinental North America (e.g. Bickford et al. 1986; Van Breemen & Davidson 1988). The tectonomagmatic setting of these granite-rhyolite provinces ("silicic LIPs" in the sense of Ernst 2014) is matter of ongoing research, and proposed models invoke a combination of protracted arc magmatism, arc accretion and associated deformation, back-arc extension and basaltic underplating (e.g. Whitmeyer & Karlstrom 2007; Bickford et al. 2015).

Sudbury Dyke Swarm

NW-striking mafic intrusions of the Sudbury Dyke Swarm are widespread throughout the Huronian Basin and cut across the Sudbury Igneous Complex. They have been dated at 1235 +7/-3 Ma (Krogh et al. 1987) and 1238 ± 4 Ma (Dudàs et al. 1994). Single dykes can be traced for tens of kilometres in outcrop and even further using potential field data (**Fig. 2.3**). In aeromagnetic maps, they show a consistent strike and regular spacing but tend to be increasingly deformed, metamorphosed, and demagnetised upon entering the Grenville orogenic front (e.g. Bethune 1997; Tschirhart & Morris 2012). The thickest dykes (≤ 300 m) can exhibit significant textural variations, from fine-grained chilled margins to pegmatoidal interiors (Dressler 1982). They are typically glomerophyric to subophitic with an average grain size of 3 mm and are composed of plagioclase (50–75 vol%), olivine (10–30 vol%), clinopyroxene (3–17 vol%), ilmenite/magnetite (≤ 10 vol%), biotite (≤ 5 vol%) and apatite (≤ 2 vol%) (Dressler 1982; Shellnutt & MacRae 2012). Within the Huronian Basin, the dykes show very little metamorphic and hydrothermal overprint; olivine is incipiently replaced by iddingsite, rarely by serpentine. Most of the olivine is entirely pristine, even close to the Grenville Front (**Fig. 2.4D**). The geochemistry of the dykes is relatively uniform and corresponds to alkaline basalt or basanite; trace element patterns are typical of modern ocean island basalt but with weakly negative Nb-Ta-Ti anomalies and high Ba/La ratios suggesting derivation from a subduction-modified and/or the lithospheric mantle (Shellnutt & MacRae 2012). The emplacement of the Sudbury Dyke Swarm has been ascribed to the breakup of the Mesoproterozoic supercontinent Columbia (e.g. Hou et al. 2008) and an ancient mantle plume either centred southeast of Sudbury (e.g. Ernst 1994) or far northwest in the Canadian Arctic (e.g. Hou et al. 2010), although these views have subsequently been challenged by Easton (2002) and Shellnutt & MacRae (2012). No mineral resources are known to be associated with the Sudbury Dyke Swarm.

Grenville Dyke Swarm

The youngest magmatic activity in the region is represented by the Grenville Dykes. These have been dated between 597 and 576 Ma (Kamo et al. 1995; Halls et al. 2015) and are the distal expression of a ~700 km parallel dyke swarm across the Grenville Province. Little is known about the Grenville Dykes in the Huronian Basin. So far, they are only known to occur in the Sudbury area and in the southern Huronian Basin (Ames et al. 2005); no such dykes have been reported in the Cobalt Embayment. Grenville Dykes strike consistently E-W (**Fig. 2.3A**) and traverse tectonic boundaries such as the Grenville orogenic front. They are also found to cut across the Sudbury Igneous Complex (e.g. Hawley 1962; Cochrane 1984; Fedorowich et al. 2006). Individual dykes can be traced for several kilometres in suboutcrop and in high-resolution aeromagnetic maps (Olaniyan et al. 2013). The dykes are typically < 15 m wide in the west as they gradually pinch out. Pyroxene, plagioclase, magnetite, and ilmenite are the principal rock forming minerals; olivine locally occurs as shielded inclusions in pyroxene, and all dykes contain traces (1–4 vol%) of primary quartz, and accessory biotite, hornblende, and apatite (Kretz et al. 1985; **Fig. 2.4F**). The texture ranges from (sub-)ophitic to equigranular; the geochemistry from tholeiitic to alkaline (Kretz et al. 1985; Seymour & Kumarapeli 1995; Ernst & Buchan 2010; Higgins et al. 2018). It appears that some of the Grenville Dykes, while originally correctly identified as such (e.g. Lumbers & Card 1977), have in more recently digitised geological maps been erroneously assigned to the Sudbury Dyke Swarm based on their similar orientation, petrography, and geochemistry. The Grenville Dykes have been linked to the breakup of Laurentia and the opening of the Iapetus Ocean (e.g. Kamo et al. 1995). In terms of mineral resources, the Grenville Dyke Swarm is considered barren.

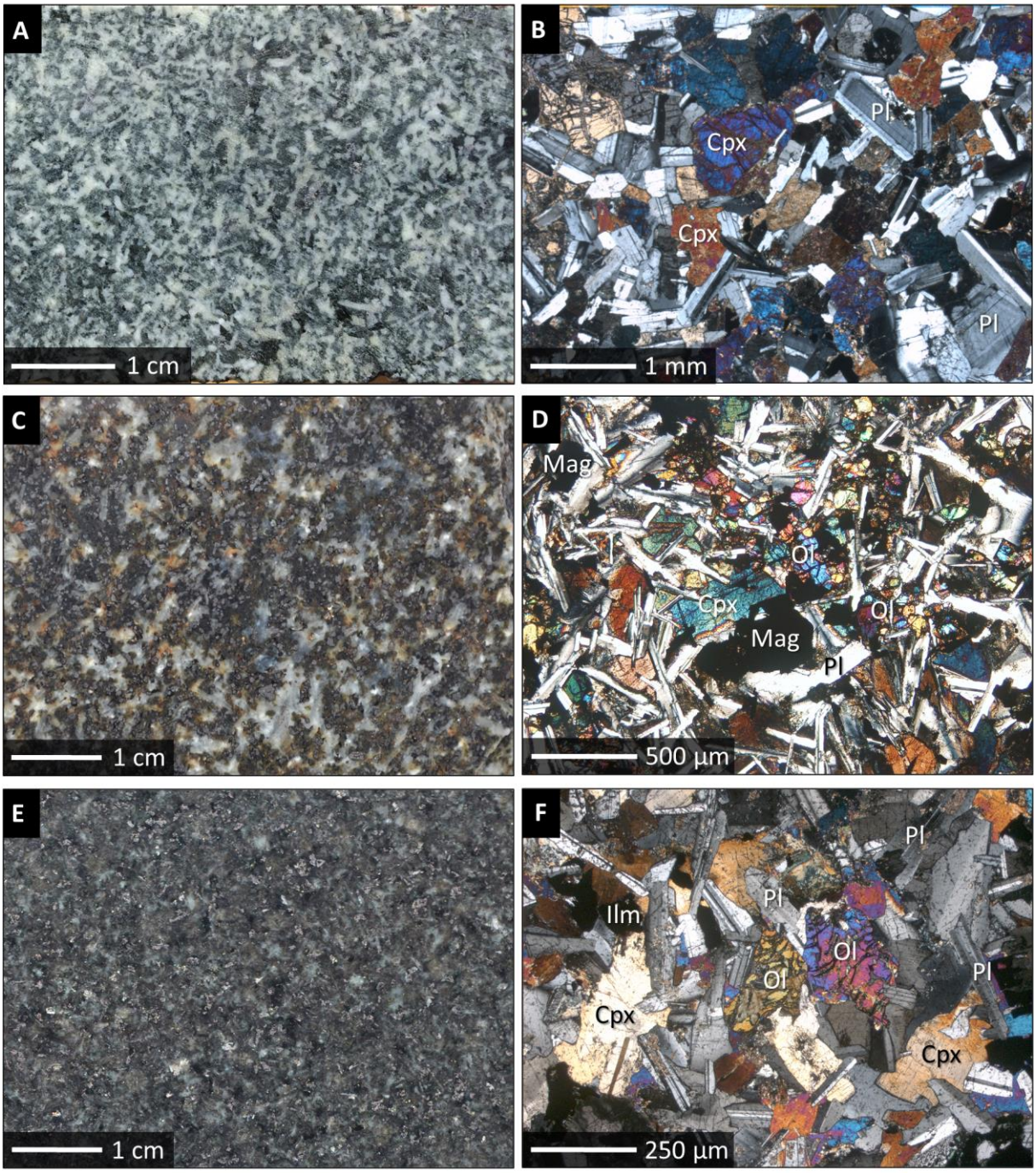

Figure 2.4 Photographs and microphotographs of representative specimens covering the three most important types of mafic intrusive rocks within the Huronian Basin; **A:** polished hand specimen of a typical leucogabbro of the Nipissing Suite (Sheppard Township); **B:** thin section of Nipissing Suite gabbro (Emerald Lake Sill, Afton Township) under transmitted and crossed polars; **C:** polished hand specimen of olivine gabbro of the Sudbury Dyke Swarm (Kukagami Lake, Kelly Township); **D:** thin section of olivine diabase of the Sudbury Dyke Swarm (Scadding Mine, Scadding Township) under transmitted light and crossed polars; **E:** Polished hand specimen of a typical diabase of the Grenville Dyke Swarm (Pardo Township); **F:** thin section of the same sample under transmitted light and crossed polars. Abbreviations: Cpx = clinopyroxene; Pl = plagioclase; Ol = olivine; Mag = magnetite; Ilm = ilmenite.

2.1.4 Sudbury Impact Structure

The Sudbury Structure is one of the oldest, largest, and best-preserved impact structures known on Earth (Earth Impact Database 2021). What has originally been proposed by Dietz (1964) and was disputed for decades thereafter (e.g. Fleet 1979; Stevenson & Stevenson 1980; Muir 1984), is now generally accepted by the scientific community. Arguments put forward to support the impact hypothesis are plenty and include: the basinal topography and oval shape of the structure (Hirt et al. 1993; Butler 1994; Golightly 1994; Roest & Pilkington 1994; Ames et al. 2002; Dreuse et al. 2010); the chaotic country rock assemblages overlying and surrounding the structure (Dressler 1984; Grieve & Osinski 2020); the presence of megaclasts and -breccias (Pattison 1979; Dressler 1984); the widespread occurrence and regular geometric distribution of pseudotachylitic breccia (Thompson & Spray 1994; Spray 1995; French 1998); shock metamorphic features in minerals (Dence 1972; French 1967, 1998; Bohor et al. 1993; Krogh et al. 1996; Joreau et al. 1996; Thomson et al. 2014; Wang et al. 2018); shatter cones centred around the supposed impact site (Dietz 1964; Guy-Bray et al. 1966); high pressure and high temperature minerals and assemblages (Stevenson 1963; Masaitis et al. 1999; Coulter et al. 2014); diaplectic glasses (French 1998); fullerenes (Becker et al. 1994; Mossman et al. 2003) – all indicative of extreme physical conditions; geochemical evidence of an extra-terrestrial component (Becker et al. 1996; Mungall et al. 2004; Ames et al. 2005; Huber et al. 2014; Petrus et al. 2015; Mougel et al. 2017); geochemical evidence of extensive crustal melting (Faggart et al. 1985; Walker et al. 1991; Dickin et al. 1992; Deutsch 1994; Lightfoot et al. 1997a; Darling et al. 2010b; Kenny et al. 2017) and de-volatilisation (O'Sullivan et al. 2016; Kamber & Schönberg 2020) without evidence of the involvement of mantle-derived magmas; and various analogies that can be drawn to other unequivocal impact structures on Moon, Mars and Earth (e.g. Morrison 1984; Osinski & Pierazzo 2012; Lightfoot 2016) or those reproduced in analogue experiments and numerical simulations (e.g. Ivanov & Deutsch 1999).

The Sudbury impact event has been dated at 1850 ± 1 Ma (Krogh et al 1984; Davis 2008; Bleeker et al. 2015). It involved a 10–15 km large projectile (Ivanov & Deutsch 1999), possibly a comet (Darling et al. 2010b; Petrus et al. 2015) or chondrite (Mougel et al. 2017), impacting at a velocity of some 10–25 km/s (asteroid) or up to 70 km/s (comet) (Osinski & Pierazzo 2012). The projectile likely struck a shallow marine foreland or epicontinental basin (Gurov et al. 2020). Formation of the Sudbury Structure followed the three universal and consecutive stages of impact cratering: (i) contact and compression, (ii) excavation, and (iii) modification (e.g. Melosh 1989; Osinski & Pierazzo 2012). These events resulted in complete vaporisation of the impactor, extensive fracturing, melting, vaporisation, displacement, and ejection of the crustal target rocks, and, after a prolonged period of crustal relaxation, the formation of a 150–260 km diameter peak ring (Scott & Benn 2001; Grieve & Osinski 2020) or multi ring basin (Deutsch et al. 1995; Spray et al. 2004). The different products of the Sudbury impact event (impactites; Stöffler & Grieve 2007) will be described below and in context to the cratering process. They fall into either of three categories:

- *Impact melt rocks* (igneous rocks formed by instantaneous bulk- and decompression melting at several thousand degrees) locally represented by the *Sudbury Igneous Complex* (SIC);
- *Pseudotachylitic breccia* (the brecciated country rock, containing a matrix generated by in situ friction melting and/or cataclasis) locally termed *Sudbury Breccia* (SUBX);
- *Post-impact rocks* (fall back, suevite and volcanic breccias and allochthonous crater fill deposits) collectively assigned to the *Whitewater Group*.

Sudbury Igneous Complex

The Sudbury Igneous Complex (SIC) (Giblin 1984), in the early literature referred to as the Sudbury Nickel Irruptive, is certainly the most iconic product of the 1.85 Ga impact event, whereby the term SIC is collectively applied to the bulk of the impact melt rocks (excluding ejecta) that are preserved within the folded centre of the former peak- or multi ring basin. Traditionally, the SIC is divided into a central layered complex termed the *Main Mass*, and a system of narrow dyke-like features surrounding the Main Mass, the *Offset Dykes* (Giblin 1984; Lightfoot 2016; **Fig. 2.5**).

The Main Mass of the SIC is a lopolith-shaped igneous body of, on average, granodioritic composition, 1.5–5 km thickness, 60 x 30 km lateral extent, and an estimated volume of some 8,000 km^3 (Grieve et al. 1991). It is geographically grouped into a North, South and East Range based on the preservation of three steeply plunging, locally overturned, limbs (**Fig. 2.5B,C**). The Main Mass is underlain by brecciated and thermally metamorphosed country rock, and concordantly overlain by the Whitewater Group. The Main Mass consists of three sub-horizontal and lateral persistent units of, from bottom to top, norite, quartz gabbro, and granophyre. The thickness proportion of these units is generally 25:15:60, and the transition between them is gradual over tens of meters (Lightfoot 2016). The norite is, in most general terms, a sulphide-poor cumulate-textured medium-grained rock with variable proportions of orthopyroxene, clinopyroxene, plagioclase, Cr-spinel, phlogopite, and quartz. The overlying quartz gabbro is similar but contains significant quantities of titanomagnetite (up to 10 vol%) plus magmatic hornblende and abundant apatite (Gasparini & Naldrett 1972). The gabbro is strongly magnetic (as opposed to the rest of the Main Mass) and, despite its limited thickness (< 300 m), most likely responsible for the extreme aeromagnetic anomaly associated with the SIC (Gupta et al. 1984; Lightfoot & Zotov 2005; Olaniyan et al. 2013). The granophyre is a coarse-grained, heterogeneous, and strongly altered granite sensu stricto, rich in quartz, plagioclase, alkali feldspar, and with minor amounts of biotite and amphibole (Therriault et al. 2002) and very plagioclase-rich towards the top (Peredery & Naldrett 1975; Anders et al. 2015). Granophyric and/or micrographic intergrowths between quartz and feldspar occur in each the norite, gabbro and granophyre, but are particularly common in the latter (Therriault et al. 2002; Stewart 2017). Between the basal norite and the footwall, a discontinuous unit may be locally developed, termed the (Contact-) Sublayer (Pattison 1979). The Sublayer is a heterogeneous igneous-textured noritic rock, rich in xenoliths, xenocrysts, and sulphides. It is interpreted as the heavily contaminated marginal facies of the Main Mass, preserved only within topographic footwall depressions (Lightfoot et al. 1997b; Prevec et al. 2000; Dreuse et al. 2010).

The Main Mass is now generally agreed upon to represent the tectonically deformed and eroded vestige of an originally circular, horizontal, more or less homogeneous, and much more extensive impact melt layer or "melt sheet" (Grieve et al. 1991; Deutsch et al. 1995; Theriault et al. 2002; **Fig. 2.5A**). Several lines of evidence indicate that this impact melt sheet was superheated beyond liquidus (Prevec & Büttner 2018, for a review), possibly in excess of 2,370°C (Timms et al. 2017). This is thought to have facilitated effective convection, igneous differentiation, and extensive thermal metamorphism and thermomechanical erosion of the country rock (Prevec & Cawthorn 2002; Péntek et al. 2011; McNamara et al. 2017; Jørgensen et al. 2018, 2019; Göllner et al. 2019). Some consider the overall differentiation trend from norite to granophyre to be the result of in-situ fractional crystallisation involving the formation of cumulates (e.g. Latypov et al. 2019), a density stratified impact melt sheet (Golightly 1994; Lightfoot et al. 2001), or alternatively, liquid-liquid immiscibility between an Fe-rich and a Si-rich melt (Zieg & Marsh 2005; Watts 2014).

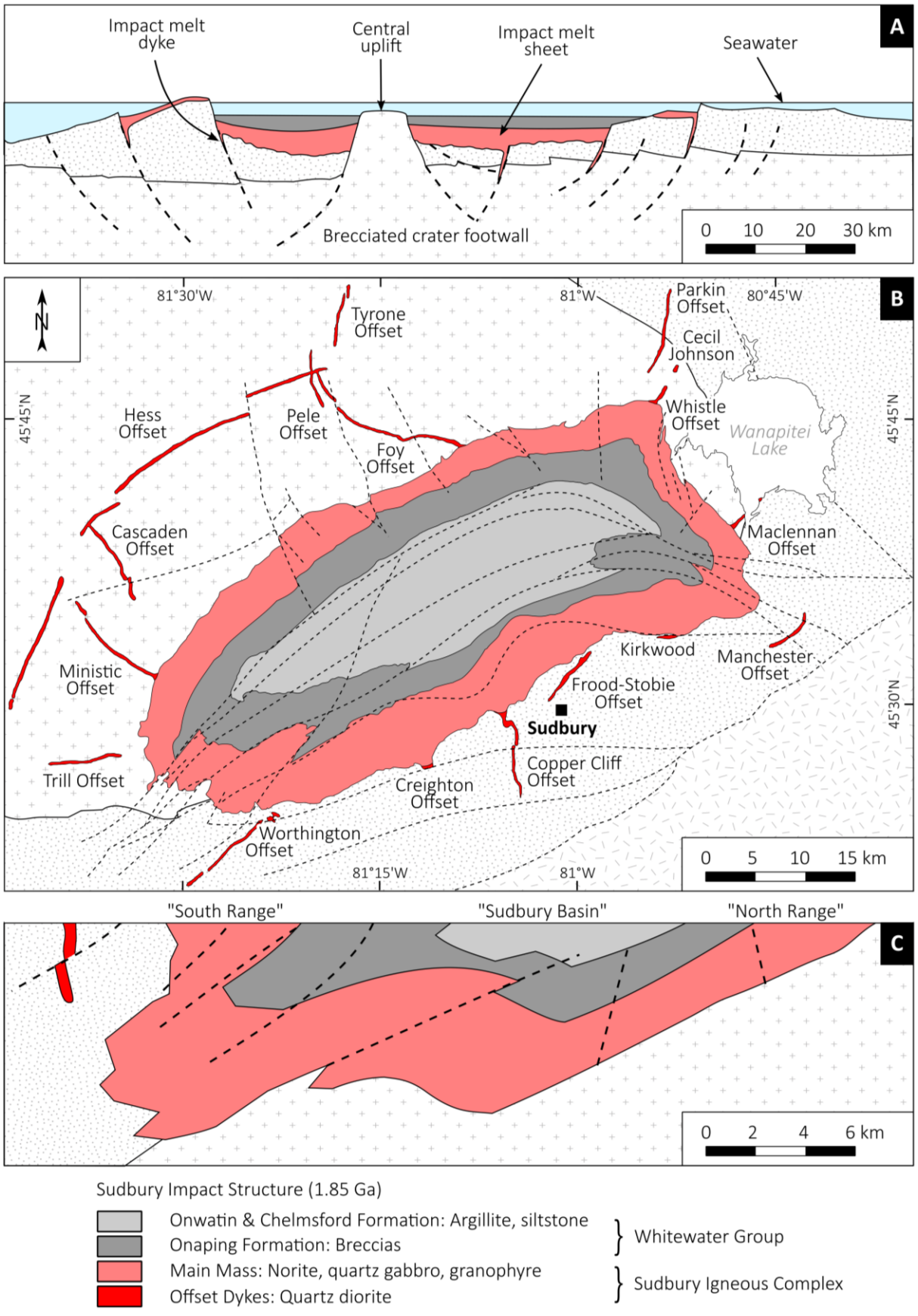

Figure 2.5 Overview over the Sudbury Impact Structure and its associated Sudbury Igneous Complex; **A:** hypothetical cross section through the Sudbury Impact Structure at the end of the crater modification stage (some 10^5–10^6 years after the impact); **B:** simplified geological map of the Sudbury Igneous Complex in its present-day configuration; **C:** geological S–N profile based on geophysical data; all after Lightfoot (2016).

The term *Offset Dyke* was coined by Coleman (1903), who used it to describe the discordant dyke-like subvertical, locally podiform, apophyses of quartz diorite that emanate from the Main Mass of the SIC. Despite their early recognition and considerable economic importance as a host of Ni-Cu-PGE sulphide (e.g. Hawley 1965), no systematic study was conducted until the landmark paper of Grant & Bite (1984). Since then, plenty of new dykes and previously unknown extension of existing dykes have been discovered (e.g. Wood & Spray 1998; Peredery 2010; Smith et al. 2013), 17 in total (Lightfoot 2016). Offset Dykes, as first noted by Grant & Bite (1984), occur in two distinct geometrically well-defined patterns around the Main Mass. Radial Offset Dykes reach at a high angle from the Main Mass outwards into the country rock. Some of these dykes are connected to the Main Mass via hundreds of meters wide funnels (e.g. Copper Cliff) and gradually pinch out at their distal extremities. Examples of radial dykes include Worthington, Trill, Cascaden, Ministic, Foy and Parkin (**Fig. 2.5B**). Concentric Offset Dykes are annular structures that strike about parallel to the outer margin of the Main Mass, but they are not physically connected to it at the current level of erosion (**Fig. 2.5B**); examples being Hess and Manchester. Some of the Offset Dykes (e.g. Frood-Stobie, Creighton, Kirkwood) are only discontinuously developed due to erosion, primary and/or secondary structural discontinuities, and cannot be reliable assigned to either the radial or concentric type. Besides, many Offset Dyke, while appearing linear and continuous in geological maps, locally exhibit complex outcrop patterns including branching, bifurcation, and en echelons (e.g. Grant & Bite 1984). All the Offset Dykes are near vertical, with a down-dip continuity of at least 500 m (locally up to 2 km), have a combined length of 130 km, and an estimated volume of 10 km^3 (Lightfoot 2016). The longest Offset Dyke is the 50 km concentric Hess Offset, studied in detail by Wood & Spray (1998) and subsequently Pilles et al. (2018b). The most distant Offset Dyke (known so far) is the Tyrone extension of the radial Foy Offset, which has been mapped up to 37 km away from the Main Mass (Tuchscherer & Spray 2002).

The petrology and geochemistry of the Offset Dykes has been investigated in numerous studies, most recently by Pilles et al. (2017, 2018a,b), Wehrle & McDonald (2019), Huber et al. (2020), Mathieu et al. (2021) and VanderWal (2021). All the Offset Dykes are fine- to medium-grained non-cumulate and locally quench-textured quartz diorites[1] with variable proportions of plagioclase, quartz, alkali feldspar, amphibole, biotite, sulphides, Fe-Ti-oxides, titanite, apatite, monazite and baddeleyite (**Fig. 2.6E**). Granophyric intergrowths between quartz and feldspar are common. Pyroxene is only preserved in those Offset Dykes close to the Main Mass and some of the low-grade metamorphic (greenschist-facies) dykes of the North Range (Grant & Bite 1984; Lightfoot 2016). Biotite and amphibole, in contrast, are the principal mafic minerals in the more distal and in all the South Range Offset Dykes. The latter minerals are either of igneous or metamorphic origin, or both (e.g. Grant & Bite 1984; Fleet et al. 1987; Lafrance et al. 2014; Warren et al. 2015).

Many Offset Dykes exhibit an internal lithological zonation, involving what has been traditionally referred to as quartz diorite (QD) and inclusion-bearing quartz diorite (IQD), the latter being typically, but not always, confined to dyke's interior (e.g. Grant & Bite 1984; Hecht et al. 2008; Pilles

[1] Some workers rejected the initial classification of the Offset Dykes as quartz diorite, and instead proposed that the rock is better classified as a quartz monzodiorite based on the position of the CIPW normative mineralogy in QAPF diagram. However, as the Offset Dykes apparently contain primary potassium-bearing minerals that are not part of the CIPW norm (biotite, hornblende), the calculated mineralogy is not representative of the actual modal mineralogy of the rock and should consequently not be used for a classification. For sake of logical consistency, Offset Dykes will still be referred to as quartz diorite in this thesis.

et al. 2018b). Where IQD contains appreciable amounts of sulphide (i.e., close to the Main Mass), the lithology has been referred to as mineralised IQD (MIQD) (Lightfoot 2016). There are, however, conflicting observations suggesting that these lithological differences are not as absolute as initially thought. Wood & Spray (1998) and Pilles et al. (2018b), for instance, have shown that sulphide mineralisation affected not only the IQD but locally also the QD facies, and that inclusions are present in both, thus rendering the distinction between QD and IQD somewhat arbitrary. To acknowledge this, variations from the original terminology have been proposed (e.g. VanderWal 2021). Said inclusions (or enclaves) characterise many, if not most, Offset Dykes. Inclusions (sensu lato) exhibit diverse origins, and many appear to be (± hornfelsed) xenoliths or xenocrysts of very local origin; examples of allochthonous or entirely exotic inclusions are, however, also known (e.g. Grant & Bite 1984; Lightfoot & Farrow 2002), and these tend to be closely associated with Ni-Cu-PGE sulphide mineralisation (Souch et al. 1969; Pattison 1979). Autoliths or anteliths of both QD and IQD within IQD are increasingly being recognised (e.g. Lightfoot & Farrow 2002; Tuchscherer & Spray 2002; Lafrance et al. 2014; Lightfoot 2016; Pilles et al. 2017, 2018b).

Despite some petrographic variability due to in situ contamination (e.g. Grant & Bite 1984) and regional metamorphism (e.g. Fleet et al. 1987), the geochemistry of the Offset Dykes is very consistent along strike and between all dykes (Lightfoot et al. 1997a). All Offset Dykes, regardless of geometry, location, or inclusion population, are of calc-alkaline affinity, have identical trace element patterns, almost identical isotope ratios, and the same radiometric ages (Ostermann et al. 1996; Corfu & Lightfoot 1996; Lightfoot et al. 1997a; Prevec et al. 2000; Darling et al. 2010b; Bleeker et al. 2015; Christoffersen 2017). The Offset Dykes have, furthermore, the same composition as vitric fragments in the Onaping Formation (Ames et al. 2002; O'Sullivan et al. 2016), which is intermediate between the composition of the Main Mass norite and granophyre. This, together with quench textures in some of the dykes (e.g. Pattison 2009; Coulter 2015), evidence of superheated emplacement temperatures (> 1,600°C; Prevec & Büttner 2018), and a lack of internal fractionation (e.g. Hecht et al. 2008), led to the proposal that the Offset Dykes preserve the initial liquid composition of the impact melt, which requires the dykes having intruded before significant cooling and differentiation of the Main Mass could occur (e.g. Spray et al. 2003; Lightfoot 2016).

Although discussed in numerous studies, many issues regarding the Offset Dykes, specifically their mode and exact timing of formation, remain controversial. Their composition and close, typically crosscutting, and locally intermingled, relationship with pseudotachylitic breccia (i.e., Sudbury Breccia) requires an early emplacement, possibly within days or years after the impact (e.g. Ames et al. 2002; Mathieu et al. 2021). Their highly symmetric distribution is yet another indication that the intrusion of the dykes was controlled by impact-generated structures, possibly fracture systems within the crater floor (Wichman & Schultz 1993). According to Wood & Spray (1998), concentric Offset Dykes could represent impact melt trapped in annular structures that were formed during the crater modification stage; radial dykes could mimic transfer faults between those listric superfaults (Scott & Benn 2001, 2002). Some have argued that the Offset Dykes were forcefully injected as clast- and sulphide-laden melt outward from the Main Mass, and experienced flow differentiation en route (Grant & Bite 1984; Pilles et al. 2018b). A variation of this model advocates for a two-stage emplacement, i.e., superheated QD melt followed by cooler (M)IQD melt, each injection separated in time by 10^2–10^4 years (Lightfoot & Farrow 2002; Hecht et al. 2008; Prevec & Büttner 2018). Other workers invoke passive downward percolation of impact melt into the structurally weakened crater footwall (Giroux & Benn 2005; Smith et al. 2013; Mathieu et al. 2021).

Sudbury Breccia

Pseudotachylitic breccia[1], locally better known under the term Sudbury Breccia (Speers 1957; Rousell et al. 2003), is an important impact-related phenomenon and one of the three major components of the Sudbury Impact Structure. It is found in all target rocks within an 80 km radius underlying and surrounding the Sudbury Igneous Complex, from Whitefish Falls and Highway 553 in the southwest (Chubb et al. 1994; Parmenter et al. 2002) as far as Temagami in the east (Simony 1964; Rousell et al. 2003). The breccia is most abundant within 15 km around the Main Mass, which is about coincidental with the maximum outcrop limit of shatter cones (Ames et al. 2005). Its distribution has been used by some workers as an indication of the original diameter of the impact structure (e.g. Deutsch et al. 1995; Spray et al. 2004) and it serves as an important stratigraphic marker to distinguish between rocks older and younger than the Sudbury impact event.

Sudbury Breccia (SUBX), or pseudotachylitic breccia (PTB) in general, consists of two components: (i) lithic and minerals clasts; and (ii) a fine-grained aphantic groundmass. The clasts are always of very local (< 100 m) derivation and exhibit a fractal grain size distribution, from µm to hundreds of meters (e.g. Rousell et al. 2003). All the clasts are themselves internally brecciated. They are typically sub- to well-rounded. The matrix shows significant variation in colour, mineralogy, and texture (**Fig. 2.6B,C**), which seems to be in part a function of the type of the host rock and of the proximity to the Sudbury Igneous Complex (e.g. Dressler 1984). The matrix ranges from cryptocrystalline, flow banded, cataclastic, spherulitic, devitrified, to subophitically recrystallised; its contact to the host rock may be sharp or gradational. The breccia occurs at very different scales, from microscopic veinlets and fracture networks to cm-wide dyklets, m-wide irregular masses, and hundreds of meter wide breccia zones. Some workers even postulated the existence of multiple (sub-)concentric ring structures ("breccia belts") around the Main Mass (e.g. Spray & Thompson 1995), including the so-called South Range Breccia Belt (Scott & Spray 2000).

Geochemical and isotopic studies have provided strong evidence that these breccias were formed in situ from their very host rock (Lafrance et al. 2008; Lafrance & Kamber 2010; Harris et al. 2013; O'Callaghan et al. 2016; Reimold et al. 2016, 2017), although there is evidence that, once formed, the breccia behaved somewhat mobile. Evidence of this includes the rotation and settling of clasts (Dressler 1984), the presence of exotic clasts (e.g. Dupuis et al. 1982), flow banding (Rousell et al. 2003), and injection veins of the matrix into dilational sites (e.g. Thompson & Spray 1996; O'Callaghan et al. 2016). The exact process by which PTB are formed is, however, not particularly well understood, and subject of a heated debate (e.g. Garde & Klausen 2018 vs. Reimold et al. 2018). Proposed mechanisms range from shock-induced decompression, cataclasis, friction melting, to acoustic fluidisation. There have even been attempts to link the formation of PTB to specific stages in the crater evolution. Some workers consider their formation an instantaneous process caused by the propagation of the shock wave (e.g. Kenkmann et al. 2000). Other workers invoke decompression melting during exhumation of a central uplift (e.g. Lieger et al. 2009; Mohr-Westheide & Reimold 2011), or high-speed slip along listric superfaults during gravitational crater re-adjustment (e.g. Spray 1997). Yet another group of workers favour seismic shaking in the aftermath of the impact as a viable mechanism of generating PTB (Garde & Klausen 2016; Spray 2016).

[1] A non-genetic, descriptive term introduced by Reimold (1998). According to Reimold et al. (2017) the term *pseudotachylite* should be reserved for endogenic friction melt products (however: Spray 1995). Note that the term *pseudotachylyte* was first used by Shand (1916) at the Vredefort Impact Structure, South Africa.

Whitewater Group

The Whitewater Group is a thick (~3 km) succession of allochthonous breccias, impact melt rocks, and post-impact sedimentary rocks overlying the Main Mass of the Sudbury Igneous Complex and preserved in the folded centre of the Sudbury Basin (**Fig. 2.5**). The Whitewater Group has been subdivided into four formations (Ames et al. 2005). These are, in ascending order, the Onaping, Vermilion, Onwatin and Chelmsford formations. The Onaping Formation is a ~1.5 km thick heterogeneous and rather chaotic assemblage of hydrothermally altered upward fining breccias, melt bodies, and tuffaceous rocks (e.g. Muir & Peredery 1984; Ames et al. 1998). It contains quartzite megaclasts derived from the Huronian Supergroup, which reach up to 100 m in diameter (Ames et al. 2009; Grieve & Osinski 2020), as well as rocks described as hyaloclastite, andesitic lapilli and bombs, devitrified lenticular to angular glass fragments, peperite, quartz dioritic enclaves, and aphantic dykes (Ames et al. 2002; Ubide et al. 2017). The Vermilion Formation is 5–50 m thick and comprises carbonate, shale, and chert (Rousell 1984). It is concordantly overlain by the 600–1,100 m thick Onwatin Formation, a sequence of sulphidic black shale, which grades upwards into greywacke (Rousell 1984). Rocks of the Onwatin Formation may contain up to 13 wt% organic carbon (O'Sullivan et al. 2016) and, in places, anthraxolite veins (e.g. Rousell 1984). The Onwatin Formation is eventually capped by an 850 m thick flysch sequence referred to as the Chelmsford Formation (Rousell 1984). The Whitewater Group, and the Onaping Formation in particular, has been subjected to various re-classifications and interpretations in recent years. Most workers now consider the Onaping Formation the chilled roof zone of the Main Mass of Sudbury Igneous Complex mixed with partially assimilated fallback material (suevite) that floated on top of the melt sheet (e.g. Grieve et al. 2010; Anders et al. 2015). Subsequent flooding of the impact basin with seawater resulted in explosive interaction with the underlying melt sheet and gave rise to thick pyroclastic deposits (e.g. Grieve et al. 2010; Ubide et al. 2017). After the melt sheet had cooled and subaquatic volcanism ceased, the basin remained largely restricted, anoxic, and possibly euxinic, was at some point colonised by microbial life, and experienced increasing detrital extra-basinal input over time (Rousell 1984; McDaniel et al. 1994a,b; Long 2004; O'Sullivan et al. 2016).

Ni-Cu-PGE mineralisation

The Sudbury Structure is unique to terrestrial impact sites in that it hosts some of the world's richest ore deposits. Since initial discovery in 1883, Sudbury's ore deposits have produced more than 12 million tons of Ni and about 12 million tons of Cu (Mudd 2010; Natural Resources Canada 2021b), which translates to some 300 billion US$ in today's commodity prices. With additional 5 million tons of combined reserves and resources, this makes the Sudbury mining camp one of the largest past, present and future producers of Ni (Lightfoot 2016), and an important source of Ag, Au, Pd, Pt, Co, Se and Te, which are gained as by-products of the Ni-Cu-PGE sulphide mineralisation. Said mineralisation occurs mainly in form of disseminated, vein-like to massive pyrrhotite–pentlandite–chalcopyrite (**Fig. 2.6F**) and affected the marginal facies of the Main Mass (the Sublayer), the proximal Offset Dykes (e.g. Frood-Stobie), and the brecciated footwall (Sudbury Breccia) in vicinity to the Main Mass (e.g. Lightfoot 2016). Consensus exists about an igneous origin of the Ni-Cu-PGE sulphide mineralisation via liquid-liquid immiscibility from the impact melt layer, followed by gravitational settling of dense and metal-charged sulphide melt droplets toward the base of the crater (e.g. Keays & Lightfoot 2004; Naldrett 2004; Dare et al. 2014; Ripley et al. 2015). Some of the deposits were subsequently affected by ductile deformation and local metal redistribution by late- and/or post-"magmatic" fluids (Mukwakwami et al. 2012, 2014; Tuba et al. 2014).

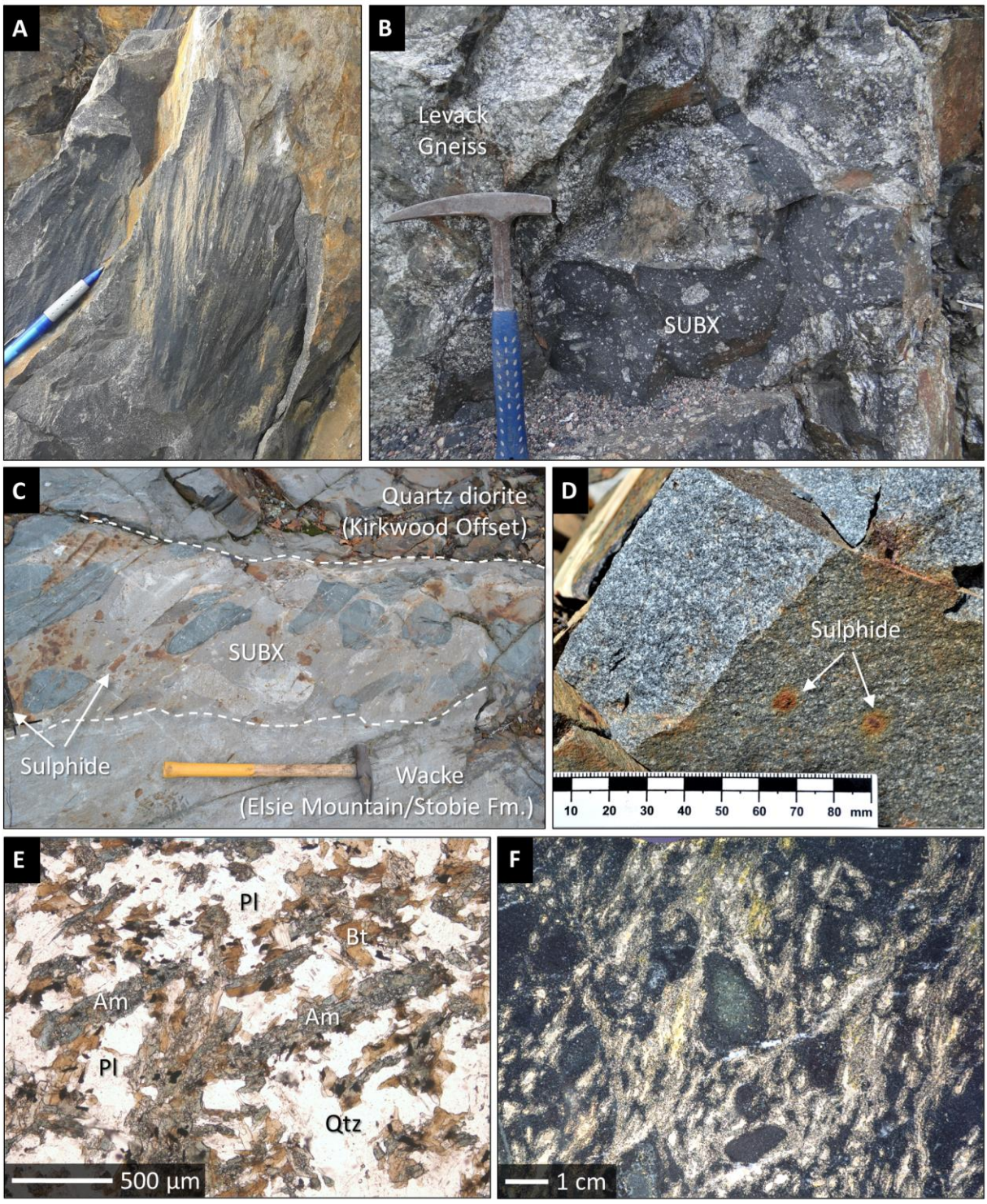

Figure 2.6 Photographs and microphotographs of some features related to the 1.85 Ga Sudbury impact event; **A:** outcrop of a shatter cone developed in Mississagi Formation sandstone (46°26 22.47N 81°00 05.32W; Walmart Supercentre, Sudbury); **B:** outcrop of black Sudbury Breccia (pseudotachylitic breccia) in Neoarchaean gneiss (46°37 50.45N 81°27 43.01W; Highway 144, near Windy Lake, Cartier Township); **C:** outcrop of quartz diorite (Kirkwood Offset Dyke) enveloped in mineralised, deformed and recrystallised Sudbury Breccia (46°33 48.06N 80°54 05.27W; Garson Township); **D:** outcrop of quartz diorite from the Cecil Johnson Offset Dyke (46°48 05N 80°51 48W; Post Creek, Parkin Township); **E:** thin section of quartz diorite from the Frood-Stobie Offset Dyke (46°33 03.54N 80°58 24.06W; Blezard Township) under transmitted light and plane polars; **F:** photograph of a polished hand specimen from the Little Stobie Deposit, showing massive base metal sulphide (predominantly pentlandite) with mafic-ultramafic inclusions (courtesy of the Mineralogical Museum of Würzburg, photographed with kind permission of Dr. Dorothée Kleinschrot). Abbreviations: SUBX = Sudbury Breccia; Am = amphibole; Bt = biotite; Pl = plagioclase; Qtz = quartz.

2.1.5 Deformation and metamorphism

In the Cobalt Embayment, including the area above and around the Temagami Anomaly, Proterozoic deformation is limited to gentle folding and faulting. Deformation of the Huronian Supergroup strata resulted in wide and open, in many places double-plunging, NW- and NE-striking syn- and anticlines. This folding is thought to have occurred prior to the emplacement of the Nipissing Suite, during the 2.4–2.2 Ga Blezardian Orogeny (Stockwell 1982; Riller & Schwerdtner 1997; Raharimahefa et al. 2014). The most prominent structures are N/NW-striking strike-slip faults of the regional Onaping Fault System, active between 2167 and 1850 Ma, and accompanied by a sinistral displacement totalling 15 km (Buchan & Ernst 1994). Some of the fault scarps (e.g. of the Upper Wanapitei River Fault) can be traced for tens of kilometres in digital elevation models, and these structures control much the drainage pattern in the region. According to Card (1978) and Easton (2000), regional metamorphism in the Cobalt Embayment did not exceed the lower to middle greenschist facies (equivalent to the biotite zone); peak metamorphic mineral assemblages reported for the Huronian Supergroup sedimentary rocks include Qtz–Ms–Ab–Sps ± Chl, Ms–Bt–Ab–Qtz, Ms–And–Prl–Ab–Qtz, Qtz–Stp, and Cc–Dol (Card 1978; Sekine et al. 2011). Retrograde metamorphism of the 2.22 Ga Nipissing Suite mafic rocks manifests in the assemblage Ep–Act–Ab–Chl ± Qtz ± Ttn (e.g. Card 1978; Dressler 1982). These secondary minerals are notably absent from the 1.23 Ga Sudbury Dykes and the 0.6 Ga Grenville Dykes.

Closer to, and south of Sudbury, there is evidence of multiple compressional, thermal, and metamorphic events related to the Penokean (1.89–1.83 Ga), Yavapai (1.77–1.70 Ga), Mazatzalian (1.7–1.6 Ga), Chieflakian (1.5–1.4 Ga) and Grenvillian (1.1–1.0 Ga) orogenies (Hu et al. 1998; Thompson et al. 1998; Corfu & Easton 2001; Bailey et al. 2004; Piercey et al. 2007; Raharimahefa et al. 2014; Papapavlou et al. 2017, 2018a). Except for the Penokean and Grenvillian, these events shaped the Sudbury Igneous Complex, which was most likely circular at the time of emplacement (e.g. Hirt et al. 1993; Roest & Pilkington 1994), into its present ovoid and synformal configuration by tilting and shortening the Main Mass and the Whitewater Group of up to 40% of their initial diameter (Clendenen et al. 1988; Lenauer & Riller 2017). This was accompanied by N-directed reverse faulting, thrusting, and folding of the Huronian Basin, and low-*P* metamorphism (< 5 kbar) locally up to the staurolite zone (Easton 2000). Amphibolite-facies metamorphism occurred both before (Pattison 1979, 1980) and after the impact (Thomson et al. 1985; Fleet et al. 1987) and likely ended prior to 1.7 Ga (Piercey et al. 2007; Bleeker et al. 2015). In the South Range, this resulted in the deformation (e.g. Hecht et al. 2008) and recrystallisation (e.g. Wehrle & McDonald 2019) of both the Offset Dykes and the Sudbury Breccia, whereas impactites in the North Range tend to preserve their primary mineralogy and texture. The Grenville Orogeny involved NW-directed thrusting and high-grade metamorphism of the southeast Huronian Basin (e.g. Easton 1992) but it had no bearing on the shape of the Sudbury Igneous Complex (Tschirhart & Morris 2012).

In addition, the entire Huronian Basin has been subjected to regional alkali metasomatism manifesting in pervasive albitisation (Meyer et al. 1987; Gates 1991), especially of sandstone-dominated formations (McLennan et al. 2000). The age of the metasomatism has been loosely dated at 1.9–1.7 Ga (Schandl et al. 1994; Fedo et al. 1997; McLennan et al. 2000), involved variable disturbance of whole-rock U-Pb, Rb-Sr and K-Ar isotope systematics, and might have been related to the Penokean and/or Yavapai Orogeny, the Killarney magmatism, the Sudbury impact event itself, or some other, hitherto unrecognised, geological event (e.g. Easton 2000; McLennan et al. 2000).

2.2 Material and Methods

2.2.1 Mapping, sampling, terminology

To accomplish the goals outlined in **Chapter 1.3**, this study makes use of a large set of lithological samples, plus material collected for reference purposes (ca. 400 kg in total), ranging from historic to more recent diamond drill cores, channel cuts, and grab samples of the in-situ bedrock. As far as possible, these were obtained by the author himself during his field work and own examination of drill cores in the years 2016, 2018 and 2019. Due to international travel restrictions (2020–), additional samples were provided by the personnel of Inventus Mining Corp. All samples were collected to meet the general criteria of good scientific practice with respect to statistical representation, volume, homogeneity, and geographical coverage. Immediately after the samples were collected, the rocks were labelled and separately kept in sealed plastic bags to avoid abrasion and cross-contamination during transport. The exact geographical position of the sample locations (± 5 m) is reported in decimal degrees latitude/longitude according to ISO 6709 (Appendix_1).

The author has also conducted, to some limited extent and assisted by Jacob VanderWal, bedrock mapping in the Rathbun and Mackelcan townships. The mapping was mainly of reconnaissance character or carried out at the scale of individual outcrops. Focus was on igneous rocks, potential mineralisation, lithological contacts and facies variations as well as on the distribution of impact-related features. Ad-hoc classification followed the nomenclature of Le Maitre et al. (2002) for igneous rocks, and Pettijohn (1975) and Lazar et al. (2015) for the description of sedimentary rocks and features. Mineral abbreviations follow Whitney & Evans (2010). For sake of brevity, use of the prefix "meta" (e.g. metadiorite, metavolcanic) is avoided. Although in Europe exclusively applied to altered mafic volcanic rocks, the term "diabase" (now officially approved by the IUGS) will be used here synonymous for "dolerite" or "microgabbro" (Le Maitre et al. 2002) mainly out of regional convention (e.g. Bowen 1910; Fahrig & Wanless 1963; Muir et al. 2016). Identification and the local Sudbury-specific nomenclature of impact-related rocks is based on Giblin (1984), Reimold & Gibson (2005), Stöffler & Grieve (2007) and Lightfoot (2016). Spelling conforms first and foremost to British English (e.g. sulphide, not sulfide) whereas all other terminology is used according to the editorial guidelines of the Ontario Geological Survey OGS (Weatherston 1996), with the notable exception of "alkaline" instead of "alkalic" (pertaining magmatic affinity).

2.2.2 Mineral identification by X-ray diffraction

As an aid to optical microscopy, qualitative mineral identification by means of X-ray diffraction (XRD) was performed on rock powders (grain size < 200 µm), using a Philips PW 1729/40 at the Department of Geodynamics and Geomaterials Research, Institute of Geography and Geology, University of Würzburg. During the mounting of the sample powder, precautions were undertaken to avoid the alignment of crystallites. The instrument operates with a CuKα anode at an acceleration voltage of 40 kV and at a probe current of 30 mA. 2Θ angles between 4° and 80° were scanned at a step size of 0.02°. Exposure time for each step was set at two seconds, resulting in a total runtime of 130 minutes per sample. Interpretation of crystallographic data was accomplished automatically using the *JADE 7* software package and an implemented crystallographic database. Some peaks, however, had to be identified (semi-)manually. The lower limit of detection of the XRD, that is, the minimum detectable amount of a phase in a given powder, approximates 5 vol%.

2.2.3 In-situ mineral chemical analyses

In addition to transmitted and reflected light microscopy, thin section specimens were investigated by electron microprobe analysis (EMPA) using a JEOL JXA 8800L superprobe at the Institute of Geography and Geology, University of Würzburg. The instrument is equipped with four wavelength-dispersive spectrometers (WDS) (LiF, PET, TAP) and detectors for backscattered electrons (BSE) and secondary electrons (SE). Synthetic metals and natural sulphides (pyrite, arsenopyrite, cinnabar, antimonite) were used as standards for the measurement of sulphides and precious metal minerals; natural silicates (andradite, orthoclase, albite, wollastonite) and synthetic oxides were used for the calibration and identification of gangue minerals. All measurements were performed under the supervision of Dr. Ulrich Schüßler and Dr. Stefan Höhn on polished and carbon-coated thin/thick sections and epoxy mounts at 15 kV acceleration voltage and 20 nA beam current. The purpose of the EMPA was twofold: First, to identify certain minerals, for example those of a very fine grain size; second, to obtain the chemical composition of minerals that typically occur in solid solution systems (feldspar, pyroxene, amphibole). To this end, (i) qualitative analyses were carried out and WDS spectra were recorded; (ii) quantitative analyses were performed using the following conditions: A counting time of 20–40 s for peaks and 10–20 s for background, a beam size of 1 µm (4–10 µm for albite, mica, and amphibole in order to prevent alkali mobility), and the implemented ZAF matrix correction procedure of Philibert & Tixier (1968).

The EMP was furthermore used to investigate opaques as well as heavy mineral separates in more detail, with special focus on base element sulphides (BMS), precious metal minerals (PMM) and the textural and mineralogical association thereof. To this end, the analytical protocol of Kawohl & Frimmel (2016) was applied: Thin (25 µm) and thick (40 µm) polished and standard-sized sections (28 x 48 mm) were systematically scanned for PMM in BSE imaging mode at a high contrast setting and ca. 300-fold magnification. Composition, shape, area, texture, and association of such minerals was carefully documented. In order to cover the wide chemical range of PMM (see Cabri 2002), and to ensure that even exotic varieties are not overlooked, complete WDS X-ray spectra were recorded, and all encountered PMM grains were carefully checked for inhomogeneities at varying contrast and brightness in BSE mode. Qualitative and semi-quantitative element distribution maps were generated using the above listed settings. High-resolution mapping (runtime > 12 hours), using 60 ms dwell time and 0.04 µm pixel size, was conducted on selected samples that had shown large, inhomogeneous grains in BSE mode and in initial, lower resolution, X-ray maps.

2.2.4 Mineral thermobarometry

Most of the rocks investigated in the present study contain amphibole, either as a primary igneous constituent or as a metamorphic mineral, or both. The utility of amphibole chemistry (as determined by using an electron microprobe, **Chapter 2.2.3**) as a geobaro-, oxy-, thermo- and hygrometer has been firmly established through extensive experimental work and empirical observations. The pressure and temperature information provided by the chemical analyses of amphibole may, for example, be used to infer the depth of emplacement/level of erosion of plutonic rocks (e.g. Stone 2000; Stein & Dietl 2001) or the dynamics of magmatic plumbing systems (e.g. Ridolfi et al. 2008; Hartung et al. 2017), not to mention the various applications in the field of metamorphic petrology. Below follows a brief review of the different amphibole geothermobarometers that have emerged over the last decades, their requirements, and limitations.

Holland & Blundy (1994) proposed two different thermometers applicable to coexisting hornblende-plagioclase pairs at conditions of 400–1,000°C and 1–15 kbar. Thermometer A, which is based on the equilibrium reaction edenite + 4quartz = tremolite + albite, and thermometer B, which is based on the equilibrium edenite + albite = richterite + anorthite. Both equations are suited for quartz-bearing rocks, whereas only the second equation may also be applied to silica undersaturated systems. According to Anderson (1996) and Bachmann & Dungan (2002), the edenite-richterite thermometer (B) of Holland & Blundy (1994) (**Eq. 2.1**) is preferable for igneous systems, especially when combined with the barometer of Anderson & Smith (1995) (**Eq. 2.10**). Holland & Blundy's (1994) edenite-richterite thermometer (B) reads as follows:

$$T\,[\pm 313K] = \frac{81.44 - 33.6X_{Na}^{M4} - (66.88 - 2.92P[kbar]X_{Al}^{M2} + 78.5X_{Al}^{T1} + 9.4X_{Na}^{A})}{0.0721 - 0.0083144\ln\left(\frac{27X_{Na}^{M4}X_{Si}^{T1}X_{An}^{Plag}}{64X_{Ca}^{M4}X_{Al}^{T1}X_{Ab}^{Plag}}\right)} \quad \textbf{(2.1)}$$

where X is the molar fraction of the species or component in the phase or crystallographic site.

A single-phase thermometer has been proposed by Ridolfi & Renzulli (2012). It is suited for calcic amphiboles with a Fe# < 0.5, formed in both calc-alkaline and alkaline magmas between 800 and 1,130°C, between 1.2 and 22 kbar, and has an alleged accuracy of ± 35.5°C:

$$T\,[\pm 35.5°C] = 17.098 - 1322.3Si - 1035.1Ti - 1208.2Al - 1230.4Fe - 1152.9Mg - 130.4Ca + 200.54Na + 29.408K + 24.410\ln P \quad \textbf{(2.2)}$$

Most recently, a Ti-in-amphibole thermometer has been developed by Liao et al. (2021), which should only be applied to amphibole that crystallised < 1,000°C in H_2O-satturated subalkaline systems in the presence of other Ti-bearing phases (ilmenite, rutile, titanite). Their equation is:

$$T\,[\pm 35°C] = \frac{2400}{1.52 - \log Ti} - 273 \quad \textbf{(2.3)}$$

As first noted by Hammarstrom & Zen (1986), a linear relationship seems to exist between the total Al content of amphibole and the crystallisation pressure, provided that other variables such as the bulk composition, temperature, and oxygen fugacity are controlled for. This led to the development of a first empirical, though relatively imprecise, single-phase Al-in-hornblende barometer (**Eq. 2.4**). Subsequent studies provided experimental refinements of the original formulation (**Eq. 2.5–2.8**). Most of these equations were all calibrated for a pressure range of 2–8 kbar, ideally require hornblende occurring in textural equilibrium with quartz, plagioclase, K-feldspar, biotite, Fe-Ti oxide and titanite, and have an alleged accuracy between ± 0.5 and ± 3 kbar. From the structure of these equations it is evident that low-Al amphibole will essentially return negative values. Thus, these barometers are not suited for amphibole that crystallised at low pressure.

Hammarstrom & Zen (1986):	$P\,[\pm 3\ kbar] = -3.92 + 5.03Al$	**(2.4)**
Hollister et al. (1987):	$P\,[\pm 1\ kbar] = -4.76 + 5.64Al$	**(2.5)**
Johnson & Rutherford (1989):	$P\,[\pm 0.5\ kbar] = -3.46 + 4.23Al$	**(2.6)**
Thomas & Ernst (1990):	$P\,[\pm 1\ kbar] = -6.23 + 5.34Al$	**(2.7)**
Schmidt (1992):	$P\,[\pm 0.6\ kbar] = -3.01 + 4.76Al$	**(2.8)**

By acknowledging the apparently non-linear relationship between the Al content in amphibole and pressure, especially < 2.5 kbar, Mutch et al. (2016) calibrated a new barometer that is applicable to amphibole having crystallised in granitic systems at 725 ± 75°C and 0.8–10 kbar. They claimed an accuracy of ± 16% for the obtained pressure by using the following equation:

$$P\ [\text{kbar}] = 0.5 + 0.331 \times Al + 0.995 \times (Al)^2 \quad \textbf{(2.9)}$$

All the above equations were calibrated for fO_2 close to the NNO buffer, and at H_2O saturated near-solidus conditions. However, Anderson & Smith (1995) and Anderson (1996) noted that pressure is not the only determining factor of Al in amphibole, but temperature and oxygen fugacity can influence site occupancy as well. Anderson & Smith (1995), therefore, recommended only to use amphiboles with $Fe^{3+}/(Fe^{3+}+Fe^{2+}) \geq 0.25$ and Fe# ≤ 0.65. They then developed a new barometer (**Eq. 2.10**) that corrects for temperature (e.g. as determined by the Holland & Blundy amphibole-plagioclase thermometer, or by independent means such as Zr-in-titanite), thereby also acknowledging the possibility that amphibole may crystallise as a phenocryst far above the solidus.

$$P\ [\pm 0.6\ \text{kbar}] = -3.01 + 4.76Al - \left\{\frac{(T[°C] - 675)}{85}\right\} \times \{0.53Al + 0.005294 \times (T[°C]) - 675)\} \quad \textbf{(2.10)}$$

Another barometer was calibrated by Ridolfi & Renzulli (2012). They formulated a whole set of new equations (accuracy ± 11.5%) that are based on an extensive compilation of published experimental data, and applicable to a wide range of pressures (1.3–22 kbar) in both calc-alkaline and alkaline systems. As can be seen from **Equation 2.11**, their barometer also takes variables such as the Ti content into account, which may substitute for Al in Ti-rich systems and can, therefore, lead to an underestimation of the actual pressure (e.g. Anderson & Smith 1995).

$$\ln P\ [\text{Mbar}] = 125.93 - 9.5876Si - 10.116Ti - 8.1735Al - 9.2261Fe - 8.7934Mg - 1.6659Ca + 2.4835Na + 2.5192K \quad \textbf{(2.11)}$$

2.2.5 Heavy mineral separation

In this study, zircon ($ZrSiO_4$) and baddeleyite (ZrO_2) were the preferred minerals for radiometric age dating. However, because of their expected small grain size and low abundance in most of the studied lithotypes (fine-grained mafic dykes with < 150 ppm Zr), large amounts of rock samples were required. These were collected throughout the field sessions and subsequently shipped to Würzburg, Germany, for further processing. First, soil and organic coatings as well as weathering crusts were removed using water, steel brush and a diamond-bladed rock saw, respectively. The material was then grinded in a stainless-steel jaw crusher down to gravel size, followed by very gentle and short-interval (1–2 seconds) pulverisation using a tungsten carbide disc mill, until all material could pass the 250 µm automated shaking sieve. Precautions were undertaken to minimise the potential of cross-contimanation by vigorous cleaning of the jaw crusher, and by flushing the disc mill with pure quartz sand in between every sample exchange. Heavy mineral separation and removal of clay-sized particles was achieved using a commercial Wilfley table at the Department of Geosciences, University of Frankfurt, and under the supervision of Dr. Wolfgang Dörr. Random samples were captured throughout the shaking procedure from different parts of the

table and studied under a stereo- and polarisation microscope for their yield. The final heavy mineral fraction (centre left part of the table) was dried overnight, and magnetite/pyrrhotite was removed on the next day using a hand magnet. Further separation of minerals according to their paramagnetic susceptibility was performed using a commercial Frantz isodynamic magnetic separator at the Institute of Geography and Geology, University of Würzburg. In order to remove stepwise all the matrix silicates (e.g. amphibole, epidote), the procedure was repeated several times using different inclination, slope, voltage, and speed. The two resulting fractions were continuously checked for their mineral content using a stereomicroscope. As it was anticipated that density liquid separation would not significantly improve the quality of the heavy mineral concentrate, the least magnetic mineral fraction obtained after five runs was used for hand picking. Grains deemed most suitable for dating were mounted via gravitational settling in epoxy resin and then ground until maximum grain exposure in plain. Coated with carbon, these mounts were first investigated using the BSE imaging and element mapping mode of the electron microprobe (**Chapter 2.2.3**). There, mineral grains were studied for homogeneity and potential internal structures such as, zonation, resorption, cracks, inclusions, shock features, metamictisation, and based on this, suitable spots for subsequent U-Pb age dating were identified.

2.2.6 U-Pb mineral dating

The U-Pb dating was performed by Dr. Axel Gerdes and Dr. Leo Millonig at the Frankfurt Isotope & Element Research Centre, University of Frankfurt, Germany, using a ThermoScientific ElementXr sector field ICP-MS. The instrument is equipped with a RESOlution (Resonetics) 193 nm ArF excimer laser system (COMpex Pro 102, Coherent) and coupled to a two-volume ablation cell (Laurin Technic S155). Operating conditions were 20 ns pulse width, 7 Hz repetition rate, 2 J/cm^2 energy density, and 1,300 W forward power. Static laser ablation was carried out in a Helium atmosphere (300 mL/min) using a spot size of 50 µm for apatite and titanite, and 33 µm for zircon, respectively. Each analysis consisted of a sequence of steps, beginning with four pules of pre-ablation in order to remove potential surface contamination, followed by 18 s of background acquisition, 18 s of sample ablation (~0.6 µm/s), and 20 s of gas blank. The sample stream was mixed with Argon (1,100 mL/min) in the ablation funnel. Upon introduction into the mass spectrometer through a Nylon 6 tube, a small amount of Nitrogen gas (5 mL/min) was also added to prevent the formation of polyatomic species. Detection of the incoming ions occurred via time-resolved peak jumping of the electrostatic analyser. Dwell times for the different atomic masses 206, 207, 208, 232 and 238 were 6.4 ms, 7.5 ms, 3.0 ms, 2.0 ms and 4.6 ms, respectively. Downhole U/Pb fractionation and instrumental mass biases were corrected for by normalising the raw data against the primary reference material Zircon GJ-1 (Jackson et al. 2004). All raw data were processed offline using the VBA spreadsheet of Gerdes & Zeh (2006, 2009), and final ages were calculated using the software *IsoplotR* (Vermeesch 2018), with a $^{238}U/^{235}U$ ratio of 137.818 ± 0.0225 (Hiess et al. 2012), a ^{238}U decay constant of 0.000155125 ± 8.3 x 10^{-8} $Myrs^{-1}$, and a ^{235}U decay constant of 0.000998485 ± 6.7 x 10^{-7} $Myrs^{-1}$ (Jaffey et al. 1971). Additional information about the underlying statistics of the data processing can be obtained from, for example, Millonig et al. (2012), or the *IsoplotR* user manual of Vermeesch (2018). Common Pb correction was achieved by first plotting the data in a Tera-Wasserburg diagram (Tera & Wasserburg 1972), and then using the y-intercept of this free regression as an approximation of the initial $^{207}Pb/^{206}Pb$ ratio (e.g. Simonetti et al. 2006; Chew et al. 2011, 2014; Kirkland et al. 2017).

In order to verify the accuracy and precision of the method, two matrix-matched secondary (external) reference materials, Durango Apatite and Namaqualand Titanite, were included in the measurement routine. Durango Apatite is an international standard from the Cerro de Mercado IOA Deposit, which is known for its exceptionally large, yellow green fluorapatite crystals. The age of this apatite has been very precisely, though indirectly, determined by ^{40}Ar–^{39}Ar dating of its host rock, that is, 31.44 ± 0.18 Ma (McDowell et al. 2005). Namaqualand Titanite is an in-house standard previously dated at 1023 ± 3 Ma using ID-TIMS (Müller et al. 2018). Treated as unknowns, repeated measurements of the two standards during the analytical session yielded 31.50 ± 0.68 Ma (*n*=15) for Durango Apatite, 999.6 ± 10 Ma (*n*=10) and 999.2 ± 8.1 Ma (*n*=15) for Namaqualand Titanite (Appendix_3). These ages are in accordance with their certified ages.

2.2.7 Whole-rock geochemical analyses

Whole-rock concentrations of major elements, minor elements (TiO_2, P_2O_5, MnO), plus the approximate concentration of Zr, were obtained by conventional alkaline fusion and X-ray fluorescence (XRF) (e.g. Norrish & Hutton 1969). Prior to the lab work, the samples were washed with deionised water and cleaned from soil and organic coatings using a steel brush and a compressed-air gun. Weathering crusts and, where desired, visible alteration features and inhomogeneities, were removed with a diamond-bladed rock saw. After pulverisation using a stainless-steel jaw-crusher and a tungsten carbide disc mill, 600 ± 1 mg of dry rock powder was stepwise fused in platinum crucibles together with 3,600 ± 1 mg lithium meta/tetra borate flux (Merck Spectromelt A12 or XRF Scientific, composed of 66% $Li_2B_4O_7$ and 34% $LiBO_2$) and 1,000 to 1,500 mg oxidant (NH_4NO_3) and then quenched to glass discs. This fusion procedure required continuous homogenisation by gentle shaking of the crucibles and is depicted in **Figure 2.7**. Loss on ignition (LOI) is reported, according to the recommendations of Lechler & Desilets (1987), as percent weight loss on dry 1,000 mg aliquots ignited at 1,000°C for four hours in a Muffle furnace using fire clay crucibles.

The resulting homogeneous glass discs were analysed with a commercial PANalytical Minipal4 energy dispersive X-ray fluorescence spectrometer (EDS-XRF) at the Department of Geodynamics and Geomaterials Research, Institute of Geography and Geology, University of Würzburg. The instrument is equipped with a Rh tube, an Al filter, and a Si drift detector. Measurement conditions were 9–14 kV, 250–350 µA, and 300–600 s per element. For calibration of the XRF, seventeen international standards, ranging in composition from basalt (BCR-1, BE-N, BHVO-1, BIR1, BM, BR, GSR-3), diabase (DNC-1, W2), gabbro/norite (MRG-1, NIM-N), diorite (DR-N), syenite (SY-2, SY-3), andesite (AGV-1, GSR-2) to quartz latite (QLO-1) with values from Govindaraju (1989) were used. External reproducibility of the EDS-XRF, including the error of crushing, fusing, weighing, and measuring, was better than 0.6% (expressed as relative standard deviation RSD) for major elements, except for Na_2O with 2.6% RSD. The error for each element was calculated as follows:

$$\text{RSD [\%]} = 100\,\frac{\text{Standard deviation}}{\text{Mean}} \qquad \textbf{(2.12)}$$

The RSD for the external reproducibility was obtained on 23 replicates of the same sample (a Tertiary alkaline basalt, Rhön, Germany), prepared by 23 different students (in order to factor in potential human biases). 25 re-runs of standard BIR-1 gave an internal precision better than 0.2% RSD, except for MgO (0.5%) and Na_2O (3.4%). The only relevant detection limit for this study was 0.01 wt% for P_2O_5 based on three times the standard deviation of the procedural blank intensities.

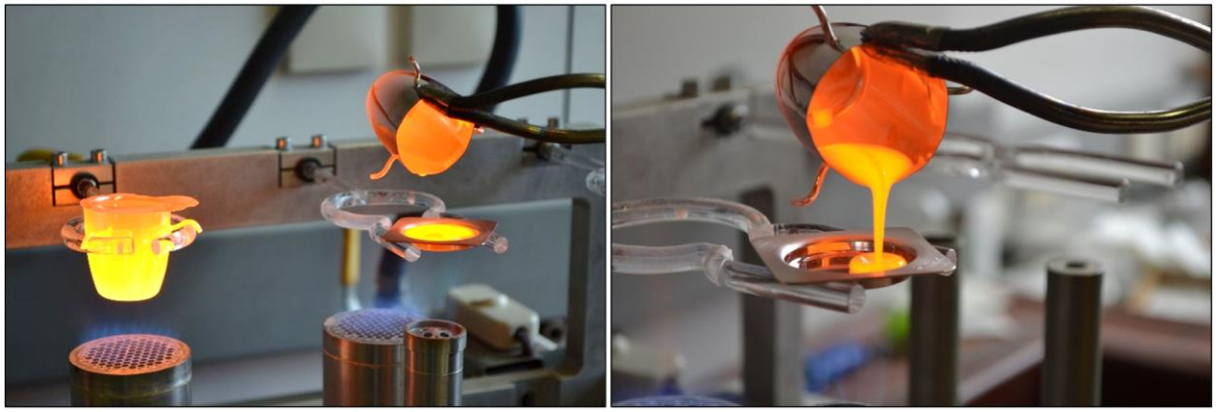

Figure 2.7 Alkaline fusion of powdered rock specimens in platinum crucibles and subsequent pouring and quenching of the homogenous melt into a platinum mould.

Aliquots of the rock powders were sent to the Department of Geological Sciences, University of Cape Town, where they were analysed by Christel Tinguely for their trace element concentrations by means of inductively coupled plasma-mass spectrometry (ICP-MS). The instrument used was a Thermo-Fisher X-Series II quadrupole ICP-MS. 50 mg of sample powder were dissolved in sealed Teflon beakers for 48 h on a hotplate using a mixture of HF and HNO_3, evaporated until dryness, diluted again in 5% HNO_3, doped with 10 ppb Rh, In, Re and Bi, and eventually analysed against five-point calibration curves with the isotopes ^{103}Rh, ^{187}Re and ^{209}Bi as internal standards. Precision, accuracy, and detection limits were determined through the analysis of USGS and international rock standards (Jochum et al. 2005) as well as total procedural blanks (TPB). The latter were < 0.065 ppm for Pb; < 0.030 ppm for Ba, Nb, Zr, Sr, Cu, and Ni; and < 0.009 ppm for all other elements. Within-run precision was better than 3% RSD for all elements, as was the precision between duplicate analyses. The potential of incomplete dissolution of possible zircon grains and thus erroneously low Zr and Hf concentrations was tested by duplicate Zr analyses using conventional alkaline fusion and EDS-XRF techniques (as described above). In each case, the Zr concentrations measured on the ICP-MS were equal or above the relatively imprecise Zr concentrations measured on the EDS-XRF, therefore, providing confidence that all zircon was successfully dissolved. This was also verified trough repeated measurements of the USGS and international rock standards, which were always within the certified range of Zr concentrations. Furthermore, Zr concentrations measured on the ICP-MS at Cape Town were cross-checked against duplicate analyses performed by the commercial AGAT Laboratories, Toronto (see below).

A smaller subset of rock powders (17 samples of drill core AT-14-01) was analysed by Dr. Vinciane Debaille, assisted by Sabrina Cauchies, for its trace element composition at the Laboratoire G-Time, University of Brussels (Belgium), also by means of ICP-MS. About 50 mg powdered samples were dissolved for two days with a mixture of HF:HNO_3 (1:3) followed by 6N HCl to ensure complete digestion. The solutions were measured on an Agilent 7700 Q-ICP-MS using 5% HNO_3. Oxide formation in the mass range 151 to 167 was monitored and corrected for by using pure solutions of Ba, Pr, Nd, and Ce. Again, the USGS standard BHVO-2 (Jochum et al. 2005) was measured regularly during the sessions to check the precision of the measurements, which was always within the accepted range of the standard. The internal reproducibility (expressed as RSD) for six repetitions of the BHVO-2 during the analytical sessions was better than 3%, except for Tm (6%) and Lu (6%). The external reproducibility, including the error introduced by the dissolution procedure, was obtained on a replicate of sample AT-14; it was found to be better than 3.7% (RSD).

Sulphide-bearing samples are not suited for fusion in platinum crucibles given the inevitable reaction between sulphide melt and the crucible to form a glassy slag. In addition to this problem, such samples are typically enriched in chalcophile and siderophile elements. These are important metallogenetic tracers, but their accurate determination requires special treatment and facilities neither available at Cape Town nor Brussels. Specimens containing visible sulphide were therefore shipped to the commercial AGAT Laboratories, Toronto. There, major and trace element concentrations were determined. Most of them, including those of Si, Zr, REE, Cu, Ni and S, were obtained by sodium peroxide fusion within glassy carbon crucibles, followed by inductively coupled plasma-optical emission spectrometry (ICP-OES) and ICP-MS. Gold was determined by fire assay and atomic absorption spectroscopy (AAS), and PGE concentrations by NiS collection fire assay (Ir, Ru, Rh, Pt, Pd, by ICP-MS finish; Os by neutron activation finish). Precision, accuracy, and detection limits were determined through the analysis of internal rock standards as well as procedural blanks. According to AGAT, the precision between duplicate analyses was better than 10%, except for Rh with 16%. Lower limits of detection were 0.1 wt% for major and minor element oxides, 1 ppb for Ir, Ru, and other precious metals except Os with 10 ppb, and generally < 0.1 ppm for all other trace elements except for Ta, Y and Zr (0.5 ppm), Hf, Nb (1 ppm), Ni, Pb, V (5 ppm).

2.2.8 Whole-rock Nd-Sr-Pb isotope analyses

Radioisotope ratios of selected whole-rock samples were obtained by Dr. Petrus Le Roux, Department of Geological Sciences, University of Cape Town, through conventional wet chemistry and mass spectrometry. Again, 50 mg-aliquots of the rock powders were digested in a mixture of HF and HNO_3, heated at 140°C, and kept for 48 h in sealed Teflon beakers, dried, and re-dissolved in 2M HNO_3. Chromatographic separation, matrix removal and pre-concentration to 50-ppb solutions was achieved through sequential column chemistry following the protocols of Pin et al. (1994), Pin & Zalduegui (1997) and Míková & Denková (2007) for the elution of Sr and Nd, and conventional single-pass anion chemistry for the separation of Pb as described by Fölling et al. (2000) and Pin et al. (2014). All isotope ratios were measured on a Nu Instruments NuPlasma high-resolution multicollector (HR MC-) ICP-MS equipped with a Nu Instruments DSN-100 nebuliser. Mass bias by (i) instrumental drift, (ii) isobaric interferences (^{87}Rb on ^{87}Sr; ^{204}Hg on ^{204}Pb; ^{144}Sm on ^{144}Nd; plus various oxides/nitrates) and (iii) isotope fractionation during the sample introduction and during the measurement was all monitored, handled and corrected for by using the approach described by Will et al. (2014), Harris et al. (2015) and Howarth et al. (2019). This involved (i) the use of JNdi-1 (Tanaka et al. 2000), NIST SRM987 and NIST SRM981 (Galer & Abouchami 1998) as bracketing standards, (ii) subtraction of isobaric interferences based on natural abundance ratios (Böhlke et al. 2005), and (iii) application of the exponential law (e.g. Albarède et al. 2015), and, in case of the Pb analyte, additional spiking with Thallium (^{205}Tl/^{203}Tl 2.3889) from NIST SRM997 (Longerich et al. 1987; Thirlwall 2002). Reproducibility of the Nd-Sr-Pb isotope analyses was verified through repeated measurements of the Hawaiian basalt standard BHVO-2. This standard was used because of its well-established matrix composition (Jochum et al. 2005; Weis et al. 2005), which closely matches that of the investigated samples.

As most of the variation in Nd and Sr isotope ratios in terrestrial samples occurs within the third or fourth decimal place, the measured ^{143}Nd/^{144}Nd and ^{87}Sr/^{86}Sr ratios are presented in a more accessible way by using the epsilon (ε) notation (e.g. Papanastassiou & Wasserburg 1970; DePaolo & Wasserburg 1976a,b). The ε value for a sample at any given time, t, is calculated as follows:

$$\varepsilon Nd_{CHUR}^{Sample}(t) = \left[\frac{\left(\frac{^{143}Nd}{^{144}Nd}\right)_{Sample,\,t}}{\left(\frac{^{143}Nd}{^{144}Nd}\right)_{CHUR,\,t}} - 1\right] 10^4 \quad \textbf{(2.13)}$$

And:

$$\varepsilon Sr_{CHUR}^{Sample}(t) = \left[\frac{\left(\frac{^{87}Sr}{^{86}Sr}\right)_{Sample,\,t}}{\left(\frac{^{87}Sr}{^{86}Sr}\right)_{CHUR,\,t}} - 1\right] 10^4 \quad \textbf{(2.14)}$$

where CHUR (= Chondritic Uniform Reservoir) is the hypothetical isotope composition of the unfractionated Earth (DePaolo & Wasserburg 1976a,b). The present-day $^{143}Nd/^{144}Nd$ of CHUR is 0.512638 according to Jacobsen & Wasserburg (1980) and Hamilton et al. (1983), and the present-day $^{87}Sr/^{86}Sr$ of the Bulk Earth is 0.7045 according to DePaolo (1988). The present-day $^{143}Nd/^{144}Nd$ and $^{87}Sr/^{86}Sr$ of the sample can be directly measured on the mass spectrometer.

Back-calculation of ε to any other t≠0 in the Earth's history requires the amount of parent isotopes in the sample to be known. First, the present-day $^{147}Sm/^{144}Nd$ of the sample needs to calculated using the following equation:

$$\left(\frac{^{147}Sm}{^{144}Nd}\right)_{Sample,\,calculated} = 0.531084\frac{c_{Sm}}{c_{Nd}} + 0.1442294\left(\frac{^{143}Nd}{^{144}Nd}\right)_{Sample,\,measured} \quad \textbf{(2.15)}$$

where c are the measured element concentrations of Sm and Nd (in ppm) in the sample, and 0.531084 and 0.1442294 are constants derived from the natural isotopic abundance ratios and atomic weights (e.g. Faure 1986; Janoušek et al. 2016).

Accordingly, the $^{87}Rb/^{86}Sr$ ratio is calculated:

$$\left(\frac{^{87}Rb}{^{86}Sr}\right)_{Sample,\,calculated} = 2.6939\frac{c_{Rb}}{c_{Sr}} + 0.2832\left(\frac{^{87}Sr}{^{86}Sr}\right)_{Sample,\,measured} \quad \textbf{(2.16)}$$

where c are the measured element concentrations of Rb and Sr (in ppm) in the sample, and 2.6939 and 0.2832 are constants derived from the natural isotopic abundance ratios and atomic weights (e.g. Faure 1986; Janoušek et al. 2016).

Then, the daughter isotope ratios of the sample at the time, t, can be calculated using the conversion of the general radiometric age equation, that is:

$$\left(\frac{^{143}Nd}{^{144}Nd}\right)_{Sample,\,t} = \left(\frac{^{143}Nd}{^{144}Nd}\right)_{Sample,\,measured} - \left(\frac{^{147}Sm}{^{144}Nd}\right)_{Sample,\,calculated} \left(e^{\lambda t} - 1\right) \quad \textbf{(2.17)}$$

And:

$$\left(\frac{^{87}Sr}{^{86}Sr}\right)_{Sample,\,t} = \left(\frac{^{87}Sr}{^{86}Sr}\right)_{Sample,\,measured} - \left(\frac{^{87}Rb}{^{86}Sr}\right)_{Sample,\,calculated} \left(e^{\lambda t} - 1\right) \quad \textbf{(2.18)}$$

where λ is the decay constant for $^{147}Sm = 6.54 \times 10^{-12}$ yrs^{-1} (Lugmair & Marti 1978) and $^{87}Rb = 1.42 \times 10^{-11}$ yrs^{-1} (Steiger & Jäger 1977), respectively.

The daughter isotope ratios of CHUR at the time, t, are obtained from the following equations:

$$\left(\frac{^{143}Nd}{^{144}Nd}\right)_{CHUR,\,t} = 0.512638 - 0.1697\left(e^{\lambda t} - 1\right) \quad \textbf{(2.19)}$$

And:

$$\left(\frac{^{87}Sr}{^{86}Sr}\right)_{CHUR,\,t} = 0.7045 - 0.0827\left(e^{\lambda t} - 1\right) \quad \textbf{(2.20)}$$

where 0.512638, 0.1697, 0.7045 and 0.0824 are the present-day $^{143}Nd/^{144}Nd$, $^{147}Sm/^{144}Nd$, $^{87}Sr/^{86}Sr$ and $^{87}Rb/^{86}Sr$ ratios of CHUR, respectively (Jacobsen & Wasserburg 1980; DePaolo 1988; Rollinson 1993), and λ is the respective decay constant.

It proved particularly useful during this study to model so-called "mantle extraction ages" (denoted with t_{DM}) for the rocks and reference materials, i.e., hypothetical ages equivalent to their mean crustal residence time. The mantle extraction age is mathematically defined as the intercept between the ε evolution line of the sample and the ε evolution line of the depleted mantle:

$$\varepsilon Nd_{CHUR}^{Sample,\,t} = \varepsilon Nd_{CHUR}^{DM,\,t} \quad \textbf{(2.21)}$$

$$\left[\frac{\left(\frac{^{143}Nd}{^{144}Nd}\right)_{Sample,\,t}}{\left(\frac{^{143}Nd}{^{144}Nd}\right)_{CHUR,\,t}} - 1\right] 10^4 = \left[\frac{\left(\frac{^{143}Nd}{^{144}Nd}\right)_{DM,\,t}}{\left(\frac{^{143}Nd}{^{144}Nd}\right)_{CHUR,\,t}} - 1\right] 10^4$$

$$\left[\frac{\left(\frac{^{143}Nd}{^{144}Nd}\right)_{Sample} - \left(\frac{^{147}Sm}{^{144}Nd}\right)_{Sample}\left(e^{\lambda t} - 1\right)}{0.512638 - 0.1697(e^{\lambda t} - 1)} - 1\right] 10^4 = \left[\frac{0.51316 - 0.214\left(e^{\lambda t} - 1\right)}{0.512638 - 0.1697(e^{\lambda t} - 1)} - 1\right] 10^4$$

with depleted mantle (DM) values as given by Goldstein et al. (1984) and McCulloch & Black (1984); for a list of alterative values see Rollinson (1993).

Solving the equation above for t (the model age in years) yields the following equation:

$$t_{DM} = \frac{1}{\lambda} \ln\left[\frac{\left(\frac{^{143}Nd}{^{144}Nd}\right)_{Sample} - 0.51316}{\left(\frac{^{147}Sm}{^{144}Nd}\right)_{Sample} - 0.214} + 1\right] \quad \textbf{(2.22)}$$

Equation 2.22 is based on the assumption that the depleted mantle followed a simple linear isotopic evolution since it deviated 4.6 billion years ago from the undifferentiated Earth. However, DePaolo (1981a,b) has shown that the evolution of the depleted mantle is better described by a quadratic polynomial:

$$\varepsilon Nd_{CHUR}^{DM}(t_x) = 0.25t_x^2 - 3t_x + 8.5 \quad \textbf{(2.23)}$$

where +8.5 is the present-day εNd of the depleted mantle and t_x is the time before present in Ga.

A mantle extraction age is then obtained from the intercept between the linear sample evolution line (left term) and the quadratic depleted mantle evolution curve (right term):

$$\left(\frac{\varepsilon Nd_{CHUR}^{Sample,\,t} - \varepsilon Nd_{CHUR}^{Sample,\,0}}{t_{Sample}}\right) t_x + \varepsilon Nd_{CHUR}^{Sample,\,0} = 0.25t_x^2 - 3t_x + 8.5 \quad \textbf{(2.24)}$$

where t_{Sample} is the crystallisation age of the rock (in Ga). It is either known or assumed for the purpose of this calculation, and accordingly the εNd at t_{Sample} is calculated. Solving the equation above for t_x eventually leads to:

$$t_x = 2\left[-\left(\frac{\varepsilon Nd_{CHUR}^{Sample,\,t} - \varepsilon Nd_{CHUR}^{Sample,\,0}}{-t_{Sample}} - 3\right) - \sqrt{\left(\frac{\varepsilon Nd_{CHUR}^{Sample,\,t} - \varepsilon Nd_{CHUR}^{Sample,\,0}}{-t_{Sample}} - 3\right)^2 - \left(\left|\varepsilon Nd_{CHUR}^{Sample,\,0}\right| + 8.5\right)}\right] \quad \textbf{(2.25)}$$

where t_x is equivalent to the mantle extraction age (in Ga), t_{Sample} is the known (or assumed) crystallisation age of the studied igneous rock (in Ga), subscript 0 and t denote the εNd of the sample at the present-day (0) and the at the assumed age (t), respectively. Testing **Equation 2.25** with the raw data provided by Prevec et al. (2000) yielded results nearly identical (± 10 Ma) with the model ages reported by Prevec et al. (2000). Nevertheless, all literature data presented here have been recalculated using the same formulation and constants (i.e., **Eq. 2.25**) in order to make meaningful comparisons.

For samples with $^{147}Sm/^{144}Nd$ ratios < 0.13, it is reasonable to assume a linear evolution for the sample since its deviation from the depleted mantle, whereas samples with $^{147}Sm/^{144}Nd$ > 0.13 had likely undergone more than one event of Sm/Nd fractionation (e.g. during crustal anatexis). In the latter case, a two-stage mantle extraction age may be calculated (e.g. Janoušek et al. 2016):

$$t_{DM} = \frac{1}{\lambda}\ln\left[\frac{\left(\frac{^{143}Nd}{^{144}Nd}\right)_{Sample} - \left(e^{\lambda t} - 1\right)\left(\left(\frac{^{147}Sm}{^{144}Nd}\right)_{Sample} - 0.12\right) - 0.513151}{0.12 - 0.219} + 1\right] \quad \textbf{(2.26)}$$

where t_{DM} is the two-stage mantle extraction age, t is the known (or assumed) crystallisation age of the studied igneous rock, λ is the decay constant of ^{147}Sm, 0.12 is the present-day $^{147}Sm/^{144}Nd$ of the continental crust (Taylor & McLennan 1985), 0.219 is the $^{147}Sm/^{144}Nd$ of the depleted mantle, and 0.513151 is the $^{143}Nd/^{144}Nd$ of the depleted mantle according to Liew & Hofmann (1988).

Lead isotopes are mostly presented in their absolute raw form using measured ratios. Like for Nd and Sr isotopes, it is possible to calculate (or estimate) initial Pb isotope ratios if the age of the rock is known (or to be assumed) and U, Th and Pb concentrations are available. For example, the initial $^{207}Pb/^{204}Pb$ ratio for any time, t, may be obtained from the following equation:

$$\left(\frac{^{207}Pb}{^{204}Pb}\right)_{Sample,\ t} = \left(\frac{^{207}Pb}{^{204}Pb}\right)_{Sample,\ measured} - \left(\frac{^{235}U}{^{204}Pb}\right)_{Sample,\ calculated} \left(e^{\lambda t} - 1\right) \quad \textbf{(2.27)}$$

where λ is the decay constant for $^{235}U = 9.8485 \times 10^{-10}$ yrs^{-1} (Steiger & Jäger 1977). First, however, the $^{235}U/^{204}Pb$ of the sample needs to be calculated:

$$\left(\frac{^{235}U}{^{204}Pb}\right)_{Sample,\ calculated} = \frac{c_U}{c_{Pb}} \times \frac{m_{Pb}}{238.02891} \times \frac{0.72}{\%^{204}Pb} \quad \textbf{(2.28)}$$

where c denotes the measured element concentrations of U and Pb in the sample, 238.02891 is the atomic mass of U (Wieser 2006), 0.72 is the isotopic percentage abundance of ^{235}U (Rosman & Taylor 1998), m is the atomic mass of Pb in the sample, and $\%^{204}Pb$ is the proportion of ^{204}Pb of the total Pb. There are, however, some problems with this approach, which mainly arise from (i) a paucity of reported U, Th and Pb concentration data in the relevant literature; (ii) the high aqueous solubility of U^{6+}; and (iii) the preferential incorporation of Pb into feldspar – a mineral highly susceptible to alteration. Thus, any fluid-induced U/Th/Pb fractionation will result in an under-/overcorrection of the radiogenic Pb ingrowth (e.g. Darling et al. 2010a,b; McNamara et al. 2017).

To circumvent the above problems, an alternative approach of modelling initial Pb isotope ratios was introduced by Dickin et al. (1996) and Darling et al. (2010a): The $^{207}Pb/^{204}Pb$ for any time, t, may be obtained by projecting the measured $^{207}Pb/^{204}Pb$ ratio back parallel to the reference isochron for t to the corresponding $^{206}Pb/^{204}Pb$ ratio of Stacey & Kramers (1975) growth curve:

$$\left(\frac{^{207}Pb}{^{204}Pb}\right)_{t,\ modelled} = \left(\frac{^{207}Pb}{^{204}Pb}\right)_{Sample} - m_t\left(\frac{^{206}Pb}{^{204}Pb}\right)_{Sample} + m_t\left(\frac{^{206}Pb}{^{204}Pb}\right)_{S\&K,\ t} \quad \textbf{(2.29)}$$

where m is the slope of the reference isochron for the time t, and subscript S&K denotes the corresponding Pb isotope ratio of the Stacey & Kramers (1975) evolution curve at t.

For the age of the Sudbury impact event (1850 Ma) the equation is as follows:

$$\left(\frac{^{207}Pb}{^{204}Pb}\right)_{1850\ modelled} = \left(\frac{^{207}Pb}{^{204}Pb}\right)_{Sample} - 0.113\left(\frac{^{206}Pb}{^{204}Pb}\right)_{Sample} + 0.113 \times 15.464 \quad \textbf{(2.30)}$$

where 0.113 is the slope of the 1850 Ma reference isochron, and 15.464 is the $^{206}Pb/^{204}Pb$ ratio of the Stacey & Kramers (1975) growth curve at 1850 Ma. Modelled $^{207}Pb/^{204}Pb$ isotope ratios are obviously different from the initial ratios calculated using the more traditional approach. However, the advantage of this is that any sample can be corrected for decay, even where U, Th and Pb concentrations where either not reported and/or potentially affected by secondary mobility. This, in turn, allows for meaningful comparisons between different datasets, and also the calculation of isotopic mixing models (e.g. Darling et al. 2010a,b; McNamara et al. 2017).

Afton Offset Dyke

3.1 Summary

The discovery of impact-related quartz diorite is reported at Afton Township, 45 km northeast of Main Mass of the Sudbury Igneous Complex. The impactite was intersected at the bottom of Canadian Continental's 2,200 m deep diamond drill hole (AT-14-01) into the magnetic peak of the Temagami Anomaly, located between Sturgeon River and Emerald Lake. The discordant and up to 52 m thick quartz diorite units occur, together with pseudotachylitic breccia, within a Neoarchaean volcano-sedimentary greenstone belt succession beneath a relatively thin Palaeoproterozoic Huronian-Nipissing cover. Megacrystic feldspar quartz porphyry and banded iron formation represent the footwall and hangingwall, respectively, to which the dyke exhibits either sharp (initially chilled, now sheared) or strongly brecciated contacts.

Quartz diorite in drill core AT-14-01 is an aphantic fine-grained rock composed of plagioclase, biotite ± quartz ± actinolite ± magnetite. Much of the original mineralogy and texture is, however, obscured by retrograde metamorphism at greenschist-facies conditions as well intense hydrothermal alteration. Although any attempt to extract dateable minerals (zircon, baddeleyite) has not yet met with success, the whole-rock geochemical and isotopic data obtained in this study clearly identify the quartz diorite as a crustal melt rock and therefore as impact generated. The argumentation is mainly based on a combination of immobile trace element data and whole-rock Nd-Sr-Pb isotope systematics. These have revealed remarkable similarities to published data on other impact melt-related dykes of the 1.85 Ga Sudbury impact event, locally referred to as Offset Dykes. This is also supported by an imprecise whole-rock Pb-Pb errorchron date of 1711 ± 114 Ma, and an 1846 ± 76 Ma Rb-Sr date of, however, questionable significance. It is concluded that quartz diorite in drill core AT-14-01 is another, hitherto unrecognised Offset Dyke of the 1.85 Ga Sudbury Igneous Complex in a very distal area of the impact structure so far not known for Offset Dykes. Although no mineralisation was noted, these findings raise the general possibility to discover other, more proximal, and then perhaps better endowed Offset Dykes east of the Sudbury Igneous Complex. Exactly how the dyke was emplaced is beyond this study and requires additional drilling and, ideally, the discovery of a mappable surface expression. Interestingly tough, geochemical and isotopic fingerprinting (Ce/Yb ratios, Pb isotopes) implies that the Afton Offset Dyke could be a North Range radial Offset Dyke, the closest analogy being Ministic, Foy, or Parkin.

Further, this chapter demonstrates – as an alternative approach to U-Pb mineral dating – the utility of whole-rock geochemistry in conjunction with whole-rock Nd-Pb isotope analyses as a time, material, and cost-efficient means of identifying Sudbury-related impact melt rocks, even where hydrothermal processes and metamorphism have altered the rock beyond recognition, and erosion/deformation erased any physical evidence of a direct connection to the Sudbury Igneous Complex. The approach introduced in this chapter will be applied throughout the rest of the thesis.

A modified version of this chapter has been published as:
Kawohl, A., Frimmel, H. E., Bite, A., Whymark, W. E., & Debaille, V. (2019). Very distant Sudbury impact dykes revealed by drilling the Temagami geophysical anomaly. ***Precambrian Research***, 324, 220-235. **doi.org/10.1016/j.precamres.2019.02.014**

3.2 Local Geology

The study area comprises the Afton and Scholes townships, located some 75 km northeast of the City of Sudbury. These townships are bordered by longitudes 80°25 05W and 80°09 50W, and latitudes 46°58N and 46°53N. Access is provided via the Glen Afton Highway 805 and secondary gravel and logging roads. The area is of particular interest because it extends across the magnetic peak of the regional 1,200 km^2 large Temagami Anomaly, and it occurs close to its gravity peak. Both townships have previously been mapped by Meyn (1977) and exploration companies (e.g. Innes 1984), and some of the following information were taken from these studies, whereas other information are based on the writer's own drill core examinations and field work.

The western third of Afton Township, around Sturgeon River (**Fig. 3.1**), is marked by a profound lack of bedrock exposure, as it is largely covered by swamp, dead arms, and alluvium. Gabbro of the 2.22 Ga Nipissing Suite supposedly underlies much of the area immediately around the drilling location. This gabbro is part of one of the largest coherent members of the Nipissing Suite known so far, in the literature referred to as the "Emerald Lake Intrusion" (e.g. Lightfoot & Naldrett 1996a, p. 20). The bulk of this presumably sheet-like intrusion consists of medium-grained orthopyroxene gabbro, with minor fine-grained quartz gabbro (diabase) at the lower margin, and pods and veins of vari-textured or pegmatoidal gabbro, diorite, and granophyre, localised predominantly towards the roof zone. An apparent thickness of the intrusion between 50 and 360 m has been inferred from previous drilling programs, although an upper intrusive contact is yet to be found (Meyn 1977). Its geochemistry and lithological diversity make the Emerald Lake Intrusion a typical example of a moderately differentiated sill of the Nipissing Suite (Lightfoot & Naldrett 1996a), as they are common throughout the Cobalt Embayment. This sill intruded sedimentary rocks of the Gowganda Formation, which are locally exposed in the western and northern corners of Afton Township, and north of Scholes Township. There, the Gowganda Formation is more or less flat lying and consists of locally massive, locally laminated, mudstone and siltstone (50% of the formation), wacke (25%), and matrix-supported conglomerate (25%), the latter containing dropstones of sedimentary rocks, pink granite, and subordinate greenstone, ranging in size from pebbles to 3 m-large boulders (Meyn 1977). Metamorphism of the Palaeoproterozoic units reached the lower greenschist facies at maximum; deformation is restricted to N-S oriented lineaments interpreted as faults, and tectonic fabrics are largely absent (Meyn 1977; Card 1978).

The crystalline basement below the Palaeoproterozoic cover is locally exposed as erosive windows to the southern extension of the 2.7–2.6 Ga Abitibi Subprovince. One such window is the Emerald Lake Greenstone Belt (**Fig. 3.1**), an assemblage of volcanic, hypabyssal, and sedimentary rocks, ranging in composition from tholeiitic and calc-alkaline basalt to rhyolite, and including, shale, wacke, and banded iron formation, respectively (Meyn 1977; Bennett 1978). Syn- to late volcanic quartz-feldspar porphyric dykes and ultramafic lamprophyres have been reported by Innes (1984), whereas rocks of the tonalite-trondhjemite-granodiorite (TTG) suite and volcanic rocks of komatiitic affinity are absent. The Emerald Lake Greenstone Belt appears to be closely related to the Abitibi outliers at Temagami and Cobalt (see Ayer et al. 2006). Their volcanic successions likely represent former submarine pyroclastic deposits and submarine lava flows as indicated by pillow structures, extensive VMS-type alteration, and their intercalation with limestone, turbidite, and pyritic black shale.

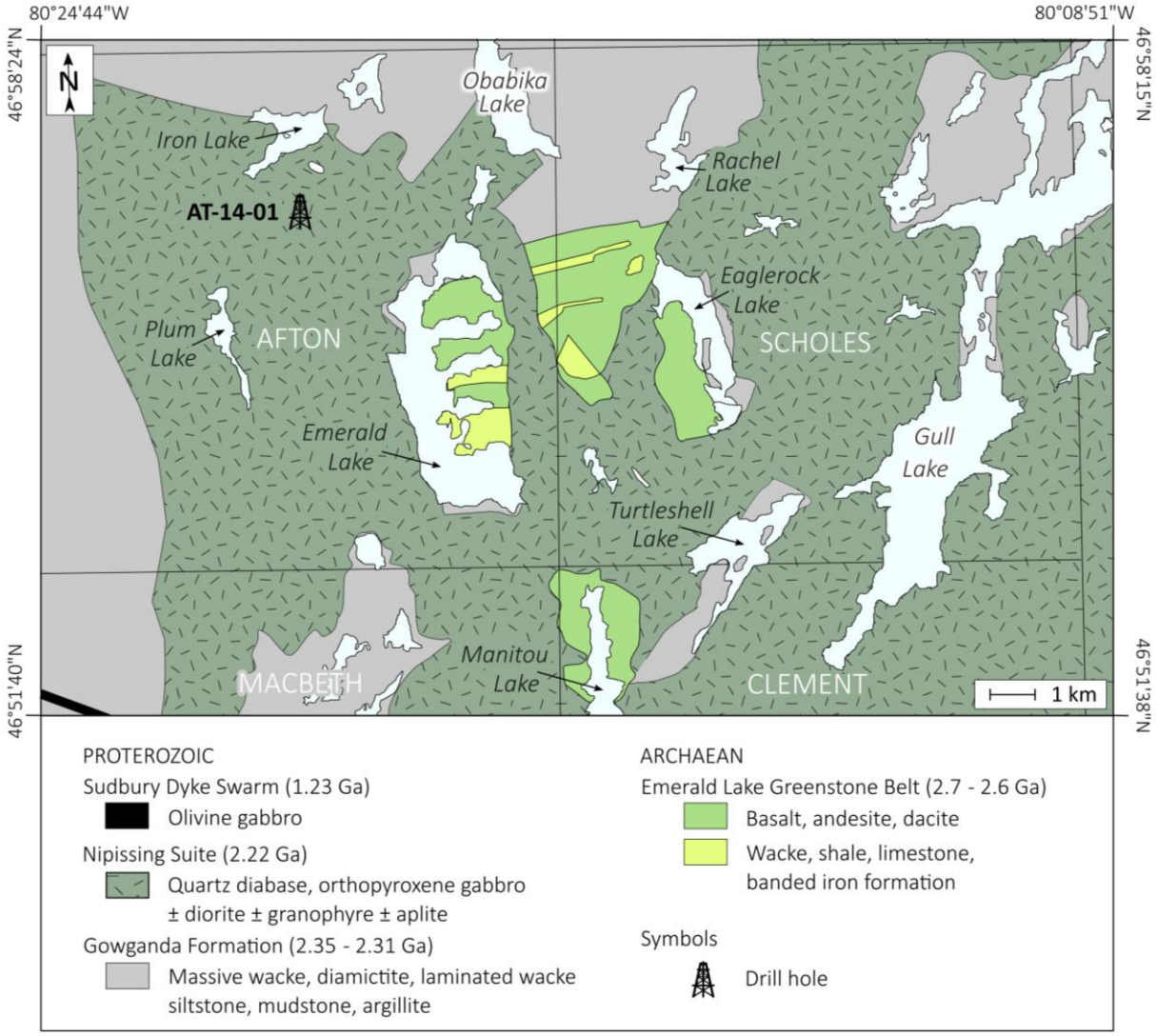

Figure 3.1 Geological map of the Afton and Scholes townships showing the regional geological and lithostratigraphic context of drill hole AT-14-01; after Meyn (1977) and Ayer et al. (2006).

At least two units of 100 m-thick Algoma-type BIF, dipping 60–85° south (Innes 1984) and striking NE, are present within the Emerald Lake Greenstone Belt. The BIF is embedded within mafic volcanic rocks and chloritic schist and it is mainly composed of laminated magnetite and chert; coarse-grained vuggy pyrite is not uncommon. Greenschist-facies metamorphic conditions prevail, and several episodes of hydrothermal alteration were noted, including syn-depositional seafloor alteration, intrusion-related hydrothermal alteration, and late carbonate-quartz-tourmaline veining and brecciation. Tectonic fabrics occur in form of penetrative schistosity in the chloritic metavolcanic and pyroclastic rocks; folding, microfaulting and a variety of soft-sediment deformation features can be observed in several BIF outcrops, muck piles, and in dumped core material.

The youngest geological unit in the study area is a NW-striking dyke of alkaline olivine gabbro related the 1.23 Ga Sudbury Dyke Swarm (**Fig. 3.1**). The dyke is several tens of meters wide, associated with topographic ridges and valleys, and its orientation is clearly visible on aeromagnetic maps as a distinctive linear feature. The dyke's primary mineralogy and texture seems well preserved, even pristine olivine is present. Considering the ease at which olivine would have been altered to serpentine, magnesite or chlorite, the fresh mineralogy of the dyke indicates that its emplacement post-dated regional metamorphism and metasomatism.

3.3 Drill Core Stratigraphy

Borehole AT-14-01 (NQ size, diameter = 4.76 cm) targeted the magnetic peak of the Temagami Anomaly at Afton Township, coordinates 46°56 31N 80°21 08W. Originally drilled in 2014 with an azimuth of 90° to a depth of 1,071 m, a downhole extension followed in 2015 to a final depth of 2,200 m. The recovered drill core was first logged by Kleinboeck (2015) and has been re-visited for the present study, thus, only a summary of the overall stratigraphy (**Fig. 3.2**) is presented here. For insights, the reader is referred to the detailed log of Kleinboeck (2015). AT-14-01 intersected a massive gabbro from 0 to 321 m (**Fig. 3.2A**), which bears all the hallmarks of the Nipissing Suite gabbro as exposed on surface and elsewhere in the Southern Province. This is followed by sandstone, siltstone, and conglomerate of the Gowganda Formation, and from a depth of ~600 m to 2,000 m, a volcano-sedimentary assemblage likely of Archaean age and equivalent to the rocks of the Emerald Lake Greenstone Belt. These are felsic to intermediate porphyric volcanic rocks (10% of the drill core) and subordinate aphyric and strongly altered, crudely bedded, tuffaceous, pyroclastic and volcaniclastic rocks (~22%). Megacrysts of zoned alkali feldspar, up to 5 cm in diameter, as well as 1 cm-large phenocrysts of embayed blueish quartz are common in this strongly sericitised porphyry (**Fig. 3.2B**), which bears strong resemblance to the porphyric rocks described at Emerald Lake (e.g. Innes 1984). A 3 m-thick massive chert-pyrite breccia overlies the volcanic pile at 932 m and is interpreted as the product of exhalative hydrothermal activity, which is also reflected by a pervasive phyllic alteration noted throughout the volcanic succession. Veinlets of black sulphidic pseudotachylite (Sudbury Breccia) cut the aphyric volcanics at 1,388 m (**Fig. 3.2C**), and a heterolithic breccia of similar appearance also occurs within the shale unit from 1,539–1,546 m. Two thick packages of banded iron formation make up 20% of drill core AT-14-01. These are predominantly of the oxide facies (chert-magnetite microbands and mesobands), devoid of jasper, and interlayered with chlorite schist, stilpnomelane-siderite schist, and pyritic chert. Folding and microfaulting is common throughout, whereas brecciation (**Fig. 3.2D**) tends to increase with depth and peaks at around 2,000 m. Some of these BIF breccias might in fact be pseudotachylitic breccia as well, although testing this hypothesis is beyond the scope of this study. Wacke constitutes the remaining 10% of the total drill core length. It occurs between the lower and upper BIF and is bracketed between two units of > 50 m thick cherty and graphitic black shale that contains boudinaged lenses and cm-large framboids of pyrite or marcasite (**Fig. 3.2E**). The black shale eventually grades into sulphidic BIF over some metres.

Finally, two suspicious quartz diorite bodies, 25 and 52 m in thickness, were encountered within another feldspar porphyry unit (**Fig. 3.2F**) and brecciated iron formation at depths below 2,000 m. This fine-grained quartz diorite (**Fig. 3.2G**) displays a clear intrusive and cross-cutting relationship with the ambient feldspar porphyry. Contacts to this porphyry are sharp, undulating, and in one place sheared and re-healed with chlorite, stilpnomelane and calcite. Neoblasts of biotite were noted within the porphyry, at the intrusive contact, and likely reflect contact metasomatism. The nature of the contact between the quartz diorite and the iron formation remains ambiguous, but it is marked by a strong brecciation (either primary intrusive, impact-related, or tectonic in origin) and by the abundance of chlorite. For the purpose of this study, seventeen halved diamond drill core specimens, each 15–25 cm in length, were obtained at regular sampling intervals throughout the quartz diorite, and after a petrographic examination, subjected to whole-rock geochemical and isotopic analyses. The results obtained on these samples will be detailed below.

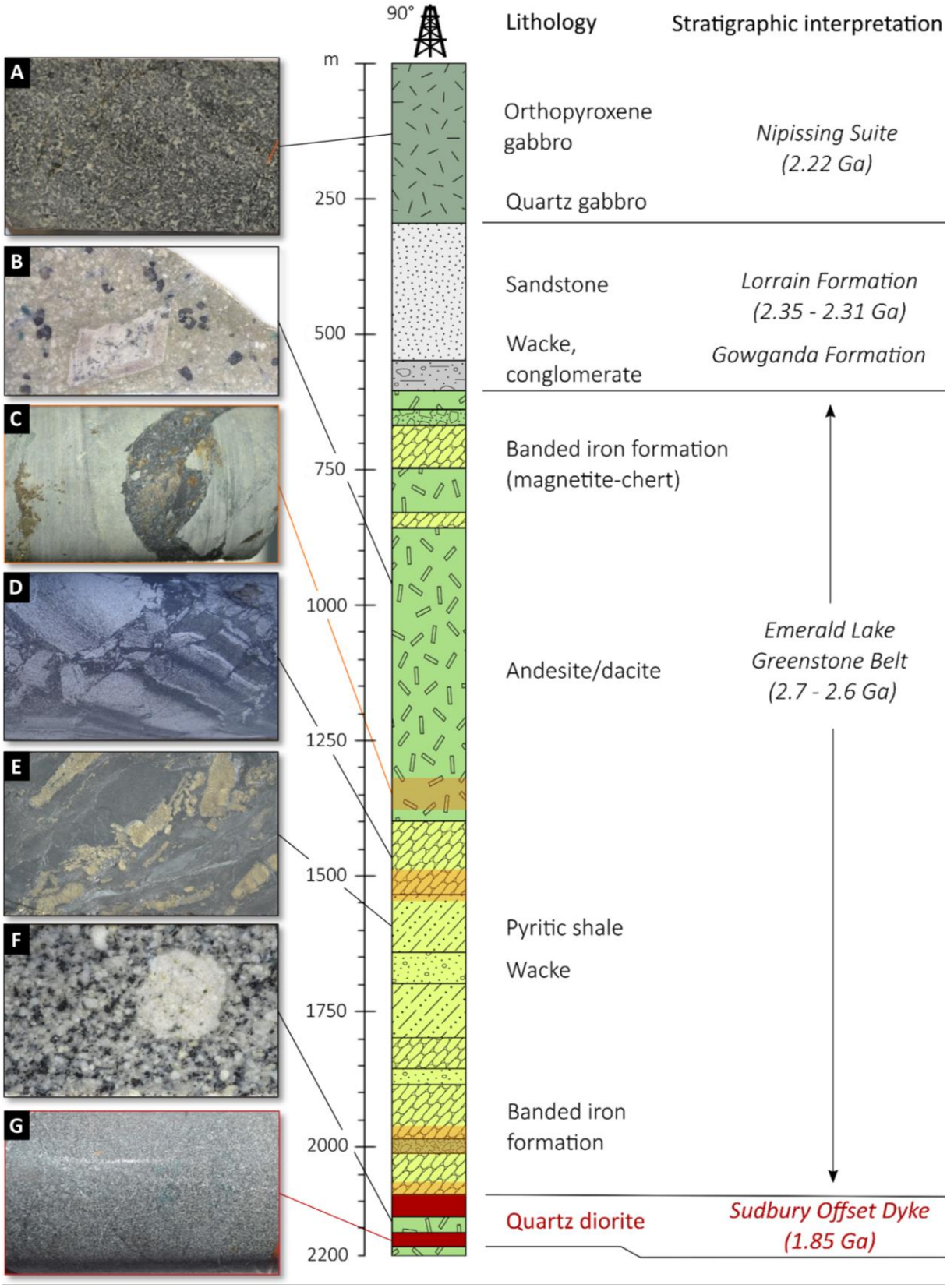

Figure 3.2 Lithological profile of drill core AT-14-01 with exemplary core photographs (left) and stratigraphic interpretation (right); **A:** medium-grained Nipissing Suite gabbro; **B:** porphyric volcanic rock with phenocrysts of quartz and feldspar; **C:** aphyric sulphide-bearing volcanic rock cut by pseudotachylite; **D:** brecciated banded iron formation; **E:** pyrite framboids in cherty black shale; **F:** feldspar quartz porphyry; **G:** quartz diorite; core diameter (= the height of each panel) is 4.76 cm; colour code as in Figure 3.1.

3.4 Petrography

The quartz diorite intersected at the bottom of AT-14-01 is greyish green in drill core and dark grey on polished surfaces, massive, aphantic and texturally uniform. In hand specimen, it has a relatively high density and magnetic susceptibility compared to the adjacent porphyry. The quartz diorite appears chilled against the country rock, becoming slightly coarser grained away from the contact, gradually, over a few decimetres. Any possible quench texture (spherulitic or even glassy) that might have been present originally is, however, obscured by the strong alteration. The freshest and most coarsely grained intersection of the quartz diorite is found at 2,160 m (**Fig. 3.3A–D**) and displays a texture that might be described as holocrystalline, inequigranluar and subophitic to interstitial. Sub- to euhedral, twinned, and zoned plagioclase laths (0.5–1 mm in length) constitute 60 vol%, locally up to 85 vol%, of the rock; their aspect ratio is typically 4:1. The interstitial spaces between plagioclase are commonly filled with either by biotite, quartz and sericite, or a cryptocrystalline mixture of ferromagnesian minerals (**Fig. 3.3C,D**). Plagioclase has been, to variable degrees and especially in its cores, replaced by a cryptocrystalline and almost opaque mineral aggregate including epidote and chlorite. This saussuritisation is, in places, so extreme that hardly any plagioclase is preserved and that the original igneous texture is no longer apparent. Close to the intrusive contacts, the texture of the quartz diorite becomes very fine grained (< 0.1 mm) and most strongly affected by the alteration. A fault gouge, filled with chlorite, carbonate and stilpnomelane, is developed at the contact between the quartz diorite and the porphyry at 2,120 m but no shearing or penetrative tectonic fabric was observed elsewhere within the two dykes. Biotite is the second most abundant mineral after plagioclase/epidote, and by far the most abundant ferromagnesian mineral in all the quartz diorite samples. It is of flaky habit, of olive-green colour, in places converted to chlorite, and occurs at modal amounts of 25 vol% homogeneously distributed throughout. There is every reason to assume that biotite is of primary origin in these samples. However, biotite also occurs as cm-long veinlets together with granular epidote indicating short-distance remobilisation by late-/post magmatic fluids (**Fig. 3.3F**). Pale green amphibole (actinolite) occurs as mm-sized needles and bundles at around 5 vol%. Magnetite is a minor constituent of the rock, present at up to 3–5 vol%. Its distribution is, however, relatively irregular, its habit bimodal. On one hand, magnetite occurs as subangular grains with sharp and well-defined grain boundaries and occasionally with lamella of Fe-Ti oxide, which is typical of a magmatic origin. On the other hand, magnetite also occurs together with titanite, clay, carbonate, and undefinable Fe-Ti-oxides as a cryptocrystalline, semi translucent mineral aggregate (**Fig. 3.3G**), here and in the following referred to as leucoxene, and it considered being of secondary origin. Among the few accessory minerals identified there is, in decreasing order of abundance, anhedral interstitial quartz, anhedral calcite, pyrite, and apatite. Calcite and pyrite occur together with chlorite in patches (**Fig. 3.3H**) and are certainly not part of the magmatic paragenesis, whereas the regular distribution, abundance and overall appearance of quartz indicates a primary origin, hence the petrographic rock classification as quartz diorite.

An inclusion-bearing facies occurs between 2,081 and 2,086 m, in the centre of the upper quartz diorite. It contains angular to subrounded mm- to dm-sized strongly brecciated xenoliths of BIF and chlorite schist. Xenocrysts of quartz and magnetite are very abundant in this part of the dyke, which likely reflect disintegration of these locally derived xenoliths. Fragments of chlorite schist are in turn replaced by biotite, possibly due to contact metasomatism by the intrusion of the dyke.

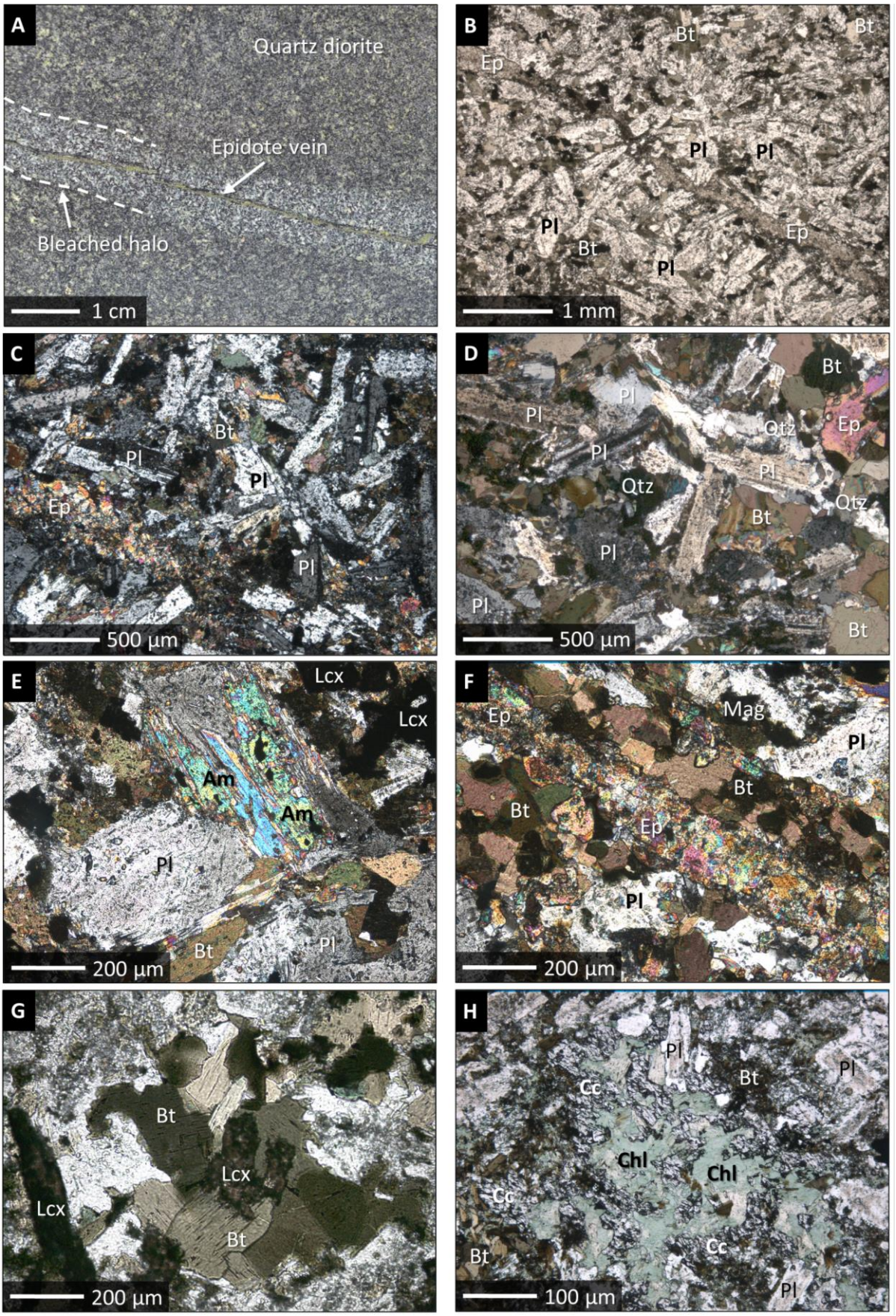

Figure 3.3 Photograph and microphotographs of the quartz diorite in drill core AT-14-01; **A:** polished drill core (sample AT-21); **B, G, H:** thin sections under transmitted light and plane polars; **B–F:** thin sections under transmitted light and crossed polars. Abbreviations: Pl = plagioclase; Bt = biotite; Ep = epidote; Qtz = quartz; Am = amphibole; Lcx = leucoxene; Mag = magnetite; Chl = chlorite; Cc = calcite.

3.5 Geochemistry

General characteristics

Quartz diorite in drill core AT-14-01 has a relatively uniform, subaluminous, subalkaline and in terms of SiO_2 (53.4–56.2 wt%) intermediate composition (**Tab. 3.1**), with 11–13 wt% Fe_2O_3 (representing total iron) and 3.5–3.9 wt% MgO. The Mg# (=100×molar MgO/[MgO+FeO]) lies between 39 and 43. The LOI ranges from 1.0 to 6.6 wt% and reflects the variable amount of hydrous silicates and carbonates in those samples. The rock is characterised by moderate concentrations of Cr (7–88 ppm) and Ni (43–91 ppm), except for three outliers with up to 308 ppm Cr and 203 ppm Ni. Despite its relatively primitive character with respect to mineralogy, Mg#, Cr and Ni, the quartz diorite is markedly enriched in incompatible lithophile elements, for example, K_2O (1.3–3.2 wt%), U (1.1–1.3 ppm), Th (6.5–7.2 ppm), ΣREE+Y (169–186 ppm) and Zr (139–155 ppm). Its CIPW normative mineralogy is as follows: 52 vol% plagioclase, 17 vol% orthoclase, 15 vol% hypersthene, 10 vol% diopside, and 4 vol% quartz, corresponding to a hypothetical rock density of 2.9 g/cm^3.

Igneous rock classification

According to the TAS diagram (**Fig. 3.4B**), the quartz diorite's composition corresponds to andesite (intrusive equivalent diorite), trachyandesite (monzodiorite) or basaltic andesite. The AFM plot furthermore classifies the rock somewhat ambiguously as calc-alkaline or tholeiitic (**Fig. 3.4C**). Although the isocon method demonstrates little secondary mobility of most major elements (**Fig. 3.4A**), classification plots using typically immobile trace elements (Ti, Nb, Y, Zr, Th) are generally preferred. In such diagrams (e.g. **Fig. 3.4D**), the samples plot within the field of basalt/gabbro, stretching to the field of andesite/diorite. Most classification schemes suggest a calc-alkaline to shoshonitic (high-K) magmatic affinity (e.g. **Fig. 3.4E**). This classification is in broad agreement with the trace element patterns for the quartz diorite (**Fig. 3.4F**), which exhibit the diagnostic features of (calc-alkaline) subduction-zone magmatism, namely, the decoupling and enrichment of LILE from and over HFSE. This is evident from positive anomalies of Rb, Ba, K, Pb relative to the composition of the primitive mantle, and negative anomalies of Ti, Nb and Ta, in all 17 samples.

Nd-Sr-Pb isotopes

A summary of whole rock radioisotope data for the quartz diorite is presented in **Table 3.2**. All 17 samples define a narrow range in $^{143}Nd/^{144}Nd$ corresponding to a very un-radiogenic εNd between –27.61 and –26.01. The spread in $^{143}Nd/^{144}Nd$ ratios is outside the analytical uncertainty and accompanied by subtle variations in $^{147}Sm/^{144}Nd$, however, without a linear relationship and without age significance. Neodymium model ages (t_{DM}) are between 2540 Ma and 2910 Ma, and 2760 Ma on average. The $^{87}Sr/^{86}Sr$ isotope ratio is very radiogenic although it varies considerably from 0.710 to 0.734. A good correlation exists between the measured $^{87}Sr/^{86}Sr$ ratio and the calculated $^{87}Rb/^{86}Sr$ ratio. An ordinary least square regression passing through all 17 samples gives an errorchron with a slope 1846 ± 76 Ma (*IsoplotR*; Vermeesch 2018) but with a significant dispersion. The $^{206}Pb/^{204}Pb$ ratio ranges from 15.77 to 19.38, $^{207}Pb/^{204}Pb$ from 15.22 to 15.59, and $^{208}Pb/^{204}Pb$ from 35.67 to 41.15. The spread in uranogenic Pb isotope ratios makes it possible to construct a whole-rock errorchron (n=17) of 1780 +320/-330 Ma using *Isoplot/Excel* of Ludwig (2003), or 1711 ± 114 Ma using *IsoplotR* (Vermeesch 2018). The modelled initial $^{207}Pb/^{204}Pb$ ratio at 1850 Ma (the absolute age of the Sudbury impact event) ranges from 15.14 to 15.22.

Table 3.1 Major element oxide concentrations (wt%) and trace element concentrations (ppm) in quartz diorite from drill core AT-14-01, Afton Township

	AT-36	AT-38	AT-39	AT-64	AT-40	AT-41	AT-14	AT-15	AT-58	AT-17	AT-19	AT-59	AT-20	AT-21	AT-22	AT-24	AT-25
Depth [m]	2109.00	2105.00	2097.50	2096.20	2091.00	2089.20	2166.00	2165.00	2165.00	2159.50	2157.00	2156.90	2156.30	2155.00	2153.50	2149.50	2148.20
SiO_2	53.4	53.7	53.4	53.6	53.5	53.9	54.5	54.5	54.7	55.8	55.3	55.6	55.5	55.8	56.2	53.6	54.3
TiO_2	1.08	1.09	1.08	1.09	1.07	1.08	1.09	1.12	1.11	1.15	1.16	1.17	1.16	1.15	1.18	1.10	1.11
Al_2O_3	13.7	13.8	13.7	13.8	13.7	13.7	13.8	14.0	14.0	14.3	14.3	14.4	14.2	14.4	14.3	13.8	14.0
Fe_2O_3	11.3	11.7	11.3	11.5	11.5	11.2	11.5	12.1	11.7	12.2	12.3	12.4	12.2	12.2	12.6	11.3	11.7
MgO	3.8	3.9	3.7	3.7	3.7	3.5	3.5	3.7	3.5	3.6	3.6	3.6	3.7	3.9	3.8	3.5	3.7
CaO	5.4	4.8	5.3	4.9	6.2	5.8	6.8	6.2	6.6	5.6	5.7	5.6	5.5	5.4	4.6	5.2	5.2
MnO	0.15	0.15	0.14	0.12	0.12	0.11	0.14	0.14	0.14	0.15	0.16	0.15	0.16	0.16	0.16	0.14	0.14
Na_2O	4.0	4.0	3.9	4.0	4.0	4.2	2.9	3.0	2.9	3.3	3.3	3.6	3.4	3.7	4.0	4.1	4.2
K_2O	2.72	3.24	2.65	2.76	1.45	1.33	1.87	2.24	2.26	2.50	2.42	2.39	2.50	2.30	2.05	2.91	2.27
P_2O_5	0.09	0.07	0.08	0.09	0.10	0.10	0.11	0.09	0.11	0.08	0.09	0.09	0.08	0.07	0.06	0.04	0.08
LOI	5.5	4.8	5.6	5.0	6.6	6.3	4.7	4.0	3.8	1.1	1.0	1.2	1.1	1.1	1.5	4.6	5.3
Total	101.10	101.22	100.85	100.60	101.86	101.30	100.86	101.03	100.76	99.79	99.39	100.07	99.44	100.04	100.42	100.32	101.93
Cr	11.2	21	7.5	12.2	81	11.8	296	51	18.6	32	308	65	244	88	45	13.5	11.5
Ni	45	52	43	45	86	48	195	67	51	58	203	74	170	91	67	46	47
Cu	111	103	117	119	101	114	119	115	121	106	90	107	101	73	61	118	120
Rb	149	189	136	139	62	49	72	82	87	46	38	39	42	37	38	127	103
Sr	491	561	462	423	542	527	744	732	843	1019	1155	1127	1203	1126	875	514	370
Zr	147	147	145	147	146	150	145	139	144	148	149	142	149	146	155	148	150
Nb	7.5	7.5	7.2	7.4	9.8	7.7	16.9	8.4	8.1	8.6	18.6	9.3	15.3	10.2	9.1	7.7	7.4
Ba	458	550	517	562	331	332	560	637	642	947	1000	961	1020	982	819	669	535
La	33.6	32.9	33.3	33.8	33.1	34.1	35.1	33.8	34.6	34.9	35.0	34.6	35.1	32.8	32.3	31.3	33.9
Ce	65	66	65	66	65	68	68	66	67	69	69	68	69	65	65	64	66
Pr	7.9	7.6	7.5	7.6	7.7	8.1	8.0	7.9	7.9	7.9	8.1	8.1	8.2	7.8	7.6	7.4	7.6
Nd	30.8	29.8	30.0	30.4	29.7	31.8	30.5	30.2	29.9	31.4	32.1	30.7	31.9	29.8	29.8	29.0	29.8
Sm	5.5	5.7	5.5	5.8	5.5	5.8	5.9	6.0	5.7	6.1	6.1	6.0	6.1	6.0	5.6	5.5	5.5
Eu	1.68	1.53	1.58	1.68	1.59	1.60	1.63	1.60	1.66	1.63	1.64	1.46	1.64	1.38	1.34	1.44	1.57
Gd	4.9	4.9	5.0	4.9	4.9	4.9	5.3	5.1	5.5	5.4	5.5	5.5	5.4	5.3	5.3	5.1	5.4
Tb	0.57	0.60	0.59	0.58	0.57	0.57	0.65	0.67	0.65	0.65	0.70	0.68	0.69	0.63	0.66	0.63	0.65
Dy	3.1	2.9	3.2	3.1	3.0	3.1	3.8	3.8	3.8	3.9	3.9	4.1	4.0	3.7	3.8	3.8	3.7
Ho	0.53	0.53	0.58	0.56	0.56	0.56	0.71	0.67	0.69	0.70	0.71	0.68	0.71	0.65	0.69	0.71	0.67
Er	1.46	1.42	1.50	1.51	1.56	1.48	1.85	1.79	1.90	1.92	2.06	1.93	1.94	1.92	1.88	1.92	1.89
Tm	0.22	0.20	0.23	0.21	0.20	0.21	0.26	0.25	0.24	0.26	0.26	0.25	0.27	0.28	0.26	0.26	0.26
Yb	1.43	1.38	1.36	1.44	1.38	1.43	1.64	1.66	1.56	1.71	1.61	1.66	1.66	1.63	1.69	1.70	1.70
Lu	0.23	0.21	0.21	0.23	0.21	0.23	0.25	0.23	0.24	0.25	0.25	0.29	0.27	0.27	0.24	0.25	0.25
Y	14.3	14.0	14.4	13.9	14.7	14.5	18.7	17.7	18.5	19.0	19.2	18.2	18.8	18.6	18.9	17.8	17.8
Hf	3.8	3.7	3.9	3.8	3.7	3.9	3.7	3.7	3.5	3.8	3.7	3.7	3.9	3.6	4.1	3.9	3.9
Ta	0.53	0.49	0.48	0.50	0.52	0.48	0.56	0.54	0.53	0.55	0.59	0.53	0.55	0.53	0.52	0.53	0.52
Pb	6.2	11.0	11.3	9.7	11.4	4.8	12.3	11.2	12.2	15.4	14.6	14.1	14.8	14.6	20.8	27.9	43.4
Th	6.5	6.8	6.5	6.7	6.7	6.7	6.9	6.8	6.7	7.2	7.1	7.1	7.2	7.0	7.2	7.0	6.8
U	1.2	1.1	1.1	1.1	1.1	1.1	1.2	1.2	1.2	1.2	1.2	1.2	1.2	1.2	1.3	1.2	1.2

Table 3.2 Summary of whole-rock Nd-Sr-Pb isotope data for quartz diorite intersected in drill core AT-14-01, Afton Township

	$\frac{^{143}Nd}{^{144}Nd}$	±2σ	$\frac{^{147}Sm}{^{144}Nd}$	εNd present	εNd 1850 Ma	1-stage t_{DM}	$\frac{^{87}Sr}{^{86}Sr}$	±2σ	$\frac{^{87}Rb}{^{86}Sr}$	$\frac{^{87}Sr}{^{86}Sr_{1850}}$	$\frac{^{208}Pb}{^{204}Pb}$	±2σ	$\frac{^{207}Pb}{^{204}Pb}$	±2σ	$\frac{^{206}Pb}{^{204}Pb}$	±2σ	$\frac{^{207}Pb}{^{204}Pb_{1850}}$
AT-14	0.511298	13	0.117	–26.13	–6.95	2760 Ma	0.715811	8	0.280	0.70835	38.6961	32	15.4805	9	17.7970	9	15.22
AT-15	0.511276	13	0.120	–26.56	–8.17	2897 Ma	0.716820	8	0.324	0.70818	38.8245	27	15.4724	9	17.7485	8	15.21
AT-17	0.511252	12	0.117	–27.04	–8.34	2852 Ma	0.711776	8	0.131	0.70830	37.5967	25	15.3429	8	16.6996	7	15.20
AT-19	0.511244	17	0.115	–27.20	–7.82	2788 Ma	0.710665	10	0.095	0.70813	37.7978	25	15.3470	8	16.7932	7	15.20
AT-20	0.511280	9	0.115	–26.50	–7.36	2751 Ma	0.710862	9	0.101	0.70817	37.6443	31	15.3652	10	16.8109	9	15.21
AT-21	0.511298	11	0.122	–26.14	–8.39	2913 Ma	0.710429	10	0.095	0.70790	37.6221	25	15.3272	8	16.7120	7	15.19
AT-22	0.511263	11	0.119	–26.83	–7.32	2892 Ma	0.710872	12	0.126	0.70752	36.7148	29	15.2713	9	16.2197	8	15.19
AT-24	0.511255	12	0.115	–26.97	–7.56	2763 Ma	0.726431	11	0.716	0.70735	36.1687	29	15.2509	10	16.0588	8	15.18
AT-25	0.511287	14	0.111	–26.35	–6.39	2626 Ma	0.728671	12	0.807	0.70717	35.6667	24	15.2173	8	15.7691	7	15.18
AT-36	0.511282	12	0.108	–26.46	–5.61	2541 Ma	0.732724	11	0.880	0.70928	41.1497	26	15.5381	8	18.8262	8	15.16
AT-38	0.511248	17	0.115	–27.12	–7.74	2804 Ma	0.733651	10	0.977	0.70762	37.8948	28	15.3335	10	16.9720	9	15.16
AT-39	0.511254	12	0.111	–26.99	–6.46	2657 Ma	0.731453	9	0.854	0.70871	38.3395	26	15.3609	9	17.2746	8	15.16
AT-40	0.511255	13	0.112	–26.97	–6.74	2686 Ma	0.720708	13	0.331	0.71188	38.6533	31	15.3785	10	17.4073	14	15.16
AT-41	0.511223	10	0.110	–27.61	–7.28	2691 Ma	0.719547	12	0.269	0.71237	40.2583	28	15.5865	9	19.3769	9	15.14
AT-58	0.511282	10	0.115	–26.45	–7.28	2737 Ma	0.715774	11	0.299	0.70781	38.5325	28	15.4418	8	17.4739	8	15.21
AT-59	0.511305	12	0.135	–26.01	–7.35	2787 Ma	0.710667	12	0.100	0.70800	37.9210	25	15.3568	8	16.8618	8	15.20
AT-64	0.511276	10	0.115	–26.56	–7.41	2748 Ma	0.733426	12	0.953	0.70804	38.7832	36	15.3845	11	17.4853	10	15.16
Average	0.511269		0.115	–26.70	–7.30	2758 Ma	0.720017		0.432	0.70852	38.1332		15.3739		17.1993		15.18

$^{147}Sm/^{144}Nd$ and $^{87}Rb/^{86}Sr$ ratios were calculated using measured Sm, Nd, Rb and Sr concentrations, which are given in Table 3.1;
2σ uncertainties of $^{147}Sm/^{144}Nd$ and $^{87}Rb/^{86}Sr$ are < 3% based on the propagated analytical error of Sm, Nd, Rb and Sr concentration data;
$^{143}Nd/^{144}Nd$ ratios are normalised to $^{146}Nd/^{144}Nd = 0.72190$;
2σ uncertainties of $^{143}Nd/^{144}Nd$ are < 0.004% based on the long-term in-house reproducibility of BHVO-2;
2σ uncertainties of $^{87}Sr/^{86}Sr$ are < 0.007% based on the long-term in-house reproducibility of BHVO-2;
2σ uncertainties of $^{208}Pb/^{204}Pb$, $^{207}Pb/^{204}Pb$ and $^{206}Pb/^{204}Pb$ are < 0.18%, < 0.09% and < 0.5%, respectively, based on the long-term in-house reproducibility of BHVO-2;
For sake of readability, all listed 2σ absolute internal errors only refer to the last significant decimal digits of the measured isotope ratios;
εNd values were calculated relative to CHUR with $^{147}Sm/^{144}Nd = 0.1967$ and $^{143}Nd/^{144}Nd = 0.512638$;
One-stage Nd model ages (t_{DM}) were calculated according to DePaolo (1981a,b);
$^{207}Pb/^{204}Pb_{1850}$ was calculated according to Darling et al. (2010a)

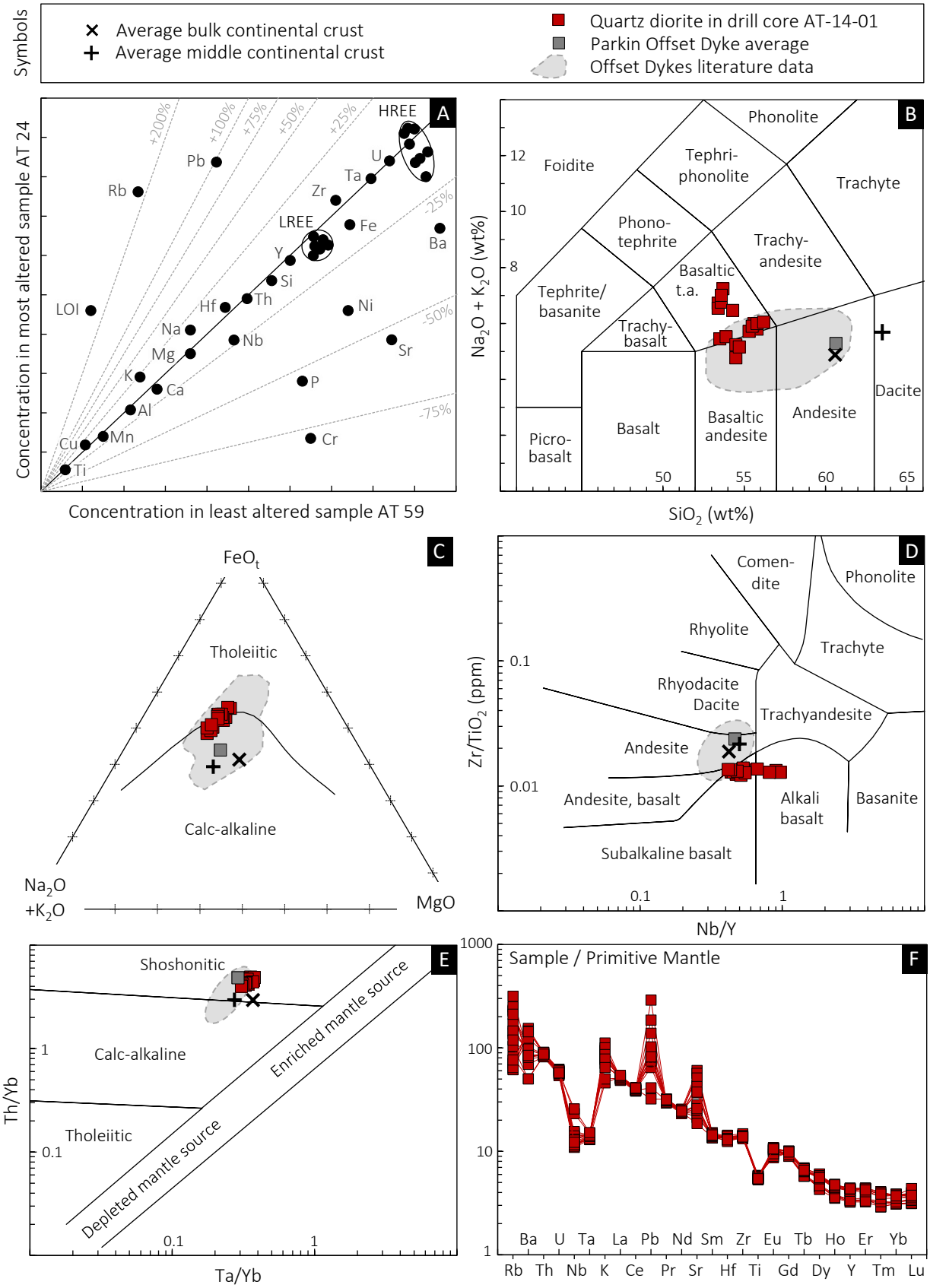

Figure 3.4 A selection of plots used to illustrate the effects of metasomatism on, and the geochemical classification and magmatic affinity of, the quartz diorite in drill core AT-14-01; **A:** isocon diagram after Grant (1986) as a means of testing for secondary element mobility; **B:** TAS classification after Le Bas et al. (1986); **C:** AFM plot after Irvine & Baragar (1971); **D:** discrimination plot after Winchester & Floyd (1977); **E:** discrimination plot after Pearce (1983); **F:** spidergram with normalisation values after McDonough & Sun (1995); crustal values from Rudnick & Gao (2013), Offset Dyke data (excluding outliers) are mainly from Lightfoot et al. (1997c); 2σ-error bars are in each panel smaller than the symbol size.

3.6 Interpretation

Assessment of post-depositional alteration

The macro- and microscopic appearance of the rocks intersected in drill core AT-14-01 has already revealed that effectively all lithotypes therein experienced hydrothermal alteration to some extent and regional metamorphic overprint at least at lower greenschist-facies conditions. Hydrothermal alteration is, for instance, reflected by the LOI, which varies considerably throughout the quartz diorite. The LOI approximates the amount of CO_2 and H_2O and was found to correlate well with the modal amount of hydrous silicates and calcite in those samples. A low LOI of 1.0–1.5 wt% in the samples from 2,060 m is in line with petrographic observations that this portion of the quartz diorite had largely escaped post-depositional alteration (see **Fig. 3.3A–C**). Consequently, the samples AT-19, 20, 21, 22 and 59 (**Tab. 3.1**) should be most representative of the protolith's composition. But how has alteration affected element concentrations and isotope ratios? Traditional wisdom suggests most elements – except the alkali metals and alkaline earth metals – should have remained relatively unaffected by low-*T* alteration unless a very high fluid:rock ratio.

Secondary element mobility can be quantitatively assessed using the isocon method (Grant 1986), i.e., a direct comparison between sample pairs: Contrasting the measured element concentrations of the freshest sample (AT-59) with the most strongly altered but nearby sample (AT-24) reveals that the concentrations of most elements have remained constant within the analytical uncertainty. This is demonstrated by Ti, Al, Th and Ta (typically immobile elements under greenschist-facies conditions; Pearce 1996), which define an isocon with a slope of 1.0, and most other elements plot on, or close to, this line (**Fig. 3.4A**). The slope of the isocon, in turn, suggests little if any volume change during fluid-rock interaction. The elements Na (+14%), K (+22%), Ca (–7%), Ba (–30%), Rb (+226%), Sr (–54%) and Pb (+98%), in contrast, do show mobility, likely due to the breakdown of primary feldspar. It is also possible that the apparent mobility of K, Ba and Rb resulted from primary variations in the modal amount of biotite. Iron (–9%), Ni (–38%) and Cr (–79%) show some mobility as well, whereas the apparent loss of P (–56%) is likely an analytical artefact (P_2O_5 concentrations are close to the detection limit of the EDS-XRF). Overall little element mobility (except for Na, K, Ca, Rb, Ba, Pb, Sr) is also supported by constant inter-element ratios (**Fig. 3.4D,E**), by smooth, parallel and uniform trace element patterns (**Fig. 3.4F**), and by optimal alteration indices (after Nesbitt & Young 1982; Large et al. 2001). Consequently, most of the geochemical data obtained from the quartz diorite should be representative of the protolith.

The measured Nd isotope ratios do not show any correlation with the intensity of alteration (approximated by the volatile content; **Fig. 3.5A**) and are therefore considered representative of the igneous photolith as well; mobility of Sm, Nd and the calculated $^{147}Sm/^{144}Nd$ can be ruled out on the basis of the isocon method (**Fig. 3.4A**). The Pb isotope ratios do not show any correlation with the LOI either (**Fig. 3.5B,C**) but scatter randomly around the average. The Sr isotope ratio, however, does exhibit a strong positive correlation with the LOI (**Fig. 3.5D**), indicating interaction with crustal fluids. The $^{87}Sr/^{86}Sr$ ranges from 0.710 even in the least altered sample, to 0.734 in one of the most altered endmembers, Rb/Sr ratios have a large spread (from 0.03 to 4.5), so do any hypothetical initial $^{87}Sr/^{86}Sr$ ratios. In view of the likely disturbance of the Rb-Sr system, Sr isotopes are not expected to provide any meaningful petrogenetic information (especially if the Rb-Sr mobility was not recent) and are therefore omitted from further discussion.

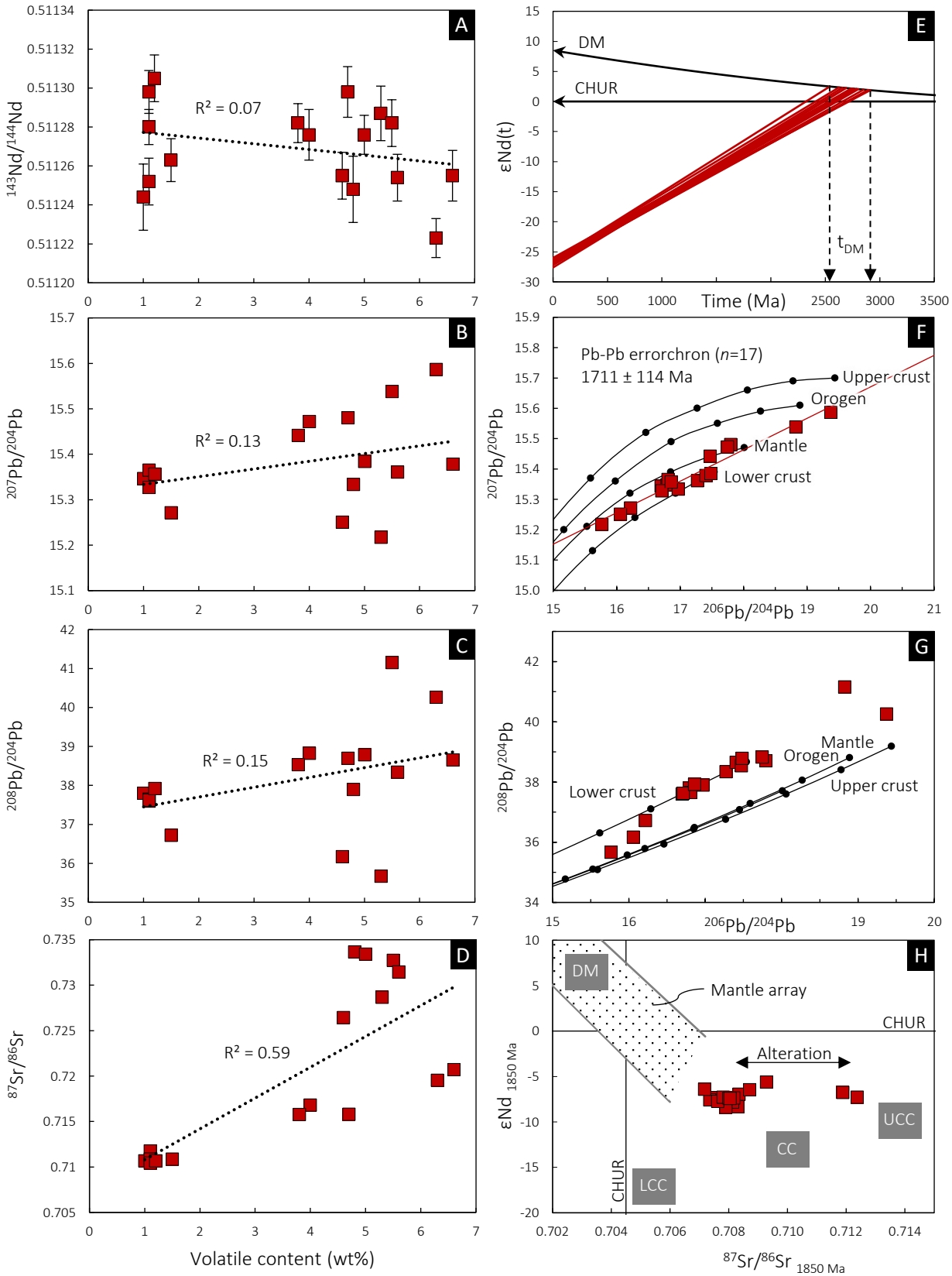

Figure 3.5 Bivariate plots of whole-rock Nd, Pb and Sr isotope ratios for quartz diorite in drill core AT-14-01; **A–D:** measured isotope ratios vs. whole-rock volatile content, illustrating the effects of fluid-rock interaction on the isotopic composition; **E:** neodymium isotope evolution diagram with εNd displayed as a function of time; depleted mantle curve (DM) after DePaolo (1981a,b); **F–G:** lead isotope ratio plots with growth curves after Zartman & Doe (1981) for different reservoirs, with 400 Ma-increments until present; **H:** plot of the initial εNd vs. the initial $^{87}Sr/^{86}Sr$; upper (UCC) and lower continental crust (LCC) after Faure (1986); error bars represent 2σ internal errors but are smaller than the symbol size in most of the panels.

Quartz diorite in AT-14-01 – an Offset Dyke?

The 25 and 52 m-thick quartz diorite intersected in drill hole AT-14-01 into the magnetic peak of the Temagami Anomaly does not resemble, in terms of petrography, geochemistry and isotopic composition, any of the known igneous rocks in the Huronian Basin (**Chapter 2.1.3**). The quartz diorite is certainly no member of the 2.22 Ga Nipissing Suite, nor is it related to the 1.23 Ga Sudbury Dyke Swarm or the 0.6 Ga Grenville Dyke Swarm, as these have a distinct mineralogy, geochemistry, and metamorphic history (cf. Lightfoot & Naldrett 1996a,b; Shellnutt & MacRae 2012). Unlike Archaean diorites typically found in the Abitibi (e.g. Bennett 1978; Hurley 1985; Sutcliffe et al. 1993; Beakhouse 2011), the quartz diorite in drill core AT-14-01 is fine-grained, aphyric, and – despite its mafic mineralogy and overall intermediate calc-alkaline composition – abnormally enriched in incompatible lithophile elements, but conversely also marked by high abundances Fe, Mg, Cr and Ni. As such, it shares many geochemical traits with models of the average continental crust (e.g. Rudnick & Gao 2013, and references therein; **Fig. 3.4B,E** and **Tab. 3.3**) and the composition of so-called post-Archaean shales (pelitic sedimentary rocks representative of the bulk composition of the respective hinterland; Taylor & McLennan 1985, not shown). Such composition would require the assimilation of unrealistically large volumes of crustal material and is thus difficult to reconcile with a mantle-derived magmatic origin of the quartz diorite. It is instead typical of breccias and melt-bearing rocks formed by hypervelocity impacts involving large-scale homogenisation of crustal rocks (e.g. French 1998; Koeberl 2013; Dressler & Reimold 2001; Osinski et al. 2018). The unusual nature of the quartz diorite, the recognition of pseudotachylite in the same drill core, and the proximity to the Sudbury Igneous Complex, all invariably lead to the question as to whether quartz diorite in drill core AT-14-01 could also be impact-related.

Table 3.3 Geochemical data demonstrating the strong crustal affinity of the quartz diorite (QD) in drill core AT-14-01, with major element oxides in wt% and trace element concentrations in ppm.

	SiO_2	Al_2O_3	TiO_2	Fe_2O_3	MgO	CaO	Na_2O	K_2O	Zr	Ce	Yb	Nb	Th	U	Pb	Ni	Cr
QD (*n*=17)	54.5	14	1.12	11.8	3.7	5.6	3.7	2.3	147	64	1.6	9.8	6.9	1.2	15	82	78
MCC [1]	63.5	15	0.69	6.0	3.6	5.3	3.4	2.3	149	53	2.2	10	6.5	1.3	15	34	76

[1] Average composition of the middle continental crust according to Rudnick & Gao (2013)

If the quartz diorite was impact related, it would most likely have been an Offset Dyke of the 1.85 Ga Sudbury Igneous Complex. These impact melt dykes are also of quartz dioritic, monzodioritic to granodioritic composition, and can reach for up to 37 km from the Main Mass into the country rock (e.g. Tuchscherer & Spray 2002). However, conclusive evidence to support this hypothesis fails because of limited drill core data, lack of outcrops, and the absence of a robust radiometric age. Pitfalls of dating the Offset Dykes, were, for example, documented by Ostermann et al. (1996), and include the overall low whole-rock Zr concentrations, the scarcity of newly grown zircon/baddeleyite, and the prevalence of inherited minerals. As a matter of fact, recent attempts to extract datable minerals (zircon, baddeleyite) from the quartz diorite in drill core AT-14-01 have not been successful (Wesley Whymark, pers. comm. 2020). In the absence of outcrops and an absolute formation age, an alternative approach must be used to confirm its origin by the Sudbury impact event. Fortunately, the Offset Dykes are all characterised by a unique and uniform geochemical and isotopic composition, which makes it possible to compare the measured analyses with previously published data. A similar approach of geochemical and isotopic "fingerprinting" has recently been used by Latypov et al. (2019) in order to identify melanoritic (very Zr-poor) autoliths within the Main Mass of the Sudbury Igneous Complex.

Similarities between the quartz diorite and other Offset Dykes are already apparent with respect to major element concentrations (**Fig. 3.5B–C**). Although the composition of the quartz diorite in drill core AT-14-01 is not identical with the average composition of the Offset Dykes (after Lightfoot et al. 1997c), most of the 17 analyses are within the range of previously published data. The few outliers towards higher alkali metal concentrations and lower silica might be explained by secondary element mobility (as it has already been demonstrated for Na, Ca, and Fe; **Fig. 3.5A**) in the course of epidotisation, chloritisation, and carbonatisation. Trace elements, most of which have been shown to be immobile, reveal a clearer picture: Aside from the classification plots in **Figure 3.5D,E**, where the new data and the reference values form tight clusters, a direct comparison of normalised trace element patterns shows a nearly identical composition (**Fig. 3.6**). The spidergram demonstrates that the trace element geochemistry of the quartz diorite is almost indistinguishable from that of the Offset Dykes, not only in terms of element ratios (e.g. Th/U, Nb/Ta, Zr/Hf, Ce/Yb), but also absolute abundances. A perfect fit exists, for example, in the concentrations of Zr, Hf, Nb, Ta, and the REE. Despite the alteration-induced variability, the average concentrations of Rb, Ba and K also match the reference values. The only noteworthy discrepancy exists for Sr, as it appears to be anomalously enriched in the quartz diorite compared to the average Offset Dyke. However, Sr concentrations are extremely variable among the 17 studied samples and, as discussed earlier, have most likely been affected by secondary mobility.

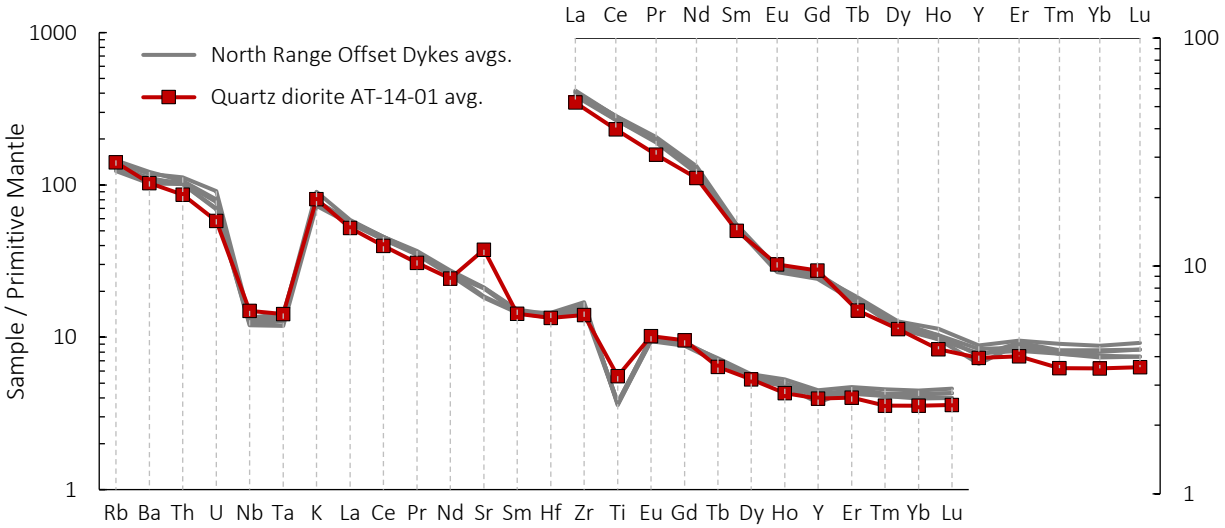

Figure 3.6 Primitive mantle-normalised trace element abundances for the quartz diorite in drill core AT-14-01 and, for comparison, selected Offset Dyke averages of the Sudbury Igneous Complex (Parkin, Foy, Ministic); normalisation values from Sun & McDonough (1989); literature data from Lightfoot et al. (1997c).

Aside from these trace element considerations, studies by Faggart et al. (1985), Naldrett et al. (1986), Deutsch (1994) and Prevec et al. (2000) have established a strong crustal affinity of the Sudbury Igneous Complex in terms of $^{143}Nd/^{144}Nd$ and $^{147}Sm/^{144}Nd$ ratios, reflected by a low εNd (between –6 and –9) at 1850 Ma, i.e., way outside the array of typical mantle-derived rocks. These workers have also shown that the model age of the Sudbury Igneous Complex, that is, the theoretical time elapsed since the rocks (lower Sm/Nd) were separated from the depleted mantle reservoir (higher Sm/Nd) by partial melting, is significantly older than the impact itself, viz. 2.75 Ga on average. Model age and highly negative εNd were interpreted by these authors as entirely inherited from the crustal precursor rocks (juvenile 2.75 Ga Abitibi Subprovince crust and its erosional product, the Huronian Supergroup) that became reworked and more or less homogenised in the

course of impact melt formation. The same isotopic features were found in the quartz diorite of drill core AT-14-01; the present-day εNd of the quartz diorite is nearly identical with the εNd of the Sudbury Igneous Complex as reported in the literature (**Fig. 3.7A**). In full awareness that outliers exist in either data set, depleted mantle model ages, which include information about the Sm/Nd ratio, also overlap with those of the Offset Dykes and the Main Mass of the Sudbury Igneous Complex (**Fig. 3.7B**). Although such model age is not unique to the impact melt-derived rocks of Sudbury (Neoarchaean magmatic rocks would have the same t_{DM} of ca. 2.75 Ga), the *combination* of εNd_0 and t_{DM} suggests that both the Offset Dykes and the quartz diorite share a common source with the same Sm/Nd ratio and experienced the same radiogenic ingrowth of ^{143}Nd.

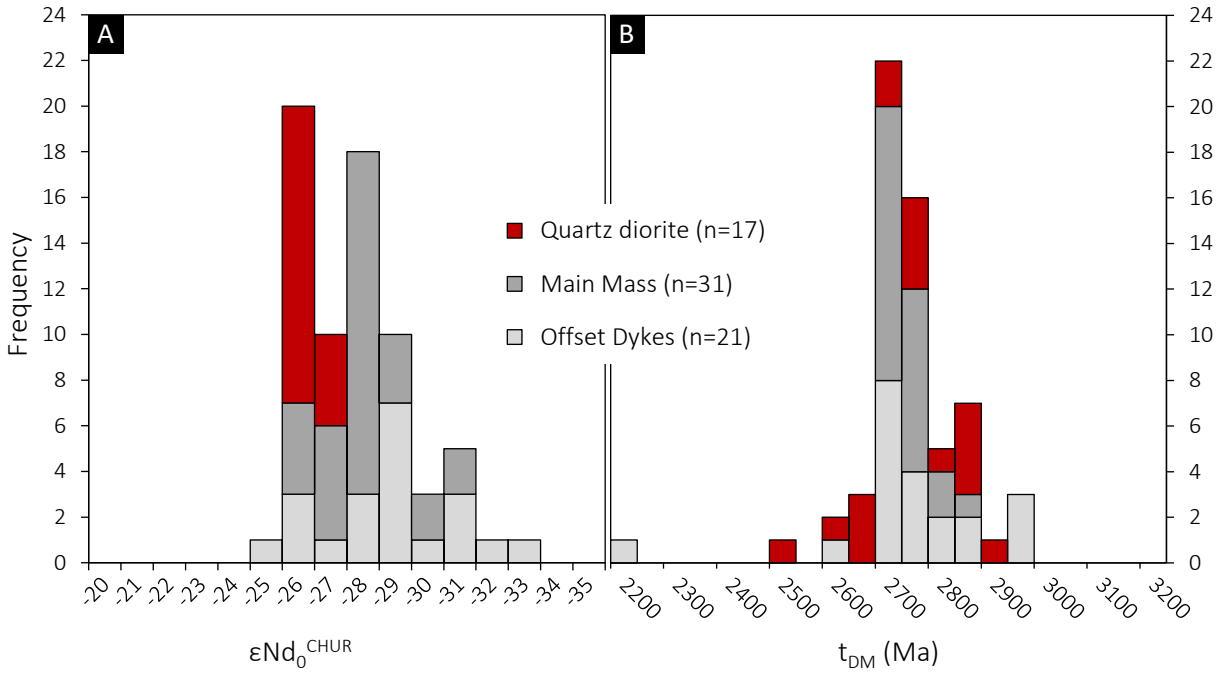

Figure 3.7 Neodymium isotope histograms for the quartz diorite in drill core AT-14-01 and, for comparison, literature data for the Sudbury Igneous Complex; **A:** frequency of the present-day εNd^{CHUR}; **B:** frequency of depleted mantle model ages; literature data are recalculated from Faggart et al. (1985), Prevec et al. (2000), Latypov et al. (2019), plus five previously unpublished data for the Offset Dykes (n=1) and the Main Mass (n=4) (this study, see Appendix_2); not shown are data for the heavily contaminated Sublayer because these are not representative of the initial impact melt composition (e.g. Prevec et al. 2000).

Additional support for an impact melt origin comes from whole-rock Pb isotopes. Like Nd isotopes, the very radiogenic Pb isotope systematics of the Sudbury Igneous Complex are consistent with impact-induced reworking of older crustal material (e.g. Darling et al. 2010b; Petrus et al. 2016), possibly coupled with impact-induced volatile loss of Pb (O'Sullivan et al. 2016; McNamara et al. 2017). In contrast to Sm and Nd, the elements U, Th and Pb are readily fractionated by a range of intra-crustal processes and are more susceptible to later disturbance, accordingly large is the spread of Pb isotope data for the Sudbury Igneous Complex and its host rocks (Darling et al. 2010b). Nevertheless, the Pb isotope ratios determined for the 17 quartz diorite samples from drill core AT-14-014 overlap closely with those previously obtained on other Offset Dykes and the Main Mass. This holds true for thorogenic Pb (**Fig. 3.8A**), uranogenic Pb (**Fig. 3.8B**), and the decay-corrected $^{207}Pb/^{204}Pb_{1850}$ (**Tab. 3.2**), and thus not only implies identical time integrated Th/U ratios, but identical inheritance common Pb. In view of the large variability in reference Pb isotope ratios (**Fig. 3.8**, McNamara et al. 2017), the excellent overlap is of even greater statistical significance and provides strong support for an impact melt-origin of the quartz diorite in question.

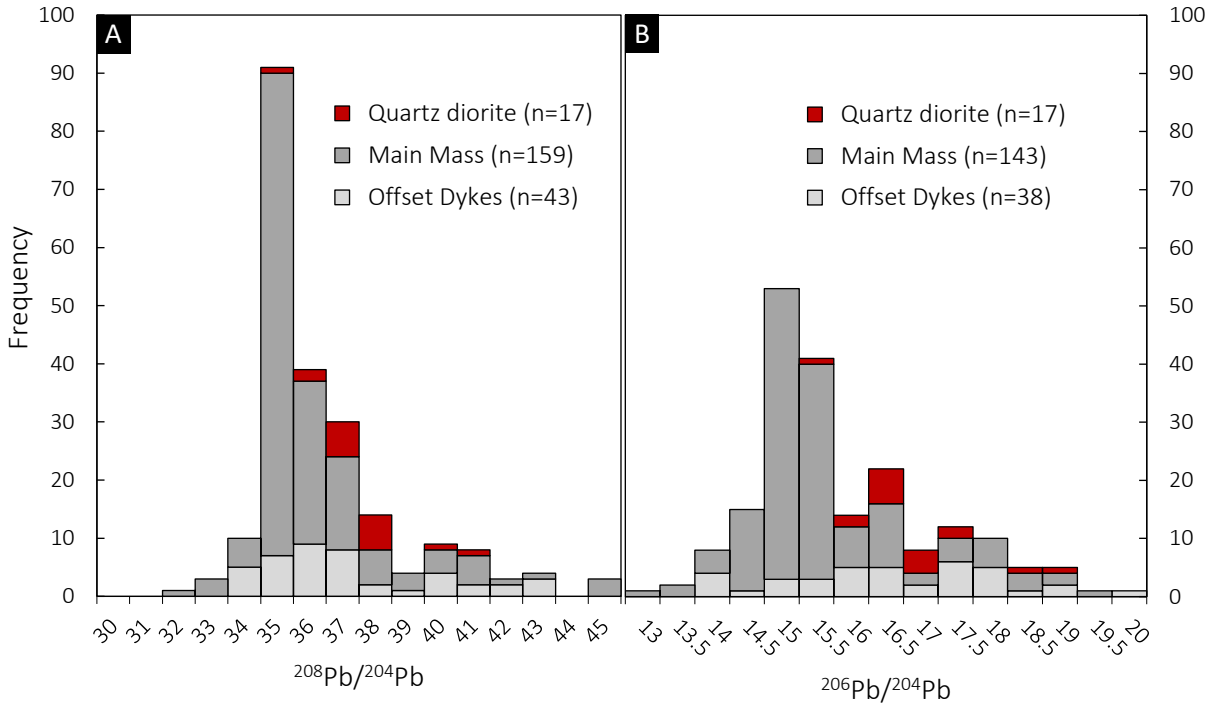

Figure 3.8 Lead isotope histograms for the quartz diorite in drill core AT-14-01 and, for comparison, literature data for the Sudbury Igneous Complex; **A:** frequency of the thorogenic Pb isotope ratios; **B:** frequency of the uranogenic Pb isotope ratios; literature data on whole-rock samples and feldspar are from Dickin et al. (1996, 1999), Darling et al. (2010b), Lafrance et al. (2014) and McNamara et al. (2017), plus five previously unpublished data for the Offset Dykes (n=1) and the Main Mass (n=4) (this study, see Appendix_2); not shown are data for the heavily contaminated Sublayer and the sulphide ores because these were likely not in isotopic equilibrium with, and are therefore not representative of, the initial impact melt composition (McNamara et al. 2017).

The spread in uranogenic Pb isotope ratios in the quartz diorite is sufficiently large to construct a whole-rock errorchron of 1780 +320/–330 Ma or 1711 ± 114 Ma. This date could further help to constrain the emplacement of the rock and to assess its putative relation to the Sudbury impact event, but its interpretation is not unambiguous. The first thing to note is the good linear regression between $^{208}Pb/^{204}Pb$, $^{207}Pb/^{204}Pb$ and $^{206}Pb/^{204}Pb$ for all 17 samples. Second, Th and U concentrations and ratios are constant whereas Pb concentrations vary. Third, there is no geochemical evidence of igneous differentiation within the quartz diorite (e.g. stratigraphic variations in Zr, MgO, or Mg#). Theoretically, the spread in Pb isotope ratios could be a simple consequence of *early* loss of Pb (or gain of Th, U) during hydrothermal alteration (thereby increasing the radiogenic ingrowth of Pb). In this case, the errorchron would erroneously date the timing of the Pb-loss, not the crystallisation age. However, the exact opposite appears true, i.e., a gain of Pb during metasomatism (**Fig. 3.4A**), with no systematic alteration of Pb isotopes (**Fig. 3.5B,C**). Consequently, the spread in Pb isotopes could have also been caused by subtle primary inhomogeneities in Th/Pb and U/Pb as one would expect for a crustal, not necessarily well-homogenised, impact melt. It could also be that the different isotope ratios are linked to different modal proportions of feldspar, since feldspar is known to incorporate more common Pb than most other rock-forming minerals. In these cases, the errorchron dates might be interpreted as the igneous crystallisation age of the quartz diorite. Although none of the above presented hypotheses can be excluded, it is interesting to note that the above date of 1780 Ma, despite its large uncertainty, is outside the known age of most other dyke swarms within the Huronian Basin, but it overlaps with the 1850 ± 1 Ma U-Pb age of the Sudbury impact event (Krogh et al. 1984; Davis 2008; Bleeker et al. 2015).

Discrimination between North- and South Range Offset Dykes

Evidently, the quartz diorite in drill core AT-14-01 and the Sudbury Igneous Complex were produced from the same crustal material with the same Sm/Nd and U/Th/Pb, μ, κ, and common Pb, and experienced the same radiogenic ingrowth of ^{143}Nd, ^{208}Pb, ^{207}Pb and ^{206}Pb. Otherwise the strong similarity in the Nd and Pb isotope systematics would be difficult to explain. Together with identical trace element patterns they provide convincing evidence that the quartz diorite is the product of an impact related melt, here suggested to be a hitherto unrecognised Offset Dyke. Its discovery, however, opens a range of new questions. For instance, how was it emplaced and how can its unusual apparent thickness (50 m), depth (> 2 km) and distant position (45 km) be reconciled with current models of the impact process? Theoretically, the Afton Offset Dyke could represent the distant termination of a radial Offset Dyke analogues to the Tyrone extension of the Foy Offset. Alternatively, it could be part of a concentric dyke, for example, an extension of Manchester or Hess, or a second, outer ring structure; it could also be a discontinuous, breccia hosted Offset Dyke analogues to Frood-Stobie. Also, whether the Afton Offset Dyke represents just the extension of one of the known, or a completely new Offset Dyke, remains at this stage unclear. Most of these questions are beyond the available data and require additional drilling and, ideally, outcrops. Nonetheless, below follows an attempt to tackle these problems from a geochemical perspective.

Lightfoot et al. (1997a) were the first to notice, based on hundreds of analyses, that subtle geochemical variations exist between the different Offset Dykes, yet little variation exists within a given dyke. These differences are most pronounced between North Range and South Range and were attributed by Lightfoot et al. (1997a) to inhomogeneities in the melt sheet composition, resulting from the assimilation of different country rocks (Neoarchaean gneiss and granitoid in the North Range, Palaeoproterozoic sedimentary rocks and intrusions in the South Range).

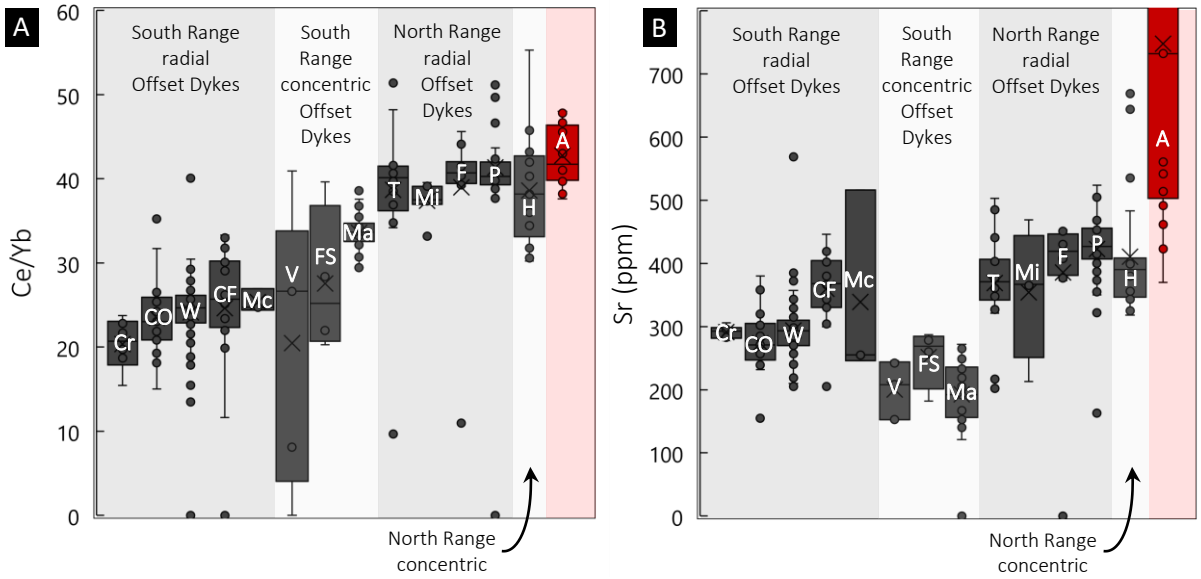

Figure 3.9 Box and whisker plots comparing selected geochemical parameters of the Afton Offset Dyke with those of other Offset Dykes, differentiated by geographical location (North vs. South Range) and dyke geometry (radial vs. concentric); **A:** Ce/Yb ratios; **B:** Sr concentrations; literature data are from Lightfoot et al. (1997c), Wood & Spray (1998), Scott & Spray (2000), Coulter (2015) and Pilles (2016). Abbreviations: Cr = Creighton; CO = Copper Cliff Offset; W = Worthington; CF = Copper Cliff Funnel; Mc = McConnel; V = Vermillion; FS = Frood-Stobie; Ma = Manchester; T = Trill; Mi = Ministic; P = Parkin; H = Hess; A = Afton.

This is especially evident from whole-rock Ce/Yb ratios and Sr concentrations, but a less bimodal distribution also exists with respect to Th, U, Nb, and Ta, and ratios thereof. In this respect, the high Ce/Yb ratio of 38–48 that characterises the Afton Offset Dyke (**Fig. 3.9A**) is typical of all the North Range Offset Dykes and Parkin in particular. Lightfoot et al. (1997a) further noted that differences also exist between radial and concentric Offset Dykes in the South Range. This difference is not observed in Ce/Yb ratios, but it is statistically significant in terms of absolute Sr concentrations and reveals the following trend (**Fig. 3.9B**): South Range concentric dykes have the lowest Sr concentrations, followed by South Range radial dykes, North Range concentric dykes, and eventually, North Range radial dykes. The reason for this somewhat counterintuitive relation is not clear, but it is interesting to note that, despite extensive secondary element mobility, the Sr concentrations in the Afton Offset Dyke do overlap with those of the North Range radial dykes.

Regional differences in trace element abundances between North and South Range Offset Dykes are mirrored by their Pb isotope ratios (**Fig. 3.10**), with those in the South Range having systematically higher time-integrated U/Pb ratios but lower Th/Pb. Darling et al. (2010a,b) proposed that this bimodality resulted from the assimilation of isotopically distinct footwall rocks by the impact melt *prior* to the emplacement of the Offset Dyke, although more local effects, such as the assimilation of wall rocks (post-emplacement), could have played a role as well. In terms of Pb isotopes, the Afton Offset Dyke displays a clear North Range affinity (**Fig. 3.10**, **Fig. 3.11**), suggesting that it was derived from the same melt pool, or interacted with the same wall rocks, as the Foy, Parkin, Ministic and Hess Offset Dykes. Among those North Range Offset Dykes, the best overlap exists with the radial ones, especially Parkin, i.e., the very Offset Dyke closest to the drilling site, and hosted by both Neoarchaean and Palaeoproterozoic country rock. The similarity between the Parkin and the proposed Afton Offset Dyke is particularly interesting as it implies a close genetic relation that is yet to be understood. Perhaps the Afton Offset represents a distal and strongly displaced extension of the Parkin Offset Dyke, perhaps a nearby dyke that was fed by the Parkin, or at least a dyke that evolved in a very similar fashion from the same batch of impact melt.

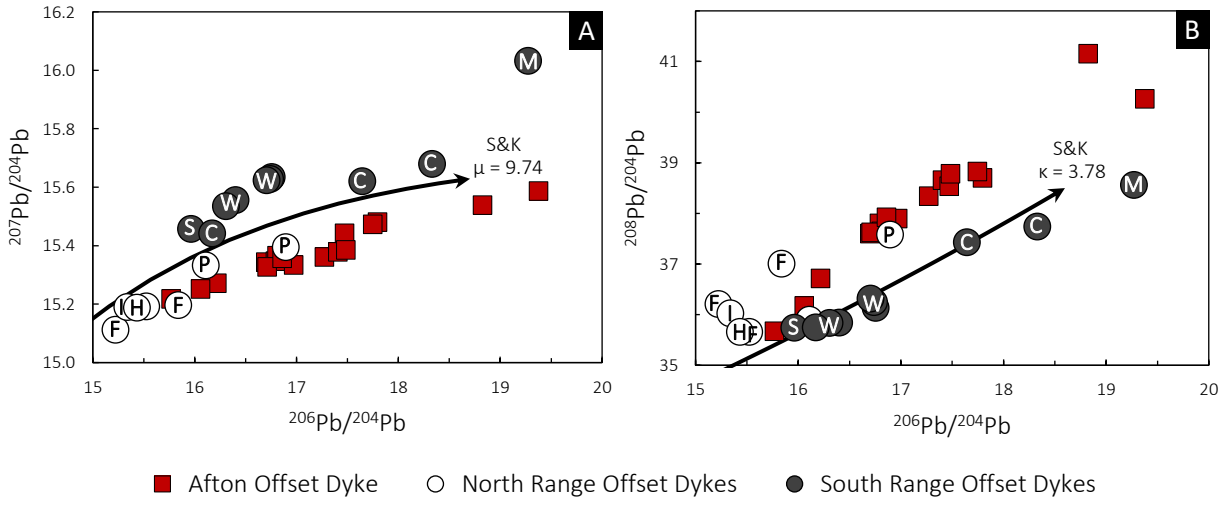

Figure 3.10 Bivariate plots comparing the Pb isotope composition of the Afton Offset Dyke with that of other Offset Dykes; **A:** uranogenic Pb; **B:** thorogenic Pb; note how the Offset Dykes in the North Range and in the South Range of the Sudbury Igneous Complex form two isotopically distinct groups, indicating that they evolved with a different μ and κ; for comparison, the two-stage growth curves after Stacey & Kramers (1975) are shown; literature data are from Darling et al. (2010b). Abbreviations: F = Foy; I = Ministic; H = Hess; P = Parkin; S = Frood-Stobie; W = Worthington; C = Copper Cliff; M = Manchester.

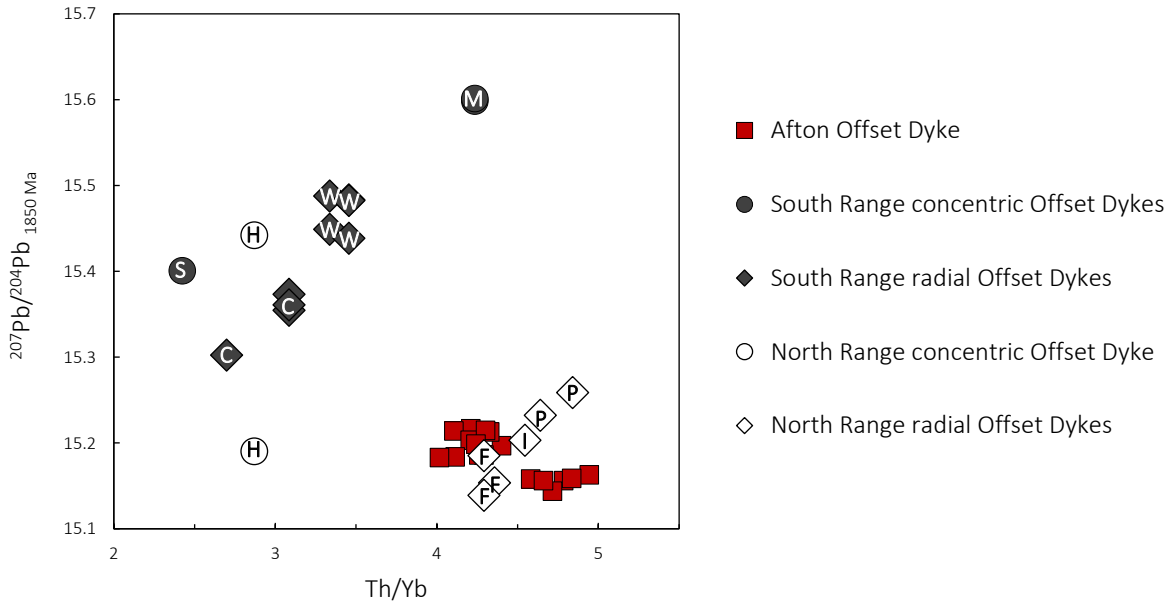

Figure 3.11 Scatter plot comparing the whole-rock Th/Yb ratio vs. the decay corrected $^{207}Pb/^{204}Pb$ ratio of different Offset Dykes, differentiated by geographical location (North vs. South Range) and dyke geometry (radial vs. concentric); Th/Yb ratios are averages based on Lightfoot (2016), Wood & Spray (1998) and Pilles (2016); Pb isotopes from Darling et al. (2010b). Abbreviations: F = Foy; I = Ministic; H = Hess; P = Parkin; S = Frood-Stobie; W = Worthington; C = Copper Cliff; M = Manchester.

A brief note on the (limited) economic potential

In view of the fact that Offset Dyke-hosted Ni-Cu-PGE mineralisation accounts for as much as 50% of the total metal resources of the Sudbury Mining Camp (e.g. Keays & Lightfoot 2004), the discovery of a new Offset Dyke in the Afton Township seems, at first sight, of great economic significance. However, only those dykes proximal to the Main Mass of the Sudbury Complex are actually mineralised (e.g. Frood-Stobie, Copper Cliff, Vermillion, Worthington, Whistle-Parkin), whereas Offset Dykes in a distant position to the impact site (e.g. Hess, Manchester, Tyrone) only contain traces, if any, sulphide (see, for example, Lightfoot 2016; Smith 2017). Unfortunately, no test exists to discriminate geochemically between barren and fertile Offset Dykes, and the only available criterion is their simple lateral distance to the outer margin of the Main Mass (~6 km according to the currently active mines). The reason for this spatial gradient in the metal endowment is not fully understood, as is the emplacement of the Offset Dykes in general, but it appears to be related to the thickness of the original impact melt sheet and/or the limited capability of the impact melt dykes to transport dense (4–5 g/cm^3) sulphide melt over a larger distance. Theoretically, in a distant position of the crater, the thickness of the impact melt sheet would have been too small and, as a simple consequence of mass balances (e.g. Ames et al. 2002; Lightfoot & Farrow 2002; Lightfoot 2016), would have not been able to generate significant amounts of Ni-Cu-PGE sulphide melt by liquid-liquid immiscibility, metal scavenging, and eventual gravitational accumulation of the metal-laden sulphide melt into larger reservoirs. Alternatively, in case of a lateral (horizontal) emplacement of the Offset Dykes (Grant & Bite 1984; Giroux & Benn 2005; Pilles et al. 2018b), the expected decreasing flow velocity, increasing lack of pathways (breccias, fissures in the crater floor) and increasing degrees of undercooling, all would have probably prevented any sulphide melt from being injected deep into the country rock. Thus, the mere distance of the Afton Offset Dyke to the Main Mass (45 km) renders its ore potential unlikely, supported by the fact that no base- or precious metal mineralisation was intersected in the AT-14-01 deep hole.

Laura Offset Dyke

4.1 Summary

Prompted by the identification of an impact-related "Offset Dyke" at Afton Township, ongoing exploration efforts have led to the discovery of another Offset Dyke at Mackelcan Township, 25–30 km northeast of the Main Mass of the Sudbury Complex. The proposed Laura Offset Dyke (so named after its discovery outcrop at Laura Creek), extends continuously over a length of more than 4 km, striking between N05°W and N10°E. Several shallow diamond drill holes reveal that the dyke has a down-dip continuity of at least 80 m, and a true width between 10 and 15 m. The dyke is hosted by brecciated argillite of the Firstbrook Member (Gowganda Formation) and consists of two lithofacies: A medium-grained inclusion-poor quartz diorite (IQD) with < 1 vol% inclusions; and a fine-grained and apparently inclusion-free schlieren-textured quartz diorite (QD) most likely representing the quenched, extensively altered, and strongly contaminated marginal facies of the IQD. The volume proportion of IQD:QD approximates 10:1. However, a clear field, petrographic and geochemical distinction is barely possible; the transition between the two facies is gradual with all respects, as is the intrusive contact of the dyke against the brecciated host rock.

The IQD that constitutes the Laura Offset Dyke is medium-grained equigranular hypidiomorphic rock composed mainly of plagioclase, quartz, and micrographic intergrowths thereof. Chlorite, sericite, epidote, and carbonate are omnipresent, in places rock-forming, and evidently the result of pervasive texturally destructive fluid-rock interaction. Where primary textures are remotely preserved, at least five different types of inclusions could be discerned: (i) Quartzite; (ii) feldspar-rich enclaves; (iii) actinolitic enclaves; (iv) epidosite; and (v) exotic quartz diabase. These likely represent a combination of locally derived (contact-metasomatised) xenoliths and miarolitic cavities. No Cu-Ni-PGE sulphide mineralisation is currently known to be associated with the dyke.

Geochemically, the dyke exhibits a considerable compositional heterogeneity that is in part attributed to be an inherent feature, and in part attributed to secondary element mobility induced through metasomatism and regional metamorphism at lower greenschist facies conditions. Relatively fresh, inclusion-poor and thus likely the least-contaminated samples of the quartz diorite have, on average, a strong mid-/upper crustal (calc-alkaline to shoshonitic) affinity, both in terms of immobile trace elements (150 ppm Zr; 0.85 wt% TiO_2; Th/Yb = 3; Nb/Yb = 4), and whole-rock Nd and Pb isotope ratios ($\varepsilon Nd_0 = -28$; $^{147}Sm/^{144}Nd = 0.11$; $t_{DM} = 2700$ Ma; $\mu = 12$; $\kappa = 3.5$). These features identify the dyke as crustal in origin and therefore as being related to the 1.85 Ga Sudbury impact event. In terms of Ce/Yb and $^{207}Pb/^{204}Pb_{1850}$ ratios, the Laura Offset Dyke has a clear South Range affinity – much like the Worthington, Copper Cliff, and Manchester Offset Dykes – which is arguably the result of contamination with the local country rock after the dyke's emplacement, rather than due to inherited isotopic heterogeneities. The strike of the Laura Offset Dyke makes it a possible analogue to the concentric Hess and Manchester Offset Dykes, but at a greater distance to the Main Mass (25 km), suggesting that the ring defined by Manchester, Hess, and Laura was not perfectly circular. Alternatively, the Laura Offset Dyke could delineate a second, more distant annular through within what might have originally constituted a ~200 km multi-ring basin.

4.2 Local Geology

Mackelcan Township is centred around 46°50N 80°37W, some 45 km northeast of the City of Sudbury, and 10 km northeast of Wanapitei Lake. It borders McConnell Township to the north, McCarthy Township to the east, Rathbun Township to the south, and Aylmer Township to the west. Mackelcan Township covers approximately 100 km² and extends across the eastern part of the Temagami geophysical anomaly. The magnetic peak of the Temagami Anomaly occurs 20 km, the gravity peak 15 km, northeast. Access is provided by the Kukagami Road that joins the Trans-Canada Highway about 10 km east of the town Wahnapitae. After following the Kukagami Road for 25 km north, the Bushy Bay Road and then several unnamed logging and drill roads lead to the area of interest. Water access is provided by the north arm of Matagamasi Lake. Field work by the author and the company involved was preceded by reconnaissance mapping of Ontario Geological Survey (Dressler 1982; Gates 1991). For detailed insights into the local geology, the reader is referred to these publications; a generalised overview is presented in **Figure 4.1.**

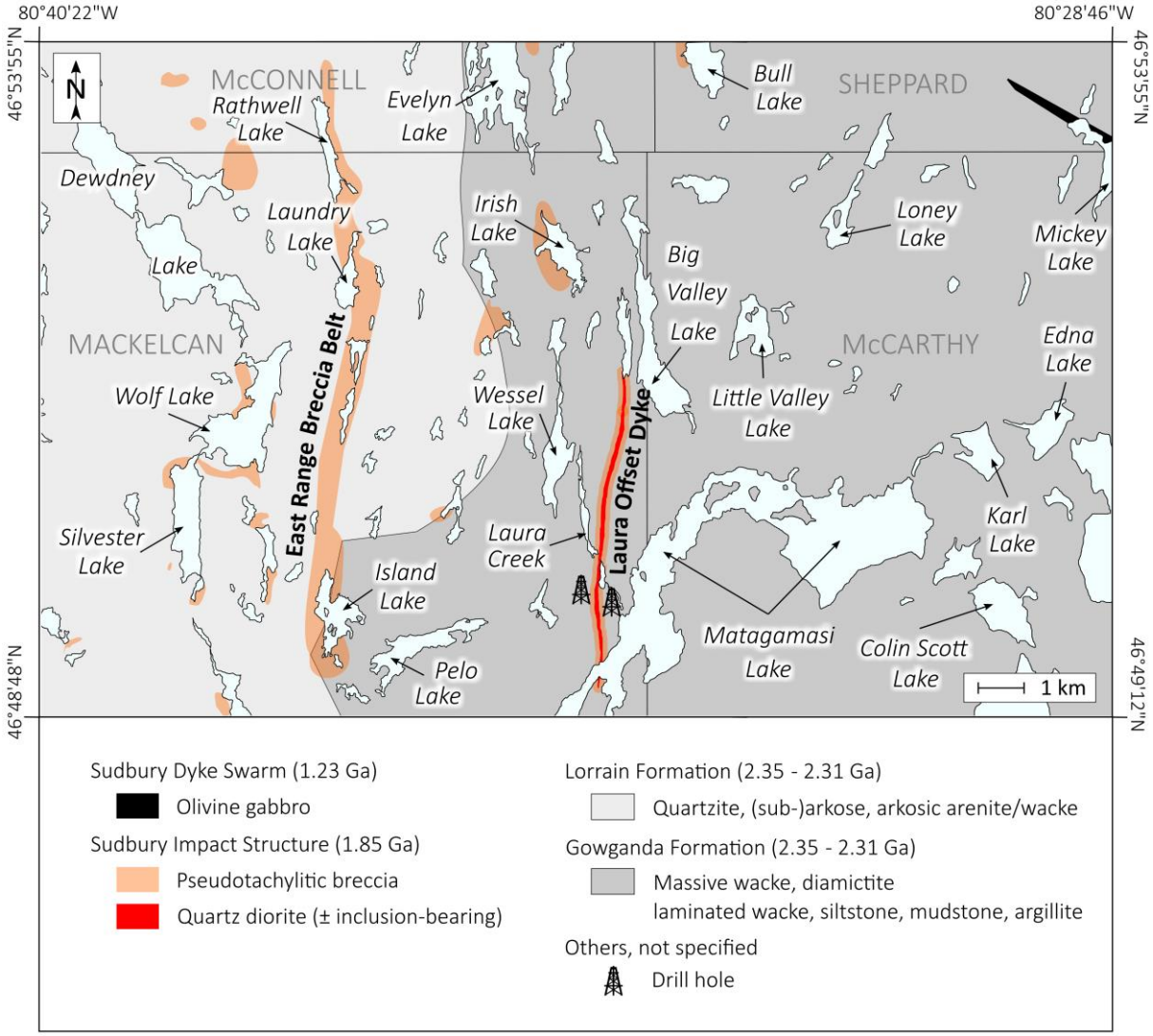

Figure 4.1 Geological map of the Mackelcan and McCarthy townships showing the regional geological and lithostratigraphic context of the quartz diorite at Laura Creek; in part based on maps of Dressler (1981a, 1982) and Whymark (2019).

The entire Mackelcan Township is underlain by Palaeoproterozoic sedimentary rocks of the Cobalt Group (upper Huronian Supergroup). Sandstone of the Lorrain Formation predominates in the western half of the township, pelitic sedimentary rocks of the Gowganda Formation in the east. Although the contact between the two units is not directly exposed in the study area, it is thought to strike approximately N-S based on geophysical evidence (e.g. Easton et al. 2020) and a significant change in outcrop abundance and in relief across the supposed contact.

The Lorrain Formation is a thick and relatively homogeneous package of fluviatile arenite. Dressler (1982) estimated its total preserved thickness at 3,400 m; drilling at Wolf Lake revealed an apparent thickness of 670 m and a gradual transition to the underlying Gowganda Formation (Schandl 2002). In the study area, the Lorrain Formation encompasses quartzofeldspathic rocks ranging from quartzite, (sub-)arkose, arkosic arenite and arkosic wacke. A thickly bedded massive sub-arkose is by far the most common lithology, and wacke becomes more abundant in the lowermost parts of the formation (e.g. Schandl 2002). Sedimentary structures are only really apparent at the outcrop scale and include thick planar bedding, through-cross stratification, and layers of quartz pebbles. Colours range in outcrop from dull white, light grey to different shades of green, beige, pink and brick red, all of which reflects different styles of post-depositional alteration and the presence of different secondary minerals such as hematite, chlorite, carbonate, or albite. Prograde metamorphism is evident by sutured quartz grains that exhibit bulging crystallisation. Lack of biotite, however, indicates that the upper greenschist facies (biotite zone) was either not attained or that biotite was replaced by retrograde chlorite, thus constraining the metamorphic temperature between 280 and 390°C (e.g. Stipp et al. 2002). Rocks of the Lorrain Formation are typically cemented with chlorite and quartz, locally also with albite and carbonate. Silicified lithotypes, such as the quartzite from Wolf Mountain and Cobalt Hill, are very resistant to weathering and erosions. These quartzites are associated with a significant relief (> 100 m).

The Gowganda Formation is likewise thick and extensive but less well exposed due to a higher susceptibility to erosion. In most general terms, the formation is a heterogeneous sequence of wacke, siltstone, and mudstone. The rocks were deposited between ~2.35 and 2.31 Ga in a glaciogenic to pro-deltaic environment (e.g. Young et al. 2001). A two-fold subdivision of the Gowganda Formation in the Cobalt Embayment has been proposed (e.g. Rainbird & Donaldson 1988). The Coleman Member, which is abundant in the east of the study area, in McCarthy Township, comprises massive non-stratified greenish wacke with an occasional matrix-supported conglomerate facies (diamictite). Clasts are highly variable in size and shape, and they lack any sorting. The most common clast lithology is a pink granite. The Firstbrook Member, which conformably overlies the Coleman Member, comprises (from bottom to top) thinly and rhythmically bedded siltstone, mudstone, and eventually sandstone; dropstones are mostly absent (e.g. Rainbird & Donaldson 1988). Argillaceous units of the Firstbrook Member display a diagnostic varve-like bedding of alternating light- and dark grey laminae and may be magnetic and graphitic in places. Unfortunately, these relatively soft rocks are rarely exposed within the study area. The Firstbrook Member is most commonly observed in the eastern part of Mackelcan Township, near the contact to the overlying Lorrain Formation, which confirms an overall younging direction of the Huronian strata from east to west. Rocks of the Gowganda Formation were metamorphosed under lower greenschist-facies conditions as evident by the ubiquitous presence of chlorite and sericite, and the replacement of detrital plagioclase by epidote. Quartz-carbonate-chlorite veining can be intense, and it is locally accompanied by Cu-Au mineralisation. Deformation is restricted to gentle folding and faulting.

Breccias related to the Sudbury impact event ("Sudbury Breccia") are widespread, but their identification often strongly depends on the outcrop quality. Sudbury Breccia is typically found as irregular masses and dykes in all types of country rock, where it appears preferentially developed along contacts between host rocks of varying competence (e.g. arkose–mudstone) or utilising planes of prior weakness such as faults, joints, and bedding plains. Veinlets of ultracataclasite and recrystallised pseudotachylite turned out to be ubiquitous in the region but may be macroscopically mistaken for chlorite veinlets. A massive (megaclastic) type of Sudbury Breccia (**Fig. 4.2A**) is more easily recognised in the field, with continuous exposure over 14 km along a N-trending lineament from Matagamasi as far as Chiniguchi Lake, with an additional 15 km of discontinuous exposure further north and south. Interestingly, this belt strikes concentrically around the Sudbury Igneous Complex. By analogy to the South Range Breccia Belt (Scott & Spray 1999), it will be referred to as the *East Range Breccia Belt*. Sudbury Breccia shows significant petrographic diversity. Mono-, bi- and heterolithic, matrix- and clast supported varieties exist; clasts range in diameter from a few mm to at least 12 m and have a fractal grain size distribution. They are typically sub-rounded with aspect ratios < 2. Most clasts are of very local derivation and underwent little displacement or rotation. Some exceptions of allochthonous or even exotic clasts do, however, occur in the centre of the breccia belt. These could not be linked to any lithology in the vicinity, or in some cases, are entirely exotic (e.g. **Fig. 4.2B**). The texture of the breccia matrix ranges from homogeneous (**Fig. 4.2A**) to flow-banded (**Fig. 4.2C**), cataclastic, devitrified, intersertal, to vesicular and amygdaloidal. Injection dykes of breccia matrix into dilational sites within the ambient host rock were also observed (**Fig. 4.2C**). Locally, these resemble isoclinal or sheath folds.

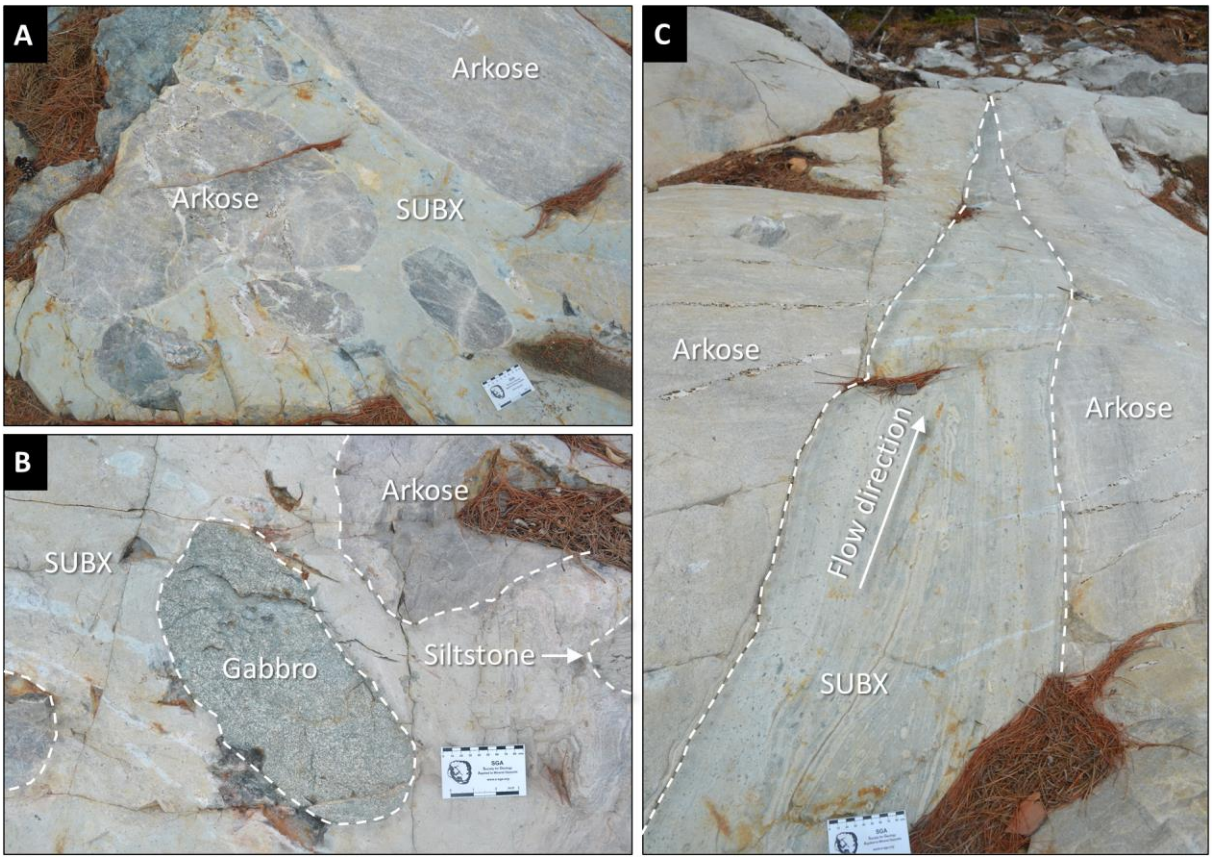

Figure 4.2 Photographs of Sudbury Breccia within the East Range Breccia Belt; **A:** clasts of arkose (Lorrain Formation) in megaclastic Sudbury Breccia; **B:** clasts of exotic gabbro (likely Nipissing Suite) and laminated siltstone (Gowganda Formation); **C:** injection dyke of Sudbury Breccia matrix into brecciated arkose (Lorrain Formation); length of the card = 9 cm; all outcrops are at Island Lake (46°49 36.47N 80°37 18.06W).

4.3 Field Relations

In search for any surface expression of the Afton Offset Dyke (**Chapter 3**), another quartz diorite dyke was discovered (in outcrop) during the field work of 2019 at Laura Creek, eastern Mackelcan Township. The dyke was first recognised on the basis of a historic exploration adit of unknown age and ownership (46°49 56.03N 80°34 25.84W), apparently sunk in order to exploit auriferous quartz veins that crosscut the quartz diorite. It was subsequently possible to trace the dyke over a length of 4,350 m in (sub-)outcrop, from Matagamasi Lake (McCarthy Bay) in the south (46°49 15.83N 80°34 25.59W), as far as Big Valley Lake in the north (46°51 32.93N 80°34 09.39W). Although no exposure could be found further north, it is likely that the dyke extends for additional 4 km as far as Evelyn Lake, judging from the continuation of the topographic lows and lineaments in between. The dyke is ca. 10–15 m wide, exclusively hosted by laminated Gowganda Formation argillite (the Firstbrook Member) and strikes between N05°W and N10°E. The strike parallels that of the East Range Breccia Belt (**Fig. 4.1**), and the dyke itself appears to occupy another narrow (< 30 m) but less well-defined belt of monomict, argillite-hosted Sudbury Breccia.

Outcrop stripping uncovered extensive quartz-carbonate veining within the dyke and its host rock. This was followed by an induced polarisation survey, and in the winter of 2019/2020, diamond drilling of five shallow diamond holes dipping between 40 and 80° and totalling 530 m (VanderWal 2020a,b,c,d; Whymark 2020). Although drilling failed to intersect mineralisation, it provided first insights into the subsurface structure of the dyke and its relationship with the host rock. Drilling revealed an essentially tabular geometry of the dyke, a down-dip continuity for at least 80 m, a true width between 10 and 15 m, and sharp to transitional contacts against the brecciated country rock. These observations are summarised in **Figure 4.3** and will be detailed below.

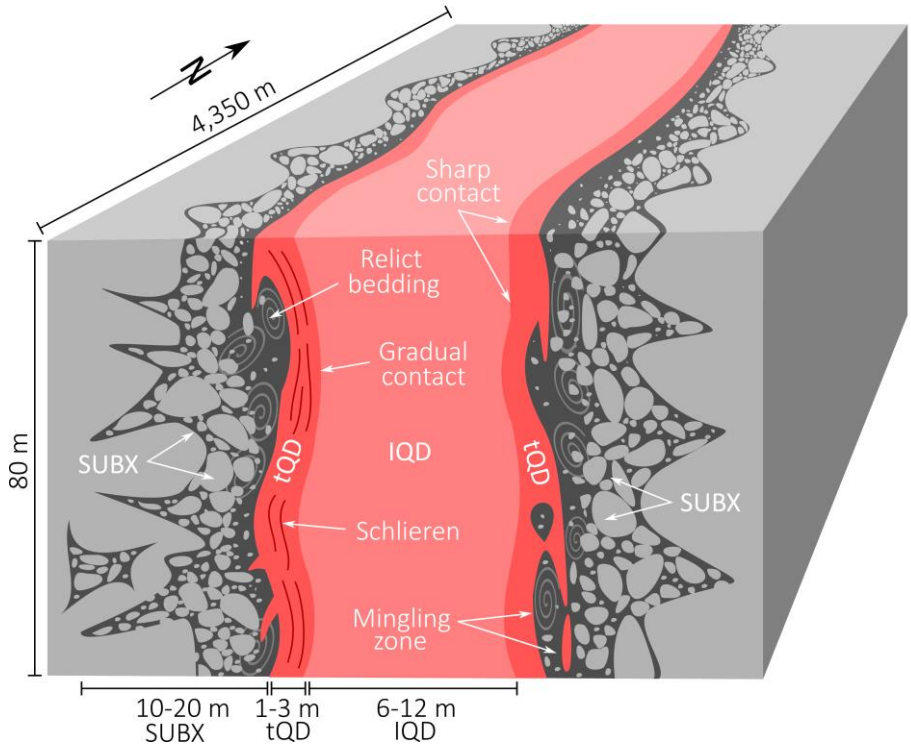

Figure 4.3 Idealised block diagram illustrating the contact relations of and textural features associated with the proposed Laura Offset Dyke; based on field observations and drill cores; not drawn to scale. Abbreviations: SUBX = Sudbury Breccia; tQD = transitional quartz diorite; IQD = inclusion-bearing quartz diorite.

Gowganda Formation

Laminated argillite of the Firstbrook Member (Gowganda Formation) represents the footwall and the hangingwall of the dyke. The argillite consists of varve-like laminae of greyish green siltstone and dark grey mudstone, each between 1 mm and 15 cm thick and laterally persistent. Some mudstone-rich intervals exhibit significant magnetism in the field likely due to the abundance of finely dispersed magnetite. Rice grain-shaped 2 mm large carbonate porphyroblasts and cubes of pyrite occur disseminated throughout, together with quartz-carbonate stockworks and localised quartz-rich crackle breccia. Some samples are extensively foliated. Bedding of the argillite on either site of the dyke dips chaotically and does not follow the regional dip direction of the Cobalt Group, which is either due to small scale folding and faulting (as indicated in vertical gradient aeromagnetic maps; Easton et al. 2020) or due to impact-related brecciation and associated clast rotation. The latter interpretation is favoured because, with closer proximity to the dyke, the argillite becomes increasingly fractured and eventually grades into flow-textured pseudotachylitic breccia.

Sudbury Breccia

Pseudotachylitic breccia distal to the dyke (ca. 20 m) is characterised by a random network of microfractures with little or no displacement. This type of breccia gives gradually way to a more matrix-supported variety closer to the dyke. The latter strongly resembles the typical argillite-hosted Sudbury Breccia (e.g. Parmenter et al. 2002; VanderWal 2021). The bedding of the host rock is heavily deformed (boudinaged, disjointed, and convoluted); the breccia matrix is flow-banded, rarely massive, and typically wraps around clasts of mudstone and argillite. Some of the clasts preserve the original bedding of their host rock and occur in either sharp or gradual contact to the matrix. The size of the clasts is difficult to quantify; they range from a few cm to possibly 1 m in diameter and are typically well rounded. Drag folds around and snowball-like or sigmoid disintegrations of laminated clasts into a laminated matrix were locally observed.

Quartz diorite

Quartz diorite weathers dull white to beige in outcrop; it weathers salmon pink to brick red where cut by extensional quartz-carbonate veins. Rectangular jointing is common. The width of the dyke cannot be reliably ascertained in the field due to a lack of outcrops and the gradual to brecciated nature of the contact. However, drilling indicates a width of 6–15 m. Its contact to the host rock appears subvertical on a larger scale, and highly irregular on the core/outcrop scale. The dyke has been tentatively divided into two facies (VanderWal 2020a,b,c): A *transitional quartz diorite* (tQD) and an *inclusion-bearing quartz diorite* (IQD). The tQD is found along the intrusive contact of the dyke and possibly represents a chilled margin. The rock is non-magnetic, aphantic, greyish green, and of indistinct appearance; it may be easily mistaken for sheared siltstone. tQD is characterised by dark schlieren parallel to the dyke's margin, a diffuse contact against SUBX, and a thickness of 1–3 m. tQD grades over 1–2 m inwards into IQD. The transition can be abrupt, but it is more commonly of gradual nature. The contact between the two units is locally obscured by bodies of SUBX that seem to have spalled off the wall rock and into the dyke, and by apophyses of tQD reaching into the wall rock. The transition between tQD and IQD is marked by the disappearance of schlieren, the appearance of inclusions, and a change in texture from aphantic to phaneritic. IQD is non-magnetic and for most parts texturally uniform, but it becomes slightly coarser in the centre of the dyke. Four types of inclusions were noted. They make up < 1 vol% of the IQD, range in size from mm's to dm's, and display no preferred orientation, and are found evenly distributed throughout.

4.4 Petrography

Inclusion-bearing quartz diorite

The inclusion-bearing quartz diorite from Laura Creek is a non-magnetic greyish green meso- to melanocratic, massive, equigranular, texturally uniform rock with an average grain size of 0.5 mm and crosscut by epidote- and quartz-carbonate veins (**Fig. 4.4A**). In thin section, the rock reveals to be composed predominantly of feldspar within a hypidiomorphic to intergranular texture; primary mafic minerals are absent. The principal rock-forming minerals are, in decreasing order of abundance, plagioclase (50–75 vol%), chlorite (20–25 vol%), carbonate (0–35 vol%), sericite (5–10 vol%), quartz (5–10 vol%), epidote (≤ 5 vol%), leucoxene (< 1 vol%), and apatite (< 0.1 vol%).

Plagioclase occurs as up to 1 mm large tabular sub- to anhedral sutured grains (aspect ratio between 5:1 and 3:1) surrounded by quartz, and in many places intergrown with quartz in a myrmekitic manner. These myrmekitic or micrographic intergrowths (**Fig. 4.4B**) may locally account for up to 30 vol% of the rock. Tabular plagioclases displays polysynthetic twinning of the albite law, a normal faint (gradual) core-rim zonation, retrograde metamorphic replacement by epidote, and extensive hydrothermal alteration to sericite (**Fig. 4.4C,D**). The anorthite-rich cores are always more affected by these processes than the albite-rich rims, the latter being well preserved (**Fig. 4.4C**). It is possible that some of the sericite is secondary after K-feldspar, but microprobe analyses failed to identify any relicts of such. Chlorite occurs as bundles and irregular shaped aggregates interstitial between plagioclase and quartz. Two types of chlorite could be discerned based on interference colour: A golden-brown generation appears to be pseudomorphic after a primary, long-prismatic ferromagnesian mineral (amphibole?); a purple generation of chlorite seems to be related to metasomatism. The purple chlorite generation also occurs in close association with porphyroblastic epidote. Carbonate (calcite ± ankerite) is omnipresent. The carbonates vary in habit from anhedral to euhedral rhombic, and in size from a few µm up to 5 mm (**Fig. 4.4C**). They typically contain minute inclusions of sericite. Quartz is likely a primary constituent of the rock. It occurs mainly as undeformed, anhedral angular interstitial grains of less than 0.2 mm in size and evenly distributed throughout; as up to 1 mm large anhedral subangular optical continuous crystals poikilitically enclosing tabular plagioclase; or as irregular vermicular crystals intergrown with feldspar. Granular quartz locally exhibits a weak undulose extinction, sub-grain formation, and bulging grain boundaries. Leucoxene is found disseminated throughout the inclusion-bearing quartz diorite. It occurs as skeletal rhombic or skeletal octahedral semi-opaque mineral aggregates of < 0.2 mm in size. Microprobe analyses revealed leucoxene to be composed of ilmenite, surrounded by cryptocrystalline selvages of hematite, rutile, titanite and pyrite. Apatite is an accessory constituent. It is found as very small (< 10 µm) acicular grains enclosed in plagioclase and quartz. So far, no zircon or baddeleyite has been observed in thin section.

Some samples of the inclusion-bearing quartz diorite are notably sheared and exhibit a planar fabric defined by chlorite and sericite (**Fig. 4.4E**), which is locally overgrown by later, post-kinematic carbonate porphyroblasts. Furthermore, quartz-carbonate veins crosscut the rock at a high angle to this foliation, and they also cut across earlier epidote veins (**Fig. 4.4F**). While the epidote veins are confined to the inclusion-bearing quartz diorite, the quartz-carbonate veins cut across all lithological contacts. Both types of veins contain traces of pyrite; however, traces of galena, chalcopyrite and free gold have been observed only in the quartz-carbonate veins.

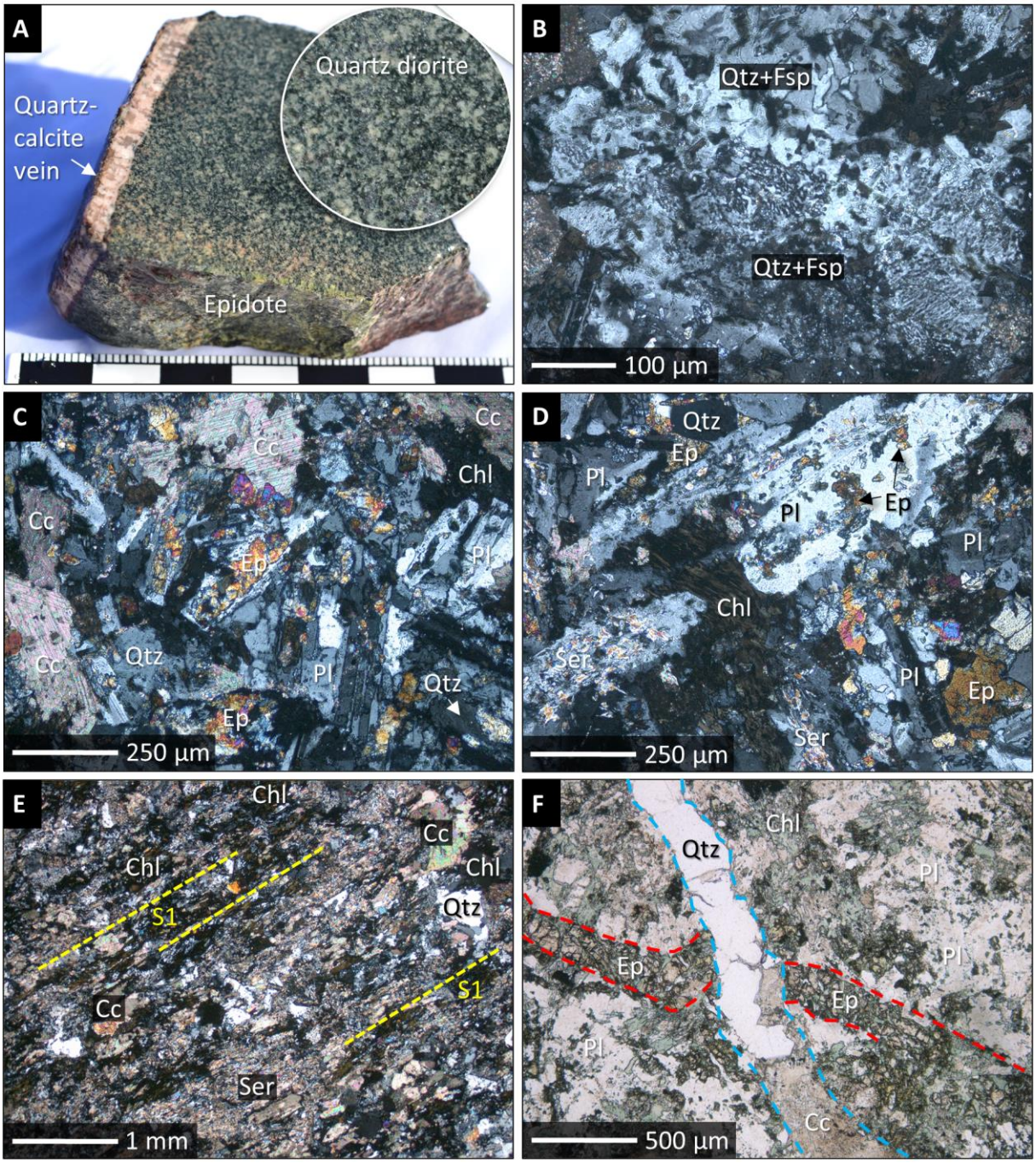

Figure 4.4 Photographs and microphotographs of the inclusion-bearing quartz diorite from Laura Creek, Mackelcan Township; **A:** polished hand specimen (sample LC06); **B:** thin section of the same sample under transmitted light and crossed polars, showing micrographic (granophyric) intergrowths between quartz and feldspar; **C–D:** close-up images (sample LC13) under transmitted light and crossed polars, highlighting the retrograde metamorphic and the hydrothermal replacement of feldspar by epidote and sericite, respectively; with quartz, calcite and chlorite as interstitial minerals; **E:** strongly altered and foliated specimen of the quartz diorite (sample LC01) under transmitted light and crossed polars; **F:** thin section under transmitted light and plane polars, showing the two types of hydrothermal veins thar are found within the quartz diorite; **G:** photograph of a drill core specimen (sample DH1-3 and DH1-3B), showing quartzite xenoliths and an igneous-textured mafic enclave; **H:** thin section of the same specimen (DH1-3B) under transmitted light and plane polars; broken line marks the contact between matrix and mafic enclave; **I:** same thin section under transmitted light and crossed polars; **J:** photograph of a drill core, showing two types of enclaves within the quartz diorite; **K:** thin section under transmitted light and crossed polars, showing an actinolite enclave; **L:** same spot under crossed polars; **M:** thin section under transmitted light and plane polars, showing an epidosite enclave; **N:** same spot under crossed polars. Abbreviations: Fsp = feldspar; Pl = plagioclase; Chl = chlorite; Ser = sericite; Cc = calcite; Qtz = quartz; Ep = epidote.

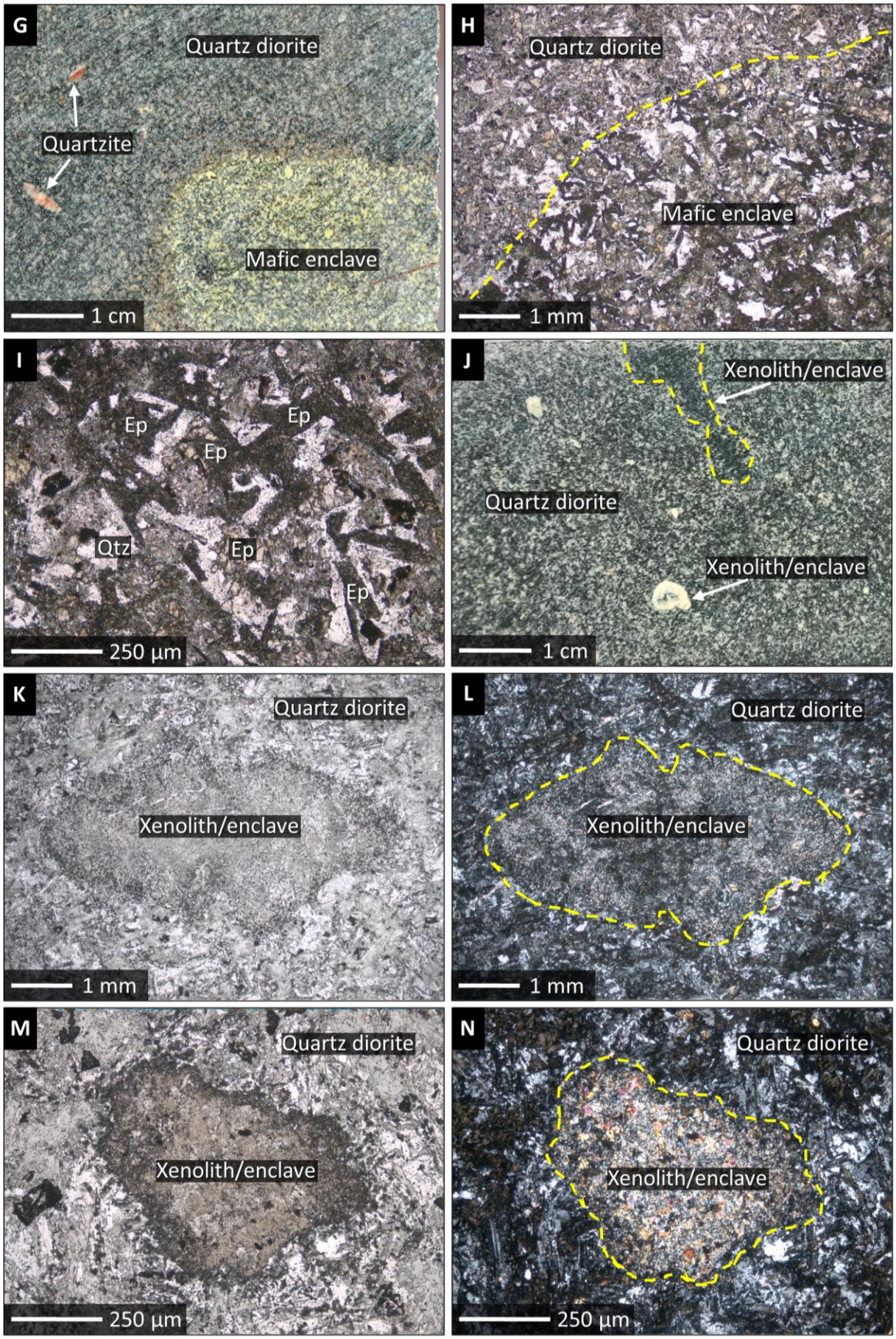

Figure 4.4 (continued)

Inclusions/enclaves

At least five different types of inclusions/enclaves have been noted throughout the IQD and distinguished based on microscopic features. Inclusions account for less than 1 vol% of the total rock, range in size from mm's to dm's, and are found relatively evenly distributed throughout. However, no attempt has been made to systematically assess their distribution nor orientation, as the initial sampling strategy focused primarily on the quartz dioritic matrix.

Quartzite xenoliths are readily identifiable in hand specimen. The xenoliths are well-rounded, pebble-sized, and in sharp contact to the quartz dioritic matrix. They are semi-transparent in hand specimen and locally fractured; in thin section, they are polycrystalline and monomineralic. Quartzite inclusions likely represent refractory xenoliths of the local country rock, either derived from pre-existing quartz veins, or from sedimentary pebbles in the Cobalt Group.

Igneous-textured mafic enclaves with well-defined margins ("ghost clasts") represent the largest yet most enigmatic type of inclusion (**Fig. 4.4G**). They range in size from a few cm to 0.5 m, and in shape from spherical to amoeboid, locally boudinaged, and appear plastically deformed. Petrographically, the enclaves resemble the quartz diorite in terms of mineral content and texture; tabular plagioclase and interstitial quartz are the main rock-forming minerals (**Fig. 4.4H,I**). The only aspect in which the enclaves differ from the quartz diorite is their extent of alteration or metamorphic overprint. Some of the enclaves, for instance, are composed of up to 75 vol% epidote (both granular and pseudomorphic after plagioclase). The transition between such epidote-rich enclaves is relatively sharp in hand specimen, and gradual over less than 1 mm in thin section (**Fig. 4.4H,I**). Conversely, some igneous-textured enclaves are bleached relative to the matrix.

Feldspathic enclaves are the most common type of inclusion. They are typically < 1 cm in diameter, amoeboid to subangular in shape, milky white to pale green in hand specimen, and in sharp contact to the host rock (**Fig. 4.4J**). In thin section, they are shown to be composed predominantly of sericite possibly after alkali feldspar. It is conceivable that these feldspathic enclaves are fragments of the local country rock, or blebs of immiscible (more felsic) xenomelt. A phenocryst origin is unlikely considering their very heterogeneous size, shape, and irregular spatial distribution.

Actinolite enclaves range in size from 2 mm to at least 5 cm. Their shape is highly irregular patchy, and the contact to the matrix is gradational, which makes their identification in hand specimen as well as any attempt to assess their abundance difficult. Actinolite enclaves are dark green and aphantic in hand specimen (**Fig. 4.4J**). In thin section (**Fig. 4.4K,L**) they revealed to be composed of colourless to pale green amphibole ± chlorite. The amphibole occurs as fibrous masses and radiating optical homogeneous bundles, locally intergrown with, and perhaps replaced by, grey chlorite. There is no evidence of amphibole replacing other minerals. Although a xenolith origin of this type of inclusion cannot be ruled out, it is equally possible that these actinolite enclaves represent miarolitic cavities. This would be consistent with their rather diffuse contact, irregular shape, fibrous and monomineralic nature, and the absence of relict textures or pseudomorphs.

Epidosite enclaves were only recognised in thin section and appear relatively scarce. They are less < 1 mm in diameter, spherical, and with sharp contacts (**Fig. 4.4M,N**). They are monomineralic and composed granular, locally fibrous, epidote, and resemble the epidosite of **Chapter 6**. In contrast to the epidote-rich "ghost clasts", the epidosite enclaves preserve no relict igneous textures.

4.5 Geochemistry

General characteristics

Geochemical data of representative grab- and drill core samples from the quartz diorite at Laura Creek are presented in **Table 4.1**. The rock is characterised by a metaluminous, subalkaline and in terms of SiO_2 (50–65 wt%) intermediate composition. The rock is low in TiO_2 (0.85 wt%), rich in Fe_2O_3 (7–12 wt%) but low in MgO (3–6 wt%); Mg# lies between 39 and 43. The LOI ranges from 2.3 to 8.8 wt% and reflects the variable amounts of hydrous silicates (esp. chlorite) and carbonates in those samples. In spite of its relatively evolved character with respect to SiO_2, Mg# and Zr (130–187 ppm), the rock has quite high concentrations of Cr (148–312 ppm) and Ni (62–155 ppm), yet likewise high concentrations of incompatible lithophile elements such as, Th (4–11 ppm), Nb (6–12 ppm), and ΣREE+Y (115–300 ppm). The CIPW normative mineralogy is as follows: 14 vol% quartz, 53 vol% plagioclase, 7 vol% orthoclase, 23 vol% hypersthene, and 2 vol% corundum.

Igneous rock classification

The quartz diorite's composition conforms to basaltic andesite (plutonic equivalent: gabbroic diorite) according to the TAS diagram (**Fig. 4.5B**). In the AFM plot, the rock straddles the boundary between calc-alkaline and tholeiitic affinity (**Fig. 4.5C**). Although the isocon method implies little secondary mobility of most major elements (**Fig. 4.5A**), classification plots using typically fluid immobile trace elements (Ti, Nb, Y, Zr, Th) are generally preferred. In such diagrams (e.g. **Fig. 4.5D**), the samples fall entirely within the field of andesite/diorite. Most classification schemes employing immobile trace elements further support a calc-alkaline to shoshonitic (high-Th, high-K) affinity (e.g. **Fig. 4.5E**). This agrees with mantle-normalised trace element patterns (**Fig. 4.5F**), which exhibit the diagnostic features of (calc-alkaline) arc magmatism; there are pronounced negative Nb-Ta-Ti anomalies, and positive Pb-Sr anomalies. A significant variability is observed among the normalised abundances of K, Rb and Ba, and this results in ambiguously negative to positive anomalies. All REE patterns are uniform and subparallel, marked by a distinct LREE enrichment, a steep slope in the MREE, flat HREE, and a negative Eu anomaly (0.6–0.9) throughout. As seen in **Figure 4.5**, the quartz diorite's composition corresponds to the bulk continental crust.

Nd-Sr-Pb isotopes

A summary of whole-rock radioisotope data for the quartz diorite is presented in **Table 4.2**. All samples (n=10) are quite uniform with respect to their $^{143}Nd/^{144}Nd$ and have very un-radiogenic εNd_0 between –29.45 and –26.74. The calculated $^{147}Sm/^{144}Nd$ ratio ranges from 0.104 to 0.115. There is a weak linear correlation between $^{143}Nd/^{144}Nd$ and $^{147}Sm/^{144}Nd$ (R^2 = 0.70) but without age significance. One-stage Nd model ages (t_{DM}) are between 2588 Ma and 2768 Ma, and 2692 Ma on average. The $^{87}Sr/^{86}Sr$ isotope ratio is very radiogenic with values between 0.718 and 0.728. Some correlation (R^2 = 0.65) exists between the measured $^{87}Sr/^{86}Sr$ ratio and the calculated $^{87}Rb/^{86}Sr$ ratio (ranging from 0.258 to 0.553). The corresponding errorchron (least square regression using *IsoplotR;* Vermeesch 2018) yields, however, only an imprecise datum of 1795 ± 455 Ma (n=10) with a y-intercept at 0.7126 ± 0.027. The $^{206}Pb/^{204}Pb$ ratio ranges from 16.5 to 20, $^{207}Pb/^{204}Pb$ from 15.57 to 15.97, and $^{208}Pb/^{204}Pb$ from 35.8 to 39. The spread in the uranogenic Pb isotope ratios is well correlated (R^2 = 0.94) but yields a questionable Mesoproterozoic (~1.5 Ga) errorchron date. The modelled initial $^{207}Pb/^{204}Pb$ ratio at 1850 Ma ranges from 15.38 to 15.50.

Table 4.1 Major element oxide concentrations (wt%) and trace element concentrations (ppm) in inclusion-bearing quartz diorite, Laura Creek, Mackelcan Township

	LC01	LC02	LC04	LC05	LC06	LC07	LC09	LC10	LC11	LC12	LC13	DH1-1	DH1-3	DH3-1	DH3-2	DH4-1	DH4-2	DH5-1	DH5-2	DH5-3	1-3B
Lat.	46°49 55	46°49 57	46°50 05	46°50 08	46°50 09	46°50 21	46°50 28	46°50 31	46°51 17	46°51 28	46°51 29	51.83 m	48.51 m	9.58 m	20.05 m	29.38 m	37.36 m	98.38 m	101.84 m	103.60 m	48.51 m
Long.	80°34 27	80°34 25	80°34 23	80°34 25	80°34 22	80°34 22	80°34 21	80°34 21	80°34 09	80°34 09	80°34 09	52.00 m	48.67 m	9.71 m	20.20 m	29.63 m	37.49 m	98.50 m	101.92 m	103.73 m	48.67 m
SiO_2	53.6	55.8	49.7	55.9	56.7	54.0	55.4	51.8	54.2	53.3	52.3	54.3	56.3	64.5	54.7	54.9	60.0	55.0	55.4	57.0	52.7
TiO_2	0.86	0.86	0.87	0.78	0.87	0.84	0.88	0.97	0.71	0.74	0.84	0.89	0.88	0.74	0.86	0.93	0.70	0.95	0.85	0.74	0.80
Al_2O_3	15.7	15.8	18.2	15.3	16.2	15.3	15.8	16.9	14.5	14.9	16.3	15.8	16.0	15.1	15.5	16.5	14.9	16.6	15.7	14.7	15.3
Fe_2O_3	9.7	9.4	11.6	11.4	10.0	9.3	9.4	12.3	8.4	9.8	11.2	9.9	10.0	6.8	9.6	10.2	7.7	10.4	9.7	8.7	11.5
MgO	4.9	4.9	6.1	6.0	5.5	4.8	4.8	5.9	4.5	4.8	4.4	5.4	5.5	3.3	5.0	5.7	4.0	5.6	4.8	4.6	4.6
CaO	4.9	4.3	3.0	2.3	3.7	4.8	4.4	2.6	5.3	4.7	3.4	5.0	2.7	1.7	6.4	2.8	4.4	2.8	6.1	6.3	10.5
MnO	0.19	0.15	0.21	0.19	0.18	0.16	0.17	0.21	0.25	0.21	0.26	0.17	0.14	0.08	0.19	0.16	0.15	0.18	0.17	0.16	0.13
Na_2O	2.6	2.3	3.0	3.2	3.2	2.7	3.1	3.5	3.0	2.7	3.4	2.9	2.0	4.5	2.4	3.4	3.7	3.6	2.9	3.0	0.33
K_2O	1.29	1.32	1.70	0.22	0.53	1.25	1.00	0.58	0.71	0.53	0.86	0.77	2.37	0.64	0.73	0.88	0.55	0.62	0.42	0.28	0.46
P_2O_5	0.08	0.08	0.04	0.03	0.05	0.09	0.08	0.01	0.06	0.04	< 0.01	0.09	0.06	0.10	0.09	0.05	0.10	0.05	0.09	0.11	0.14
LOI	6.2	4.9	5.5	4.1	3.3	6.2	5.5	5.1	8.8	8.5	7.1	5.0	4.2	2.3	5.1	4.6	3.9	3.5	4.3	4.7	4.4
Total	100.04	99.66	99.86	99.48	100.13	99.40	100.38	99.80	100.34	100.08	99.93	100.12	100.09	99.76	100.55	100.05	100.04	99.38	100.23	100.20	100.70
Cr	246.2	182.6	175.8	160.0	176.1	160.8	164.2	188.5	148.1	164.8	169.2	271.7	188.9	150.0	175.1	194.3	153.3	191.5	193.0	312.2	193.8
Ni	111.0	83.55	98.64	108.2	97.97	67.85	71.36	94.37	77.61	90.97	92.12	136.6	85.55	61.95	74.36	97.11	77.88	113.7	89.27	155.2	76.23
Cu	55.13	64.00	5.580	16.13	94.03	32.62	38.83	56.08	51.43	34.44	18.85	27.08	16.25	11.87	63.84	16.58	93.55	28.03	28.91	47.80	31.26
Rb	58.50	35.24	60.56	5.742	15.54	34.22	37.64	30.02	18.86	14.36	31.74	20.71	34.07	15.39	22.41	71.41	27.34	43.72	14.79	10.20	6.144
Sr	453.3	488.0	210.0	285.2	503.2	368.2	433.9	262.1	414.8	403.4	273.4	465.2	288.2	337.9	573.1	685.9	547.4	563.1	627.4	636.5	945.1
Y	20.31	16.92	15.32	18.95	21.26	19.13	20.27	25.91	17.34	16.42	16.90	21.17	19.22	19.03	21.01	45.40	25.81	36.61	21.88	19.13	21.86
Zr	139.2	139.0	187.1	167.2	143.6	149.7	139.8	152.1	151.6	145.7	146.5	135.8	138.3	161.8	129.1	149.2	150.2	147.1	143.6	130.0	112.6
Nb	9.333	6.578	8.967	7.856	6.924	7.065	6.578	7.184	7.784	7.337	6.917	10.41	7.494	7.898	6.479	7.086	8.231	7.160	7.466	12.31	6.347
Ba	140.5	138.2	291.2	28.03	108.4	182.2	182.4	92.84	74.41	89.07	128.7	232.7	310.6	61.61	160.1	322.6	175.7	544.9	276.7	188.0	29.80
La	23.42	22.31	35.88	36.27	29.22	20.66	26.49	35.86	31.11	27.05	25.66	32.56	18.47	37.24	28.70	60.17	48.18	51.38	29.81	31.49	24.47
Ce	44.09	48.85	69.59	67.98	59.56	43.34	54.46	60.11	64.43	56.87	55.22	63.42	38.65	71.15	58.04	95.16	82.78	83.49	60.43	62.94	54.07
Pr	5.404	5.450	7.064	8.053	6.895	5.024	6.412	7.825	7.477	6.611	6.200	7.648	4.687	8.567	6.939	13.15	11.02	11.92	7.241	7.647	6.730
Nd	20.60	21.51	30.56	30.33	26.92	17.99	24.97	29.84	26.11	23.29	24.11	26.76	16.25	28.54	23.62	44.33	36.87	41.15	24.17	26.67	23.29
Sm	3.687	4.085	5.971	5.347	5.081	3.211	4.733	5.406	4.479	4.067	4.601	5.665	3.753	5.634	4.951	9.416	7.346	8.593	5.068	5.536	5.324
Eu	1.097	1.076	1.111	0.930	1.303	0.912	1.244	1.341	1.178	1.121	1.168	1.425	0.996	1.440	1.392	2.048	1.691	2.085	1.398	1.543	1.647
Tb	0.538	0.519	0.553	0.600	0.660	0.519	0.622	0.705	0.590	0.550	0.558	0.749	0.593	0.694	0.703	1.374	0.900	1.144	0.720	0.687	0.768
Gd	3.733	3.559	5.165	4.344	4.604	3.301	4.302	4.932	4.089	3.773	4.135	5.000	3.729	4.743	4.606	8.879	6.229	7.698	4.672	4.734	5.054
Dy	3.450	3.224	3.574	3.561	4.016	3.182	3.835	4.424	3.195	2.998	3.337	4.186	3.457	3.631	3.830	7.735	4.763	6.431	3.964	3.714	4.203
Ho	0.709	0.635	0.554	0.674	0.773	0.680	0.740	0.866	0.625	0.593	0.637	0.850	0.749	0.733	0.805	1.609	0.943	1.305	0.819	0.739	0.848
Er	2.255	1.932	2.083	2.075	2.277	2.061	2.192	2.665	1.856	1.768	1.910	2.486	2.147	2.183	2.258	4.697	2.715	3.854	2.308	2.116	2.304
Tm	0.327	0.277	0.239	0.307	0.319	0.296	0.301	0.386	0.259	0.250	0.271	0.353	0.323	0.320	0.331	0.706	0.380	0.559	0.343	0.300	0.320
Yb	2.230	1.866	2.037	2.175	2.167	1.981	2.010	2.625	1.727	1.670	1.842	2.306	2.032	2.090	2.100	4.495	2.415	3.611	2.146	1.899	1.985
Lu	0.343	0.289	0.289	0.341	0.333	0.318	0.307	0.405	0.276	0.273	0.286	0.360	0.321	0.326	0.315	0.714	0.375	0.570	0.323	0.292	0.299
Hf	3.483	3.544	4.534	4.314	3.786	3.645	3.598	3.927	3.686	3.576	3.751	4.120	3.393	4.089	3.150	3.695	4.434	4.231	3.450	3.803	2.868
Ta	0.371	0.431	0.493	0.518	0.407	0.391	0.394	0.411	0.426	0.388	0.397	0.916	0.797	0.546	0.614	0.457	0.759	0.790	0.563	0.556	0.357
Pb	7.682	8.074	4.754	5.337	7.749	5.113	5.826	5.193	35.81	21.53	15.88	8.258	6.492	5.842	9.211	9.469	8.169	10.96	10.83	10.79	17.86
Th	5.593	4.478	8.054	8.646	4.932	5.122	4.599	6.227	6.968	5.776	5.155	5.348	4.981	9.582	4.734	10.48	11.11	9.548	5.406	6.268	4.088
U	0.893	0.816	1.582	1.480	0.871	0.893	0.863	1.198	1.197	0.941	1.137	0.945	1.394	2.161	0.947	1.710	2.762	1.479	1.058	1.251	1.097

Note: Analyses LC01 to LC13 are grab samples; analyses DH1-1 to DH3-5 are diamond drill cores (for details see VanderWal 2020a,b,c,d; Whymark & VanderWal 2020; Whymark 2020)

Table 4.2 Summary of whole-rock Nd-Sr-Pb isotope data for (inclusion-bearing) quartz diorite at Laura Creek, Mackelcan Township

	$^{143}Nd/^{144}Nd$	±2σ	$^{147}Sm/^{144}Nd$	εNd present	εNd 1850 Ma	1-stage t_{DM}	$^{87}Sr/^{86}Sr$	±2σ	$^{87}Rb/^{86}Sr$	$^{87}Sr/^{86}Sr_{1850}$	$^{208}Pb/^{204}Pb$	±2σ	$^{207}Pb/^{204}Pb$	±2σ	$^{206}Pb/^{204}Pb$	±2σ	$^{207}Pb/^{204}Pb_{1850}$
Inclusion-bearing quartz diorite																	
LC01	0.511255	14	0.108	–26.98	–5.97	2588 Ma	0.723420	13	0.553	0.70870	37.0237	25	15.7080	9	17.8568	9	15.44
LC02	0.511255	12	0.115	–26.98	–7.54	2768 Ma	0.721013	12	0.399	0.71039	37.0376	22	15.6955	8	17.6895	9	15.44
LC05	0.511141	17	0.106	–29.21	–7.81	2715 Ma	0.718171	10	0.258	0.71131	38.7084	30	15.9216	10	20.0344	10	15.40
LC06	0.511250	13	0.114	–27.08	–7.47	2756 Ma	0.717668	11	0.286	0.71004	37.3098	28	15.7183	10	17.9597	10	15.44
LC08	0.511128	11	0.105	–29.45	–7.63	2687 Ma	0.722125	12	0.372	0.71223	38.6892	25	15.8191	9	19.3164	8	15.38
LC09	0.511250	10	0.114	–27.07	–7.63	2768 Ma	0.724069	13	0.439	0.71238	37.5817	24	15.7324	8	18.2706	8	15.41
LC10	0.511237	14	0.109	–27.33	–7.57	2649 Ma	0.728008	11	0.515	0.71430	38.9738	27	15.9735	10	19.9983	10	15.46
LC11	0.511162	14	0.104	–28.80	–6.63	2612 Ma	0.722668	12	0.327	0.71395	35.7896	33	15.5724	12	16.4685	9	15.46
LC12	0.511192	10	0.105	–28.20	–6.72	2613 Ma	0.722394	9	0.300	0.71439	36.8259	26	15.6909	9	17.1331	9	15.50
LC13	0.511267	17	0.115	–26.74	–6.56	2765 Ma	0.727214	14	0.519	0.71340	37.1830	28	15.6954	10	17.3735	8	15.48
Average	0.511214		0.110	–28.78	–7.13	2692 Ma	0.722675		0.397	0.71211	37.5123		15.7527		18.2101		15.44
Igneous-textured mafic enclave																	
DH1-3B	0.511305	11	0.138	–26.01	–12.13	3594 Ma	0.708708	10	0.218	0.70290	35.8008	30	15.5270	11	16.5402	10	15.41

$^{147}Sm/^{144}Nd$ and $^{87}Rb/^{86}Sr$ ratios were calculated using measured Sm, Nd, Rb and Sr concentrations, which are given in Table 4.1;
2σ uncertainties of $^{147}Sm/^{144}Nd$ and $^{87}Rb/^{86}Sr$ are < 3% based on the propagated analytical error of Sm, Nd, Rb and Sr concentration data;
$^{143}Nd/^{144}Nd$ ratios are normalised to $^{146}Nd/^{144}Nd = 0.72190$;
2σ uncertainties of $^{143}Nd/^{144}Nd$ are < 0.004% based on the long-term in-house reproducibility of BHVO-2;
2σ uncertainties of $^{87}Sr/^{86}Sr$ are < 0.007% based on the long-term in-house reproducibility of BHVO-2;
2σ uncertainties of $^{208}Pb/^{204}Pb$, $^{207}Pb/^{204}Pb$ and $^{206}Pb/^{204}Pb$ are < 0.18%, < 0.09% and < 0.5%, respectively, based on the long-term in-house reproducibility of BHVO-2;
For sake of readability, all listed 2σ absolute errors only refer to the last significant decimal digits of the measured isotope ratios;
εNd values were calculated relative to CHUR with $^{147}Sm/^{144}Nd = 0.1967$ and $^{143}Nd/^{144}Nd = 0.512638$;
One-stage Nd model ages (t_{DM}) were calculated according to DePaolo (1981a,b);
$^{207}Pb/^{204}Pb_{1850}$ was calculated according to Darling et al. (2010a)

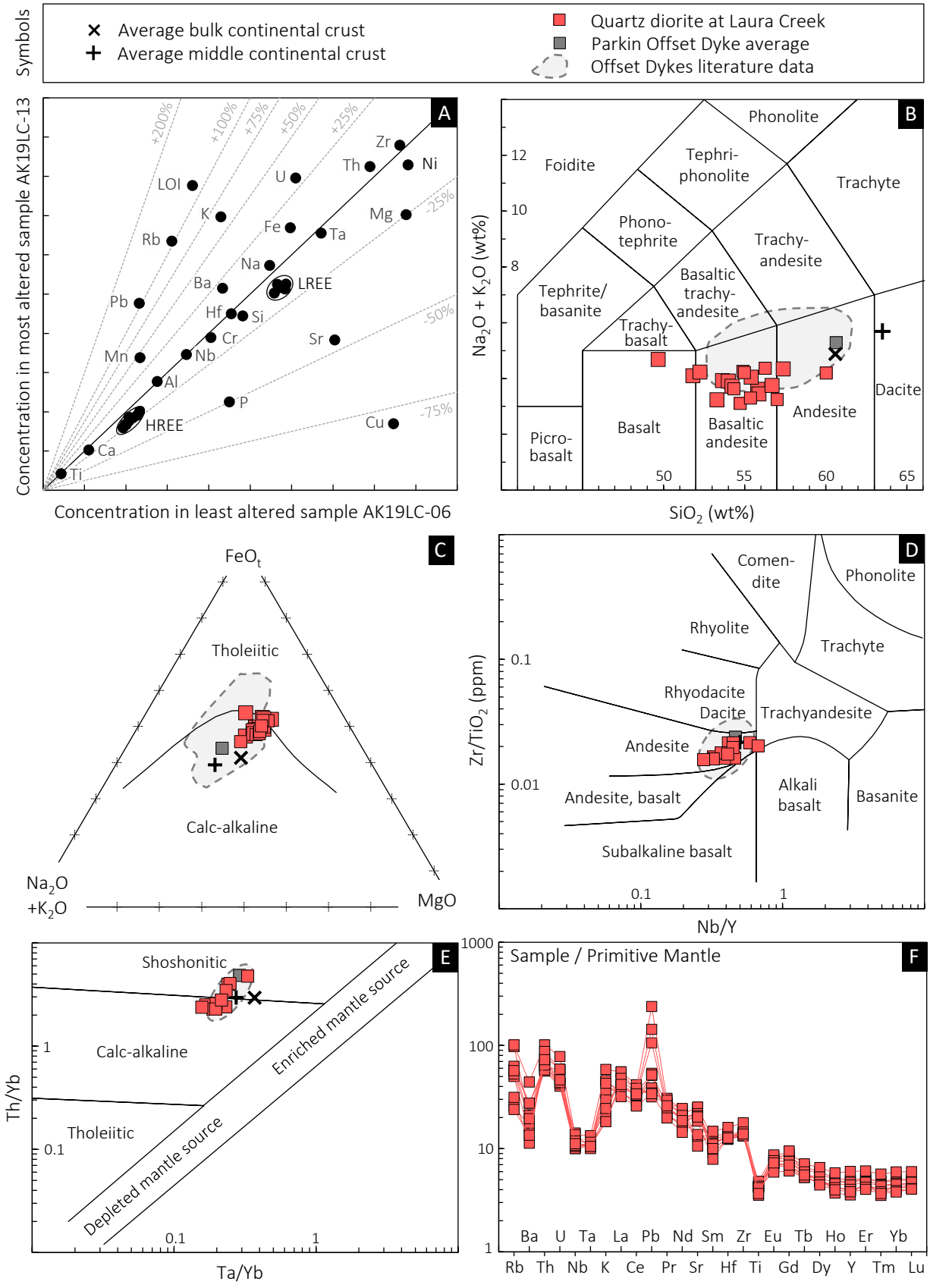

Figure 4.5 Selected plots used to illustrate the effects of metasomatism on, and the geochemical classification and magmatic affinity of, the (inclusion-bearing) quartz diorite from Laura Creek, Mackelcan Township; **A:** isocon diagram after Grant (1986) to test for secondary element mobility; **B:** TAS classification after Le Bas et al. (1986); **C:** AFM plot after Irvine & Baragar (1971); **D:** discrimination plot after Winchester & Floyd (1977); **E:** discrimination plot after Pearce (1983); **F:** spidergram with normalisation values after McDonough & Sun (1995); crustal values from Rudnick & Gao (2013), Offset Dyke data (excluding outliers) are mainly from Lightfoot et al. (1997c); 2σ-error bars are in all panels smaller than the symbol size.

4.6 Interpretation

Assessment of post-depositional alteration

Quartz diorite from Laura Creek underwent extensive sub-solidus alteration as evident from a lack of preservation of primary igneous minerals and textures, and a preponderance of carbonates and hydrous silicates (**Fig. 4.4**). Some of these changes are likely related to regional greenschist-facies metamorphism and are expected to have occurred under isochemical conditions (simple hydration), whereas others (sericitisation, carbonatisation, silicification) are more erratic, seem to be related to later crosscutting hydrothermal veining, and imply an open system behaviour of certain elements. Thus, it is first necessary to assess the extent of secondary element mobility, and to identify those immobile elements that are representative of the protolith's composition.

The isocon method after Grant (1986) offers a straightforward approach to element mobility. Contrasting the composition of the freshest sample available (LC06) with that of the most intensely altered sample from a nearby locality (e.g. LC13) reveals that most elements (esp. HFSE) remained constant within the analytical uncertainty, because they plot on, or close to, a straight line (an isocon) through the origin (**Fig. 4.5A**). The slope of this regression line is close to one, indicating that – despite volatile gain (LOI +115%) – volume change was negligible. Interestingly, Ca, Na, Al, and Si seemingly remained constant as well, indicating that epidotisation and chloritisation were isochemical processes, and are merely a consequence of retrograde metamorphism. Only Sr (–46%), Ba (+19%), and Pb (+105%) appear mobile possibly due to local metal redistribution following the breakdown of magmatic feldspar, and their overall higher solubility. Sericitisation could explain the apparent gain of K (+62%) and Rb (+104%) as well as the large scatter in the TAS diagram (**Fig. 4.5B**), but primary heterogeneities cannot be ruled out. Relatively low element mobility, at least for HFSE, is further supported by constant inter-element ratios (**Fig. 4.5D,E**), uniform trace element patterns (**Fig. 4.5F**), and optimal alteration indices (not shown).

The discussion of fluid mobility also applies to radiogenic isotope ratios. Due to the low capacity of most fluids to carry trivalent REE (e.g. Bau 1991), it is not expected that Sm or Nd were significantly mobilised during low-/medium-grade metamorphism or mild metasomatism, nor should have Sm/Nd elemental fractionation taken place unless the fluid:rock ratio was exceptionally high (e.g. DePaolo & Wasserburg 1979). Immobility of these elements and their isotopes is supported by constant Sm/Nd, $^{143}Nd/^{144}Nd$, and $^{147}Sm/^{144}Nd$ ratios. There is no correlation between the $^{143}Nd/^{144}Nd$ ratio and the whole-rock volatile content, the latter serving as an alteration proxy (**Fig. 4.6A**). Lead isotope ratios, in contrast, show a systematic change with increasing volatile content (**Fig. 4.6B,C**), which holds true for both uranogenic Pb ($R^2 = 0.35$) and thorogenic Pb ($R^2 = 0.44$). Conversely, there is no correlation between the isotope ratios and the U, Th and Pb concentrations, although there is evidence (**Fig. 4.5A**) of both U and Pb having been mobile to a certain extent. Consequently, the Pb isotope data must be treated with caution, and the ~1.5 Ga Pb-Pb errorchron likely reflects the timing of the metasomatism. The Sr isotope ratio shows an irrational scatter way outside the analytical error, even in those samples that were classified as least altered. This scatter persists in the initial $^{87}Sr/^{86}Sr_{1850}$. Further, $^{87}Sr/^{86}Sr$ varies with volatile content ($R^2 = 0.21$) (**Fig. 4.6D**), perhaps due to interaction with crustal (radiogenic) fluids. In face of disturbance in potentially all samples (see **Fig. 4.5A**, **Fig. 4.6H**), Sr isotopes are considered being of no petrogenetic significance, the Rb-Sr errorchron date of ~1.8 Ga as geologically meaningless.

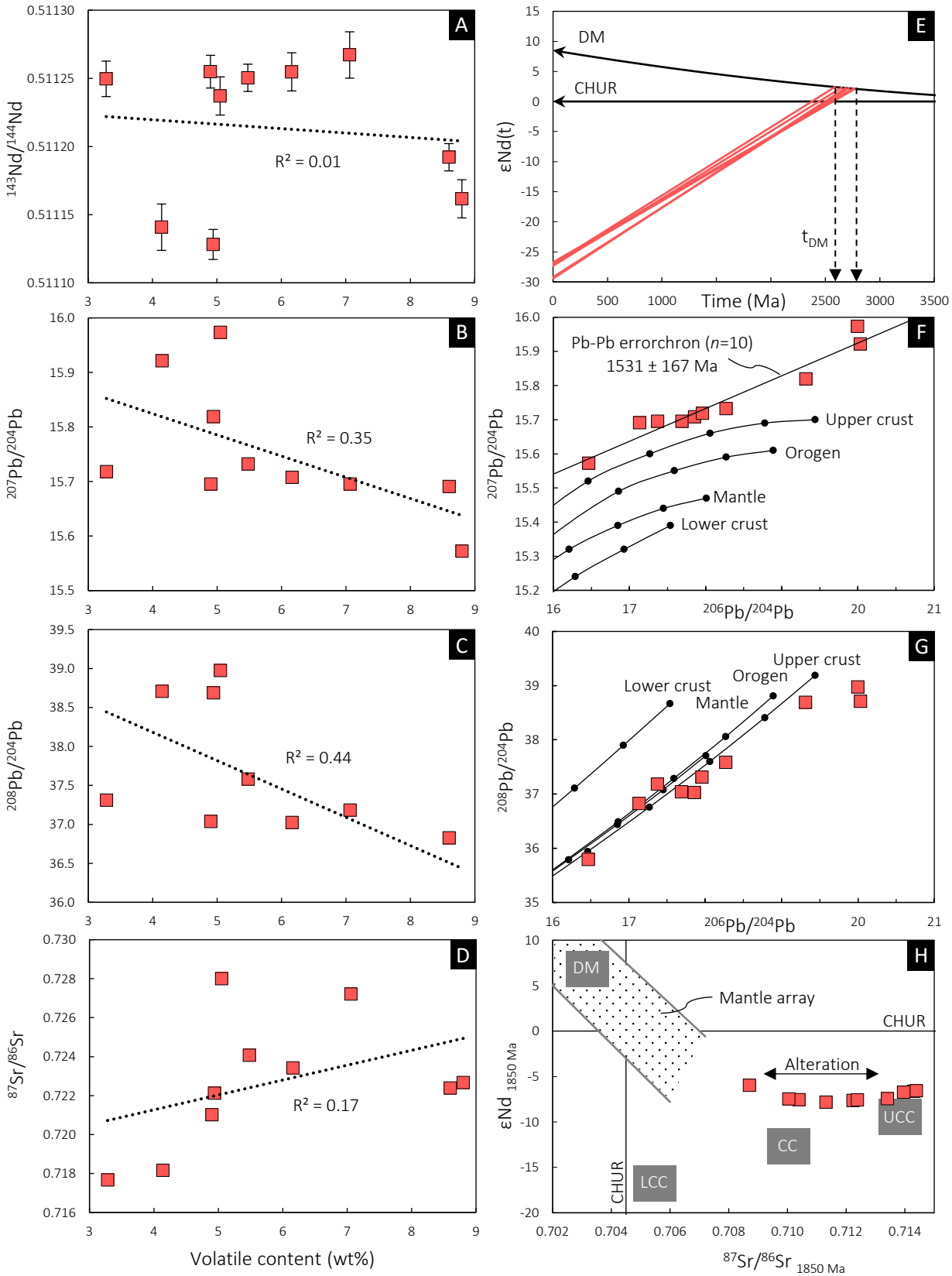

Figure 4.6 Bivariate plots of whole-rock Nd, Pb and Sr isotope ratios for (inclusion-bearing) quartz diorite from Laura Creek, Mackelcan Township; **A–D:** measured isotope ratios vs. whole-rock volatile content, illustrating the effects of fluid-rock interaction on the isotopic composition; **E:** neodymium isotope evolution diagram with εNd displayed as a function of time; depleted mantle evolution curve (DM) after DePaolo (1981a,b); **F–G:** lead isotope ratio plots with growth curves after Zartman & Doe (1981) for different reservoirs, with 400 Ma-increments until present; **H:** plot of the initial εNd vs. the initial $^{87}Sr/^{86}Sr$; error bars represent 2σ internal errors but are smaller than the symbol size in most of the panels.

Evidence of an impact melt origin

The quartz diorite from Laura Creek, though recognised as being part of a larger dyke, differs in many aspects (orientation, lithology, potential field data, geochemistry) from magmatic dykes and dyke swarms known in the wider region (see **Chapter 2.1.3**). Instead, its close spatial association with Sudbury Breccia, its proximity to the Afton Offset Dyke (~20 km), its orientation conspicuously parallel to the East Range Breccia Belt (**Fig. 4.1**), and its mere classification as a calc-alkaline inclusion-bearing quartz diorite, all raise the question whether the dyke from Laura Creek could also be impact-related, perhaps another Offset Dyke of the Sudbury Igneous Complex.

As discussed before in **Chapters 2.1.4** and **3.6**, igneous rocks of the 1.85 Ga Sudbury impact event – the quenched impactites (the Offset Dykes) in particular – have a unique geochemical and isotopic fingerprint, thereby providing an alternative means to their identification, especially where field relations are equivocal, and the opportunity for radiometric age dating is limited (e.g. Latypov et al. 2019). Having provided evidence that the measured trace element concentrations and isotopic ratios (expect for Rb, Ba, K, Ca, Sr, Mg, Pb) are representative of the protolith, these now invite to test for such geochemical correlation. Comparing the average composition of the quartz diorite from Laura Creek with the average composition of the Offset Dykes reveals nearly identical trace element patterns (**Fig. 4.7**). The quartz diorite and the Offset Dykes, for example, have the same steep slope in normalised REE (Ce/Yb_N 7.5), the same weakly negative Eu anomaly, and almost identical absolute REE abundances. They also share the same Nb/Ta, Zr/Hf, Th/U, Th/Nb, Nb/Y and Zr/Ti (**Fig. 4.5D,E** and **Fig. 4.7**), which are sensitive ratios as to the type of a melt source, the degree of fractional crystallisation, and the extent of lithospheric contamination (e.g. Hofmann 1997; Pearce 2008), all of which provides strong evidence of a genetic relationship between the Sudbury Igneous Complex and the dyke in question. Also note how well these features correspond to the estimated bulk composition of the continental crust (**Fig. 4.5D,E**; Rudnick & Gao 2013), exactly as one would expect for impactites generated by large-scale melting and homogenisation of calc-alkaline rocks (the Abitibi Subprovince) and their sedimentary derivatives (the Huronian Supergroup) (cf. Koeberl 2013). Thus, the trace elements, and to a lesser extent also the major elements, are consistent with the quartz diorite being a product of the Sudbury impact event.

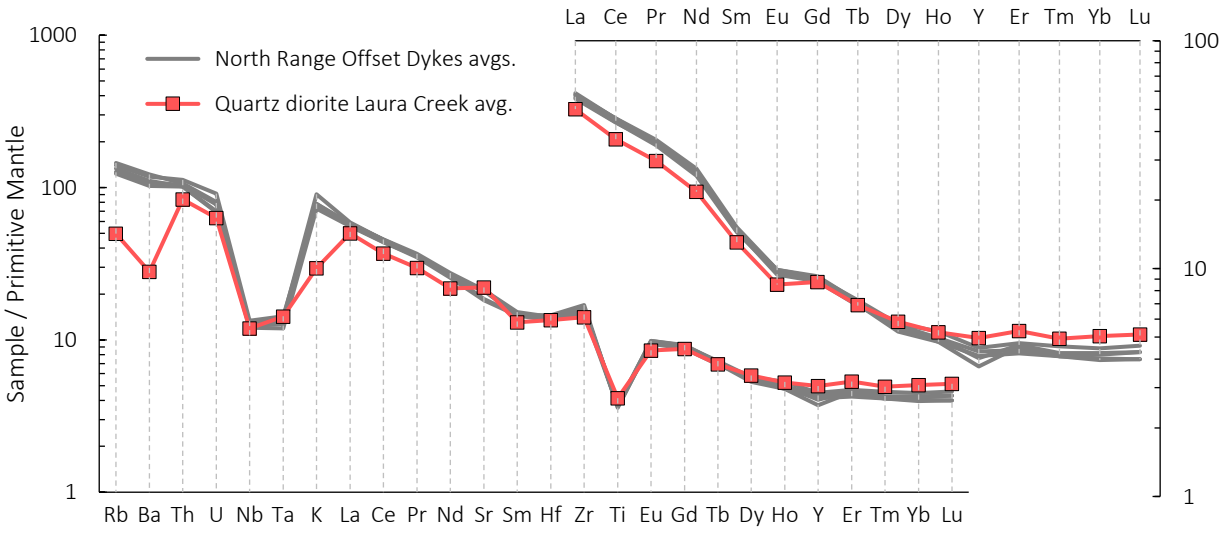

Figure 4.7 Primitive mantle-normalised trace element abundances of the quartz diorite from Laura Creek and, for comparison, selected Offset Dyke averages of the Sudbury Igneous Complex (Parkin, Foy, Ministic); normalisation values are from Sun & McDonough (1989); literature data are from Lightfoot et al. (1997c).

Aside from these trace element considerations, many studies have established a unique and very crustal isotopic signature of the Sudbury Igneous Complex (e.g. Faggart et al. 1985; Naldrett et al. 1986; Deutsch 1994; Dickin et al. 1999; Prevec et al. 2000; Darling et al. 2010b; Petrus et al. 2016; Kenny et al. 2017; McNamara et al. 2017). The same signature also characterises the quartz diorite from Laura Creek. For instance, both the Sudbury Igneous Complex and the quartz diorite have a low (i.e., a very un-radiogenic) $^{143}Nd/^{144}Nd$ ratio, reflected in a strongly negative present-day εNd (**Fig. 4.8A**). They also have the same $^{147}Sm/^{144}Nd$ ratio of 0.11. Further, the model age of the quartz diorite (t_{DM} = 2700 Ma) is exactly as expected for an allochthonous impactite generated by large-scale crustal melting and homogenisation of a 2.75 Ga juvenile crust (the Abitibi Subprovince) and its sedimentary derivatives (the Huronian Supergroup), and it is (within ± 50 Ma) identical to the model age of the Sudbury Igneous Complex (**Fig. 4.8B**). Put in other words, the strong resemblance in Sm-Nd isotope systematics indicates that the quartz diorite from Laura Creek and the Sudbury Igneous Complex have the same time-integrated Sm/Nd and experienced the same radiogenic ingrowth of ^{143}Nd, thereby providing strong indication of a genetic relationship.

Similarly, the Pb isotope signature can be used to argue for an impact melt origin (e.g. Darling et al. 2010b; Koeberl 2013), as both the Sudbury Igneous Complex and the dyke from Laura Creek cluster around a measured $^{208}Pb/^{204}Pb$ ratio of 35 (**Fig. 4.9A**), a measured $^{206}Pb/^{204}Pb$ ratio of 16 (**Fig. 4.9B**), and a modelled $^{207}Pb/^{204}Pb_{1850}$ of 15.4 (see also: McNamara et al. 2017). This not only implies identical time integrated Th/U ratios, but identical inheritance of common Pb. Such Pb isotope signature is, of course, no definite proof of an impact origin. However, in combination with the above presented petrographic criteria, trace element patterns, and Nd isotope features, ample of evidence exists to accept the working hypothesis that the quartz diorite from Laura Creek represents another Offset Dyke of the Sudbury Igneous Complex.

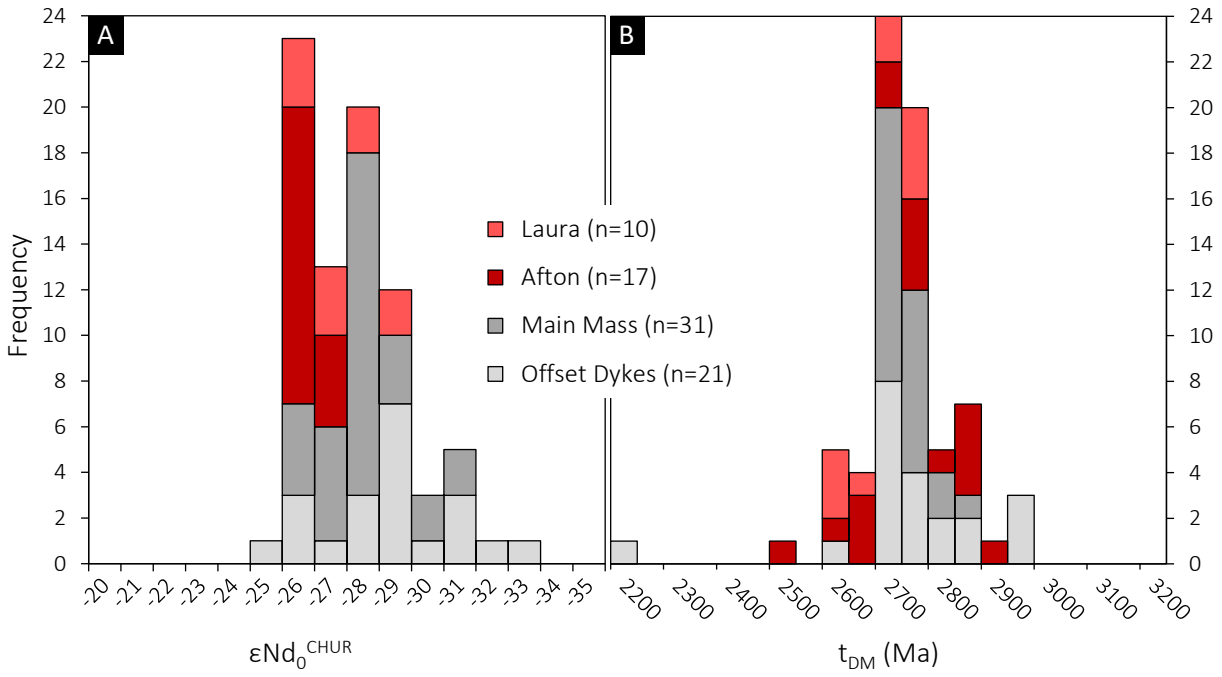

Figure 4.8 Neodymium isotope histograms for the (inclusion-bearing) quartz diorite from Laura Creek, Mackelcan Township and, for comparison, literature data for the Sudbury Igneous Complex; **A:** frequency of the present-day εNd^{CHUR}; **B:** frequency of depleted mantle model ages; literature data are recalculated from Faggart et al. (1985), Prevec et al. (2000), Latypov et al. (2019), plus five previously unpublished data (Appendix_2) for the Offset Dykes (*n*=1) and the Main Mass (*n*=4), and data for the herein discovered Afton Offset Dyke (*n*=17); not shown are data for the heavily contaminated Sublayer because these are not representative of the initial impact melt composition (e.g. Prevec et al. 2000).

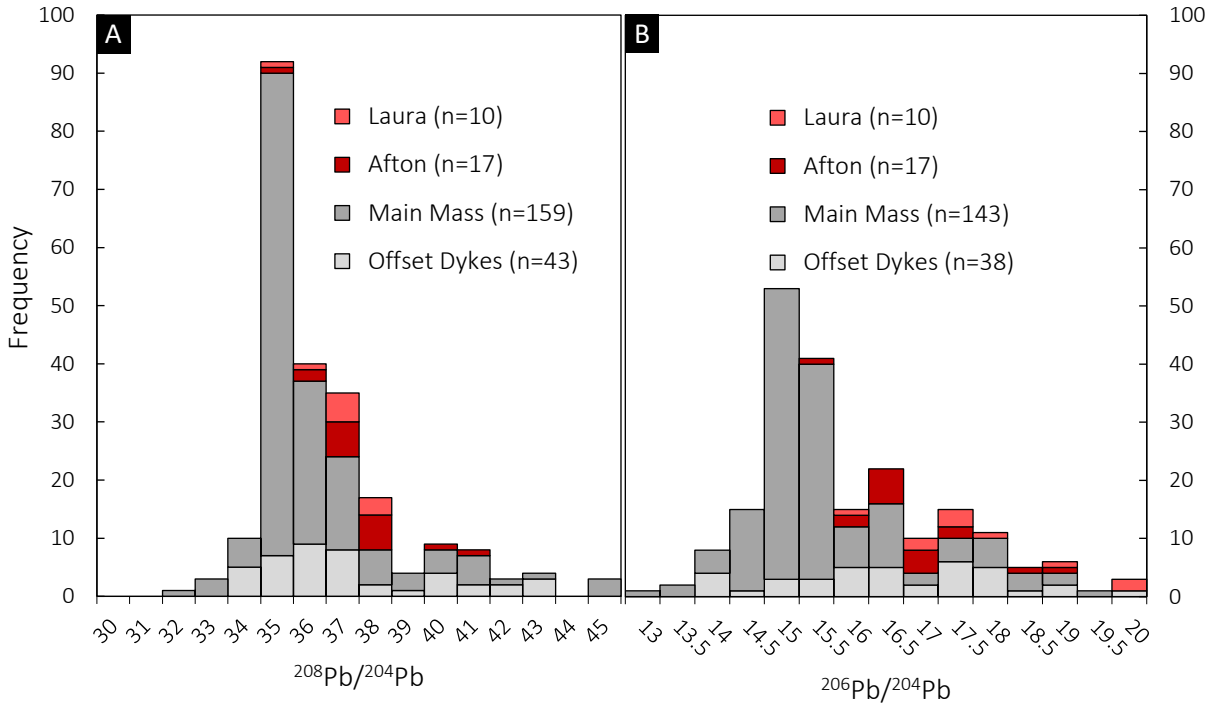

Figure 4.9 Lead isotope histograms for the quartz diorite from Laura Creek and, for comparison, literature data for the Sudbury Igneous Complex; **A:** frequency of the thorogenic Pb isotope ratios; **B:** frequency of the uranogenic Pb isotope ratios; literature data on whole-rock samples and feldspar are from Dickin et al. (1996, 1999), Darling et al. (2010b), Lafrance et al. (2014) and McNamara et al. (2017), plus five previously unpublished data (Appendix_2) for the Offset Dykes (*n*=1) and the Main Mass (*n*=4), and the herein discovered Afton Offset Dyke (*n*=17); not shown are data for the heavily contaminated Sublayer and the sulphide ores because these were likely not in isotopic equilibrium with, and are therefore not representative of, the initial impact melt composition (McNamara et al. 2017).

Geochemical and isotopic discrimination

Having made the case for the "*Laura Offset Dyke*", it is now worth considering how the dyke is related to the 18 other Offset Dykes within the Sudbury Impact Structure, and the nearby Afton Offset in particular. As discussed before (**Chapter 3.6**), Lightfoot et al. (1997a) recognised systematic compositional differences between those Offset Dykes in the North Range of the Sudbury Impact Structure (Trill, Ministic, Cascaden, Foy, Parkin, Hess), and those Offset Dykes located in the South Range (Worthington, Vermillion, Creighton, Copper Cliff, Frood-Stobie, Kirkwood-McConnel, Manchester) as well as subtle differences between radial and concentric Offset Dykes. According to Lightfoot (2016), these regional differences are especially pronounced with respect to Ce/Yb ratios and Sr concentrations. In that sense, a compilation of published geochemical data for the different Offset Dykes (**Fig. 4.10**) reveals a strong South Range affinity of the proposed Laura Offset Dyke. Its Ce/Yb ratio (20–30), for example, is identical to the Copper Cliff, Worthington, Kirkwood-McConnel and Manchester Offset Dykes, but it also overlaps to a certain degree with the Ce/Yb of the Frood-Stobie and Vermillion Offset Dykes (**Fig. 4.10A**). All the North Range Offset Dykes, in contrast, have invariably higher Ce/Yb ratios (> 30) than the Laura Offset Dyke, suggesting that its melt source and/or subsequent evolution was distinct from the Offset Dykes in the North Range. This geographical divide also exists, but is less pronounced, with respect to Sr concentrations (e.g. Lightfoot 2016). Unfortunately, the large range in Sr concentrations within the Laura Offset Dyke (likely due to metasomatism) does not permit to make a clear distinction; there is a substantial overlap with all groups and types of Offset Dykes (**Fig. 4.10B**).

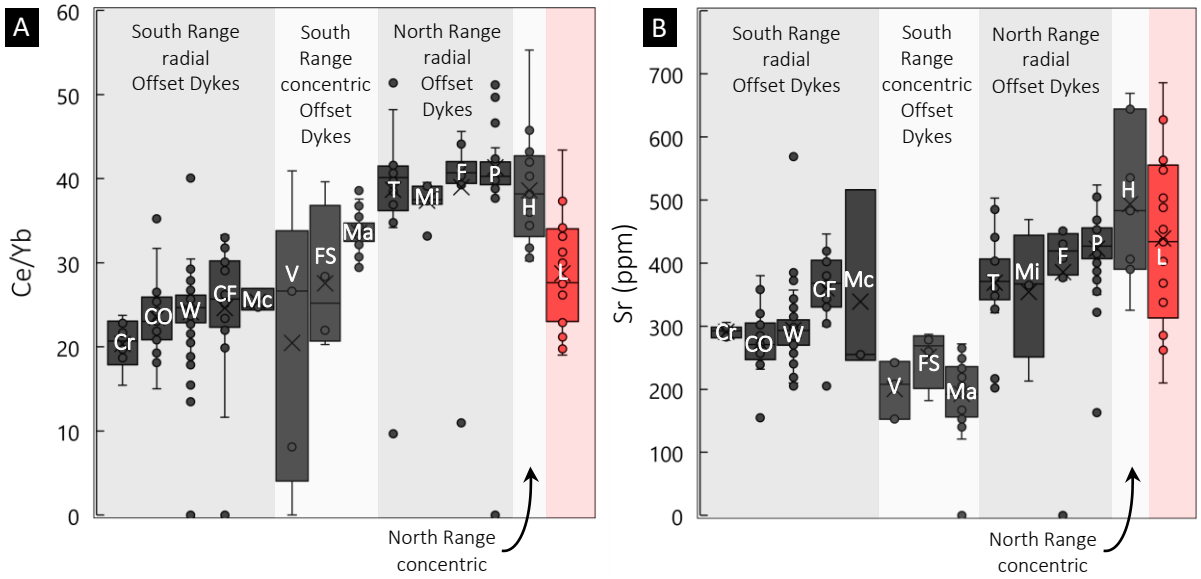

Figure 4.10 Box and whisker plots comparing selected geochemical parameters of the Laura Offset Dyke with those of other Offset Dykes, differentiated by geographical location (North vs. South Range) and dyke geometry (radial vs. concentric); **A:** Ce/Yb ratios; **B:** Sr concentrations; literature data are from Lightfoot et al. (1997c), Wood & Spray (1998), Scott & Spray (2000), Coulter (2015) and Pilles (2016). Abbreviations: Cr = Creighton; CO = Copper Cliff Offset; W = Worthington; CF = Copper Cliff Funnel; Mc = McConnel; V = Vermillion; FS = Frood-Stobie; Ma = Manchester; T = Trill; Mi = Ministic; P = Parkin; H = Hess; L = Laura.

Systematic differences between North- and South Range Offset Dykes are most pronounced with respect to Pb isotopes (Darling et al. 2010b), for the Offset Dykes in the South Range have a systematically higher $^{207}Pb/^{206}Pb$ and lower $^{208}Pb/^{206}Pb$ ratio relative to the Offset Dykes in the North Range (**Fig. 4.11**), although both groups are aligned along an 1850 Ma reference isochron, which reflects their co-genetic evolution. The observed dichotomy in Pb isotope composition could have had two potential causes (e.g. McNamara et al. 2017). Theoretically, the impact melt sheet and the Offset Dykes might have not been completely homogenised at the time of their emplacement.

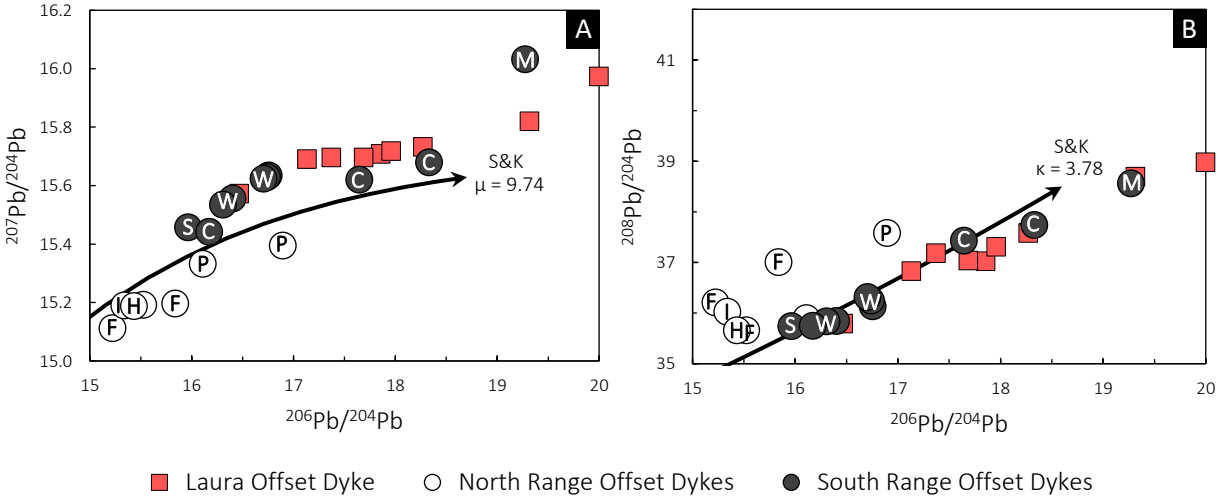

Figure 4.11 Bivariate plots comparing the Pb isotope composition of the Laura Offset Dyke with that of other Offset Dykes; **A:** uranogenic Pb; **B:** thorogenic Pb. Note how the Offset Dykes in the North Range and in the South Range of the Sudbury Igneous Complex form two isotopically distinct groups, indicating that they evolved at a different μ and κ; for comparison, the two-stage growth curves after Stacey & Kramers (1975) are shown; literature data are from Darling et al. (2010b). Abbreviations: F = Foy; I = Ministic; H = Hess; P = Parkin; S = Frood-Stobie; W = Worthington; C = Copper Cliff; M = Manchester.

Alternatively, the Offset Dykes could have assimilated different types of country rock during or *after* their emplacement, viz. high-$^{207}Pb/^{206}Pb$ Huronian Supergroup sedimentary rocks in the South Range, and low-$^{207}Pb/^{206}Pb$ Archaean granite and gneiss in the North Range. Irrespective of what the cause of the Pb isotope heterogeneity might have been, it becomes clear that the Laura Offset Dykes shares the same isotopic traits as the typical South Range Offset Dyke, because it falls on the same trend relative to the Stacey & Kramers (1975) evolution line. Its Pb isotope signature resembles especially that of the Copper Cliff and the Worthington Offset Dyke (**Fig. 4.11**), which is in good agreement with the trace element considerations from above (**Fig. 4.10A**). A common theme of these two Offset Dykes is that they are predominantly hosted by siliciclastic sedimentary rocks and that they had experienced lower amphibolite-facies metamorphic overprint.

Finally, a clear "South Range affinity" of the Laura Offset Dyke is indicated using modelled initial $^{207}Pb/^{204}Pb$ ratios (following Darling et al. 2010a) in combination with fluid-immobile trace elements, for instance, the Th/Yb ratio. In such plot (**Fig. 4.12**), the different Offset Dykes form two distinct clusters corresponding to North- and South Range. The plot also highlights a narrow isotopic and geochemical variability among the different North Range Offset Dykes, and a considerably heterogeneity among the South Range Offset Dykes. This appears to be a reflection of the different host rocks, with the North Range being characterised by relatively monotonous a lithology, and the South Range by a considerable lithological diversity. Somewhat paradoxically, the Hess Offset Dyke does not follow this trend, perhaps because it dissects, and thus assimilated, a range of different lithotypes, in contrast to the other North Range Offset Dykes. Irrespective of this, the Laura Offset Dyke corresponds to the typical South Range group. As such, it differs significantly from the Afton Offset Dyke, despite their proximity to each other. This, in turn, implies that the systematic differences between the Offset Dykes are not a consequence of their location relative to the impact site, or large-scale inhomogeneities in the composition of the impact melt sheet, but rather a consequence of the assimilation of different types of host rock *after* the intrusion.

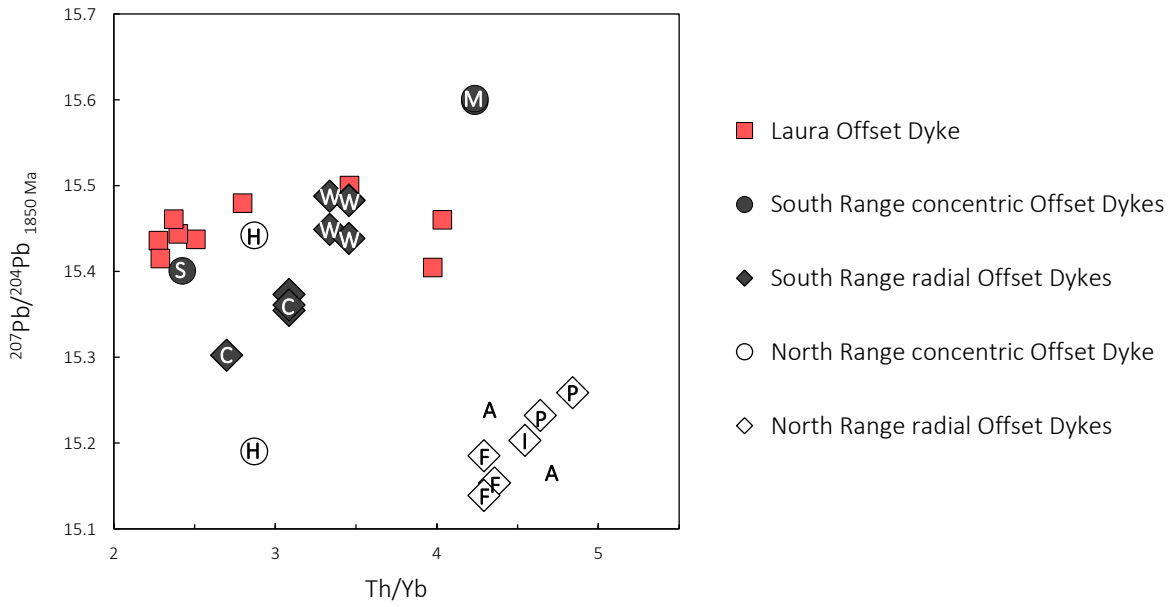

Figure 4.12 Scatter plot comparing the whole-rock Th/Yb ratio vs. the decay corrected $^{207}Pb/^{204}Pb$ ratio of different Offset Dykes, differentiated by geographical location (North vs. South Range) and dyke geometry (radial vs. concentric); Th/Yb ratios are averages based on Lightfoot (2016), Wood & Spray (1998), and Pilles (2016); Pb isotopes from Darling et al. (2010b) and this study. Abbreviations: A = Afton; F = Foy; I = Ministic; H = Hess; P = Parkin; S = Frood-Stobie; W = Worthington; C = Copper Cliff; M = Manchester.

Comparison with Manchester and Hess

Although the above present field relations, geochemical and isotopic data have provided strong evidence of an impact melt origin, the proposed Laura Offset Dyke differs in some respects from most other Offset Dykes, expect for the Manchester and the Hess (**Fig. 2.5B**), as detailed below.

A peculiar feature of the Laura Offset Dyke is its strike between N05°W and N10°E (**Fig. 4.1**), which is about parallel to the outer margin of the Main Mass. This sub-concentric strike distinguishes Laura from most other Offset Dykes; it does, however, also characterise the 5 km long Manchester Offset Dyke in the South Range, and especially the 50 km long Hess Offset Dyke in the North Range. All three dykes have in common that they are 10–30 m wide, dip sub-vertically, and are hosted by extensive zones of Sudbury Breccia (e.g. Grant & Bite 1984; Wood & Spray 1998; Smith et al. 2013). It therefore seems as if the Laura Offset Dyke is, in terms of geometry and contact relations, a close analogue to the Hess and Manchester, perhaps their extension, or a second (more distal) concentric dyke. The latter interpretation is favoured because the Laura Offset Dyke occurs more than 14 km away from the outermost reported occurrence of shatter cones east of the Main Mass (Guy-Bray et al. 1966; Dressler 1982, 1984; Grieve et al. 2008), whereas Hess and Manchester still occur within the zone of shock metamorphism (likely within the former transient cavity; Spray et al. 2004). Under the reasonable assumption that the distribution of shock features was initially circular around the impact site, and in the absence of evidence that the dyke was significantly deformed or structurally displaced afterwards, the Laura Offset Dyke most likely represents another, more distal, circumferential dyke within the Sudbury Impact Structure.

Unlike most other dykes within the Sudbury Impact Structure, the Laura, Manchester, and Hess Offset Dykes have a very low inclusion content and a high QD/IQD ratio of > 10 (Lightfoot 2016); inclusions constitute less than 1 vol% of the Laura Offset Dyke and is not clear whether the lithology should actually be classified as IQD (the arbitrary distinction and gradual nature between QD and IQD has been pointed out before in **Chapter 2.1.4**). The reason for the lack of inclusions is currently not known. Maybe it is a diagnostic feature of all distal and/or concentric Offset Dykes, in contrast to the more proximal dykes, which are expected to have formed and evolved in a highly dynamic environment, including multiple injections, resorption, flow differentiation, exhumation and collapse of a central uplift (Pilles et al. 2018b; Prevec & Büttner 2018; Mathieu et al. 2021).

Another mutual characteristic of the Laura, Manchester and Hess Offset Dykes is their unusual quartz-rich modal composition; granophyric intergrowths locally account for up to 30 vol% of the quartz diorite in either dyke (Grant & Bite 1984; Wood & Spray 1998; and this study). Grant & Bite (1984) and Lightfoot et al. (1997a) speculated that this could be the result of local contamination by siliceous wall rocks such as, Serpent Formation sandstone (~80 wt% SiO_2; Fedo et al. 1997) at Manchester, and Neoarchaean granite (70 wt% SiO_2; Meldrum et al. 1997) at Hess. Conversely, the Laura Offset Dyke is hosted by relatively silica poor Gowganda Formation argillite (~65 wt% SiO_2; Young 1969) and still contains a disproportionally large modal amount of granophyre. Alternatively, the abundance of granophyre could point to a more evolved, stronger fractionated composition of the impact melt relative to other Offset Dykes (Wood & Spray 1998), although geochemical data on neither Hess, Manchester nor Laura support this interpretation (see: Lightfoot et al. 1997a,c; Pilles et al. 2017). It remains to be established whether the quartz-rich composition of Laura, Hess, and Manchester Offset Dykes is merely a function of the host rock, or maybe an inherent feature of all distal and/or continuously developed concentric Offset Dykes.

Origin of the mafic enclaves

Another issue that remains to be addressed is the origin of the igneous-textured mafic enclaves within the inclusion-bearing quartz diorite of the Laura Offset Dyke (**Fig. 4.4**). In an attempt to constrain their origin, one of the enclaves (sample DH3-1B) has been analysed for its trace element- and isotopic composition. As can be seen in **Figure 4.13**, the sample differs geochemically from the average Offset Dyke. Although the enclave has a similar major element composition, similar MREE and HREE abundances, the same Nb/Ta ratio, and the same negative Ti anomaly, there are noteworthy discrepancies with respect to LREE, Zr, Hf, Nb, Ta, Th and U (as well as Rb, Ba, K, and Sr, but these were most likely affected by fluid-rock interaction). While it cannot be ruled out that other elements, such as U and the LREE, were likewise affected by the alteration (epidotisation), the lower concentrations of Zr, Nb and Th in the enclave relative to the quartz diorite are suspicious. It appears that these igneous-textured enclaves, at least the one analysed here, are genetically unrelated to the Offset Dykes. This conclusion finds additional support in the whole-rock isotope data. As evident from **Table 4.2**, the enclave has a significantly higher $^{147}Sm/^{144}Nd$ ratio (0.14) than the Laura Offset Dyke, and a much older model age (t_{DM}) of 3600 Ma. The enclave has, furthermore, a lower $^{87}Sr/^{86}Sr$ ratio and a lower $^{207}Pb/^{204}Pb_{1850}$ ratio than its host rock.

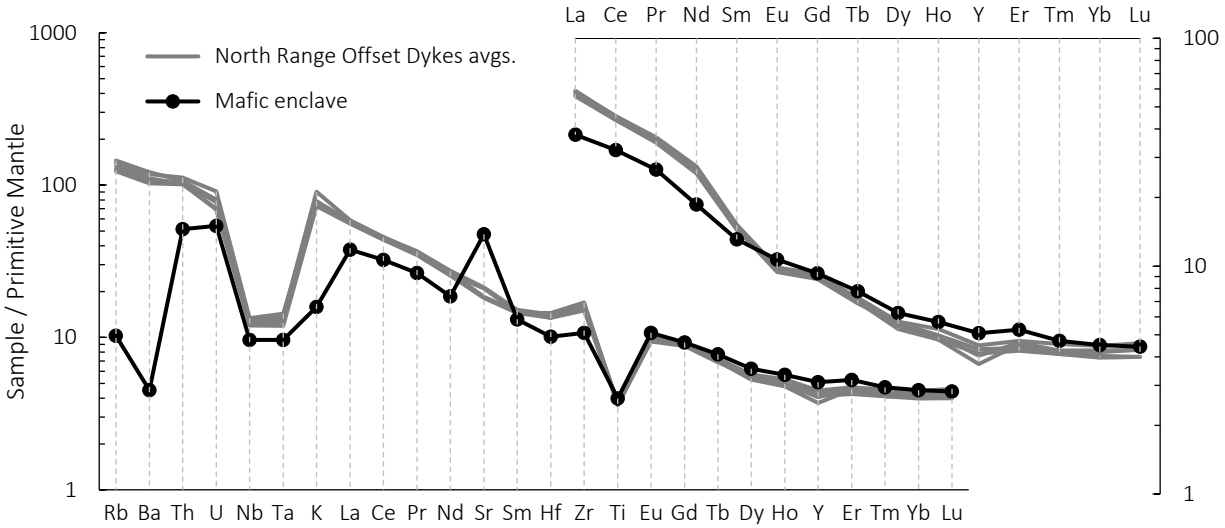

Figure 4.13 Primitive mantle-normalised trace element abundances of a mafic enclave within the Laura Offset Dyke and, for comparison, selected Offset Dyke averages of the Sudbury Igneous Complex; normalisation values are from Sun & McDonough (1989); literature data are from Lightfoot et al. (1997c).

Based on the above evidence it is proposed that the mafic, igneous-textured enclaves within the Laura Offset Dyke are xenoliths, affected to some extent by contact metasomatism (albite-epidote hornfels facies; see also: Boast & Spray 2006) and perhaps melt infiltration (see: Wang et al. 2020). They were likely derived from a pre-existing, unexposed, mafic lithology. As the enclaves have a similar mineralogy and composition as their host rock (i.e., the impact melt), and because of their refractory composition in general, the mafic xenoliths were not completely digested by the superheated impact melt. Their high liquidus temperature likely accounts for their relatively high abundance compared to the rarely observed, more fusible, sedimentary xenoliths. The exact origin of the xenoliths remains unclear, but a potential source rock (a quartz diabase of the 2.17 Ga Biscotasing Dyke Swam) might have already been identified in this study (**Chapter 8**). That said, it is interesting to note that exotic gabbroic clasts, either of the Nipissing Suite or the Biscotasing Dyke Swarm, were observed within Sudbury Breccia just 8 km west of Laura Creek (**Fig. 4.2B**).

Ni-Cu-PGE mineralisation potential

A final aspect that requires consideration is the economic potential that might or might not be associated with the Laura Offset Dyke. While Offset Dykes in general constitute an important source of Ni, Cu, and PGE, and bearing in mind that Offset-hosted deposits account for half of the total historic metal production of the Sudbury mining camp (e.g. Keays & Lightfoot 2004), not all the dykes are as equally well endowed. Disproportionally large quantities of ore are, for example, associated the Frood-Stobie, Copper Cliff, and the Worthington Offset Dyke and, to a lesser extent, also with the proximal Foy, Vermillion, and Whistle-Parkin. Others, such as Trill, Cascaden, Hess, Manchester, Tyrone (distal Foy), or Cecil-Johnson, are only hosts of subeconomic disseminated base metal mineralisation (Smith et al. 2013; Coulter 2015; Smith 2017) whereas some may only contain pyrite, if any sulphide (Anders 2016; Pilles 2016). The metal enrichment of an Offset Dyke seems to be unrelated to factors such as, lithology; its geochemical affinity (including bulk-rock Cu/Ni, Ce/Yb); the type and abundance of inclusions; the geometry, continuity, length, or width of the dyke; the type of the country rock; the extent of brecciation; the level or erosion; or the degree of metamorphism/alteration (Lightfoot 2016).

From our current understanding, only two parameters seem to have favoured the concentration of economic amounts of Ni-Cu-PGE sulphide into a given Offset Dyke: (1) Its proximity to the Main Mass (typically < 7 km based on the sphere of currently operating mines), and/or (2) the existence of a physical connection to the Main Mass via funnels (as is the case for Copper Cliff, Foy, Whistle). As discussed before in **Chapter 3.6**, both parameters are indirectly related to the initial thickness of the impact melt sheet (a thicker melt sheet contains more metals) (Ames et al. 2002; Lightfoot & Farrow 2002; Lightfoot 2016), and the availability of pathways and structural traps (typically higher in the centre of an impact structure). In this sense, not only does the Laura Offset Dyke lack any known physical attachment to the Main Mass, but it also occurs at a much greater distance to the Main Mass (25–30 km) than most other Offset Dykes. Thus, from a pure theoretical perspective, and under the reasonable premise that the distribution of impact melt and structural features within the Sudbury Impact Structure was relatively symmetric, the Laura Offset Dyke should be only of limited economic significance, as should be the even further Afton Offset Dyke (45 km).

And indeed, no sulphide other than erratic (and clearly secondary) pyrite, galena and chalcopyrite was observed within the Laura Offset Dyke despite considerable and ongoing exploration efforts (e.g. Whymark 2020). There is also no evidence of the existence of base metal sulphide/arsenide that could have potentially resulted from the metamorphic/hydrothermal remobilisation of a pre-existing (igneous) ore body. One might argue that the Laura Offset Dyke has a considerable down-dip continuity (possibly as deep as the other Offset Dykes), that sulphide melt could have percolated into the dyke (e.g. Giroux & Benn 2005), and that economic concentrations of Ni-Cu-PGE are somewhere hidden at depth. However, the total absence of both magmatic and hydrothermal base metal sulphide at surface and along the entire 4.3 km strike length, not even of traces, is highly suspicious of that theory, and rather indicates that the Laura Offset Dyke – as interesting as its discovery might appear from an academic viewpoint – is barren throughout. Whether the quartz-carbonate veins that cut across the Laura Offset Dyke have any economic value (e.g. with respect to gold) is yet to be established, as is the nature of their relationship to the dyke. The possibility remains nonetheless that other, more proximal, and therefore perhaps better endowed (or even ore-bearing) Offset Dykes exist within the East Range, maybe in the Aylmer, Rathbun or Scadding townships, 5–15 km northeast of the Main Mass of the Sudbury Igneous Complex.

Rathbun Offset Dyke

5.1 Summary

A third Offset Dyke was discovered at Rathbun Lake, central Rathbun Township, 15 km east of the Main Mass of the 1.85 Ga Sudbury Igneous Complex. The Rathbun Offset Dyke, an inclusion-bearing amphibole quartz diorite, is very limited in exposure and lacks any known physical connection to the Main Mass. It likely represents the erosional remnant and the basal termination of an originally much more voluminous Offset Dyke, whether radial, concentric, or discontinuous. As far the emplacement of the Rathbun Offset Dyke is concerned, there is textural, geochemical, and isotopic evidence of extensive thermomechanical erosion of the local country rock (Nipissing Suite gabbro) by the parental superheated (> 1,200°C) impact melt. The presence of primary igneous hornblende suggests that the quartz diorite crystallised under hydrous conditions (~6 wt% H_2O) likely as a result of the assimilation and dehydration of volatile-bearing xenoliths and country rock, at a pressure between 0.8–1.3 kbar. These data are consistent with an emplacement of the dyke at the base of the 3–5 km thick Sudbury impact melt sheet that is now preserved as the Main Mass.

The Rathbun Offset Dyke is here shown to be spatially and genetically associated with high-grade PGE-Cu-Ni sulphide mineralisation, previously known as the *Rathbun Lake occurrence*, and previously interpreted as epigenetic in origin and related to the 2.22 Ga Nipissing Suite. The following chapters therefore provide a detailed characterisation and re-interpretation of the Rathbun Lake occurrence in light of its potential impact origin. A primary assemblage is identified and interpreted as igneous. It consists of disseminated to semi-massive net-textured chalcopyrite, loop-textured pentlandite, trellis-textured titanomagnetite ± Pd-Bi-Te minerals ± $PtAs_2$ (sperrylite) ± native gold. Grab samples average ~40 g/t Pd+Pt+Au at a Cu/(Cu+Ni) of > 0.9 and a Pd/Ir of > 100,000. This assemblage was likely formed by a highly fractionated sulphide melt, and it bears as such strong resemblance to the footwall deposits underneath the Sudbury Igneous Complex. Hydrothermal overprint at lower greenschist-facies conditions produced a secondary assemblage of pyrite/marcasite, violarite, covellite ± millerite. It involved local remobilisation into pyrite-chalcopyrite stringers and veinlets and led to the textural liberation of PGE minerals from their sulphide hosts. Micron-scale X-ray mapping revealed a progressive in-situ replacement of magmatic Pd-Bi-Te minerals, where in contact with hydrous silicates, by Sb- and Hg-bearing Pd minerals such as temagamite, Pd_3HgTe_3. The timing and nature of this hydrothermal overprint remains uncertain, but a connection to later regional metamorphism and faulting, followed by supergene weathering, seems most plausible. Alternatively, alteration could have occurred autometasomatically when a hydrous fluid phase was expelled from the crystallising sulphide melt.

All in all, these findings advocate for a new subtype of distal Offset Dyke-hosted mineralisation in an area so far not known for Offset Dykes. This opens new perspectives in the search for unconventional ore deposits within the 200 km-large Sudbury Impact Structure.

Parts of this chapter have been published in a modified form as:
Kawohl, A., Whymark, W. E., Bite, A., & Frimmel, H. E. (2020). High-Grade Magmatic Platinum Group Element-Cu(-Ni) Sulfide Mineralization Associated with the Rathbun Offset Dike of the Sudbury Igneous Complex (Ontario, Canada). ***Economic Geology***, 115(3), 505-525. **doi.org/10.5382/econgeo.4717**

5.2 Local Geology

Rathbun Township is located 10–15 km northeast of Sudbury. It extends across the 10 km-large Wanapitei Lake and covers the southwestern part of the Temagami Anomaly. It borders the 1.85 Ga Sudbury Igneous Complex to the west, which is one of the main reasons why the township looks back on more than 100 years of extensive mineral exploration. Numerous occurrences, past-producing as well as active mines are found in the township, including impact-related Ni-Cu-PGE sulphide mineralisation (Capre, Nickel Rim, Victor Deep, MacLennan, Rathbun Lake showing – this chapter). For detailed insights into the geology of the Wanapitei Lake area, the reader is referred to Dressler (1982) and Gates (1991). For reasons outlined below, the focus of this chapter will be placed on the eastern part of Rathbun Township, specifically the area around Portage Bay, Matagamasi Lake and Rathbun Lake. Access to these locations is provided by Highway 17 coming from Sudbury, then turning into Kukagami Road and heading for 30 km northwards along the Bushy Bay Road as far as Poulton Lake. Some outcrops around Portage Bay may be accessed by boat only. In contrast to much of the eastern part of the Temagami Anomaly, outcrop conditions in the Portage Bay area are quite good, especially alongside roads and other manmade excavations. Another advantage of the area is, despite its proximity to Sudbury, the absence of black smelter coatings, which typically obscure much of the outcrops in the South Range of the Sudbury Igneous Complex. This invites for a more detailed description of the local geology.

The oldest rocks in the Portage Bay area are sedimentary rocks of the upper Huronian Supergroup (Cobalt Group), deposited sometime between 2.35 and 2.31 Ga in a glaciogenic to fluvial environment (Caquineau et al. 2018; Hill et al. 2018). Wacke, silt- and mudstone of the Gowganda Formation prevail; arenites of the overlying Lorrain Formation are only present in the northern corner of the township and in a small enclave to the south, around Bassfin Lake (**Fig. 5.1**). Typical features observed in the Gowganda Formation include Archaean dropstones (mostly granitoids), rhythmical bedding, and, in places, conglomeratic layers. A greenish-grey massive and uniform wacke, however, is the aerially most extensive lithology of the Gowganda Formation; laminated argillite is locally found north of Rathbun Lake and in the Bassfin Lake area. Sedimentary features typically observed in the Lorrain Formation rocks include thin layers of quartz pebbles, planar and through cross-stratification. The thickness of the Cobalt Group in the area is not known.

Rocks of the Huronian Supergroup were, in many places, intruded by tholeiitic magmas of the 2.22 Ga Nipissing Suite, forming predominantly up to 1 km-thick sills, rarely dykes. An exceptionally well-studied member of the Nipissing Suite is exposed at Portage Bay, stretching across Matagamasi and Kukagami Lake, and extending as far as Scadding Bay to the south. The so-called Wanapitei Intrusion (not to be confused with the 1.75 Ga Wanapitei *Complex* in the Grenville Province; Prevec 1995) is a lopolith-like body that received considerable attention throughout the past as a Cu-Ni-PGE prospect. Dated at 2109 ± 40 Ma using the K-Ar method (Edgar 1986) it was confirmed as a member of the Nipissing Suite (see also: Dressler 1982; Lightfoot & Naldrett 1996a). The lopolith could have originally exceeded 8 km in diameter and 800 m in true thickness (Edgar 1986); the three separate lobes of the intrusion measure 3 x 1 km. Their basal intrusive contacts dip steeply and face a common centre at Bassfin Lake (**Fig. 5.1**). Thermal metamorphism of the country rock (laminated wacke) is restricted to less than 2 m of baking (Edgar 1986). A basal unit of fine-grained quartz diabase (< 5 vol% quartz) is typically present, but more than 98 vol% of the Wanapitei Intrusion consists of massive, medium-grained, and Nipissing Suite-typical

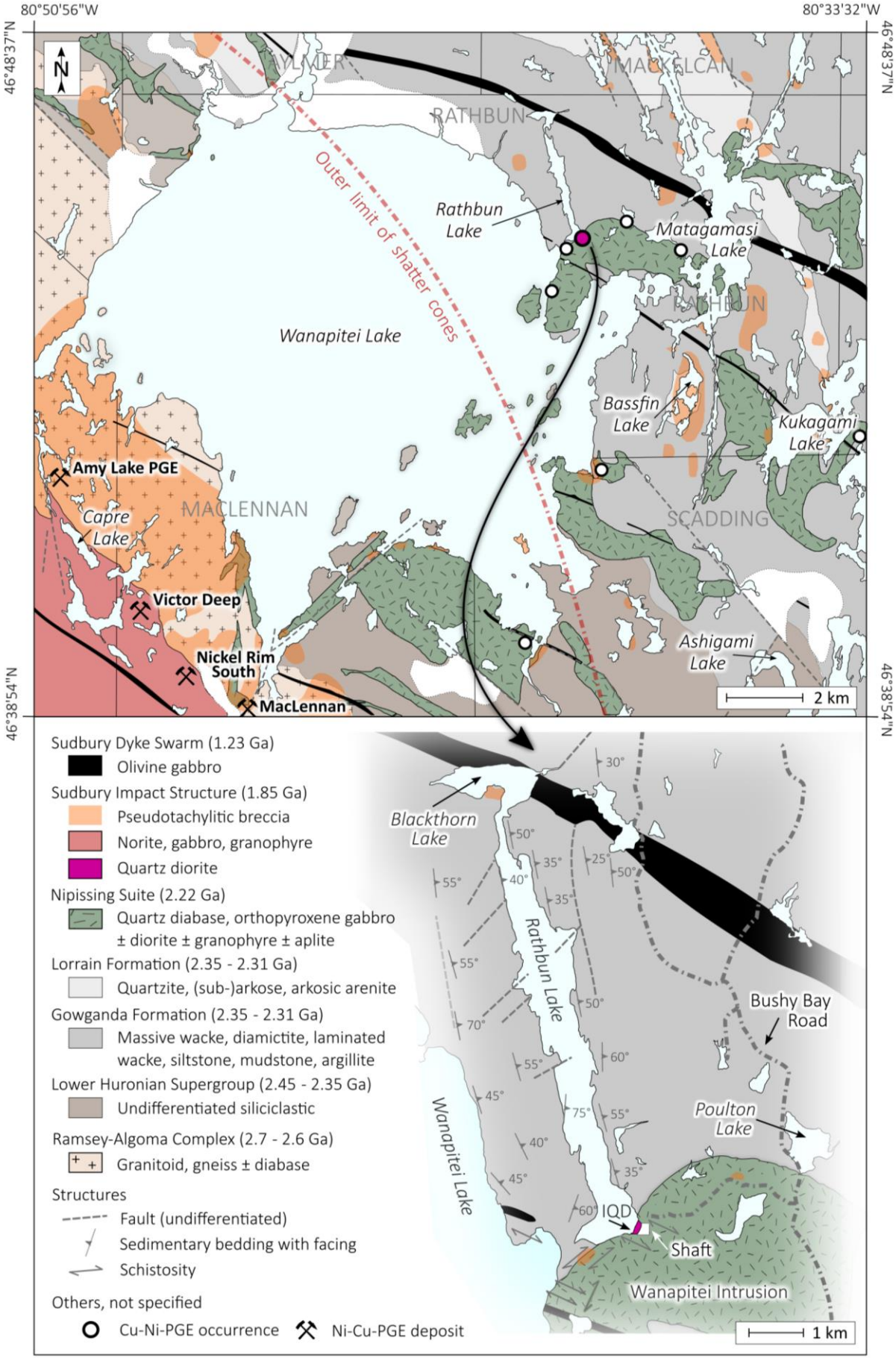

Figure 5.1 Geological map of Wanapitei Lake; based on maps of Ogden (1957), Dressler (1981a, 1981b, 1982), Ames et al. (2005), Whymark (2019) and additional mapping by the author.

orthopyroxene gabbro without macroscopic evidence of igneous layering (however: Finn & Edgar 1986; Finn et al. 1982). Pegmatoidal segregations occur here and there, but always > 100 m above the basal contact. The author would like to note that some of these pegmatoidal segregations, with their cm-sized prismatic augite and hornblende crystals, are very similar to the features observed in the Shakespeare Lopolith, the only economically mineralised member the Nipissing Suite, 70 km west of Sudbury (Sproule et al. 2007; Dasti 2014; Davey et al. 2019). The Wanapitei Intrusions, furthermore, contains irregular, metres to tens of metres wide zones of disseminated (up to 3 vol%) blebby or globular chalcopyrite and pyrrhotite ± pentlandite. This type of mineralisation is not confined to any stratigraphic level within the lopolith, specific lithology, nor rock texture; it is found in each of the three lobes, in the basal quartz diabase, in the orthopyroxene gabbro, in the more plagioclase-rich leucogabbro, and even in felsic differentiates near the roof zone, although it is not found in the sedimentary footwall rocks. Consensus exists about a magmatic origin of this sulphide (Lightfoot & Naldrett 1996a; Jobin-Bevans 2000; Lightfoot 2016, p. 91).

A more controversial but to the scientific community and the local mining industry well-known PGE-Cu-Ni occurrence is found on the northern contact of the northern lobe of the Wanapitei Intrusion, exposed directly on surface at the shore of Rathbun Lake (formerly known as Boucher Lake or McLarens Lake). Patented in 1889/1890, the first reference to the Rathbun Lake occurrence was made in the Sudbury Journal of June 4, 1891 (as cited in Gates 1991, p. 203):

> *"The Bonanza Nickel Company, the announcement of whose incorporation was made in the Ontario Gazette recently (…) the property of which they will operate is in F.4 township 42 (Rathbun) on the shore of Lake Wahnapitae, where they have 80 acres on which the showing is excellent, as will be shown by the following analysis of samples by Prof. Hayes: nickel, 4.10 per cent, copper, 12.50 per cent, gold $12.10 per ton, platinum $37.50 per ton. The company is in the hands of live practical men. Mr. Wells, the President, will direct the operations in mining and smelting. A water-jacketed smelter capable of treating about fifty tons of ore per day will be put up, and is expected that everything will be completed so that mining may begin this summer."*

The ambitious plans of the Bonanza Nickel Company did not go beyond the sinking of a 13.5 m-deep prospect shaft vertical into the occurrence, the timbered and collapsed remnants of which were still in place at the time of writing. The property was acquired in the 1950s by Dolmac Mines Ltd., who conducted mapping, surface sampling, shallow drilling and dewatering of the shaft, but eventually failed to locate additional mineralisation or an extension of the existing showing. Although grab samples collected by Dolmac returned impressive values of up to 10 g/t Pt and 30 g/t Pd (Koulomzine 1955), the project came yet to another halt. With the economy's growing demand for Pt and Pd especially since the 1980s, several other companies and individuals began to explore the Rathbun Lake area, drilling included, but all without success.

As the showing went through several phases of outcrop stripping, blasting, trenching, excavation and muck piling, an in-situ study of the mineralisation is no longer possible. For information about the original mineralisation one must rely on historic company reports and drill logs (Ogden 1957, 1958; Dressler 1982) and the study of muck piles (Koulomzine 1955; Rowell & Edgar 1986; Lightfoot et al. 1991). The available information summarise as follows: The mineralisation in form of massive chalcopyrite (50 vol%), pyrite (45 vol%), magnetite (5 vol%) and traces of pyrrhotite, millerite, violarite, covellite, arsenopyrite, sperrylite, native gold and Pd-Bi-Te minerals, was

described as a lenticular or vein-like body (striking roughly E-W), up to 12 m long and 0.6 m wide, surrounded by a halo of disseminated sulphide, and located at the lower contact between the Wanapitei Intrusion and the Gowganda Formation. The host rock was described as a fractured, strongly altered variety of the Nipissing Suite diabase/gabbro, rich in quartz, hornblende, chlorite, epidote, and biotite. The host rock was apparently referred to as a sharp-walled "grey dyke" in drill logs by Ogden (1958) and interpreted as a silicified fault breccia by Rowell & Edgar (1986).

All the Palaeoproterozoic rocks in the Portage Bay area were affected by gentle folding and regional metamorphism not exceeding the greenschist facies (see also Dresser 1982). This is evident from metamorphic assemblages in the Nipissing Suite gabbro, which include actinolite, chlorite, epidote, quartz and titanite. Most of the Wanapitei Intrusions, however, preserves a relatively pristine mineralogy and texture. Exceptions are autometasomatically altered zones in and around pegmatitic segregations, where patches of epidote, amphibole, and pink feldspar (and scapolite?) are common. The main metamorphic minerals in the Cobalt Group are sericite, chlorite, and biotite; garnet is absent, and no penetrative foliation was observed, nor has it been reported in the literature. The Portage Bay area lies outside the sphere of high-pressure shock metamorphism related to the 1.85 Ga Sudbury impact event (e.g. Dressler 1982; Ames et al. 2005) and way outside the thermal aureole surrounding the Sudbury Igneous Complex (Prevec & Cawthorn 2002; Jørgensen et al. 2019). Pseudotachylitic breccia (termed Sudbury Breccia) occur scattered throughout the study area, typically found at lithological contacts. Quite impressive examples of megaclastic Sudbury Breccia can be found around Poulton Lake, and especially around Bassfin Lake.

The structural geology around Wanapitei Lake and Portage Bay is dominated by subparallel N-striking faults and shears (**Fig. 5.1**). The largest of these is known as the Upper Wanapitei River Fault (WRF), which can be traced for a hundred kilometres along strike. A significant topography and both lateral and possibly vertical displacements are associated with the WRF, and many potential splays have been mapped in the study area, including the MacLaren Lake and MacLaren Creek faults. It is possible that the linear morphology of Rathbun Lake is also structurally predetermined. Buchan & Ernst (1994) included the WRF into the Onaping Fault System, a regional system of left-lateral faults across the south-central Superior Craton and related to the uplift of Kapuskasing zone. Structures of the Onaping Fault System are thought to have acted as pathways for hydrothermal fluids on a regional, basin-wide scale. Structurally controlled albitisation and silicification (± carbonate, chlorite) can be observed in many places and always in spatial association with the Nipissing Suite gabbro, locally resulting in (sub-)economic Cu-Au mineralisation (Scadding Mine, Crystal/Comstock, McVittie Property), massive quartz veins (Bonanza Lake), and hydraulic breccias of potential use as a dimension stone (Aylmer Quarry) (e.g. Gates 1991).

NW-striking dykes of 1.23 Ga olivine gabbro are, once more, the youngest rocks in the study area. They are part of the regional Sudbury Dyke Swarm and have previously been studied in detail by Shellnutt & MacRae (2012). Individual dykes are typically between 10 and 100 m wide, can be traced for tens of kilometres in outcrop and even further in the subsurface using aeromagnetic maps. Their emplacement post-dated regional hydrothermal alteration, and it post-dated major folding and/or faulting (e.g. Tschirhart & Morris 2012). Only dykes in the southern-most part of the Huronian Basin were affected by the 1.1–1.0 Ga Grenville Orogeny, where metamorphic grade and the intensity of deformation rapidly increase (e.g. in southern Scadding Township).

5.3 Field Relations

Field work in the Portage Bay-Rathbun Lake area was completed in 2018 and 2019 with the principal observations documented below. In 2018, inclusion-bearing quartz diorite was discovered at two localities, in outcrop at the above mentioned Rathbun Lake PGE-Cu-Ni occurrence (46°45 50.80N 80°39 21.17W), and as boulders in a nearby muck pile (46°45 54.44N 80°39 16.20W).

The inclusion-bearing quartz diorite crops out immediately northeast to the old shaft, along the NE-striking contact between the Wanapitei Intrusion (Nipissing Suite) and the Gowganda Formation (**Fig. 5.2A**). The inclusion-bearing lithology visually resembles the local fine-grained (marginal) facies of the Nipissing Suite gabbro and can be easily overlooked in the field, even in wet outcrop and on freshly broken surfaces (**Fig. 5.2B**). In addition, much of the outcrop is obscured by a gossan. For the same reasons it was not possible identify the exact contact relationships nor the actual outcrop dimension of the inclusion-bearing lithology with certainty, but it is estimated to be 5 m^2 judging from the size of the gossan and the presence of gabbro and wacke three metres on either site of the shaft. The orientation of the inclusion-bearing quartz diorite remains unclear.

The Gowganda Formation in and around the outcrop consist of massive, crudely laminated to massive wacke or siltstone. It dips ca. 50° southeast, where it plunges below fine-grained gabbro of the Wanapitei Intrusion, the latter becoming increasingly coarser grained further east of the contact. The gabbro does not differ from the typical Nipissing Suite gabbro elsewhere in the township and consequently it does not require a more detailed description. A parallel set of sulphidic shears was observed five metres north of the shaft, cutting across gabbro and wacke (**Fig. 5.2C**). These N-striking structures dip almost vertically and seem to have mobilised sulphide, predominantly pyrite, over a short distance along strike and, to a lesser extent, also diffusive and along secondary, perpendicular joints into the host rock. The structures are easily recognised in the field by their sulphide burns and they are filled with a fine material that is interpreted as a fault gouge.

Angular boulders of up to 1 m in size are found close to and pilled below the shaft (**Fig. 5.2A**), together with dumped fragments of older 3-cm diamond drill cores. Access to the historic underground workings is not possible anymore and so this material provides the only possibility to study the subsurface geology. Most of the rubble and all the core material feature a fine- to medium grained, unaltered, undeformed, and barren gabbro that evidently belongs to the regional Nipissing Suite. Boulders of the Gowganda Formation were also overserved. They feature a dark grey, green to brown, very fine-grained and very brittle sedimentary rock. Some of the sedimentary boulders contain slickensides, chlorite veins, crenulation cleavage, or exhibit conchoidal fracturing. Dusty malachite coatings were occasionally observed. Rusty chunks of massive sulphide occur in abundance, and it was already possible to discern pyrite-rich and chalcopyrite-rich samples in the field. The same material, though less weathered, was found in a ca. 100 m^2 waste rock pile ~150 m to the north of the Rathbun Lake occurrence. Most of the waste rock there could be assigned with confidence to the local Nipissing Suite gabbro. Boulders of the inclusion-bearing lithology were also recovered after some digging. There is no doubt that the waste rock originally came from the Rathbun Lake occurrence. This is supported by the presence of blasting mats. As usage of these was not common practice until the latter half of the 20th century, blasting, excavation, and transportation must have occurred fairly recent (Winston Whymark, pers. comm. 2019). Speculations about another second historic shaft, closer to the muck pile, could not be confirmed.

No Sudbury Breccia occurs at the showing, not even in a 200 m radius around it; only 400 m southwest, at the outlet between Rathbun and Wanapitei Lake, Nipissing-hosted Sudbury Breccia was observed. The breccia is developed close to the lower contact of the Wanapitei Intrusion and contains traces of disseminated chalcopyrite (< 0.25 vol%). Channel sampling from this outcrop suggests that the sulphide was originally derived from magmatic sulphide in the host rock. It seems to have been reworked, but not necessarily upgraded, during the brecciation. A barren gabbro breccia was also found at a logging road some 300 m southwest of Poulton Lake; extent unknown. It is not clear whether the apparent scarcity of Sudbury Breccia in the Rathbun Lake area is representative of its actual distribution or whether it is the mere consequence of a lack of outcrops and its indistinct field appearance, especially if monomict and hosted by fine-grained gabbro only.

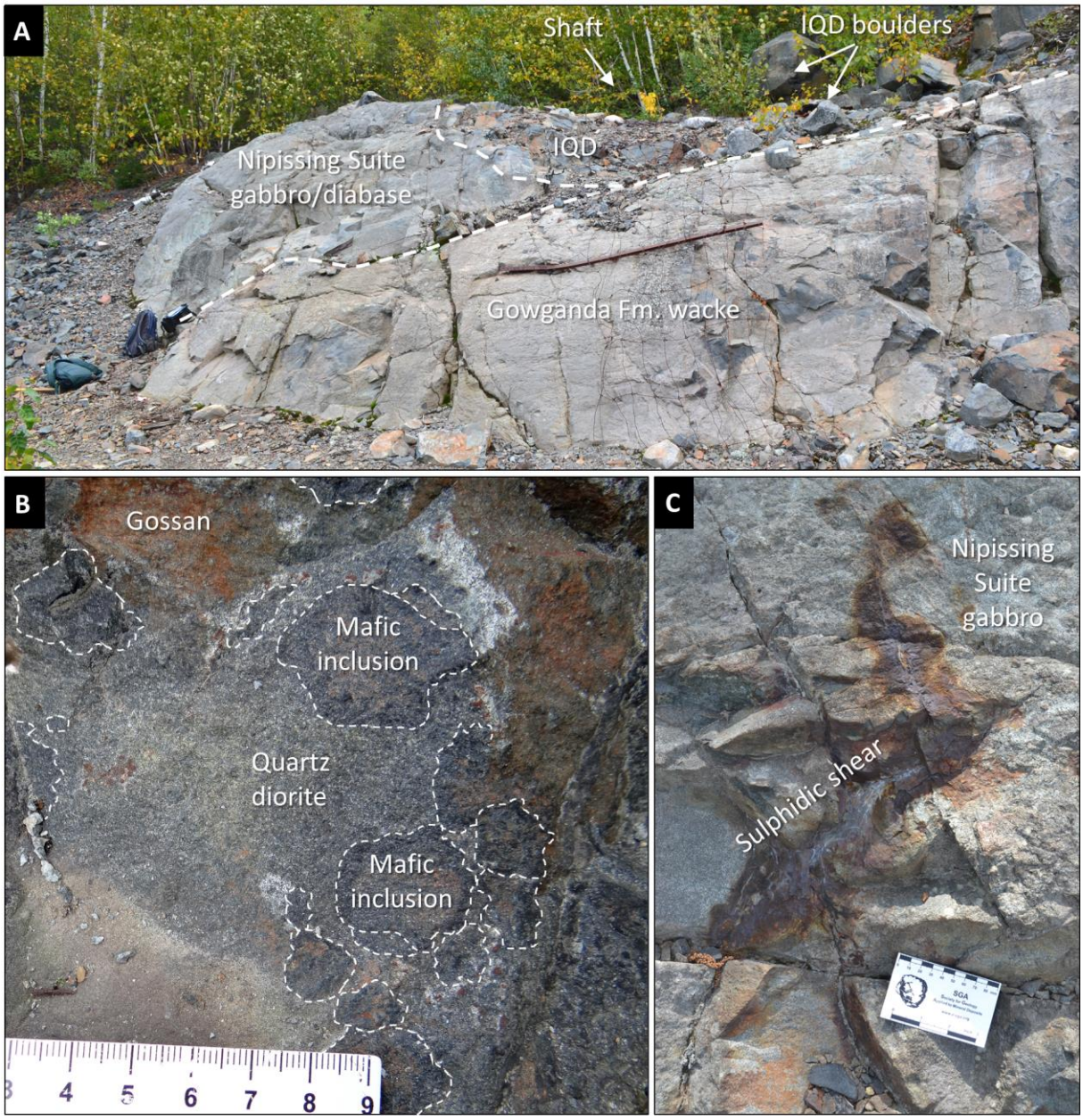

Figure 5.2 Field photographs of the Rathbun Lake occurrence, Rathbun Township (46°45 50.80N 80°39 21.17W); **A:** the Rathbun Lake occurrence in outcrop, looking south; **B:** the inclusion-bearing quartz diorite in outcrop (right next to the shaft); **C:** sulphidic shears in country rock (5 m north of the shaft); broken lines delineate inferred lithological contacts; 50-cm backpacks and 9-cm card for scale. Abbreviation: IQD = inclusion-bearing quartz diorite.

5.4 Petrography

Inclusion-bearing quartz diorite (matrix)

In outcrop, the inclusion-bearing quartz diorite from Rathbun Lake is almost indistinguishable from the typical fine-grained Nipissing Suite gabbro. Only polished grab samples and channel cuts across the outcrop (**Fig. 5.3**) reveal the composite nature of the rock, with abundant dark grey aphantic inclusions set in a light grey phaneritic matrix. The inclusions are well rounded, between a few mm and 10 cm in diameter, and exhibit sharp but undulating contacts with the matrix. The groundmass has an inequigranluar to ophitic texture and consists of 45 vol% altered plagioclase, 35 vol% quartz, 20 vol% amphibole (**Fig. 5.4A**), conforming to mineralogy and modal proportions typical of a quartz diorite. Plagioclase is up to 0.8 mm large, of tabular to acicular subhedral to euhedral habit (aspect ratios between 5:1 and 10:1), compositionally zoned, and arranged in a decussate manner. Pseudomorphic replacement of plagioclase by epidote and sericite is omnipresent (**Fig. 5.4A–C**) and affected predominantly the anorthite-rich cores of the feldspar, while albite-rich rims being preserved. Exceptions are pristine plagioclase inclusions within quartz. Quartz occurs as up to 3 mm-large, optical continuous, undeformed, anhedral poikilitic grains enclosing plagioclase, biotite, and amphibole. Subhedral to euhedral amphibole is olive green in thin section (**Fig. 5.4A–C**), up to 1.5 mm in length, and lacks compositional zoning. It is considered a primary mineral because there is no evidence of amphibole replacing earlier ferromagnesian minerals such as pyroxene. Amphibole is, however, in part or entirely, replaced by chlorite (**Fig. 5.4D**). Accessory minerals (< 1 vol%) are skeletal magnetite and ilmenite, tabular biotite (converted to chlorite), and acicular apatite. Metamict halos around tiny (< 10 µm) inclusions of zircon or monazite were observed in biotite and chlorite. Granular epidote occurs disseminated throughout as well as concentrated in cross-cutting veins. Notwithstanding the hydrothermal alteration and the pseudomorphic replacement of primary minerals, the igneous texture of the quartz diorite is generally preserved. Only adjacent to hydrothermal veins has the rock been completely overprinted.

Mafic and sedimentary inclusions

Two types of inclusions have been observed; igneous-textured mafic inclusions prevail. They are dark grey phaneritic to almost black and aphantic in hand specimen (**Fig. 5.3**). Mafic inclusions are characterised by a spherical to amoeboid shape, sharp and undulating contacts to the matrix, dark concentric rims, and diameters of up to 10 cm. Finger-like intergrowths between the matrix and the inclusions can be locally observed as well as fragmentation of larger mafic inclusions into smaller droplets, giving rise to ocelli-like textures. Mafic inclusions are essentially gabbroic and composed to > 90 vol% of equal proportions of fresh plagioclase and clinopyroxene, typically within a spherulitic texture (**Fig. 5.4E,F**). A relict ophitic texture is indicated in some coarser-grained inclusions, but intense uralitisation has obscured much of the protolith. Clusters of tremolite and talc occur at 10 and 1 vol%, respectively, and are likely the alteration product of orthopyroxene. Accessory phases are quartz, biotite, and ilmenite, and occur dispersed throughout. Arkosic wacke constitutes less than 1% of the inclusion population. Their contacts to the matrix are blend, gradual and less well-defined. Sedimentary inclusions preserve their original bedding and are composed of fine-grained (40 µm) sub-rounded feldspar and mono- to polycrystalline quartz, embedded in a brown, cryptocrystalline micaceous groundmass. Locally, biotite is recrystallised to mm-large flakes, possibly because of thermal metamorphism; veins of chlorite are common.

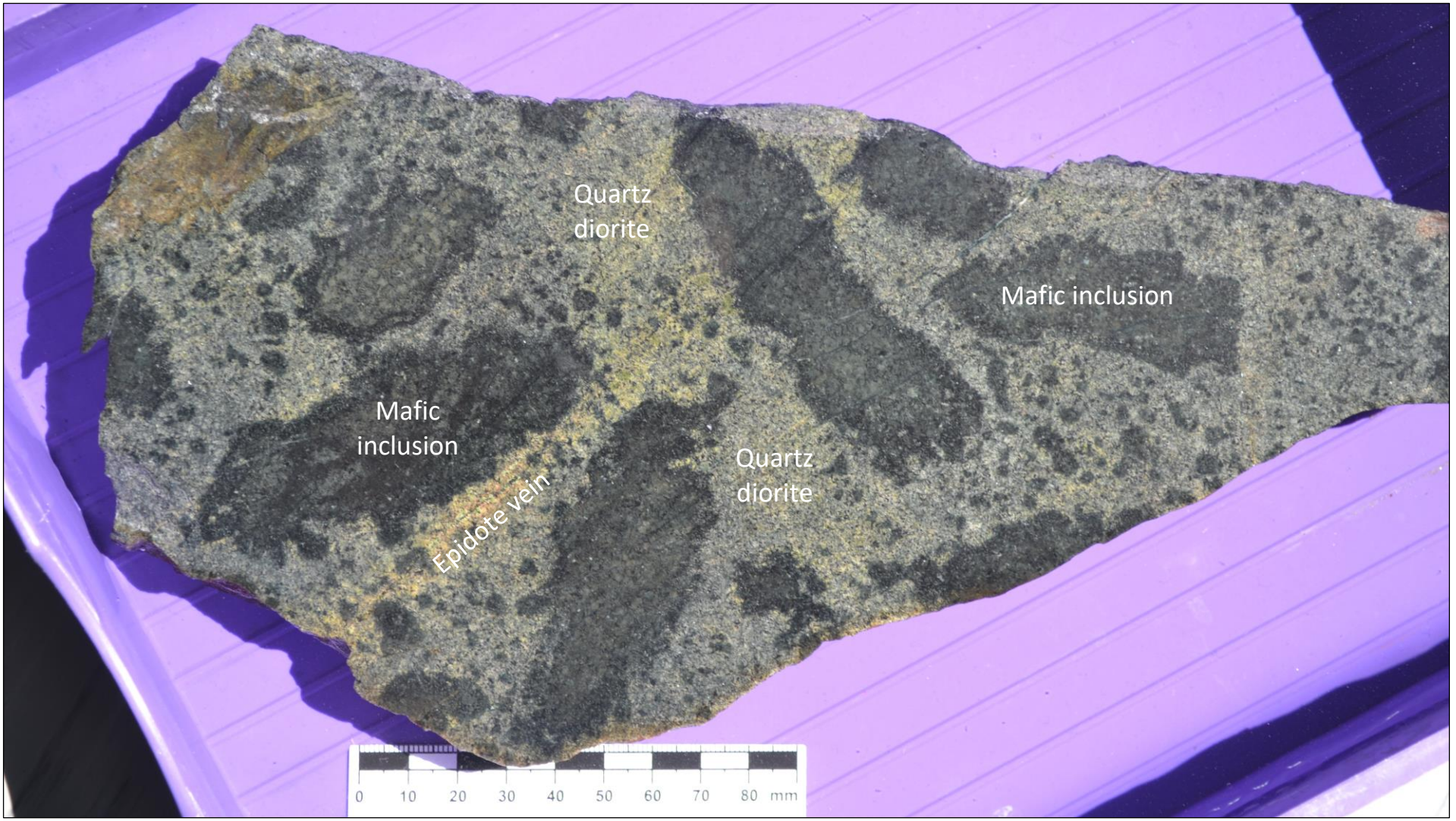

Figure 5.3 Photograph of the inclusion-bearing quartz diorite from Rathbun Lake, Rathbun Township (46°45 50.80N 80°39 21.17W); the specimen shown in this image is a piece of a channel cut; the slab has been polished using diamond-sand paper, and photographed under water for contrast enhancement; note the dark reaction rims around the mafic inclusions as well as the apparent disintegration of the mafic inclusions into smaller ones; also note the green epidote vein; 9-cm card for scale.

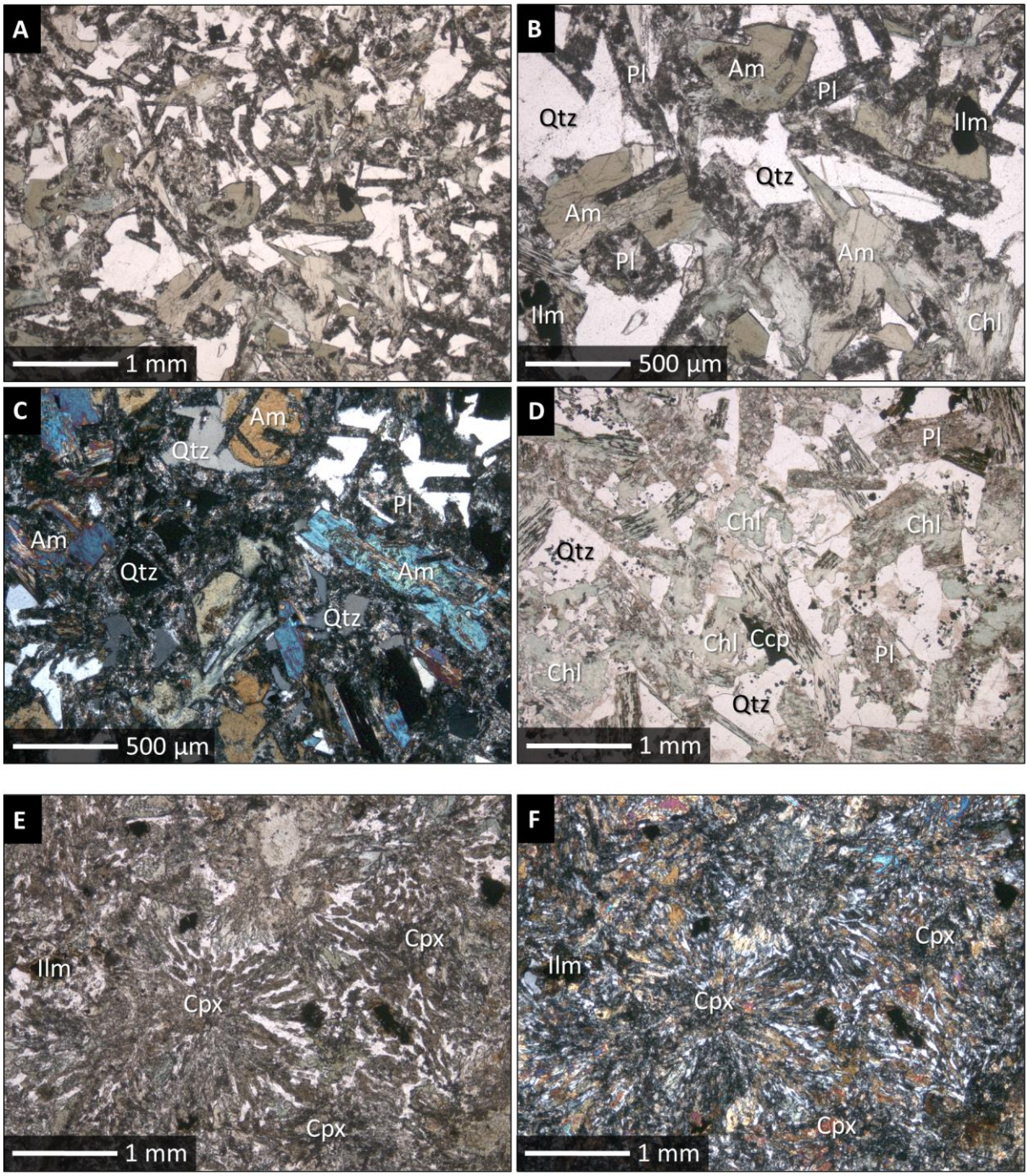

Figure 5.4 Microphotographs of the inclusion-bearing quartz diorite from Rathbun Lake, Rathbun Township; **A:** thin section under transmitted light and plane polars, showing a relatively fresh specimen of the quartz dioritic matrix, with plagioclase and amphibole in an ophitic texture, and enclosed in optical continuous quartz; **B:** same spot but enlarged, plane polars; **C:** Quartz diorite under transmitted light and crossed polars; **D:** altered quartz diorite under transmitted light and plane polars, showing chlorite and epidote pseudomorphically replacing amphibole, biotite, and plagioclase, respectively; note how the original texture is still preserved; **E:** thin section under transmitted light and plane polars showing one of the mafic inclusions; note the spherulitic texture of radiating plagioclase and clinopyroxene; also note the ilmenite grains surrounded by biotite; **F:** same image under crossed polars. Abbreviations: Am = amphibole; Qtz = quartz; Pl = plagioclase; Ilm = ilmenite; Chl = chlorite; Ep = epidote; Ccp = chalcopyrite; Cpx = clinopyroxene.

5.5 Thermobarometry

Analytical results

Representative mineral-chemical analyses of amphibole from the inclusion-bearing quartz diorite are reported in **Table 5.1**, together with structural formulae calculated on the basis of 13 cations per formula unit (excluding Na, Ka, Ca), and with a stochiometric Fe^{3+}/Fe^{2+} determination following the approach as outlined by Holland & Blundy (1994). The analysed amphibole is calcic, i.e., $Ca_{M4} \geq 1.50$; $(Na+K)_A < 0.50$; $Ca_A < 0.5$, and consistently classified as magnesio hornblende according to Leake et al. (1997). The mineral does not exhibit any resolvable core-rim-zonation with respect to major elements, but it shows a considerable range in composition reflecting either sub-solidus processes such as incipient replacement by chlorite or actinolite, or small-scale compositional heterogeneity of the quartz dioritic melt from which the amphibole had crystallised. The SiO_2 content ranges from 48 to 55 wt%; Al_2O_3 ranges from 2.6 to 7.4 wt%. All analyses have elevated TiO_2 contents of up to 1.4 wt%, and 0.85 wt% on average, which is typical of amphibole formed at high temperature. Na_2O contents are as much as 1.4 wt%, and 0.94 wt% on average. The total Al content ranges from 0.4 to 1.3 cations per formula unit. The Fe# = Fe/(Fe+Mg) ranges from 0.26 to 0.43, and the $Fe^{3+}/(Fe^{3+}+Fe^{2+})$ ranges from 0.42 to 0.76. These values indicate relatively high oxygen fugacity (e.g. Spear 1981; Anderson & Smith 1995).

Temperature determinations

Although mineral chemical data were obtained on plagioclase-hornblende pairs, these were not used for the Holland & Blundy (1994) temperature calculations for the following reasons. Firstly, the omnipresent saussuritisation (± sericitisation) evidently obscured the primary composition of the plagioclase. Secondly, almost all plagioclase grains exhibit a continuous core-rim zonation from An_{79} to An_{34}, which leads to an unreasonably large temperature range when using the calculations of Holland & Blundy (1994), even if only the albite-rich rims are considered. Thirdly, the few plagioclase grains that do appear fresh do not occur in contact and therefore not necessarily in textural/chemical equilibrium with hornblende. Thus, instead of using hornblende-plagioclase exchange thermometry, temperatures were determined using the single-phase amphibole thermometer of Ridolfi & Renzulli (2012). Their equations yielded a reasonable average temperature (± 1 std.) of 718 ± 32°C (*n*=74), which is consistent with the results of the Ti-in-amphibole thermometer of Liao et al. (2021), which gave 681 ± 92°C (*n*=74). These values lie above or close to the H_2O saturated granite solidus of ~650°C (e.g. Lambert & Wyllie 1974; Holtz & Johannes 1994), which is one of the prerequisites for the application of most amphibole barometers. The high temperature obtained on the hornblende is consistent with textural evidence of a primary igneous origin. The temperature of 718 ± 32°C or 681 ± 92°C also far exceeds the lower greenschist metamorphic conditions previously established for the area (≤ 350°C; Card 1978; Dressler 1982; Easton 2000), and it precludes that significant sub-solidus re-equilibration had taken place.

Pressure determinations

A prerequisite in the successful application of the various Al-in-hornblende barometers is the presence of an appropriate buffer assemblage (e.g. Hammarstrom & Zen 1986). The hornblende in question occurs in textural equilibrium with quartz, feldspar, biotite, apatite, and Fe-Ti-oxide, and so the system should meet the basic requirement of Si-, K-, Al-, and Ti- saturation. Application

of the various linear Al-in-hornblende barometers yielded, nevertheless, a considerable range in pressure, and in part negative values. The equation of Hollister et al. (1987), for example, gave 1.4 ± 0.5 kbar (*n*=65). However, as noted before, their calculation was only calibrated for 4–6 kbar, which is outside the obtained pressure range. The equation of Johnson & Rutherford (1989) yielded similar results, namely 1.2 ± 0.4 kbar (*n*=65). However, their barometer was only calibrated for 2–8 kbar. The same holds true for the equation of Schmidt (1992), which gave 2.1 ± 0.6 kbar (*n*=69) and again, in part negative values. Evidently, the linear Al-in-hornblende barometers are not suited for such Al-poor amphibole. The barometer of Mutch et al. (2016), which does apply to amphibole formed at low pressure, yielded an average of 1.9 ± 0.4 kbar (*n*=74). This pressure is intermediate between all the above results. The barometer of Anderson & Smith (1995) takes all three intensive parameters (*P*, *T*, fO_2) into account, and it is therefore considered relatively reliable (e.g. Anderson et al. 2008). In order to control for oxygen fugacity, Anderson & Smith (1995) recommended only to use amphibole with $Fe^{3+}/(Fe^{3+}+Fe^{2+}) \geq 0.25$ and Fe# ≤ 0.65, which is a criterion met by all analyses of this study. Using the equation of Anderson & Smith (1995) in concert with the respective temperatures derived from Ridolfi & Renzulli (2012) or Liao et al. (2021), an average pressure of 1.3 ± 0.3 kbar (*n*=74) was obtained. These values compare well with the results obtained by the barometer of Mutch et al. (2016). Finally, the barometer of Ridolfi & Renzulli (2012). It was calibrated against the largest experimental dataset, claims the highest accuracy of all barometers, and can be applied to pressures as low as 1.3 kbar. Their barometer, in conjunction with their single-phase thermometer, gave an average of 0.86 ± 0.23 kbar (*n*=74). For reasons discussed above, the author places most confidence in the results obtained via Anderson & Smith (1995), Mutch et al. (2016) and Ridolfi & Renzulli (2012).

Depth of emplacement

With the crystallisation conditions now being constrained to ca. 700 ± 50°C and 0.8–1.3 kbar, the results can be used to calculate the emplacement depth/level of erosion of the quartz diorite. Assuming a uniform density of 2,650 kg/m³ (the average density of the Huronian Supergroup sedimentary rocks; Card et al. 1984), a lithostatic pressure of 0.86 ± 0.23 kbar would have been attained at 3,300 ± 900 m below palaeosurface; a pressure of 1.3 ± 0.3 kbar equates to 5,000 ± 1,100 m. Assuming a magmastatic instead of a lithostatic pressure, with an average density of an andesitic hydrous impact melt (ca. 2,530 kg/m³ at 1,150°C; Warren et al. 1996), the same pressure would have been reached at the bottom of a 3,400 m-thick or a 5,200 m-thick melt column. Regardless of the choice of the density, which does not greatly change the outcome, these numbers seem quite realistic, considering that the inclusion-bearing quartz diorite from Rathbun Lake occurs at the intrusive contact between the Nipissing Suite and the Gowganda Formation. The overlying (now eroded) Lorrain Formation has an average thickness of 1–2 km elsewhere in the Huronian Basin; the Gordon Lake and Bar River formations have an estimated thickness of ~1 km each (Young et al. 2001; Long 2004). Unfortunately, the pre-erosional extent of the latter two formations is not known, and so whether they were initially present in the Rathbun Lake area is speculative. Interestingly, the calculated depth closely corresponds to the maximum thickness (5 km) of the Main Mass of the Sudbury Igneous Complex (**Chapter 2.1.4**). It also corresponds to the average thickness of the Main Mass (2.5 km) plus the average thickness of the Onaping Formation (1.5 km) (e.g. Lightfoot 2016). The implications of this in relation to the origin of the quartz diorite from Rathbun Lake, and its association with so-called footwall-type mineralisation, will be discussed in more detail in **Chapter 5.8**.

Table 5.1 Representative electron microprobe data and structural formulae for amphibole in the inclusion-bearing quartz diorite from Rathbun Lake

SiO_2	TiO_2	Al_2O_3	Cr_2O_3	FeO	MgO	CaO	MnO	Na_2O	K_2O	Sum	Tetrahedral site				M1, M2, M3 sites								M4 site				A site		
wt%	wt%	wt%	wt%	wt%	wt%	wt%	wt%	wt%	wt%	wt%	Si	Al(IV)	Ti(IV)	Σ	Al(VI)	Ti	Cr	Fe3+	Mg	Fe2+	Mn	Σ	Fe2+	Ca	Na	Σ	Na	K	Σ
52.5	0.65	3.39	0.03	16.7	13.7	10.6	0.29	0.84	0.17	98.95	7.45	0.55	0.00	8.00	0.01	0.07	0.00	0.92	2.90	1.07	0.03	5.00	0.00	1.61	0.23	1.84	0.00	0.03	0.03
50.5	0.48	6.13	0.05	15.1	14.1	11.0	0.27	0.93	0.44	98.94	7.14	0.86	0.00	8.00	0.16	0.05	0.01	0.93	2.97	0.85	0.03	5.00	0.00	1.66	0.26	1.92	0.00	0.08	0.08
54.3	0.81	2.62	0.04	11.8	17.1	11.4	0.11	0.61	0.14	98.87	7.55	0.43	0.02	8.00	0.00	0.07	0.00	0.69	3.54	0.68	0.01	5.00	0.00	1.71	0.16	1.87	0.00	0.02	0.02
52.3	0.62	3.42	0.00	15.6	14.6	10.9	0.27	0.83	0.17	98.81	7.40	0.57	0.03	8.00	0.00	0.04	0.00	0.92	3.08	0.93	0.03	5.00	0.00	1.66	0.23	1.89	0.00	0.03	0.03
54.3	0.86	2.67	0.08	11.1	17.6	11.1	0.07	0.75	0.11	98.66	7.52	0.44	0.04	8.00	0.00	0.05	0.01	0.82	3.64	0.47	0.01	5.00	0.00	1.65	0.20	1.85	0.00	0.02	0.02
52.1	0.60	3.44	0.04	16.5	14.1	10.5	0.31	1.04	0.14	98.66	7.38	0.57	0.04	8.00	0.00	0.02	0.00	1.03	2.98	0.92	0.04	5.00	0.00	1.59	0.28	1.87	0.00	0.03	0.03
52.3	0.17	4.55	0.00	14.5	14.8	11.1	0.29	0.65	0.29	98.63	7.37	0.63	0.00	8.00	0.12	0.02	0.00	0.88	3.11	0.83	0.03	5.00	0.00	1.68	0.18	1.86	0.00	0.05	0.05
50.6	0.20	5.57	0.01	15.1	14.6	11.1	0.33	0.75	0.39	98.62	7.15	0.85	0.00	8.00	0.08	0.02	0.00	1.10	3.07	0.69	0.04	5.00	0.00	1.67	0.21	1.88	0.00	0.07	0.07
49.3	1.21	7.02	0.07	13.9	14.2	11.0	0.25	1.03	0.50	98.55	7.00	1.00	0.00	8.00	0.17	0.13	0.01	0.82	3.00	0.83	0.03	5.00	0.00	1.68	0.28	1.97	0.00	0.09	0.09
50.9	0.18	5.20	0.05	15.3	14.7	11.0	0.30	0.69	0.33	98.55	7.18	0.82	0.00	8.00	0.04	0.02	0.01	1.18	3.09	0.63	0.04	5.00	0.00	1.66	0.19	1.85	0.00	0.06	0.06
51.1	1.04	3.83	0.00	17.5	13.0	10.6	0.29	1.04	0.18	98.49	7.34	0.65	0.02	8.00	0.00	0.09	0.00	0.87	2.77	1.22	0.03	5.00	0.00	1.63	0.29	1.92	0.00	0.03	0.03
48.1	1.36	7.20	0.00	15.3	13.4	11.1	0.15	1.19	0.73	98.47	6.91	1.09	0.00	8.00	0.13	0.15	0.00	0.78	2.87	1.06	0.02	5.00	0.00	1.71	0.29	2.00	0.04	0.13	0.17
49.0	1.28	6.50	0.05	13.8	14.8	11.1	0.17	1.16	0.56	98.38	6.96	1.04	0.00	8.00	0.05	0.14	0.01	0.90	3.14	0.75	0.02	5.00	0.00	1.69	0.31	2.00	0.01	0.10	0.11
52.5	0.08	3.92	0.08	15.3	14.8	10.7	0.35	0.45	0.21	98.37	7.39	0.61	0.00	8.00	0.04	0.01	0.01	1.17	3.10	0.63	0.04	5.00	0.00	1.61	0.12	1.73	0.00	0.04	0.04
49.0	1.24	6.44	0.02	14.6	13.9	11.2	0.17	1.05	0.60	98.32	7.02	0.98	0.00	8.00	0.11	0.13	0.00	0.74	2.98	1.02	0.02	5.00	0.00	1.73	0.27	2.00	0.02	0.11	0.13
48.4	1.41	6.91	0.00	14.9	13.5	11.1	0.22	1.04	0.68	98.22	6.96	1.04	0.00	8.00	0.13	0.15	0.00	0.78	2.90	1.01	0.03	5.00	0.00	1.71	0.29	2.00	0.00	0.12	0.12
50.3	0.21	5.72	0.00	15.3	14.2	10.9	0.33	0.75	0.40	98.15	7.16	0.84	0.00	8.00	0.11	0.02	0.00	1.08	3.00	0.74	0.04	5.00	0.00	1.66	0.21	1.87	0.00	0.07	0.07
53.9	0.01	1.31	0.03	17.6	12.5	12.3	0.22	0.18	0.05	98.14	7.87	0.13	0.00	8.00	0.10	0.00	0.00	0.12	2.72	2.03	0.03	5.00	0.00	1.92	0.05	1.97	0.00	0.01	0.01
54.6	0.73	2.60	0.05	11.2	17.6	10.4	0.08	0.78	0.12	98.13	7.55	0.42	0.03	8.00	0.00	0.05	0.01	1.01	3.64	0.28	0.01	5.00	0.00	1.54	0.21	1.75	0.00	0.02	0.02
48.6	1.25	6.71	0.04	13.6	14.5	11.4	0.18	1.21	0.59	98.02	6.97	1.03	0.00	8.00	0.11	0.13	0.00	0.71	3.10	0.92	0.02	5.00	0.00	1.75	0.25	2.00	0.08	0.11	0.19
51.2	0.12	5.73	0.05	15.8	13.2	10.5	0.46	0.67	0.30	98.01	7.28	0.72	0.00	8.00	0.24	0.01	0.01	1.01	2.80	0.87	0.06	5.00	0.00	1.60	0.18	1.78	0.00	0.05	0.05
48.7	1.29	6.65	0.05	14.7	13.7	11.0	0.25	1.02	0.52	97.98	6.99	1.01	0.00	8.00	0.12	0.14	0.01	0.83	2.94	0.94	0.03	5.00	0.00	1.69	0.28	1.98	0.00	0.10	0.10
50.3	0.48	5.58	0.00	14.8	14.5	10.8	0.30	0.86	0.40	97.98	7.15	0.85	0.00	8.00	0.09	0.05	0.00	1.05	3.07	0.71	0.04	5.00	0.00	1.65	0.24	1.89	0.00	0.07	0.07
48.3	1.39	7.04	0.03	13.7	14.3	11.2	0.22	1.19	0.57	97.92	6.92	1.08	0.00	8.00	0.11	0.15	0.00	0.81	3.06	0.84	0.03	5.00	0.00	1.71	0.29	2.00	0.04	0.10	0.15
49.1	0.91	6.28	0.00	14.9	13.8	11.2	0.24	1.06	0.54	97.92	7.06	0.94	0.00	8.00	0.13	0.10	0.00	0.78	2.96	1.01	0.03	5.00	0.00	1.72	0.28	2.00	0.01	0.10	0.11
48.5	0.94	6.66	0.00	15.4	13.7	11.0	0.25	0.91	0.61	97.92	6.97	1.03	0.00	8.00	0.10	0.10	0.00	0.97	2.92	0.87	0.03	5.00	0.00	1.70	0.25	1.95	0.00	0.11	0.11
48.2	1.28	7.05	0.04	13.8	14.4	11.1	0.18	1.26	0.58	97.87	6.91	1.09	0.00	8.00	0.10	0.14	0.00	0.85	3.08	0.80	0.02	5.00	0.00	1.70	0.30	2.00	0.05	0.11	0.16
47.6	1.33	7.39	0.00	14.0	14.1	11.2	0.13	1.38	0.66	97.84	6.87	1.13	0.00	8.00	0.12	0.14	0.00	0.75	3.03	0.94	0.02	5.00	0.00	1.73	0.27	2.00	0.12	0.12	0.24
52.3	0.23	3.80	0.07	13.2	14.6	12.8	0.18	0.42	0.20	97.81	7.56	0.44	0.00	8.00	0.20	0.03	0.01	0.06	3.14	1.54	0.02	5.00	0.00	1.98	0.02	2.00	0.10	0.04	0.14
50.2	0.20	5.49	0.08	15.0	14.4	10.9	0.33	0.75	0.34	97.81	7.16	0.84	0.00	8.00	0.08	0.02	0.01	1.11	3.06	0.68	0.04	5.00	0.00	1.67	0.21	1.88	0.00	0.06	0.06
48.2	1.20	6.71	0.07	14.4	14.3	11.1	0.26	1.08	0.52	97.77	6.91	1.09	0.00	8.00	0.05	0.13	0.01	0.98	3.05	0.75	0.03	5.00	0.00	1.70	0.30	2.00	0.00	0.09	0.10
49.3	1.28	6.05	0.00	13.2	15.0	11.1	0.16	1.13	0.50	97.71	7.05	0.95	0.00	8.00	0.07	0.14	0.00	0.80	3.19	0.78	0.02	5.00	0.00	1.70	0.30	2.00	0.01	0.09	0.10
49.0	1.04	6.36	0.03	13.8	14.6	10.9	0.20	1.22	0.57	97.71	7.02	0.98	0.00	8.00	0.09	0.11	0.00	0.85	3.11	0.80	0.02	5.00	0.00	1.68	0.32	2.00	0.02	0.10	0.12
48.6	1.05	6.47	0.06	14.1	14.2	11.1	0.19	1.27	0.57	97.65	7.00	1.00	0.00	8.00	0.10	0.11	0.01	0.77	3.06	0.93	0.02	5.00	0.00	1.72	0.28	2.00	0.08	0.10	0.18
48.3	1.31	6.73	0.04	14.7	13.6	11.1	0.21	1.02	0.58	97.64	6.98	1.02	0.00	8.00	0.12	0.14	0.00	0.79	2.93	0.98	0.03	5.00	0.00	1.71	0.29	2.00	0.00	0.11	0.11
48.9	1.15	6.53	0.04	13.4	14.6	11.2	0.19	1.05	0.54	97.61	7.01	0.99	0.00	8.00	0.12	0.12	0.00	0.80	3.13	0.81	0.02	5.00	0.00	1.71	0.29	2.00	0.01	0.10	0.10
48.1	1.36	6.97	0.04	13.5	14.4	11.3	0.19	1.20	0.59	97.61	6.93	1.07	0.00	8.00	0.11	0.15	0.00	0.73	3.08	0.90	0.02	5.00	0.00	1.75	0.25	2.00	0.08	0.11	0.19
48.4	1.31	6.59	0.04	14.1	14.1	11.1	0.25	1.11	0.51	97.57	6.97	1.03	0.00	8.00	0.09	0.14	0.00	0.83	3.03	0.87	0.03	5.00	0.00	1.71	0.29	2.00	0.02	0.09	0.11
48.7	1.22	6.55	0.01	13.7	14.4	11.0	0.21	1.14	0.52	97.52	6.99	1.01	0.00	8.00	0.10	0.13	0.00	0.84	3.09	0.81	0.03	5.00	0.00	1.69	0.31	2.00	0.01	0.09	0.11

5.6 Ore Mineralogy

PGE-Cu±Ni sulphide mineralisation had affected to various degrees the inclusion-bearing quartz diorite and adjacent country rock at Rathbun Lake, as is evident from field observations and the study of numerous grab samples, which, according to Rowell & Edgar (1986), are considered representative of the historic underground workings. Chalcopyrite is the most abundant base metal sulphide and occurs either (i) as semi-massive net-textured ± inclusion-bearing sulphide (40–80 vol%; **Fig. 5.6A**), or (ii) together with pyrite and epidote as disseminated (< 1 vol%) to patchy net-textured sulphide (< 40 vol%; **Fig. 5.6B,C**). This textural and mineralogical bimodality likely reflects to different generations of mineralisation and, together with the newly discovered inclusion-bearing quartz diorite, adds to the complexity of this poorly understood Rathbun Lake mineral occurrence. Consequently, a more detailed characterisation is warranted and provided below.

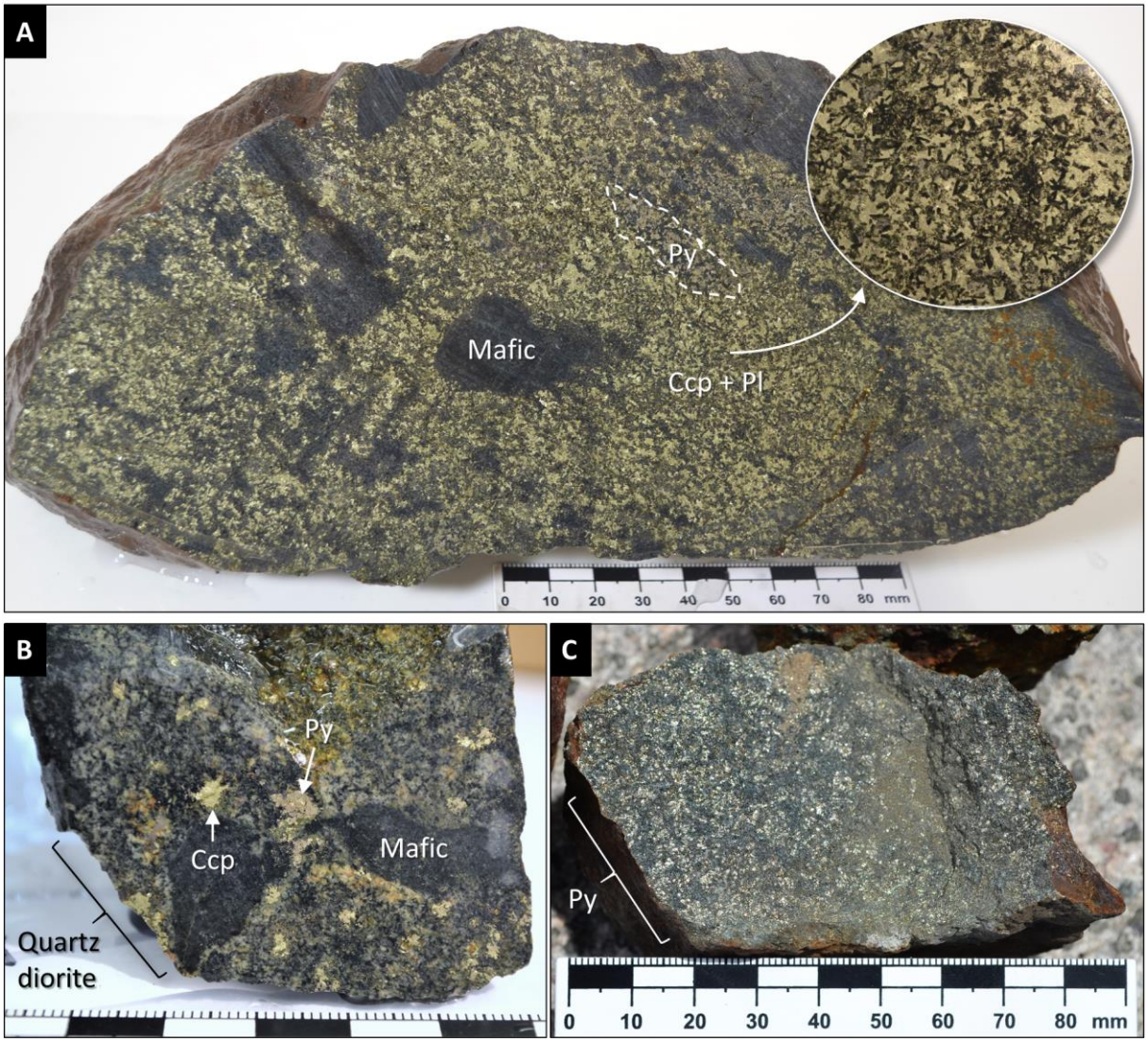

Figure 5.6 Photographs of grab samples from the Rathbun Lake occurrence, showing different sulphide assemblages and textures; **A:** semi-massive net-textured mafic inclusion-bearing chalcopyrite (± violarite) with pyrite patches; green laths are altered plagioclase grains; **B:** disseminated chalcopyrite and pyrite in mafic-inclusion bearing quartz diorite; the mafic inclusions in this specimen are rimmed with a feldspathic leucosome and with patches of epidote; **C:** semi-massive pyrite and subordinate chalcopyrite in a glomerophyric-like texture; host rock unidentifiable. Abbreviations: Ccp = chalcopyrite; Pl = plagioclase; Py = pyrite.

Primary assemblage

Least altered samples of the net-textured, presumably primary, sulphide (e.g. **Fig. 5.6A**) are characterised by a loosely packed framework of saussuritised plagioclase and chloritised amphibole embedded in a matrix of 40–80 vol% interconnected chalcopyrite (**Fig. 5.7A,B**). Interstitial textures between chalcopyrite and fresh silicates are common in samples with < 50 vol% sulphide. Chalcopyrite also occurs as tiny inclusions in plagioclase (**Fig. 5.7C**), and vice versa (**Fig. 5.7A,B**), indicating that these minerals crystallised simultaneously. Traces of pentlandite (~1 vol%) occur as granular, in places loop-textured, rounded grains of up to 2 mm diameter, predominantly located at the margins of larger chalcopyrite grains (**Fig. 5.7D,E**). Pentlandite is pseudomorphically replaced by violarite, with the presence of relic pentlandite confirmed by electron microprobe analyses. Although elsewhere replacement of pyrrhotite by violarite has been noted (e.g. Nickel et al. 1974), this was not observed in any of the samples from Rathbun Lake, as these are free of pyrrhotite. Lamellae of chalcopyrite are present in some of the pentlandite grains and vice versa. Magnetite is an accessory (< 0.1 vol%) phase of the net-textured sulphide, occurring as subhedral to euhedral (sub-)angular 30–100 μm large crystals dispersed throughout, but always in association with chalcopyrite. Two types of magnetite could be distinguished based on the presence or absence of Fe-Ti oxide exsolution lamellae. Magnetite without lamellae is preferentially found at the contact between chalcopyrite and silicates (**Fig. 5.7C**), whereas magnetite with Fe-Ti exsolutions occurs in the interior of chalcopyrite (**Fig 5.7F,G**). Sphalerite is another, although extremely rare, accessory mineral, significantly less abundant than magnetite. Sphalerite occurs as anhedral lobate grains of < 150 μm in size, typically enclosed within chalcopyrite.

In the primary, chalcopyrite-rich sulphide assemblage, a total of 422 discrete grains of precious metal minerals (PMM) were identified in seven standard-sized thin sections. The median size of the PMM is 11 μm. They always occur in association with base metal sulphide and are evenly distributed within a thin section. The majority of PMM are Pd-(Bi-)Te minerals (95.3 vol%), with kotulskite, Pd(Bi,Te), merenskyite $Pd(Bi,Te)_2$, and michenerite, PdBiTe identified. Qualitative WDS scans on these minerals reveal Pt concentrations below the detection limit. No composite grains between the above listed minerals were observed. Although only four grains of sperrylite ($PtAs_2$) were identified, they were all very large (e.g. **Fig. 5.7D**), ranging in size from 30 to 150 μm. Consequently, as the Pd-bearing minerals are small and the Pt-bearing minerals large, the total PMM count is not representative of the Pd/Pt ratios of these samples. In addition to the Pd-bearing minerals, a few grains of gold (AuAg), Ag-Bi-Te and Pt-Bi-Te phases were also found. Irrespective of their composition, all PMM occur at or near the edges of chalcopyrite, at the contact between sulphide and silicate. PMM are rarely enclosed in chalcopyrite, but where they are, they tend to have a spherical habit. In contrast, PMM at the sulphide-silicate interface typically display a concave shape into the sulphide, and a straight contact to the silicate. Only few PMM occur in association with pentlandite or magnetite. Even where PMM are hosted only by silicates (typically chlorite, rarely epidote), they are still in close proximity (< 200 μm) to chalcopyrite. PMM which, at first sight, appear to be entirely surrounded by silicate, still exhibit sub-micron intergrowths with apexes of chalcopyrite, hence the high number of PMM at the chalcopyrite-silicate interface.

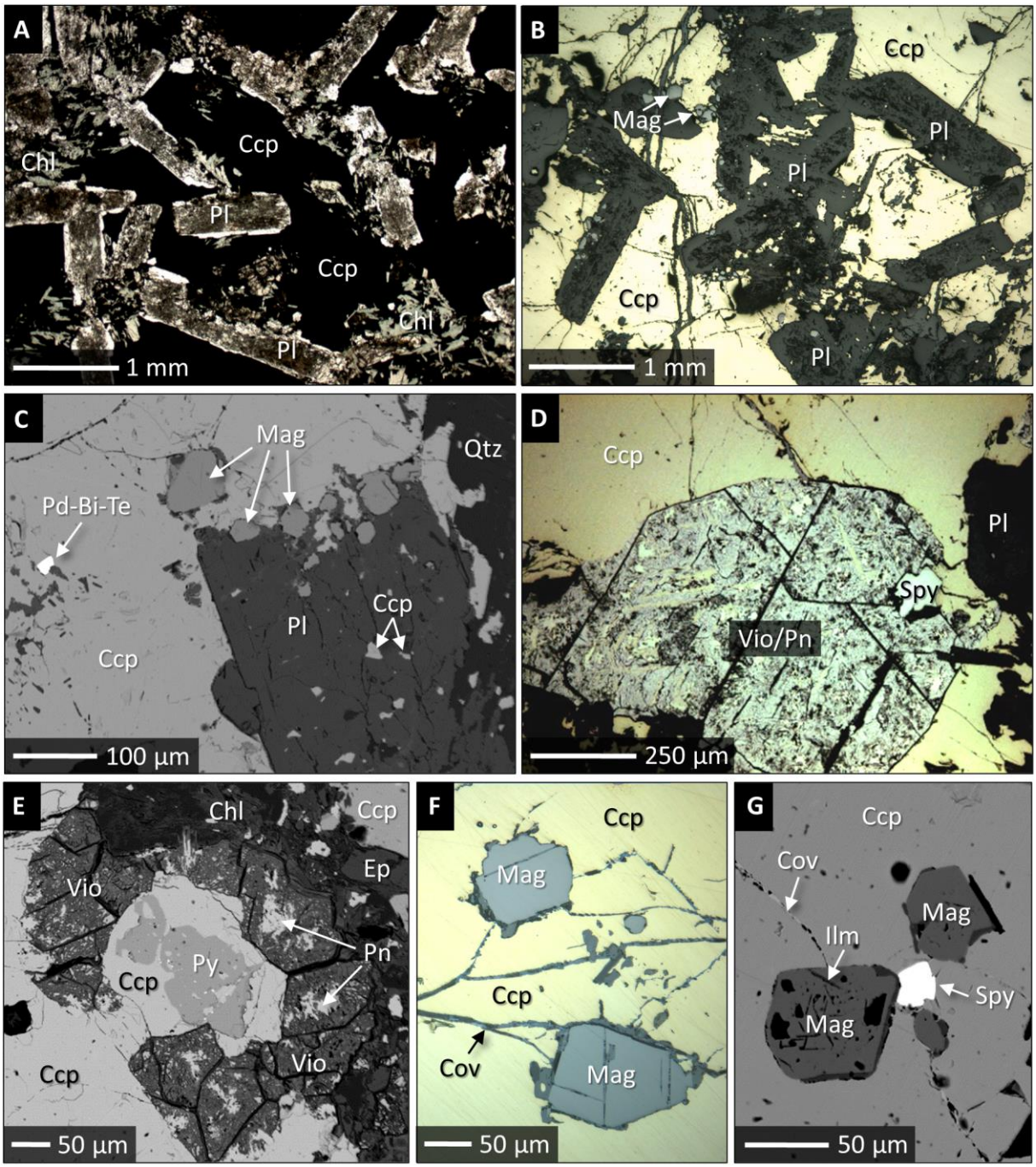

Figure 5.7 Representative microphotographs of mineralised samples from the Rathbun Lake occurrence; **A:** thin section of the sample in Fig. 5.6A under reflected light and plane polars, showing net-textured chalcopyrite enclosing altered grains of plagioclase; note the strongly saussuritised cores of plagioclase and the fresh rims of albite; **B:** same thin section under reflected light; note the abundant magnetite clusters typically found along the sulphide-silicate interface; **C:** BSE images showing magnetite grains preferentially developed at the contact between chalcopyrite and plagioclase; **D:** thin section under reflected light showing granular pentlandite (now altered to violarite) enclosed in chalcopyrite; note the typical octahedral cleavage of the original pentlandite; **E:** BSE image showing a loop-textured (atoll-like) grain of pentlandite (pseudomorphically replaced by violarite) together with chalcopyrite and pyrite; **F:** thin section under reflected light showing magnetite enclosed in chalcopyrite, and covellite as fracture infill; **G:** BSE image showing a large grain of sperrylite and trellis-textured magnetite grains (with exsolution lamellae of ilmenite), all enclosed in chalcopyrite. Abbreviations: Ccp = chalcopyrite; Pl = plagioclase; Chl = chlorite; Mag = magnetite; Qtz = quartz; Vio = violarite; Pn = pentlandite; Spy = sperrylite; Ep = epidote; Cov = covellite; Ilm = ilmenite.

Secondary assemblage

In agreement with Rowell & Edgar (1986), much of the pyrite and covellite in those samples that contain chalcopyrite, pentlandite and magnetite, is regarded as secondary because of them replacing other minerals, and their close association with hydrous silicates, veinlets, and deformation features. Pyrite is the most abundant sulphide in these samples, amounting to 50–85 vol% of the total sulphide, and it occurs in different forms. Angular pyrite is typically intergrown with chalcopyrite and, in places, overgrown by another type of anhedral and porous pyrite or marcasite. The euhedral type predominates and occurs as both patches and decimetre-long veinlets, where it is found together with interstitial chalcopyrite, disseminated throughout the quartz diorite, and cutting the adjacent Gowganda Formation wacke. Vein-type pyrite hosts inclusions of chalcopyrite, whereby some of these inclusions resulted from the coalescence of pyrite grains. Sulphide veinlets tend to follow a pervasive rock foliation defined by chlorite (S_1), where they were affected by later crenulation (S_2). In thin section, both pyrite and chalcopyrite occur as replacements after chlorite along its cleavage planes and as symplectitic intergrowths. Remobilisation of sulphide is also evident in outcrop in the form of sulphide-bearing, vertical, N-striking shear zones, 4 m north of the shaft, within the Gowganda Formation wacke (**Fig. 5.2C**). Rare millerite (< 0.1 vol% of total sulphide) was observed in thin section as part of disseminated sulphide patches within the quartz diorite. Millerite is of granular habit, up to 300 µm in diameter, and typically associated with pyrite, less frequently with chalcopyrite. Electron microprobe analyses indicate that millerite is locally replaced by violarite as well. Molybdenite, galena, arsenopyrite and Co-rich gersdorffite (NiAsS) are both small and rare accessory phases; they were only identified by using the electron microprobe. They occur in close spatial relationship with secondary sulphides and hydrous silicates, disseminated throughout the quartz diorite and wacke, and never as inclusions in chalcopyrite. Grain boundaries of, and fractures in, chalcopyrite are rimmed and filled with covellite.

In the secondary sulphide assemblage, 603 grains of PMM in nine thin sections were identified. Their median size is 10 µm. Again, Pd-(Bi-)Te minerals, including Bi-rich and Bi-poor kotulskite, merenskyite and michenerite, predominate (86 vol%). Compared to the primary assemblage, they occur more frequently as clusters, ragged grains and as satellite grains, i.e., detached from chalcopyrite, and entirely surrounded by secondary silicates (chlorite, epidote, stilpnomelane). In addition, they are frequently associated with secondary sulphides and arsenides, such as covellite, pyrite and arsenopyrite, though they do not occur in veinlets. PMM in the secondary assemblage tend towards a more irregular shape, especially where they are in contact with hydrous silicates (e.g. **Fig. 5.8C**). In contrast to the primary assemblage, the secondary assemblage is marked by the presence of Sb-and Hg-bearing PMM. The following minerals were identified: Potarite, PdHg, temagamite Pd_3HgTe_3, testiopalladite, PdTe(Te,Sb) and Sb- and Hg-bearing Pd-Bi-Te (or µm-sized intergrowths of the former), all of which are associated with hydrous silicates, chalcopyrite, its alteration product covellite, or pyrite. In places, they form composite grains with each other.

Microprobe X-ray mapping has demonstrated that most PMM grains are compositionally homogenous. This is true for PMM both in the primary and secondary assemblages. Some exceptionally large PMM in the secondary assemblage do show, however, a non-uniform distribution of major element concentrations, including Pd, Bi, Te, Hg and Sb. One PMM, for example, displays a core-rim zonation from Te-rich and Sb-free to Te-free and Sb-rich composition (**Fig. 5.8A**). Note how this pattern fits into the textural position of this particular PMM, with the PMM's contact to chlorite being enriched Sb, whereas the Te-rich core is bound on either side by chalcopyrite.

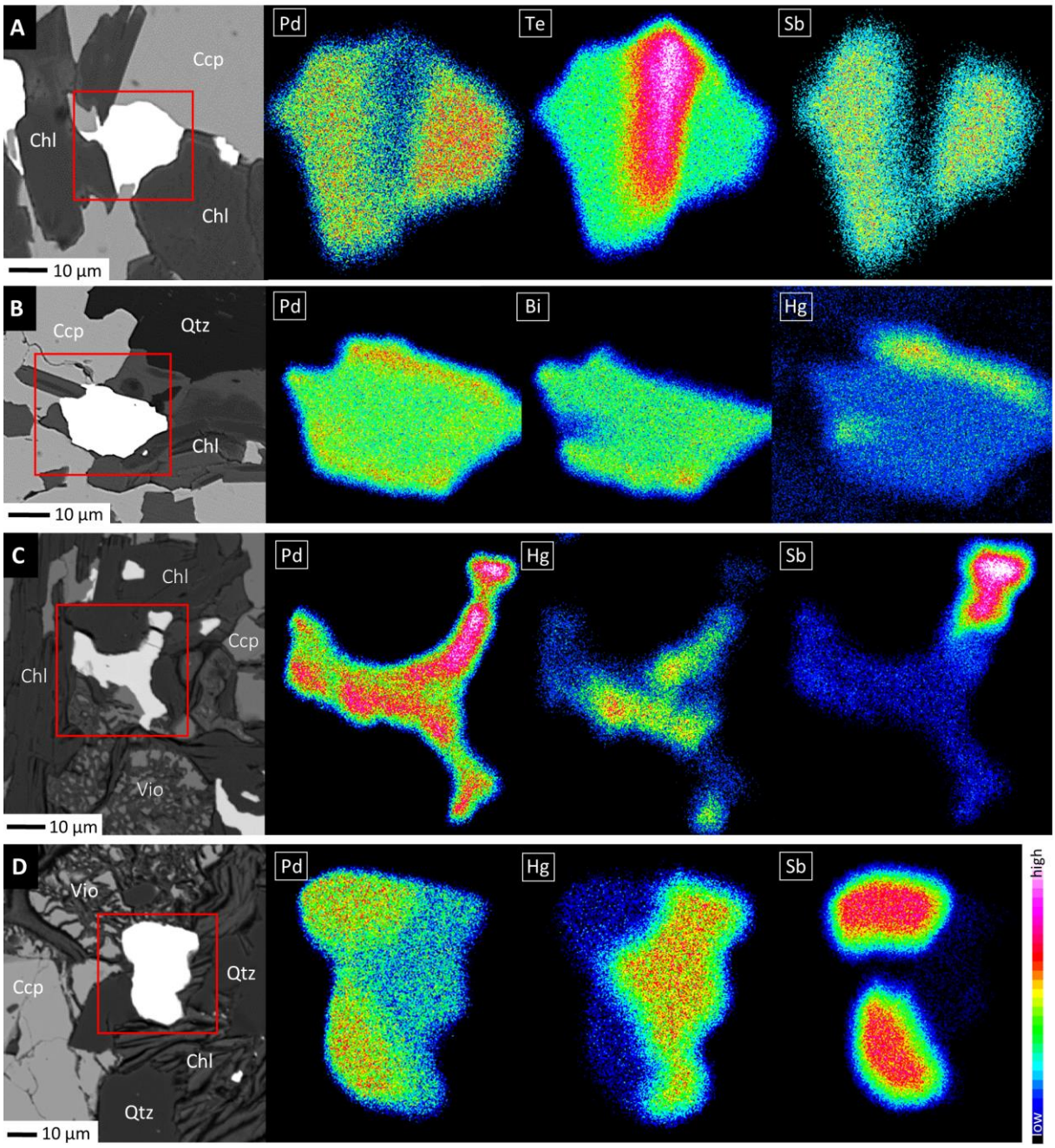

Figure 5.8 Qualitative x-ray maps of element distribution in precious metal minerals; intensities of Pd (Lα), Te (Lα), Sb (Lα), Hg (Lα) and Bi (Mα) are given in counts per second; pixel size is 0.04 µm.

Another grain shows a similar distribution (**Fig. 5.8B**): The part of the PMM, that is truncated by chlorite, is depleted in Bi and enriched in Hg. This antithetic correlation between Bi and Te on the one side and Pd, Hg, and Sb on the other side could have various reasons. Theoretically, the noted inhomogeneities could be due to composite grains hidden in the third dimension or to exsolution. However, no discrete (sub)grain boundaries that are conformable to the chemical zonation could be observed in BSE images or under reflected light, thus ruling out the above possibilities. Based on the PMM's textural position and the irregular nature of compositional zonation in the Hg- and Sb-bearing phases, it is more likely that these inhomogeneities are related to fluid-induced diffusion. The mapped PMM could represent partly altered Pd-Bi-Te grains, in which alteration failed to replace the entire grain because of its exceptionally large size. Smaller grains were completely altered, resulting in the endmember compositions PdHg, Pd_3HgTe_3 and PdTe(Te,Sb).

5.7 Geochemistry

General characteristics

Whole-rock major and trace element concentrations for inclusion-bearing quartz diorite from Rathbun Lake are listed in **Table 5.2**. The data reveal a clear geochemical distinction between matrix and inclusions as well as mixing relations thereof. Mafic inclusions are subalkaline, subaluminous, and basic in terms of SiO_2 (51–52 wt%); sedimentary inclusions are subalkaline, peraluminous and likewise poor in SiO_2 (47 wt%); the matrix is subalkaline, sub- to peraluminous and intermediate (53–56 wt% SiO_2). The LOI is typically between 1.1 and 3.5 wt%. It is highest in the chlorite-rich sedimentary inclusions, followed by the quartz dioritic matrix (where amphibole is the dominating hydrous mineral), followed by the overall anhydrous mafic inclusions. Mafic inclusions have a higher and very constant Mg# (64) compared to the matrix (46–63), but they have similar and more uniform concentrations of TiO_2 (0.6 wt%), Ni (140 ppm) and Cr (230 ppm). In either lithology, P_2O_5 concentrations are close to the detection limit of the EDS-XRF. Sedimentary inclusions are, as expected from their petrography, rich in Al_2O_3 (19 wt%) and K_2O (3.2 wt%). The largest discrepancy between matrix and inclusions exists, however, with respect to incompatible lithophile elements. Sedimentary and especially the mafic inclusions are, for instance, poor in Zr (≤ 47 ppm), Nb (≤ 5 ppm), Th (≤ 3 ppm), U (≤ 1 ppm) and ΣREE+Y (≤ 82 ppm), compared to the quartz diorite matrix, which has variable but generally high concentrations of Zr (up to 158 ppm), Nb (up to 9.6 ppm), Th (up to 9 ppm), U (up to 3.4 ppm), and ΣREE+Y (up to 148 ppm).

The CIPW normative mineralogy of the matrix of the inclusion-bearing quartz diorite is as follows: 56 vol% plagioclase, 20 vol% hypersthene, 9 vol% orthoclase, 8 vol% quartz and 5 vol% diopside. Some samples are notably corundum-normative (~1 vol%) at the expense of normative diopside. Mafic inclusions are normatively composed of 52 vol% plagioclase, 24 vol% hypersthene, 14 vol% diopside, 7 vol% orthoclase, and 2 vol% quartz. The density of the matrix, calculated based on its normative mineralogy, is 2.9 g/cm^3, whereas the density of the mafic inclusions is 3.0 g/cm^3. Sedimentary inclusions are corundum- and olivine normative.

Igneous rock classification

According to total alkalis vs. silica (TAS) diagram (**Fig. 5.9B**), the composition of the inclusion-bearing quartz diorite conforms to that basaltic andesite (intrusive equivalent: gabbroic diorite) or basaltic trachyandesite (gabbroic monzodiorite); the composition of the mafic inclusions conforms to basalt (gabbro). Most samples of the quartz dioritic matrix are calc-alkaline but with a tendency towards tholeiitic affinity; mafic inclusions are tholeiitic (**Fig. 5.9C**). Although it is not entirely clear if and to what extent major elements have been mobilised in the course of alteration, classification plots using typically immobile trace elements (Ti, Nb, Y, Zr, Th) are generally preferred over plots using potentially mobile major elements (Na, K, Si, Fe, Mg). According to such diagrams (e.g. **Fig. 5.9D**), the matrix is dioritic, and the mafic inclusions are gabbroic. Most classification schemes, including **Figure 5.9E** and others not shown here (e.g. Jensen 1976; Hastie et al. 2007; Ross & Bédard 2009), support a calc-alkaline magmatic affinity for the matrix, and they suggest – somewhat ambiguously – a tholeiitic to calc-alkaline affinity for the mafic inclusions. This classification agrees with mantle-normalised trace element patterns of both lithotypes (**Fig. 5.9F**). For there are pronounced negative Nb-Ta-Ti anomalies and weakly positive K-Pb-Sr anomalies in the patterns of the quartz dioritic matrix, which is typical of (calc-alkaline) arc magmatism

or tholeiitic magmatic rocks that chemically interacted with (assimilated) large volumes of material from the continental crust. The same anomalies (i.e., negative Nb-Ta-Ti, positive Pb-Sr) are also found in the mafic inclusions, where they are, however, less pronounced. Normalised multielement diagrams also highlight differences between the quartz dioritic matrix and the mafic inclusions, the former displaying a wider range in composition and a broad bandwidth of trace element patterns, the latter having a much narrower range in composition and overall lower normalised trace element abundances. Furthermore, there are subtle yet noteworthy differences in the slope of the normalised REE patterns, the normalised Th/U ratio, and the normalised Zr/Hf ratio. The Eu anomaly, expressed as $Eu_N/(Sm_N \times Gd_N)^{0.5}$, is throughout negative in the quartz dioritic matrix (0.65–0.90), but it is virtually absent (~1) in the mafic inclusions. Little geochemical difference exists between the mafic inclusions and the quartz dioritic matrix in terms of Cr, Ni and V concentrations. Note that the inclusion-bearing massive sulphide sample (SULF-1; **Tab. 5.2**) is geochemically more akin to the quartz dioritic matrix, rather than resembling the composition of the mafic inclusions, which is evident in elevated concentrations of, for example, U and Th.

Nd-Sr-Pb isotopes

A summary of whole-rock radioisotope data for matrix separates from the inclusion-bearing quartz diorite is presented in **Table 5.3**. All eight samples display a range in $^{143}Nd/^{144}Nd$ corresponding to an εNd between –26.75 and –23.62. The $^{147}Sm/^{144}Nd$ ratios are between 0.117 and 0.128 and correlate well ($R^2 = 0.75$) with the measured $^{143}Nd/^{144}Nd$ ratio. An ordinary least square regression passing through all eight data points using *IsoplotR* (Vermeesch 2018) yields an errorchron date of 1923 ± 423 Ma. One-stage Nd model ages (t_{DM}) are between 2816 Ma and 2999 Ma, and 2916 Ma on average. The $^{87}Sr/^{86}Sr$ isotope ratio varies from 0.719 to 0.727, and the $^{87}Rb/^{86}Sr$ ratio from 0.333 to 0.772. These data do not permit to calculate any statistically robust isochron. The Sr isotope model age varies greatly; it is 2903 Ma on average. Note the similarity between Sr model age and Nd model age. The measured $^{206}Pb/^{204}Pb$ ratio ranges from 22.61 to 30.32, $^{207}Pb/^{204}Pb$ from 16.32 to 17.29, and $^{208}Pb/^{204}Pb$ from 37.63 to 40.89, all of which are highly correlated with each other ($R^2 > 0.95$). The spread in uranogenic Pb isotope ratios makes it possible to construct a whole-rock errorchron, which, depending on the statistical approach, has either a slope equivalent to 1883 ± 1 Ma (York/maximum likelihood regression; MSWD = 18,000) or 2021 ± 76 Ma (ordinary least square regression). The modelled initial $^{207}Pb/^{204}Pb$ ratio at 1850 Ma (the absolute age of the Sudbury impact event) ranges from 15.55 to 15.61.

Table 5.3 also includes Nd-Sr-Pb isotope data for two of the mafic inclusions. The $^{143}Nd/^{144}Nd$ ratios is, within analytical uncertainty, identical between the two samples. It corresponds to a present-day εNd of –19.33 and –20.43. The $^{147}Sm/^{144}Nd$ ratio is 0.139 and 0.136, and the one-stage Nd model age (t_{DM}) is 2897 Ma and 2879 Ma. The measured $^{87}Sr/^{86}Sr$ isotope ratio is 0.721 for both samples; the measured Rb/Sr element ratio is 0.179 and 0.184; the calculated $^{87}Rb/^{86}Sr$ isotope ratio is 0.685 and 0.700. The Rb-Sr isotope data correspond to model ages of 2003 Ma and 2083 Ma. The measured $^{206}Pb/^{204}Pb$ ratio is 18.27 and 18.69, $^{207}Pb/^{204}Pb$ 15.76 and 15.82, and $^{208}Pb/^{204}Pb$ is 36.89 and 37.10. The narrow spread in radiogenic isotope ratios prevent the calculation of any statistically meaningful isochron. From these isotopic features it becomes evident, however, that the mafic inclusions differ quite significantly from the quartz dioritic matrix in that they are less radiogenic (i.e., higher $^{143}Nd/^{144}Nd$ ratio, lower $^{87}Sr/^{87}Sr$ ratio and lower $^{206}Pb/^{204}Pb$, $^{207}Pb/^{204}Pb$, $^{208}Pb/^{204}Pb$ ratios).

Table 5.2 Major element oxide concentrations (wt%) and trace element concentrations (ppm) in inclusion-bearing quartz diorite, Rathbun Lake, Rathbun Township

	Inclusion-bearing quartz diorite (matrix)													Sulphide	Mafic and sedimentary inclusions				
	IQD-1	IQD-2	IQD-3	IQD-4	IQD-5	IQD-6	IQD-7	IQD-8	IQD-9	IQD-10	IQD-11	IQD-12	IQD-13	SULF-1	MAF-1	MAF-2	MAF-3	MAF-4	SED-1
SiO_2	54.89	54.22	52.53	53.86	55.08	54.83	53.84	54.78	56.19	54.59	54.77	54.77	54.73	29	51.40	51.54	51.33	51.62	47.22
TiO_2	0.64	0.71	0.63	0.23	0.68	0.66	0.64	0.69	0.68	0.72	0.74	0.45	0.69	0.56	0.60	0.62	0.58	0.60	0.96
Al_2O_3	15.59	15.43	15.09	18.22	15.71	15.57	15.40	16.19	16.24	15.84	15.93	17.29	16.35	9.55	14.85	14.98	14.80	15.00	18.89
Fe_2O_3	9.67	9.35	10.41	7.88	9.43	9.55	9.80	10.84	10.20	9.18	8.89	8.22	10.84	27.2	10.51	10.43	10.25	10.61	14.33
MgO	6.17	5.98	7.46	5.89	5.79	6.11	6.36	5.32	4.93	5.80	5.43	5.68	4.04	2.53	8.27	8.19	8.16	8.33	6.10
CaO	7.07	7.89	8.48	6.21	7.22	7.12	7.37	5.61	5.21	7.07	7.04	6.39	7.42	2.7	10.31	9.96	10.17	8.53	3.54
MnO	0.13	0.13	0.16	0.13	0.12	0.13	0.14	0.10	0.09	0.12	0.11	0.12	0.09	0.06	0.18	0.17	0.17	0.18	0.10
Na_2O	2.63	3.48	2.20	2.98	2.59	2.98	2.36	2.08	2.27	3.03	3.01	3.20	1.92	1.12	1.75	1.91	1.73	2.17	2.29
K_2O	1.21	0.90	1.18	1.89	1.18	1.13	1.20	1.18	1.21	1.42	1.37	1.54	1.06	0.2	0.91	0.92	0.82	1.18	3.21
P_2O_5	< 0.02	0.06	< 0.02	0.19	0.05	0.04	< 0.02	0.19	0.13	0.05	0.07	0.07	0.29	0.03	< 0.02	< 0.02	< 0.02	< 0.02	0.02
LOI	2.13	1.92	1.73	2.74	2.11	1.93	1.98	3.54	3.41	2.16	2.14	2.28	3.13	13.0	1.14	1.40	1.46	1.68	3.19
Total	100.13	100.07	99.87	100.22	99.96	100.05	99.09	100.52	100.56	99.98	99.50	100.01	100.56	85.95	99.92	100.12	99.47	99.90	99.85
V	187.8	204.2	202.8	69.20	194.3	190.5	194.7	185.3	180.6	157.4	192.8	100.9	158.4	142	233.9	221.5	224.9	215.6	257.0
Cr	270.4	181.3	407.1	187.7	234.2	218.9	309.6	231.0	201.1	168.9	168.3	157.6	179.8	180	299.3	295.5	244.1	227.3	304.7
Ni	148.7	120.7	214.9	100.4	138.1	121.9	244.6	125.2	91.59	119.3	100.2	102.4	108.1	881	162.0	171.3	136.0	145.9	170.9
Cu	123.6	161.6	130.7	52.90	126.2	129.4	122.7	141.5	71.26	153.9	157.2	101.7	103.0	134,000	121.2	124.0	128.2	152.9	47.52
Rb	38.09	31.81	40.49	63.46	50.83	35.50	37.81	42.42	37.54	49.26	46.08	65.21	29.00	5.6	39.23	34.69	28.60	44.11	131.5
Sr	245.4	287.5	214.1	266.4	311.7	258.6	243.1	424.4	294.8	273.4	319.9	310.2	607.2	175	213.0	194.3	190.6	200.8	267.4
Y	15.75	16.78	15.40	15.49	19.27	16.29	16.18	22.96	19.38	15.51	15.18	16.34	21.27	4.8	16.25	15.58	15.58	15.37	14.60
Zr	74.35	87.56	55.31	33.40	85.33	77.74	66.17	124.6	158.2	76.30	81.29	51.04	74.14	54.4	42.50	42.61	40.18	42.40	47.28
Nb	7.720	6.686	9.615	3.134	8.286	5.971	8.639	8.553	8.048	6.216	6.765	4.794	5.367	4	3.971	5.056	2.600	3.762	4.111
Ba	212.7	174.1	278.2	342.5	223.7	199.8	217.7	197.8	207.2	239.7	244.1	299.8	120.2	30	239.5	221.9	180.7	231.4	612.9
La	15.49	16.32	12.58	18.92	17.90	15.67	15.30	24.50	21.91	15.72	16.69	19.44	21.94	11.4	10.04	10.25	10.55	11.76	22.82
Ce	33.28	35.34	27.31	40.93	37.80	35.27	33.95	50.22	45.36	34.35	36.29	39.31	46.44	20.5	21.38	22.36	22.83	25.91	45.39
Pr	4.010	4.128	3.351	5.020	4.525	4.229	4.071	5.879	5.313	4.191	4.263	4.717	5.235	2.16	2.656	2.735	2.852	3.101	5.364
Nd	15.50	16.35	13.43	20.00	18.05	16.49	16.01	23.17	20.74	16.31	16.78	18.45	19.94	7.3	11.18	11.43	11.93	12.55	21.63
Sm	3.279	3.344	2.922	4.044	3.679	3.481	3.368	4.835	4.230	3.396	3.393	3.572	4.211	1.3	2.582	2.575	2.726	2.746	3.985
Eu	0.765	0.795	0.796	0.860	0.832	0.761	0.771	1.375	1.108	0.692	0.703	0.841	1.568	0.55	0.783	0.775	0.773	0.741	1.250
Tb	0.465	0.477	0.434	0.464	0.528	0.462	0.453	0.669	0.572	0.465	0.462	0.470	0.611	0.15	0.443	0.429	0.435	0.422	0.457
Gd	3.045	3.180	2.857	3.498	3.455	3.049	2.978	4.562	3.997	3.086	3.070	3.212	4.150	1.05	2.713	2.701	2.811	2.675	3.506
Dy	2.997	3.050	2.865	2.899	3.384	2.977	2.968	4.004	3.559	2.863	2.792	2.870	3.811	0.9	2.876	2.836	2.950	2.814	2.795
Ho	0.578	0.599	0.555	0.541	0.666	0.579	0.572	0.791	0.695	0.563	0.545	0.565	0.734	0.18	0.588	0.572	0.577	0.556	0.525
Er	1.698	1.764	1.691	1.541	1.984	1.694	1.702	2.300	2.065	1.599	1.560	1.628	2.127	0.55	1.726	1.715	1.746	1.680	1.497
Tm	0.240	0.248	0.241	0.212	0.282	0.244	0.245	0.327	0.292	0.208	0.219	0.213	0.282	0.1	0.253	0.239	0.246	0.238	0.210
Yb	1.568	1.680	1.644	1.393	1.892	1.620	1.623	2.167	2.010	1.475	1.419	1.535	1.851	0.5	1.714	1.634	1.642	1.603	1.355
Lu	0.246	0.258	0.247	0.213	0.293	0.254	0.252	0.345	0.319	0.231	0.221	0.240	0.278	0.09	0.267	0.253	0.261	0.249	0.215
Hf	2.123	2.356	1.571	1.064	2.393	2.207	1.966	3.256	3.995	2.176	2.321	1.568	2.119	1	1.212	1.286	1.178	1.239	1.325
Ta	0.525	0.541	0.351	0.370	0.579	0.572	0.533	0.620	0.712	0.600	0.629	0.511	0.546	< 0.5	0.195	0.219	0.228	0.322	0.335
Pb	5.140	7.663	5.291	5.100	5.975	4.971	5.210	4.468	4.960	3.944	4.641	6.625	3.742	55	6.616	5.964	6.340	4.543	6.030
Th	6.678	8.348	4.176	5.588	8.921	6.816	6.039	3.991	5.116	6.589	7.168	7.517	3.696	4	1.925	2.336	2.172	2.809	3.292
U	2.554	2.751	1.561	2.256	2.798	2.630	2.258	3.038	3.421	1.908	2.677	1.897	3.195	1.42	0.646	0.806	0.791	1.122	1.058

Note: SULF-1 is a sample of semi-massive inclusion-bearing sulphide that was analysed by the commercial AGAT Laboratories, Toronto

Table 5.3 Summary of whole-rock Nd-Sr-Pb isotope data for the inclusion-bearing quartz diorite from Rathbun Lake, Rathbun Township

	$^{143}Nd/^{144}Nd$	±2σ	$^{147}Sm/^{144}Nd$	εNd present	εNd 1850 Ma	1-stage t_{DM}	$^{87}Sr/^{86}Sr$	±2σ	$^{87}Rb/^{86}Sr$	$^{87}Sr/^{86}Sr_{1850}$	$^{208}Pb/^{204}Pb$	±2σ	$^{207}Pb/^{204}Pb$	±2σ	$^{206}Pb/^{204}Pb$	±2σ	$^{207}Pb/^{204}Pb_{1850}$
Inclusion-bearing quartz diorite (matrix separates)																	
IQD-2	0.511339	15	0.124	–25.33	–7.99	2904 Ma	0.719213	13	0.502	0.70585	40.1859	34	16.5932	10	24.3260	14	15.59
IQD-5	0.511340	14	0.123	–25.32	–7.88	2889 Ma	0.722759	13	0.644	0.70560	40.8861	21	16.6515	8	25.2823	15	15.54
IQD-8	0.511360	10	0.126	–24.93	–8.19	2956 Ma	0.724871	14	0.475	0.71223	38.3990	29	16.8808	8	27.2522	12	15.55
IQD-9	0.511312	11	0.123	–25.87	–8.44	2941 Ma	0.724481	14	0.548	0.70988	38.2017	23	16.7545	9	26.1418	13	15.55
IQD-10	0.511331	14	0.126	–25.50	–8.69	2999 Ma	0.725715	10	0.691	0.70731	39.6524	27	16.6066	9	25.0744	12	15.52
IQD-11	0.511292	12	0.122	–26.25	–8.57	2940 Ma	0.724569	12	0.593	0.70877	39.5598	35	16.4940	11	24.2096	12	15.50
IQD-12	0.511267	16	0.117	–26.75	–7.84	2816 Ma	0.726631	13	0.772	0.70606	38.9942	23	16.3167	8	22.6103	10	15.51
IQD-13	0.511427	14	0.128	–23.62	–7.23	2884 Ma	0.720473	13	0.333	0.71161	37.6299	24	17.2941	9	30.3172	14	15.61
Mafic inclusions																	
MAF-1	0.511647	11	0.139	–19.33	–5.77	2897 Ma	0.721482	13	0.700	0.70282	36.8875	25	15.7575	9	18.2665	7	15.44
MAF-2	0.511590	15	0.136	–20.43	–6.06	2879 Ma	0.721794	15	0.685	0.70354	37.1029	20	15.8188	8	18.6921	8	15.45

$^{147}Sm/^{144}Nd$ and $^{87}Rb/^{86}Sr$ ratios were calculated using measured Sm, Nd, Rb and Sr concentrations, which are given in Table 5.2;
2σ uncertainties of $^{147}Sm/^{144}Nd$ and $^{87}Rb/^{86}Sr$ are < 3% based on the propagated analytical error of Sm, Nd, Rb and Sr concentration data;
$^{143}Nd/^{144}Nd$ ratios are normalised to $^{146}Nd/^{144}Nd = 0.72190$;
2σ uncertainties of $^{143}Nd/^{144}Nd$ are < 0.004% based on the long-term in-house reproducibility of BHVO-2;
2σ uncertainties of $^{87}Sr/^{86}Sr$ are < 0.007% based on the long-term in-house reproducibility of BHVO-2;
2σ uncertainties of $^{208}Pb/^{204}Pb$, $^{207}Pb/^{204}Pb$ and $^{206}Pb/^{204}Pb$ are < 0.18%, < 0.09% and < 0.5%, respectively, based on the long-term in-house reproducibility of BHVO-2;
For sake of readability, all listed 2σ absolute errors only refer to the last significant decimal digits of the measured isotope ratios;
εNd values were calculated relative to CHUR with $^{147}Sm/^{144}Nd = 0.1967$ and $^{143}Nd/^{144}Nd = 0.512638$;
One-stage Nd model ages (t_{DM}) were calculated according to DePaolo (1981a,b);
$^{207}Pb/^{204}Pb_{1850}$ was calculated according to Darling et al. (2010a)

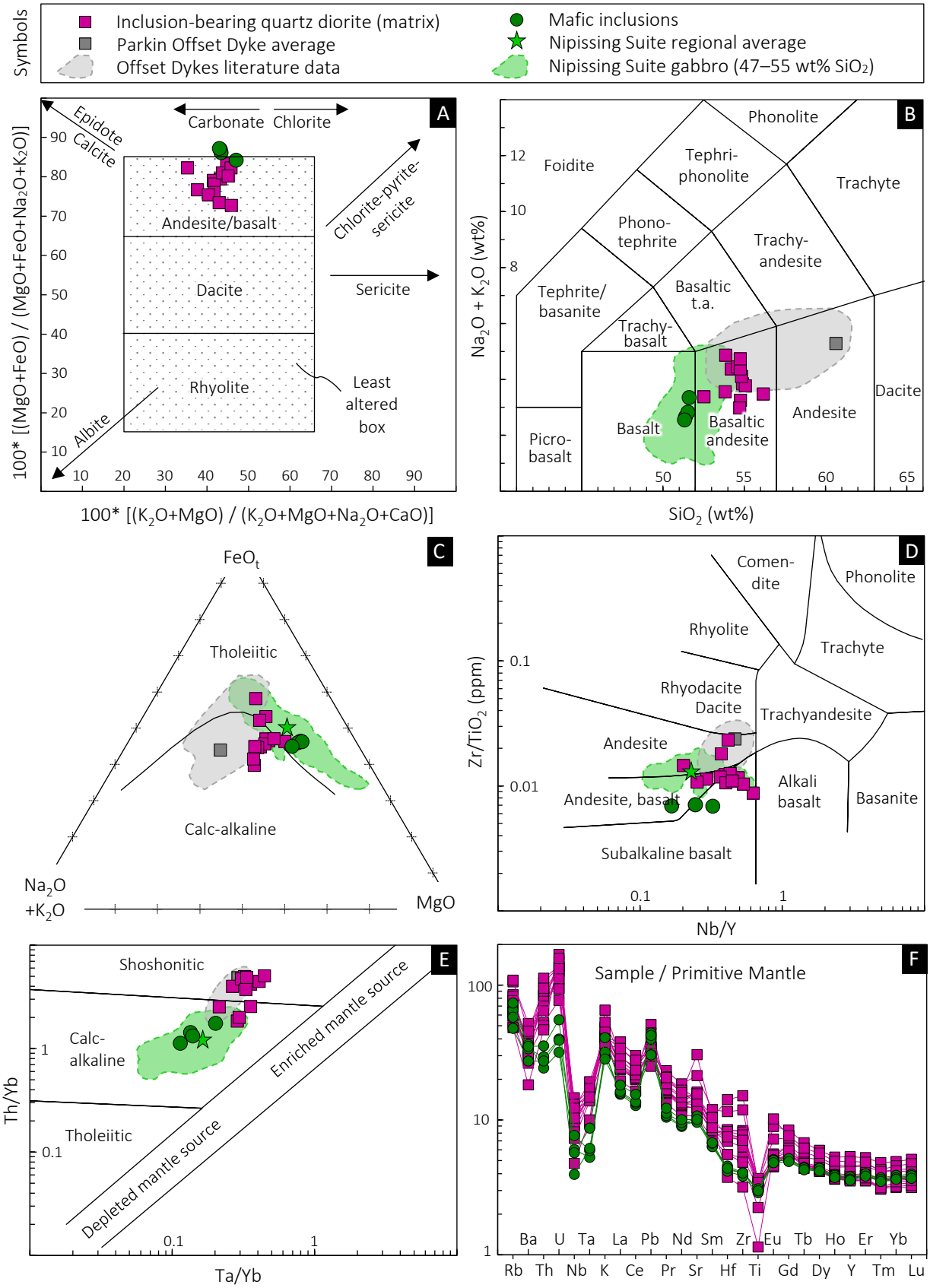

Figure 5.9 A selection of plots used to illustrate the effects of metasomatism on, and the geochemical classification and magmatic affinity of, the inclusion-bearing quartz diorite from Rathbun Lake; **A:** alteration box plot after Large et al. (2001); **B:** TAS classification after Le Bas et al. (1986); **C:** AFM plot after Irvine & Baragar (1971); **D:** discrimination plot after Winchester & Floyd (1977); **E:** discrimination plot after Pearce (1983); **F:** spidergram with normalisation values after McDonough & Sun (1995); Offset Dyke data (excluding outliers) are mainly from Lightfoot et al. (1997c); data for the Nipissing Suite are from Lightfoot & Naldrett (1996b) and Jobin-Bevans (2016); 2σ error bars are in each panel smaller than the symbol size.

Chalcophile and siderophile elements

Assay results for grab samples from the Rathbun Lake occurrence together with reference samples for mineralised Nipissing Suite gabbro from Rathbun Township are presented in **Table 5.4** (for lithophile element concentrations of one of these samples see **Tab. 5.2**). The Rathbun Lake samples are characterised by variable S content, ranging from < 0.2 wt% (macroscopically invisible sulphide) to 23.4 wt% (corresponding to massive sulphide). Copper ranges from 0.07 to 22.8 wt%, Ni from 0.09 to 1.12 wt%. The Cu/(Cu+Ni), which may be seen an index for magmatic sulphide fractionation (Lightfoot 2016), is typically > 0.9. All samples are characterised by an extreme enrichment in PGE+Au. Palladium, for instance, occurs at concentrations ranging from 6 to 63 ppm; Pt from 0.06 to 33 ppm. The Pd/Pt ratio lies between 0.6 and 473. Iridium, Os, Rh and Ru, on the other hand, occur at very low concentrations (ppb range) close to, or even below, the detection limit. This results in extremely high Pd/Ir ratios and PPGE/IPGE ratios in the range of 10^3–10^5. Some Ni-enriched samples, however, show slightly higher concentrations of Ir (2–28 ppb) hence lower Pd/Ir. Gold has, compared to Pd and Pt, overall lower but more uniform concentrations (0.25–10 ppm). Bismuth, Pb and Zn (not shown) occur at concentrations of ca. 5–50 ppm each; Ag, Sb and Sn < 5 ppm; As 74–410 ppm. Interestingly, there is no correlation between the whole-rock concentrations of Cu, S and PGE. A complete decoupling of S+Cu+Ni and PGE+Au is evident from samples < 1 wt% S, as these retain extremely high metal tenors. It is evident that this sulphide-poor PGE-rich mineralisation differs from the typical disseminated Cu-Ni-PGE mineralisation in the local Nipissing Suite gabbro (**Tab. 5.4** and Lightfoot et al. 1991; Jobin-Bevans 2016).

Table 5.4 Summary of whole-rock PGE, Au, Cu, Ni and S concentrations for the Rathbun Lake occurrence

S (wt%)	Cu (wt%)	Ni (wt%)	Cu/Cu+Ni	Au (ppb)	Pd (ppb)	Pt (ppb)	Rh (ppb)	Ru (ppb)	Ir (ppb)	Os (ppb)	Pd/Ir	Reference
Semi-massive and disseminated sulphide, Rathbun Lake occurrence												
18.30	11.50	1.12	0.91	3,170	53,000	6,325	n.a.	n.a.	n.a.	n.a.	n.a.	[1]
17.80	12.40	0.87	0.93	1,050	24,000	3,275	n.a.	11	0.05	10	480,000	[1]
16.00	13.90	0.95	0.94	6,410	17,700	2,550	n.a.	n.a.	n.a.	n.a.	n.a.	[1]
13.10	4.20	0.32	0.93	4,400	34,500	3,050	37	n.a.	n.a.	n.a.	n.a.	[1]
6.80	3.20	0.66	0.83	1,630	6,650	1,750	47	n.a.	0.19	n.a.	34,817	[1]
3.50	2.96	0.38	0.89	565	34,500	1,155	n.a.	n.a.	0.10	7	345,000	[1]
2.90	1.78	0.74	0.71	n.a.	23,090	929	n.a.	n.a.	0.05	n.a.	461,800	[1]
2.40	1.77	0.20	0.90	1,260	11,100	58	n.a.	n.a.	0.09	n.a.	123,333	[1]
23.40	19.90	0.22	0.99	250	23,000	1,800	17	< 5	0.1	< 3	230,000	[2]
19.40	9.10	0.22	0.98	890	35,000	74	14	20	0.3	6	116,667	[2]
18.40	8.30	0.26	0.97	1,300	37,000	18,000	8	< 5	0.3	11	123,333	[2]
9.40	4.70	0.16	0.97	950	19,000	33,000	3	40	0.2	23	95,000	[2]
2.40	2.30	0.36	0.86	2,800	12,000	190	23	15	28.0	3	429	[2]
22.00	22.80	0.10	1.00	452	62,500	976	7	< 1	< 1	< 10	> 62,500	this study
17.70	13.20	0.42	0.97	7,300	28,000	5,079	52	2	< 1	< 10	> 28,000	this study
13.00	13.40	0.09	0.99	1,180	35,800	1,740	n.a.	n.a.	n.a.	n.a.	> 35,800	this study
12.90	12.80	0.36	0.97	2,770	16,800	18,400	8	< 1	< 1	< 10	> 16,800	this study
9.87	6.81	0.42	0.94	9,580	5,500	9,300	50	2	2	<10	4,790	this study
8.42	2.01	1.05	0.66	3,800	24,000	503	256	5	5	<10	760	this study
7.17	0.78	0.52	0.60	1,940	14,400	1,269	13	< 1	< 1	< 10	> 14,400	this study
5.47	3.26	0.30	0.91	3,790	35,700	5,734	13	< 1	< 1	< 10	> 35,700	this study
4.16	1.61	0.32	0.83	1,850	6,300	963	12	< 1	< 1	< 10	> 6,300	this study
0.79	0.46	0.25	0.65	8,990	13,400	1,270	70	11	4	< 10	2,248	this study
0.75	0.44	0.24	0.65	5,770	11,500	1,370	65	8	6	< 10	962	this study
0.29	0.06	0.27	0.18	8,990	7,250	876	37	7	7	< 10	1,284	this study
0.17	0.07	0.18	0.28	7,910	8,460	1,020	60	3	4	< 10	1,978	this study
Disseminated sulphide in Nipissing Suite gabbro, Rathbun Township												
1.79	0.58	0.16	0.79	517	325	260	109	7	10	23	33	this study
1.77	0.70	0.30	0.70	432	623	226	131	5	7	12	89	this study
0.88	0.36	0.15	0.71	305	256	107	82	2	4	< 10	64	this study
4.44	1.29	0.41	0.76	974	317	477	159	5	6	< 10	53	this study

References: [1] Lightfoot et al. (1991); [2] Rowell & Edgar (1986); n.a. = not analysed or not available; note that 1 ppm = 1,000 ppb

5.8 Interpretation

Assessment of post-depositional alteration

The macro- and microscopic appearance of the inclusion-bearing quartz diorite from Rathbun Lake revealed limited and non-pervasive hydrothermal/metamorphic overprint at conditions that had likely not exceeded the lower greenschist facies (< 350°C). This is evident from the pseudomorphic replacement of primary amphibole and biotite by chlorite, plagioclase by saussurite, pyroxene by tremolite and talc, as well as crosscutting veins of epidote, chlorite, and pyrite. Before the geochemical and isotopic features of the rocks will be discussed in more detail, it its necessary to assess if and how alteration had affected the measured geochemical and isotopic composition.

The isocon method is one way of assessing the extent of secondary element mobility (Grant 1986). The approach works by directly comparing a pair of whole-rock samples (altered vs. fresh) from the same lithology and then assumes that all observed differences in composition are the result of secondary element mobility. When applied to the inclusion-bearing quartz diorite two problems become evident: First, the identification of fresh and altered endmembers is almost impossible. Second, any potential metasomatic changes are masked by contamination with ubiquitous (micro-)xenoliths and other primary inhomogeneities of the rock (e.g. schlieren). This severely limits the use of the isocon method and the quantification of fluid-induced element mobility.

The alteration box plot after Large et al. (2001) offers an alternative, semi-quantitative approach to metasomatism. It makes use of whole-rock oxide concentrations and has the advantage of having originally been calibrated specifically for igneous rocks. It also allows to identify different alteration trends and mineralogical changes by plotting vectors toward normative minerals (e.g. chlorite, albite, epidote). A major disadvantage is that trace elements are not considered. The alteration box plot shows that both the quartz diorite matrix and the mafic inclusions are relatively fresh; their major element composition corresponds to that of a typical unaltered andesite or basalt, with no discernible trend towards epidote/calcite, chlorite, or sericite (**Fig. 5.9A**).

The inclusion-bearing quartz diorite has only a narrow range in volatile content (2.0–3.5 wt% LOI) most of which is due to the presence of primary amphibole and modal variations thereof. The LOI, therefore, does not serve as good alteration proxy. To test whether the isotopic composition has been altered, all measured isotope ratios have been, instead of the LOI, contrasted against the Chemical Index of Alteration* (CIA) of Nesbitt & Young (1982). In doing so, the $^{143}Nd/^{144}Nd$ ratios show no trend with increasing alteration (higher CIA) and are therefore considered representative of the igneous protolith (**Fig. 5.10A**). Uranogenic Pb isotope ratios show a weak positive correlation with the CIA, which could suggest limited mobility of U and/or Pb (**Fig. 5.10B**). The thorogenic Pb isotope ratio, in contrast, shows a strongly negative correlation with increasing CIA (**Fig. 5.10C**). Theoretically, this could have been the result of early Pb loss, e.g. during alteration of feldspar, thereby increasing the time-integrated Th/Pb ratio. More likely, however, is it the result of primary inhomogeneities. This would agree with the significant variability in terms of Th concentrations, whereas Pb concentrations remain relatively constant. The Sr isotope ratios show no significant trend but a random scatter way outside the analytical uncertainty (**Fig. 5.10D**).

* CIA = 100 molar $[Al_2O_3/(Al_2O_3+CaO+K_2O+Na_2O)]$; where CaO only refers to Ca in silicates

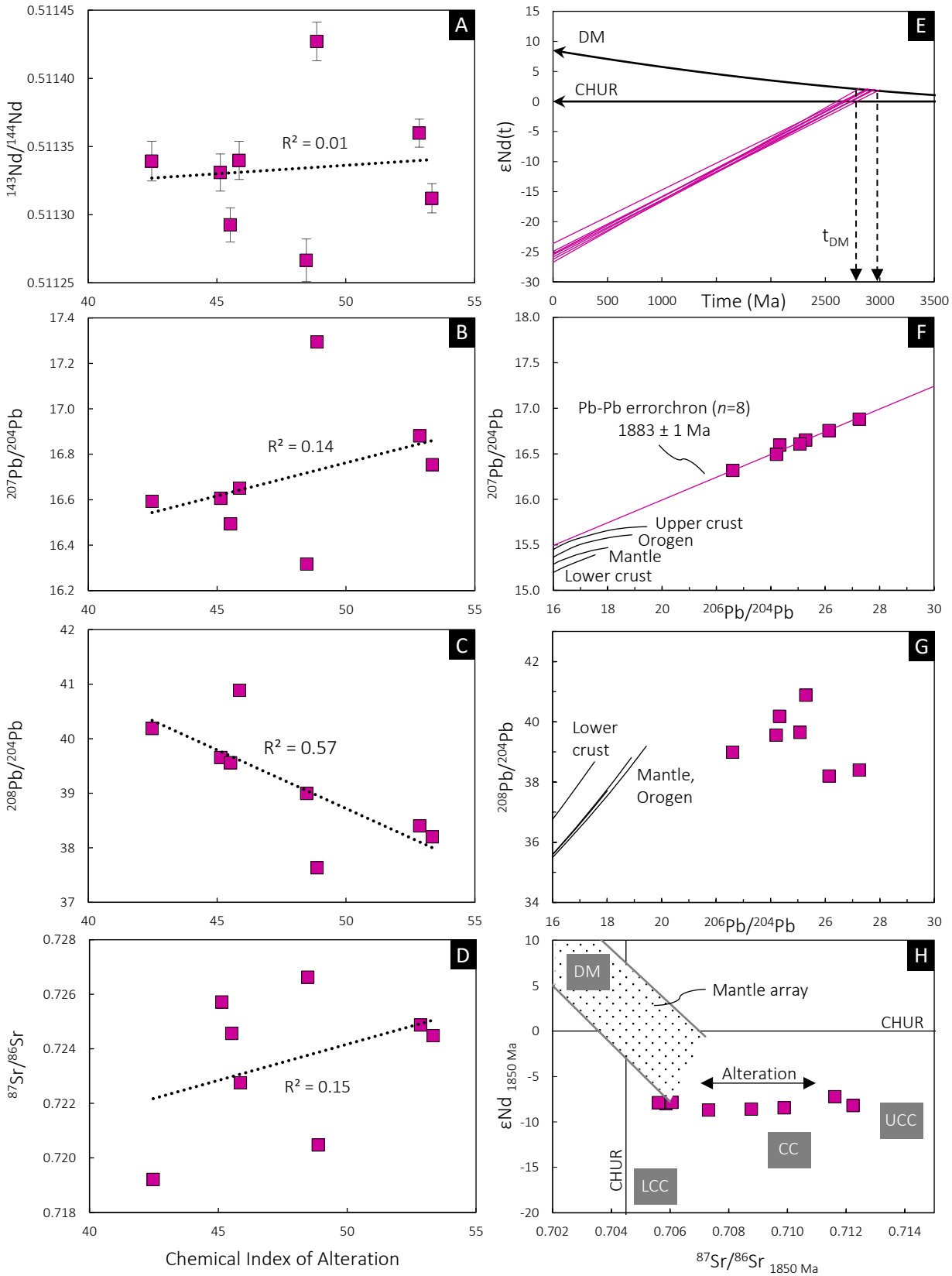

Figure 5.10 Bivariate plots of whole-rock Nd, Pb and Sr isotope ratios for the inclusion-bearing quartz diorite from Rathbun Lake; **A–D:** measured isotope ratios vs. the Chemical Index of Alteration (after Nesbitt & Young 1982), illustrating the effects of fluid-rock interaction on the isotopic composition; **E:** neodymium isotope evolution diagram with εNd displayed as a function of time; depleted mantle curve (DM) after De-Paolo (1981a,b); **F–G:** lead isotope ratio plots with growth curves after Zartman & Doe (1981) for different reservoirs; **H:** plot of the initial εNd vs. the initial $^{87}Sr/^{86}Sr$; crustal reservoirs after Faure (1986); error bars represent 2σ internal errors but are smaller than the symbol size in most of the panels.

Another Offset Dyke of the Sudbury Igneous Complex

Exploration of the Rathbun Lake area dates back to the late 19th century with first official reports made by Koulomzine (1955) and subsequent work conducted by the OGS (Dressler 1982), Flag Resources Ltd. and many other individuals since (Finn et al. 1982; Rowell & Edgar 1986; Lightfoot et al. 1991; Lightfoot & Naldrett 1996a; Jobin-Bevans 2000). Despite this considerable amount of work, no study has yet documented (at least not knowingly) the presence of inclusion-bearing quartz diorite at Rathbun Lake nor in the entire Rathbun Township. From a petrographic point of view, this quartz diorite differs in its clast- and quartz-rich nature and in the presence of primary amphibole from any other Proterozoic rock in the wider area. This includes the local Nipissing Suite gabbro and differentiated varieties thereof, sedimentary rocks of the Cobalt Group, and olivine diabase of the 1.23 Ga Sudbury Dyke Swarm (Dressler 1982). The petrography of the inclusion-bearing quartz diorite, however, bears strong resemblance to the impact melt-derived dykes of the Sudbury Igneous Complex (e.g. Lightfoot 2016). These so-called Offset Dykes display considerable petrographic diversity across the 200 km-large Sudbury Impact Structure; thus it may come as no surprise that the strongest similarity exists with Whistle Offset Dyke (Lafrance et al. 2014), which is the very Offset Dyke closest (~16 km) to the Rathbun Lake occurrence. Not only does the Whistle Offset Dyke contain Cu-sulphide veins and abundant fragments of surrounding basement rocks (including Archaean metagabbro and diabase), but it has the same mineralogy and texture as the quartz diorite found at Rathbun Lake (**Fig. 5.11**; Lafrance et al. 2014). This invariably leads to the suggestion that the quartz diorite at Rathbun Lake is also another Offset Dyke of the Sudbury Igneous Complex. Unequivocal evidence for this impact hypothesis requires a precise radiometric age, for instance, obtained via U-Pb on zircon/baddeleyite, or Ar-Ar on hornblende/biotite. Alas, this proved to be difficult due to the Zr-poor, xenolith-rich, hydrothermally altered nature of the inclusion-bearing quartz diorite. In the absence of an absolute formation age, an alternative approach is required to confirm its origin by the 1.85 Ga Sudbury impact event.

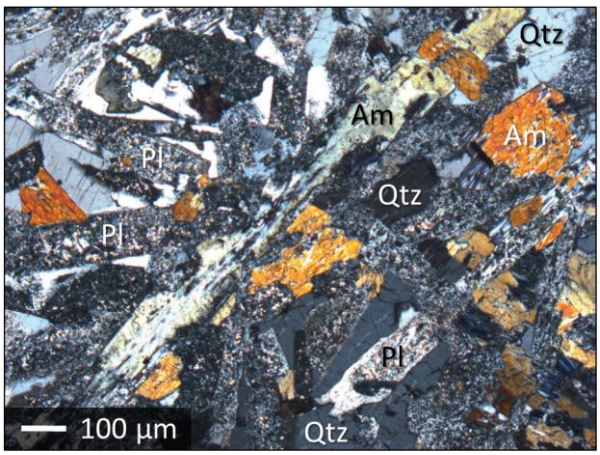

Figure 5.11 Microphotograph of a thin section from the Whistle segment of the Whistle-Parkin Offset Dyke northwest of Wanapitei Lake (ca. 46°56 26N 80°52 27W) showing the typical quartz diorite, composed of altered plagioclase and amphibole in an ophitic texture with quartz; under transmitted light and crossed polars; note the strong resemblance of this sample to the inclusions-bearing quartz diorite from Rathbun Lake; the photograph shown here is originally from Lafrance et al. (2014, p. 474, their figure 6c) with minor modifications (i.e., labelling) made by the author. Abbreviations: Am = amphibole; Pl = plagioclase; Qtz = quartz.

Bulk melting by hypervelocity impact constitutes an effective means of target rock homogenisation (e.g. Dressler & Reimold 2001; Kenny et al. 2017; Osinski et al. 2018). Fortunately, this resulted in a distinctive geochemical and isotopic composition of the Sudbury Igneous Complex compared to individual rocks in the target area of the bolide (e.g. Darling et al. 2010b; O'Callaghan et al. 2016). Whole-rock geochemistry in combination with radioisotopes (e.g. Nd, Hf, Pb) should thus make it possible to identify units related to the Sudbury Igneous Complex (e.g. Latypov et al. 2019). Indeed, major element concentrations for the quartz diorite from Rathbun Lake compare

quite well with previously published data for the Offset Dykes (**Fig. 5.9B,C**). The Copper Cliff Offset Dyke, for example, has concentrations of 55.3 wt% SiO_2, 0.94 wt% TiO_2, 4.43 wt% MgO, 6.71 wt% CaO, 12.0 wt% Fe_2O_3, and 4.31 wt% Na_2O+K_2O (Grant & Bite 1984). These values are similar to the Rathbun Lake quartz diorite, viz. 54.5 wt% SiO_2, 0.63 wt% TiO_2, 5.77 wt% MgO, 6.9 wt% CaO, 9.6 wt% Fe_2O_3, and 4.0 wt% Na_2O+K_2O, on average. Notably, both the Offset Dykes and the Rathbun Lake quartz diorite straddle the boundary of tholeiitic and calc-alkaline affinity in the AFM plot (**Fig. 5.9C**). This appears characteristic of all the impact melt rocks of the Sudbury Igneous Complex (e.g. Grant & Bite 1984) and the Vredefort Impact Structure (e.g. Huber et al. 2020) as these did not follow any of the typical magmatic differentiation trends, but instead represent a mixture target rocks of variable tholeiitic, calc-alkaline, and alkaline affinity.

Similarities between the Rathbun Lake quartz diorite and the Offset Dykes are especially evident from trace element concentrations. Zirconium, Th and Nb, for example, are significantly enriched in the quartz diorite relative to the local Nipissing Suite gabbro (cf. Lightfoot & Naldrett 1996b; Jobin-Bevans 2016) or the Gowganda Formation (cf. Young 2001), but they resemble the typical Offset Dyke quite well (cf. Lightfoot et al. 1997a,c). This can be illustrated in the plot Nb/Y vs. Zr/Ti among others, in which data for the Rathbun Lake quartz diorite and the Offset Dykes form tight overlapping clusters (**Fig. 5.9D**). Thorium in combination with Nb or Ta have previously been demonstrated effective in tracing crustal contamination (e.g. Pearce 2008) and are therefore useful to differentiate between crustal (i.e., impact-related) and mantle-derived igneous rock. In the Ta/Yb vs. Th/Yb plot (**Fig. 5.9E**), samples from the Rathbun Lake quartz diorite populate the same field as the Offset Dykes and the average continental crust as defined by Rudnick & Gao (2013). A combination of all trace elements, irrespective of their susceptibility to alteration, is presented in **Figure 5.12**. It reveals broad similarities between the quartz diorite and the Offset Dykes but also some discrepancies that are worth a more detailed discussion (see below). It should be born in mind, however, that the inclusion-bearing quartz diorite has a large geochemical variability and exhibits omnipresent contamination with the mafic inclusions, hence trace element patterns that are intermediate between, and sub-parallel to, the mafic inclusions and average Offset Dyke.

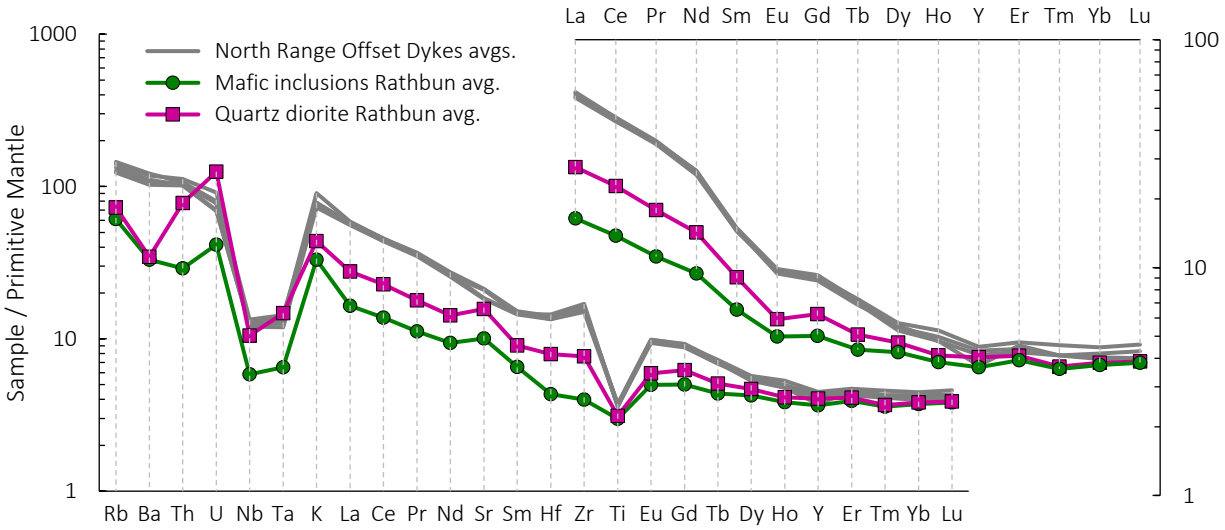

Figure 5.12 Primitive mantle-normalised trace element diagrams for the inclusion-bearing quartz diorite from Rathbun Lake and, for comparison, selected Offset Dykes of the Sudbury Igneous Complex (Parkin, Foy, Ministic); normalisation values are from Sun & McDonough (1989); literature data are from Lightfoot et al. (1997c).

Studies by Faggart et al. (1985), Naldrett et al. (1986), Deutsch (1994) and Prevec et al. (2000) have established a strong crustal affinity of the Sudbury Igneous Complex in terms of $^{143}Nd/^{144}Nd$ ratios. This is best exemplified using depleted mantle model ages (t_{DM}), which, for rocks with Sm/Nd ratio < 0.12, should equal their mean crustal residence time. The t_{DM} of the Sudbury Igneous Complex reported in these studies is not 1.85 Ga, as would be expected for an igneous rock formed by partial melting of the Earth's mantle at that time, but 2.75 Ga. Model age and highly negative εNd are considered inherited from the crustal precursor rocks (juvenile 2.75 Ga crust and its erosional product, the Huronian Supergroup) that became homogenised during impact melt formation (e.g. Faggart et al. 1985; Darling et al. 2010b; Petrus et al. 2016; Kenny et al. 2017). Broadly similar isotopic features were also observed in the Rathbun Lake quartz diorite (**Fig. 5.13**), viz. an εNd of –27 to –24, a $^{147}Sm/^{144}Nd$ ratio of 0.117 to 0.128, and an average t_{DM} of 2.9 Ga. This suggests that both the Offset Dykes and the quartz diorite share a common source and experienced the same radiogenic ingrowth of ^{143}Nd. Slight deviations from the Offset Dyke average, as shown in the histograms of **Figure 5.13**, are easily explained by contamination with local country rock, either gabbro or wacke. The Nd isotope composition of the Huronian Supergroup would be, however, indistinguishable from that of the Offset Dykes (cf. McLennan et al. 2000) and should thus not have had a profound effect on the measured Nd isotope ratios. Mafic rocks of the Nipissing Suite, in contrast, have distinctly higher εNd0, a high Sm/Nd and older model ages (t_{DM} > 3000 Ma) (Lightfoot & Naldrett 1996a). The Nipissing Suite gabbro is, therefore, the most likely source of contamination. This mixing relationship will be explored in more detail later this chapter.

It is concluded, based on petrographic evidence, and strong similarities in geochemistry and isotopic composition, that the inclusion-bearing quartz diorite from Rathbun Lake is another hitherto unrecognised Offset Dyke of the Sudbury Igneous Complex.

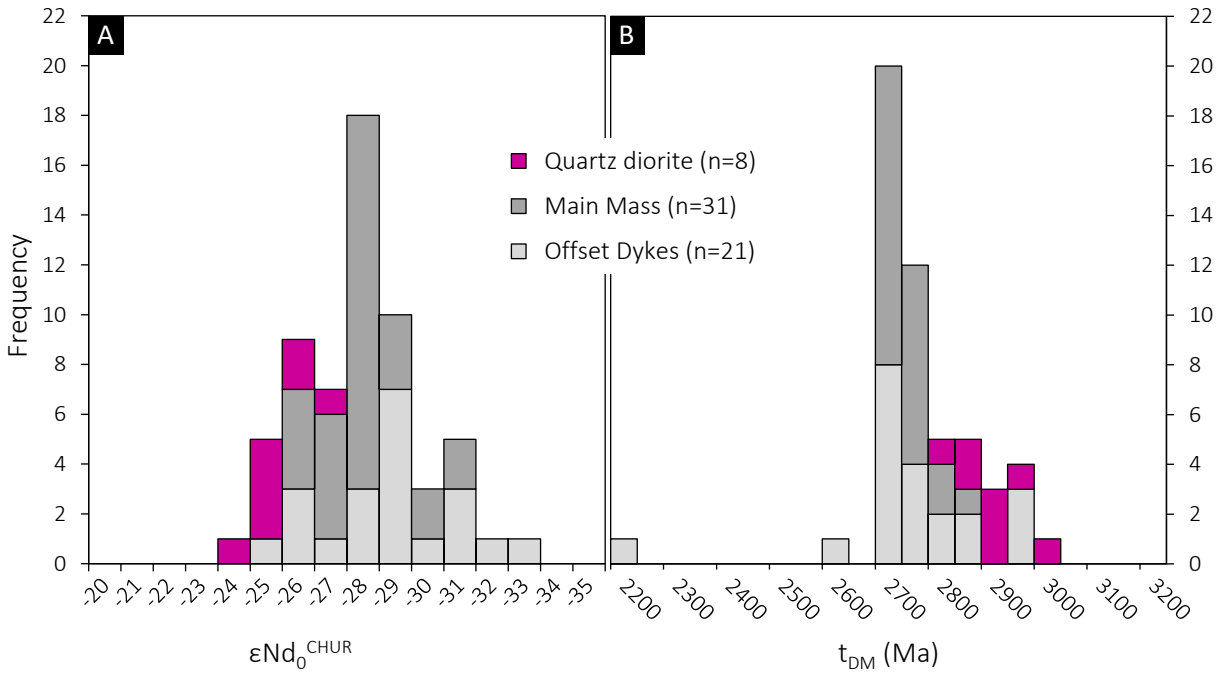

Figure 5.13 Neodymium isotope histograms for the inclusion-bearing quartz diorite from Rathbun Lake and, for comparison, literature data for the Sudbury Igneous Complex; **A:** frequency of the present-day εNd^{CHUR}; **B:** frequency of depleted mantle model ages; literature data recalculated from Faggart et al. (1985), Prevec et al. (2000), Latypov et al. (2019), plus five unpublished data for the Offset Dykes (*n*=1) and the Main Mass (*n*=4) (this study; Appendix_2); not shown are data for the heavily contaminated Sublayer because these are not representative of the initial impact melt composition (e.g. Prevec et al. 2000).

Origin of the mafic inclusions

Now that the impact origin of the inclusion-bearing quartz diorite has been established and the rock identified as another Offset Dyke of the Sudbury Igneous Complex, a discussion on the origin of the mafic inclusions follows. Such rock and mineral fragments are an integral part of almost all types of impactites (e.g. Stöffler & Grieve 2007), accordingly diverse can their possible origin be. In any impact structure, most fragments are typically derived from the immediate basement (xenoliths), but studies have also reported reworked fragments of early formed impact melt rocks (autoliths, anteliths) or even of the projectile itself (Maier et al. 2006; Latypov et al. 2019; Wang et al. 2020). The study of inclusions in the Sudbury Igneous Complex has a long tradition (Scribbins et al. 1984; Lightfoot et al. 1997b; Prevec et al. 2000; Cohen et al. 2000; Wang et al. 2018, 2020). This is because, early on, geologists have recognised the common association of Ni-Cu-PGE sulphide and inclusions, especially the more mafic and ultramafic exotic types (Souch et al. 1969; Pattison 1979). The case of the Rathbun Offset Dyke testifies once more to this enigmatic relationship.

The mafic inclusions from Rathbun Lake have a fine-grained spherulitic texture indicative of quenching of basic melts (e.g. Lofgren 1971; Holness et al. 2012). Although this texture is typically found in the chilled margins of sills and dykes, it provides no reliable source information per se. What is clear is that the mafic inclusions differ petrographically from the quartz dioritic matrix, and they must have been in disequilibrium with the impact melt as is evident from their deeply embayed shapes, their dark concentric rims, and the feldspar-rich fringes (leucosome?) surrounding them. Any possibility that these mafic inclusions represent anteliths of early formed quartz diorite, as reported in some of the Offset Dykes (Tuchscherer & Spray 2002; Lightfoot & Farrow 2002; Pilles et al. 2017, 2018b) can, therefore, be ruled out. An impact melt-origin of the mafic inclusions is also odds with their geochemical composition, which was found to be more primitive than the initial undifferentiated impact melt of the Sudbury Igneous Complex (**Fig. 5.12**).

Given that diabase and gabbro of the Nipissing Suite occurs in direct contact with the Rathbun Offset Dyke, it is the most likely source of these mafic inclusions. A geochemical comparison reveals indeed striking similarities. Mafic inclusions have, for instance, major element concentrations of 51 wt% SiO_2, 0.6 wt% TiO_2, and a tholeiitic affinity according to the AFM plot, all of which is typical of the Nipissing Suite (e.g. Lightfoot et al. 1993; Lightfoot & Naldrett 1996b; Jobin-Bevans 2016), especially its gabbroic units, which have been least affected by alteration or AFC processes. The similarity is even more profound with respect to lithophile trace elements. Both the mafic inclusions and the gabbroic rocks of the Nipissing Suite have < 60 ppm Zr, < 2.5 ppm Th, relatively flat REE patterns, and pronounced negative Nb-Ta-Ti anomalies (**Fig. 5.14**). Assuming that Rb, Ba and Sr have not been significantly mobilised during alteration, their abundances also match those of the typical Nipissing Suite gabbro. Granted, rocks of the Nipissing Suite show a considerable range in composition across the Huronian Basin, but their regional average corresponds very closely to the composition of the mafic inclusions (**Fig. 5.14**). Further insights come from Nd isotope systematics. Mafic inclusions have the same isotopic features as the Nipissing Suite, namely, a high $^{147}Sm/^{144}Nd$ ratio of 0.135, an εNd_0 between –15 and –20, and a one-stage Nd model age (t_{DM}) of ca. 3000 ± 500 Ma (cf. Lightfoot & Naldrett 1996a). The geochemistry and isotopic composition of the mafic inclusions is, therefore, consistent with their very local origin as xenoliths. As most mafic inclusions exhibit what is interpreted as quench textures, it is conceivable that they were derived from the chilled Nipissing Suite-Gowganda Formation contact along the northern margin of the Wanapitei Intrusion (**Fig. 5.2A**) and thus have not been significantly displaced since.

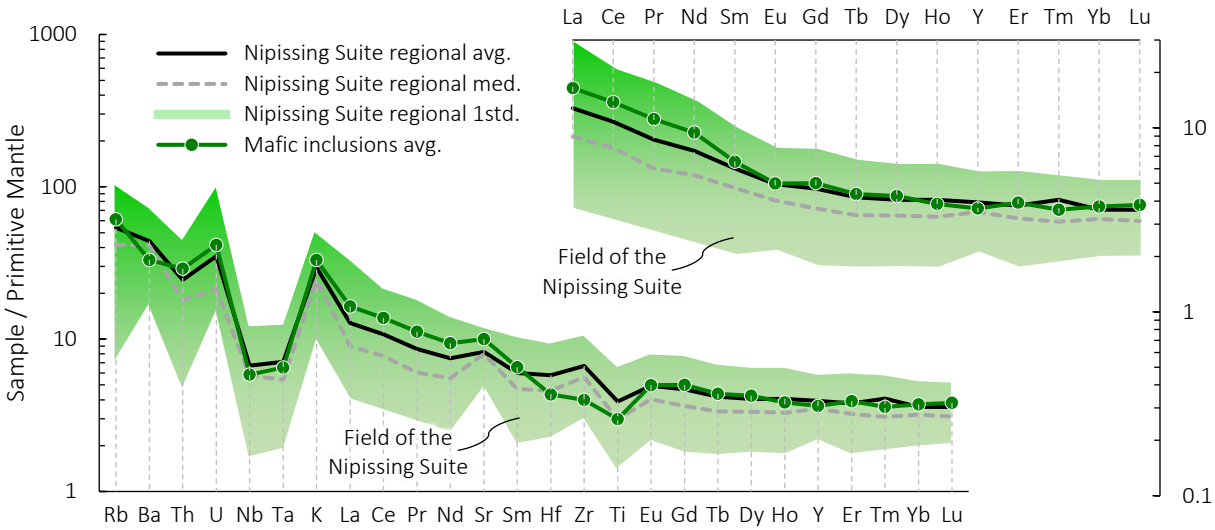

Figure 5.14 Primitive mantle-normalised trace element diagrams for mafic inclusions from the Rathbun Offset Dyke in comparison to gabbroic rocks (47–55 wt% SiO_2) of the Nipissing Suite; normalisation values are from Sun & McDonough (1989); data for the Nipissing Suite are from Lightfoot & Naldrett (1996b), Jobin-Bevans (2016), Hagen (2020) and this study (Appendix_1); regional average, median and standard deviation were calculated from more than 500 analyses excluding altered and mineralised outliers with < 47 wt% SiO_2 as well as differentiated and contaminated outliers with > 55 wt% SiO_2.

Geochemical modelling of xenolith assimilation

The spherical and in places amoeboid shape of the mafic inclusions bears some resemblance mafic enclaves in granites, or to embayed phenocrysts in volcanic rocks, for example, of olivine in basalt, or quartz in rhyolite. Such embayed phenocrysts are clear evidence of crystal-melt disequilibrium and generally interpreted as resorption phenomena. A similar disequilibrium relation seems to exist between the mafic inclusions (xenoliths) and the quartz dioritic matrix from Rathbun Lake, supported by textural features such as (i) the visible fragmentation of larger mafic inclusions in to smaller ones, giving rise to ocelli-like textures; (ii) feldspar-rich patches in vicinity to the many of mafic inclusions, which could be interpreted as a leucosome; (iii) dark and fine-grained reaction rims around mafic inclusions, perhaps as a result of hydration, thermal metamorphism, or alternatively, representing the more refractory phases (restite) at an assumed xenolith-melt interface.

To test if and to what extent the mafic inclusions were assimilated by the impact melt, and how this had influenced the composition of the quartz diorite, geochemical mixing models have been performed. The theory behind this is that, if assimilation (assuming bulk melting) had occurred, the composition of the matrix should correspond to a mixture between the mafic inclusions and the undifferentiated, uncontaminated impact melt. If the mafic inclusions where the only contaminant, then the trend defined by the inclusions, matrix and Offset Dykes should be a binary mixing line. **Figure 5.15** shows a compilation of simple element-element scatter plots, each with a calculated mixing line between the xenoliths and the typical quartz dioritic Offset Dyke. Two features become evident; first, there is a significant scatter of the quartz dioritic matrix, even on the hand specimen scale; second, matrix samples fall indeed on, or close to, the binary mixing lines between Nipissing Suite and Offset Dykes. According to the lever rule, each plot points to a relatively consistent contaminant-to-assimilant proportion of 40:60 to 60:40. These mixing proportions are in good agreement with the normalised trace element diagram of **Figure 5.13**, which has also indicated a quartz diorite:Nipissing Suite gabbro mixing proportion of approximately 50:50.

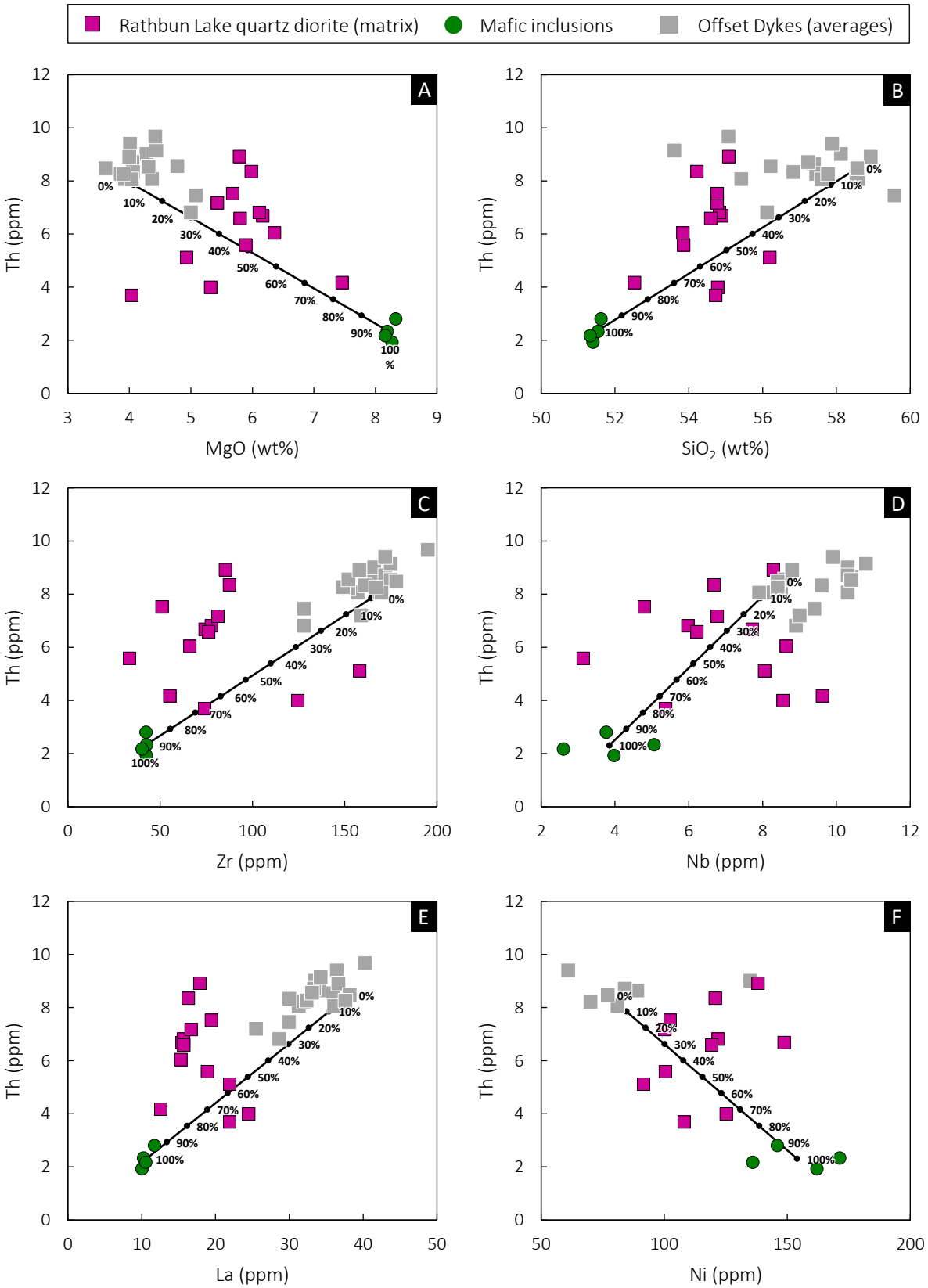

Figure 5.15 Scatter plots of relatively fluid immobile elements, used to infer the extent of crustal contamination in the inclusion-bearing quartz diorite from Rathbun Lake; each panel shows a binary mixing line between the undifferentiated impact melt composition (represented by the Offset Dykes) and the mafic inclusions (samples MAF-1, MAF-2, MAF-3, and MAF-4); with 10% increments using the quartz diorite from the Parkin Offset Dyke as a starting composition; literature data from Lightfoot et al. (1997c); 2σ error bars are in each panel smaller than the symbol size.

Neodymium isotope systematics are another way of quantifying the assimilation of the mafic inclusions by the hot, likely superheated, impact melt. **Figure 5.16** shows the calculated (non-linear) mixing trend between the mafic inclusions and the Parkin Offset Dyke, with the $^{143}Nd/^{144}Nd$ ratio on the y-axis, and the reciprocal Nd concentration on the x-axis. In agreement with trace element considerations above, the isotopic composition of the matrix can be explained by ~60% admixture of mafic inclusions to the initial undifferentiated impact melt.

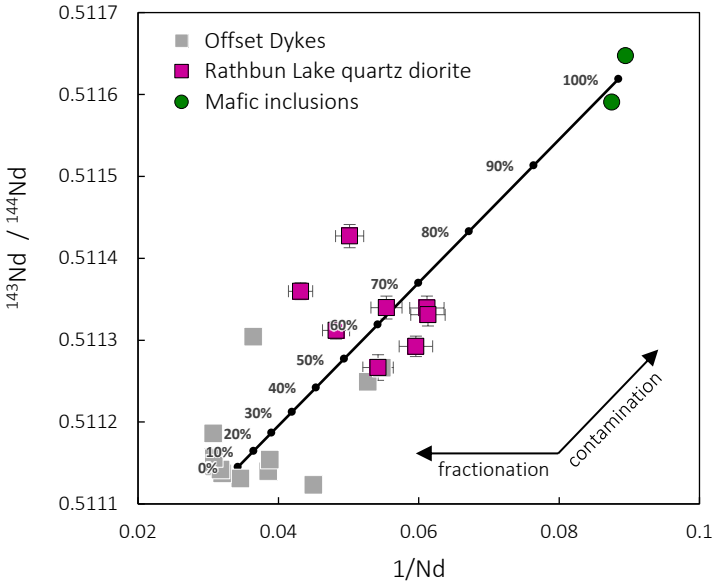

Figure 5.16 Reciprocal Nd concentrations vs. measured $^{143}Nd/^{144}Nd$ ratios used to ascertain crustal contamination in the inclusion-bearing quartz diorite (matrix) from Rathbun Lake; also shown is a binary mixing line between the undifferentiated impact melt composition (represented by the Offset Dykes) and the mafic inclusions; with 10% increments using the average quartz diorite from the Parkin Offset Dyke as a starting composition; literature data are averages based on Lightfoot et al. (1997c) and Prevec et al. (2000); error bars are 2σ internal errors.

Geochemical and isotopic models demonstrate that the matrix composition of the inclusion-bearing quartz diorite from Rathbun Lake can be accommodated by a ca. 40:60 mixture between impact melt and the locally derived mafic xenoliths. Not only does this provide additional, though indirect, evidence of an impact origin of the inclusion-bearing quartz diorite, but it also testifies to the superheated temperature the impact melt must have had at the time of emplacement to allow for assimilation to such an extent. Application of the software *Melts* (Gualda & Ghiorso 2015) predicts complete melting of the mafic inclusions at 1,250°C, assuming H_2O-rich conditions, an oxygen fugacity around the QFM buffer, and assuming that the Offset Dyke was emplaced at a paleodepth of 3–5 km (~1 kbar). This temperature corresponds closely to the experimentally determined basalt liquidus (e.g. Green & Ringwood 1967) and provides a minimum estimate of the emplacement temperature for the impact melt. Textural and geochemical evidence suggests, however, that the mafic inclusions did undergo melting. Therefore, temperatures must have exceeded 1,250°C by a substantial extent, perhaps by several hundred degrees, based on analogue experiments on phenocryst/xenocryst resorption rates (e.g. Donaldson 1985; Thornber & Huebner 1985) and in consideration that high temperatures must have kept sustained long enough before the impact melt solidified, and this in spite of all the energy that was consumed for the assimilation. These observations are in strong favour of a superheated temperature as it has been proposed before for the Offset Dykes of the Sudbury Igneous Complex, that is, 1,500–1,800°C (Ostermann et al. 1996; Coulter et al. 2014; Prevec & Büttner 2018), although studies on other, smaller, impact structures imply even greater temperatures exceeding 2,370°C (e.g. Timms et al. 2017). Thermomechanical erosion of the local wall rock seems to have played an important role in the emplacement of the Rathbun Offset Dyke as well as its textural and geochemical evolution. Assimilation of H_2O-bearing country rock (± hydrated gabbro) at high confining pressure would probably also explain the unusual presence of primary igneous hornblende in the Rathbun Offset Dyke.

A re-interpretation of the Rathbun Lake PGE-Cu±Ni occurrence

Because of very low crustal abundances (Rudnick & Gao 2013) and a limited solubility in most low-*T* aqueous fluids (e.g. Barnes & Liu 2012), cases of hydrothermal PGE mineralisation are extraordinarily rare; only a handful of epigenetic PGE occurrences are known worldwide. One of these, according to the classification by Maier (2005), is Rathbun Lake. This widespread yet questionable view dates back to the work of Rowell & Edgar (1986), who presented a series of arguments that the extremely high Pd (63 g/t), Pt (33 g/t) and Au (10 g/t) grades at Rathbun Lake could be due to fluid-mediated leaching from, and metasomatic replacement of, the local 2.22 Ga Nipissing Suite gabbro. Their argumentation was primarily based on the presence of Hg-, Sb-, Te-, Bi- and As-bearing platinum group minerals, the abundance of typical hydrothermal sulphides such as pyrite, arsenopyrite, molybdenite or covellite, the lack of typical magmatic sulphides, the gangue type (epidote, quartz, chlorite), the allegedly brecciated nature of the host rocks and – for most magmatic deposits – the unusually high (Pd+Pt)/(Os+Ir+Ru) ratios and Pd/Ir ratios.

The study of Rowell & Edgar (1986) was well received by the scientific community and was published just as a renewed discussion about the role of fluids in the formation of PGE deposits emerged (e.g. Ballhaus & Stumpfl 1986; Boudreau et al. 1986; Mountain & Wood 1988). Suffice to say, the discovery of a new type of epigenetic mineralisation style would open entirely new economic perspectives as an alternative exploration target to the market-dominating orthomagmatic reef-type deposits. Even more, the work of Rowell & Edgar (1986) sparked sudden interest in the regionally widespread but, until then, heavily underexplored Nipissing Suite as a potential host of high-grade PGE-Cu-Ni mineralisation. This prompted a whole series of follow-up studies to investigate the geology and economic potential of the Nipissing Suite in more detail (e.g. Lightfoot & Naldrett 1989, 1996a,b; Lightfoot et al. 1991, 1993; Noble & Lightfoot 1992; Keays et al. 1995; Jobin-Bevans et al. 1997; Vaillancourt et al. 2001). These studies altogether failed, however, to locate similar PGE occurrences throughout the entire magmatic province, similarly as they failed to explain why high-grade PGE mineralisation only occurs at Rathbun Lake. Some 35 years later, the Rathbun Lake occurrence is still considered by many scholars as Nipissing Suite-related (e.g. Keays & Lightfoot 2020), and as an archetype of epigenetic PGE mineralisation. An impact origin, although informally discussed by local exploration geologist long before the discovery an inclusion-bearing quartz diorite at Rathbun Lake, has never been tested so far.

In this context, the discovery of an Offset Dyke sheds a completely new light on the Rathbun Lake occurrence, calling not only its age but its alleged hydrothermal origin into question. Could this occurrence also be genetically related to the Sudbury impact event? The occurrence shares, indeed, many features typical of a very specific type of mineralisation known exclusively from Sudbury: Footwall-type mineralisation, named after its position in the brecciated basement of the Sudbury Impact Structure, is characterised by extremely high Cu and PGE grades, vein-like ore bodies, and a plethora of different platinum group minerals. The formation of these so-called "sharp-walled Cu veins" is now widely considered the end-product of extreme magmatic sulphide fractionation, and not the product of hydrothermal processes (e.g. Naldrett et al. 1999; Hanley et al. 2011; Dare et al. 2014; Lightfoot 2016). A step-by-step comparison with these footwall deposits will demonstrate their remarkable similarity with the Rathbun Lake occurrence. It will further be shown that all the features previously cited as evidence of a hydrothermal (epigenetic) origin are in fact – and by analogy to the footwall deposits – in favour of a (late-)magmatic origin of the Rathbun Lake occurrence, syngenetic with the emplacement of the Rathbun Offset Dyke.

It has long been known that the sulphide deposits at Sudbury become increasingly Cu-rich and Ni-poor with depth (Keays & Crocket 1970), and by now there is consensus that such compositional zonation is due to fractional crystallisation (Naldrett 2004; Lightfoot 2016). According to our current understanding of orthomagmatic sulphide deposits and the Sudbury Igneous Complex as a differentiated impact melt sheet, immiscible sulphide droplets began to unmix from the impact melt as it cooled, settled towards topographic depressions on the crater floor and there, they underwent fractionation and sub-solidus modification. Experimental studies have shown that the first solid to crystallise at 1,190°C from such a sulphide melt is always rich in Fe and Ni. This high-*T* phase, called monosulphide solid solution (MSS), is not stable below 650°C, and pyrrhotite and pentlandite will inevitably exsolve from it. Copper, on the other hand, behaves differently. It is not incorporated in the crystal structure of the MSS but will be concentrated into a residual Cu-Fe-S ±Ni bearing liquid. At around 880°C, this Cu-rich liquid will crystallise into its own high-*T* phase, the so-called intermediate solid solution (ISS) (e.g. Naldrett 2004). Equally unstable, down-temperature evolution causes the ISS to transform into the stable assemblage chalcopyrite ±cubanite ±pentlandite (e.g. Naldrett 2004). Because of its high density (4.5 g/cm^3; Mungall & Su 2005), low viscosity (< 0.1 Pa s; Dobson et al. 2000) and solidus (880°C), a (Cu-rich) sulphide melt can be highly mobile and thus able to physically separate from an early solidified MSS, thereby providing a means of Cu/Ni fractionation. A Cu-rich sulphide melt may even migrate over larger distances and is capable of percolating into the underlying footwall of a given intrusion (Saumur & Cruden 2017; Staude et al. 2017; Barnes et al. 2020a), provided sufficient permeability and temperature of the substrate. At Sudbury, the product of this process is preserved in form of vein stockworks in the brecciated footwall of the Main Mass (the "sharp-walled Cu veins"; **Fig. 5.17A**). Interestingly, the original ore body of Rathbun Lake was also described as vein-like (Koulomzine 1955). Although it is not possible to study the mineralisation there in situ anymore, grab samples from the showing do resemble the typical footwall mineralisation (compare **Fig. 5.6A** and **Fig. 5.17B**).

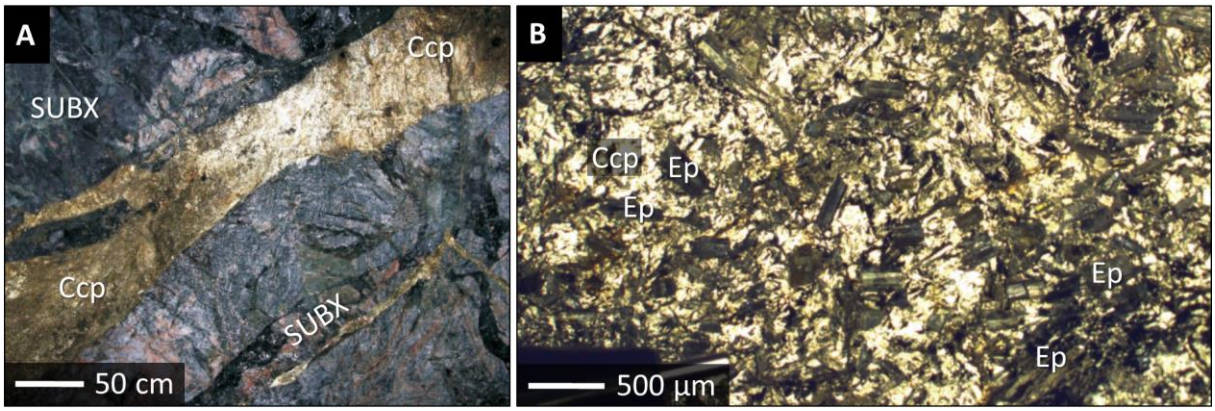

Figure 5.17 Photographs of the sharp-walled Cu-veins in the footwall of the Sudbury Igneous Complex as a possible analogy to the Rathbun Lake mineralisation; **A:** massive chalcopyrite vein from the McCreedy East Deposit; photograph from Dare et al. (2014, p. 346); **B:** close-up photograph of a massive chalcopyrite vein from the Broken Hammer Deposit; photograph from Hall et al. (2020, p. 1158).

A basic hallmark of all footwall deposits (e.g. McCreedy, Strathcona) is their high Cu/(Cu+Ni) ratio and a principal paragenesis dominated by chalcopyrite with lesser amounts of other minerals (cubanite, pentlandite) that may exsolve from a Ni-bearing ISS. The sulphide from Rathbun Lake has essentially the same mineralogy as these footwall deposits and the same highly fractionated Cu/(Cu+Ni) ratio of ≥ 0.9, as illustrated in the mineral assemblage plot of **Figure 5.18**.

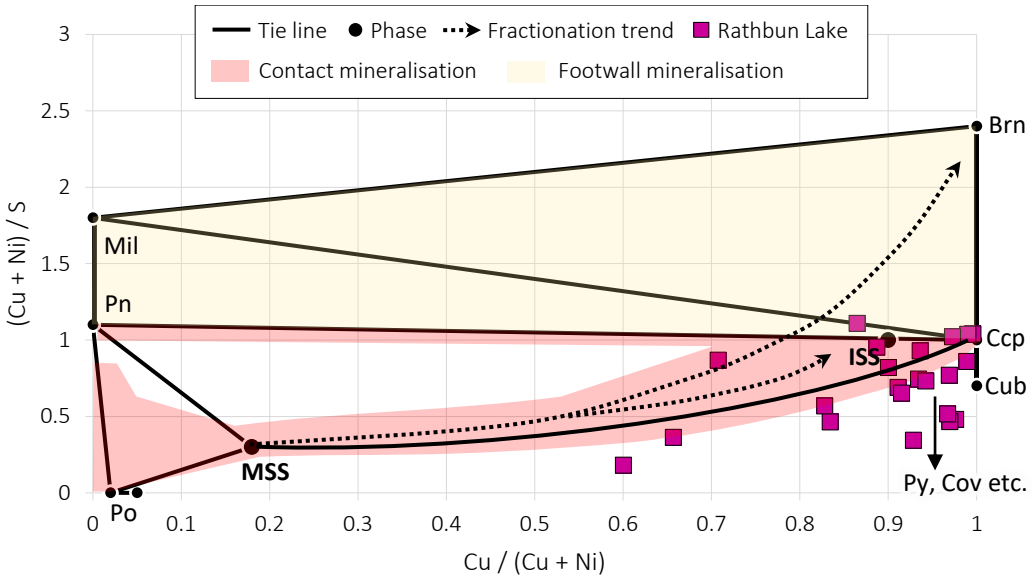

Figure 5.18 Mineral assemblage plot after Lightfoot (2016); this plot establishes a link between whole-rock Cu, Ni and S concentrations and specific igneous mineral assemblages, with Cu/(Cu+Ni) as a fractionation index and (Cu+Ni)/S as metal tenor (not considering the diluting effects of pyrite, arsenides etc.). Abbreviations: Brn = bornite; Ccp = chalcopyrite; Cub = cubanite; Cov = covellite; ISS = intermediate solid solution; Mil = millerite; MSS = monosulphide solid solution; Pn = pentlandite; Po = pyrrhotite; Py = pyrite.

Furthermore, the oriented intergrowths between pentlandite and chalcopyrite (**Fig. 5.7D**) are a strong indication that these two minerals exsolved from one homogenous precursor, by implication, an ISS. Similar textures were described before only for massive chalcopyrite-veins of the McCreedy East footwall deposit by Dare et al. (2014), who proposed that these pentlandite lamellae originally exsolved from a Ni-bearing ISS and subsequently coarsened to granular pentlandite. At Rathbun Lake, these lamellae seem well-preserved, perhaps as a consequence of undercooling that prevented subsequent ripening. Loop-textured pentlandite, present in some samples from Rathbun Lake (e.g. **Fig. 5.7C**), is additional evidence of a magmatic origin (Barnes et al. 2020b). Another feature of Rathbun Lake consistent with a magmatic origin is the abundance of dispersed and euhedral magnetite, either with or without Fe-Ti oxide exsolutions. Although Rowell & Edgar (1986) interpreted this magnetite as hydrothermal, similar magnetite was described from the Sudbury footwall deposits, where it is considered magmatic in origin (Dare et al. 2012, 2014; Lightfoot 2016). It is either a product of direct crystallisation from the sulphide melt (Naldrett 1969; Craig & Kullerud 1969) or was formed by the reaction of sulphide melt with surrounding silicates (Fonseca et al. 2008; Lesher 2017). In fact, both types of magnetite might be present in the studied samples: A trellis-textured magnetite enclosed in chalcopyrite, which possibly crystallised directly from the sulphide melt; a homogeneous type of magnetite found in contact with primary silicates, which possibly formed by the process advocated by Fonseca et al. (2008).

Apart from analogous mineral assemblages, it is also worth considering similarities in trace element abundance between Rathbun Lake and the footwall deposits. That is, the fractionation trend outlined above with respect to Cu/(Cu+Ni) (**Fig. 5.18**) is typically accompanied by systematic variations in the precious metals, whose distribution is controlled by different partition coefficients between MSS and ISS. While Co, IPGE (Ir, Ru, Os) and Rh are preferentially incorporated into the early MSS, other metals (Pd, Pt, Au, Ag) and TABS (Te, As, Bi, As, Sb, Sn) do not enter the MSS. Instead, they remain in the residual Cu-rich melt (Barnes & Ripley 2016). At Sudbury, this contrasting partitioning behaviour resulted in IPGE-Co-enriched Ni-sulphide ores (contact deposits),

i.e., the former MSS cumulates on the crater floor, and Pd-Pt-Au-Ag-enriched Cu-sulphide ores (ISS cumulates/footwall deposits) (Li et al. 1992; Naldrett et al. 1999; Dare et al. 2014; Lightfoot 2016). Consequently, the Pd/Ir ratio, which might serve as another fractionation index, can exceed several 100,000 in the footwall deposits (e.g. Li et al. 1992; Barnes & Lightfoot 2005; Dare et al. 2014). Similar high Pd concentrations and Pd/Ir ratios of Cu-sulphide ores have been reported not only from Sudbury but also Norilsk-Talnakh (e.g. Duran et al. 2017) and Lac des Iles (e.g. Duran et al. 2016) among other magmatic deposits. Duran et al. (2017) successfully reproduced the observed metal variations at Norilsk with Rayleigh fractionation modelling by using published partition coefficients. Given that the ore deposits at Norilsk experienced no metamorphic and hydrothermal overprint, this is an important finding as it demonstrates that fluids are not required in the formation of Pd-rich, high-Pd/Ir base metal sulphide ores. Thus, the high Pd/Ir ratio of the Rathbun Lake occurrence (up to 480,000) does not necessarily reflect the higher fluid mobility of Pd over Ir (e.g. Keays et al. 1982), as implied by Rowell & Edgar (1986), but is likewise consistent with magmatic sulphide fractionation. Interestingly, Rowell & Edgar (1986) reported one sample that is anomalously high in Ir (28 ppb) and, at the same time, has the lowest Cu/(Cu+Ni) (0.86) and lowest Pd/Ir (429) of all their samples (**Tab. 5.4**). This sample may be interpreted as less evolved, maybe a mixture of MSS and ISS. The high Ir in this particular sample significantly above the mantle value of 3.2 ppb (McDonough & Sun 1995) effectively rules out a hydrothermal origin because of the extremely low solubility of Ir in any hydrothermal fluid (e.g. Keays et al. 1982; Lesher 2017). It is, however, consistent with sequestration by magmatic sulphide. In **Figure 5.19**, the Ni-PGE-Au-Cu concentrations of the Rathbun Lake occurrence are compared to those of the Sudbury footwall deposits; the similarity is striking, regardless of the metal tenor.

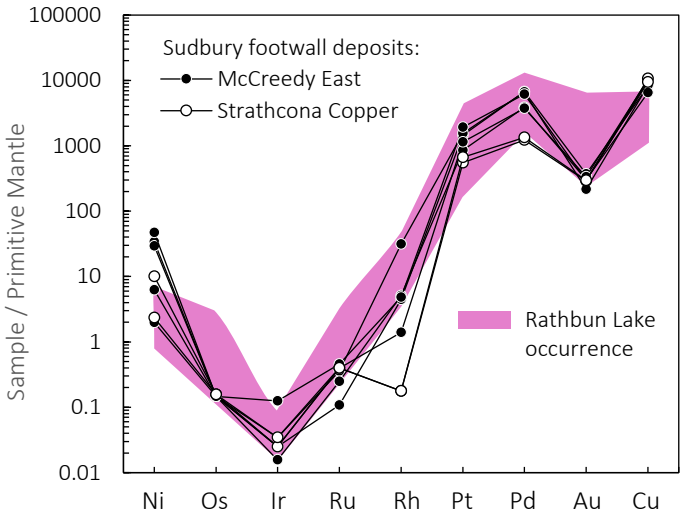

Figure 5.19 Primitive mantle-normalised Ni-PGE-Au-Cu concentrations from the Rathbun Lake occurrence and, for comparison, the typical composition of the sharp-walled Cu veins (footwall mineralisation) in and beneath the Sudbury Igneous Complex; notice the strong resemblance of these patters to each other; the strong enrichment of Cu, Pd, Pt and Au over Ni, Os, Ir, Ru and Rh is typical of ores derived from a highly fractionated sulphide melt; data for McCreedy East from Dare et al. (2014); data for Strathcona Copper from Li et al. (1992); mantle values from Sun & McDonough (1989).

The final step of PGE-sulphide fractionation is still a matter of research. Experimental studies (e.g., Tomkins 2010; Liu & Brenan 2015; Bai et al. 2017; Piña et al. 2020) and examples from natural analogues (Cabri & Laflamme 1976; Holwell & McDonald, 2010; Dare et al. 2014; Piña et al. 2015) imply that Pd, Pt, Au and various other metals that remain in the residual Cu-rich melt are in fact incompatible with ISS. These will be concentrated in very late-stage liquids together with TABS. Although PGE-TABS-rich liquids are expected to have very low viscosities and low solidi (Prichard et al. 2004; Tomkins 2010), in most cases they are trapped by the ISS and the surrounding framework of silicates. Both ISS and PGE-TABS liquid eventually crystallise, giving rise to the typical chalcopyrite-PMM assemblages (Cabri & Laflamme 1976; Dare et al. 2014). This may have also

been the case at Rathbun Lake, where discrete PMM are not only abundant, but occur is close textural association with chalcopyrite. The observed scarcity of Pt and Au minerals compared to Pd minerals is consistent with whole-rock PGE+Au concentrations. This and the lack of correlation between Cu, S and PGE suggests that a significant portion of PGE+Au occur as discrete minerals (i.e., PMM) rather than in solid solution in sulphides. Furthermore, there is no evidence (e.g. acicular, vermicular, flame-like or symplectitic textures) that PMM were formed by solid state exsolution or eutectic crystallisation. Rowell & Edgar (1986) argued for an independent precipitation of PMM out of a hydrothermal fluid, because of their textural preference for the edges of chalcopyrite. However, the location of PMM at the silicate-sulphide interface is very typical of magmatic deposits (Godel et al. 2010; Holwell & McDonald 2010). It therefore appears that the observed PMM attached to chalcopyrite represent late-magmatic liquids that were expelled from the crystallising Cu-sulphide (e.g. Prichard et al. 2004). Furthermore, Rowell & Edgar (1986) speculated that Te-Bi-As-bearing PMM might be diagnostic of hydrothermal occurrences. However, these minerals are in fact among the most common PMM in magmatic systems (e.g. O'Driscoll & González-Jiménez 2016), especially in those that have undergone crustal contamination (Platreef: Hutchinson & Kinnaird 2005; Norilsk: Duran et al. 2017), and they are the prevalent type of PMM in the footwall deposits of the Sudbury Complex (Cabri & Laflamme 1976; Li & Naldrett 1993; Farrow & Watkinson 1997; Dare et al. 2014; Hall et al. 2020). Experiments by Bai et al. (2017) and Scholten et al. (2018) support a (late-)magmatic origin of sperrylite in these footwall deposits.

Note that the Rathbun Lake PGE-Cu-Ni occurrence, although undoubtedly hosted by an Offset Dyke, differs from the typical offset-related ore deposits elsewhere around Sudbury in two respects: Its Ni/Cu ratio of < 0.1 is much lower than the average ore composition (Ni/Cu ~0.5) from offset deposits (Keays & Lightfoot 2004), and it is free of pyrrhotite, whereas pyrrhotite is the principal Fe sulphide in the Offset Dyke deposits. However, this difference would be easily explained if the Rathbun Lake represents only the deepest and highly fractionated part of a now eroded offset-hosted mineral system with the overlying contact ore having been eroded. This is somewhat similar to the Frood mineral system that is hosted by the inclusion-bearing quartz diorite of the Frood Offset Dyke. There, the ore body is also fractionated from surface (Fe-Ni-rich) to a depth of about 1.3 km (Cu-PGE-rich) as it narrows (Hawley 1965; Lightfoot 2016). It would also explain the very limited extent of the Rathbun Offset Dyke, suggesting that its current exposure of 5 m^2 represents only the lowermost termination of an originally much more voluminous dyke.

It remains to be established why the Rathbun Offset Dyke was mineralised in the first place. Offset Dykes at a similar distance to the Main Mass (~15 km) are generally regarded barren as their metal endowment steadily decreases with increasing distance. Maybe dyke-internal flow differentiation (Giroux & Benn 2005; Pilles et al. 2018b) and/or structural traps (Lightfoot & Farrow 2002) for both sulphide melts and mafic inclusions (e.g. faults, lithological contacts, branching, footwall irregularities) played a crucial role in the formation of the Rathbun Lake occurrence. Alternatively, the incorporation and assimilation of mafic xenoliths (perhaps accompanied by devolatilisation) could have led to changes in the rheological behaviour of the impact melt, to changes in the bulk density, viscosity, and wetting properties (e.g. Lesher 2017), thus facilitating the local deposition of base metal sulphide. Another possibility is that the impact melt sheet was extraordinarily thick above the study area for there seems to be a tight correlation between the size of sulphide deposits and the thickness of the overlying Main Mass as a simple consequence of mass balance (Lightfoot 2016): The thicker the impact melt sheet, the more metals available, the more

sulphide can separate, the thicker the contact mineralisation, the more PGE remained in the residual liquid. Maybe the Rathbun Offset Dyke occupied a concentric fault system that acted as a pond for impact melt and sink of sulphide melt, in a similar fashion as footwall embayments did beneath the Main Mass (Dreuse et al. 2010; Ripley et al. 2015; Lightfoot 2016; **Fig. 5.20**). This notion of Rathbun Lake representing a former topographic low beneath a relatively thick portion of the melt sheet is also borne out by the barometric evidence presented in **Chapter 5.5**.

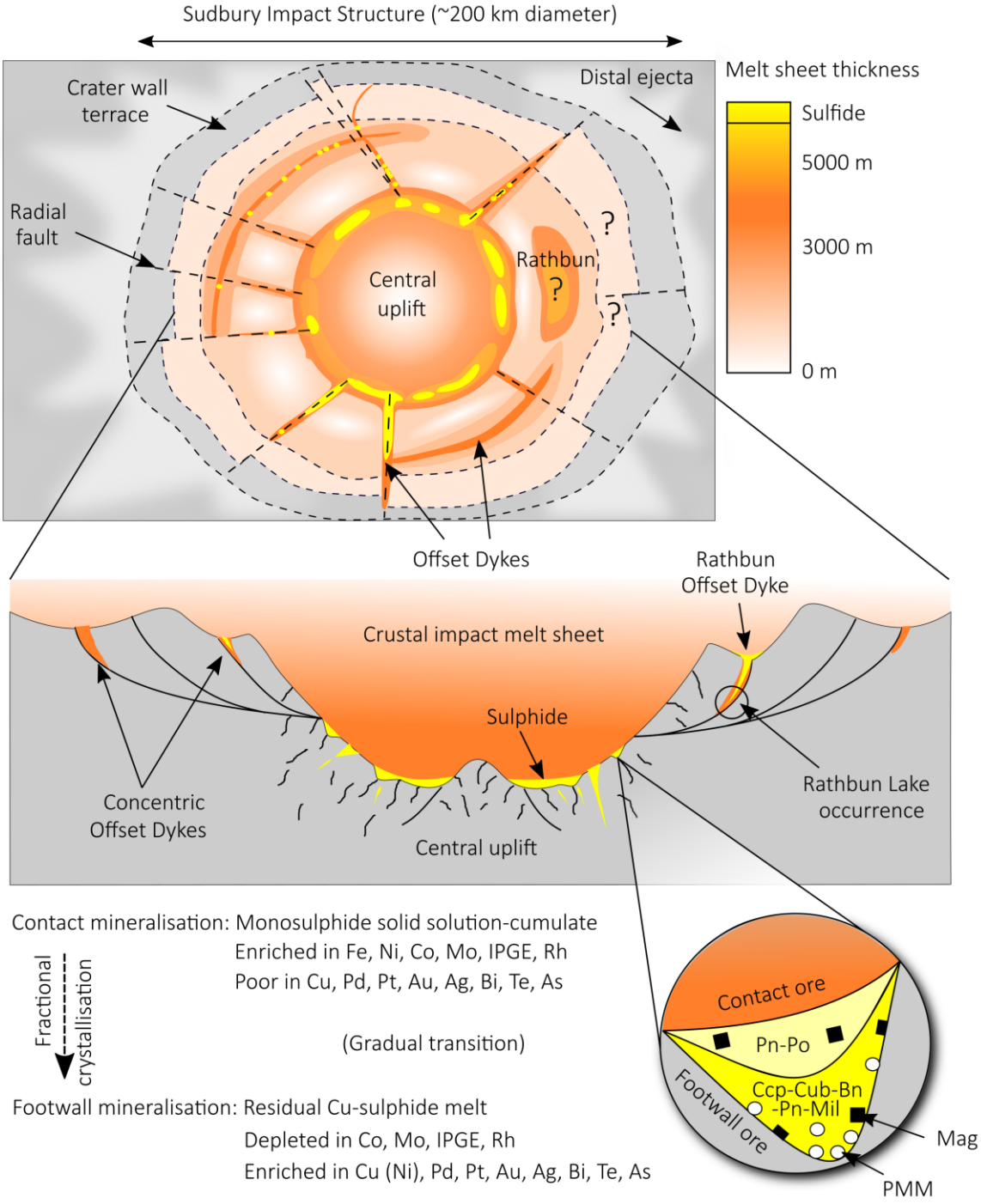

Figure 5.20 Emplacement and distribution of Offset Dykes and massive sulphide within the Sudbury Impact Structure; **A:** reconstructed "bathymetric" map of the initial impact melt sheet during the crater modification stage; massive sulphide was apparently localised in areas of maximum melt sheet thickness and footwall topography (throughs and embayments); also shown is the distribution of all known Offset Dykes (corrected for deformation); **B:** the Sudbury Impact Structure in cross section (not drawn to scale); inset illustrates the mineralogical and compositional zoning of the ore deposits into contact- and footwall type.

Although an igneous origin of the Rathbun Lake occurrence is beyond question, there is mineralogical and textural evidence of a certain hydrothermal component. This is especially true for the assemblages Chl + Qtz + Ep + Alb and Ccp + Py + Vio/Mil ± Cov, which are diagnostic of lower greenschist-facies metamorphism of mafic rocks and low-temperature alteration of magmatic sulphide, respectively (e.g. Bucher & Frey 2002; Holwell et al. 2017). The same assemblages have been reported worldwide, including many well-known magmatic deposits where pyrrhotite, pentlandite and chalcopyrite are the primary sulphides. Examples include the Bushveld Complex (e.g. Smith et al. 2014; Junge et al. 2019), the Great Dyke (Li et al. 2008), Lac des Iles (Duran et al. 2016), Kevitsa (Le Vaillant et al. 2016), Kambalda (Nickel et al. 1974), several deposits in the Abitibi (Misra & Fleet 1974) and structurally modified deposits at Sudbury itself (Lightfoot 2016).

In fact, the mineral violarite, $FeNi_2S_4$, was first described by Clark & Catlett (1889) in the Vermillion Mine, a high-grade PGE-Cu-Ni sulphide deposit hosted by the Vermillion Offset Dyke south of Main Mass (Grant & Bite 1984; Szentpéteri et al. 2003). Since then, it has been documented in many other deposits, where it is always considered a supergene alteration product of pentlandite (Misra & Fleet 1974), less frequently also of pyrrhotite (Nickel et al. 1974). Due to its wide distribution and metallurgical significance, the formation conditions of violarite are particularly well constrained. Experimental work by Kullerud (1963) and Craig (1971) in the Fe-Ni-S system, for example, indicates that violarite is not stable above 460°C. Michener & Yates (1944) reported on pentlandite-bearing drill cores, which had already shown incipient secondary formation of violarite, pyrite, marcasite ±millerite after some 35 years of weathering. An experimental study by Tenailleau et al. (2006) implies that this replacement takes place at temperatures as low as 20°C within 5–10 years under typical surface conditions, for instance, via reactions:

$$\text{Pentlandite} + 2.75\ O_2(g) + 5.5\ H_2S(aq) \rightleftharpoons 2.25\ \text{Violarite} + 2.25\ \text{Pyrite} + 5.5\ H_2O \quad \textbf{(5.1)}$$

$$\text{Pentlandite} + 1.625\ O_2(g) + H_2S(aq) + 4.5\ H^+ \rightleftharpoons 2.25\ \text{Violarite} + 2.25\ Fe^{2+} + 3.25\ H_2O \quad \textbf{(5.2)}$$

Both reactions are accompanied by a ~11% volume increase (Tenailleau et al. 2006). This could have resulted in fracturing, thereby creating a secondary porosity and additional pathways for fluids. Note that **Reaction 5.1** can also account for the common association of pyrite/marcasite and violarite in the samples from Rathbun Lake (corresponding to the pyrite-zone of supergene profiles; Nickel et al. 1974). Additional Fe, Ni and S may have been released following the replacement of violarite to millerite, NiS (e.g. Tenailleau et al. 2006), although there remains ambiguity as to the origin of millerite in the studied samples, whether igneous or supergene, as there remains general ambiguity as to its origin in the Sudbury footwall deposits (e.g. Lesher 2017; Gore 2020). The same discussion applies to covellite, CuS, a very common supergene alteration product of chalcopyrite (e.g. McKinstry 1959; Sillitoe & Clark 1969): Replacement of chalcopyrite by covellite could have resulted in the liberation of Fe and S only to be re-deposited as pyrite/marcasite:

$$\text{Chalcopyrite} + 0.5\ O_2(g) + H_2S(aq) \rightleftharpoons \text{Covellite} + \text{Pyrite} + H_2O \quad \textbf{(5.3)}$$

It is, however, unlikely that all observed FeS_2 (up to 85 vol% in some samples) is due to the breakdown of base metal sulphide alone. Sulphidation of primary pyrrhotite has previously been invoked to explain pyrite-rich alteration assemblages in magmatic ore deposits (Djon & Barnes 2012; Duran et al. 2016; Piña et al. 2016; Holwell et al. 2017) and this process could well account for the absence of pyrrhotite and the predominance of pyrite/marcasite at Rathbun Lake.

Note that sulphidation of pyrrhotite produces an excess in Fe^{2+}. If this process occurred simultaneously with the breakdown of magmatic silicates (plagioclase, pyroxene, amphibole), it is conceivable that the excess Fe was consumed to form Fe-bearing hydrous silicates such as chlorite, stilpnomelane, amphibole or epidote. This would explain the frequently observed intergrowths between those hydrous silicates and pyrite at the Rathbun Lake occurrence. In a similar fashion, one could explain the formation molybdenite, arsenopyrite, Co-rich gersdorffite and galena – all present at trace amounts at Rathbun Lake and with a strong textural affinity towards chlorite. Arsenic could have been derived from the breakdown of primary As-bearing minerals or sourced from the sedimentary rocks in the footwall; the corresponding metals could have been leached from primary sulphides and silicates in the host and/or the country rock (e.g. Mo, Ni and Co from pentlandite; Pb from detrital or magmatic feldspar). On a side note, these accessory sulphides and arsenides are also common accessories in the hydrothermally altered footwall deposits, especially in the south of the Sudbury Igneous Complex, where the Main Mass is underlain by metasedimentary rocks (Lightfoot 2016, p. 314). Arsenides are common accessories in the mineralised parts of the Worthington (Lightfoot & Farrow 2002), Vermillion (Szentpéteri et al. 2003) and Copper Cliff Offset Dyke (Szentpéteri et al. 2002; Huminicki et al. 2004).

In contrast to silicates and sulphides, alteration seems to have had little effect on the PMM. This is particularly evident from a statistical comparison between the PMM populations (**Fig. 5.21**): Pd-Bi-Te minerals dominate in all samples, regardless of the intensity of sub-solidus alteration. Moreover, no statistically significant difference in grain size could be found, apart from PMM's tendency towards more irregular crystal faces (corrosion?) in the altered samples. Only the textural relationship between matrix and PMM seems to have changed in response to alteration. That is, in relatively fresh samples, the PMM preferentially occur together with chalcopyrite; in altered samples, they preferentially occur together with covellite, pyrite or silicates. Notable here is the high proportion of satellite grains, i.e., PMM that are detached from sulphide and now entirely enclosed in silicates. Given that PGE+Au are relatively insoluble in most hydrothermal fluids (compared to Cu, Ni, Fe and S) and thus experience re-distribution on a local scale at best (e.g. Barnes & Liu 2012; Holwell et al. 2014; Smith et al. 2014; Le Vaillant et al. 2016), satellite PMM are widely considered immobile textural relicts (e.g. Seabrook et al. 2004; Li et al. 2004; Hutchinson & Kinnaird 2005; Godel & Barnes 2008; Holwell et al. 2015). Whether whole-rock PGE+Au grades and -ratios (e.g. Pd/Pt, Pd/Ir) were affected by the alteration is, however, beyond the scope of this study; pursuing this question further would require detailed knowledge about the PGE+Au concentrations in the sulphides (e.g. pyrite), a statistically larger set of samples, and greater sample volumes to minimise nugget effects that are caused by, for example, large sperrylite crystals.

Of specific interest is the presence of temagamite, Pd_3HgTe_3, in the Rathbun Lake occurrence, as it could provide constraints on the nature of the involved fluid(s). Curiously, the mineral was first described by Cabri et al. (1973) in the nearby Temagami Greenstone Belt (**Chapter 2.1.1**), where it was found in association with mafic intrusion-hosted Cu-Ni-PGE sulphides. The available literature indicates that the presence of temagamite is restricted to hydrothermally/metamorphically modified magmatic sulphide occurrences (e.g. Beaudoin et al. 1990; Watkinson & Melling 1992; Seabrook et al. 2004; Bursztyn & Olivo 2010; Smith et al. 2014). This is likely because temagamite is unstable above 500°C; at greater temperature, Pd_3HgTe_3 decomposes into PdTe and Hg vapour (Cabri et al. 1973). Given the high volatility of Hg (boiling point of Hg^0 = 357°C, but likely depending on the speciation in fluids), alteration must have still occurred in a temperature regime that

prevented outgassing of Hg, perhaps aided by rapid self-sealing of the system. Mercury concentrations are very low (ppb range) in both the Earth's mantle and in mantle-derived magmas (e.g. McDonough & Sun 1995). This makes the local Nipissing Suite gabbro an unlikely source of Hg. It is also unlikely that Hg was derived from the impact melt rocks themselves, given their high formation temperature > 1,600°C and the well-established impact-induced volatile loss of even moderately volatile elements such as Zn, Cs, Rb and Pb (Kamber & Schönberg 2020). The most likely origin of Hg in the Rathbun Lake occurrence is, therefore, leaching of the local sedimentary rocks, especially if organic carbon was present (e.g. in the Espanola Formation).

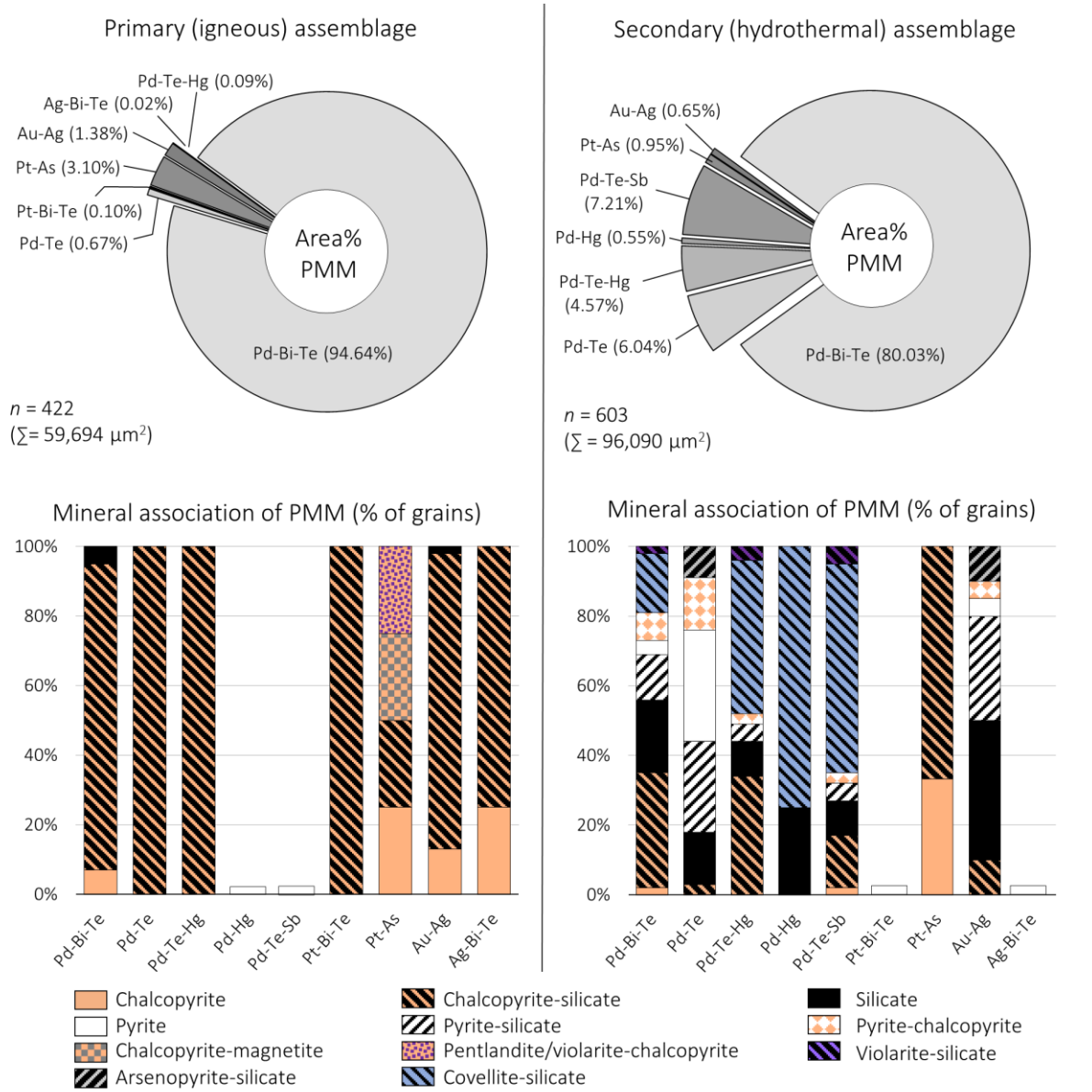

Figure 5.21 Statistical analysis of the relative proportions of precious metal minerals (PMM) and their textural association at the Rathbun Lake occurrence; pie charts show the relative proportion of PMM (in vol %) and bar charts show the mineralogical-textural association of the different PMM (in grain %); grains in composite PMM are classified individually.

By analogy to Hg diffusion through gold particles (Frimmel & Gartz 1997), the diffusive replacement of Pd minerals is expected to have operated on timescales of some 10^3–10^4 years. Most Pd minerals at Rathbun Lake are, however, not homogeneous with respect to their Hg content; rather, they show evidence of incomplete replacement toward PdHg and Pd_3HgTe_3, where in contact with

secondary silicates (**Fig. 5.8**). This incomplete homogenisation could point to a very short-lived hydrothermal event that affected Rathbun Lake, to a low fluid:rock ratio, and/or to rapid cooling and exhumation. Based on microscopic deformation features (kink bands, crenulation, fractures), sulphide-bearing shears in outcrop, the observations made in previous studies (Dressler 1982; Rowell & Edgar 1986), and bearing in mind that Hg in geological systems is typically confined to near-surface hydrothermal processes (Barnes & Seward 1997), it is likely that the alteration was related to faulting, possibly associated with regional deformation and metamorphism, sometime between 1.8 Ga and 1.4 Ga (Papapavlou et al. 2017, 2018a). A possible candidate is the nearby Wanapitei River Fault, part of the Palaeoproterozoic NNW-striking Onaping Fault System (Buchan & Ernst 1994). Previous studies on Rathbun Lake have already stressed the importance of potential splays related to this fault system as they may have acted as conduits for fluid circulation (Koulomzine 1955; Rowell & Edgar 1986). This notion is supported by the report of secondary Sb- and Hg-bearing PGE and Te minerals in an Archaean mafic intrusion of the nearby Temagami Greenstone Belt (Cabri et al. 1973); in the 2.45 Ga River Valley mafic intrusion 20 km southeast of Rathbun Lake (Holwell et al. 2014); in the hydrothermal Cobalt Hill Cu-Au occurrence 20 km north of Rathbun Lake (Schandl 2004); in the Broken Hammer footwall deposits north of the Main Mass of the Sudbury Igneous Complex, 30 km to the east (Péntek et al. 2013). All these occurrences have in common that they are spatially associated with (the same?) regional N-trending structures.

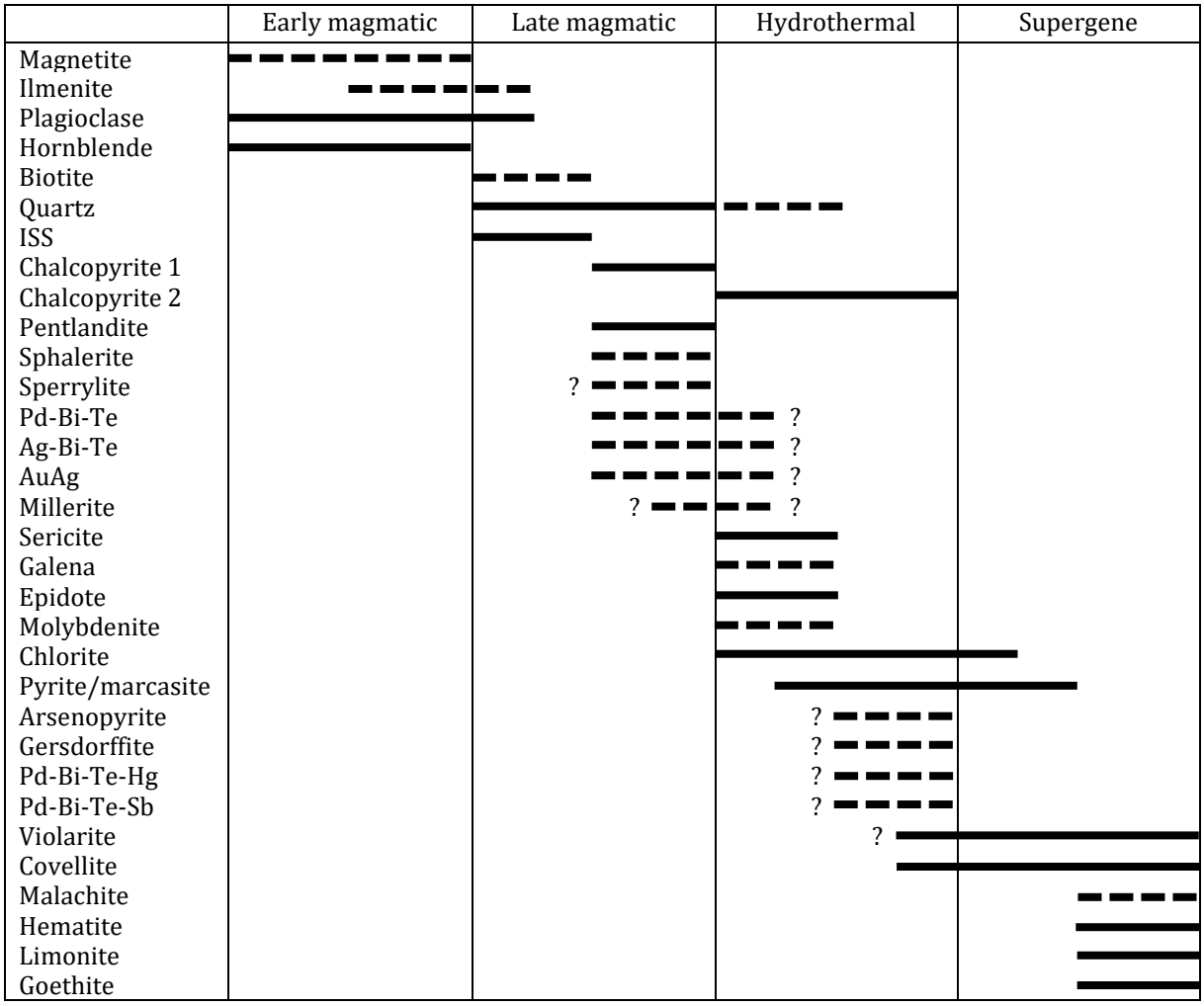

Figure 5.22 Proposed paragenetic sequence for the PGE-Cu-Ni sulphide mineralisation (the Rathbun Lake occurrence) associated with newly discovered Rathbun Offset Dyke.

Tholeiitic Diabase

6.1 Summary

A mafic dyke was discovered in Mackelcan Township, where it was emplaced into sedimentary rocks of the Lorrain Formation, Cobalt Group. The dyke is non-magnetic, measures 8–10 m in width, and could be traced in (sub-)outcrop for 10 km along strike (between N30°E and N60°E). Field evidence and microscopic studies reveal that the dyke is, in many places, crosscut by and incorporated as clasts into pseudotachylitic breccia (Sudbury Breccia), indicating that the dyke's emplacement must have predated the 1.85 Ga Sudbury impact event, whereas the maximum possible intrusion age is constrained by the depositional age of the sedimentary host rock (~2.31 Ga).

Petrographically, the dyke classifies as quartz diabase although it exhibits a considerable range in mineralogy and texture, and an overall trend for post-magmatic alteration to increase from northeast to southwest. Fresh samples consist of clinopyroxene + plagioclase ± quartz ± ilmenite; moderately altered samples of actinolite + plagioclase + epidote ± quartz ± leucoxene; strongly altered portions are essentially monomineralic epidosites or composed chlorite ± quartz. Most of the observed changes can be attributed to retrograde metamorphism at greenschist-facies conditions, whereas the pervasive epidotisation and chloritisation seems related to shearing and hydrothermal alteration at a higher fluid:rock ratio. Alteration is pervasive close to Sudbury Breccia or in vicinity to N-trending structures, suggesting both acted as conduits for circulating fluids.

Alteration was accompanied by a significant element mobility and the disturbance of whole-rock Rb-Sr and U-Pb isotope systematics, leaving only the HFSE and REE as immobile petrogenetic tracers. Relatively fresh samples a characterised by 50–52 wt% SiO_2, 6–8 wt% MgO, 40–60 ppm Zr, a La/Sm ratio of 2.8, and weakly negative Ti-Nb-Ta anomalies when normalised against the primitive mantle. These are all features typified by the mafic rocks of the regional 2.22 Ga Nipissing Suite, and it is therefore proposed that the tholeiitic quartz diabase dyke is another member of this suite. This correlation is further supported by similar whole-rock Nd isotope systematics (εNd_0 between –14 and –8; $^{147}Sm/^{144}Nd$ between 0.13 and 0.18; εNd_{2220} between –3 and +1).

Although most intrusions of the Nipissing Suite occur as sills concordant with the bedding of the host rocks, discordant narrow dykes (like the one identified in this study) are not uncommon, and these are traditionally interpreted as magmatic feeders. However, the Nipissing dyke of this study is not connected to any larger intrusive body at the current level of erosion. It also occurs in a rather unusual, very shallow stratigraphic level no more than 2–3 km below palaeosurface. If the Nipissing Suite represents the erosional remnant of a former flood basalt province, the dyke identified here would be the closest analogue of what one might consider a subvolcanic fissure vent.

Although no mineralisation is directly hosted by the diabase, the dyke occurs adjacent (< 500 m) to the hydrothermal breccia-hosted Cu-Co-Au (± Cr ± Ni) occurrences of Cobalt Hill and Wolf Lake. Mass balance calculations indicate that metasomatic leaching of the dyke during a pervasive epidotisation and chloritisation could have provided some of the required metals, in particular Cu, Cr, and Pb. The age of these occurrences, the heat- and fluid source(s), remain enigmatic.

6.2 Local Geology

Mackelcan Township is located about 45 km northeast of Sudbury, and 10 km northeast of Lake Wanapitei. It borders McConnell Township to the north, McCarthy Township to the east, Rathbun Township to the south, and Aylmer Township to the west. The area can be accessed via the Trans-Canada Highway coming from Sudbury, passing the town of Wahnapitae, and then turning north into Kukagami Road. Following this and the subsequent Bushy Bay Road for 40 km north, access to the Wolf Lake area is provided by gravel and logging road. Field work by the author and the exploration company involved was preceded by reconnaissance mapping of Ontario Geological Survey (Dressler 1981a, 1982; Gates 1991), and the reader is referred to these publications for a detailed description of the local geology; a summary is presented in **Figure 6.1** and down below.

The surface geological makeup of the area encompasses siliciclastic sedimentary rocks of the Cobalt Group; no igneous rocks of the 2.22 Ga Nipissing Suite or the 1.23 Ga Sudbury Dyke Swarm are present, at least not at surface. Sandstone of the ca. 2.35–2.31 Ga Lorrain Formation is aerially extensive and covers most of Mackelcan Township. According to Dressler (1982) and Goad & Rowell (1985), these rocks conformably rest upon the Gowganda Formation, the latter being exposed only in the eastern corner of the study area and will not be considered further. The Lorrain Formation is a very thick unit. Dressler (1982) estimated its total preserved thickness at 3,400 meters; drilling in the Wolf Lake revealed a true thickness of 670 m and a gradual transition to the underlying Gowganda Formation (Schandl 2002). In the study area, the Lorrain Formation is composed of relatively homogeneous and monotonous sandstone, which can be further classified as quartzite, (sub-)arkose and arkosic arenite. Of these, arkose is by far the most common lithology, and wacke becomes more abundant in the lowermost parts of the formation (e.g. Schandl 2002). Sedimentary structures are rarely observed in outcrop, but may include planar bedding, through-cross stratification, and layers of quartz pebbles. Colours range in outcrop from dull white, light grey to different shades of green, beige, pink and brick red, all of which reflects different styles of post-depositional alteration and the presence of different secondary minerals such as hematite, chlorite, carbonate, or albite. Prograde metamorphism is implied by bulging recrystallisation of quartz grains that occur in mutual contact with each other, and by the replacement of detrital feldspar by sericite and saussurite. Lack of biotite, however, indicates that the upper greenschist facies (biotite zone) was either not attained or that biotite was replaced by retrograde chlorite, thus constraining the metamorphic overprint to ca. 280–390°C (e.g. Stipp et al. 2002). Rocks of the Lorrain Formation are typically cemented with chlorite and quartz, locally also with albite and carbonate. Silicified lithotypes, such as the quartzite from Wolf Mountain and Cobalt Hill, are very resistant to weathering and erosions, creating a significant relief (> 100 m).

While the Lorrain Formation appears largely undeformed on regional geological maps (e.g. Dressler 1982), a more complex picture is revealed by geophysical surveys (e.g. Buchan & Ernst 1994; Easton et al. 2020) and recent field work. Numerous lineaments, some not evident at surface, seem to displace magnetic and gravity features in the basement, and the hydrography in the region appears to be, at least in part, structurally controlled. One example is Silvester Lake (**Fig. 6.1**). Another example includes the Laundry Lake Structure, a regional > 10 km long lineament that encompasses Rathwell Lake, Laundry Lake, and Island Lake. The Laundry Lake Structure has previously been interpreted as a syncline based on the facing of sedimentary bedding (e.g. Lumbers & Card 1977), but geophysical data also reveal a certain strike-slip component. The Laundry Lake

Fault (Dressler 1982) could be a splay of the N-striking Upper Wanapitei River Fault, which is in turn part of the regional Palaeoproterozoic Onaping Fault System (Buchan & Ernst 1994). In addition, there are multiple small-scale reversals in the orientation of sedimentary bedding, for example, in the Wolf Lake area. This could point to the existence of parasitic fold structures that have not previously been recognised.

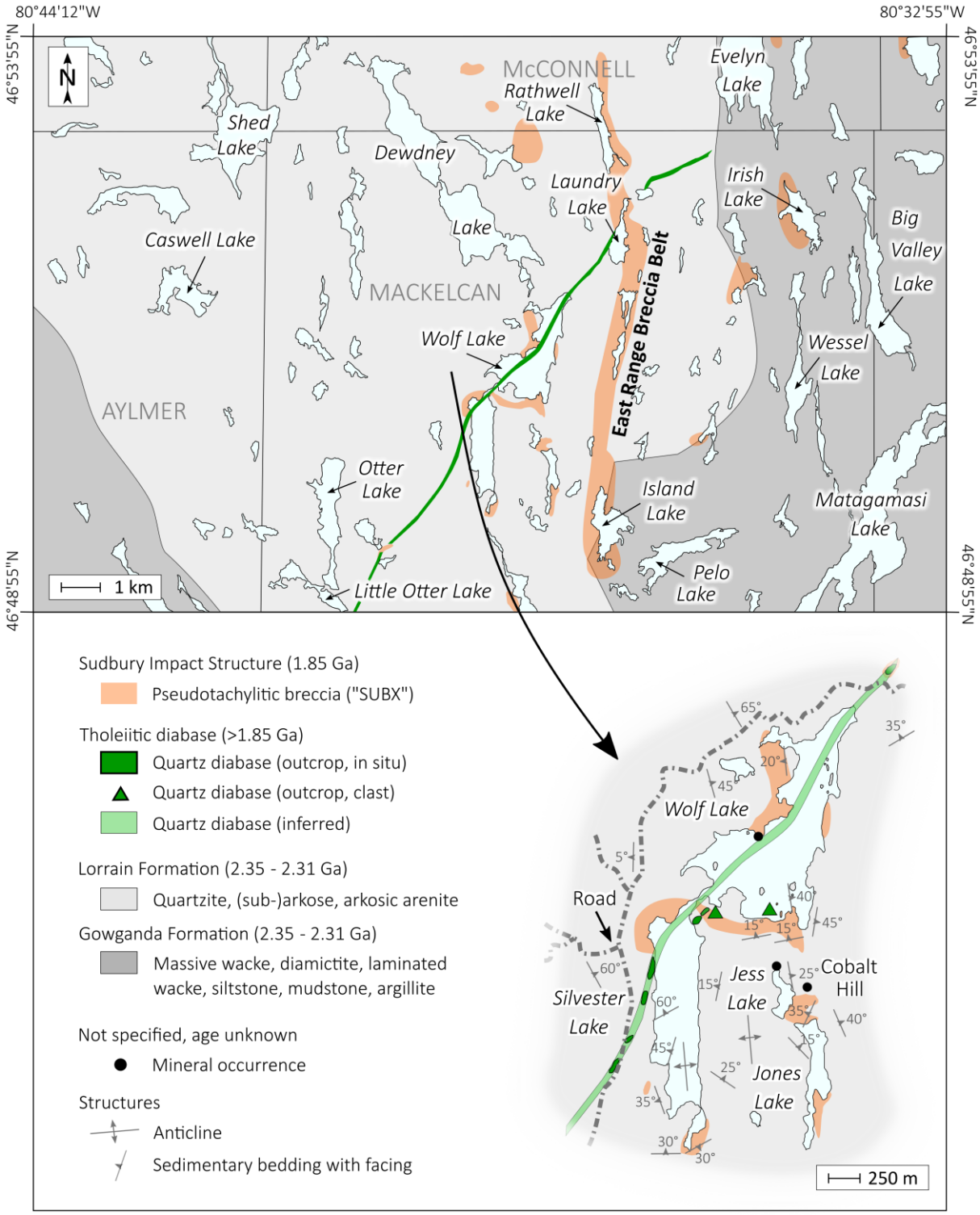

Figure 6.1 Geological map of Mackelcan Township showing the regional geological and lithostratigraphic context of the tholeiitic quartz diabase dyke; based on maps of Dressler (1981a, 1982), Gates (1991), Whymark (2019) and additional mapping by the author in the course of this study.

Two types of breccia are present in the study area. Mosaic breccia in form of pipes, lenses, and irregular bodies – and likely of hydraulic origin – falls into the first category (**Fig. 6.2A–C**). This kind of breccia is associated with a pervasive hydrothermal alteration and, in a few places, host of sub-economic base and precious metal mineralisation. Prominent examples include the Wolf Lake (46°51 12.0N 80°38 14.7W) and Cobalt Hill occurrences (46°50 33.0N 80°37 52.8W). Mineralisation at Wolf Lake occurs in form of chalcopyrite, covellite, malachite, and vuggy pyrite. It is marked by Cu > (Ni+Co) at up to 4 wt% Cu, and the entire mineralisation is hosted by pink albitised quartzite breccia and quartz-carbonate stockworks that extend for several hundred meters into the subsurface (e.g. Gates 1991). Visible Au grading up to 687 g/t over 0.5 m has lately been reported (Whymark 2019). The Cobalt Hill occurrence, despite being separated only 1.2 km from the Wolf Lake occurrence and likewise hosted by albitised Lorrain Formation breccia, displays a somewhat different style of mineralisation. For instance, metallic ratios are characterised by a Cu < (Ni+Co); Au grades are more constant but overall lower (1.2–23 g/t); Pt and Pd concentrations are elevated above the background. Schandl (2002, 2004) studied drill core 92-1 into the Cobalt Hill showing (**Fig. 6.2A–C**) and reported on pyrite as the principal sulphide, with tiny inclusions of millerite, gersdorffite, chalcopyrite, pentlandite, and coloradoite (HgTe). Interestingly, Schandl (2002, 2004) also found Cr-V-bearing chlorite and mica (fuchsite) at Cobalt Hill. When the author re-examined the same drill core in 2018 as well as a muck pile below the old adit at Cobalt Hill (46°50 33.03N 80°37 53.17W), the accessory presence of fuchsite could be confirmed (**Fig. 6.2B**).

As noted by Gates (1991), both occurrences seem to be spatially and genetically related to a regional Na metasomatism (albitisation) that affected large parts of the Huronian Basin, from Davis Township in the east as far as Espanola in the west (e.g. Meyer et al. 1987). Attempts to date this regional metasomatism, which is accompanied by Cu-Au mineralisation elsewhere (e.g. the Scadding Mine) yielded U-Pb monazite dates of 1701 ± 3.6 Ma (*n*=1), 1727 ± 3.6 Ma (*n*=20), 1699 ± 3.6 Ma (*n*=8) and 1916 ± 13 Ma (*n*=13) (Schandl et al. 1994). It should be noted, however, that these dates were obtained only two samples south of Wanapitei Lake, just a few kilometres north of the Grenville orogenic front, and that the textural position of the dated monazite grains is not known. Thus, it is possible that these dates reflect a younger thermal/metamorphic overprint (e.g. the Yavapai Orogeny, or the Killarney magmatic event) and not the actual timing of the Na metasomatism. Evidence of a more prolonged, or maybe of two separate metasomatic events (2.22–1.68 Ga) within the Huronian Basin was provided by Fedo et al. (1997), McLennan et al. (2000) and Potter & Taylor (2009). Schandl (2002, 2004) considered the possibility of a hidden (ultra-)mafic intrusion as both a heat and metal source for Cobalt Hill. Schandl & Gorton (2007), elaborating on their earlier work, drew comparison to ICOG-type mineralisation and alteration. They proposed that the Scadding Mine, and by implication, the Wolf Lake-Cobalt Hill occurrences, represent "*modified iron oxide-copper-gold (IOCG) deposit*[s] *in which Fe sulfides dominate over Fe oxides*" (Schandl & Gorton 2007, p. 1415), ignoring the fact that none of the described or observed features matches the modern definition of an IOCG system (cf. Groves et al. 2010).

A second type of breccia, Sudbury Breccia, is far more widespread than previous studies have indicated. Field work made it possible to outline an extensive and discrete 14 km long breccia zone (or "belt"). By analogy to the South Range Breccia Belt (e.g. Scott & Spray 1999) this will in the following be referred to as the *East Range Breccia Belt (ERBB)*. The ERBB extends from Matagamasi Lake in the south, as far as Chiniguchi Lake in the north, and it is between 100 and 400 m wide, although its lateral confines are gradational. The ERBB broadly coincides with the Laundry

Lake Structure, but enclaves of Sudbury Breccia were also noted, for example, around Wolf Lake, and in many places without any link to structures. Sudbury Breccia in the Wolf Lake-Silvester Lake area can be described as monomict and matrix supported. Rock and mineral clasts (mainly arkose and quartzite) are subrounded, have a roughly fractal grain size distribution, range in diameter from millimetres to several decimetres, and are embedded in fine grained micro- to cryptocrystalline quartzofeldspathic ±vesicular matrix. The matrix is in places homogeneous, in other places remarkably striated/flow banded. A spectacular example of the latter occurs on a small island on Wolf Lake (**Fig. 6.2D**). The texture of convoluted flow banding there strongly resembles the clastic type of Sudbury Breccia sensu Rousell et al. (2003). It also bears resemblance to sheath folds in pseudotachylite from the Vredefort Impact Structure, South Africa (Berlenbach & Roering 1992). The outcrop is important in as such it provides constrains as to the relative timing of the alteration in the area. Pink (hematised and apparently albitised) fragments of arkose indicate that metasomatism preceded the brecciation. In the same outcrop, two chloritic clasts of < 10 cm in diameter were found. Tests with a hand magnet indicated the presence of abundant magnetite and/or pyrrhotite in those clasts. It is not clear whether they were derived from a mafic dyke or from a chloritic hydrothermal breccia similar to that of **Figure 6.2A–C**, but either way, the outcrop provides evidence for the existence of an exotic pre-1.85 Ga lithology in the area that is not exposed nearby.

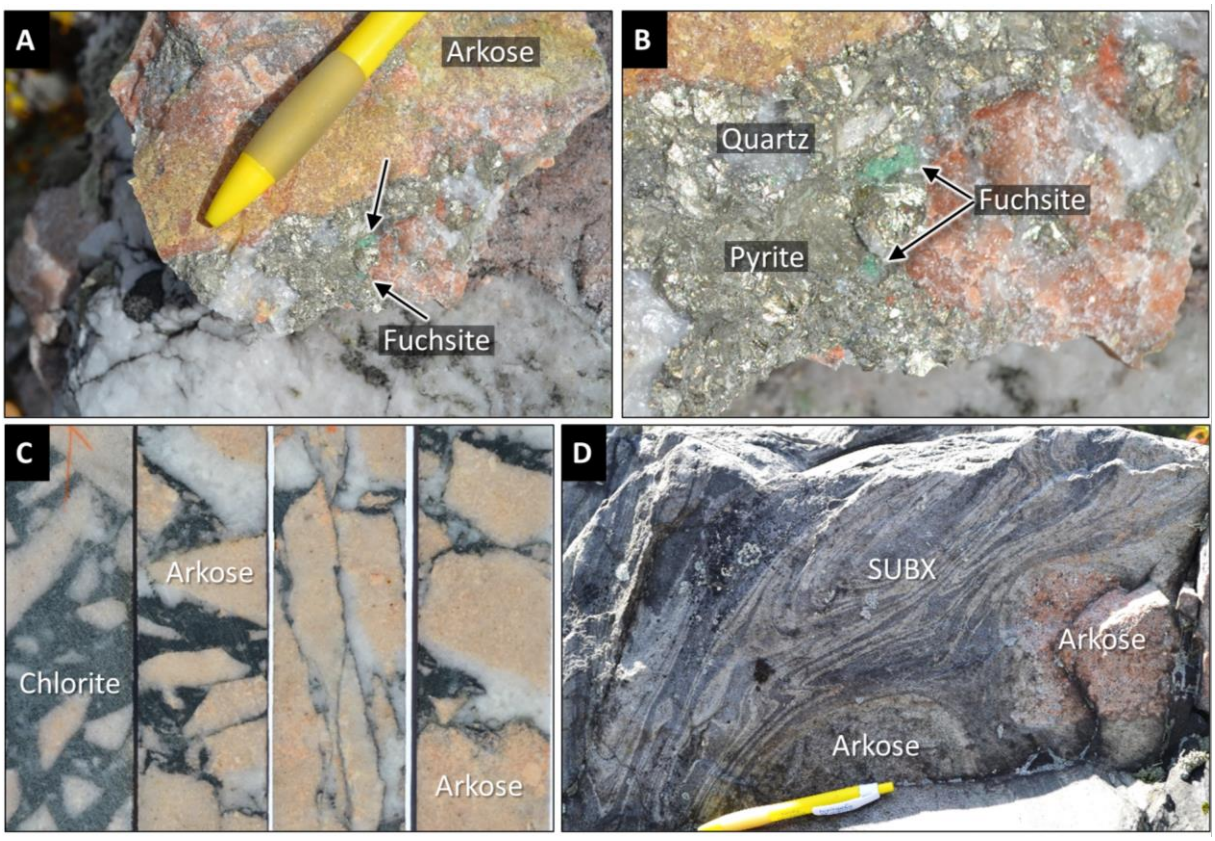

Figure 6.2 Photographs showing the two types of breccias found around Wolf Lake, Mackelcan Township; **A:** hand specimen obtained from the muck pile below the Cobalt Hill occurrence, showing a hydrothermal breccia with pyrite and accessory green fuchsite (46°50 33.0N 80°37 52.8W); **B:** same photograph as before, but enlarged; **C:** hydrothermal mosaic breccia intersected in Flag Resources' historic drill core 92-1 at Cobalt Hill, showing angular and bleached clasts of Lorrain Formation arkose in a matrix of chlorite; note the chlorite coatings on top of the paleo vertical possibly due to settling in a stagnant environment; drill core diameter is 3.65 cm; **D:** outcrop of flow-banded pseudotachylitic breccia (Sudbury Breccia, SUBX) at Wolf Lake, showing clasts of arkose in a cataclastic quartzofeldspathic matrix (46°50 53.7N 80°38 06.8W).

6.3 Field Relations

In 2018, an exotic mafic lithology was discovered between Silvester Lake and Wolf Lake, both in outcrop and in dumped diamond drill cores of past exploration activities in the area. Although very scattered and discontinuous in outcrop, it was subsequently possible to trace the outcrops, which turned out to be part of a larger dyke, for 9.7 km along strike, from Little Otter Lake in the southwest, almost as far as Evelyn Lake in the northeast (**Fig. 6.1**). The dyke strikes relatively consistently – but not without some undulation – between N30°E and N60°E, and it occurs on both sides of the East Range Breccia Belt. Judging from its orientation, little, if any, displacement of the mafic dyke around the breccia belt and other structures had occurred. The true thickness of the dyke is typically 8–10 m; contacts to the country rock (Lorrain Formation quartzite and arkose) are blend, sometimes sharp, locally brecciated, but in most places, the intrusive contact is not exposed. The dyke appears homogeneous in texture with little grain-size variation throughout, and free of xenoliths. No currently known mineralisation is associated with the dyke. The dyke seems to have been metamorphosed under greenschist-facies conditions, as it is aphantic, relatively soft in hand specimen and rich in epidote and chlorite. For most parts, no metamorphic fabric was observed. However, in a few outcrops around Silvester Lake, slickenfibres of epidote and slickensides of chlorite were noted. The only "fresh" outcrops could be found far northeast, at a road outcrop between Laundry Lake and Evelyn Lake (46°52 49.27N 80°36 18.66W), before the dyke eventually disappears. No extension of the dyke could be found east of the N-striking Gowganda-Lorrain contact, either due to erosion, or because the dyke preferentially exploited fractures within the competent and brittle Lorrain Formation quartzite and arkose.

A peculiar feature of the mafic dyke is its intimate spatial relationship with pseudotachylitic breccia of the 1.85 Ga Sudbury impact event (Sudbury Breccia), which is predominantly found at its intrusive contact to the Lorrain Formation. This is consistent with a general and well-established trend for Sudbury Breccia to occur along lithological contacts between rocks of different physical properties such as, competence, density, or water content (e.g. Rousell et al. 2003). At the passage between Wolf Lake and Silvester Lake (**Fig. 6.1**), a 5 m^2-large outcrop was found with clasts of the mafic dyke nested inside Sudbury Breccia. The rounded clasts, although strongly affected by epidotisation, clearly originated from the mafic dyke nearby. This lends support that the dyke must be older than the impact and the Sudbury Breccia. Similar observations were made in many other locations, for example, west of Silvester Lake, and in the gorge that connects Wolf Lake and Laundry Lake (46°51 01N 80°37 18W). This narrow gorge, striking N35°E, likely formed by the preferential erosion of the relatively soft mafic dyke compared to the hard and resistant quartzite and quartzite-hosted Sudbury Breccia surrounding it. A similar, less pronounced, lineament is associated with the northeastern-most extension of the mafic dyke, between Laundry Lake and Evelyn Lake (46°52 55.89N 80°36 0.63W), as can be seen, for example, in digital elevation models.

6.4 Petrography

The freshest, least altered samples of the dyke were found at a road outcrop just south of Evelyn Lake (**Fig. 6.1**). They are dark grey to dark green in hand specimen (**Fig. 6.3A**), medium grained (1 mm on average), and display a salt-pepper texture of mafic minerals (70 vol%) and felsic minerals (30 vol%). In thin section (**Fig. 6.3B–D**), the rock is characterised by a holocrystalline, equigranular, subophitic and hypidiomorphic texture typical of fine-grained gabbro. It is mainly composed of clinopyroxene and feldspar. Clinopyroxene is of subhedral habit and occurs as (sub-)angular crystals of up to 2 mm in size. Fresh individuals of clinopyroxene display a high relief, sharp, either curved or straight, grain boundaries, and no intrinsic colour. Altered grains, in contrast, are marked by a pronounced pleochroism from olive green to brown, and by frayed, highly irregular grain boundaries due to the incipient pseudomorphic replacement by fibrous amphibole (uralite) ± ilmenite. Clinopyroxene, mainly augitic in composition, occurs as, in places, single twins with herringbone-like exsolutions of pigeonite. Sector zoning was observed in some of the grains. Triple junctions between pyroxene and feldspar are common. Feldspar occurs either as mm-large, anhedral crystals (aspect ratio < 2:1), or as sub- to euhedral lathy crystals (aspect ratio 10:1). The former variety lacks twinning typical of feldspar, and it is, even in the freshest samples, strongly altered to sericite; epidote is absent. The euhedral needles of feldspar are, in general, better preserved, especially where they are enclosed in pyroxene. Because of their polysynthetic twinning, high extinction angles and their chemical composition, they have been identified as calcic plagioclase. Leucoxene, a semi-translucent to opaque aggregate of Fe-Ti minerals involving ilmenite, magnetite, hematite, and titanite, occurs as an accessory (< 1 vol%) dispersed throughout, and it forms amoeboid to dendritic (skeletal) grains of up to 3 mm in diameter. Quartz was found as another accessory yet omnipresent mineral, also interstitial between pyroxene and feldspar. Quartz is typically anhedral, undeformed and appears monocrystalline. It is best seen under plane polars in altered samples. Quartz also forms complex aggregates together with sericite, which are interpreted as relict granophyric intergrowths between quartz and feldspar (**Fig. 6.3C,D**). In these intergrowths, feldspar appears altered whereas quartz appears fresh. Needles of apatite and cubes of pyrite are small and rare accessory minerals. Chlorite was occasionally observed; it occurs in close association with leucoxene and appears to be secondary after magmatic biotite and/or hornblende. These biotite-leucoxene intergrowths are similar to the features observed in mafic xenoliths (Nipissing Suite gabbro) within in the Rathbun Offset Dyke (**Chapter 5**).

Increasing alteration of mafic dyke samples close to, and especially within, the East Range Breccia Belt, manifests in the obliteration of the original igneous texture, the complete pseudomorphic replacement of pyroxene by fibrous green amphibole, and the replacement of plagioclase by saussurite (**Fig. 6.3E,F**). Primary minerals are reduced to ghost-like outlines, separated only by pristine relicts of interstitial quartz. In these samples, brown semi-transparent leucoxene occurs at the expense of opaque leucoxene; the modal amount of pyrite and chlorite increases slightly.

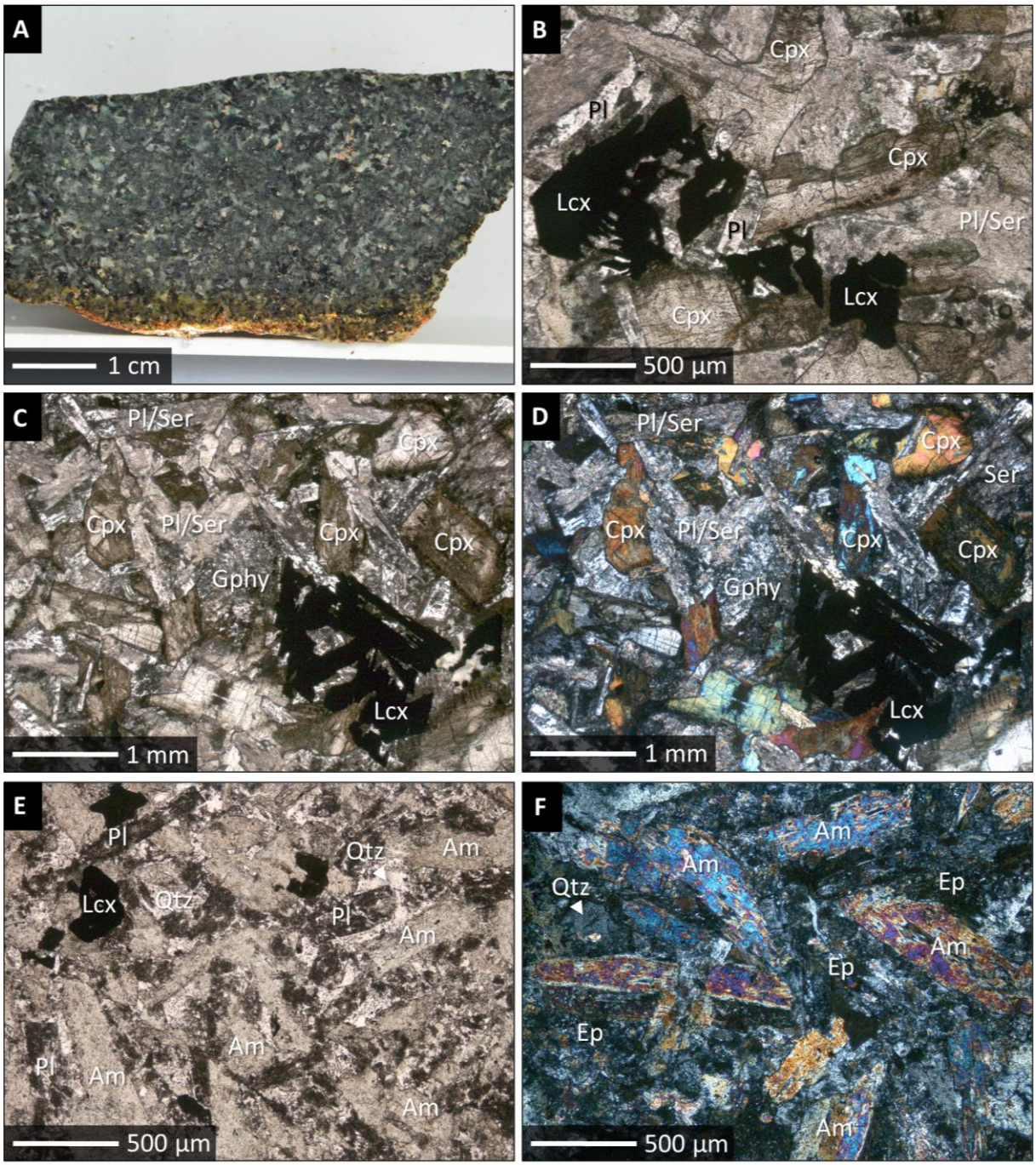

Figure 6.3 Photograph and microphotographs of the freshest and of moderately altered samples of the tholeiitic quartz diabase dyke from Mackelcan Township; **A:** hand specimen of the pristine sample AK19-35 (polished and photographed under water for contrast enhancement); **B–C:** thin sections of AK19-35 under transmitted light and plane polars, showing slightly uralised clinopyroxene and sericitised plagioclase in a subophitic texture together with accessory interstitial granophyre and skeletal leucoxene; **D:** same spot under transmitted light and crossed polars; **E:** moderately altered sample AK18-3 under transmitted light and plane polars, showing amphibole (actinolite) after pyroxene, and epidote/saussurite after plagioclase, and interstitial quartz, and accessory leucoxene; **F:** same thin section under transmitted light and crossed polars. Abbreviations: Cpx = clinopyroxene; Pl = plagioclase; Ser = sericite; Gphy = granophyric intergrowth; Lcx = leucoxene; Ep = epidote; Qtz = quartz; Am = amphibole.

Brecciation and the intensity of hydrothermal alteration of the mafic dyke is most extreme at and around Wolf Lake. Hand specimens collected from there have completely lost their primary magmatic texture due to a strong deformation and a pervasive propylitic alteration. Hand specimens of the mafic dyke from Wolf Lake are cut by numerous green veins (**Fig. 6.4A**), which, at first glance, could be easily mistaken for hydrothermal features such as, chlorite-epidote veins. They have a random orientation, shrink and swell, and are arranged in an anastomosing, dendritic, in places also ladder-like manner. A closer examination under the microscope (**Fig. 6.4B**) shows that these veins are not of hydrothermal origin, but pseudotachylitic breccia. They display the defining hallmarks of Sudbury Breccia as listed, for example, in Rousell et al. (2003), i.e., sharp irregular breccia walls, rounded rock and mineral clasts with a fractal grain-size distribution (that is, an inverse relationship between the clast size and abundance), embedded in an aphantic, cryptocrystalline matrix. The term "matrix" is here applied somewhat arbitrary given that there is a continuum in grain size. Some of the clasts are elongated and oriented parallel to the breccia margin (**Fig. 6.4B**). Mafic clasts preserve the original, though secondary, mineralogy and texture of their host lithology, indicating that the metamorphism and alteration pre-dated the brecciation, yet it cannot be ruled out that some of the observed alteration post-dated the brecciation, selectively replacing the fine-grained, perhaps initially glass-bearing, matrix. Some fragments of polycrystalline quartz have also been found. These probably originated from the adjacent Lorrain Formation quartzite and are regarded as parautochthonous (= locally remobilised). The spectrum of Sudbury Breccia also includes tiny microfractures (**Fig. 6.4C**) and centimetre to decimetre-wide breccia veins and breccia bodies (**Fig. 6.4D**), preferentially found along the intrusive contact of the dyke. Narrow, cryptocrystalline and almost opaque veinlets of Sudbury Breccia are in fact omnipresent in every mafic sample collected along the East Range Breccia Belt. The veinlets resemble mylonitic shears in thin section. However, in contrast to microfractures resulting from endogenic processes, these Sudbury Breccia veinlets have a random orientation and lack any displacement. Their arrangement is locally perpendicular to each other, locally dendritic, which bears some resemblance to dendritic shock veins or fracture systems known from other impact structures (e.g. Garde & Klausen 2016). Under the microscope, these veins also bear strong resemblance to pseudotachylitic breccia previously described within mafic host rocks (cf. Kovaleva et al. 2018a). **Figure 6.4D** shows a more massive example of heterolithic Sudbury Breccia developed at the intrusive contact between the mafic dyke (incompetent) and the Lorrain Formation quartzite (competent). Note the green opaque-rich, contorted and plastically deformed clast in the centre of this image, whilst clasts of mono- and polycrystalline quartz are still intact and exhibit sharp contacts against the matrix. This likely reflects competence differences between the two host rocks and the different susceptibility of hydrous and anhydrous minerals to undergo friction melting (e.g. Spray 2010).

Some parts of the diabase dyke underwent extreme metasomatic changes, especially at the south shore of Wolf Lake and in vicinity to the Cobalt Hill occurrence (**Fig. 6.4D–F**). There, centimetre-thick hydrothermal veins of epidote ± quartz ± chlorite were found to cut across the dyke, or pervasively replacing the entire diabase. The alteration is in places so extreme that the magmatic protolith has been entirely replaced by hydrous silicates, producing almost monomineralic domains: epidosite, chlorite fels, and transitional variants between the two. The epidosite is composed of more than 80 vol% epidote; chlorite and quartz make up the remainder 20 vol% (**Fig. 6.4E,F**); titanite is an accessory. Epidote occurs typically in a granular interlobate texture at a grain size of less than 100 µm. In places, epidote also occurs as fibrous masses indicating ataxial growth. In hand specimen, the fibrous epidote can be seen to form slickenfibres (**Fig. 6.4D**).

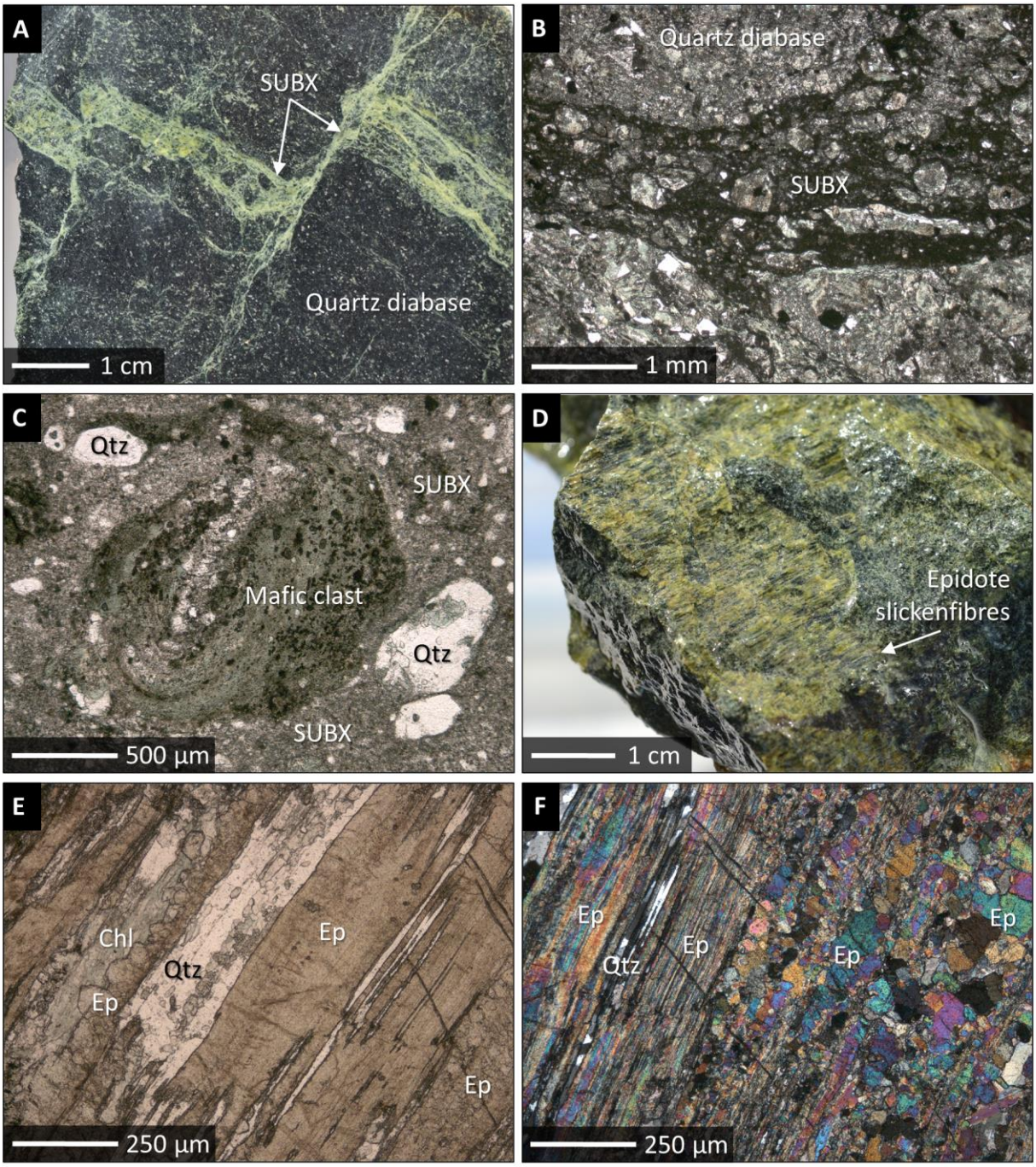

Figure 6.4 Photographs and microphotographs of strongly altered and brecciated samples of the tholeiitic quartz diabase dyke from Mackelcan Township; **A:** polished hand specimen (sample WO-4) collected from the south shore of Wolf Lake, near Cobalt Hill, showing veinlets of altered pseudotachylite (Sudbury Breccia, SUBX) cutting across the quartz diabase; **B:** thin section of the same sample under transmitted light and plane polars, showing a braided vein of pseudotachylitic breccia cutting the mafic dyke and carrying well-rounded lithic and mineral clasts of the host rock; **C:** thin section under transmitted light and plane polars, showing heterolithic matrix-supported Sudbury Breccia developed at the intrusive contact between the mafic dyke and the Lorrain Formation, with clasts of quartzite and a highly contorted chloritic clasts, likely derived from the quartz diabase dyke nearby; **D:** photograph of a hand specimen from the same outcrop (sample WO-5), showing the quartz diabase being pervasively replaced by fibrous epidote; **E:** thin section of the same sample under transmitted light and plane polars, showing the mafic dyke being replaced by granular and fibrous epidote, chlorite, and quartz; **F:** both fibrous and granular epidote under transmitted light and crossed polars. Abbreviations: SUBX = Sudbury Breccia; Qtz = quartz; Ep = epidote; Chl = chlorite.

6.5 Geochemistry

General characteristics

Major- and trace element concentrations of representative grab samples of the quartz diabase from the Wolf Lake area, Mackelcan Township, are presented in **Table 6.1** and reveal a subalkaline, subaluminous and in terms of SiO_2 (48–52 wt%) basic composition. Concentrations of Fe_2O_3 and MgO are with 11–13 wt% and 6–8 wt% relatively uniform, respectively. The corresponding Mg# ranges from 54 to 61. A notable exception is the strongly altered sample WO3 with up to 13 wt% MgO (Mg# 70). The dyke has a narrow range in TiO_2 between 0.6 and 0.8 wt%, and P_2O_5 values close to the detection limit of the EDS-XRF (~0.02 wt%). The LOI, on the other hand, is highly variable, ranging from 1.8 wt% in relatively fresh samples, to 9.7 wt% in sample WO3. The overall primitive character of the dyke is also reflected in its trace element abundances, such as, high Cr (83–228 ppm) and Ni (97–176 ppm), and complementary low Zr (42–63 ppm), Th (1.3–2.3 ppm), Nb (2–8 ppm), and low ΣREE+Y (32–84 ppm). Its CIPW normative mineralogy is 52 vol% plagioclase, 23 vol% hypersthene, 14 vol% diopside, 4 vol% orthoclase, 2 vol% ilmenite and magnetite, and 3 vol% of either olivine or quartz; sample WO3 is corundum normative (9 vol%). The hypothetical density of the fresh diabase, according to its normative mineralogy, is 3.0 g/cm^3.

Igneous rock classification

The quartz diabase's composition conforms to basalt/gabbro according to the TAS diagram (**Fig. 6.5B**). A tholeiitic magmatic affinity is indicated by the AFM plot (**Fig. 6.5C**) for all but one strongly altered sample. Given severe metasomatic changes (**Fig. 6.5A**), classification plots using typically immobile trace elements (Ti, Nb, Y, Zr, Th) are generally preferred (e.g. Pearce 2008). In such diagrams (e.g. **Fig. 6.5D**), the samples plot within the field of subalkaline basalt. Although classification schemes employing Th (e.g. **Fig. 6.5E**; Hastie et al. 2007, not shown) suggest a calc-alkaline magmatic affinity, normalised trace element patterns (**Fig. 6.5F**) are more typical of a tholeiitic basalt. This is evident from a lack of a LILE-HFSE decoupling as expressed in a lack pronounced negative anomalies of Ti, Nb and Ta. Thus, for sake of simplicity, and in order to distinguish it from another quartz diabase dykes in the area (**Chapter 8**), the rock will be referred to as tholeiitic.

Nd-Sr-Pb isotopes

A summary of whole-rock radioisotope data for the quartz diabase is presented in **Table 6.2**. All eight samples have a wide range in $^{143}Nd/^{144}Nd$ corresponding to an εNd_0 from –14.34 in the freshest sample, to –5.23 is the most strongly altered sample. The $^{147}Sm/^{144}Nd$ ratios are between 0.129 and 0.167 and do not correlate with the measured $^{143}Nd/^{144}Nd$ ratios. One-stage Nd model ages (t_{DM}) are between 2583 Ma and 2857 Ma; two-stage model ages are between 2011 Ma and 2224 Ma. The $^{87}Sr/^{86}Sr$ isotope ratio is extremely high (radiogenic) and varies greatly, from 0.745 to 0.791. The calculated $^{87}Rb/^{86}Sr$ ratio ranges from 0.263 to 1.945. The spread in Rb-Sr isotope ratios is, however, without age significance, irrespective of which and how many samples are used for a regression. The $^{206}Pb/^{204}Pb$ ratio ranges from 16.61 to 27.69, $^{207}Pb/^{204}Pb$ from 15.07 to 16.35, and $^{208}Pb/^{204}Pb$ from 34.90 to 40.64. There is a good linear correlation between the different Pb isotope ratios ($R^2 > 0.8$), which is typical of rocks formed in a cogenetic suite, but it is of questionable age significance. Using *IsoplotR* (Vermeesch 2018), an ordinary least square regression in $^{204}Pb/^{206}Pb$ vs. $^{207}Pb/^{206}Pb$ space (n=8) yields an inverse errorchron date of 1721 ± 282 Ma.

Table 6.1 Major element oxide concentrations (wt%) and trace element concentrations (ppm) in tholeiitic quartz diabase, Mackelcan Township

	AK19-34	S2_97*	AK19-35	S2_98*	S2_91*	LAU-9	S2_08*	S2_09*	WO-3	WO-4	WO-5	WO-6	WO-7	WO-8	AK18-3	S2_76*	S2_77*	S2_78*	S2_79*	S2_80*
Lat.	46°52 38	46°52 39	46°52 49	46°52 41	46°52 46	46°52 02	46°52 21	46°52 24	46°50 56	46°50 56	46°50 56	46°50 56	46°50 54	46°50 29	46°48 53	46°48 53	46°49 00	46°48 49	46°49 20	46°49 20
Long.	80°36 46	80°36 45	80°36 19	80°36 43	80°36 32	80°37 19	80°37 02	80°37 01	80°38 32	80°38 32	80°38 32	80°38 32	80°38 37	80°38 54	80°40 24	80°40 24	80°40 20	80°40 26	80°40 04	80°40 04
SiO_2	51.3	50.6	51.7	51.1	49.7	51.3	47.8	50.4	51.5	51.0	50.1	51.0	50.6	50.6	50.8	50.5	50.3	49.3	50.2	50.5
TiO_2	0.81	0.82	0.80	0.79	0.83	0.83	0.60	0.82	0.83	0.78	0.81	0.79	0.80	0.81	0.81	0.80	0.82	0.78	0.84	0.81
Al_2O_3	14.15	14	14.28	13.2	13.7	14.16	12.8	13.7	14.93	14.30	14.30	14.27	13.98	14.15	14.04	13.9	13.9	14	14.2	13.9
Fe_2O_3	11.64	11.9	11.29	12.6	12.2	11.89	11	11.7	12.32	12.51	12.46	12.70	12.17	11.97	11.84	11.8	12	11.6	12.4	12.2
MgO	7.39	7.58	6.72	6.49	7.42	7.20	7.59	6.75	12.74	7.63	7.82	7.36	8.12	7.77	7.77	7.51	7.36	6.67	7.65	7.46
CaO	8.19	10.2	8.25	12.8	10.4	10.55	7.38	9.28	0.96	6.56	8.60	4.77	8.94	8.86	9.08	9.62	9.07	8.65	9.03	8.49
MnO	0.22	0.25	0.18	0.18	0.2	0.21	0.2	0.17	0.12	0.17	0.19	0.13	0.20	0.19	0.30	0.3	0.29	0.2	0.22	0.22
Na_2O	2.31	2.16	3.87	1.01	2.72	1.95	2.36	2.11	1.41	2.56	1.98	2.94	1.64	2.18	2.23	2.21	2.62	3.5	2.4	2.76
K_2O	0.36	0.33	1.28	0.08	0.19	0.20	0.61	0.33	0.30	1.11	0.65	0.91	0.85	0.79	0.61	0.66	0.67	0.42	0.43	0.38
P_2O_5	< 0.02	0.08	< 0.02	0.07	0.08	< 0.02	0.05	0.07	< 0.02	< 0.02	< 0.02	< 0.02	< 0.02	< 0.02	< 0.02	0.06	0.07	0.09	0.08	0.07
LOI	4.49	2.12	1.94	1.76	2.82	2.13	9.68	3.36	5.58	3.57	2.65	5.59	2.47	2.51	2.23	3.24	2.99	4.62	3.09	3.25
Total	100.90	100.04	100.33	100.08	100.26	100.42	100.07	98.69	100.66	100.19	99.54	100.42	99.72	99.86	99.67	100.60	100.09	99.83	100.54	100.04
V	241.2	251	228.8	229	252	258.1	218	254	278.6	250.8	256.1	255.9	189.4	256.0	246.8	240	251	234	257	254
Cr	102	190	225.1	180	150	228	100	83	112.5	161.8	163.1	111	165.8	144.2	155.1	109	84	104	99	101
Ni	118.9	118	97.91	97	113	175.8	122	100	149.2	153.5	160	120.8	151.8	141.6	143.1	106	98	97	107	108
Cu	144.7	138	107.0	63	168	102.2	108	143	18.59	119.9	88.36	113.5	125.3	129.4	140.8	149	135	110	113	110
Rb	10.57	9.4	66.44	1.6	3.6	6.009	36.7	10.4	14.29	111.6	27.57	70.34	37.05	30.61	19.70	21.4	19.4	11.4	13.2	10.7
Sr	281.9	396	103.3	464	278	368.4	314	471	33.04	314.3	316.5	127.7	204.5	278.1	271.9	292	368	177	286	310
Zr	54.51	51	62.60	47.4	51.4	57.05	41.7	59.3	58.81	55.68	55.73	55.6	52.87	52.96	52.94	60.3	61.6	58.8	63.4	55.8
Nb	2.789	2	3.396	2	3	7.658	2	2	2.787	4.134	4.044	2.721	4.707	3.528	4.081	3	3	3	3	3
Ba	102	n.a.	96.19	n.a.	n.a.	62	n.a.	n.a.	20.98	73.73	144.4	99.76	220.4	359.3	258.4	n.a.	n.a.	n.a.	n.a.	n.a.
La	5.257	6.2	8.901	6.1	6.1	5.874	6	7.1	1.823	6.142	5.89	5.467	5.86	5.494	5.579	7.1	7.2	11.9	7.4	7.3
Ce	11.85	13.6	18.21	13.3	13.8	13.08	12.2	15.5	5.146	13.68	13.11	11.91	13.31	12.58	12.98	15	15.3	24.1	15.7	15.4
Pr	1.581	1.78	2.356	1.72	1.83	1.754	1.51	1.99	0.679	1.831	1.753	1.551	1.783	1.735	1.707	2.02	2.09	3.06	2.15	2.09
Nd	6.685	8.3	10.09	8.2	8.5	7.911	6.7	9.1	3.142	8.306	7.99	6.83	7.938	7.911	7.822	8.9	8.8	11.8	9.3	8.8
Sm	1.982	2.3	2.454	2.1	2.2	2.201	1.8	2.5	1.059	2.252	2.213	1.87	2.158	2.149	2.124	2.5	2.5	3	2.7	2.4
Eu	0.711	0.75	0.935	0.93	0.81	0.774	0.64	0.88	0.279	0.754	0.699	0.625	0.691	0.74	0.704	0.84	0.89	1.07	0.86	0.88
Gd	2.467	2.79	3.096	2.7	2.79	2.722	2.15	2.98	1.608	2.713	2.701	2.448	2.61	2.547	2.566	3	2.92	3.34	2.97	2.97
Tb	0.404	0.44	0.473	0.42	0.44	0.43	0.34	0.47	0.302	0.442	0.431	0.419	0.422	0.418	0.408	0.51	0.5	0.55	0.53	0.5
Dy	2.562	2.78	3.070	2.73	2.81	2.836	2.13	3.2	2.09	2.867	2.864	2.774	2.756	2.71	2.739	3.1	3.01	3.35	3.24	3.02
Ho	0.517	0.55	0.596	0.57	0.56	0.557	0.42	0.62	0.444	0.576	0.564	0.565	0.553	0.545	0.537	0.66	0.66	0.73	0.69	0.66
Er	1.504	1.61	1.756	1.69	1.59	1.679	1.32	1.78	1.351	1.682	1.656	1.626	1.604	1.582	1.590	1.71	1.84	1.86	1.8	1.8
Tm	0.213	0.21	0.241	0.23	0.23	0.226	0.18	0.25	0.202	0.238	0.23	0.23	0.208	0.222	0.218	0.26	0.27	0.3	0.26	0.25
Yb	1.403	1.5	1.589	1.6	1.5	1.521	1.2	1.6	1.346	1.554	1.542	1.456	1.49	1.466	1.454	1.6	1.7	1.7	1.7	1.6
Lu	0.218	0.23	0.240	0.23	0.22	0.235	0.2	0.26	0.221	0.242	0.233	0.22	0.23	0.227	0.220	0.26	0.31	0.26	0.27	0.26
Y	14.30	14.8	16.76	15	14	14.85	10.4	15.6	11.83	16.06	15.21	15.17	14.86	14.8	14.53	16.4	16.3	16.9	17	15.7
Hf	1.585	2	1.752	1	2	1.551	1	2	1.633	1.521	1.545	1.498	1.524	1.477	1.477	2	2	2	2	2
Ta	0.197	< 0.5	0.243	< 0.5	< 0.5	0.208	< 0.5	< 0.5	0.19	0.177	0.184	0.188	0.186	0.17	0.224	< 0.5	< 0.5	< 0.5	< 0.5	< 0.5
Pb	5.770	21	4.763	< 5	< 5	9.728	20	5	1.329	3.644	3.483	8.547	3.685	5.248	99.73	175	39	9	14	12
Th	1.324	1.5	2.283	1.4	1.5	1.529	1.3	1.7	1.479	1.627	1.608	1.525	1.558	1.443	1.469	1.8	1.8	1.8	1.8	1.7
U	0.730	0.53	0.668	0.46	0.59	0.527	0.59	0.55	1.146	0.463	0.44	0.535	0.362	0.454	0.522	0.55	0.61	4.2	0.67	0.72

Samples denoted with an asterisk (*) were analysed at the commercial AGAT Laboratories, Toronto (see Whymark 2019 for details); n.a. = not available or not analysed

Table 6.2 Summary of whole-rock Nd-Sr-Pb isotope data for tholeiitic quartz diabase, Mackelcan Township

	$\frac{^{143}Nd}{^{144}Nd}$	±2σ	$\frac{^{147}Sm}{^{144}Nd}$	εNd present	εNd 2220 Ma	1-stage t_{DM}	2-stage t_{DM}	$\frac{^{87}Sr}{^{86}Sr}$	±2σ	$\frac{^{87}Rb}{^{86}Sr}$	$\frac{^{87}Sr}{^{86}Sr_{2220}}$	$\frac{^{208}Pb}{^{204}Pb}$	±2σ	$\frac{^{207}Pb}{^{204}Pb}$	±2σ	$\frac{^{206}Pb}{^{204}Pb}$	±2σ
LAU-9	0.512202	12	0.164	–8.50	+0.91	2583 Ma	2011 Ma	0.774637	15	0.263	0.766200	36.8718	24	15.5838	8	17.7143	8
WO-3	0.512370	14	0.129	–5.23	–7.24	(12000 Ma)	(2687 Ma)	0.790641	20	1.389	0.746120	40.6402	32	16.3512	10	27.6867	18
WO-4	0.512191	16	0.131	–8.72	+0.68	2620 Ma	2150 Ma	0.769090	14	1.174	0.731450	36.9408	29	15.3994	10	17.8616	9
WO-5	0.512187	12	0.129	–8.81	–0.42	2857 Ma	2224 Ma	0.745824	15	0.446	0.731530	36.8054	25	15.3755	8	17.6779	8
WO-6	0.512164	9	0.130	–9.24	–0.30	2807 Ma	2216 Ma	0.788928	15	1.707	0.734210	34.8991	24	15.0726	8	15.6141	7
WO-7	0.512183	11	0.167	–8.87	+0.41	2670 Ma	2168 Ma	0.744625	13	0.699	0.722220	36.5427	22	15.3807	8	17.7606	8
WO-8	0.512197	13	0.164	–8.61	+0.70	2621 Ma	2148 Ma	0.746419	13	0.508	0.730140	35.7711	29	15.2593	10	16.7232	8
AK19-35	0.511903	13	0.147	–14.34	–0.13	2611 Ma	2205 Ma	0.751134	12	1.945	0.688790	37.1360	30	15.6176	10	18.3853	9
AK19-34	0.512210	11	0.179	–8.35	–3.33	3942 Ma	2762 Ma	0.742474	14	0.311	0.732500	36.1961	80	15.4301	10	17.7009	8

$^{147}Sm/^{144}Nd$ and $^{87}Rb/^{86}Sr$ ratios were calculated using measured Sm, Nd, Rb and Sr concentrations, which are given in Table 6.1;
2σ uncertainties of $^{147}Sm/^{144}Nd$ and $^{87}Rb/^{86}Sr$ are < 3% based on the propagated analytical error of Sm, Nd, Rb and Sr concentration data;
$^{143}Nd/^{144}Nd$ ratios are normalised to $^{146}Nd/^{144}Nd = 0.72190$;
2σ uncertainties of $^{143}Nd/^{144}Nd$ are < 0.004% based on the long-term in-house reproducibility of BHVO-2;
2σ uncertainties of $^{87}Sr/^{86}Sr$ are < 0.007% based on the long-term in-house reproducibility of BHVO-2;
2σ uncertainties of $^{208}Pb/^{204}Pb$, $^{207}Pb/^{204}Pb$ and $^{206}Pb/^{204}Pb$ are < 0.18%, < 0.09% and < 0.5%, respectively, based on the long-term in-house reproducibility of BHVO-2;
For sake of readability, all listed 2σ absolute errors only refer to the last significant decimal digits of the measured isotope ratios;
εNd values were calculated relative to CHUR with $^{147}Sm/^{144}Nd = 0.1967$ and $^{143}Nd/^{144}Nd = 0.512638$;
One-stage Nd model ages (t_{DM}) were calculated according to DePaolo (1981a,b);
Two-stage Nd model ages (t_{DM}) were calculated according to Liew & Hofmann (1988) using a $^{147}Sm/^{144}Nd = 0.106$ for the contaminant, which is the regional average crustal composition as approximated by the composition of the Sudbury Igneous Complex (e.g. Prevec et al. 2000)

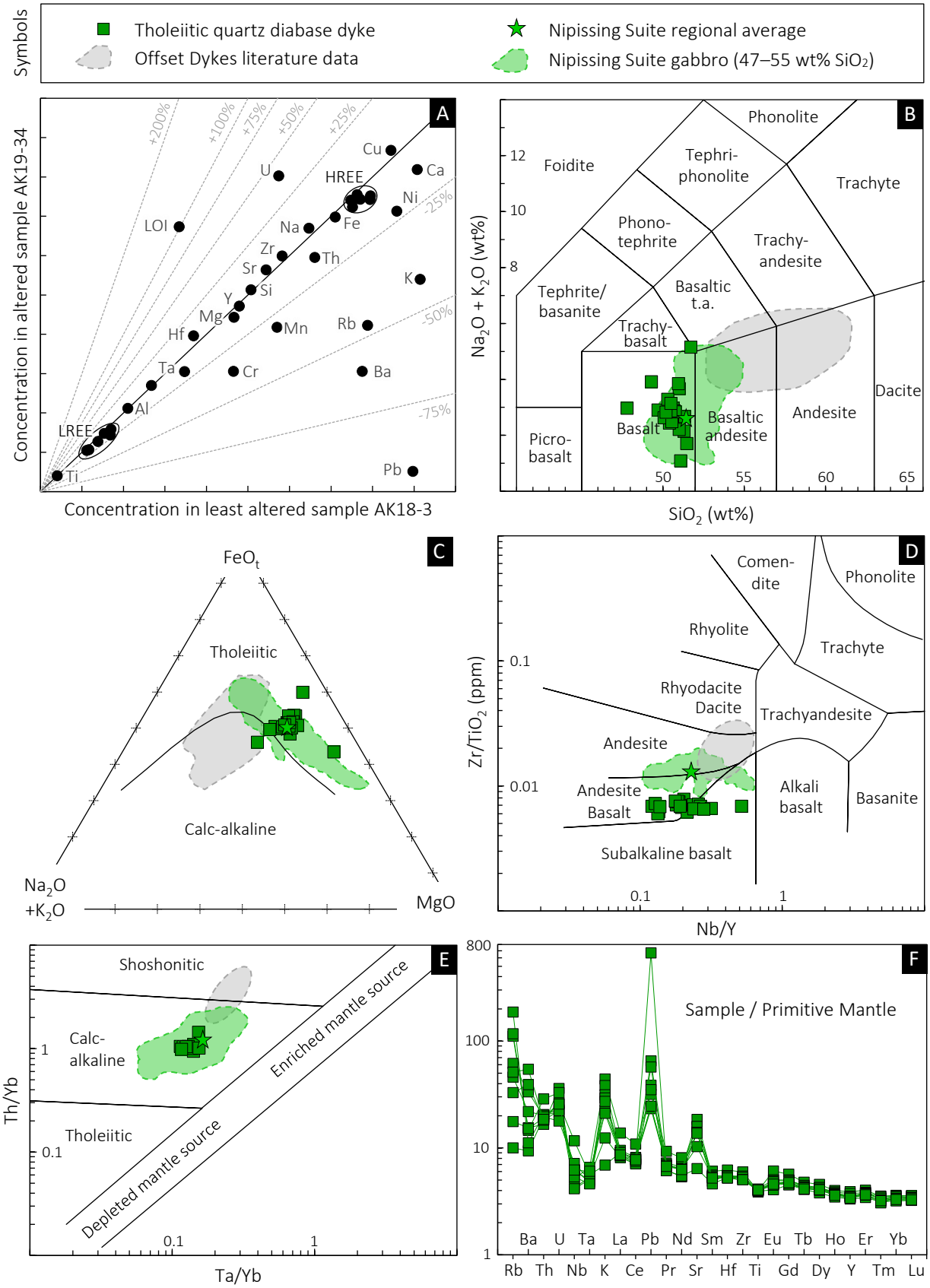

Figure 6.5 A selection of plots used to illustrate the effects of metasomatism on, and the geochemical classification and magmatic affinity of, the tholeiitic quartz diabase from Mackelcan Township; **A:** isocon diagram after Grant (1986); **B:** TAS classification after Le Bas et al. (1986); **C:** AFM plot after Irvine & Baragar (1971); **D:** discrimination plot after Winchester & Floyd (1977); **E:** discrimination plot after Pearce (1983); **F:** spidergram with normalisation values after McDonough & Sun (1995); Offset Dyke data (excluding outliers) are mainly from Lightfoot et al. (1997c); data for the Nipissing Suite are from Lightfoot & Naldrett (1996b) and Jobin-Bevans (2016); propagated 2σ error bars are typically smaller than the symbol size.

6.6 Interpretation

Assessment of post-depositional alteration

The macro- and microscopic appearance of the quartz diabase has already revealed hydrothermal alteration to some, in places significant, extent, and regional retrograde metamorphic overprint at greenschist-facies conditions. The latter is evident from the pseudomorphic replacement of pyroxene by actinolite and chlorite, and plagioclase by epidote and albite. While this metamorphism is expected to have occurred under isochemical conditions (except for H_2O), there is also evidence of metasomatism in form a pervasive epidotisation and chloritisation, which is expected to have affected the chemical composition of the rock to some degree. Furthermore, sedimentary rocks in the vicinity of the dyke were affected by Na-metasomatism in form of a pervasive albitisation (see also Gates 1991; Schandl 2002, 2004). Therefore, it is necessary to quantify these potential metasomatic changes before interpreting the lithogeochemical data in a petrogenetic context.

The most straightforward approach to metasomatism is a simple chemical comparison of sample pairs, also known as the isocon method (Grant 1986). Contrasting the measured element concentrations of one of the freshest samples (AK18-3) with one of the most strongly altered but nearby sample (AK19-34) reveals that the concentrations of most elements have remained constant within the analytical uncertainty. Elements that are traditionally considered least mobile, such as Ti, Zr, Al, Y, are well correlated between the two samples ($R^2 > 0.99$) and define an isocon (a straight line through the origin) with a slope of one (**Fig. 6.5A**). Most elements plot on, or close to, this isocon, which implies they have not been significantly mobilised either. The concentrations of Si, Ti, Al, Fe, Mg, Na, REE+Y, Zr, Hf, Nb, Ta and Sr are therefore considered representative of the magmatic protolith. Some elements, however, do show mobility. The isocon method implies that K was effectively leached form the rock (–41%) and lost to the fluid. The same holds true for Rb (–46%), Ba (–61%), Pb (–94%), Ca (–13%), Mn (–27%), Cr (–34%) and Ni (–17%). Uranium, in contrast, was apparently added to the system (+40%). While the loss of K, Rb, Ba, Pb and Ca is easily explained by the secondary breakdown of feldspar, and Mn, Ni and Cr by the replacement of pyroxene by amphibole and/or chlorite, the apparent mobility of U is somewhat conspicuous. Overall little element mobility (except for U, K, Ca, Rb, Ba, Pb, Sr) is also supported by smooth and uniform trace element patterns (**Fig. 6.5F**), by optimal alteration indices (Nesbitt & Young 1982; Large et al. 2001; not shown), and constant inter-element ratios. Consequently, the geochemical data obtained on the quartz diabase dyke (**Tab. 6.1**) should be representative of the protolith.

In terms of isotopic disturbance, only the measured $^{87}Sr/^{86}Sr$ ratio shows a strongly positive correlation ($R^2 = 0.67$) with the volatile content of the sample (LOI; **Fig. 6.6**). Substantiated by the established Rb mobility (**Fig. 6.5A**) and the highly variable Rb/Sr ratio, it is clear that the Rb-Sr isotope system must have been open at some time in the history. It is, however, unlikely that the high $^{87}Sr/^{86}Sr$ ratio of almost (sic!) 0.79 was simply due to a metasomatic gain of Sr, because most hydrothermal fluids, even those of crustal origin, do not exceed a $^{87}Sr/^{86}Sr$ ratio of ~0.71 (Rollinson 1993). Such an extremely high $^{87}Sr/^{86}Sr$ ratio requires a significant and non-recent addition of Rb to the system (i.e., alkali metasomatism), or loss of Sr. The other isotope ratios, $^{143}Nd/^{144}Nd$, $^{207}Pb/^{204}Pb$, $^{208}Pb/^{204}Pb$, show no significant correlation with the rock's volatile content. Instead, they show and increase in random scatter with increasing hydration. Samples with a volatile content of < 3 wt% form tight clusters and should be most representative of the magmatic protolith.

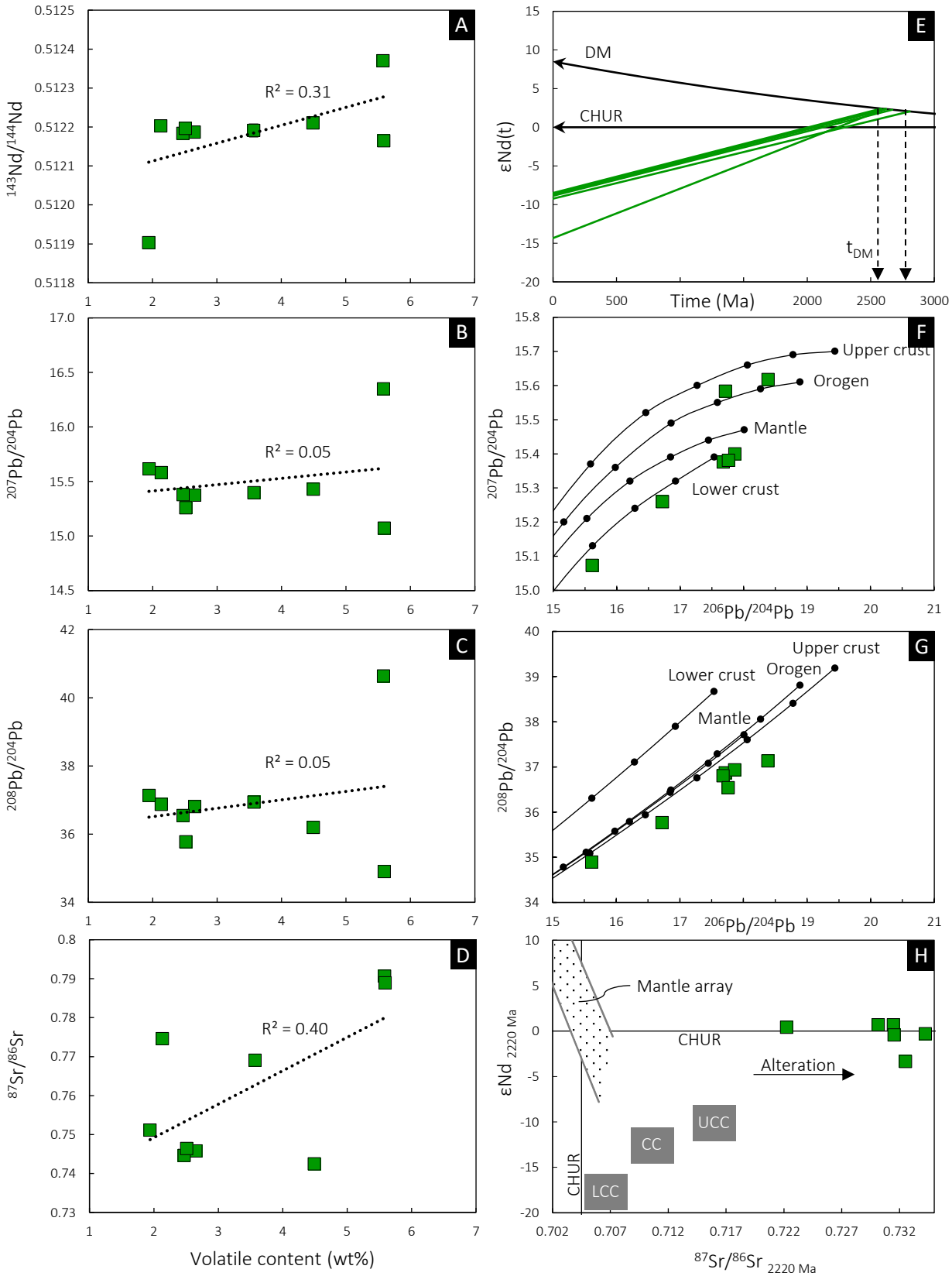

Figure 6.6 Bivariate plots of whole-rock Nd, Pb and Sr isotope ratios for tholeiitic quartz diabase from the Wolf Lake area, Mackelcan Township; **A–D:** measured isotope ratios vs. whole-rock volatile content, illustrating the effects of fluid-rock interaction on the isotopic composition; **E:** neodymium isotope evolution diagram with εNd displayed as a function of time; depleted mantle curve (DM) after DePaolo (1981a,b); **F–G:** lead isotope ratio plots with growth curves after Zartman & Doe (1981) for different reservoirs, with 400 Ma-increments until present; **H:** plot of the initial εNd vs. the initial $^{87}Sr/^{86}Sr$; error bars represent 2σ internal errors but are smaller than the symbol size in most of the panels.

Relationship to the Sudbury impact event

When the dyke was discovered in 2018, it was initially assumed to be another Offset Dyke of the Sudbury Igneous Complex. This hypothesis was based on (i) the remarkable continuity of the dyke along strike (almost 10 km); (ii) its orientation approximately radial to the Main Mass of the Sudbury Igneous Complex; (iii) its close spatial relationship to mega-breccias within the East Range Breccia Belt; (iv) its normative and modal quartz content. However, the above observations clearly rule out any genetic relationship with the Sudbury impact event for the following reasons. Firstly, it has been shown that the tholeiitic quartz diabase dyke must be older than the impact event because it is crosscut by pseudotachylitic veins (**Fig. 6.4A,B**), and because it is found as highly altered clasts in Sudbury Breccia. Secondly, the geochemistry of the dyke does not remotely resemble the composition of the Offset Dykes, nor any other type of impact melt rock found within the Sudbury Structure. This is evident from the geochemical classification diagrams (**Fig. 6.5**), and from a direct comparison of trace element patterns (**Fig. 6.7**). With 40–60 ppm Zr, the dyke differs significantly from the impact melt rocks of Sudbury, which have invariably higher Zr (80–300 ppm); the Nb-Ta-Ti anomalies are less pronounced in the dyke compared to the typical calc-alkaline impact melt rock; the REE a depleted in the dyke relative to the impact melt rocks, and their normalised abundances have a completely different slope. With < 52 wt% SiO_2, the dyke is also more basic than any impact-generated lithology from the Sudbury Igneous Complex, including norite and quartz gabbro, which are the most primitive units of the Main Mass (e.g. Lightfoot 2016, p. 206, 214). Furthermore, the Nd isotope features do not match those of the Offset Dykes, since the diabase dyke has a much higher Sm/Nd ratio and a much lower εNd. As discussed before, the impact melt rocks of Sudbury have a narrow range in $^{147}Sm/^{144}Nd$ of ~0.11, whereas the mafic dyke in question has a $^{147}Sm/^{144}Nd$ of 0.13–0.18. Accordingly, the Nd model age of the dyke differs significantly from that of the Sudbury Igneous Complex. These differences are not simply explained by processes such as post-magmatic alteration or contamination, and so they provide evidence that the impact melt rocks and the mafic dyke cannot share a common source. It follows that the dyke must be the manifestation of a magmatic event older than the 1.85 Ga Sudbury impact, but younger than the ~2.31 Ga upper Huronian Supergroup into which it was emplaced.

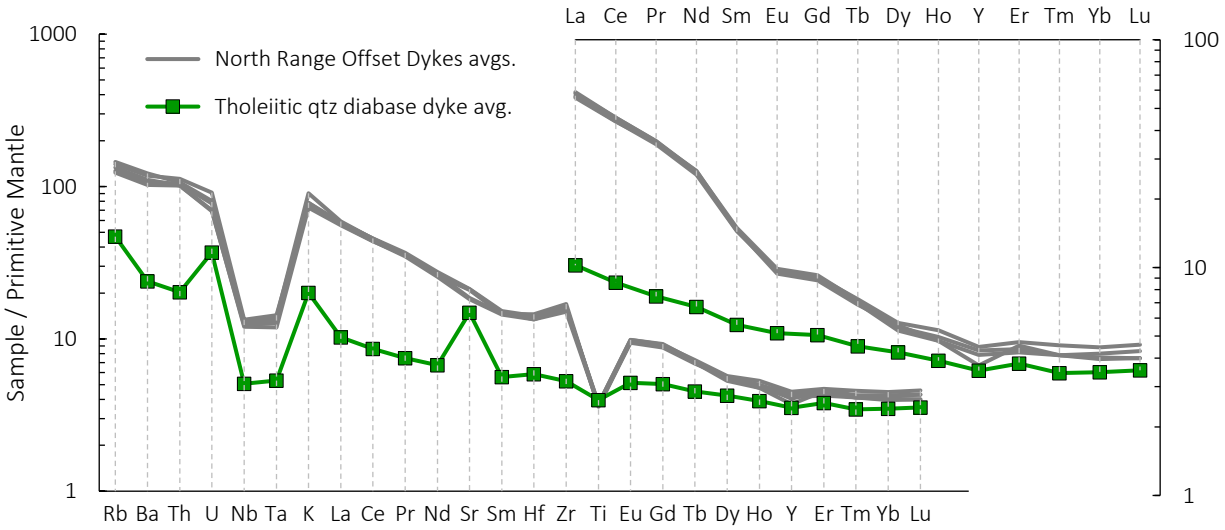

Figure 6.7 Primitive mantle-normalised trace element diagrams for the tholeiitic quartz diabase dyke from Mackelcan Township and, for comparison, selected Offset Dykes of the Sudbury Igneous Complex (Parkin, Foy, Ministic); normalisation values are from Sun & McDonough (1989); literature data are from Lightfoot et al. (1997c).

Relationship to the Nipissing Suite

Cross-cutting field relations constrain the intrusion age of the dyke between 2310 Ma and 1850 Ma. This already rules out the possibility that the dyke is genetically related to the 0.6 Ga Grenville Dyke Swarm, or any other mafic dyke swarm younger than the impact event. It also eliminates the possibility that the tholeiitic dyke is part of the ~2480 Ma Matachewan Dyke Swarm (e.g. Heaman 1997). Although the Matachewan Dykes are, like the diabase of this study, quartz tholeiitic, they only occur at the base of the Huronian Supergroup, and never within the Cobalt Group (upper Huronian Supergroup). In addition, the Matachewan Dykes have a completely different orientation (N-NW) than the tholeiitic dyke from Mackelcan Township (NE). It is also clear that the tholeiitic quartz diabase dyke cannot be one of the so-called yet ill-defined "trap dykes" (e.g. Dressler 1984; Grant & Bite 1984). These trap dykes are so far only known from the immediate Sudbury region, where they strike very consistently E-W, and have recently been dated to 1700 Ma (Bleeker et al. 2015), i.e., they are younger than the Sudbury impact event. All this leaves only two options. Either the new dyke is related to the regional 2220 Ma Nipissing Suite, or it is the manifestation of a previously unrecognised magmatic event. Unequivocal evidence would require an absolute radiometric age, but the rock is very poor in Zr (≤ 60 ppm) and thus expected to be poor in zircon and baddeleyite, which compromises its applicability for U-Pb mineral dating.

In order to test whether the dyke is related to the Nipissing Suite, its geochemical composition has been compared to an extensive set of lithogeochemical data (Lightfoot & Naldrett 1996b; Jobin-Bevans 2016; Davey et al. 2019; Hagen 2020). In the classification plots of **Figure 6.5** it was already shown that the dyke lies well within the compositional field defined by the Nipissing Suite, a genetic link to which is also indicated in the scatter plots of **Figure 6.8**. There, different element concentrations are contrasted against the MgO concentration as an index of the degree of magmatic differentiation. All these plots reveal geochemical trends interpreted as magmatic differentiation trends emanating from one homogeneous parental magma. Analyses of the tholeiitic quartz diabase dyke lie exactly on the magmatic differentiation trend(s) defined by the Nipissing Suite, thereby providing first evidence of a genetic relationship.

The vast majority of intrusions assigned to the Nipissing Suite occur in form of sills concordant with the sedimentary bedding, and typically emplaced along the contact between rocks of contrasting competency such as, between the Gowganda Formation and the Lorrain Formation. Dykes, on the other hand, are very rare for the Nipissing Suite. The few examples of Nipissing Suite dykes that do exist have previously been interpreted as magmatic feeders of larger sills (e.g. Lightfoot et al. 1993; Lightfoot & Naldrett 1996a) and they tend to form a continuum with the NE-striking Senneterre Dyke Swarm in Quebec (e.g. Davey et al. 2019). Lightfoot & Naldrett (1996a) have shown that the dykes in the Nipissing Suite possess a very uniform composition that matches the composition of the least evolved rocks of the suite, the chilled margins. Dykes should therefore represent the best approximation of the parental, unfractionated magma composition. If the studied tholeiitic dyke was such a feeder dyke too, it would be expected to have the same geochemical features as the parental magma of the Nipissing Suite. However, the plots of **Figure 6.8** indicate that this was not the case. Instead, the composition of the dyke is systematically displaced towards a higher degree of magmatic differentiation. For instance, the dyke is lower in MgO, CaO, and Ni than the typical feeder or chilled margin, but it is richer in incompatible lithophile elements (e.g. Na, Zr, Th). As such, the dyke is more like the average quartz diabase and the orthopyroxene gabbro of the Nipissing Suite, suggesting that minor fractional crystallisation presumably occurred.

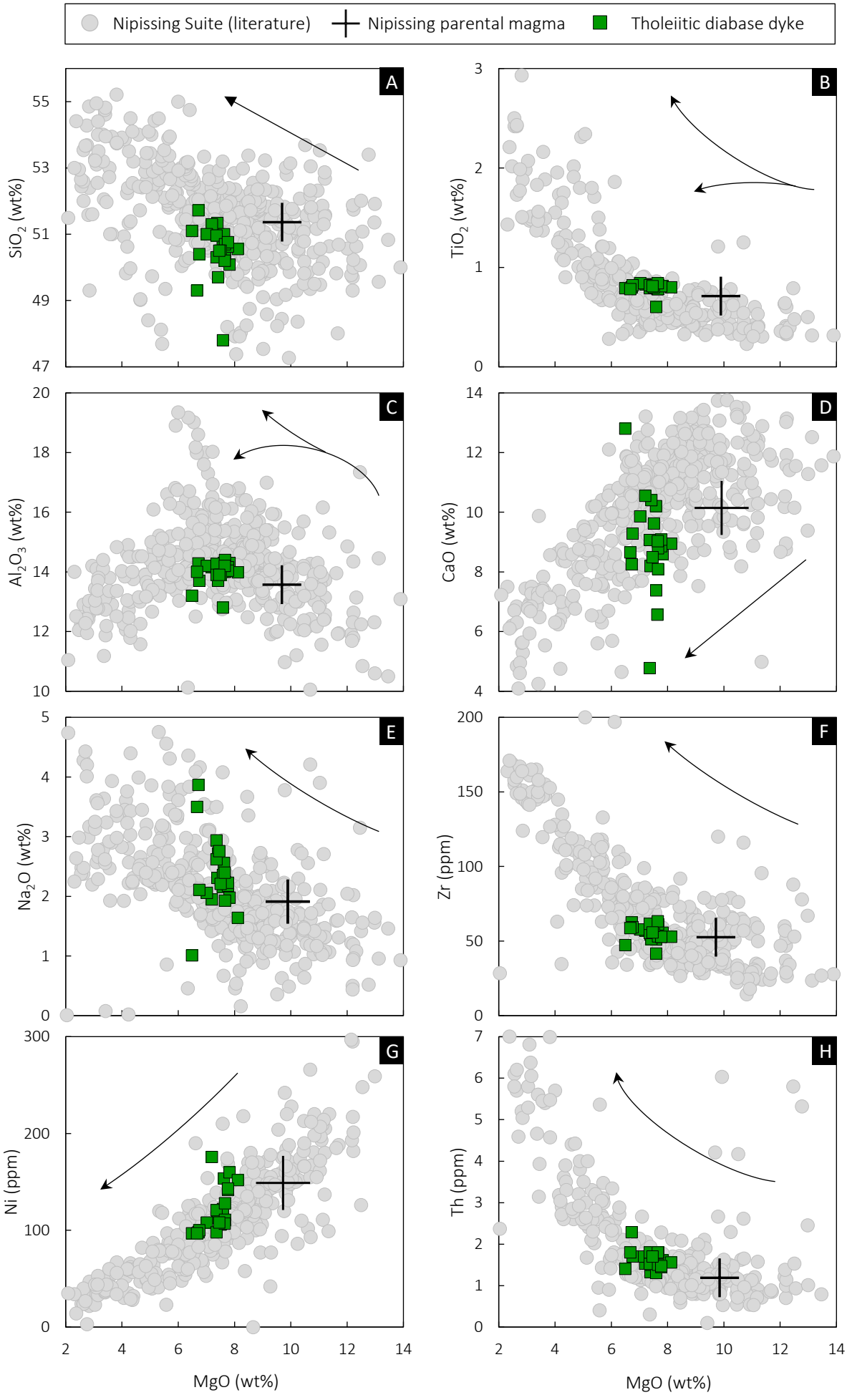
Nipissing Suite (literature)
Nipissing parental magma
Tholeiitic diabase dyke
A
B
C
D
E
F
G
H
SiO2 (wt%)
TiO2 (wt%)
Al2O3 (wt%)
CaO (wt%)
Na2O (wt%)
Zr (ppm)
Ni (ppm)
Th (ppm)
MgO (wt%)
MgO (wt%)

↑ **Figure 6.8** Scatter plots used to highlight chemical variations across the Nipissing Suite, with MgO as differentiation index; also shown are approximate vectors for fractional crystallisation and crustal assimilation, and the average composition of the parental magma of the Nipissing Suite; literature data are from Lightfoot & Naldrett (1996b) and Jobin-Bevans (2016) and were filtered for 47–55 wt% SiO_2.

The similarity between the tholeiitic quartz diabase dyke and the average Nipissing Suite gabbro is also demonstrated in **Figure 6.9**. In this graph, the average trace element pattern of the tholeiitic quartz diabase dyke is plotted together with the regional median and average composition of gabbroic rocks belonging to the Nipissing Suite. The patterns reveal to be almost indistinguishable, and they overlap with respect to several geochemical key parameters (e.g. La/Sm_N, La/Yb_N, Th/U_N, Th/Nb_N, Ti/Ti*). Exceptions are Rb, Ba and Sr, which have arguably been mobilised during regional metamorphism and alteration and are not representative of the protolith's composition. In summary, the almost identical trace element patterns provide strong support that the tholeiitic diabase dyke is a previously unrecognised member of the Nipissing magmatic suite.

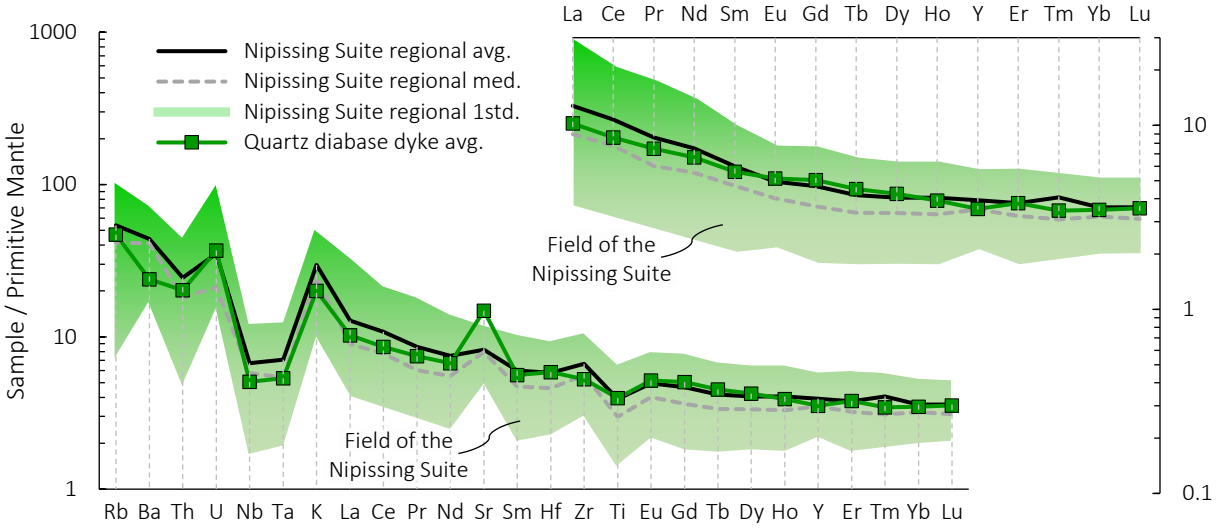

Figure 6.9 Primitive mantle-normalised trace element diagrams for the tholeiitic quartz diabase dyke from Mackelcan Township in comparison to gabbroic rocks (47–55 wt% SiO_2) of the Nipissing Suite; normalisation values are from Sun & McDonough (1989); data for the Nipissing Suite are from Lightfoot & Naldrett (1996b), Jobin-Bevans (2016), Hagen (2020) and this study (Appendix_1); regional average, median and standard deviation were calculated based on more than 500 analyses excluding altered and mineralised outliers with < 47 wt% SiO_2 as well as differentiated and contaminated outliers with > 55 wt% SiO_2.

A genetic link between the tholeiitic quartz diabase dyke and the Nipissing Suite is additionally supported by the same whole-rock Sm-Nd isotope systematics. For example, the dyke has a present-day εNd value between –9 and –14. These values overlap, within the analytical uncertainty (εNd ± 0.5), with the εNd previously reported for the Nipissing Suite (cf. Lightfoot & Naldrett 1996a; Davey et al. 2019). The dyke is further characterised by a very high $^{147}Sm/^{144}Nd$ ratio > 0.13, which is again similar to the $^{147}Sm/^{144}Nd$ ratio determined for the Nipissing Suite, and which is fundamentally higher than reported for any other known igneous rock in the wider region. Accordingly, the tholeiitic dyke and the Nipissing Suite have one-stage Nd model ages considerably older (2.5–3.5 Ga) than their (assumed) intrusion age of 2.22 Ga. These model ages are, obviously, without geological significance, but they indicate that the tholeiitic dyke and the magma of the Nipissing Suite evolved at the same time integrated Sm/Nd ratio. Interestingly, the two-stage Nd model age for the tholeiitic diabase dyke (**Tab. 6.2**) is between 2.2 and 2.4 Ga. These values correspond, within the analytical uncertainty (± 50 Ma), to the absolute emplacement and crystallisation age of the 2.22 Ga Nipissing Suite, thus providing further proof for a genetic relationship.

Although the above presented geochemical and isotopic data leave very little doubt about a genetic relationship between the tholeiitic diabase dyke and the Nipissing Suite, one feature is not entirely consistent with the available reference data for the Nipissing Suite: With an initial εNd_{2220} between –1 to +3, the dyke has a more depleted signature than the rest of the Nipissing Suite (**Fig. 6.10A**). Theoretically, this discrepancy could be explained by the dyke having experienced lesser degrees of crustal contamination compared to the more voluminous Nipissing Suite intrusions (e.g. the Triangle Mountain Sill), therefore preserving a more depleted mantle signature (i.e., superchondritic εNd_i). This theory is predicated on the fact that narrow mafic dykes, where laminar flow prevails, are not capable of assimilating large quantities of country rock (e.g. Campbell 1985; Huppert & Sparks 1985), whereas the latent heat and the continuous replenishment of larger magmatic bodies enables them to interact with large volumes of country rock (e.g. DePaolo 1981c; Lightfoot & Naldrett 1989). Wether crustal contamination was responsible for the apparent isotopic variations across the Nipissing Suite can be easily tested by contrasting the εNd_{2220} against geochemical proxies of crustal assimilation (e.g. SiO_2, Ce/Pb, Th/Yb, or Th/Nb). As can be seen in **Figure 6.10B**, the available data for the Nipissing Suite exhibit two opposing trends in terms of εNd_{2220} vs. Th/Yb. Some samples show an inverse correlation between εNd_{2220} and Th/Yb, which is indeed consistent with those samples having experienced a higher degree of crustal input. However, most other samples show a wide range in εNd_{2220} while maintaining a uniform and relatively low Th/Yb ratio. Maybe this reflects variations in the composition of the mantle source, for which Lightfoot et al. (1993) suggested it contained minor amounts of recycled crustal material. Alternatively, it could be explained by interaction with the subcontinental lithospheric mantle. Be this as it may, the isotopic data point to a previously unrecognised isotopic heterogeneity across the Nipissing Suite. A more comprehensive dataset, ideally supported by high-precision U-Pb ages, is nonetheless required to confirm this hypothesis. If correct, variations in mantle source and/or the existence of separate magmatic pulses could explain why some of the Nipissing Suite members are strongly mineralised with respect to Cu-Ni-PGE (e.g. Shakespeare) whereas others are barren.

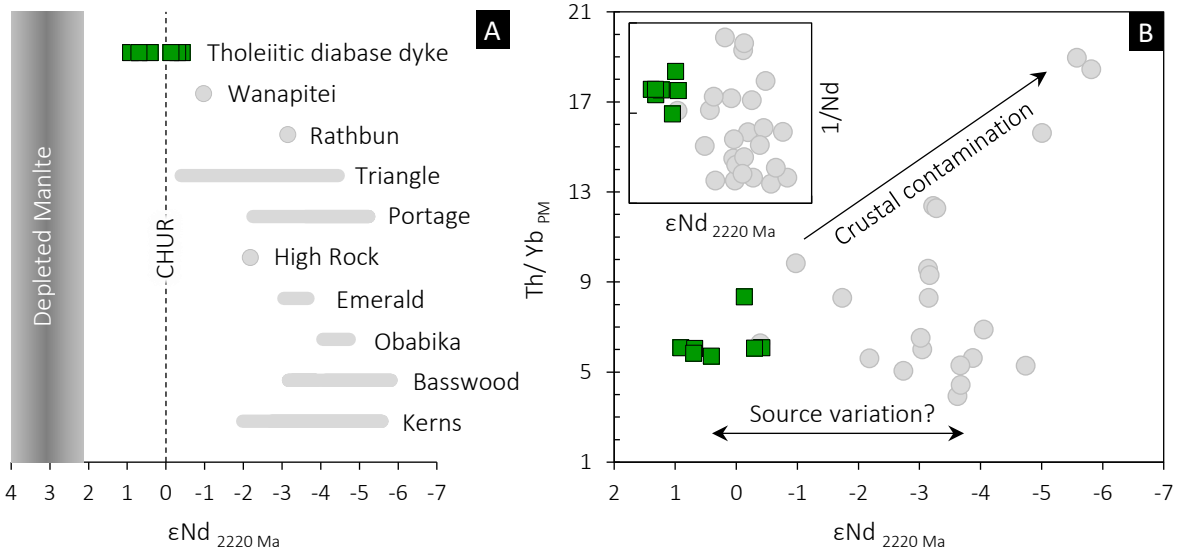

Figure 6.10 Neodymium isotope ratios of the tholeiitic quartz diabase dyke from Mackelcan Township in comparison to other members of the Nipissing Suite; **A:** variations in the initial εNd value for different members of the Nipissing Suite and the tholeiitic quartz diabase dyke; depleted mantle calculated according to DePaolo (1981a,b); **B:** the initial εNd value vs. the primitive mantle-normalised Th/Yb ratio; literature data are recalculated after Lightfoot & Naldrett (1996a,b) and Davey et al. (2019); data for the Wanapitei Intrusion and for xenoliths within the Rathbun Offset Dyke are from this study (Appendix_1; Appendix_2).

Relationship to epigenetic Cu-Co-Au mineralisation

The intention of this subchapter is to explore the close spatial, and thus perhaps even genetic, relationship between the tholeiitic diabase dyke (herein identified as a member of the Nipissing Suite) and the epigenetic Cu-Co-Au mineralisation of Cobalt Hill and Wolf Lake. As already noted by Schandl (2002, 2004), the local presence of pentlandite, millerite, gersdorffite and especially Cr-V-mica (fuchsite) in those occurrences, corroborated by elevated whole-rock concentrations of Cr, Co, and Ni (e.g. Whymark 2020), indicates that the mineralising fluid was derived from, or at least interacted with, mafic-ultramafic rocks. Because of the overall low capacity of most hydrothermal fluids to carry significant amounts of Cr, Ni or V (e.g. Humphris & Thompson 1978; Shervais 1982), together with their low background concentrations in the sedimentary rocks of the Lorrain Formation (< 15 ppm; e.g. Jobin-Bevans 2016), an extraformational, but still relatively proximal, metal source is likely required to explain the local enrichment of Cr, Ni, and V (and by association, of Cu, Au, and PGE) in these hydrothermal breccias. So far, studies have not been able to identify such mafic-ultramafic source, which led Schandl (2002, 2004) to speculate about the existence of a deep-seated intrusion having provided the required heat, fluid, and metals. The discovery of a mafic lithology at Wolf Lake now invites to reassess this hypothesis.

In **Chapter 6.3** it has been shown that the quartz diabase was pervasively sheared and hydrothermally altered to almost monomineralic domains of epidote, chlorite, and quartz (**Fig. 6.4**), and this especially in vicinity to the Cobalt Hill and Wolf Lake occurrences, suggesting that alteration was most intense in these areas. Of note, the alteration of the diabase seems to have led to a systematic depletion of Cu (and other metals) relative to the fresh portions of the same dyke. For example, the altered sample WO3 contains 19 ppm Cu, whereas the fresh sample AK19-35 contains 107 ppm Cu. This translates to a relative loss of 83%. The most likely explanation for the very low Cu concentration is that Cu was initially hosted by magmatic sulphide but was subsequently lost to whatever fluid had interacted with the rock. The isocon method (Grant 1986) reveals that mobility of Cu was also accompanied by a loss of Pb, Rb, Ba, Sr, Ca, K and Eu (elements that are typically retained by feldspar), and by a significant loss of Cr and Mn (typically hosted by pyroxene) (**Fig. 6.11A,B**). Interestingly, the method also reveals a fractionation of LREE relative to the HREE, which is indicative of a high fluid:rock ratio (e.g. Campbell et al. 1984; MacLean 1988; Bau 1991; Schandl & Gorton 1991; Valsami & Cann 1992; Lahaye et al. 1995). From the apparent gain of U (up to +200%) it may be inferred that the fluid was relatively oxidised (e.g. Langmuir 1978).

The main implication from this is that metasomatic leaching of the diabase dyke could have provided at least some of the base metals for the Cobalt Hill and Wolf Lake occurrences. A simple mass balance calculation demonstrates that the dyke, although being of small volume, contains (and thus, can liberate) a significant amount of base metal. For example, 80%-leaching of a 10 x 10 x 10 m-large segment of the diabase dyke (density 2.9 g/cm^3) containing initially 150 ppm Cu (a Nipissing Suite-typical value) would liberate 350 kg of Cu. In case of less effective leaching (e.g. 15%), a 1,000 x 100 x 10 m-large dyke segment would still provide 65 tons of Cu.

If there was a genetic link between dyke and mineralisation, as indirectly implied by this study, this could help guiding future exploration activities in the area. Based on these new findings, it is recommended that further exploration should focus primarily on the immediate vicinity of the diabase dyke and its extrapolated trend to the northeast and southwest, as this is where the highest mineralisation potential would be expected. Fuchsite, due to its prominent appearance, could

serve as a vector toward mineralisation, as, besides the local enrichment of Cr, also increased concentrations of Cu, Ni, and Co (and possibly PGE, Au, Ag) are to be expected. These observations also have wider implications for base metal prospectivity as it is conceivable that epigenetic mineralisation similar to that of Cobalt Hill and Wolf Lake could exist in similar setting elsewhere in the Huronian Basin. However, it has yet to be shown what exactly was responsible for the intense alteration, and questions about the nature and source of the fluids involved remain unanswered. It also remains to be shown whether the alteration occurred before, synchronous, or after the impact event, and what the nature of the relationship between the hydrothermal breccias and the impact-generated breccias really was.

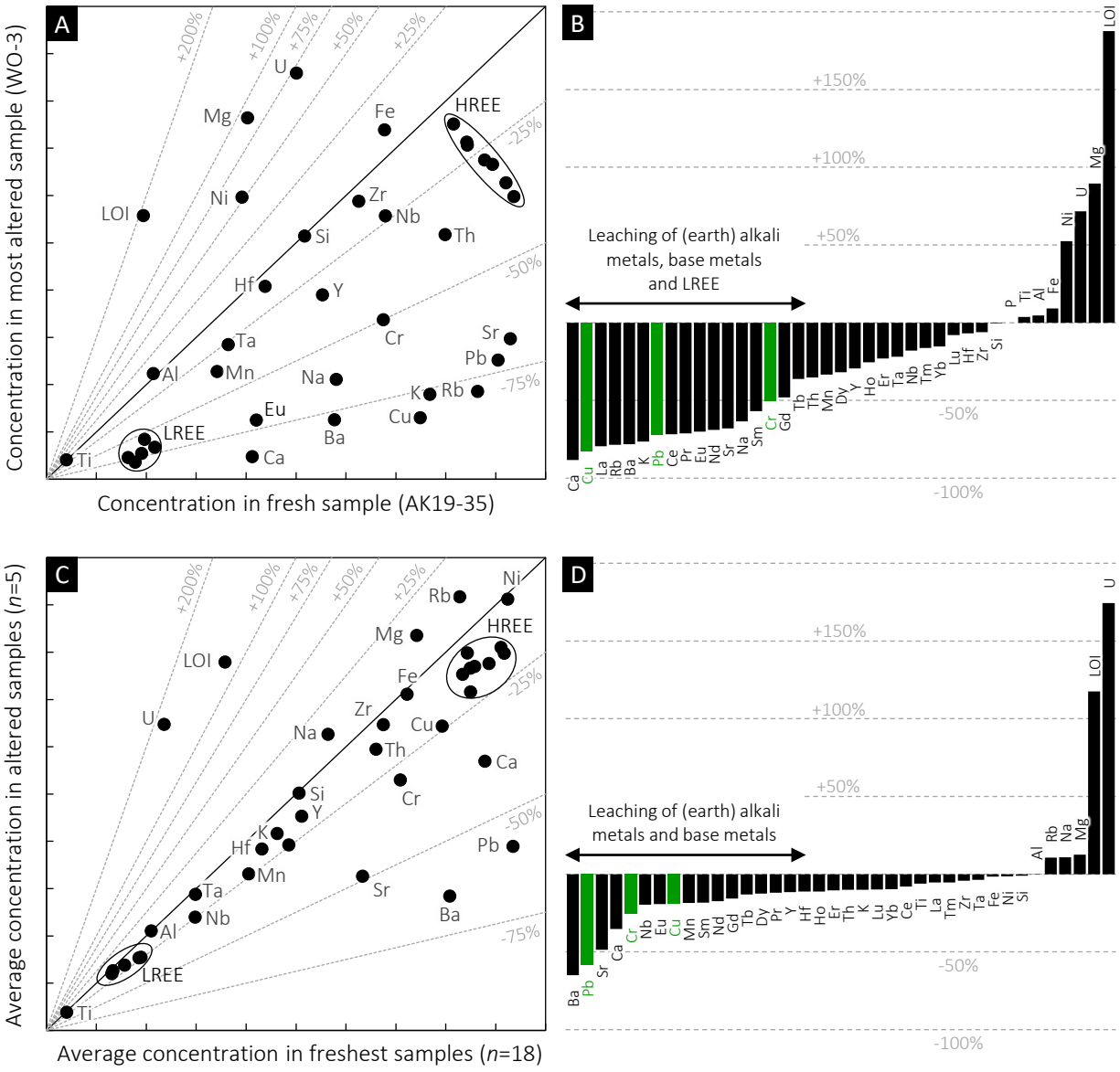

Figure 6.11 Effects of metasomatism on the whole-rock geochemical composition of the tholeiitic quartz diabase dyke from Wolf Lake; **A:** diagram contrasting the measured composition of the chloritised sample WO3 with that of the freshest sample AK19-35; the isocon was constructed assuming constant concentrations Ti, Al, Si and Zr; **B:** element gains and losses (in %) calculated relative to the isocon; **C:** diagram contrasting the average composition of the altered samples with the average composition of the freshest samples; the isocon also assumes immobility of Ti, Al, Si and Zr; **D:** calculated gains and losses (in %) relative to the isocon; note that all plots imply a fluid-induced loss of Cu, Cr and Pb.

Alkaline Diabase

7.1 Summary

Low-grade metamorphic ultrabasic dykes occur both in outcrop (Mackelcan Township) and in a deep drill core (Sheppard Township), above and into Temagami Anomaly, respectively. The dykes were emplaced into sedimentary rocks of the Cobalt Group and show field evidence of subsequent reworking into impact-generated megabreccias (Sudbury Breccia). Consequently, the dyke's emplacement must have occurred prior to the 1.85 Ga Sudbury impact event.

Geochemically, the dykes are ultrabasic, alkaline, Ol- and Ne-normative. They show a pronounced enrichment in HFSE, particularly in P_2O_5 (0.2–0.7 wt%), TiO_2 (2.0–3.5 wt%), Nb (20–50 ppm), and Zr (100–240 ppm). Their trace element signature is almost identical to that of modern ocean island basalts (OIB), but different from any other igneous rock known in the wider region. The dykes show, furthermore, no evidence of crustal contamination (Th/Nb ≤ 0.1). A strong depletion in HREE (Tb/Yb_N 1.8–2.5) is consistent with a deep (residual garnet-bearing) mantle origin, whereas a super-chondritic Zr/Hf (37–47), chondritic Nb/Ta (16–22), and negative K-Zr-Hf-Ti anomalies indicate derivation from a lithospheric mantle source that had experienced carbonatite metasomatism prior to low degrees (3–10%) of partial melt extraction, or alternatively, a hornblende-rich mantle. LA-ICP-MS dating of magmatic titanite, separated from the least altered non-brecciated part of one of the dykes, yielded a weighted mean ^{207}Pb-corrected $^{238}U/^{206}Pb$ date of 1872 ± 3 Ma (2σ; MSWD = 0.92; *n*=48). This date is interpreted as the magmatic crystallisation age of the dyke as it is consistent with a whole-rock Pb-Pb errorchron of 1895 ± 7 Ma, and mantle extraction ages deduced from whole-rock Nd isotopes (t_{DM} 1950 Ma; εNdi +2.5). These findings point to the existence of a hitherto unrecognised magmatic event having affected the Huronian Basin shortly before the Sudbury impact. Based on age, orientation (NW), and geochemistry, the dykes are interpreted as the southeast extension of the 1.88–1.86 Ga Circum-Superior Large Igneous Province, and in detail, as possible equivalents to the ~1870 Ma Haig Intrusions in Hudson Bay region.

The dykes' geochemistry (Mg# 44–57; 70–360 ppm Cr; 60–210 ppm Ni) suggests they crystallised from a relatively evolved magma that underwent fractionation crystallisation at depth. The presence of such evolved rocks above the Temagami Anomaly opens the possibility of genetically related ultramafic cumulates at a deeper crustal level. Indirect evidence of this comes from accessory magmatic Ti-Al-rich pargasite in one of the dykes, which records crystallisation at 3.7–4.4 kbar corresponding to a paleodepth of 15–20 km. This suggests that the pargasitic amphibole was likely a phenocryst phase that either crystallised en route during magma ascent, or in a deep-crustal chamber residing at a current depth of 10–15 km. Curiously, this depth coincides with the causative body of the Temagami Anomaly as predicted by independent geophysical models.

The recognition that rocks of similar age and origin as the well-endowed Raglan Formation and the Thompson Nickel Belt are present above the Temagami Anomaly increases the prospectivity of the area for magmatic Ni-Cu-PGE sulphide deposits. However, the low degree of partial melting calculated for the dykes was likely insufficient to have enriched the melts in chalcophile elements. There is also no clear evidence of sulphide segregation based on MgO/Ni and Cu/Zr systematics.

7.2 Local Geology

Mackelcan Township

Mackelcan Township is located about 45 km northeast of Sudbury, Ontario, and 10 km northeast of Lake Wanapitei. It extends across the western, less magnetic part of the Temagami Anomaly and occurs close to the gravity peak of this regional geophysical feature. The area can be accessed coming from Sudbury along Highway 17 and then following the Kukagami and Bushy Bay roads northwards, passing Dewdney and Wolf Lake. From there, gravel and logging roads lead to the glacially polished and recently stripped outcrops east of Laundry Lake (46˚52 03N 80˚36 54W).

The geology of the study area around Laundry Lake is similar to that of Wolf Lake (see **Chapter 6.2**) and has been described before by Dressler (1982). Laundry Lake lies on the axis of a wide and open double-plunging syncline dominated by thick (> 1 km) and massive (sub-)arkose, quartz wacke and quartzite. These rocks have been stratigraphically assigned to the Lorrain Formation of the Cobalt Group (upper Huronian Supergroup). The Lorrain Formation is generally undeformed to slightly inclined with sedimentary dips facing west and west-northwest. Minor parasitic folding is indicated by multiple reveals of the dip and facing of sedimentary bedding (e.g. near Wolf Lake), although this could well be the result of impact-related brecciation (see below). Metamorphic grade is sub-greenschist to lower greenschist. Sedimentary rocks underlying Lorrain Formation, i.e., siltstone and wacke of the Gowanda Formation, are exposed some 1.5 km east of Laundry Lake, at Irish, Wessel, and Island Lake. The Gowganda Formation siltstone in those areas shows very well-developed rhythmical bedding typical of the Firstbrook Member (e.g. Rainbird & Donaldson 1988), but owing to their softness, these rocks are only rarely exposed. A recent high-resolution aeromagnetic survey (Easton et al. 2020) revealed that the Gowganda Formation near the supposed contact to the Lorrain Formation had been quite extensively folded.

Laundry, Rathwell, and many other lakes and creeks in the area form part of a regional N-S oriented lineament, previously referred to as the Laundry Lake Structure and interpreted as a fault (Dressler 1982) or syncline (Lumbers & Card 1977). This lineament is associated with some of the most spectacular examples of pseudotachylitic breccia (Sudbury Breccia) east of the 1.85 Ga Sudbury Igneous Complex. The *East Range Breccia Belt* – so-called in reference to the well-known South Range Breccia Belt (see Scott & Spray 2000) – defines a linear and up to 500 m wide array of continuously exposed Sudbury Breccia, stretching across 14 km, from Matagamasi Lake in the south, to Chiniguchi Lake in the north. Small enclaves of Sudbury Breccia were also noted outside the East Range Breccia Belt, for example, at Wolf, Irish, Wessel, and Island Lake. Breccias in and around the belt are predominantly monomict and hosted by Lorrain Formation rocks, less frequently polymict and hosted in, or at the contact with, Gowganda Formation siltstone. Both matrix- and clast-supported varieties occur, the former being present as hair-like (<1 cm-thick) dendritic fracture systems, the latter as massive, irregular shaped breccia bodies. Individual clasts range in size from a few mm up to at least 10 m; their shape is typically subrounded to rounded, whilst angular clasts are almost never observed. Contacts to the matrix are generally sharp and well-defined. The provenance of clasts within the East Range Breccia Belt is certainly local, although some notable exceptions of parautochthonous clasts do occur. These include exotic gabbroic clasts from Island Lake – likely derived from a now eroded sill of the Nipissing Suite; and siltstone clasts at Laundry Lake – possibly derived from the Gowganda Formation. The colour of

the clasts can vary significantly within a given outcrop, indicating vigorous mixing of different target rocks during breccia formation. Displacement of some metres as well as clast rotation of > 90° is also evident by the orientation of cross-cutting pre-1.85 Ga quartz veins (**Fig. 7.1**). Albitised clasts of arkose weather dull white in outcrop; clasts affected by quartz-hematite veining weather reddish brown; and strongly brecciated and microfractured clasts of any lithology are dark grey, almost black, in outcrop. The matrix displays a large variability as well, ranging in colour from white, beige, grey, green to black, and locally grading into each other. Rock and mineral clasts occur throughout and in places aligned parallel to the breccia margins, although most of the clasts exhibit no preferred orientation. Sudbury Breccia matrices with at least some sort of flow-texture can be observed in every outcrop, however, best examples are found in breccia outcrops hosted in laminated siltstone, possibly due to the inheritance of primary sedimentary structures and a breccia emplacement comparable to soft-sediment deformation or fluidisation. Another, well-known feature of Sudbury Breccia observable within the East Range Breccia Belt are injection dykes. These are local, short-distance protrusions of clast-poor breccia matrix into dilational sites (e.g. Thompson & Spray 1996, Rousell et al. 2003). Analogues features have been reported before in the South Range Breccia Belt, and in the Vredefort Impact Structure, South Africa (e.g. Riller et al. 2010). Injection dykes that reach from the main zone of brecciation into the country rock range in length from a few cm to 6 m, and in shape from pockets to wedges. Some of these injection dykes exhibit u- and o-shaped flow laminations in cross section and are interpreted as sheath folds based on similar features documented in pseudotachylite at Vredefort (Berlenbach & Roering 1992).

Figure 7.1 Photograph of a typical outcrop of megaclastic pseudotachylitic breccia (Sudbury Breccia, SUBX) within the East Range Breccia Belt; clasts of Lorrain Formation arkose (2.35–2.31 Ga), brecciated to variable degrees, are embedded in a fine-grained greyish and flow-textured matrix; displaced and dead-end quartz veins indicate the rotation of clasts; the black clasts are also arkose, but they are strongly microfractured and rich in aphantic recrystallised pseudotachylite; the outcrop shown here is from the Laundry Lake stripping zone, coordinates 46°51 59N 80°36 57W, ca. 45 km northeast of Sudbury; hammer length = 50 cm.

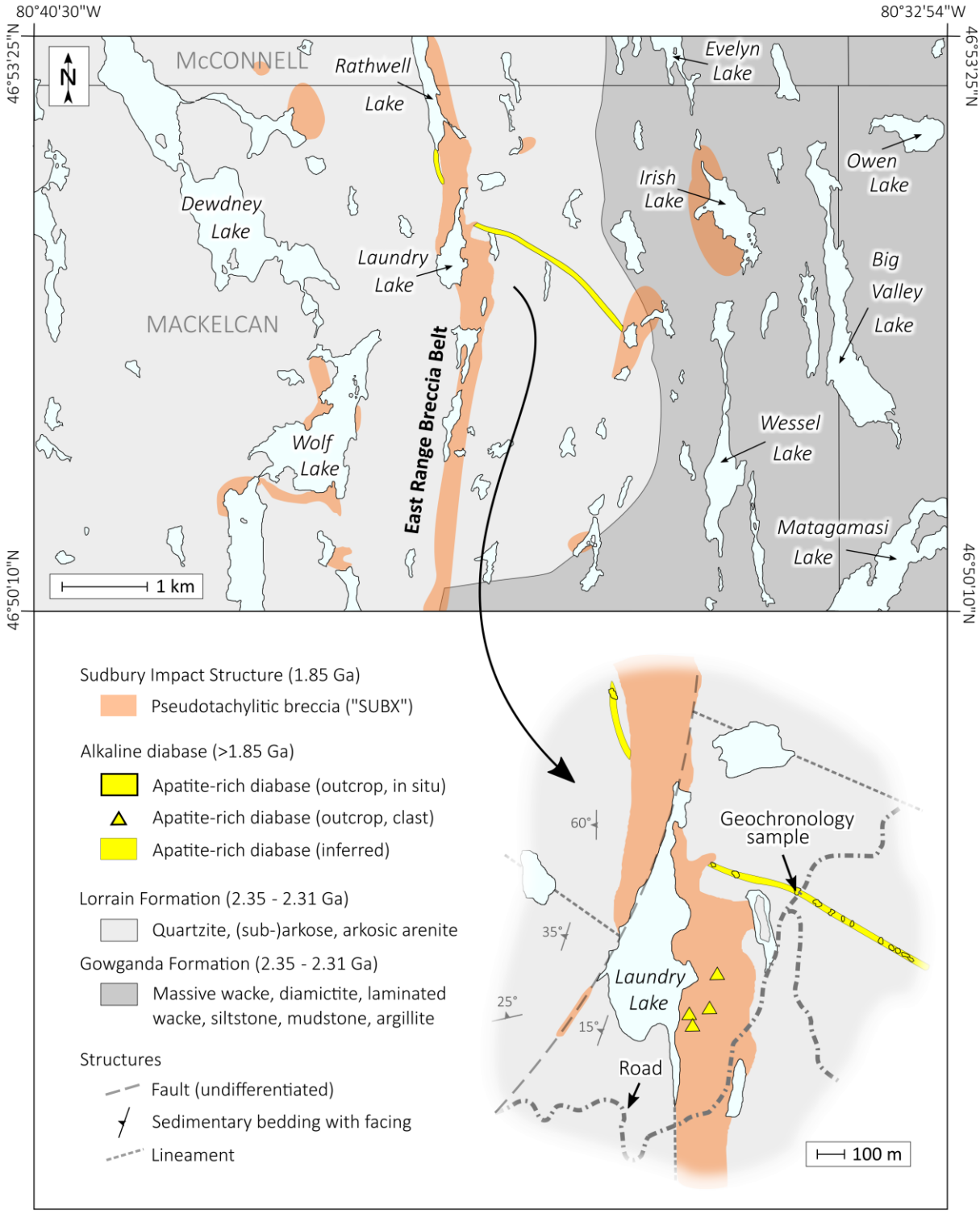

Figure 7.2 Geological map of Mackelcan Township showing the regional geological and lithostratigraphic context of the alkaline diabase dyke; in part based on maps of Dressler (1981a, 1982), Whymark (2019) and additional mapping by the author in the course of this study.

Sheppard Township

Sheppard Township lies 55 km northeast of Sudbury. Both the gravity and magnetic field of the Temagami Anomaly reach their maximum in this area, which prompted Falconbridge Ltd. in 1991 and subsequently the Wallbridge Mining Company in 2000 to drill the area. A vibroseismic survey was conducted 1991, with the results published in Milkereit & Wu (1996). Geologically, however, little is known about Sheppard Township due to limited accessibly and a lack of bedrock exposure. Apparently, Gowganda Formation wacke and siltstone account for > 99% of the (sub-)outcrop (e.g. Dressler 1982; Christopher 1992). These rocks are massive to poorly stratified in outcrop, flat lying, and locally carry dropstones of pink granitoid and green metavolcanic rocks. Laminated argillite of the Firstbrook Member only occurs in the western corner of the township; gabbro of the 2.22 Ga Nipissing Suite has been mapped in the southeast corner. Intrusive mafic rocks typical of the Nipissing Suite were also intersected in at least two drill holes in Sheppard Township (e.g. Meecham & Truscott 1992; Hagen 2020), indicating that these rocks are more widespread (at depth) than their limited outcrop suggests. The youngest rock in the area is a NW-striking olivine diabase dyke. A few occurrences of Sudbury Breccia have been reported, but their true extent remains unclear. A prominent NNW-striking fault across Harvey Lake has been mapped by Christopher (1992) as well as numerous minor faults throughout the township, striking N, NW, and NE.

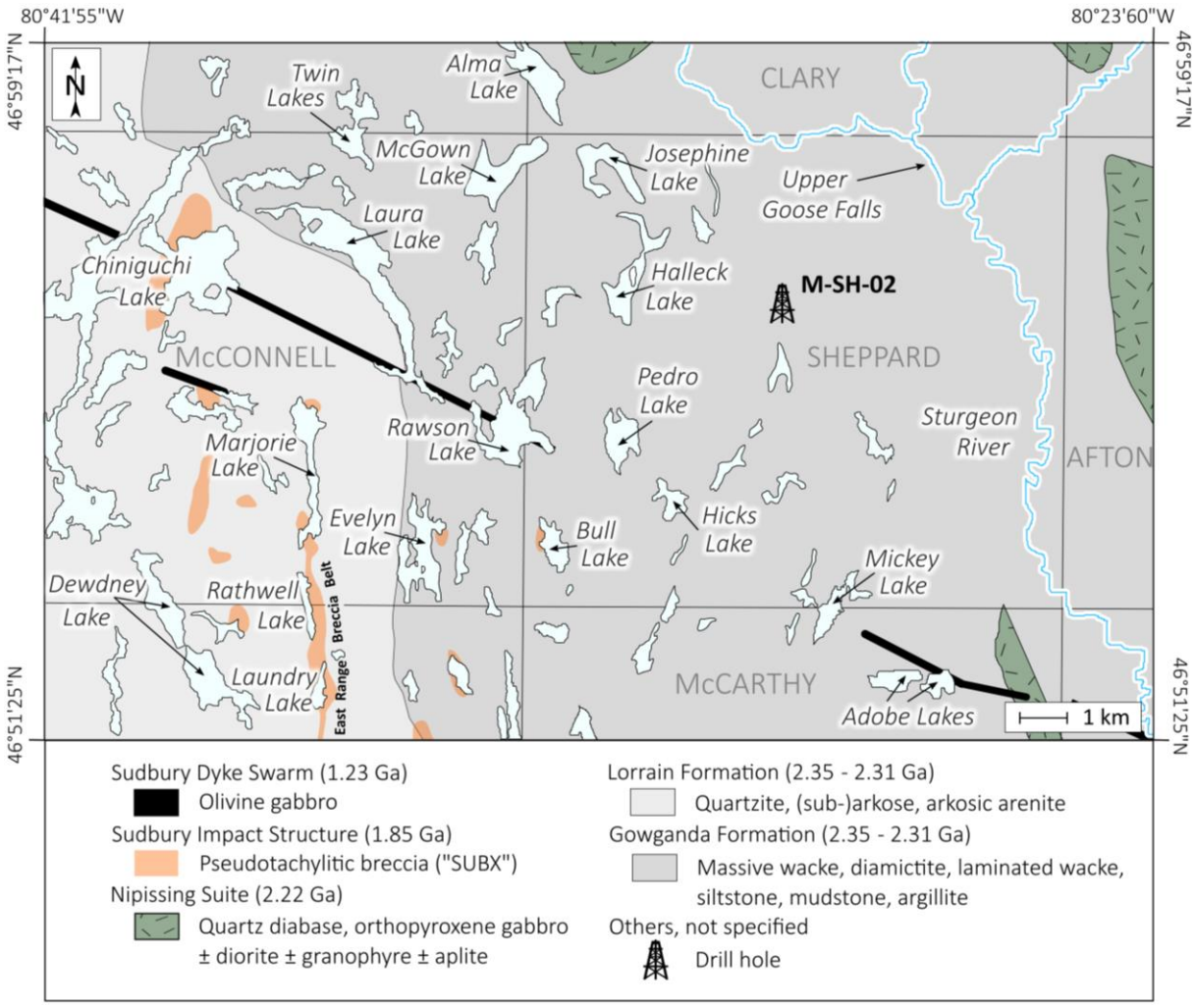

Figure 7.3 Geological map of Sheppard Township showing the regional geological and lithostratigraphic context of drill hole M-SH-2; based on maps of Lumbers & Card (1977), Dressler (1981a), Christopher (1992), and Whymark (2019).

7.3 Field Relations

In 2018, a dyke-like intrusion of alkaline diabase was discovered, cut by a gravel road in Mackelcan Township (46˚52 18N 80˚36 36W). The dyke has a distinctive appearance in outcrop compared to the more fine-grained tholeiitic dyke described in **Chapter 6**, and it has therefore been recognised as part of a separate intrusion. It was subsequently possible to trace the dyke for 2 km along strike, from Laundry Lake in the northwest, almost as far as Wessel Lake in the southeast. The dyke strikes between N40˚W and N65˚W, and its contour is clearly visible in high-resolution aeromagnetic maps, and as a prominent lineament both in the field and in satellite images. Only one outcrop could be found west of Laundry Lake (**Fig. 7.2**). This single outcrop did not permit to determine any orientation, so it is not clear if and how the dyke has been displaced by or along the East Range Breccia Belt. However, the outcrop west of Laundry Lake is associated with a N-trending valley, which, provided it reflects the true orientation of the dyke, would indicate clockwise rotation of the western block. Conversely, magnetic maps and other lineaments indicate a simple lateral displacement of this NW-striking dyke along the breccia belt without rotation. No crosscutting relationship between the NW-striking alkaline diabase dyke and the NE-striking tholeiitic diabase dyke is evident in the field. The alkaline diabase had intruded into quartzite and arkose of the Lorrain Formation to which it shows sharp, curvy planar, fine-grained, and sub-vertically dipping, contacts. No sign of contact metamorphism was observed in the field. At its thickest part at the gravel road, the dyke measures 7 m in width. Xenoliths are mostly absent. In a few locations, however, rafts of country rock (pebble-rich arkose) do occur, which had apparently spawled of the wall rock. A dyke-parallel apophysis into the country rock was noted in at least one outcrop. The texture of the dyke is homogeneous along strike; little jointing in general and no tectonic fabric other than pseudotachylitic veining was observed. Hematite staining is common at the intrusive contact as well as quartz-carbonate-hematite veining throughout.

Outcrop stripping uncovered additional exposures of alkaline diabase east of Laundry Lake (**Fig. 7.4**). In these glacially polished outcrops, the (presumably) same diabase was observed as clasts within massive megaclastic Sudbury Breccia, together with clasts of locally derived arkose and quartzite. This provides undisputable evidence that the dyke must be older than the 1.85 Ga Sudbury impact event. The mafic (diabase) clasts vary considerably in size and shape, ranging from a few cm (**Fig. 7.4B**) to 12 m (**Fig. 7.4A**) and from subrounded (**Fig. 7.4C**) to wispy and highly contorted (**Fig. 7.4B**), respectively, but their igneous texture seems, at least in part, preserved. Furthermore, all clasts are internally brecciated and cut by black, locally white-weathering, veins and stockworks of pseudotachylite. Although formation of such impact-related breccias is widely considered an in-situ process (e.g. Lafrance & Kamber 2010; Reimold et al. 2017), clasts of the alkaline diabase do occur at a significant distance from the closest outcrop of the dyke. The fact that up to 10 m-large clasts of the diabase have been found as far as 600 m south of the actual dyke indicates either (i) significant lateral and energetic transport was involved during the brecciation, or (ii) a more proximal source of the clasts, maybe in form of a second parallel dyke further south. Such parallel dyke might be associated with a distinctive NW-trending lineament observed west of Laundry Lake (**Fig. 7.2**), although no additional outcrop of a diabase dyke could be found there.

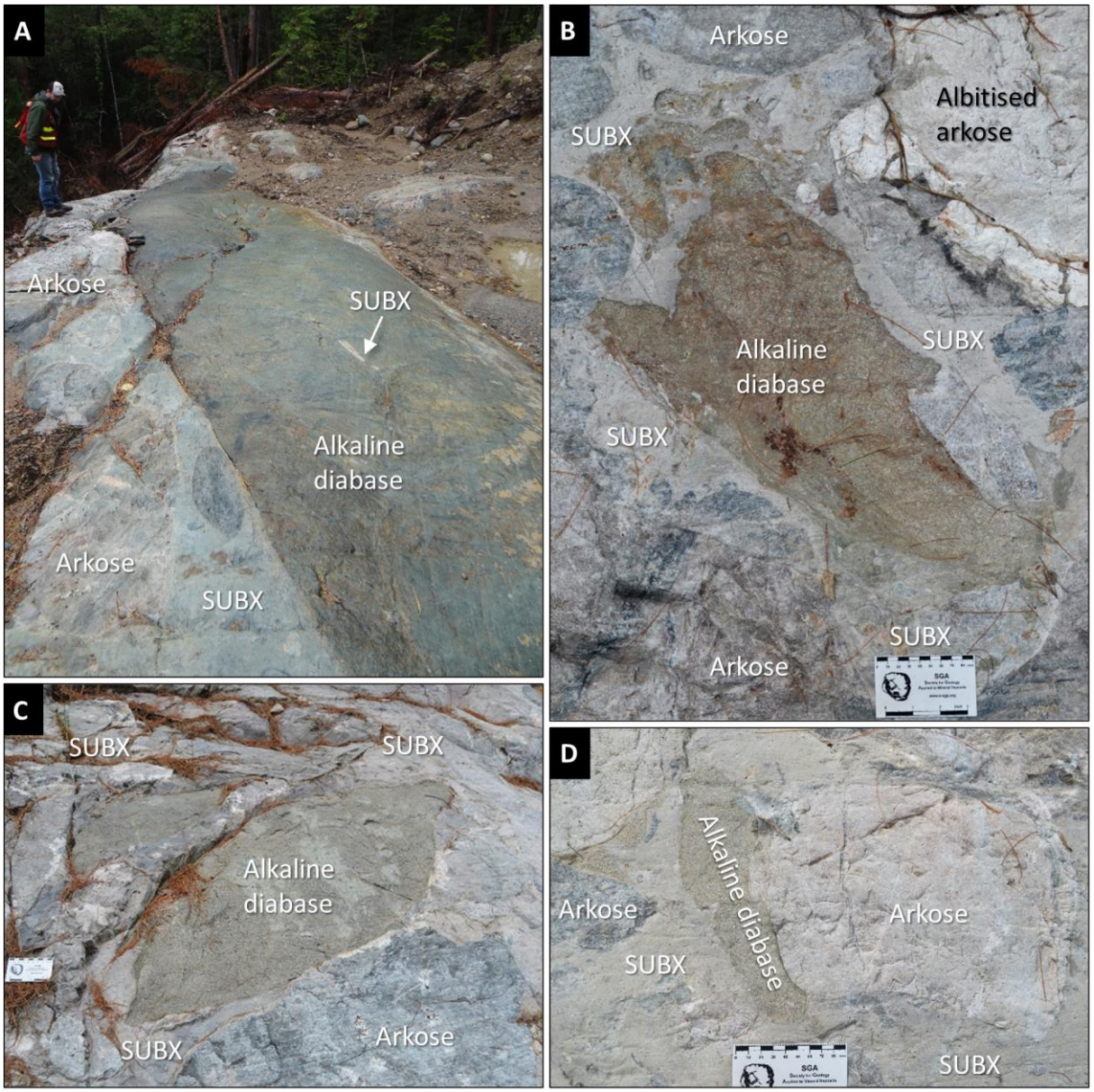

Figure 7.4 Photographs of the alkaline diabase in outcrop near Laundry Lake (Mackelcan Township) showing its intimate spatial relationship to Sudbury Breccia (SUBX); **A:** stripped and wet outcrop (46°52 05N 80°36 52W) showing a megaclast of the alkaline diabase embedded in heterolithic Sudbury Breccia together with clasts of Lorrain Formation arkose; **B:** stripped and dry outcrop (46°51 59N 80°36 57W), showing contorted clasts of alkaline diabase together with clasts of Lorrain Formation arkose, embedded in beige Sudbury Breccia matrix; one of these arkose clasts is strongly albitised; other clasts appear dark grey due to the abundance of pseudotachylite; **C:** stripped and dry outcrop (46°51 59N 80°36 57W) with two clasts of the alkaline diabase embedded in Sudbury Breccia; **D:** same outcrop showing a possible intrusive contact between bleached and albitised Lorrain Formation arkose and the alkaline diabase, preserved as a composite clast in Sudbury Breccia; dark veinlets are pseudotachylite; Wesley Whymark and 9-cm card for scale.

7.4 Drill Core Stratigraphy

Hole M-SH-2 (NQ size, diameter 4.76 cm) was drilled by Falconbridge Ltd. in 1991 in Sheppard Township, coordinates 46˚56 29N 80˚30 01W. It was the first drill program directly aimed at targeting the cause of the Temagami Anomaly and was conducted where the anomaly reaches its gravity peak. Originally, drilling was performed at an azimuth of 90˚, but the drill head was deflected within the first few metres, resulting in a total offset of 800 m to the east of the planned position at a final depth of 2,200 m. Drill core M-SH-2 was logged by Meecham & Truscott (1992) and intersected an almost complete sequence through the Huronian Supergroup as well as relatively thin mafic sill of the Nipissing Suite (**Fig. 7.5**). The uppermost 960 m of the core are rocks of the Gowganda Formation – massive siltstone and wacke with pebbles and dropstones (grey tonalites and green mafic metavolcanics) of up to 15 cm in diameter. The Gowganda Formation grades downhole into wacke, siltstone, and arenite, which are, according to Meecham & Truscott (1992), part of the Serpent Formation. The Serpent Formation is, in turn, underlain by 100 m of laminated limestone and calcareous siltstone typical of the Espanola Formation. The remaining formations (Bruce, Mississagi, Ramsey Lake, McKim) are each 50–100 m thick (**Fig. 7.5**). Finally, a 200 m-tick interval of the Matinenda Formation was intersected at the bottom of the hole. A 180 m thick gabbro of the Nipissing Suite had intruded the Gowganda Formation between 961 and 1,141 m. The sill consists of barren, massive, medium-grained, locally foliated, Nipissing Suite-typical gabbro; very coarse-grained or even pegmatoidal patches are rare. The gabbro has fine-grained chilled margins of several metres in thickness (Meecham & Truscott 1992; Hagen 2020).

Pseudotachylitic breccia (Sudbury Breccia, SUBX) occurs in form of stockworks, veins (mm- and cm-scale) and irregular bodies (dm-scale), scattered throughout the drill core. The Sudbury Breccia matrix shows, where hosted by siliciclastic sedimentary rocks, very well-developed flow textures (**Fig. 7.5A**), and colours ranging from black, grey to green. In addition to this impact-related brecciation, extensive hydrothermal alteration was noted throughout the drill core, including a pervasive epidotisation, chloritisation and carbonatisation. For example, numerous quartz-carbonate veins occur within the Gowganda Formation wacke/siltstone. The veins are relatively regular spaced, locally straight, locally curved, up to 3 cm thick, with diffusive bleaching haloes (**Fig. 7.5B**). They locally contain traces of pyrite, chalcopyrite, and galena. In addition, visible gold was discovered during a recent reassessment of the core (Jacob VanderWal, pers. comm. 2020). Massive yet barren quartz veins (up to 3 m thick), containing chlorite, zoisite and possibly fuchsite, were observed in the Nipissing Suite gabbro at 1,045 m. The gabbro is heavily sheared at ca. 1,030 m and altered to chlorite. In other places, the gabbro is crosscut by quartz crackle breccia, and by up to 10 cm-thick veins of massive milky quartz ± ankerite (**Fig. 7.5C**).

During a 2018 re-examination of drill core M-SH-2, a new lithology has been discovered: Fine- to medium grained green diabase – presumably a dyke – occurs within the upper part of the intersected Huronian Supergroup sequence, from 1,369 m to 1,377 m. The diabase was originally misidentified as Gowganda Formation wacke when the core was first logged (Meecham & Truscott 1992). The diabase is about 8 m thick, non-magnetic, green in colour, mostly aphantic with margin-parallel veining and, therefore, difficult to distinguish from the chloritised sedimentary rocks in its footwall and hanging wall; contacts on either side to the Gowganda Formation/Serpent Formation are gradational over some decimetres. The diabase will be described in more detail below.

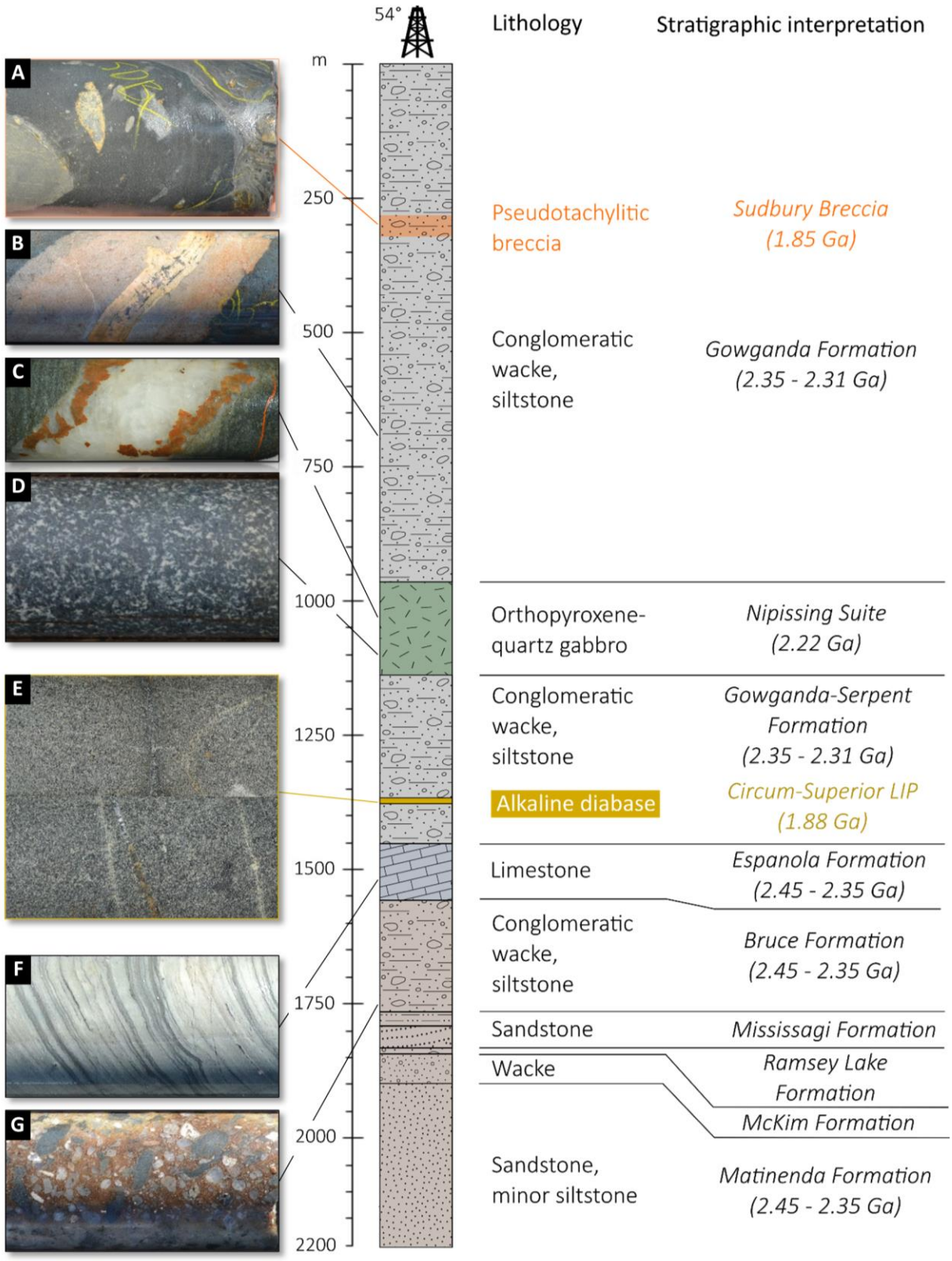

Figure 7.5 Lithological profile of drill core M-SH-2 with exemplary core photographs (left) and stratigraphic interpretation (right); **A:** flow-banded pseudotachylitic breccia (Sudbury Breccia) in Gowganda Formation argillite; **B:** ankerite vein with bleaching halo in Gowganda Formation diamictite; **C:** a massive quartz vein with marginal ankerite cutting across Nipissing Suite gabbro; **D:** typical medium-grained Nipissing Suite gabbro; **E:** quartered drill cores of the alkaline diabase dyke; **F:** laminated Espanola Formation limestone/ calcareous siltstone; **G:** pebbly Bruce Formation wacke with rusty (pyrite/limonite-bearing) matrix; core diameter (= the height of each panel) is 4.76 cm; colour code as in Figures 3.1, 4.1, 5.1, 6.1, 7.2, and 7.3.

7.5 Petrography

Macroscopically, the alkaline diabase from Mackelcan Township can be described as a medium-grained (1–3 mm), equigranular, texturally uniform, melanocratic (colour index 75), massive and non-foliated rock of olive colour. The diabase contains disseminated cubes of pyrite and is mottled with 3 mm-large patches of epidote. Veinlets, veins, and irregular-shaped bodies of Sudbury Breccia occur throughout and can be observed not only in outcrop, but also in hand specimen (**Fig. 7.6A**) and down to the scale of a thin section (**Fig. 7.6B**). Sudbury Breccia in the alkaline diabase has an aphantic, light green, light grey or dark-grey, non-laminated matrix, sharp breccia margins, and contains chloritic rock- and mineral clasts, in places also vesicles and chloritic amygdales. A gradual transition was observed from irregular-shaped Sudbury Breccia (up to 5 cm wide; **Fig. 7.6A**) toward hair-like dendritic fracture systems (< 1 mm; **Fig. 7.6B**). The latter resemble, at first glance, shear bands or hydrothermal veinlets and are not easily recognised as impact-related features in the field nor in hand specimen. They occur in almost every sample from the Laundry Lake stripping zones and exhibit a crosscutting relationship with later (post-impact) chlorite ± pyrite veins (**Fig. 7.6B**) and earlier (pre-impact) quartz-carbonate-hematite veins (**Fig. 7.1**).

Relatively fresh, non-brecciated samples of the diabase dyke were collected from the road outcrop mentioned above and were also used for geochronology. They preserve a relict ophitic texture of ca. 60 vol% amphibole and 40 vol% plagioclase. In those samples, two types of amphibole have been observed (**Fig. 7.6C**), which likely represent two different generations: Fibrous amphibole with pleochroism from colourless to pale green and blue green, prevails. Sub- to euhedral short prismatic amphibole grains with pleochroism from yellow to reddish brown, well-defined crystal faces and 124˚-cleavage patterns, represents the second type of amphibole. The former type of amphibole is likely a replacement product of ferromagnesian minerals (pyroxene), whereas the latter could be a primary magmatic mineral. Plagioclase occurs as subhedral 1 mm-large grains (aspect ratio 4:1), intergrown with amphibole in an ophitic to decussate texture, in which the interstitial spaces are filled with epidote and apatite. Plagioclase is invariably altered to fine and granular epidote/(clino-)zoisite. Preferential saussuritisation of the cores of individual plagioclase grains is frequently observed and apparently mimics a primary core-rim zonation. Only in rare instances is fresh plagioclase preserved, showing polysynthetic twinning. Leucoxene is a minor yet ubiquitous constituent of the rock. It occurs as relatively large (< 5 mm) skeletal grains of ilmenite enveloped in grey semi-opaque cryptocrystalline selvages.

In addition to leucoxene, euhedral (wedge-shaped) titanite with grain sizes between 100 µm and 300 µm was observed, dispersed as an accessory mineral throughout the diabase. Titanite is typically orange to brown under plane polars, sometimes opaque in thicker sections, with no evidence of it replacing primary minerals, or of titanite being replaced by, for example, ilmenite or leucoxene. Another very abundant (ca. 1 vol%) mineral is apatite. Apatite occurs as clear, colourless, low-birefringent, and euhedral (hexagonal) crystals with a habit that varies between acicular (needle-like) and stubby (short prismatic). Apatite is generally found in clusters poikilitically enclosed in plagioclase, amphibole, epidote, and in some instances, also enclosed within titanite. Occasionally, clusters of up to 30 apatite crystals were observed across domains of 1 mm^2. Examples of such apatite clusters are shown in **Figure 7.6F**. The grain size of apatite rarely exceeds 1 mm in length and 100 µm in diameter; most grains measure 200 x 50 µm. Quartz is generally absent from the diabase, except in and around secondary quartz-carbonate-hematite veins.

Samples of the diabase in vicinity to megaclastic Sudbury Breccia have completely lost their primary igneous texture due to a pervasive hydrothermal alteration. In those samples, ferromagnesian minerals have been converted to a chaotic mixture of green chlorite (with golden-brown to purple interference colours) and finely dispersed pyrite and ilmenite; saussuritisation is severe and porphyroblastic epidote and calcite is common. Sudbury Breccia underwent intense alteration as well. Its groundmass had been converted to a cryptocrystalline mixture of quartz, epidote, amphibole, chlorite, and ilmenite. Nonetheless its strong secondary overprint, the breccia resembles pseudotachylitic veins described elsewhere in mafic host rocks (e.g. Kovaleva et al. 2018a).

Alkaline diabase in drill core M-SH-2 is a fine- to medium-grained (< 2 mm) aphantic to phaneritic, equigranular, greyish green, (holo-)melanocratic rock (colour index 80–90). Hydrothermal veins are common, but no Sudbury Breccia was observed within, or close to, the diabase. Thin sections from the dyke's margins reveal a very fine-grained groundmass composed of amphibole, chlorite, epidote, biotite, and opaque minerals, which likely reflects chilling against the cooler country rock. Aligned phenocrysts of plagioclase – pseudomorphically replaced by saussurite (**Fig. 7.7B**) – occur at the dyke's margin and indicate that the magma was likely plagioclase-phyric. The Gowganda Formation wacke shows, where in contact with this diabase, porphyroblastic biotite set in a fine-grained micaceous matrix. This texture (not shown) resembles a biotite hornfels and provides, together with chilled margins along both the footwall and hangingwall, supporting evidence for an intrusive relationship between diabase dyke and the Gowganda Formation. Alkaline diabase in drill hole M-SH-2 is, therefore, not considered an exceptionally large Archaean dropstone, but a manifestation of an intrusive event younger than the ~2.31 Ga Cobalt Group.

The most coarsely grained and freshest samples of the alkaline diabase dyke (samples SH2-12; SH2-14) consist of a roughly equal modal proportion of plagioclase and amphibole in an ophitic texture (**Fig. 7.7C,E**). Plagioclase rarely exceeds 1 mm in length and is characterised by an acicular habit (aspect ratio 10:1) typical of crystallisation under disequilibrium conditions (e.g. undercooling). Actinolite occurs as fibrous bundles with pleochroism from colourless to pale green, and evidently pseudomorphic after pyroxene. Appreciable amounts (~2 vol%) of leucoxene occur disseminated throughout. Leucoxene is typically 0.3 mm large, of skeletal or dendritic habit, semi-opaque in thin section, and reddish in polished hand specimens (**Fig. 7.7A**). Among accessory constituents there is only apatite, occurring as acicular crystals of less than 25 µm in size. Apatite is significantly less abundant compared to the alkaline diabase above from Mackelcan Township.

The alkaline diabase in drill core M-SH-2 shows the most complex subsolidus alteration history of any rock described so far. Apart from an extensive metamorphic overprint at greenschist facies conditions in virtually all samples of the mafic dyke, manifesting in the typical assemblage albite-actinolite-chlorite-epidote-biotite, at least three distinct generations of hydrothermal veins have been recognised. These include veins of (i) granular (clino-)zoisite together with fibrous green amphibole; (ii) pure epidote; (iii) carbonate, quartz, and chlorite. In one thin section, a younger vein of type (iii) was found to cut across an older vein of type (i). Veins of type (ii), in turn, cut across uralised pyroxene and dissect, but not displace, leucoxene (**Fig. 7.7F**). In addition, evidence of local carbonate metasomatism was found at 1,371.5 m (sample SH2-11). In this part of the dyke, the igneous protolith has been completely obliterated. Rhombic neoblasts of calcite and pseudomorphic chlorite (with golden-brown interference colours), likely after amphibole or pyroxene, make up more than 65 vol% of sample; the remainder is a mixture of sericite and plagioclase.

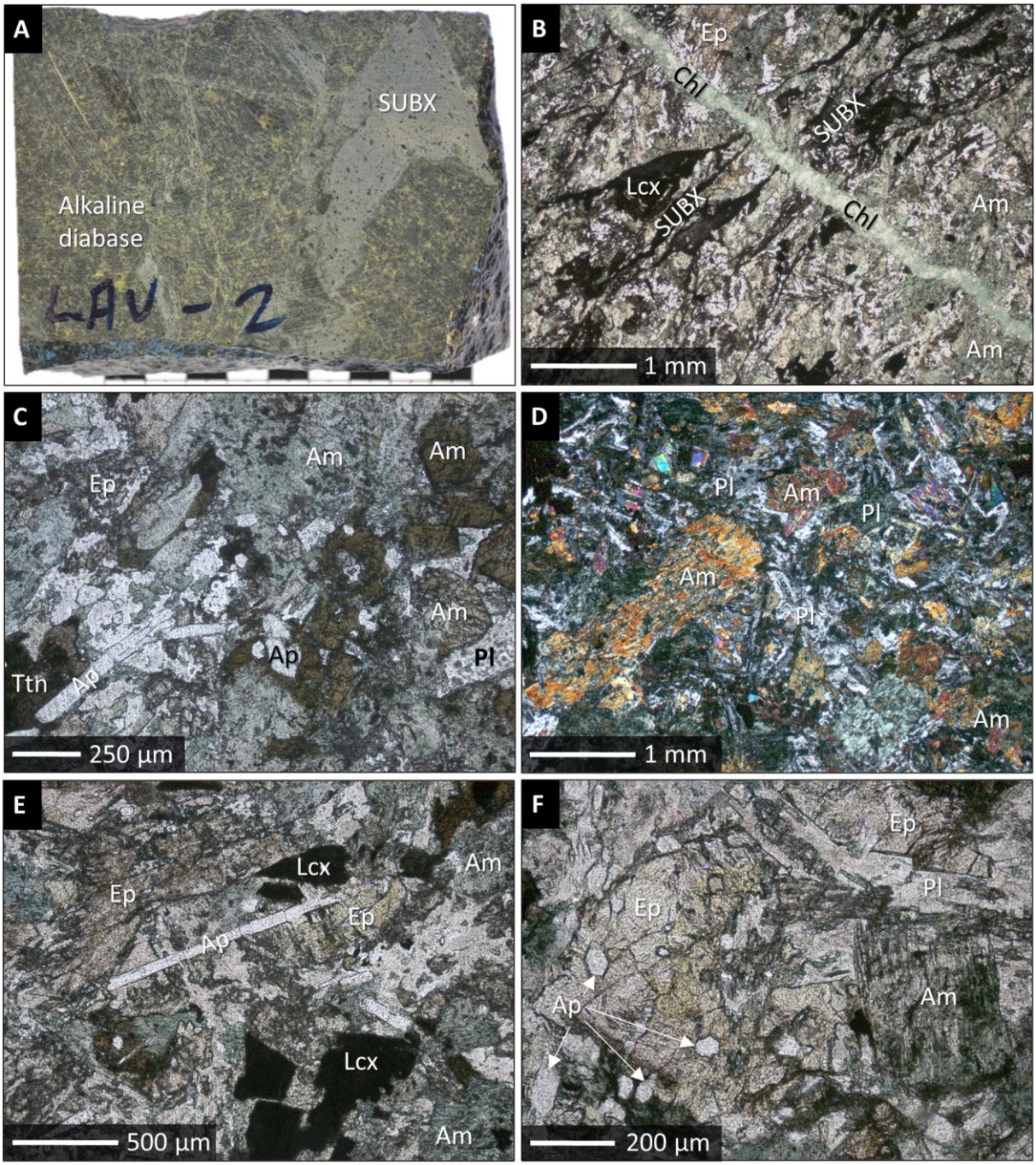

Figure 7.6 Photograph and microphotographs of the alkaline diabase from Mackelcan Township; **A:** hand specimen of a channel cut across the alkaline diabase megaclast from Laundry Lake (as shown in Fig. 7.4A); the sample contains anastomosing veins and irregular masses of pseudotachylitic breccia (Sudbury Breccia); **B:** thin section of the same sample under transmitted light and plane polars showing veinlets of dark cryptocrystalline pseudotachylitic breccia, which are in turn cut by later chlorite veins; **C:** thin section of a relatively fresh sample of the alkaline diabase dyke under transmitted light and plane polars, showing green and brown amphibole together with stubby apatite, interstitial plagioclase, anhedral epidote, and subhedral titanite; **D:** thin section of a relatively fresh and non-brecciated sample of the alkaline diabase dyke (sample AK18-7) under transmitted light and crossed polars, showing a mixture of amphibole, plagioclase, and epidote; **E:** thin section under transmitted light and plane polars, showing a strongly altered portion of the diabase dyke, with prismatic apatite; **F:** thin section under transmitted light and plane polars, showing another strongly altered sample; note the euhedral apatite crystals with well-defined hexagonal crystal faces, enclosed in an epidote poikiloblast. Abbreviations: SUBX = Sudbury Breccia; Ep = epidote; Chl = chlorite; Lcx = leucoxene; Ttn = titanite; Am = amphibole; Ap = apatite; Pl = plagioclase.

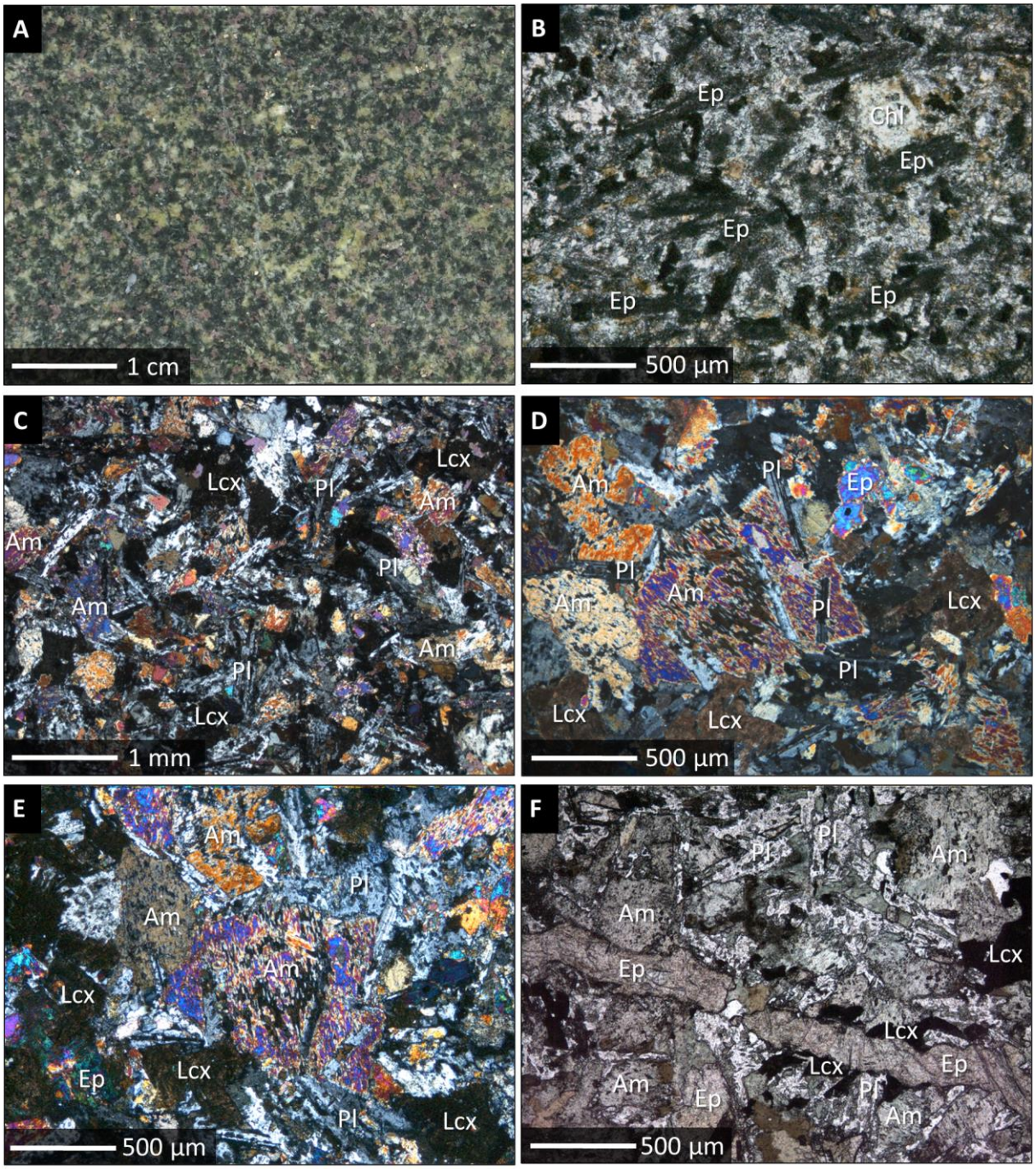

Figure 7.7 Photograph and microphotographs of the alkaline diabase dyke intersected in Falconbridge's 1991 deep drill hole M-SH-2, Sheppard Township; **A:** polished hand specimen of the drill core at 1,373 m (sample SH-14, centre of the dyke) showing a relatively coarse-grained interval of the alkaline diabase dyke; **B:** thin section under transmitted light and plane polars (sample SH2-12) showing the chilled plagioclase-phyric margin of the alkaline diabase; former plagioclase phenocrysts are crudely aligned with their long axis about parallel to the intrusive contact and they are pseudomorphically replaced by saussurite; **C:** thin section under transmitted light and crossed polars showing the freshest and most coarsely grained sample of the alkaline diabase (sample SH2-14); **D:** enlargement of the previous microphotograph under slightly de-crossed polars; **E:** same spot but rotated and with polars crossed at 90°; **F:** thin section under transmitted light and plane polars, showing a vein of epidote cutting across pre-existing leucoxene grains. Abbreviations: Ep = epidote; Chl = chlorite; Am = amphibole; Pl = plagioclase; Lcx = leucoxene.

7.6 Amphibole Chemistry

As already mentioned in the petrography section of this chapter, two different types of amphibole have been observed in the freshest samples of the alkaline diabase dyke from Mackelcan Township, and readily distinguished based on optical criteria: A fibrous green amphibole, and a prismatic brown amphibole. The former predominates by far, whereas the latter is only an accessory constituent of the rock. In order to verify these observations by objective measures, quantitative electron microprobe analyses have been performed on a representative number of amphibole grains. The data, which are presented in **Table 7.1**, reveal indeed a bimodal chemical composition, supporting the above notion that two different types of amphibole are present within the same sample. These likely represent to different generations, as will be argued below.

Using the BSE imagery mode of the electron microprobe coupled with quantitative spot analyses, it became clear that the fibrous green type of amphibole is, on the micron level, intergrown with chlorite, Fe-Ti oxide, and maybe relict pyroxene. Many analyses turned out to be contaminated by the ambient matrix, which required extensive filtering of the dataset by criteria such as Al_2O_3 content and totals. The few analyses that are considered representative of the fibrous green amphibole (**Tab. 7.1**) have a Mg# (=100×Mg/[Mg+Fe]) between 50 and 70, an $Fe^{3+}/(Fe^{3+}+Fe^{2+})$ ratio between 0.02 and 0.21, SiO_2 contents between 50 and 54 wt%, and overall low Al_2O_3 (≤ 4 wt%), TiO_2 (≤ 0.1 wt%), and low total alkali contents (≤ 1 wt%). This composition classifies the amphibole as calcic because $Ca_{M4} \geq 1.50$; $(Na+K)_A < 0.50$; $Ca_A < 0.5$, and more specifically, as (ferro-)actinolite according to scheme of Leake et al. (1997) (**Fig. 7.8**). Some analyses were found to approach the composition of actinolitic hornblende or magnesio hornblende, however, these analyses were likely contaminated by the matrix and are therefore discarded from further discussion.

Application of the thermometric and barometric equations listed in **Chapter 2.2.4** points to a low-grade metamorphic or hydrothermal (deuteric?) origin of the actinolitic amphibole generation. The equation of Ridolfi & Renzulli (2012), for example, yielded temperatures between 430 and 590°C (510 ± 55°C), which is far below the presumed solidus of the magmatic ultrabasic host rock, but above the sub- to lower greenschist-facies metamorphic conditions previously established for the area (Card 1978; Dressler 1982; Easton 2000). However, the equation of Ridolfi & Renzulli (2012) was only calibrated for the temperature interval 800–1,130°C, and accordingly these results must be treated with caution. The Ti-in-amphibole thermometer of Liao et al. (2021) gave consistently lower temperatures between 290 and 410°C (360 ± 44°C), as can be expected for actinolite occurring in equilibrium with a typical greenschist-facies assemblage. None of the linear Al-in-amphibole barometers (e.g. Hammarstrom & Zen 1986; Hollister et al. 1987; Johnson & Rutherford 1989; Liu & Ernst 1992; Schmidt 1992) gave meaningful results because of the very low Al_2O_3 content of the actinolite in question. Unreasonable results were also obtained from the barometer of Anderson & Smith (1995), probably because it is better suited for high-*T* amphibole in granitic systems. The barometer of Mutch et al. (2016), which is suited for Al-poor amphibole, yielded pressures between 0.5 and 2 kbar (0.88 ± 0.39 kbar), corresponding to an overload of ca. 3,500 m when assuming an average rock density of 2,650 kg/m^3 for the sedimentary (Huronian) overburden. Lower values, between 0.12 and 0.34 kbar (0.22 on average), were obtained using Ridolfi & Renzulli's (2012) barometer, but again, these results are outside the calibrated *P*-*T*-range and are therefore considered unreliable.

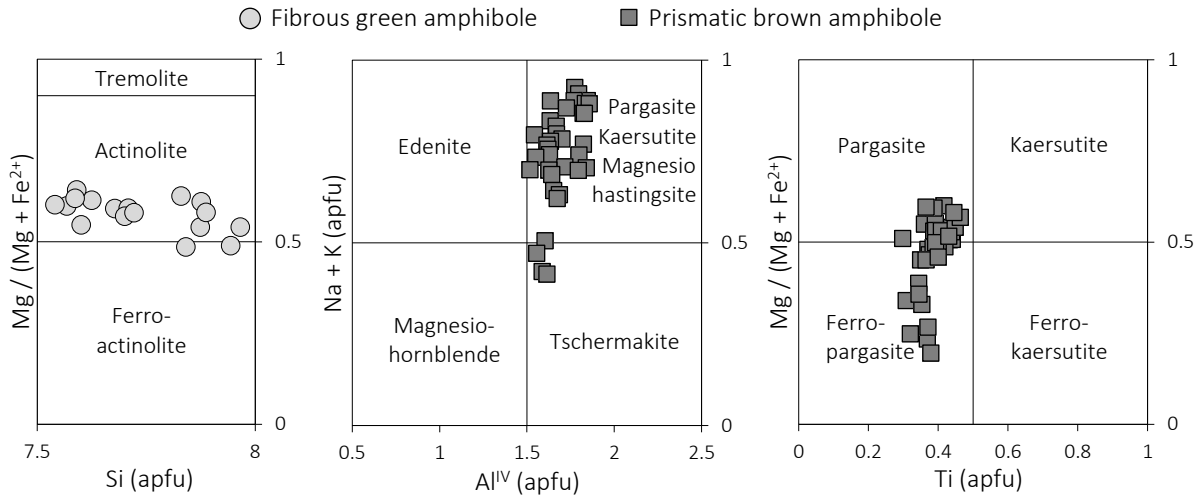

Figure 7.8 Chemical classification of the two types of amphibole in the alkaline diabase dyke from Mackelcan Township; nomenclature based on Leake et al. (1997); apfu = atoms per formula unit.

The short-prismatic brown type of amphibole occurs as rare, very bright grains in BSE images and exhibits a pronounced compositional zonation, from dark cores to bright rims. This zonation is due to a gradual outward decrease in the Mg# (65–25). The brown amphibole has a significantly higher Al_2O_3 content (8.8–11 wt%) than actinolite in the same sample. Compared to the actinolite it is also highly enriched in TiO_2 (2.6–4.1 wt%), Na_2O (1.5–2.9 wt%) and K_2O (1.0–1.6 wt%) at the expense of CaO. Consequently, the amphibole belongs to the sodic-calcic amphibole subgroup ($[Na+K]_A > 0.5$), and it is classified as titaniferous (ferro-)pargasite (**Fig. 7.8**). Such composition is inconsistent with a hydrothermal or low-grade metamorphic origin because of the low capacity of most fluids to carry Ti (e.g. van Baalen 1993). Titaniferous alkali amphiboles are, however, typical intercumulus phases in ultramafic rocks, and they are particularly common phenocrysts or mantle xenocrysts in alkaline rocks (e.g. Ridolfi & Renzulli 2012).

The notion of a magmatic origin of the pargasitic amphibole generation is quantitatively supported by a high formation temperature of 951 ± 23°C or 972 ± 29°C, as obtained by using the thermobarometers of Ridolfi & Renzulli (2012) and Liao et al (2021), respectively. Although the composition of the pargasite satisfies the requirement of Fe# ≤ 0.65 for mineral barometry, its $Fe^{3+}/(Fe^{3+}+Fe^{2+})$ ratio is lower (0.02–0.22) than the recommended minimum value of 0.25 (Anderson & Smith 1995). Another, more serious problem, is the lack of evidence of Al-saturation, as it is not clear whether the composition of the pargasite was buffered by an appropriate equilibrium assemblage. Thus, undersaturation in Al is expected to result in an underestimation of the actual crystallisation pressure. The various linear Al-in-hornblende barometers (Hollister et al. 1987; Johnson & Rutherford 1989; Liu & Ernst 1992; Schmidt 1992) yielded, nevertheless, surprisingly consistent results between 4–6 kbar (3.65 ± 0.45 kbar) corresponding to a *minimum* paleodepth of 17–24 km. Lower pressures of 2.6–4.1 kbar (10–16 km) and 3.6–4.9 kbar (14–19 km) were obtained from the equation of Ridolfi & Renzulli (2012) and Mutch et al. (2016), respectively. No meaningful values could be obtained from Anderson & Smith's (1995) equation.

These data suggest high-pressure crystallisation of the pargasitic amphibole generation prior to high-level magma emplacement into the Cobalt Group. This would mean that the pargasite is a phenocryst that crystallised at lower/mid crustal depth > 10 km below the present surface, maybe during intermittent magma storage within the crust, or en route during magma ascent.

Table 7.1 Representative electron microprobe data and calculated structural formulae for amphibole in the alkaline diabase dyke, Mackelcan Township

SiO_2	TiO_2	Al_2O_3	Cr_2O_3	FeO	MgO	CaO	MnO	Na_2O	K_2O	Sum	Tetrahedral site				M1, M2, M3 sites								M4 site				A site			
wt%	wt%	wt%	wt%	wt%	wt%	wt%	wt%	wt%	wt%	wt%	Si	Al(IV)	Ti(IV)	Σ	Al(VI)	Ti	Cr	Fe3+	Mg	Fe2+	Mn	Σ	Fe2+	Ca	Na	Σ	Na	K	Σ
Titaniferous (ferro-)pargasite																														
41.3	3.63	10.9	0.00	17.9	9.7	11.0	0.37	2.58	1.16	98.53	6.20	1.80	0.00	8.00	0.13	0.41	0.00	0.34	2.16	1.91	0.05	5.00	0.00	1.77	0.23	2.00	0.52	0.22	0.74
41.9	3.39	10.6	0.01	18.2	9.1	10.8	0.35	2.77	1.19	98.30	6.33	1.67	0.00	8.00	0.21	0.39	0.00	0.13	2.05	2.17	0.05	5.00	0.00	1.76	0.24	2.00	0.57	0.23	0.80
42.5	3.48	10.4	0.00	16.4	10.2	11.0	0.29	2.66	1.16	98.17	6.39	1.61	0.00	8.00	0.23	0.39	0.00	0.06	2.28	2.00	0.04	5.00	0.00	1.77	0.23	2.00	0.55	0.22	0.77
41.7	2.99	9.2	0.00	24.6	5.9	10.2	0.44	1.59	1.33	97.97	6.41	1.59	0.00	8.00	0.08	0.35	0.00	0.71	1.36	2.45	0.06	5.00	0.00	1.69	0.31	2.00	0.16	0.26	0.42
40.7	3.47	10.2	0.00	18.1	10.0	11.0	0.36	2.80	1.23	97.97	6.17	1.83	0.00	8.00	0.00	0.39	0.00	0.40	2.27	1.90	0.05	5.00	0.00	1.79	0.21	2.00	0.62	0.24	0.85
41.2	2.97	9.3	0.03	22.8	6.9	10.9	0.43	2.18	1.22	97.93	6.36	1.64	0.00	8.00	0.05	0.34	0.00	0.42	1.60	2.53	0.06	5.00	0.00	1.80	0.20	2.00	0.45	0.24	0.69
41.8	3.66	9.8	0.02	18.0	9.3	10.9	0.34	2.80	1.21	97.87	6.37	1.63	0.00	8.00	0.12	0.42	0.00	0.06	2.12	2.23	0.04	5.00	0.00	1.77	0.23	2.00	0.60	0.24	0.83
38.5	3.07	10.1	0.00	26.4	4.2	10.6	0.51	2.92	1.56	97.85	6.14	1.86	0.00	8.00	0.04	0.37	0.00	0.23	1.01	3.29	0.07	5.00	0.00	1.82	0.18	2.00	0.72	0.32	1.04
40.4	3.75	10.6	0.02	17.8	9.8	11.3	0.34	2.69	1.24	97.85	6.14	1.86	0.00	8.00	0.05	0.43	0.00	0.22	2.22	2.04	0.04	5.00	0.00	1.85	0.15	2.00	0.64	0.24	0.88
41.2	3.15	8.8	0.01	26.4	4.5	10.2	0.52	1.58	1.41	97.85	6.44	1.56	0.00	8.00	0.06	0.37	0.00	0.57	1.05	2.88	0.07	5.00	0.00	1.71	0.29	2.00	0.19	0.28	0.47
42.5	3.19	9.3	0.03	19.8	8.3	10.4	0.39	2.59	1.24	97.82	6.48	1.52	0.00	8.00	0.16	0.37	0.00	0.23	1.89	2.30	0.05	5.00	0.00	1.69	0.31	2.00	0.46	0.24	0.70
40.3	3.83	10.4	0.01	18.3	9.5	11.1	0.31	2.84	1.19	97.79	6.15	1.85	0.00	8.00	0.03	0.44	0.00	0.23	2.16	2.10	0.04	5.00	0.00	1.82	0.18	2.00	0.66	0.23	0.89
40.7	3.22	10.3	0.00	19.2	8.9	11.0	0.34	2.82	1.26	97.77	6.23	1.77	0.00	8.00	0.08	0.37	0.00	0.25	2.04	2.21	0.04	5.00	0.00	1.81	0.19	2.00	0.64	0.25	0.89
40.6	3.63	10.6	0.01	17.1	10.1	11.3	0.31	2.76	1.21	97.66	6.16	1.84	0.00	8.00	0.07	0.41	0.00	0.22	2.30	1.96	0.04	5.00	0.00	1.83	0.17	2.00	0.65	0.23	0.88
41.6	3.96	10.5	0.02	16.8	9.9	10.7	0.30	2.63	1.11	97.64	6.28	1.72	0.00	8.00	0.15	0.45	0.00	0.23	2.23	1.89	0.04	5.00	0.00	1.72	0.28	2.00	0.49	0.21	0.71
41.9	3.49	9.6	0.01	20.1	8.2	11.1	0.37	1.53	1.25	97.55	6.40	1.60	0.00	8.00	0.12	0.40	0.00	0.37	1.87	2.20	0.05	5.00	0.00	1.81	0.19	2.00	0.26	0.24	0.51
40.6	3.76	10.3	0.00	17.7	9.6	11.2	0.36	2.84	1.20	97.53	6.20	1.80	0.00	8.00	0.06	0.43	0.00	0.13	2.19	2.14	0.05	5.00	0.00	1.83	0.17	2.00	0.67	0.23	0.91
39.2	2.68	10.3	0.04	25.6	4.4	10.7	0.47	2.60	1.52	97.49	6.23	1.77	0.00	8.00	0.16	0.32	0.00	0.23	1.05	3.17	0.06	5.00	0.00	1.82	0.18	2.00	0.62	0.31	0.93
41.3	3.94	11.0	0.03	15.8	10.6	11.1	0.29	2.39	1.15	97.49	6.21	1.79	0.00	8.00	0.15	0.45	0.00	0.27	2.38	1.71	0.04	5.00	0.00	1.78	0.22	2.00	0.48	0.22	0.70
42.1	3.04	9.7	0.02	19.0	8.5	10.8	0.41	2.80	0.98	97.43	6.46	1.54	0.00	8.00	0.21	0.35	0.00	0.06	1.95	2.37	0.05	5.00	0.00	1.77	0.23	2.00	0.61	0.19	0.80
40.7	2.62	9.1	0.01	24.1	6.0	10.4	0.47	2.44	1.37	97.30	6.38	1.62	0.00	8.00	0.06	0.31	0.00	0.44	1.40	2.72	0.06	5.00	0.00	1.74	0.26	2.00	0.48	0.27	0.76
40.3	3.11	9.1	0.05	24.8	5.6	10.6	0.54	1.94	1.30	97.27	6.31	1.67	0.01	8.00	0.00	0.35	0.01	0.57	1.32	2.69	0.07	5.00	0.00	1.77	0.23	2.00	0.36	0.26	0.62
41.8	3.77	10.0	0.00	17.6	9.5	11.0	0.33	2.15	1.16	97.24	6.35	1.65	0.00	8.00	0.14	0.43	0.00	0.22	2.15	2.01	0.04	5.00	0.00	1.79	0.21	2.00	0.42	0.22	0.64
41.9	3.43	10.1	0.00	16.3	10.7	10.9	0.29	2.25	1.08	97.04	6.31	1.69	0.00	8.00	0.11	0.39	0.00	0.40	2.41	1.65	0.04	5.00	0.00	1.76	0.24	2.00	0.42	0.21	0.63
40.6	4.07	10.8	0.00	16.8	10.1	10.6	0.30	2.63	1.06	97.03	6.16	1.84	0.00	8.00	0.08	0.46	0.00	0.40	2.28	1.74	0.04	5.00	0.00	1.73	0.27	2.00	0.50	0.20	0.71
Actinolite																														
53.8	0.03	1.04	0.01	19.1	11.8	12.3	0.31	0.14	0.04	98.53	7.87	0.13	0.00	8.00	0.05	0.00	0.00	0.15	2.57	2.18	0.04	5.00	0.00	1.93	0.04	1.97	0.00	0.01	0.01
54.1	0.02	0.96	0.01	17.7	12.7	12.3	0.20	0.21	0.02	98.27	7.89	0.11	0.00	8.00	0.05	0.00	0.00	0.15	2.77	2.00	0.02	5.00	0.00	1.92	0.06	1.98	0.00	0.00	0.00
53.6	0.04	0.59	0.01	20.4	10.8	12.4	0.19	0.08	0.01	98.09	7.94	0.06	0.00	8.00	0.05	0.00	0.00	0.04	2.39	2.49	0.02	5.00	0.00	1.97	0.02	1.99	0.00	0.00	0.00
52.4	0.06	1.86	0.00	18.4	12.1	12.4	0.38	0.20	0.10	97.93	7.70	0.30	0.00	8.00	0.02	0.01	0.00	0.27	2.65	2.00	0.05	5.00	0.00	1.96	0.04	2.00	0.02	0.02	0.03
52.4	0.02	1.59	0.03	18.5	12.3	12.4	0.38	0.28	0.05	97.91	7.72	0.28	0.00	8.00	0.00	0.00	0.00	0.32	2.70	1.96	0.05	5.04	0.00	1.96	0.04	2.00	0.04	0.01	0.05
54.1	0.04	1.12	0.02	16.3	13.4	12.3	0.32	0.27	0.03	97.90	7.88	0.12	0.00	8.00	0.07	0.00	0.00	0.12	2.90	1.86	0.04	5.00	0.00	1.92	0.08	1.99	0.00	0.01	0.01
52.2	0.09	3.03	0.00	16.2	13.2	12.0	0.38	0.49	0.12	97.78	7.59	0.41	0.00	8.00	0.11	0.01	0.00	0.37	2.86	1.60	0.05	5.00	0.00	1.87	0.13	2.00	0.01	0.02	0.03
52.0	0.08	2.99	0.00	16.9	12.8	12.1	0.37	0.46	0.11	97.76	7.59	0.41	0.00	8.00	0.10	0.01	0.00	0.34	2.78	1.72	0.05	5.00	0.00	1.90	0.10	2.00	0.03	0.02	0.05
50.9	0.06	3.61	0.07	19.4	11.1	11.7	0.39	0.50	0.15	97.75	7.49	0.51	0.00	8.00	0.12	0.01	0.01	0.50	2.43	1.88	0.05	5.00	0.00	1.85	0.14	1.99	0.00	0.03	0.03
51.3	0.06	2.99	0.01	17.1	12.7	12.6	0.38	0.44	0.13	97.70	7.54	0.46	0.00	8.00	0.06	0.01	0.00	0.26	2.78	1.84	0.05	5.00	0.00	1.99	0.01	2.00	0.11	0.02	0.14
51.6	0.09	3.37	0.05	16.7	12.5	12.4	0.36	0.50	0.14	97.66	7.57	0.43	0.00	8.00	0.15	0.01	0.01	0.20	2.74	1.84	0.05	5.00	0.00	1.94	0.06	2.00	0.09	0.03	0.11
53.9	0.02	0.73	0.00	18.1	11.9	12.5	0.25	0.12	0.03	97.62	7.97	0.03	0.00	8.00	0.09	0.00	0.00	0.00	2.63	2.24	0.03	5.00	0.00	1.97	0.03	2.00	0.01	0.01	0.01
50.0	0.09	3.98	0.14	17.6	12.0	12.5	0.38	0.63	0.17	97.50	7.41	0.59	0.00	8.00	0.10	0.01	0.02	0.29	2.64	1.89	0.05	5.00	0.00	1.98	0.02	2.00	0.16	0.03	0.19

7.7 Geochronology

Due to the limited amount of core material available, no attempt was made to extract accessory minerals from the alkaline diabase in drill core M-SH-2. For radiometric age dating of the alkaline diabase from Mackelcan Township, a 30-kg whole-rock sample was subject to the heavy mineral separation routine described in **Chapter 2.2.7**. The sample was collected ca. 450 m northeast of Laundry Lake (46°52 17N 80°36 35W). This locality was chosen for several reason. Not only reaches the dyke its maximum width in this area, but it is also the most accessible, coarsest grained and least altered outcrop known so far. There are no xenoliths, breccias or pseudotachylite/ultracataclasite veins at this site, thereby minimising the potential of contamination, inheritance, or isotopic disturbance. Although zircon and baddeleyite were the minerals of choice because of their well-established utility as geochronometers, high closure temperature and high resistance to post-magmatic disturbance, none of these could be separated from the rock despite considerable effort and time investment. This might be a result of their small grain sizes or, more likely (and in agreement with BSE analyses of thin sections), the total absence of zircon and baddeleyite. Lack of discrete Zr minerals is, in fact, not uncommon in silica-poor and -undersaturated systems such as lamprophyres and other alkaline rocks, especially in the presence of primary amphibole, titanite or other minerals with a high Zr partition coefficient (e.g. Seifert & Kramer 2003; Craddock et al. 2007). The separation was nevertheless successful in that it yielded a high amount of other heavy minerals including, in decreasing order of abundance, amphibole, epidote, ilmenite, pyrite, apatite and titanite. The latter two are likewise suited for U-Pb dating as has been repeatably demonstrated throughout the literature (e.g. Storey et al. 2007; Chew et al. 2011, 2014; Kirkland et al. 2017). Consequently, U-Pb dating was performed on apatite and titanite, the results of which are presented below following a detailed characterisation of the analysed grains.

Description of titanite and apatite

Individual titanite grains are euhedral and exhibit the typical sphenoid habit (Greek *sphēn*, meaning "wedge") dominated by the {111} form. The grains are between 50–250 µm in size yet many are arguably shards of even larger crystals. Under the stereomicroscope, all titanite grains are orange, honey to amber, homogeneous, clear (almost gemmy), with smooth and lustrous crystal faces, and mostly free of inclusions. Some larger grains are rimed with epidote and amphibole or contain inclusions of apatite. Under plane polarised transmitted light (**Fig. 7.9A**), titanite is typically brown to white depending on its thickness. Although homogeneous on first sight, all titanite grains show complex grey-scale patterns in BSE images (**Fig. 7.9B–D**) corresponding to differences in the mean atomic number. As demonstrated by X-ray maps (**Fig. 7.10**) much of this zonation is explicable by a non-uniform distribution of major elements (Si, Al, Ti, Ca) across a given titanite crystal. Four different styles of compositional zoning could be discerned, all of which have been described before in the literature and appear, in combination, typical if not diagnostic of magmatic titanite (e.g. Paterson & Stephens 1992; McLeod et al. 2011; Bruand et al. 2014):

- Faint zoning with gradual transitions from light grey to dark grey
- Oscillatory zoning, marked by rhythmical to cyclic recurrence of thin concentric growth rims
- Sector zoning, locally resembling a schematic "fir-tree" (Paterson & Stephens 1992, p. 382)
- Convoluted patchy zoning (possibly another form of sector zoning)

Most grains display more than one type of zonation at a time, suggesting they are all part of the of

the same titanite generation. This is also supported by their uniform optical appearance and the lack of mineral inclusions other than apatite. Importantly, no sieve-textured titanite grains, resorption zones, nor a discrete core-rim segmentation was observed, suggesting continuous mineral growth. As expected, planar deformation features, mosaicism, or other microstructural products of shock metamorphism (cf. Papapavlou et al. 2018b) are absent; all observed fractures (radial cracks emanating from apatite inclusions (**Fig. 7.9B–D**) are considered artefacts of the sample preparation.

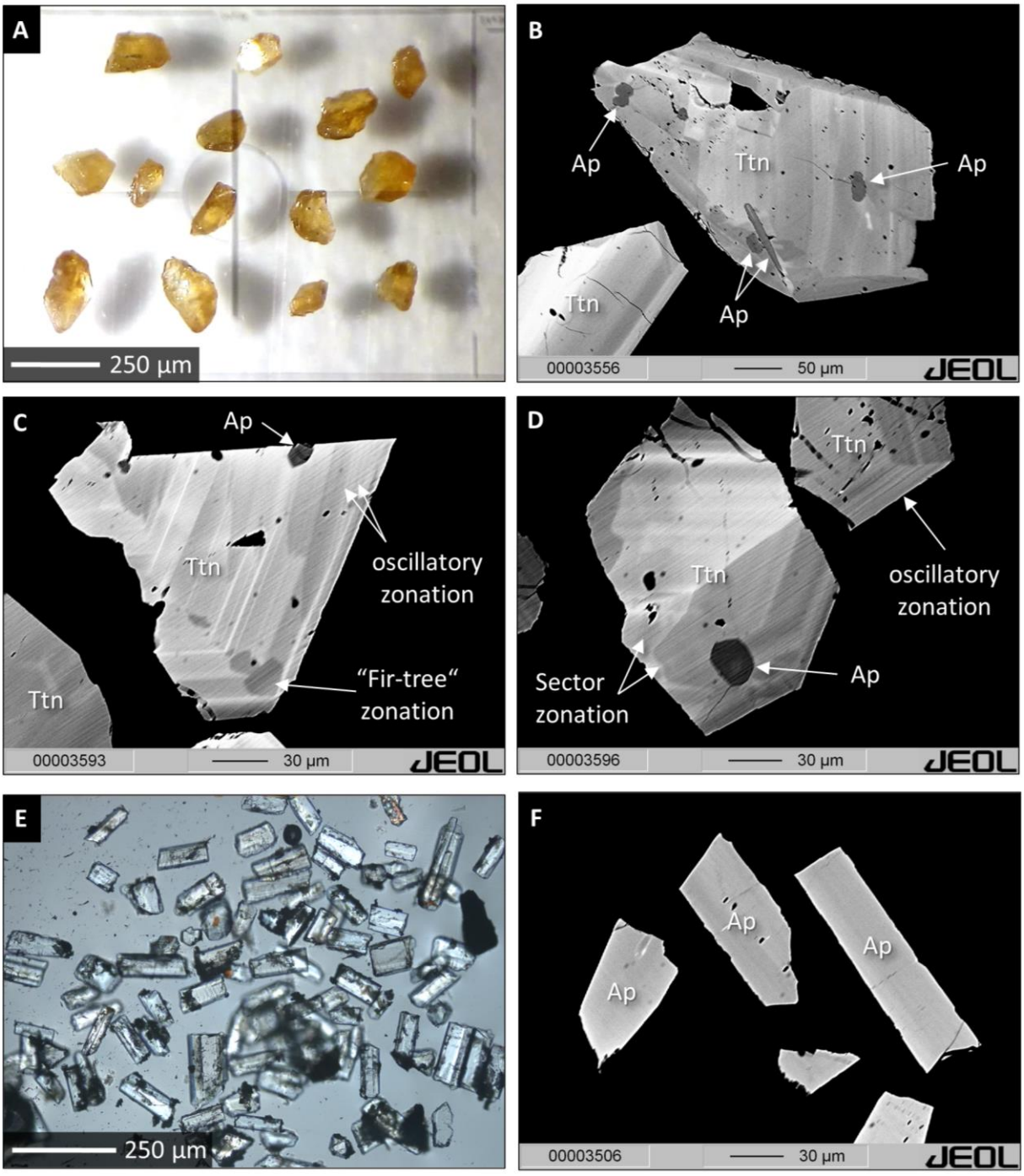

Figure 7.9 Representative microphotographs of the titanite and apatite picked for U-Pb dating; **A:** polished epoxy mount photographed through a stereomicroscope, showing grains of titanite; **B–D:** BSE images highlighting several features of these titanite grains; note the inclusions of euhedral apatite grains; **E:** polished mount under transmitted light and plane polars, showing multiple apatite grains; **F:** BSE images of these apatite grains demonstrating their compositional homogeneity. Abbreviations: Ttn = titanite; Ap = apatite.

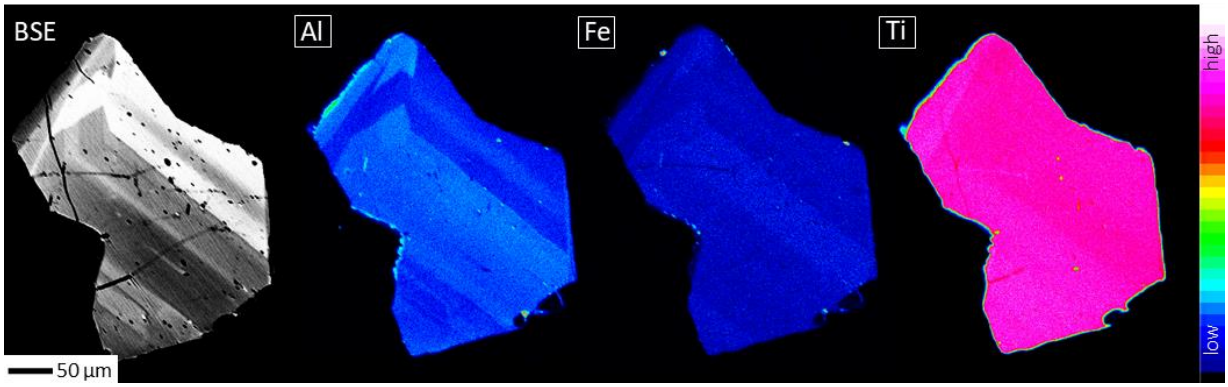

Figure 7.10 BSE image of a compositionally zoned titanite grain and three corresponding qualitative X-ray maps; intensities of Al (Kα), Fe (Kα) and Ti (Kα) are given in counts per second; pixel size is 0.04 µm.

Apatite is about two orders of magnitude more abundant than titanite in the least magnetic heavy mineral fraction. Under optical microscopes (e.g. **Fig. 7.9E**), all apatite grains are remarkably uniform with respect to length (90–120 µm), diameter (25–35 µm), habit (acicular simple prismatic dominated by the $\{10\bar{1}0\}$ form; rare instances of fully developed hexagonal pyramids $\{10\bar{1}\bar{1}\}$), and general optical appearance (colourless, clear, homogeneous, vitreous lustre), suggesting they all are part of one and the same generation. No compositional zoning was observed in BSE images (**Fig. 7.9F**) nor were any inhomogeneities recognised in EMP generated X-ray maps. No doubt, the extracted apatite is the same as observed in thin section, and the same as enclosed in titanite.

U-Pb isotope systematics

A total of 49 titanite grains were selected for U–Pb geochronology, with one spot having been analysed per grain. All of them have relatively low U and high Th concentrations (2.9–8.76 ppm U; Th/U 1.58–15.5; Appendix_3). In $^{238}U/^{206}Pb$ vs. $^{207}Pb/^{206}Pb$ space, the data define a linear array that reflects binary mixing between common Pb and radiogenic Pb (**Fig. 7.11A**). A raw, unanchored regression calculated using 48 data points (excluding one outlier with extremely high common Pb) yields a lower intercept at 1871.76 ± 8.78 Ma (MSWD = 0.49), and an initial $^{207}Pb/^{206}Pb$ ratio of 0.938 ± 0.015. The latter ratio is slightly lower than that predicted by the Stacey & Kramers (1975) crustal evolution model at 1.87 Ga ($^{207}Pb/^{206}Pb$ = 0.98), but similar to the corresponding mantle value of Zartman & Doe (1981). The error of the regression can be somewhat improved by forcing ("anchoring") the isochron through a fixed $^{207}Pb/^{206}Pb$ ratio, in this case a $^{207}Pb/^{206}Pb$ ratio 0.938 (**Fig. 7.11B**). This yielded a lower intercept at 1872 ± 4.02 Ma (MSWD = 0.48), corresponding to a weighted mean $^{238}U/^{206}Pb$ date of 1871.79 ± 3.45 Ma (MSWD = 0.92) (**Fig. 7.11C**).

Additional 69 apatite grains (69 spots) were analysed by means of LA-ICP-MS, with target domains having consistently low U but high Th concentrations (0.1–3.1 ppm U; Th/U 5.50–26.2; Appendix_3). When plotted on a Tera-Wasserburg diagram, these data also define a linear array due to variable contamination with initial common Pb (**Fig. 7.11D**). A free regression passing through all 69 data points yields a lower intercept at 1849.51 ± 6.17 Ma (MSWD = 0.67), which is similar to the above titanite date. A y-intercept at 0.9032 ± 0.0050 is, however, lower than obtained on the titanite fraction. Excluding the five analyses with the highest common lead ($^{238}U/^{206}Pb$ < 1.5), which have typically the largest influence on the slope of the isochron, gave a lower intercept at 1850.50 ± 9.31 Ma (MSWD = 0.65). A regression anchored by a $^{207}Pb/^{206}Pb$ ratio of 0.905 (i.e., the y-intercept in **Fig. 7.11D**) yields a lower intercept at 1850.74 ± 5.04 Ma (MSWD = 0.64) (**Fig. 7.11E**), and a weighted mean $^{238}U/^{206}Pb$ date of 1851.43 ± 3.34 Ma (MSWD = 1.56) (**Fig. 7.11F**).

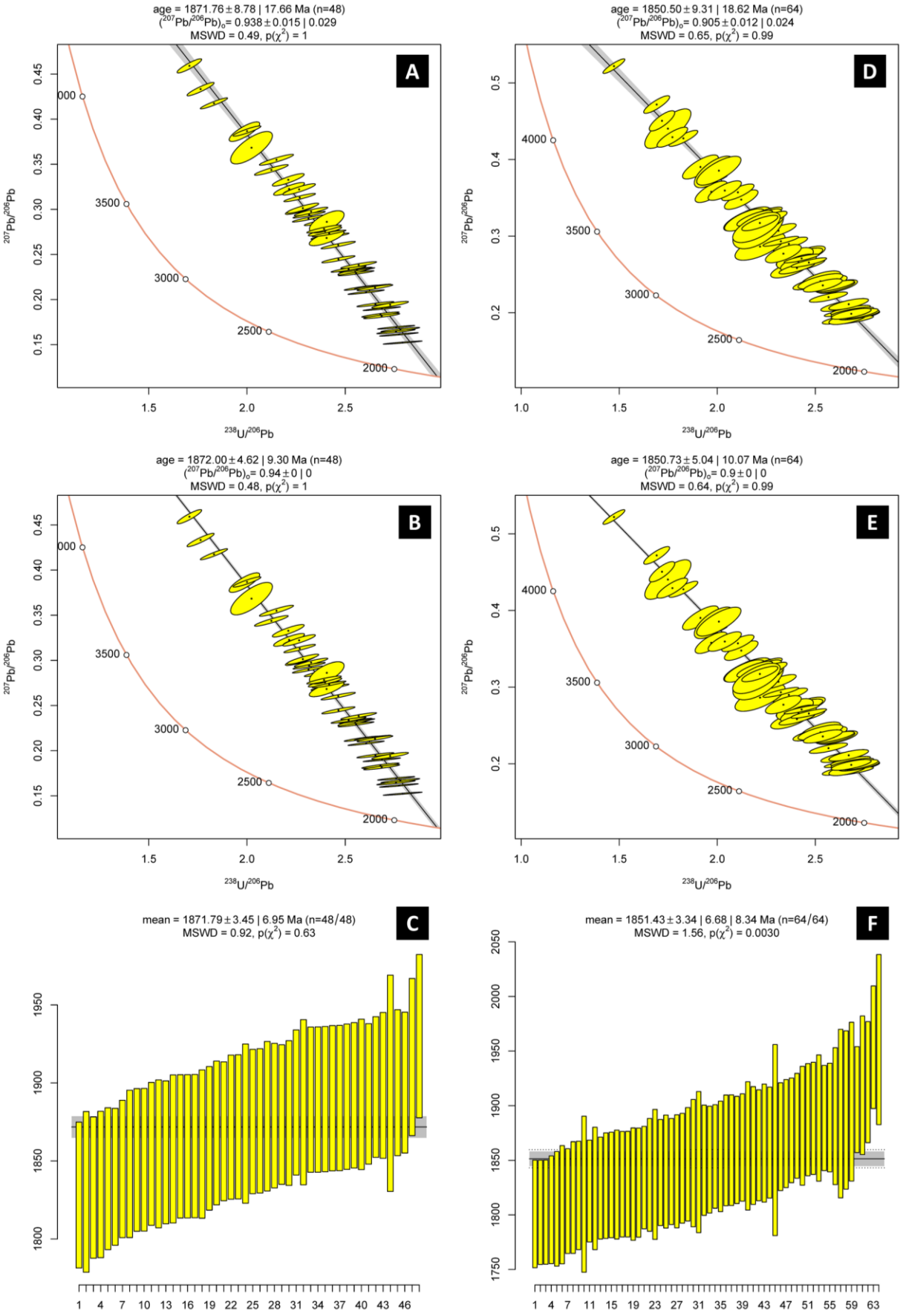

Figure 7.11 Uranium-Pb isotope plots for **A–C:** titanite; **D–F:** apatite. Individual analyses are shown as 2σ uncertainty ellipses; **A** and **D** show Tera-Wasserburg plots with unanchored regressions; **B** and **E** show anchored (^{207}Pb-corrected) regressions; **C** and **F** show weighted mean ^{207}Pb-corrected ^{206}Pb/^{238}U dates.

7.8 Geochemistry

General characteristics

Major- and trace element concentration data of selected representative samples from the alkaline diabase at Mackelcan Township, covering both clasts and the undisturbed dyke, are reported in **Table 7.2.** The rock has a uniform, subaluminous and in terms of SiO_2 (41.8–44.7 wt%) ultrabasic composition. Fe_2O_3 (representing total iron) ranges from 14.0 to 16.3 wt%, and MgO ranges from 5.6 to 7.1 wt% (Mg# 44–50). Relatively low alkali metal concentrations (< 3.5 wt% in total) are contrasted by high concentrations of CaO (10–12 wt%). The LOI is typically 2–3 wt% except for a few altered outliers with up to 7 wt% volatile content. The most prominent feature of the rock is, however, an extreme enrichment in HFSE such as, P_2O_5 (0.6–0.7 wt%), TiO_2 (3.1–3.6 wt%), Nb (35–56 ppm), Zr (148–238 ppm) and V (267–326 ppm). Concentrations of Cr (69–358 ppm) and Ni (61–214 ppm), on the other hand, are rather typical of most mafic rocks. Thorium and U show a moderate enrichment (3.6 and 0.8 ppm on average, respectively), so do the ΣREE+Y (240–300 ppm in total; La/Yb 22). The rock's CIPW normative mineralogy is as follows: 53 vol% plagioclase, 21 vol% diopside, 13 vol% olivine, 6 vol% ilmenite/magnetite, 4 vol% orthoclase, 2 vol% nepheline and 1 vol% apatite. Its hypothetical density, according to the CIPW norm, is 3.1 g/cm^3.

Geochemical data for the alkaline diabase in drill core M-SH-2, Sheppard Township, are presented in **Table 7.3**, and reveal broad similarities to the alkaline diabase found in outcrop. The rock also has a uniform, subaluminous and ultrabasic composition with equally low concentrations of SiO_2 (40.3–45.9). Fe_2O_3 ranges from 12.0 to 13.8 wt%, and MgO from 6.6 to 7.8 wt%. The LOI is generally below 5 wt% except for one chloritised and calcified specimen (sample SH2-11) with 10 wt% of volatiles. The rock is slightly less evolved compared to the diabase from Mackelcan Township, as evident from higher Mg# (53–57), and overall lower concentrations of incompatible lithophile elements, e.g., Zr (65–132 ppm), Th (avg. 2.2 ppm), U (avg. 0.5 ppm) and ΣREE+Y (98–147 ppm; La/Yb 12), whilst concentrations of Cr, Ni and V are almost the same. The more primitive character of the M-SH-2 diabase compared to its (presumed) equivalent at Mackelcan Township is also reflected in its higher modal proportions of mafic minerals according to the CIPW norm: 48 vol% plagioclase, 23 vol% diopside, 10 vol% hypersthene, 7 vol% orthoclase, 7 vol% olivine, 5 vol% ilmenite and magnetite, and 0.5 vol% apatite. The hypothetical density of the rock is 3.1 g/cm^3.

Igneous rock classification

In terms of total alkali vs. silica content (not shown), both dykes would be classified as tephrite. However, as will be discussed below, concentrations of Na and K are presumably not representative of the protolith. Using typical fluid-immobile trace elements (**Fig. 7.12A,B**), the dykes and the clasts are consistently classified as alkali basalt/gabbro. This is, for instance, demonstrated in the plot Nb/Y vs. Zr/Ti (**Fig. 7.12C**), where all data form very tight clusters within the field of alkali basalts, and corresponding to the composition of a modern ocean island basalt (OIB). An alkaline composition similar to modern OIB (and alkaline within plate basalts in general) is further supported by a range of classification schemes including the Ti/V plot (**Fig. 7.12D**); the Ti/P plot after Floyd & Winchester (1975); the Th/Ti/Hf ternary plot after (Wood 1980); the Zr/Nb/Y ternary plot after Meschede (1986), and especially the more commonly used Ta/Yb vs. Th/Yb plot (**Fig. 7.12E**) and the similar Nb/Yb vs. Th/Yb plot after Pearce (2008). Also, an OIB-like trace element signature is consistent with the normalised trace element patterns shown in **Figure 7.12F**.

Table 7.2 Major element oxide concentrations (wt%) and trace element concentrations (ppm) in alkaline diabase, Mackelcan Township

	LAU-1	LAU-2	LAU-3	LAU-5	LAU-6	LAU-10	AK18-5	AK18-6	LAU-8	AK18-7	AK19-12	AK19-13	AK19-14	AK19-15	AK19-16	AK19-17	AK19-18	AK19-19	AK19-20
Lat.	46°52 03	46°52 03	46°52 03	46°52 03	46°52 03	46°52 03	46°52 03	46°52 03	46°52 05	46°52 18	46°52 19	46°52 21	46°52 42	46°52 14	46°52 10	46°52 09	46°51 54	46°51 47	46°51 46
Long.	80°36 54	80°36 54	80°36 54	80°36 54	80°36 54	80°36 54	80°36 54	80°36 54	80°36 52	80°36 36	80°36 48	80°36 51	80°37 11	80°36 30	80°36 20	80°36 17	80°35 52	80°35 43	80°35 41
SiO_2	43.8	43.9	44.2	43.9	44.6	43.8	44.2	41.8	43.1	43.8	44.6	43.7	44.6	43.9	44.2	43.9	44.7	43.6	43.6
TiO_2	3.37	3.19	3.35	3.38	3.38	3.41	3.08	3.14	3.19	3.41	3.26	3.39	3.29	3.32	3.40	3.36	3.53	3.56	3.47
Al_2O_3	13.4	13.7	13.2	13.4	13.2	13.4	13.5	12.6	13.0	13.4	13.6	13.2	13.6	13.4	13.2	13.6	11.8	13.8	13.5
Fe_2O_3	15.5	15.2	14.7	15.7	14.0	15.5	15.0	14.4	15.4	15.5	15.1	16.3	15.1	15.5	15.2	15.5	16.2	15.9	15.7
MgO	6.0	6.0	5.9	6.0	6.3	6.0	6.5	5.7	6.1	6.0	6.3	6.1	5.7	5.9	5.9	6.4	7.1	5.9	5.6
CaO	10.6	11.1	12.1	10.3	11.1	9.7	10.8	8.5	9.5	11.1	10.1	9.8	5.6	10.6	10.2	10.3	10.7	10.0	10.4
MnO	0.23	0.22	0.22	0.22	0.22	0.22	0.22	0.15	0.24	0.24	0.22	0.23	0.16	0.23	0.22	0.22	0.22	0.25	0.22
Na_2O	3.0	2.8	2.8	2.9	2.8	3.2	2.7	3.3	2.4	2.9	3.0	3.1	4.0	2.7	3.0	2.9	2.6	2.9	3.1
K_2O	0.35	0.31	0.20	0.39	0.42	0.40	0.75	2.68	0.74	0.44	0.25	0.43	0.41	0.83	0.66	0.41	0.40	0.20	0.47
P_2O_5	0.64	0.60	0.66	0.61	0.66	0.66	0.60	0.60	0.60	0.64	0.67	0.60	0.57	0.62	0.63	0.62	0.58	0.64	0.67
LOI	2.2	2.3	2.1	2.3	2.3	2.4	2.2	7.2	5.9	2.0	2.7	2.5	7.3	2.2	2.6	2.6	2.0	2.8	2.9
Total	99.11	99.27	99.36	99.12	98.99	98.71	99.41	100.09	100.07	99.42	99.82	99.48	100.34	99.18	99.22	99.77	99.93	99.42	99.55
V	323.7	290.4	325.8	307.6	317.2	310.3	291.1	289.0	313.2	318.2	267.1	304.3	284.2	296.3	301.4	298.2	312	310.6	299.8
Cr	110.5	246.3	87	121.2	110.3	358.4	214.3	82.25	100	87.10	173.8	164.5	76.48	72.35	160.3	97.82	99.07	68.60	89.02
Ni	80.02	159.2	72.69	88.52	80.43	213.9	138.2	62.49	76.75	69.81	112.5	108.1	61.81	63.38	107.2	81.24	74.2	61.33	74.29
Cu	94.62	69.98	133	61.96	220.8	101.8	101.0	73.91	93.19	87.99	82.24	75.17	79.35	51.33	82.23	69.21	44.34	90.62	76.02
Rb	14.5	12.71	3.072	15.40	11.61	11.92	40.04	203.2	39.69	17.98	5.505	21.62	5.529	55.34	41.67	14.41	19.33	4.855	23.06
Sr	950	437.0	1294	803.9	482.1	344.1	446.9	587.7	643.3	342.8	949.1	1057	239.6	860.5	772.2	738.1	836.8	861.1	844.8
Y	29.79	27.28	28.11	27.81	27.64	29.10	26.85	25.62	26.66	28.20	26.97	27.41	24.94	26.97	27.11	26.49	25.61	29.06	28.36
Zr	206.5	166.8	185	237.1	163.4	205.8	165.9	185.5	182.5	222.7	197.4	209.9	215.6	209.0	215.3	190.5	148.2	220.2	237.3
Nb	47.74	50.08	44.18	47.21	43.77	56.17	47.97	42.59	46.02	47.36	51.91	51.66	47.70	49.27	52.36	47.93	35.37	51.23	51.88
Ba	95.93	83.13	81.02	112.2	164.6	131.8	137.8	245.5	202.5	200.0	169.7	116.2	53.85	171.6	245.3	165.0	166	296.8	352.0
La	47.97	44.81	45.13	44.56	43.42	48.10	43.18	44.03	43.27	46.45	47.42	47.09	46.03	46.44	44.23	43.51	34.51	50.97	49.12
Ce	109.6	103.0	103.3	104.4	101.0	110.4	99.37	100.6	97.27	106.9	109.2	108.4	105.2	106.0	104.4	101.4	85.99	113.7	111.5
Pr	13.9	13.42	13.24	13.54	13.30	14.17	12.96	13.07	13.12	13.77	13.81	13.59	13.07	13.43	13.06	12.86	11.1	14.74	14.02
Nd	59.65	57.25	57.1	57.68	56.63	60.29	56.35	56.62	55.53	58.64	54.67	53.40	51.60	52.66	51.99	50.70	48.83	57.43	55.27
Sm	11.21	11.20	10.94	11.04	11.06	11.45	10.82	10.65	10.26	11.21	10.07	10.03	9.511	9.854	9.748	9.644	9.549	10.77	10.28
Eu	3.499	3.316	3.497	3.444	3.457	3.511	3.334	3.197	3.375	3.481	3.247	3.186	2.879	3.184	3.230	3.133	3.27	3.499	3.348
Tb	1.238	1.096	1.176	1.172	1.104	1.199	1.107	1.047	1.145	1.182	1.178	1.183	1.114	1.178	1.184	1.151	1.083	1.273	1.183
Gd	9.68	8.864	9.225	9.185	8.784	9.556	8.761	8.417	8.981	9.413	8.867	8.745	8.285	8.696	8.760	8.585	8.609	9.473	8.815
Dy	6.585	6.164	6.23	6.319	6.248	6.617	6.204	5.825	6.193	6.484	5.790	5.799	5.434	5.818	5.865	5.793	5.849	6.285	5.832
Ho	1.137	1.042	1.071	1.086	1.028	1.143	1.041	0.976	1.055	1.111	1.017	1.021	0.940	1.025	1.038	1.014	0.98	1.094	1.021
Er	2.899	2.623	2.706	2.756	2.621	2.903	2.599	2.499	2.644	2.851	2.676	2.725	2.594	2.721	2.757	2.722	2.502	2.981	2.688
Tm	0.374	0.329	0.34	0.323	0.325	0.360	0.330	0.324	0.333	0.363	0.324	0.327	0.312	0.329	0.334	0.327	0.299	0.351	0.331
Yb	2.238	1.981	2.056	2.138	1.927	2.230	1.975	2.018	2.014	2.214	2.000	2.089	1.968	2.071	2.085	2.017	1.801	2.200	2.019
Lu	0.325	0.274	0.302	0.314	0.271	0.322	0.282	0.285	0.286	0.320	0.300	0.312	0.301	0.306	0.309	0.293	0.255	0.330	0.299
Hf	5.033	4.240	4.627	5.043	4.258	5.075	4.180	4.553	4.31	5.150	5.069	5.281	5.399	5.240	5.418	4.892	4.068	5.631	5.258
Ta	2.787	2.628	2.622	2.764	2.581	2.833	2.652	2.551	2.83	2.833	2.698	2.696	2.657	2.733	2.761	2.651	2.154	2.924	2.681
Pb	6.213	6.352	6.233	6.898	7.228	5.789	6.067	13.11	8.268	9.926	8.648	6.810	17.00	14.71	8.551	6.872	6.58	8.402	10.03
Th	3.644	3.467	3.3	3.456	3.299	3.966	3.418	3.411	3.532	3.928	3.193	3.158	3.158	3.195	3.154	3.084	2.595	3.483	3.382
U	0.797	0.791	0.745	0.599	0.778	0.860	0.762	0.880	0.762	0.833	0.742	0.763	0.780	0.740	0.848	0.805	0.914	1.030	0.800

Table 7.3 Major element oxide concentrations (wt%) and trace element concentrations (ppm) in alkaline diabase from Falconbridge's 1991 DDH, Sheppard Township

	SH2-13	SH2-12	SH2-11	SH2-10	SH2-9	MSH-02A*	SH2-14	SH2-8	SH2-7	MSH-02B*	SH2-5	SH2-4	SH2-6	MSH-02C*
Depth [m]	1369.10 m 1369.25 m	1370.30 m 1370.48 m	1371.45 m 1371.55 m	1372.90 m 1373.00 m	1373.18 m 1373.30 m	1373.18 m 1373.37 m	1373.37 m 1373.52 m	1373.64 m 1373.80 m	1374.52 m 1374.67 m	1374.52 m 1374.80 m	1375.15 m 1375.40 m	1376.00 m 1376.15 m	1376.40 m 1376.55 m	1376.40 m 1376.70 m
SiO_2	45.4	44.9	40.3	45.9	45.3	44.9	45.9	45.4	44.1	44.5	45.8	45.4	45.1	45.1
TiO_2	1.91	1.98	1.69	2.05	1.96	1.89	2.05	1.98	2.02	2	1.99	2.00	1.98	1.87
Al_2O_3	13.4	13.9	15.1	13.6	13.6	13.4	13.9	13.6	14.1	13.9	13.8	13.6	13.7	13.2
Fe_2O_3	13.7	13.3	13.8	12.7	13.4	13	13.5	13.1	13.6	13.8	13.1	13.0	12.5	12
MgO	7.4	7.1	7.8	6.7	6.8	6.63	6.9	6.6	7.0	7.12	7.3	7.2	7.5	6.88
CaO	11.2	11.5	9.3	12.5	12.9	12.6	11.5	12.9	12.2	10.9	11.4	12.4	11.6	11.8
MnO	0.23	0.23	0.22	0.20	0.21	0.21	0.21	0.21	0.22	0.22	0.22	0.22	0.22	0.21
Na_2O	1.5	1.2	1.9	1.8	1.6	1.6	1.9	1.5	1.4	1.65	1.5	0.9	0.5	0.28
K_2O	0.69	1.4	0.84	0.64	0.54	0.68	0.55	0.67	0.91	0.91	0.95	1.19	1.9	1.91
P_2O_5	0.15	0.18	< 0.02	0.23	0.21	0.25	0.19	0.21	0.18	0.25	0.18	0.20	0.19	0.23
LOI	4.2	4.3	10.1	3.9	3.5	4.01	2.7	3.3	3.5	3.74	3.3	3.2	4.4	5.97
Total	99.72	99.94	101.09	100.17	99.93	99.17	99.25	99.39	99.15	98.99	99.63	99.32	99.61	99.45
V	283.8	334.1	295.4	297.2	279.1	290	311.8	326.3	314.1	299	335.4	305.3	320.5	286
Cr	258.8	149.2	131.7	364.3	159.9	131	133.5	143	113.8	126	177.7	109.5	164.3	124
Ni	183.2	127.1	115	183.9	110.1	96	109.3	129.5	100.8	154	145.2	103.0	133.1	102
Cu	146.4	126.7	16.14	106.6	149.0	169	109.6	152.1	131.8	191	132.7	127.4	200	121
Rb	31.90	52.6	21.08	24.05	21.69	25.9	20.01	25.08	33.18	34.5	42.25	55.69	72.56	78.6
Sr	953.0	904.8	500.8	1057	1124	1042	485.6	1041	527.4	1005	956.7	1214	961.4	1018
Y	18.74	19.7	15.07	20.72	19.33	19.8	19.20	20.16	19.76	19.7	20.49	19.89	20.5	19.2
Zr	107.8	103.7	64.92	124.6	119.6	130	131.5	101.2	123.4	132	98.39	116.7	95.57	124
Nb	24.87	22.68	11.58	28.22	22.07	21	21.90	21.98	20.61	21	23.14	20.54	22.13	20
Ba	116.1	217	233.7	103.4	115.9	130	113.7	136.1	242.8	229	230	255.4	417.4	386
La	19.14	20.1	15.03	20.57	20.26	21.1	20.67	20.39	19.84	21.5	19.63	19.96	19.77	20.5
Ce	43.60	43.44	30.82	47.8	45.90	47.2	47.18	43.91	45.40	48.2	43.28	46.26	43.3	45.1
Pr	5.706	5.956	4.104	6.3	6.013	6.26	6.177	6.011	6.015	6.35	5.951	6.100	5.961	5.85
Nd	25.03	25.64	17.35	27.36	26.29	27.1	26.86	25.99	26.36	27.5	26.31	26.54	26.28	25.8
Sm	5.362	5.422	3.684	5.923	5.631	5.7	5.762	5.549	5.713	5.9	5.608	5.654	5.595	5.6
Eu	1.671	1.728	1.227	1.816	1.742	1.9	1.714	1.82	1.690	1.79	1.857	1.789	1.906	1.88
Tb	0.680	0.718	0.52	0.728	0.706	0.76	0.722	0.735	0.727	0.78	0.748	0.725	0.745	0.73
Gd	4.922	5.097	3.648	5.231	5.066	5.32	5.295	5.203	5.317	5.29	5.279	5.249	5.241	5.1
Dy	3.923	4.11	3.023	4.298	4.051	4.32	4.218	4.189	4.236	4.34	4.266	4.171	4.228	4.04
Ho	0.719	0.748	0.56	0.788	0.744	0.81	0.744	0.767	0.784	0.82	0.773	0.766	0.766	0.76
Er	1.925	1.982	1.505	2.138	2.009	2.19	2.037	2.03	2.102	2.15	2.06	2.059	2.052	2.05
Tm	0.235	0.271	0.204	0.264	0.248	0.3	0.273	0.274	0.278	0.29	0.275	0.252	0.274	0.28
Yb	1.614	1.619	1.208	1.842	1.727	1.8	1.724	1.652	1.761	1.8	1.674	1.731	1.655	1.7
Lu	0.239	0.234	0.175	0.281	0.261	0.33	0.259	0.241	0.263	0.33	0.237	0.259	0.238	0.27
Hf	2.905	2.633	1.834	3.351	3.200	3	3.311	2.58	3.143	4	2.742	3.180	2.352	3
Ta	1.116	1.261	0.641	1.280	1.215	1.2	1.232	1.29	1.193	1.3	1.27	1.204	1.246	1.2
Pb	7.129	5.768	3.266	8.851	27.63	23	12.86	14.72	15.39	19	27.3	27.70	52.72	51
Th	2.089	2.101	2.534	2.460	2.222	2.3	2.342	2.08	2.226	2.4	2.069	2.117	2.076	2.2
U	0.409	0.537	0.714	0.481	0.426	0.64	0.576	0.552	0.559	0.65	0.533	0.431	0.526	0.58

Samples denoted with an asterisk (*) were analysed at the commercial AGAT Laboratories, Toronto (see Whymark 2019, for details); n.a. = not available or not analysed

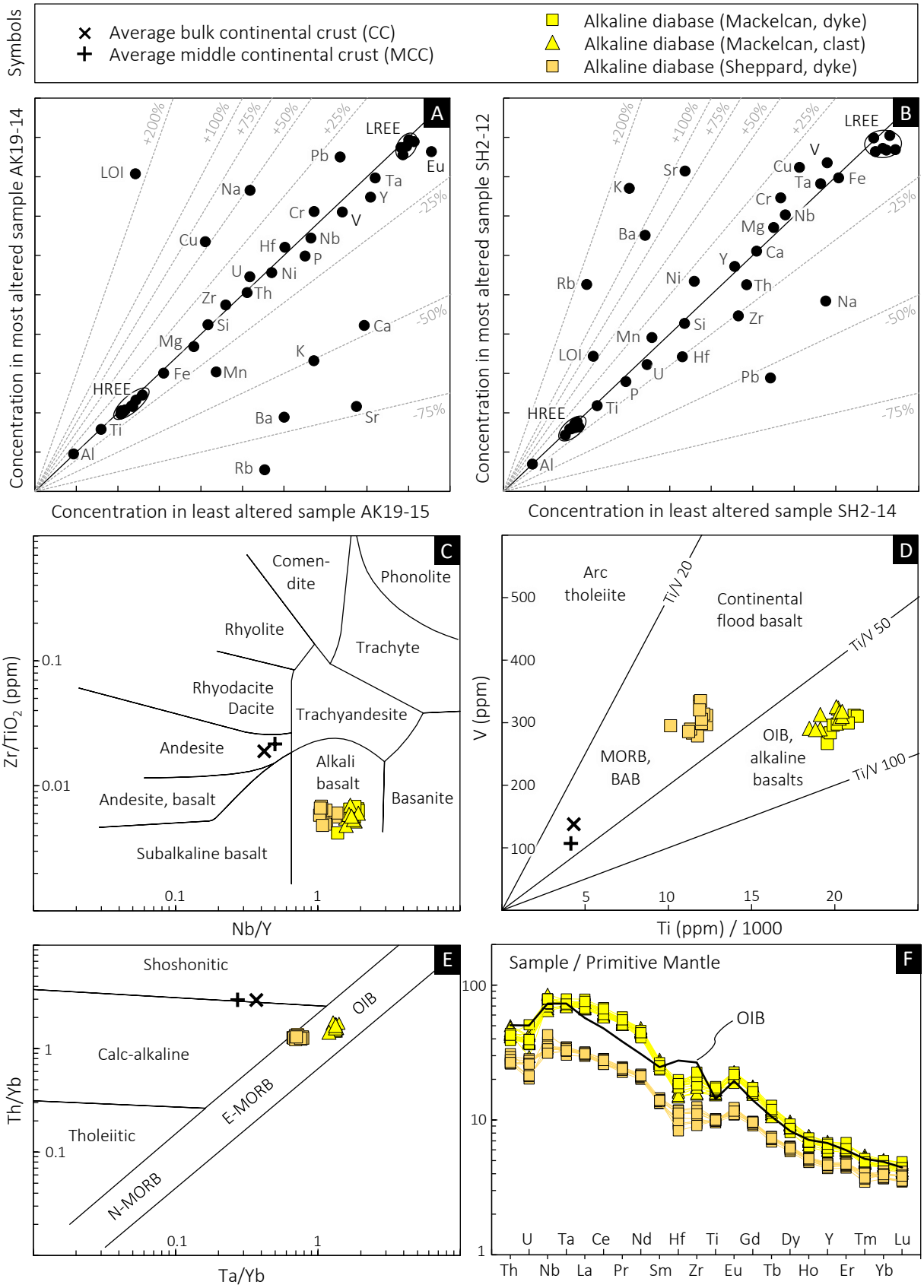

Figure 7.12 A selection of plots used to illustrate the effects of metasomatism on, and the geochemical classification and magmatic affinity of, the alkaline diabase dykes and related clasts; **A:** isocon diagram after Grant (1986) as a means of testing for secondary element mobility, applied to the diabase from Mackelcan Township; **B:** same diagram for the diabase from Sheppard Township; **C:** discrimination plot after Winchester & Floyd (1977); **D:** discrimination plot after Shervais (1982); **E:** discrimination plot after Pearce (1983); **F:** spidergram with normalisation and OIB values after McDonough & Sun (1995); crustal values from Rudnick & Gao (2013); propagated 2σ-error bars are in each panel smaller than the symbol size.

Nd-Sr-Pb isotopes

A summary of whole-rock radioisotope data for the alkaline diabase dyke and associated clasts in Sudbury Breccia from Mackelcan Township is presented in **Table 7.4**. All sample have a narrow range in $^{143}Nd/^{144}Nd$ corresponding to a quite un-radiogenic present-day εNd between –17.29 and –16.31. The $^{147}Sm/^{144}Nd$ ratio ranges from 0.113 to 0.118. There is no discernible difference in the isotopic composition between the diabase dyke and the clasts. This is aligned with the trace element data presented above and provides additional support for a genetic relationship between the clasts and the dyke. In $^{147}Sm/^{144}Nd$ vs. $^{143}Nd/^{144}Nd$ space, all nine samples define a broadly linear array, but without any age significance. One-stage Nd model ages (t_{DM}) are between 1891 Ma and 1990 Ma, and 1948 Ma on average. Interestingly, these model ages correspond closely the U-Pb ages of ca. 1872 ± 3 Ma obtained on titanite. Using the 1872 ± 3 Ma as the best age constraint on the intrusion and magmatic crystallisation for both the clasts and the dyke, initial εNd values have been calculated. The εNd_{1872} has a very narrow range, between +2.29 and +3.52. The measured $^{87}Sr/^{86}Sr$ ratio for the dyke and the clasts ranges from 0.706 to 0.771, and the calculated $^{87}Rb/^{86}Sr$ ratio from 0.245 to 1.150. These data do not permit to calculate any meaningful isochron age. The $^{87}Sr/^{86}Sr_{1872}$ ranges considerably, from 0.6988 to 0.7421. The $^{206}Pb/^{204}Pb$ ratio ranges from 16.72 to 17.70, $^{207}Pb/^{204}Pb$ from 15.38 to 15.41, and $^{208}Pb/^{204}Pb$ from 35.95 to 37.03. In terms of uranogenic lead, the samples fall on the Zartman & Doe (1981) isotopic evolution curve of the lower crust (μ = 5.9) and the mantle (μ = 8.9). The thorogenic Pb corresponds more to the mantle evolution curve (κ = 3.6), rather than to the lower crustal evolution (κ = 5.9). The very limited spread in measured Pb isotope ratios is, again, without age significance.

Table 7.4 also includes radioisotope data for seven samples of the alkaline diabase dyke intersected in the drill core from Sheppard Township. The rock has a uniform $^{143}Nd/^{144}Nd$ corresponding to an εNd between –14.28 and –13.68. The $^{147}Sm/^{144}Nd$ ratio ranges from 0.113 to 0.118. In $^{147}Sm/^{144}Nd$ vs. $^{143}Nd/^{144}Nd$ space, the samples do not define a linear array, and hence do not permit the calculation of an isochron age. The one-stage Nd model ages (t_{DM}) for the diabase form Sheppard Township ranges from 1970 Ma to 2073 Ma (2015 Ma on average). Assuming a crystallisation age of 1872 Ma, the initial εNd_{1872} ranges from +1.65 to +2.70. These values compare well to the data obtained on the alkaline diabase dyke from Mackelcan Township. The measured $^{87}Sr/^{86}Sr$ ratio has a narrow range, from 0.713 to 0.717, and the calculated $^{87}Rb/^{86}Sr$ ratio ranges from 0.254 to 0.406; the initial $^{87}Sr/^{86}Sr_{1872}$ is between 0.7051 and 0.7069. The $^{206}Pb/^{204}Pb$ ratio ranges from 15.79 to 16.94, $^{207}Pb/^{204}Pb$ from 15.32 to 15.46, and $^{208}Pb/^{204}Pb$ from 35.09 to 36.10. These values correspond to the Pb isotopic evolution curve of the mantle and of the lower crust as defined by Zartman & Doe (1981). The spread in uranogenic Pb isotope ratios is statistically significant and can be used to construct a Pb-Pb whole-rock isochron through six analyses (excluding one outlier). Using a maximum likelihood regression (York et al. 2004; Vermeesch 2018) and the 2σ uncertainties as listed in **Table. 7.4**, the data define an errorchron with a slope of 1895 ± 7 Ma (MSWD = 1,200); an ordinary least square regression gave an errorchron date of 1920 ± 231 Ma. Both regressions intercept the Stacey & Kramers (1975) evolution curve at ca. 1700 Ma. The datum obtained from these errorchrons, although being of questionable geological significance, comes close to the U-Pb titanite and apatite dates obtained on the dyke from Mackelcan Township, and it is similar to the 1-stage Nd model ages. Further, the good regression helps to define an initial Pb isotope ratio (obtained from the intercept of the isochron/errorchron with the y-axis), that is, $^{207}Pb/^{204}Pb_0 = 13.49$, and $^{207}Pb/^{206}Pb_0 = 0.11$.

Table 7.4 Summary of whole-rock Nd-Sr-Pb isotope data for the alkaline diabase dykes and related clasts, Mackelcan and Sheppard Township

	$^{143}Nd/^{144}Nd$	±2σ	$^{147}Sm/^{144}Nd$	εNd present	εNd 1872 Ma	1-stage t_{DM}	$^{87}Sr/^{86}Sr$	±2σ	$^{87}Rb/^{86}Sr$	$^{87}Sr/^{86}Sr_{1872}$	$^{208}Pb/^{204}Pb$	±2σ	$^{207}Pb/^{204}Pb$	±2σ	$^{206}Pb/^{204}Pb$	±2σ
Alkaline diabase (dyke, outcrop), Mackelcan Township																
AK18-6	0.511756	12	0.114	–17.20	+2.79	1948 Ma	0.771227	12	1.150	0.7404	35.8562	24	15.2400	8	16.3634	8
AK18-7	0.511754	16	0.115	–17.25	+2.29	1990 Ma	0.709878	16	0.342	0.7007	35.9500	23	15.3975	8	16.7208	8
AK19-14	0.511752	13	0.111	–17.28	+3.25	1911 Ma	0.749397	12	0.274	0.7421	37.2581	26	15.5139	10	17.5768	9
AK19-18	0.511802	10	0.118	–16.31	+2.59	1968 Ma	0.705808	11	0.262	0.6988	36.2318	24	15.4130	9	17.4149	8
Alkaline diabase (clast, outcrop), Mackelcan Township																
LAU-1	0.511751	14	0.113	–17.29	+2.71	1954 Ma	0.719008	11	0.245	0.7125	36.8374	31	15.3770	10	17.4611	9
LAU-3	0.511768	21	0.116	–16.98	+2.49	1974 Ma	0.711799	11	0.253	0.7050	36.6783	30	15.3827	10	17.3860	8
LAU-5	0.511778	14	0.116	–16.77	+2.74	1955 Ma	0.720681	14	0.269	0.7135	36.5871	19	15.3756	7	17.2698	6
LAU-8	0.511769	10	0.112	–16.95	+3.52	1891 Ma	0.730441	12	0.373	0.7205	36.2631	29	15.3782	9	16.9302	8
LAU-10	0.511774	12	0.115	–16.85	+2.87	1943 Ma	0.722837	15	0.298	0.7149	37.0286	23	15.4025	8	17.6995	7
Alkaline diabase (dyke, drill core), Sheppard Township																
SH2-4	0.511936	13	0.129	–13.70	+2.66	1974 Ma	0.715630	11	0.326	0.7069	35.5311	22	15.3977	8	16.2449	6
SH2-6	0.511937	10	0.129	–13.68	+2.70	1970 Ma	0.717320	10	0.406	0.7064	35.4308	28	15.3997	8	16.1739	8
SH2-7	0.511929	13	0.131	–13.83	+2.00	2040 Ma	0.713842	15	0.372	0.7039	35.5389	26	15.3692	8	16.2123	9
SH2-9	0.511930	13	0.129	–13.82	+2.37	2002 Ma	0.713569	12	0.254	0.7068	35.0852	21	15.3169	8	15.7921	7
SH2-10	0.511910	11	0.131	–14.20	+1.65	2073 Ma	0.713830	14	0.263	0.7068	35.8908	23	15.4214	7	16.7150	7
SH2-13	0.511932	15	0.129	–13.77	+2.42	1998 Ma	0.714350	12	0.292	0.7065	36.0982	26	15.4604	9	16.9439	8
SH2-14	0.511906	13	0.130	–14.28	+1.86	2051 Ma	0.713443	15	0.313	0.7051	35.5427	22	15.3679	8	16.2821	7

$^{147}Sm/^{144}Nd$ and $^{87}Rb/^{86}Sr$ ratios were calculated using measured Sm, Nd, Rb and Sr concentrations, which are given in Table 7.2 and Table 7.3;
2σ uncertainties of $^{147}Sm/^{144}Nd$ and $^{87}Rb/^{86}Sr$ are < 3% based on the propagated analytical error of Sm, Nd, Rb and Sr concentration data;
$^{143}Nd/^{144}Nd$ ratios are normalised to $^{146}Nd/^{144}Nd = 0.72190$;
2σ uncertainties of $^{143}Nd/^{144}Nd$ are < 0.004% based on the long-term in-house reproducibility of BHVO-2;
2σ uncertainties of $^{87}Sr/^{86}Sr$ are < 0.007% based on the long-term in-house reproducibility of BHVO-2;
2σ uncertainties of $^{208}Pb/^{204}Pb$, $^{207}Pb/^{204}Pb$ and $^{206}Pb/^{204}Pb$ are < 0.18%, < 0.09% and < 0.5%, respectively, based on the long-term in-house reproducibility of BHVO-2;
For sake of readability, all listed 2σ absolute errors only refer to the last significant decimal digits of the measured isotope ratios;
εNd values were calculated relative to CHUR with $^{147}Sm/^{144}Nd = 0.1967$ and $^{143}Nd/^{144}Nd = 0.512638$;
One-stage Nd model ages (t_{DM}) were calculated according to DePaolo (1981a,b)

7.9 Interpretation

Assessment of post-depositional alteration

Both the two alkaline diabase dykes and their supposed clasts within the East Range Breccia Belt underwent significant post-magmatic changes as evident from the lack of preservation of primary igneous minerals and textures, and the preponderance of hydrous silicates (epidote, actinolite, chlorite, biotite). Some of these changes are seemingly the result of retrograde metamorphism at greenschist-facies conditions and are expected to have occurred under nearly isochemical conditions (i.e., simple hydration). Others, such as carbonatisation, silicification, hematitisation, and chloritisation, are more erratically distributed, only locally pervasive, or cut as veins across lithological contacts, which implies an open system behaviour of certain elements (e.g. Ca, Si, Fe, Mg, Al). Before anything else, it is necessary to assess the extent of this secondary element mobility, and to identify those immobile elements that are representative of the protolith's composition.

Application of the isocon method (Grant 1986) to the dyke from Mackelcan Township (**Fig. 7.12A**) reveals that most elements, the HFSE in particular, are constant and highly correlated between the most altered sample (AK19-14) and the least altered sample from a nearby location (AK19-15). In fact, the elements Ti, Al, REE, Th and Zr are, within the analytical uncertainty, identical between the two endmembers such that they define an isocon with a slope of 1.0. Most other elements plot on, or close to, this isocon, suggesting they have not been significantly mobilised either. This is also supported by very constant inter-element ratios (**Fig. 7.12C–E**) and by uniform and parallel trace element patterns (**Fig. 7.12F**). Some elements, however, plot either above or below the isocon. Although primary heterogeneities cannot be ruled out, the systematic displacement of certain (typically fluid-mobile) elements is more likely the result of post-magmatic processes, such as the alteration of feldspar or biotite. The following elements were identified as having been affected by metasomatism (with net concentration changes given in brackets): Ca (–47%), Sr (–72%), Ba (–69%), K (–51%), Rb (–90%), Pb (+16%), Na (+48%), Cu (+55%), and Mn (–30%).

The same approach can also be applied to the dyke from Sheppard Township, but the selection of the endmember samples requires some clarification. At first glance, sample SH2-11 would be defined as the most-altered endmember, but it is obvious that this sample, being composed of more than 50 vol% chlorite and calcite, has completely lost its primary geochemical signature. Sample SH2-11 will therefore be omitted from any further discussion. Alternatively, SH2-12 could be defined as an altered endmember, based on the intense chloritisation, biotitisation, and epidotisation observed in this sample. Contrasting the measured whole-rock composition of SH2-12 with that of the freshest sample available (SH2-14; **Fig. 7.7A,C–E**) reveals overall limited element mobility. Again, the HFSE and the transition metals define an isocon with a slope of one, and most other elements plot on or close to this straight line. Overall little mobility is further supported by constant Zr-Ti-V-Nb-Ta-Y-Yb ratios (**Fig. 7.12C–E**), and by smooth trace element patterns (**Fig. 7.12F**). In contrast, Na (–38%), K (+155%), Rb (+163%), Sr (+86), Ba (+91), and Pb (–55%), have apparently been mobilised to a significant extent. An apparent loss of Zr and Hf is indicated by the isocon method. It is, however, more likely that sample SH2-12 (dyke's margin) was affected by wall-rock contamination compared to sample SH2-14 (centre of the dyke), or that the apparent mobility of Zr and Hf is an analytical artifact, or simply the result of an inhomogeneous distribution of primary Zr-bearing phases, rather than the result of secondary Zr-Hf mobility.

An assessment if and to what extent fluid-rock interaction led to a disturbance of whole-rock isotope systematics can be achieved, for example, by comparing the isotopic composition of fresh and altered endmembers of the same lithology. As can be seen in **Figure 7.13A**, the measured $^{143}Nd/^{144}Nd$ ratio of the dyke from Mackelcan Township is within the analytical uncertainty indistinguishable from the diabase clasts found in Sudbury Breccia, with no resolvable difference between altered and fresh sample. Also, there is no correlation between the measured Nd isotope ratio and the measured whole-rock volatile content (i.e., H_2O and CO_2), suggesting that hydration and carbonatisation did not modify the Nd isotopic composition of the rock. This is consistent with the results of the isocon method, which implied immobility of Sm and Nd (**Fig. 7.12A**), and it is entirely consistent with widely held view that neither Sm nor Nd are particularly fluid mobile (e.g. Bau 1991) unless a very high fluid:rock ratio or high temperature (DePaolo & Wasserburg 1979). The Pb isotope ratios, in contrast, exhibit a wider scatter that is outside the analytical uncertainty (**Fig. 7.13B,C**), although the data show no correlation with the volatile content. Moreover, samples containing less than 5 wt% volatiles form a relatively tight cluster with respect to their measured $^{206}Pb/^{204}Pb$, $^{207}Pb/^{204}Pb$, and $^{208}Pb/^{204}Pb$, with the implication that these samples experienced little if any disturbance and could retain the primary isotopic signature of the protolith. The isocon method, on the other hand, has indicated that Pb concentrations, and perhaps U concentrations as well, had been affected by secondary mobility. Whether the Pb isotope ratios of the alkaline diabase from Mackelcan Township have any petrogenetic significance remains therefore unclear, especially if U/Pb disturbance did not occur recently. In contrast to the Nd and Pb isotope ratios, the measured $^{87}Sr/^{86}Sr$ ratio shows a strong positive correlation with the volatile content (R^2 = 0.81). The extremely radiogenic ratios obtained for some samples (up to 0.77) indicate either interaction with radiogenic (crustal?) fluid, a metasomatic gain of Rb and/or a loss of Sr (as also indicated by the isocon method). Samples with < 2 wt% LOI form tight clusters with respect to their measured $^{87}Sr/^{86}Sr$ and should thus approximate the isotopic signature of the photolith, although it cannot be ruled out that Rb-Sr disturbance had occurred even in those samples. When initial Sr isotope ratios are plotted against the initial εNd (**Fig. 7.13H**), the data define a linear array toward an unreasonably high $^{87}Sr/^{86}Sr_{1872}$ of up to 0.74. Other samples, in contrast, have a, for pristine igneous rocks impossible low, $^{87}Sr/^{86}Sr_{1872}$ ratio of 0.6988. Such large spread in initial $^{87}Sr/^{86}Sr$ ratios at relatively constant initial $^{143}Nd/^{144}Nd$ ratios is usually interpreted as the result of metasomatic decoupling of Sm-Nd and Rb-Sr isotope systematics (e.g. Rollinson 1993, p. 260).

The alkaline diabase dyke from Sheppard Township (or at least the interval intersected in the drill core) has a narrow range in measured Nd, Sr and Pb isotope ratios. The $^{143}Nd/^{144}Nd$ ratios are for all seven samples almost identical within the quoted analytical uncertainty, and they show nor co-dependency with the volatile content (**Fig. 7.13A**). Together with constant Sm/Nd ratios, it is suggested that the $^{143}Nd/^{144}Nd$ isotope ratio is most likely representative of the protolith's composition. The Pb isotope ratios show a large random scatter around the mean, but they exhibit no correlation with the LOI (**Fig. 7.13B,C**). The isocon method, on the other hand, indicates Pb was mobile to a significant extent (+86%). The $^{87}Sr/^{86}Sr$ is weakly correlated (R^2 = 0.29) with the volatile content, which is possibly due to interaction with more radiogenic fluid(s), or metasomatic Rb-gain/Sr-loss (**Fig. 7.12A**). When the initial $^{87}Sr/^{86}Sr_{1872}$ ratio is plotted against the εNd_{1872}, (**Fig. 7.13H**), the scatter is significantly reduced, but it persists, nonetheless. The linear array defined be the data is, again, indicative of post-magmatic, fluid-induced decoupling of Sm-Nd and Rb-Sr isotope systematics. It follows that the Nd isotope signature is likely representative of the protolith, whereas the Sr isotope signature is presumably not.

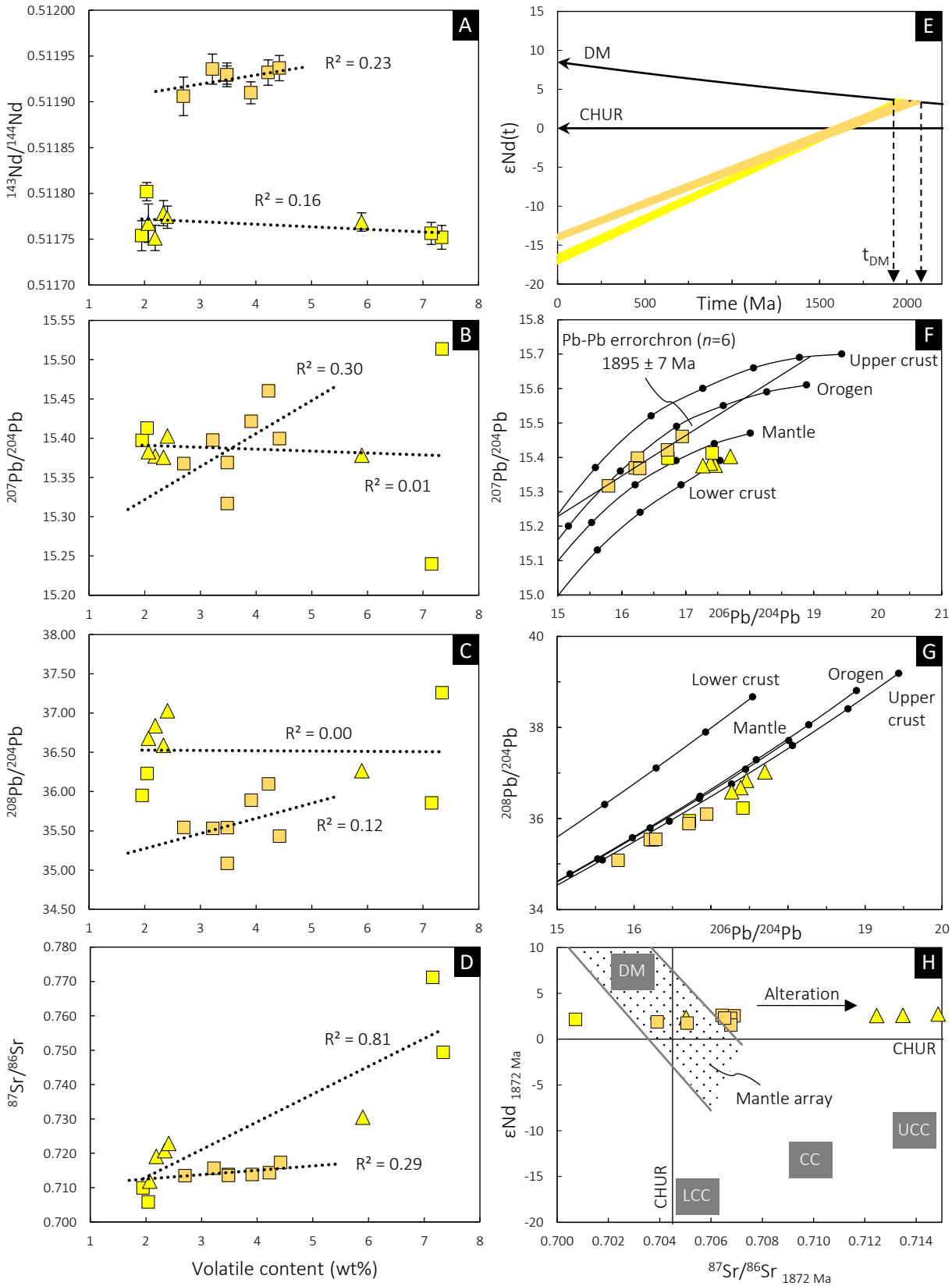

Figure 7.13 Bivariate plots of whole-rock Nd, Pb and Sr isotope ratios for the alkaline diabase dykes and related clasts (Mackelcan, Sheppard); **A–D:** measured isotope ratios vs. whole-rock volatile content, illustrating the effects of fluid-rock interaction on the isotopic composition; **E:** neodymium isotope evolution diagram with εNd displayed as a function of time; depleted mantle curve (DM) after DePaolo (1981a,b); **F–G:** lead isotope ratio plots with growth curves after Zartman & Doe (1981) for different reservoirs, with 400 Ma-increments until present; **H:** plot of the initial εNd vs. the initial $^{87}Sr/^{86}Sr$; crustal reservoirs after Faure (1986); error bars are 2σ internal errors but are smaller than the symbol size in most of the panels.

Interpretation of geochronological data

In the absence of zircon or baddeleyite, which are considered the gold standard when dating Precambrian mafic dyke swarms, one must rely on alternative geochronometers, in this case, apatite and titanite. The interpretation of such mineral dates is, however, not without its pitfalls and limitations owing to a lower precision compared to conventional U-Pb zircon/baddeleyite geochronology, the incorporation of significant amounts of common Pb, ill-defined blocking temperatures, and an overall higher susceptibility to post-magmatic disturbance. All of these aspects must be considered before it is possible to draw reliable conclusions from the apatite and titanite dates.

Apatite has a relatively low closure temperature between 350°C and 600°C for the U-Pb decay systems at a typical grain size of 10–50 μm and a cooling rate of 2–100°C/Ma (e.g. Cherniak et al. 1991; Chamberlain & Bowring 2000; Schoene & Bowring 2007; Cochrane et al. 2014), although closure temperatures has high as 770–870°C have been suggested in cases of very rapid cooling at the order of several degrees per year (e.g. Pochon et al. 2016). Titanite has a lower though poorly constrained Pb diffusivity than apatite (e.g. Kohn 2017; Holder et al. 2019; Hartnady et al. 2019; Kirkland et al. 2020) corresponding to a blocking temperature between 600°C and 800°C at a grain size of 0.1 mm and cooling rates of 1–100°C/Ma (e.g. Cherniak 1993; Scott & St-Onge 1995), which is in fact only slightly below that of zircon (> 900°C; Cherniak & Watson 2001).

Thermal modelling by Pochon et al. (2016) indicates that a 10 m-wide basaltic dyke (like the one dated in this study) would solidify and cool to ambient temperature in less than 100 years, when in contact with 300°C hot sandstone (assuming conductive heat loss, and accounting for the latent heat that is involved in the crystallisation). Such high cooling rate (5–10°C/year) can be considered virtually *instantaneous* in geological timescales, and differences in closure temperature would be negligible (Pochon et al. 2016). Therefore, apatite and titanite should be viable alternatives in dating the emplacement (= crystallisation) of small, fast-cooling mafic intrusions, provided (i) that the rocks did not experience later reheating above the respective closure temperatures, (ii) a proper assumption of the initial $^{207}Pb/^{206}Pb$ ratio can be made, and (iii) a magmatic origin of apatite and titanite can be firmly established. Fortunately, it was possible to extract a large quantity of apatite and titanite grains with variable incorporation of common Pb, and this allows for a relatively precise determination of the initial $^{207}Pb/^{206}Pb$ component by following the approach outlined by Chew et al. (2014). Reheating above the closure temperature seems, at first glance, unlikely given the diabase dyke was emplaced into a shallow crustal level (< 3 km) and that it shows no evidence of prograde metamorphism. A secondary origin of the titanite and apatite, either metamorphic or hydrothermal, seems unlikely, as will be detailed below.

The titanite dated in this study exhibits features typical of a magmatic origin, including a high Th/U ratio (Aleinikoff et al. 2002; Fedorowich et al. 2006; Jung & Hellebrand 2007; Gao et al. 2012; Rajesh et al. 2013; Li et al. 2021; Zulauf et al. 2021), and complex compositional (oscillatory *and* sector) zoning (Paterson & Stephens 1992; McLeod et al. 2011; Bruand et al. 2014). It also differs from typical metamorphic titanite with respect to habit, optical appearance, textural association, mineral inclusions or the lack thereof (cf. Corfu & Easton 2001; Gao et al. 2012; Papapavlou et al. 2017). Consequently, the weighted mean ^{207}Pb-corrected datum of 1872 ± 3 Ma obtained on 48 titanite grains is considered the best age constraint on their magmatic host rock. This is consistent with the relative age relation established in the field, and with the Nd model age obtained on the whole-rock samples (1950 Ma). Furthermore, the titanite age is consistent with the whole-rock

Pb-Pb errorchron obtained on the alkaline diabase dyke from Sheppard Township (1895 ± 7 Ma).

Although the dated apatite shows features suggesting a magmatic origin as well (acicular habit, high Th/U), its apparent age is lower than that of the supposedly cogenetic titanite. Depending on the statistical approach, apatite has either yielded an uncorrected and unfiltered date of 1849.5 ± 6 Ma (n=69), or a ^{207}Pb-corrected weighted mean of 1851.43 ± 3.34 Ma (MSWD = 0.92; n=64). The discrepancy of ~20 Ma between titanite and apatite date is outside the analytical uncertainty, and it is not simply explained by later closure to Pb diffusion as this would imply an unrealistically low cooling rate (≪ 20°C/Ma) for such a narrow mafic dyke. Theoretically, the discrepancy could be an artifact of an inappropriate choice of the initial ^{207}Pb/^{206}Pb used to anchor the regression. If, for example, the regression is anchored by a ^{207}Pb/^{206}Pb of 0.935 (the y-intercept of the titanite regression), apatite would define a datum of 1872 Ma. However, this would also increase the dispersion of the data to a level that is larger than accounted for by the analytical error (MSWD = 1.2). If the regression is forced through the terrestrial Pb evolution curve at 1870 Ma, the dispersion would be even greater (MSWD = 3.1) and thus statistically no longer acceptable (Spencer et al. 2016). It therefore appears as if the 1850 Ma date obtained on the apatite must be taken at face value. Interestingly, this date coincides with the U-Pb age of the Sudbury impact event (1850 ± 1 Ma; Krogh et al. 1984; Davis 2008; Bleeker et al. 2015), although field evidence clearly demonstrated that the host rock of the apatite must be older than the impact. The most likely explanation for this paradox is impact-induced isotopic resetting (i.e., Pb-loss) of some of the apatite grains.

Partial (never complete) isotopic resetting is a phenomenon increasingly recognised in and around both lunar and terrestrial impact structures, ranging in size from small and simple craters (< 5 km) to complex craters at the size of Sudbury, Chicxulub, and Vredefort (e.g. Nemchin et al. 2009; Moser et al. 2011; McGregor et al. 2018, 2019, 2020a,b; Timms et al. 2020). At Sudbury, age resetting of zircon is known from hornfelsed xenoliths and other footwall units within the thermal aureole of the Main Mass (Corfu & Lightfoot 1996; Prevec & Baadsgaard 2005), and it has been documented in shocked titanite grains in pseudotachylite from the Creighton Mine (Papapavlou et al. 2018b). Although a variety of mechanisms (diffusion, annealing, dissolution-reprecipitation, shock unloading) have been proposed to explain impact-induced Pb-loss, consensus exists that apatite is always more susceptible to resetting than titanite, and titanite more so than zircon (Nemchin et al. 2009; McGregor et al. 2018, 2019, 2020a,b, 2021). This order of susceptibility implies that age resetting is first and foremost controlled by volume diffusion sensu Dodson (1973).

The exact mechanism and geological process behind the age resetting in the studied apatite grains is somewhat elusive given that the sampled outcrop had shown no evidence of disturbance (no pseudotachylite, no impact melt), and that the textural position of the dated grains is not known. Maybe age resetting was caused by thermal effects imposed by the overlying (now eroded) impact melt sheet, or by the intrusion of nearby Offset Dyke. This notion would be consistent with the observations made in **Chapters 3** and **4**, and the study of Spray et al. (2004), who argued that the Main Mass was originally much more extensive, causing widespread thermal demagnetisation of pre-impact diabase dykes. Alternatively, age resetting could have occurred within a hydrothermal system initiated by the impact. This interpretation is particularly appealing because it would explain the intense alteration observed throughout the township. A similar mechanism of fluid-mediated resetting has been suggested before in other contexts to explain age discrepancies between cogenetic apatite, titanite, and zircon (e.g. Corfu & Stone 1998; Timms et al. 2020).

A distinct magmatic event in the Huronian Basin

As already reviewed in **Chapter 2.1**, mafic and ultramafic rocks are not an unusual occurrence within the Huronian Basin, for there have been at least four major magmatic episodes. These encompass the following: (i) the East Bull Lake Suite, which, together with the Matachewan Dyke Swarm, represents a large igneous province (LIP) (Ciborowski et al. 2015); (ii) the Nipissing Suite, which is considered a distal expression of the Ungava LIP related to a former mantle plume beneath Ungava Bay in northern Quebec (Lightfoot & Naldrett 1996a,b; Davey et al. 2019); (iii) the impact-generated Sudbury Igneous Complex (Prevec et al. 2000; Lightfoot et al. 1997c), and (iv) the much younger Sudbury Dyke Swarm (Condie et al. 1987; Ketchum & Davidson 2000; Shellnutt & MacRae 2012). Theoretically, the dykes discovered here could be related to any of the above, however, the lithological, geochemical, and geochronological evidence presented in this study clearly shows that these dykes are not related to any of the above but represent a distinct, separate magmatic event. The East Bull Lake and Nipissing suites, for example, have a different lithology and geochemical signature (**Tab. 7.5**). The Sudbury Dyke Swarm, though being of similar orientation and alkaline character, is strongly magnetic, which is in stark contrast to the weakly magnetic dykes of this study. The new U-Pb dates of 1850 Ma and 1872 Ma further preclude a genetic relationship of the dykes with any of these units as the East Bull Lake and Nipissing suites are much older, and the Sudbury Dyke Swarm is much younger. The only "magmatic" unit of similar age is the Sudbury Igneous Complex. Field evidence alone, however, shows already that the studied alkaline diabase dykes must have been older than the impact event because they clearly became reworked by the impact into megabreccias (**Fig. 7.4**). Apart from that, the alkaline ultrabasic nature of the studied dykes contrasts the overall calc-alkaline and siliceous nature of the Sudbury Igneous Complex. This leaves only the option of a new, hitherto unrecognised, magmatic event having affected the Huronian Basin in the target area of, and shorty before, the Sudbury impact.

Table 7.5 Comparison of the alkaline ultrabasic diabase dykes of this study with known Proterozoic mafic magmatic events in the Huronian Basin (see text above for references)

	This study	Matachewan Dykes, East Bull Lake Suite	Nipissing Suite	Sudbury Igneous Complex	Sudbury Dyke Swarm
Age	1872 ± 3 Ma	2496 – 2450 Ma	2220 Ma	1850 Ma	1235 Ma
Mode of occurrence	Dykes, clasts in impact breccia	Parallel/ radiating dyke swarm, layered intrusions	Undulating sills, lopoliths, rarely dykes	Stratified complex, dykes and breccias	Parallel/ radiating dyke swarm
Orientation	NW	N/NW	NE	Random	NW
Lithology	Gabbro, diabase	Qtz diabase, troctolite, gabbro(-norite), anorthosite	Qtz diabase, Opx gabbro, diorite, granophyre, aplite	Qtz diorite, Qtz norite, Qtz gabbro, granophyre	Ol diabase, Ol gabbro, troctolite
Metamorphism	Greenschist facies	Greenschist to amphibolite facies	Greenschist to amphibolite facies	Greenschist to amphibolite facies	None
Magnetic features	Weakly magnetic	Small but strong magnetic anomalies	Weakly to non-magnetic	Moderately magnetic depending on lithology	Strongly magnetic linear features
Affinity	Alkaline	Tholeiitic/boninitic	Calc-alkaline	Calc-alkaline	Alkaline
CIPW norm	Nepheline	Quartz	Quartz	Quartz	Nepheline
SiO_2	40 – 45 wt%	45 – 55 wt%	> 49 wt%	54 – 70 wt%	39 – 46 wt%
TiO_2	2 – 3.5 wt%	0.2 – 2 wt%	< 1 wt%	0.2 – 1.5 wt%	2 – 4 wt%
P_2O_5	0.2 – 0.7 wt%	< 0.2 wt%	< 0.1 wt%	0.1 – 0.5 wt%	0.3 – 0.8 wt%
Zr	100 – 240 ppm	10 – 200 ppm	< 100 ppm	60 – 300 ppm	100 – 400 ppm
Nb	20 – 50 ppm	1 – 10 ppm	1 – 10 ppm	4 – 15 ppm	7 – 15 ppm
εNd_0	–17 to –14	–20 to –10	–20 to –10	–30	No data
εNd_i	+1.7 to +3.5	–4 to +4	–4 to –2	–8	No data
Model age	1.95 – 2.05 Ga	2.5 – 3.0 Ga	2.8 – 3.5 Ga	2.75 Ga	No data

Correlation with the Circum-Superior LIP

A magmatic event just prior to the Sudbury impact has not been recognised before in the Huronian Basin, which raises the question what the cause of the intrusion of alkaline ultrabasic magma shortly before 1850 Ma into the Huronian Supergroup might have been. Primarily based on the titanite age, but also on the location, it is proposed that the alkaline diabase dykes are temporally and genetically related to 1.88–1.86 Ga Circum-Superior Large Igneous Province (LIP), a discontinuous magmatic belt that wraps for 3,400 km around the Superior Craton and that has been interpreted as the erosional remnant of an originally more widespread LIP (e.g. Ciborowski et al. 2017) with an inferred plume centre either near Thompson, Manitoba (e.g. Minifie et al. 2013; Ernst 2014), or right beneath the keel of the Superior Craton (Ciborowski et al. 2017; Waterton et al. 2017). The following units are currently considered part of this LIP (**Fig. 7.14**): Various mafic-ultramafic rocks of the Thompson Nickel, Fox River and Winnipegosis belts (Manitoba); volcanic and minor plutonic rocks of the Cape Smith Belt (including the Raglan Formation) and the Labrador Through (Quebec); volcanic rocks and minor lamprophyre of the Gunflint Formation and the Marquette Range Supergroup/Hemlock Formation (Michigan, Wisconsin); volcanic rocks of the Flathery Formation and subvolcanic equivalents known as the Haig Intrusions (Hudson Bay). In addition, there are a number of isolated alkaline complexes and mafic dykes located in the interior of the craton. These include the Spanish River, Borden, Cargill, Goldray and Argor carbonatites, and the Molson, Pickle Crow, Fort Albany and Wabigoon dykes. For a detailed account on the different members of the Circum-Superior LIP, the reader is referred to Ciborowski et al. (2017).

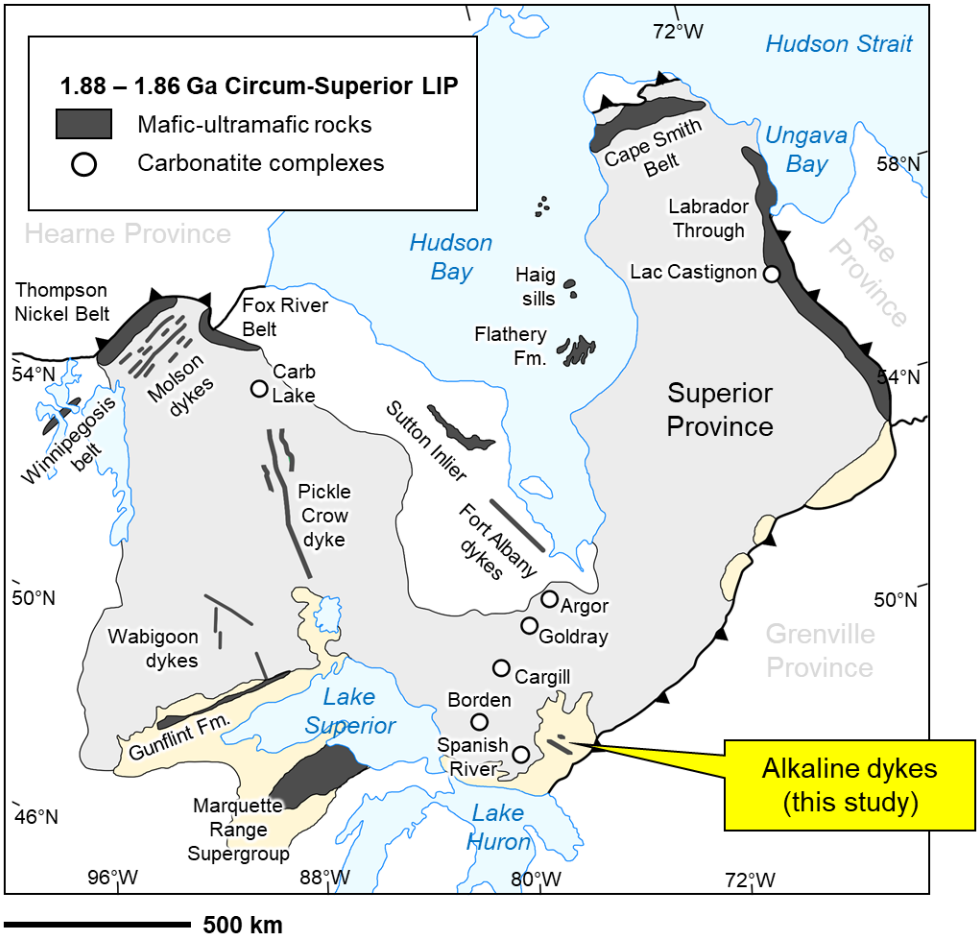

Figure 7.14 Regional geological map showing the distribution of members of the 1.88–1.86 Ga Circum-Superior Large Igneous Province; after Ernst & Bell (2010) and Ciborowski et al. (2017).

The wealth of published high-quality U-Pb dates that exist for the Circum-Superior LIP (**Fig. 7.15**) makes it possible to draw detailed comparisons with the titanite age obtained in this study. As can be seen from the compilation below, most of the magmatic activity took place between 1885 and 1870 Ma, with the earliest pulse (~1883 Ma) represented by (i) the Spanish River, Borden, Cargill and Goldray carbonatites; (ii) the various ultramafic rocks in the Cape Smith Belt and Thompson Nickel Belt; and (iii) the Molson Dyke Swarm. Apparently younger magmatic products (~1875 Ma) include the volcanic rocks of the Lake Superior region (Gunflint and Hemlock formations). The youngest known magmatic activity of the Circum-Superior LIP was the eruption of komatiites in the Winnipegosis Belt (ca. 1870–1860 Ma), and the emplacement of weakly alkaline mafic intrusions (Haig sills, Sutton Inlier, Fort Albany dykes) and volcanic rocks (Flathery Formation) in the Hudson Bay region (~1870 Ma). The latter group shows the best age overlap with the 1872 ± 3 Ma alkaline magmatism of the present study, which invites to test for a geochemical correlation.

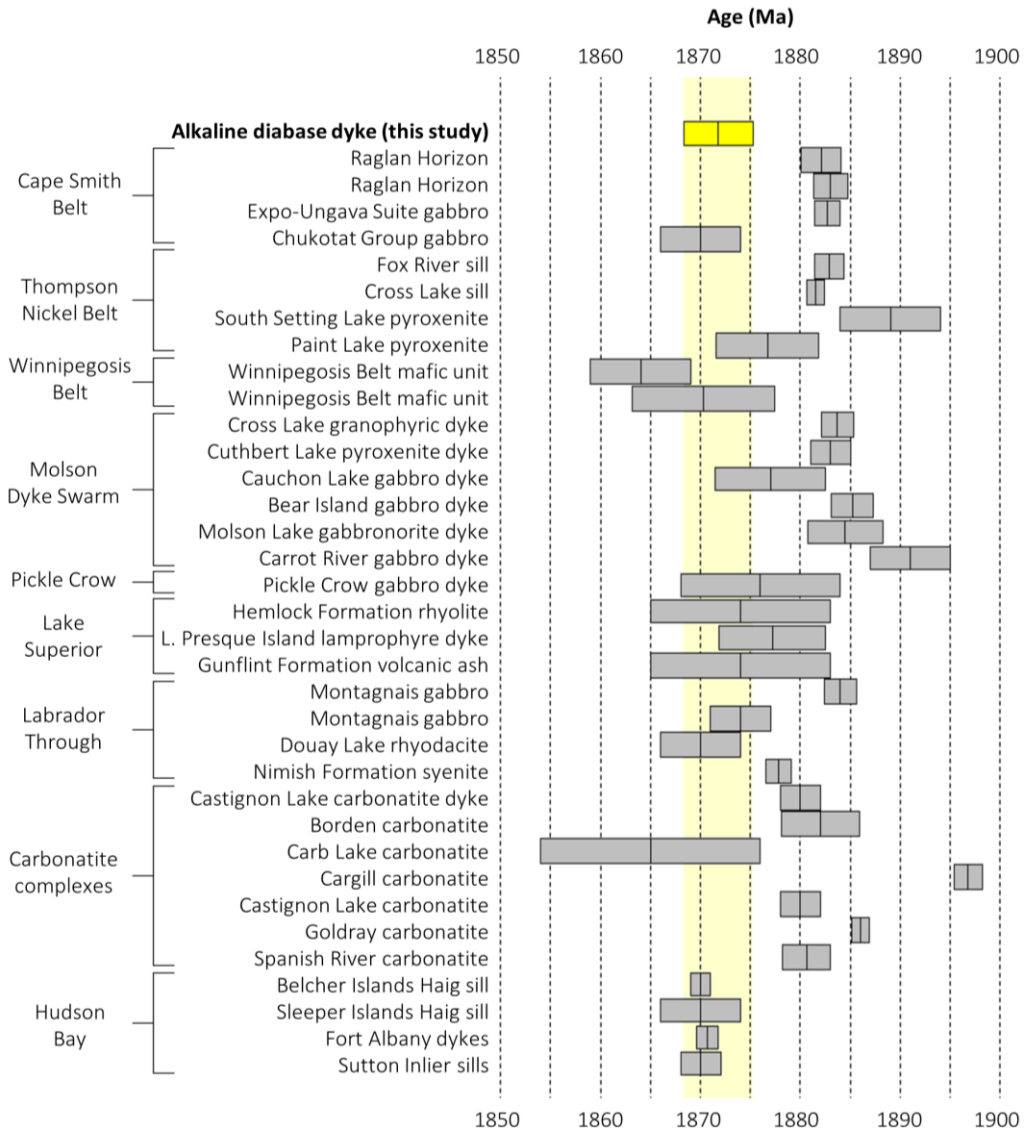

Figure 7.15 Summary of published radiometric dates for the different members of the Circum-Superior LIP; compiled after Minifie (2010), Ciborowski et al. (2017), Bleeker & Kamo (2018) and references therein; also included are four previously unpublished dates for the Haig Sills, the Fort Albany Dykes, and the Sutton Inlier (M. Hamilton, cited in Minifie 2010); all quoted dates are based on U-Pb TIMS dating of either zircon or baddeleyite, except for two Ar-Ar mineral dates for the Little Presque Island Lamprophyre (Craddock et al. 2007) and the Pickle Crow Dyke (Buchan et al. 2003); all age bars are displayed as 2σ uncertainty; the yellow array shows the 1872 ± 3 Ma U-Pb LA-ICP-MS titanite age of the alkaline diabase of the present study.

Aside from the geochronological evidence presented above, the notion of a genetic relationship between the 1.88–1.86 Ga Circum-Superior LIP and the alkaline diabase dykes is supported by similar whole-rock Sm-Nd isotope systematics. In **Figure 7.16**, the Nd isotope signature of the alkaline diabase dykes is compared to previously published data on other members of the LIP. As can be seen in **Figure 7.16A**, almost all the data define a linear array in terms of $^{147}Sm/^{144}Nd$ vs. $^{143}Nd/^{144}Nd$ corresponding to the slope of the 1880 Ma reference isochron. Such linearity is typical of rocks formed in a cogenetic suite at the same time and with the same initial $^{143}Nd/^{144}Nd$ ratio. The fact that the alkaline diabase dykes plot in the lower left corner is simply a reflection of their lower time integrated Sm/Nd ratio. Similarly, the initial εNd values compare very well between the alkaline diabase dykes and various (other) members of the Circum-Superior LIP (**Fig. 7.16B**), typical of rocks formed by the same, more or less depleted, mantle source at the same time; outliers with a negative initial εNd are explicable by crustal contamination (e.g. Desharnais 2005).

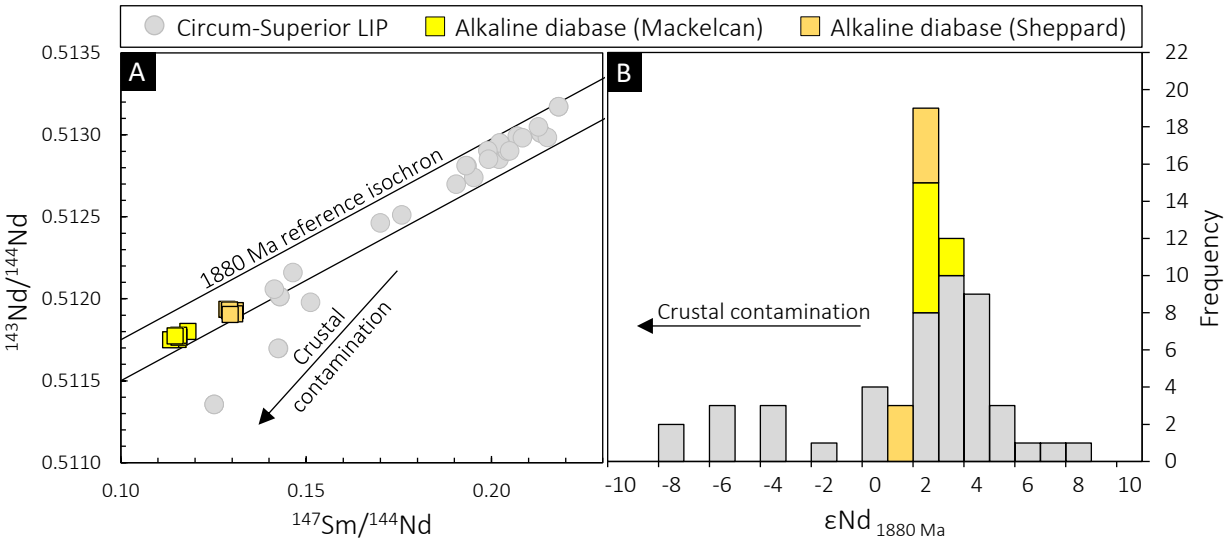

Figure 7.16 Neodymium isotope data for the alkaline diabase dykes and for the 1.88–1.86 Ga Circum-Superior Large Igneous Province; **A:** plot showing the $^{147}Sm/^{144}Nd$ vs. $^{143}Nd/^{144}Nd$ isotope ratios for the alkaline diabase dykes of the present study, compared to published data for different members of the Circum-Superior LIP; **B:** histogram comparing the initial εNd values; literature data are from Blichert-Toft & Arndt (1999), Vervoort & Blichert-Toft (1999), Desharnais (2005), Ciborowski et al. (2017), and Kastek (2019).

From **Figure 7.17** it is evident that the Circum-Superior LIP exhibits a wide compositional range, from very primitive, to highly evolved, trace element-enriched, rocks. Although the data define a broad superimposed igneous differentiation trend, Ciborowski et al. (2017) have shown that each regional group defines its own distinct differentiation trend, and that no single parental magma can account for the observed variations. The alkaline diabase dykes of the present study show some overlap with these published geochemical data. A relatively good overlap exists, for example, between the dyke from Sheppard Township and the rocks of the Hudson Bay area, which is interesting because these have a very similar age (~1870 Ma). It is, however, also clear that especially the diabase from Mackelcan Township exhibits a trend towards an extreme enrichment in incompatible trace elements. Except for lamprophyres from northern Michigan (Craddock et al. 2007), no other known member Circum-Superior LIP shows a similar HFSE and LILE enrichment. The observed mismatch does not necessarily preclude a genetic relationship, but it implies that the petrogenesis and magmatic evolution of the alkaline diabase dykes was quite distinct from the rest of the Circum-Superior LIP, for example, due to variations in the depth and/or degree of mantle melting, or variations in the mantle composition. This will be explored in more detail below.

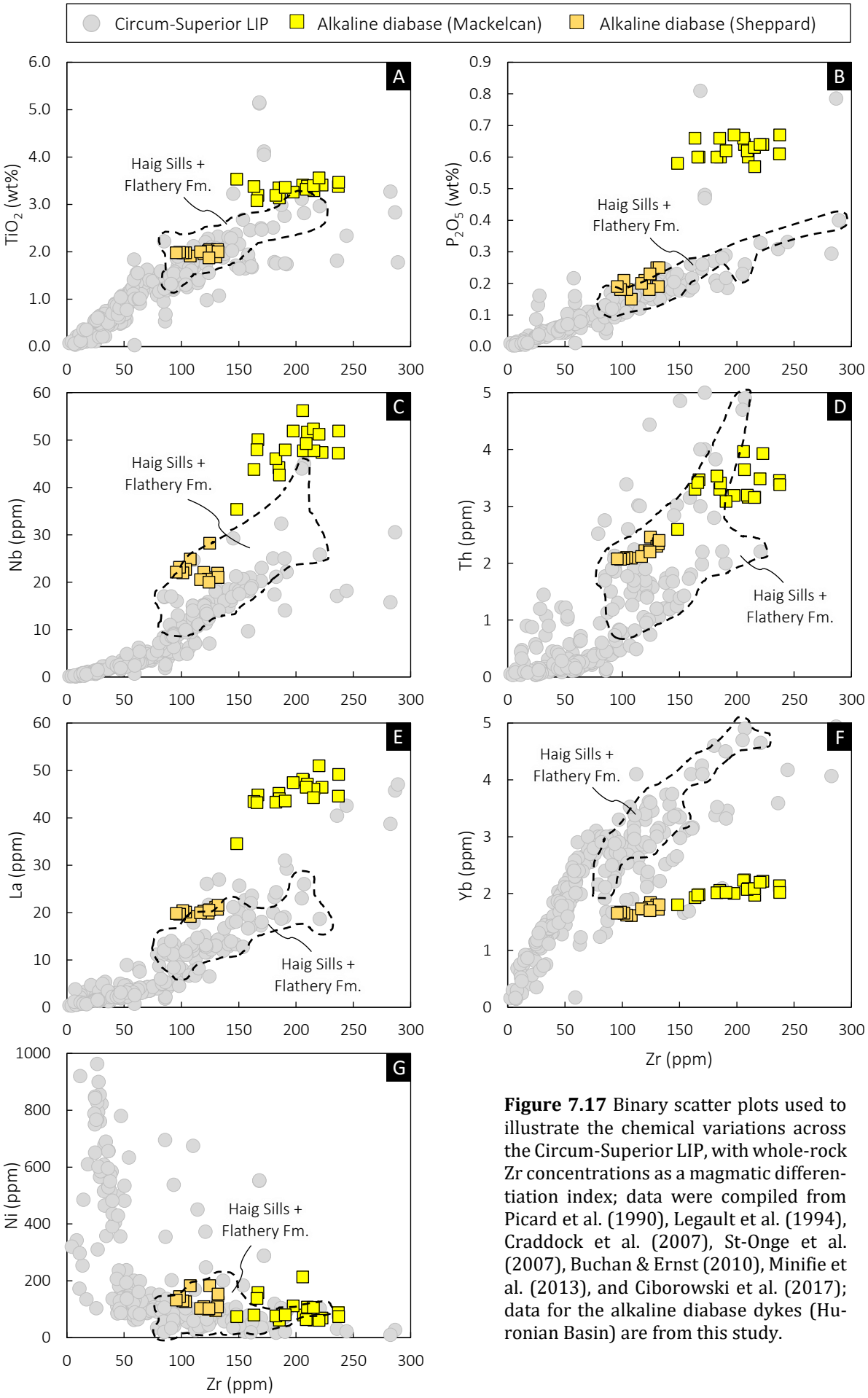

Figure 7.17 Binary scatter plots used to illustrate the chemical variations across the Circum-Superior LIP, with whole-rock Zr concentrations as a magmatic differentiation index; data were compiled from Picard et al. (1990), Legault et al. (1994), Craddock et al. (2007), St-Onge et al. (2007), Buchan & Ernst (2010), Minifie et al. (2013), and Ciborowski et al. (2017); data for the alkaline diabase dykes (Huronian Basin) are from this study.

Petrogenetic interpretation

Hot, Mg-rich primitive magmas are, by virtue, prone to assimilation of country rock (e.g. Huppert & Sparks 1985; Sparks 1986), and since the continental crust is the largest reservoir of LILE and REE (e.g. Rudnick & Gao 2013), even the smallest admixture of crustal material can obscure the primary elemental and isotopic signature of a primitive magma (DePaolo 1981c; Lesher & Arndt 1995), although in alkaline systems these effects would probably be buffered by the trace element enriched composition of the magma (e.g. Farmer 2013). The alkaline diabase dykes of the present study, despite being rich in LILE, HFSE and REE, show no evidence of such crustal contamination; they have OIB-like trace element patterns, a low SiO_2 content (≤ 45 wt%), and they are devoid of crustal xenoliths, quartz- or zircon xenocrysts. In primitive mantle-normalised trace element patterns, continental crust and contaminated magmatic rocks typically exhibit negative Nb-Ta-Ti anomalies (e.g. Taylor & McLennan 1985; Pearce 2008; Rudnick & Gao 2013). These features are not seen in the dykes of this study; they have a very low Th/Nb ratio (0.06–0.11) coupled with positive Nb-Ta anomalies (Nb/Nb* 1.0–1.5), and only a weakly negative Ti anomaly (Ti/Ti* 0.85–1.02). Also, the samples have Nb/Ta ratios of 16–22, which is significantly higher than the continental crust (12–13; Barth et al. 2000; Rudnick & Gao 2013; Hawkesworth & Kemp 2006), but typical of uncontaminated within-plate basalts (> 16; Pfänder et al. 2012). Other proxies of crustal contamination, such as Nb/U or Ce/Pb (e.g. Haase et al. 2004), are less useful here given the potential of secondary mobilisation of U and/or Pb, and the accumulation of radiogenic Pb during the last 1.87 billion years. It should be noted, however, that the Nb/U ratios of the samples (37–70) do match the typical OIB value (47 ± 10; Hofmann et al. 1986). That said, crustal contamination can be largely (though not entirely) ruled out on the basis of relatively low, but still mantle-like, εNdi values (+1.7 to +3.5), and based on the convergence of magmatic emplacement age (1872 Ma) and mantle extraction age (t_{DM} 1950–2050 Ma). If the magma had incorporated older crustal material, one would expect lower or even negative εNdi values, and model ages significantly older than 1872 Ma. In summary, the effects of crustal contamination on the geochemical and isotopic composition of the alkaline diabase dykes are considered negligible.

Another process that can affect the composition of a magma is fractional crystallisation. All samples are characterised by low MgO (≤ 7 wt%), moderate Mg# (44–57) as well variably low Cr (70–360 ppm) and Ni (60–210 ppm). These values are relatively low compared to primary magmas (MgO: 10–15 wt%; Mg#: ~70; Cr: 1,000 ppm; Ni: 400–500 ppm, e.g. Frey et al. 1978; Hart & Davis 1978; Hess 1992) in equilibrium with a typical upper mantle mineral assemblage, with the implication that the magma parental to the dykes underwent fractionation of olivine, pyroxene, and possibly Cr-spinel. In SiO_2-poor systems, however, fractionation of these minerals should not affect the ratios of HFSE, REE nor LILE because of mineral/melt partition coefficients below unity (e.g. Rollinson 1993; Adam & Green 2006), although it does affect their absolute abundances through passive enrichment in the residual melt. Lack of a distinct negative Eu anomaly (Eu/Eu* 0.94–1.1) and the presence of a variably positive Sr anomaly (Sr/Sr* 0.26–2.70, and 1.3 on average) argue against significant fractionation of plagioclase prior to the dyke's emplacement. Removal of other phases (apatite, biotite, amphibole, ilmenite) seems unlikely because this would have resulted in a depletion in P_2O_5, Ba and TiO_2 (among others) relative to other elements of similar compatibility. It is, therefore, concluded that the dykes crystallised from relatively evolved second-stage magmas that precipitated olivine + pyroxene ± Cr-spinel (and possibly pargasite) at some unconstrained depth, perhaps along the crust-mantle boundary, or at some density barrier within crust. Their trace element signature should reflect the composition of the mantle source.

In order to better understand the magmatic evolution and internal differentiation of the dykes, and to test whether the two dykes crystallised from the same batch of magma, geochemical modelling has been performed using the software *PetroLog_v3.1.13* (Danyushevsky & Plechov 2011). Sample SH-13 from the chilled margin of the alkaline diabase dyke from Sheppard Township was chosen as the starting composition of the hypothetical melt, because it appears to be to most primitive sample (8.0 wt% MgO; 284 ppm Cr; 183 ppm Ni) of this study, and it is most likely to preserve the quenched liquid composition of the magma. The major and trace element geochemical trends have been modelled at five different fractional crystallisation scenarios: (i) 1 kbar, anhydrous; (ii) 1 kbar with 0.5 wt% H_2O added to the melt (which is a typical value for fresh within plate basalts; Hauri 2002); (iii) 5 kbar, anhydrous; (iv) 5 kbar, with 0.5 wt% H_2O; and (v) 10 kbar, anhydrous. In each scenario, lithostatic pressure was kept constant, initial oxygen fugacity set at the NNO (nickel-nickel oxide) buffer, and ideal crystal-liquid fractionation was assumed. The results of this modelling in comparison with the measured whole-rock data are shown in **Figure 7.18**.

The models predict that, in each scenario, ortho- and/or clinopyroxene will be the first liquidus phase; only in the anhydrous scenario at 1 kbar is olivine supposed to crystallise. Plagioclase joins the sequence typically after ca. 40% of the crystallisation has commenced, and ilmenite will crystallise with or without magnetite relatively late, once Ti-saturation is reached. These mineral assemblages broadly match those observed in thin section (e.g. **Fig. 7.7**), with the exception of olivine. As can be seen in **Figure 7.18**, all the samples from Sheppard Township exhibit a significant scatter that makes the identification of geochemical trends difficult. Only a few elements, including Ti, Ca, Na, P, Zr, La and Nb, define linear trends. All of these elements are negatively correlated with MgO, a behaviour that is best predicted by models involving small amounts of H_2O, low to moderate pressure (1 kbar or 5 kbar), and less than 10% crystallisation. These conditions appear realistic and suggest that the observed internal variation within the dyke from Sheppard Township is explicable by limited fractional crystallisation involving plagioclase and pyroxene, perhaps resulting from flow differentiation during the dyke's emplacement. Conversely, the variations of Ni within this dyke are best approximated by the anhydrous model at 1 kbar and 30% crystallisation, which seems unrealistically high for such a narrow, fast cooling dyke. The anhydrous model also requires precipitation of olivine, which was not observed in thin section.

The above models can also be used to explore the magmatic relationship between the two alkaline diabase dykes. If, for example, the dyke from Mackelcan Township resulted from fractionation of the same batch of magma as the supposedly cogenetic dyke from Sheppard Township, both should lie on the same liquid line of descent. **Figure 7.18** shows that the models can broadly reproduce the compositional differences between the two dykes, but only for a few elements. The contents of SiO_2, Al_2O_3, CaO, and Zr contents of the dyke from Mackelcan Township, for example, are well matched by the 10 kbar model after 40–50% crystallisation of clinopyroxene and plagioclase. However, none of models provides a unifying solution to all observed differences, and most importantly, no model is able to reproduce the extreme enrichment in TiO_2, P_2O_5, Na_2O, and La within the dyke from Mackelcan Township. Theoretically, to achieve a melt composition with 3.5 wt% TiO_2, ilmenite crystallisation needs to be effectively suppressed, and high degrees of crystallisation (> 60%) would be required. At such high degrees of fractionation, however, the magma would no longer be basic, nor would it match the measured Zr content of 200–220 ppm unless this was counterbalanced by fractionation of Zr-bearing phases. Similarly, the high P_2O_5 and Na_2O contents would only be achieved after implausibly large degrees (> 80%) of crystallisation.

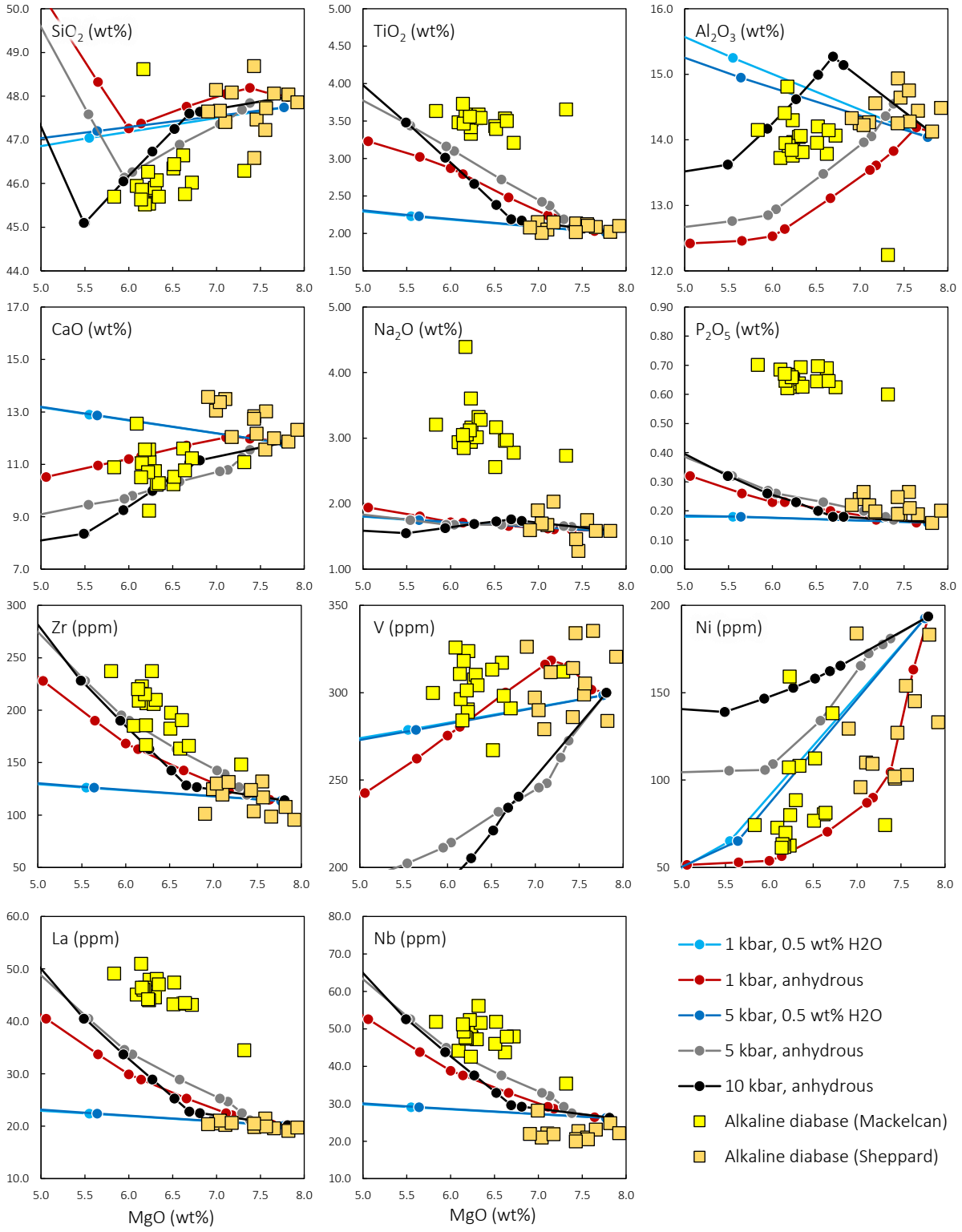

Figure 7.18 Bivariate diagrams showing the results of the fractional crystallisation modelling, with the most primitive sample (SH-13) from the alkaline diabase dyke from Sheppard Township as a starting melt composition; markers indicate increments of 10% crystallisation on the calculated liquid lines of descent; all element concentrations were recalculated on a volatile-free basis; modelling was done using *PetroLog3* (Danyushevsky & Plechov 2011) with the implemented melt oxidation state model of Borisov & Shapkin (1990); mineral-melt equilibria follow Danyushevsky (2001) for olivine, clinopyroxene and plagioclase, Bolikhovskaya et al. (1996) for orthopyroxene and pigeonite, Nielsen (1985) for spinel and ilmenite, Ariskin & Barmina (1999) for magnetite; trace element partition coefficients were taken from Zack & Brumm (1999) and Villemant et al. (1981); note the extreme enrichment in TiO_2, Na_2O, P_2O_5, and La in the alkaline diabase dyke from Mackelcan Township, which is not reproduced by any of the models.

Failure to reproduce the observed compositional differences between the two dykes via fractional crystallisation implies that another process must have been involved, for instance, melting of a heterogeneous mantle source, or changes in the depth and/or degree of mantle melting. In the absence of crustal contamination, this can be tested using whole-rock REE data. Both dykes have strongly fractionated HREE (Tb/Yb_N 1.8–2.7) and low Lu/Hf ratios (0.06–0.11), which is typical of near-solidus melts generated in the garnet stability field deep within the Earth' mantle (> 75–90 km; Robinson & Wood 1998) because of the retention of especially Yb and Lu by refractory garnet (e.g. Beard & Johnson 1993). In contrast, melts generated in the shallower, spinel-bearing mantle facies (or by > 25% melting of any mantle lithology) would exhibit unfractionated HREE ratios (Tb/Yb_N < 1.8) (e.g. Wang et al. 2002) because of uniform bulk partition coefficients < 1 for all REE. In addition, a deep melt source corresponding to a pressure of ca. 3 GPa (~100 km) is indicated by whole-rock SiO_2/Al_2O_3 ratios of 3.2–3.8 in conjunction with MgO/CaO ratios of 0.5–1.0 (cf. Gudfinnsson & Presnall 2005); a pressure of ca. 3.5 GPa (~120 km) is implied by the high Nb/Yb vs. TiO_2/Yb (Pearce 2008, p. 30). Thus, melting might have occurred within the garnet stability field of the lithospheric mantle, considering that the lithosphere beneath the southeast Superior Carton was likely 180–190 km thick at that time (e.g. Smit et al. 2014; Snyder et al. 2021).

The identification of residual garnet in the mantle source of the dykes not only places constraints on the minimum depth (> 75 km) and maximum degree of melt generation (< 25%), but it also makes it possible to calculate hypothetical melting curves as a function of different mantle compositions. For sake of simplicity, and because of the many unknowns pertaining the melting process and the nature of the mantle source involved, melt compositions have been modelled assuming instantaneous non-modal batch (equilibrium) melting as defined by Shaw (1970). The results of this modelling are presented in **Figure 7.19.**

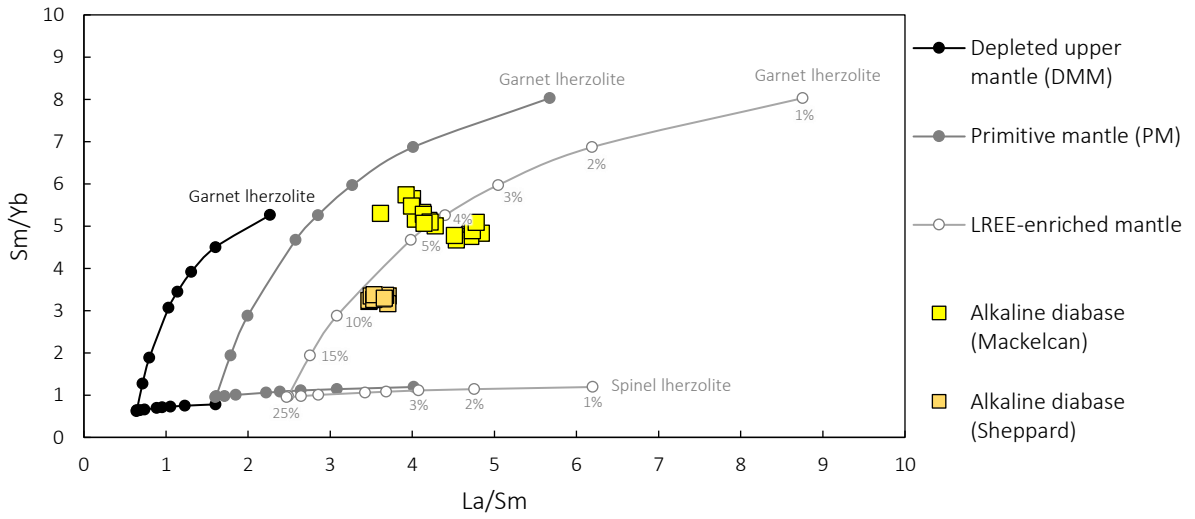

Figure 7.19 Results of the trace element melting modelling; the curves show calculated melt compositions in increments of 1%, 2%, 3%, 4%, 5%, 10%, 15% and 25% for non-modal batch melting (Shaw 1970) of three different mantle types; modal mineral and melt proportions according to Thirlwall et al. (1994), Walter (1998), Shaw et al. (2003), Peters et al. (2008), and Özdemir & Güleç (2014); mineral/melt partition coefficients from McKenzie & O'Nions (1991); modal proportions of the spinel lherzolite were 57.8% Ol, 27% Opx, 11.9% Cpx, 3.3% Spl, which melts in proportions of 10/27/50/13; modal mineralogy of the garnet lherzolite was 59.8% Ol, 21.1% Opx, 7.6% Cpx, 11.5% Grt, which enters the melt in proportions of 5/20/30/45; composition of the depleted upper mantle (DMM) after Workman & Hart (2005); primitive mantle after Sun & McDonough (1989); the hypothetical LREE-enriched mantle source represents the best fit curve assuming DMM-like values for Sm and Yb, and an adjusted La value of 1.0 ppm.

As can be seen in **Figure 7.19**, the alkaline diabase samples of the present study define a cryptic trend of increasing La/Sm with increasing Sm/Yb, which either reflects different degrees of partial melting of a garnet-bearing source, or alternatively, mixing between garnet- and spinel-bearing mantle sources or partial melts thereof. However, as also evident from **Figure 7.19**, melting of a REE-depleted (MORB-like) mantle source, whether garnet- or spinel-bearing, cannot produce the measured composition of the alkaline diabase dykes, as these have higher La/Sm ratios at a given Sm/Yb. Similarly, a primitive mantle-like source composition would result in an underestimation of the observed Sm/Yb and La/Sm ratios and would require implausible low degrees of partial melting (< 1%). The best fit is achieved assuming depleted mantle-like concentrations of Sm (0.21 ppm) and Yb (0.348 ppm), and a modelled La concentration of 1.0 ppm. High La concentrations of up to 10 ppm appear typical of metasomatically enriched subcontinental lithospheric mantle domains (SCLM) and have been reported before in many mantle-derived xenoliths elsewhere (e.g. Stosch & Seck 1980; Hartmann & Wedepohl 1990; McDonough 1990; Rudnick et al. 1993; Downes 2001; Pearson & Nowell 2002; Ionov et al. 2006; Aulbach et al. 2013; Wyman et al. 2015).

Unfortunately, the exact thickness, modal mineralogy, and chemical composition of the Palaeoproterozoic SCLM beneath the southeast Superior Craton is not known for certain (see: Hunt et al. 2012; Smit et al. 2014; Wyman et al. 2015), and the above presented melting curves, therefore, must be interpreted with caution. Also, the isobaric equilibrium melt model of Shaw (1970) is clearly an oversimplification of the natural melting process (e.g. Zou & Reid 2001), and it should be born in mind that the results of such calculations can vary to some degree, depending on the choice of the partition coefficients. Regardless of all these uncertainties, the model demonstrates that the REE signature of the alkaline diabase dyke from Mackelcan Township can be, in principle, explained by relatively low degrees (4–5%) of partial melting of a garnet-bearing LREE-enriched mantle; the REE signature of the alkaline diabase dyke from Sheppard Township can be explained by ~8% partial melting of *the same* source. These numbers seem realistic and compare well with melting degrees calculated for alkaline Na-rich within-plate basalts worldwide (e.g. Fitton & Dunlop 1985; Frey et al. 1991; Baker et al. 1997; Jung & Masberg 1998; Jung & Hoernes 2000; Zeng et al. 2010). This implies that the observed compositional differences between the two dykes could have resulted from different degrees of partial melting, rather than from changes in depth, variations in the mantle lithology, or involvement of a chemically heterogeneous mantle.

Distinguishing between differences in the degree of melting on the one hand, and subtle chemical mantle heterogeneities on the other hand, can in fact be extremely difficult, even in recent ocean island basalts (Willbold & Stracke 2006), let alone metamorphic Precambrian rocks that suffered from extensive post-magmatic element mobilisation. However, mantle heterogeneities seem rather unlikely in this case. First, the samples have uniform εNdi values and uniform initial Pb isotope ratios suggesting the mantle source had identical time integrated Sm/Nd and U/Th/Pb ratios. Second, the ratios of equally incompatible element pairs are, within the analytical error, identical between the two dykes. This is particular evident from uniform Zr/Hf (40 and 39), Nb/Ta (18 and 18) and La/Nb (0.94 and 0.92) ratios. Theoretically, these element ratios should only fractionate if either the degree of melting was extremely low (≪ 1 %) or the mantle source was heterogeneous in the first place (e.g. Willbold & Stracke 2006). Thus, the identical average Zr/Hf, Nb/Ta and La/Nb ratios, together with uniform εNdi and a lack of U-series disequilibria, are consistent with the above notion that the two dykes were generated from a chemically and mineralogically homogeneous mantle reservoir at different degrees of partial melting.

Mantle source characteristics

As already mentioned above, melting of a typical lherzolitic geochemically depleted (i.e., MORB-like) mantle source cannot explain the extreme enrichment of especially LREE in the alkaline diabase dykes, unless the mantle source had experienced some sort of LREE-enrichment as well. This is also demonstrated by the trace element patterns in **Figure 7.20**. As can be seen from this figure, non-modal batch melting of an ordinary garnet lherzolite having a DMM-like composition cannot reproduce the observed trace element signature of the alkaline diabase dykes. Firstly, the pronounced LREE enrichment can only be achieved by extremely low melt fractions (F ~0.01%). Such low fractions of near-solidus melts are, however, unlikely to ever reach the surface (e.g. McKenzie 1989). Secondly, partial melting of a DMM-like garnet lherzolite (whether depleted or "enriched", Workman & Hart 2005) will inevitably result in positive K-anomalies because the bulk partition coefficients for K are far lower than for any other trace element (e.g. McKenzie & O'Nions 1991; Salters et al. 2002). Thirdly, melting of a DMM-like garnet lherzolite cannot lead to negative Zr-Hf-Ti anomalies because the bulk partition coefficient of these elements is similar to that of Sm, Eu, and Gd (e.g. McKenzie & O'Nions 1991; Salters et al. 2002). Fourthly, superchondritic Zr/Hf ratios (37–47) observed in the alkaline diabase dykes are difficult to reconcile with the above melting models unless (a) the high Zr/Hf ratio was inherited from the source region; or (b) some mineral phase other than olivine, pyroxene, garnet, or spinel (McKenzie & O'Nions 1991; Green et al. 2000; Salters et al. 2002) fractionated Zr from Hf during the melting process. Evidently, some kind of source enrichment, or a non-peridotitic mantle lithology, is required to explain the geochemical characteristics of the alkaline diabase dykes. This notion is entirely in keeping with the general consensus that alkaline Ne-normative intraplate basalts with OIB-like trace element signatures cannot be generated by melting of a "dry" and depleted peridotite (e.g. Frey et al. 1978; Hirschmann et al. 2003; Prytulak & Elliott 2007; Pilet et al. 2008, 2011) calling instead for a metasomatically enriched lithospheric mantle as a potential source (e.g. Pilet 2015; Rooney et al. 2017).

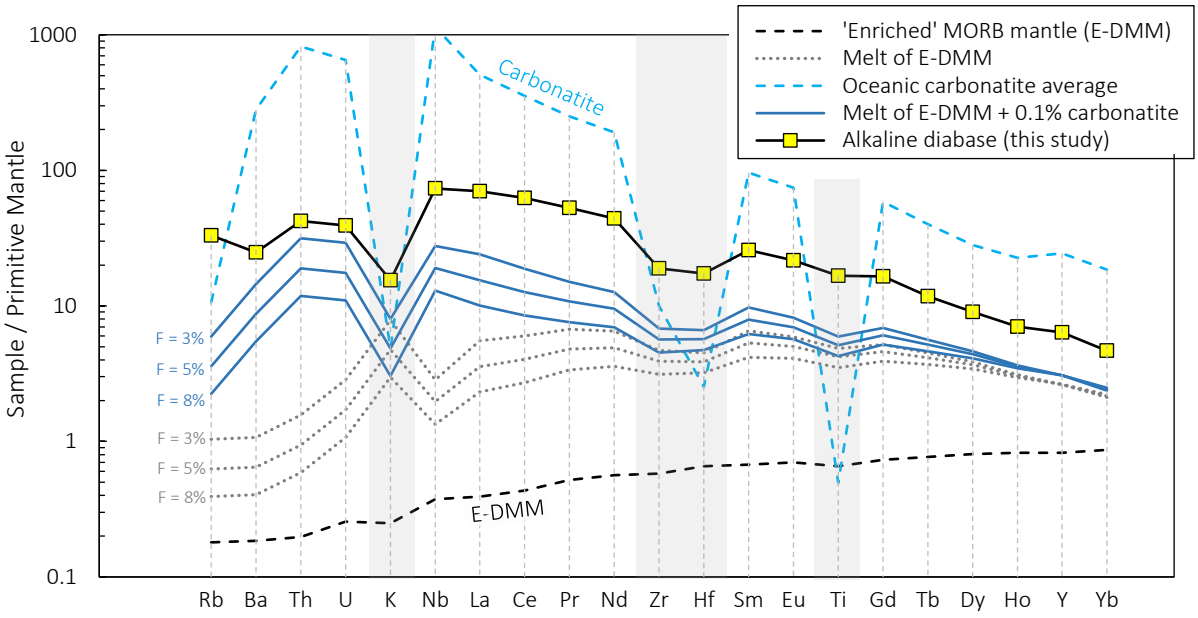

Figure 7.20 Primitive mantle-normalised trace element abundances for the alkaline diabase of the present study compared to calculated melt compositions obtained from non-modal batch melting models; parameters as defined in Figure 7.19; composition of the "enriched" DMM after Workman & Hart (2005); also shown is the average composition of oceanic calcio carbonatites from the Cap Verde Islands (Hoernle et al. 2002; Doucelance et al. 2010; Murão et al. 2010); normalisation values after Sun & McDonough (1989).

An elegant solution to explain the composition of alkaline basalts involves re-melting of a lithospheric mantle source that had previously been metasomatised by low-viscosity carbonatite melts (Zeng et al 2010; Foley & Fisher 2017; Zhang et al. 2017; Shea & Foley 2019; Liu et al. 2021). The hypothesis is based on the fact that carbonatites, which are spatially and genetically often associated with alkaline intraplate magmatism, typically exhibit an extreme enrichment in LREE, Th, U, Nb and Ta of up to 1,000-times the chondritic value, a pronounced depletion in Rb, K, Pb, Zr, Hf and Ti relative to elements of similar incompatibility, and super-chondritic Zr/Hf ratios (e.g. Dupuy et al. 1992; Hoernle et al. 2002; Bizimis et al. 2003; **Fig. 7.20**). Studies from xenoliths have shown that carbonatite melts infiltrating peridotitic mantle domains will essentially impose their distinct trace element signature upon the peridotite, resulting in highly enriched mantle metasomes with high LREE/HREE ratios and depletions in K, Pb, Zr, Hf, Ti (e.g. Yaxley et al. 1991, 1998; Hauri et al. 1993; Ionov et al. 1993; Coltorti et al. 1999; Rudnick et al. 1993; Gorring & Kay 2000; Laurora et al. 2001; Neumann et al. 2002; Rosatellia et al. 2007). Thermal reactivation of such carbonated mantle sources, containing as little as 0.1–0.25 wt% CO_2, has been shown to be able of generating Ti-rich high-CaO/Al_2O_3 Ne-Di-Ol-normative OIB-like silicate melts at 3 GPa and melting degrees of 1–5% (Hirose 1997; Dasgupta et al. 2007) with trace element patterns closely resembling those of at least some natural intraplate Na-rich alkali basalts and basanites (e.g. Dixon et al. 2008; Zeng et al. 2010; Dai et al. 2017; Gómez-Ulla et al. 2018; Shea & Foley 2019).

The hypothesis of a carbonated lithospheric mantle beneath the southeast Superior Craton is particularly appealing considering that the 1.88 Ga Spanish River Carbonatite (Rukhlov & Bell 2010) occurs just 100 km west of the study area. The occurrence of additional carbonatite complexes of similar age across the Superior Craton (Rukhlov & Bell 2010; **Fig. 7.14**) testifies that carbonatite magmatism (and by implication, mantle metasomatism) was widespread. To assess whether such carbonated mantle was also present in the source region of the 1872 Ma alkaline magmatism in the Huronian Basin, trace element modelling has been performed following a modified version the approach of Dixon et al. (2008) and Zeng et al. (2010), the results of which are illustrated in **Figure 7.20**. The modelling reveals that non-modal batch melting of a slightly carbonated garnet lherzolite (DMM + 0.1% carbonatite) can, in theory, produce melt compositions with a weakly negative Ti anomaly (Ti/Ti* ~0.8), strongly negative K-Zr-Hf anomalies (K/K* < 0.5, Hf/Hf* < 0.5), and moderate LREE enrichment over HREE (La/Yb_N 4–23), and superchondritic Zr/Hf (35–55), all characteristics that are found in the alkaline diabase dykes of the present study. In agreement with the modelling results of **Figure 7.19**, the best match is achieved for a melt degree between 5% and 8% (followed by fractional crystallisation of olivine or pyroxene). Lower degrees of melting would result in La/Yb_N ratios far greater than is observed in the alkaline diabase dykes; higher degrees and the "carbonatite fingerprint" would gradually disappear. A carbonated mantle source would also account for the relatively high P_2O_5/TiO_2 ratio of up to 0.21 in the alkaline diabase dykes. Experimental work (Baker & Wyllie 1992) indicates that P_2O_5 is highly soluble in carbonatite melts, whereas TiO_2 has a very low solubility, hence the high P_2O_5/TiO_2 ratio of up to 20 found in carbonatites (e.g. Sage 1987; Hoernle et al. 2002; Doucelance et al. 2010; Murão et al. 2010), far exceeding the P_2O_5/TiO_2 ratio of the primitive mantle (0.1; Palme & O'Neill 2013).

In conclusion, low degrees (< 10%) of deep melting (~3 GPa) of a carbonated mantle metasom offers a viable explanation for almost all observed major, minor, and trace element features of the alkaline diabase dykes (except for the highly fluid-mobile elements Ba, Rb, Sr, Pb), thus implying a close genetic association between diabase and previously documented carbonatite magmatism

in the region as locally represented by the Spanish River Carbonatite (Rukhlov & Bell 2010).

As an alternative to carbonated mantle domains, melting of hydrous mineral veins within the lithospheric mantle has been invoked to explain Ne-normative alkaline basalts with OIB-like trace element features (e.g. Pilet et al. 2008, 2011; Jung et al. 2012). Such hydrous veins, typically composed of Ti-rich alkali amphibole, have been extensively documented in xenoliths from other parts of the world (Wass & Rogers 1980; Dawson & Smith 1982, 1988; Zanetti et al. 1996; Konzett et al. 2000), and are believed to be stable only in the cold lithospheric mantle, but not in the hot and convecting asthenosphere (Foley 1991; Class & Goldstein 1997; Green et al. 2010). How exactly such metasomes are formed in the first place is, however, poorly understood. In brief, hornblende-rich cumulates have been interpreted in terms of percolation of low-degree (near-solidus, hence highly enriched) melts within the lithosphere, where these melts are supposed to differentiate, react with the ambient mantle (resulting in modal and cryptic metasomatism), and eventually, solidify (e.g. Best 1974; Bodinier et al. 1987; Nielson & Noller 1987; Wilshire 1987; Nielson & Wilshire 1993; Harte et al. 1993; Pilet et al. 2011). Later reheating of such veined material, e.g. during thermal perturbation of the lithospheric mantle by a rising mantle plume (e.g. Foley 1992, 2008), will preferentially melt these hornblendite-rich domains because of lower solidi than the anhydrous lherzolite, resulting in alkaline melts that may reach the surface (e.g. Pilet 2015).

As illustrated in **Figure 7.21**, high-pressure melting of a hornblende-bearing mantle satisfies almost all geochemical features of the alkaline diabase dykes, including steeply sloping REE patterns, the same negative Zr-Hf anomalies, a Zr/Hf ratio slightly above the chondritic value, and a distinct negative K anomaly. Some mismatch exists in terms of Nb, which tends to be enriched in hornblendite-derived melts relative to the alkaline diabase. There is also a noteworthy discrepancy with respect to the shape of the Ti anomaly; while the alkaline diabase dykes have a negative Ti anomaly, the experimentally generated melts tend towards a positive Ti anomaly. The similarity between the experimental data and the alkaline diabase dykes is, nevertheless, remarkable.

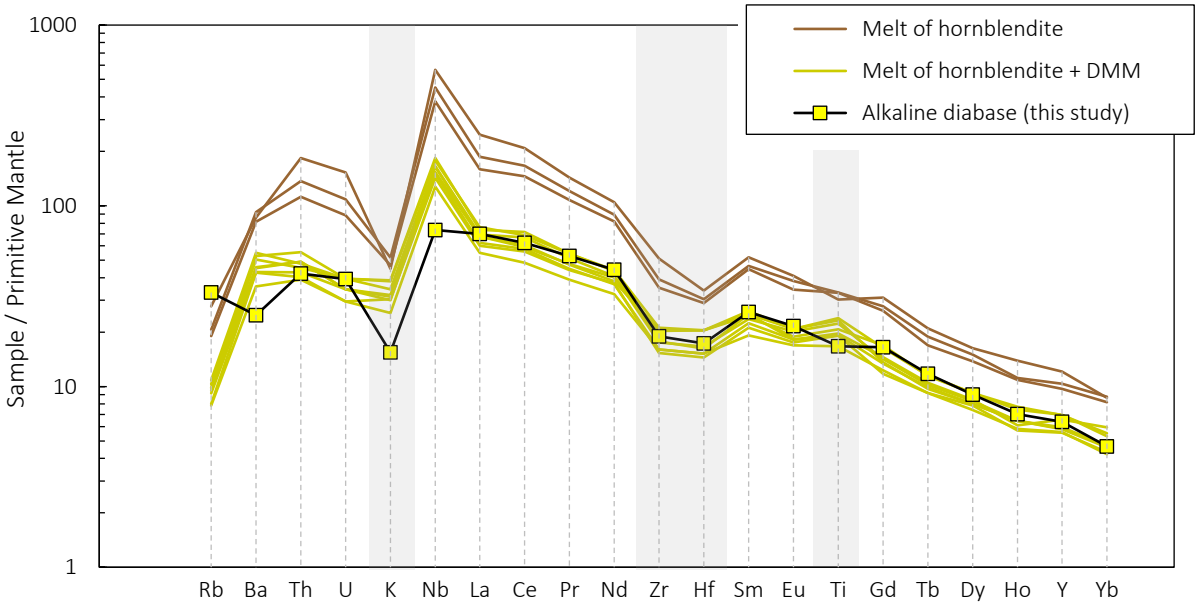

Figure 7.21 Primitive mantle-normalised trace element abundances for the alkaline diabase of the present study compared to experimentally generated liquids produced by high-pressure melting (1.5 GPa) of natural hornblendite and hornblende-rich peridotite; experimental data are from Pilet et al. (2008); normalisation values after Sun & McDonough (1989).

Experimental studies have shown that melts generated from a carbonated peridotite always have a whole-rock $(Na_2O+K_2O)/TiO_2 > 1$ (Dasgupta et al. 2007), whereas melts generated from hornblendite have a $(Na_2O+K_2O)/TiO_2 = 1$ (Pilet et al. 2008). In addition, melts from a carbonated peridotite are supposed to exhibit a negative Ti anomaly (Ti/Ti* < 1) (e.g. Zeng et al. 2010), whereas melts from a hornblendite source have a weakly positive Ti anomaly (Pilet et al. 2008). In principle, these subtle differences, although relying on a very limited set of experimental data, should make it possible to differentiate between the above presented options – a carbonated mantle source, or a hornblende-rich mantle source. In practise, however, the evidence is inconclusive, as the alkaline diabase dykes of the present study exhibit geochemical features characteristic of both source types. As can be seen in **Figure 7.22A**, the alkaline diabase dykes have a relatively uniform $(Na_2O+K_2O)/TiO_2 \approx 1$, which is typical of hornblendite-derived melts. Conversely, the negative Ti anomaly of the samples rather points to a carbonated mantle source (**Fig. 7.22B**). Maybe this apparent contradiction can be resolved by contribution from a mixed source, that is, one that contained both hydrous veins and carbonated portions (e.g. Zeng et al. 2010; Shea & Foley 2019).

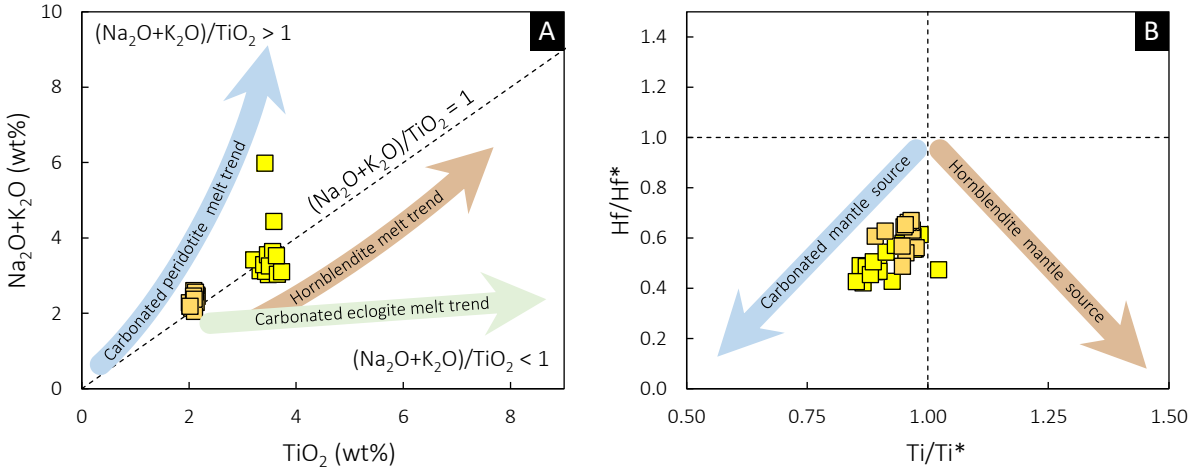

Figure 7.22 Element ratio plots used to discriminate between different metasomatic mantle sources for the alkaline diabase dykes; **A:** plot of total alkalis vs. TiO_2 to distinguish between melts generated by carbonated peridotite, carbonated eclogite/pyroxenite, and hornblendite; after Zeng et al. (2010); **B:** plot of whole-rock Ti/Ti* vs. Hf/Hf* used to distinguish between melts generated by hornblendite and carbonated peridotite.

Although the above geochemical considerations point to the involvement of a metasomatically enriched lithospheric mantle in the petrogenesis of the alkaline diabase dykes, the data alone provide no explanation as to the cause(s) and the timing of the metasomatism. Potential causes could have been slab-derived fluids and/or melts related to subduction in the late Archaean, older plume events (Matachewan, Mistassini, Marathon, Nipissing), or the Circum-Superior event itself. Some clues as to the timing of the source enrichment can be obtained from whole-rock Sm-Nd isotope systematics. The relatively un-radiogenic εNdi (+1.65 to +3.52) of the alkaline diabase dykes means that the melt source cannot have been enriched in LREE long before partial melt extraction, nor could it have been long-term depleted. This, together with model ages (1950–2050 Ma) closely resembling the intrusion age of 1872 Ma, indicates that source enrichment must have occurred relatively shortly before, or contemporaneously with, the onset of the Circum-Superior magmatism. If source enrichment had occurred long before that, decay of ^{147}Sm to ^{143}Nd would have resulted in a very radiogenic (very low εNdi) source, and any melt separated from such radiogenic source would be expected to show equally low or even negative εNdi values, and model ages far older than 1872 Ma, which is evidently not the case for the alkaline diabase dykes here.

Geodynamic implications

The observations made in the present study, although being based on a limited number of samples and outcrops, have the potential of refining existing genetic models for the 1.88–1.86 Ga Circum-Superior LIP and adding to a more comprehensive understanding of this magmatic event as whole. The currently favoured model for the Circum-Superior LIP (Ciborowski et al. 2017; Waterton et al. 2017; Bleeker & Kamo 2018) summarises as follows (**Fig. 7.23**): An upwelling mantle plume impinged beneath the Superior Craton and was deflected by the thick (~300 km) cratonic keel into areas of thinner lithosphere, specifically the rifted cratonic margins. Only there could significant decompression melting occur, and the magmas rise buoyantly through the crust, eventually erupting as voluminous komatiites and tholeiitic flood basalts. Ciborowski et al. (2017) suggested that large volumes of melt were predominantly generated in areas that had recently been affected by lithospheric extension, either through rifting or back-arc basin formation; examples are Raglan and Thompson. Other parts of the Superior Craton such as, the Huronian Basin, the Lake Superior region, and the Hudson Bay area, had not witnessed any recent extensional event (> 300 Ma before the arrival of the plume), hence the low volumes of weakly alkaline magmatic rocks in these areas (Haig Sills, Flathery Formation; Minifie 2010). The presence of 1.88 Ga carbonatites in the centre of the craton does not contradict the plume model; carbonatite melts would have been able to migrate even through the thicker, inner part of the craton because of their exceptional low viscosity and density (Hammouda & Laporte 2000; Kono et al. 2014). If the plume model is correct, then the Fort Albany, Molson, and Pickle Crow dykes could be interpreted as part of a radiating dyke swarm, the focal point of which should help to locate the plume centre (Minifie et al. 2013). However, the limited number of dykes previously assigned to the Circum-Superior LIP makes the identification of geometric dyke swarm patterns difficult and provides, at least in this case, no conclusive evidence as to the location of the plume centre, especially following the recognition that both radial and concentric dyke swarms can be associated with one and the same LIP (Buchan & Ernst 2018, 2021), and that other factors such as inherited basement structures or later deformation can define the orientation of dyke swarms as well (e.g. Jourdan et al. 2006; Will & Frimmel 2013).

While a mantle plume origin of the Circum-Superior LIP seems widely accepted (Ciborowski et al. 2017, for a list of arguments), there are some aspects still not entirely resolved by the model. Heaman et al. (2009), for example, pointed out the lack of evidence of crustal uplift prior to 1.88 Ga. They also argued against a plume based on the absence of rocks with an OIB-like trace element signature. According to Heaman et al. (2009), only OIB-like basalts would provide unequivocal evidence of a deep mantle source and thus a plume origin, whereas tholeiitic basalts and komatiites could have been generated in essentially any tectonic setting. Another weakness of the plume model was found in the absence of 1.88–1.86 Ga magmatic rocks in the southeast part of the Superior Craton, specifically the Huronian and Mistassini-Otish basins. Although these basins are located on the rifted margin of the craton and should have been well within the typical diameter of a flattened plume head (~2,500 km; Campbell 2007), there have been no reports of ~1.88 Ga magmatic rocks in neither the Huronian nor the Mistassini-Otish basins, at least so far.

As such, the discovery of 1872 Ma alkaline ultrabasic dykes with an OIB-like signature in the southeast corner of the Superior Craton fills a crucial gap in the regional magmatic record and reinforces the plume model of Ciborowski et al. (2017) and Bleeker & Kamo (2018) for the Circum-Superior LIP. The new geochronological data confirm the notion of a short lived, remarkbely synchronous yet extremely widespread magmatic event that manifested all around the Superior

Craton (and maybe even beyond; French et al. 2008). A deep mantle source is now and for the first time evidenced by the highly alkaline, OIB-like trace element signature of the newly discovered dykes. Furthermore, the geochemical "carbonatite fingerprint" establishes a direct genetic link between these dykes and the ~1.88 Ga carbonatites within the carton's interior. At issue is whether these alkaline diabase dykes were part of a larger dyke swarm (like the Molson Dyke Swarm, Manitoba), or very localised magmatic products. It also remains to be shown whether the dykes were fed vertically from a deep magma chamber, or laterally over longer distances from a possible plume centre. Based on circumstantial evidence, the former scenario is considered more plausible. Another aspect that remains to be addressed is whether the dykes, considering their shallow emplacement level (< 3 km), could have been related to a now eroded volcanic province.

As mentioned above, the alkaline diabase dykes discovered here differ in some respects from other members of the Circum-Superior LIP, which does, however, not contradict their inferred plume origin nor contradict their proposed genetic relationship to the Circum-Superior LIP. First, the dykes have an alkaline affinity, opposed to the predominantly tholeiitic to komatiitic magmatic rocks. Second, the newly discovered alkaline dykes are volumetrically minor compared to the magmatic rocks at, say, Thompson or the Cape Smith Belt. Third, the alkaline diabase dykes appear slightly younger than most other members of the Circum-Superior LIP. All of this could indicate that the dykes were formed in one of the later stages of the plume event by lower degrees of partial melting. Lower degrees of melting could be interpreted in terms of a more distal (cooler) plume setting, the fading of the plume itself, plate motion away from the steady plume (in the sense of a hot spot track), or simply a thicker lithospheric column above the melt source region (**Fig. 7.23**).

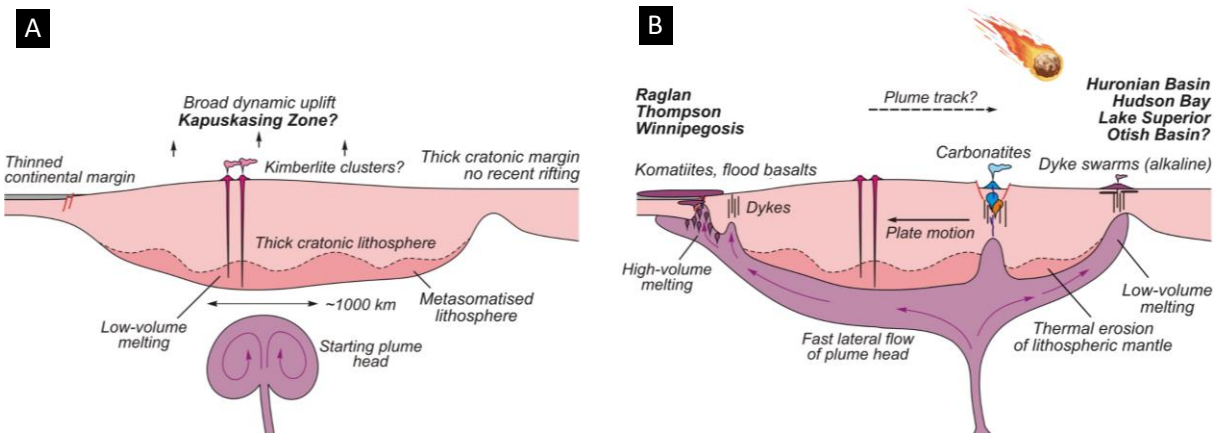

Figure 7.23 Genetic model for the Circum-Superior LIP; **A:** arrival of hot ascending asthenospheric material, likely a plume head, at the base of the Superior Craton (ca. 1890 Ma); this may have resulted in uplift of the lithosphere and the exhumation of lower crust, such as it is found in the Kapuskasing Structural Zone in the centre of the craton; the arrival of the plume head may have also caused metasomatism of the lithospheric mantle by fast rising low-viscosity carbonatite melts, or by low-volume, volatile-rich silicate melts; alternatively, metasomatism of the lithospheric mantle could have occurred during foregoing plume events, or during Neoarchaean to Palaeoproterozoic plate subduction; **B:** impingement and subsequent flattening of the plume head beneath the Superior Craton (~1883 Ma); the thick lithospheric keel of the craton caused lateral deflection of the plume into areas of thinner lithosphere, facilitating high-volume (garnet-consuming) melting in areas that had recently been affected by rifting, and low-volume (garnet-preserving) melting in areas of thicker lithosphere (or in cooler areas that were more distant to the plume); as the plate continued to migrate above the steady plume, some areas (e.g. the Huronian Basin) were eventually cut off from the plume and the heat source, whereas high-volume melt generation was sustained in other areas (e.g. Winnipegosis Belt); figures modified after Bleeker & Kamo (2018).

Ni-Cu-PGE potential

Certain members of the Circum-Superior LIP are host of economically important base metal mineralisation. At Raglan (Cape Smith Belt, Quebec), magmatic Ni-Cu-PGE sulphide mineralisation is associated with komatiitic lava flows of the so-called Raglan Formation (e.g. Lesher 2007, 2017; Mungall 2007). At Thompson, Manitoba, massive to disseminated Ni-Co-PGE sulphide mineralisation affected strongly deformed and metamorphosed ultramafic bodies of the Ospwagan Group (e.g. Peredery et al. 1982; Layton-Matthews et al. 2007). Deposits of the Thompson Nickel Belt are in fact among the world's largest producers of Nickel and in terms of total Canadian production rank second after the Sudbury Mining Camp (Mudd 2010; Lightfoot 2016). The Fox River Sill, also near Thompson, hosts sub-economic magmatic PGE-Cu-Ni (e.g. Desharnais et al. 2000). Other, younger, members of the Circum-Superior LIP, including those in the Lake Superior and Hudson Bay areas, are not associated with any known occurrences. Uranium-Pb dating (Bleeker & Kamo 2018) suggests that the above ore-forming events occurred within a narrow time frame, 1883–1881 Ma. The present study has identified 1872 ± 3 Ma alkaline ultrabasic dykes in the Huronian Basin. Although these dykes seem to be slightly younger than the main ore-forming event at Thompson or Raglan, their mere presence raises the question of their metallogenetic significance, especially after having provided evidence that these dykes are but a surface manifestation of a magmatic plumbing system, and in view of the fact that they conspicuously occur above one of the largest unexplained potential field anomalies on the Canadian Shield – the Temagami Anomaly.

The first factor to consider when assessing the metal fertility of an igneous rock is the degree of mantle melting. In the Earth mantle, base- and precious metals are generally believed to reside within discrete sulphide minerals (e.g. Lorand & Luguet 2016), and these will effectively withhold chalcophile elements, unless the degree of melting was high enough (> 17–25 %) to consume all the sulphide (e.g. Keays 1995; Rehkämper et al. 1999). This in turn means that low degrees of partial melting should not be able to release large amounts of Cu and PGE, because these elements will remain, together with residual sulphide, in the mantle. This theory was empirically tested by Jowitt & Ernst (2013), who found that alkaline members of LIPs are almost never associated with Ni-Cu-PGE deposits, whereas members formed via high degrees of melting (e.g. komatiites) tend to be well endowed, especially if they reached later S-saturation through crustal assimilation. The alkaline diabase dykes of the present study show no evidence of such crustal contamination, and they were evidently generated by very low degrees of partial melting (< 10%). However, according to Mungall et al. (2006) low degrees of melting can still lead to a chalcophile element enrichment under special circumstances. Highly oxidised conditions in the mantle could destabilise sulphide in favour of sulphate, thus releasing metals even at melting degrees as low as 5% to produce PGE-Cu rich meimechites and alkali picrites (Mungall et al. 2006). Whether such oxidised conditions prevailed in the mantle of the alkaline diabase dykes is, however, purely speculative; the high Ti/V ratio of the dykes is rather indicative a low fO_2 (Shervais 1982). On the other hand, if the dykes originated from hornblendite or a carbonated mantle source, as implied by this study, it is possible that the metasomatic agent (CO_2, H_2O) oxidised and fertilised the mantle domain. Moreover, a CO_2-rich volatile phase may even act as a transport medium for metal-charged sulphide liquids from the mantle into the crust (Blanks et al. 2020). In this context it should be noted that, contrary to Jowitt & Ernst (2013), there are indeed cases of Ni-Cu-PGE-Au enriched alkaline rocks elsewhere (e.g. Graham et al. 2017; Holwell & Blanks 2021), including the Coldwell Alkaline Complex, Ontario, or the well-known Phalaborwa Complex, South Africa. Therefore, alkaline magmatic affinity and elevated Ni-Cu-PGE potential are not per se mutually exclusive.

Another aspect worth considering is the S-saturation history of a magmatic system. Jowitt & Ernst (2013) observed that magmas that had experienced early removal of sulphide will deviate from the MgO/Ni silicate fractionation trend. This is because, once S-saturation is reached, Ni will strongly partition into the sulphide liquid, whereas Mg remains to be controlled solely by olivine. In **Figure 7.24A**, the MgO content of the alkaline diabase dykes is contrasted against their Ni content. The plot reveals that all samples fall on the silicate fractionation trend typified by (alkaline) within plate basalts, meaning there is no evidence of Ni depletion by sulphide removal. This either indicates that S-saturation was never achieved, or that the magma reached S-saturation so late that any hypothetical sulphide liquid was trapped by the silicates framework to form disseminated interstitial, and thus likely uneconomic, Ni-Cu-PGE mineralisation (e.g. Arndt et al. 2005).

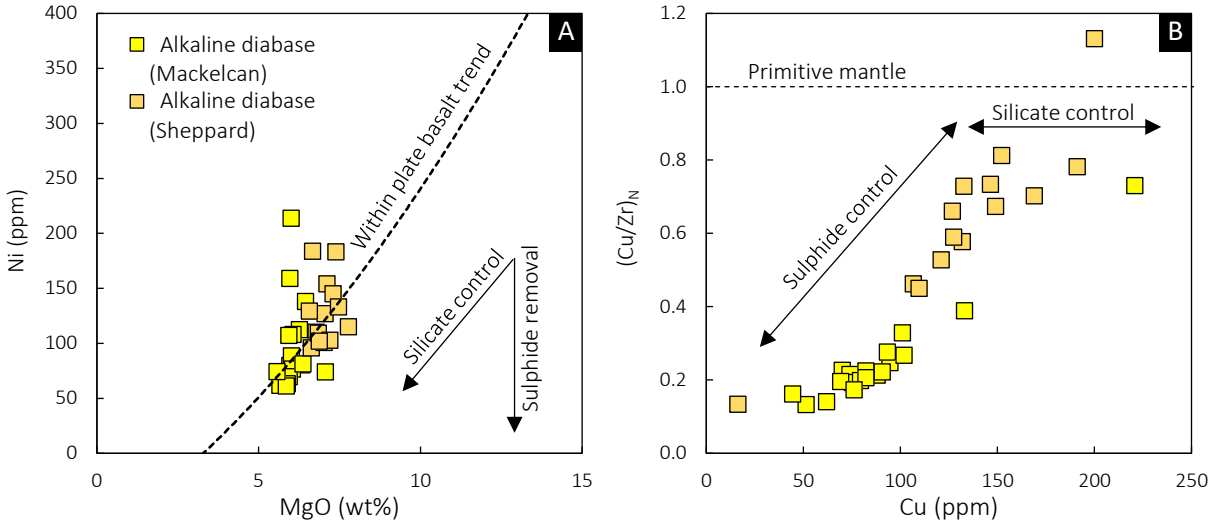

Figure 7.24 Geochemical plots used to evaluate the metallogenetic potential of the alkaline diabase dykes from the Huronian Basin; **A:** whole-rock MgO content vs. Ni content, showing the typical silicate fractionation trend defined by (alkaline) within plate basalts; after Keays & Lightfoot (2007); **B:** whole-rock Cu content vs. the primitive mantle-normalised Cu/Zr ratio; normalisation values are from Palme & O'Neill (2013).

According to Jowitt & Ernst (2013) the Cu/Zr ratio is another useful proxy in assessing the fertility of a magmatic system. The theory behind this is based on the incompatible behaviour of both Cu and Zr in S-undersaturated basic-ultrabasic magmas (Keays 1995). If, however, the magma reaches S-saturation, Cu will preferentially partition into the sulphide liquid and thereby fractionate the Cu/Zr ratio. **Figure 7.24B** shows that the alkaline diabase dykes are strongly depleted in chalcophile elements, as these have very low Cu/Zr ratios, far lower than the primitive mantle. Interestingly, the Cu/Zr ratio is positively correlated with Cu. There are three possible explanations for this trend. First, Cu could have been affected by secondary element mobility. Although the isocon method revealed some mobility of Cu, there is no systematic trend between alteration and Cu/Zr ratio. Second, the depletion in Cu could be due to sulphide loss within deeper crustal levels, which is, however, inconsistent with the MgO/Ni ratio. Third and favoured, the depletion in Cu relative to Zr could be the result of very low degrees of mantle melting. That is, analyses with a higher Cu/Zr ratio could simply reflect higher degrees of partial melting, whereas analyses with a low Cu/Zr reflect the retention of chalcophile elements in the mantle restite. This would be consistent with the above trace element considerations and would have rather negative implications for the Ni-Cu-PGE prospectivity of the alkaline dykes and whatever magmatic plumbing system they might have been related to. However, additional work is required to fully explore their Ni-Cu-PGE potential, ideally through geophysics and PGE+Au assays.

Calc-Alkaline Diabase

8.1 Summary

Another diabase dyke has been discontinuously mapped over a length of 5 km in Mackelcan Township, 45 km northeast of Sudbury. The dyke strikes northeast, cuts across sedimentary rocks of the Cobalt Group, and is in turn cut by pseudotachylitic breccia that is arguably product of the 1.85 Ga Sudbury impact event. This brackets the emplacement age of the dyke between 2.31 and 1.85 Ga. Petrographically, the dyke is described as a medium-grained aphyric quartz diabase, containing minor amounts of interstitial granophyric intergrowths between quartz and feldspar. The dyke suffered from extensive retrograde metamorphism at lower greenschist-facies conditions, resulting in the destruction of primary igneous textures, intense saussuritisation of feldspar, complete pseudomorphic replacement of ferromagnesian minerals by chlorite and actinolite, and alteration of ilmenite/magnetite to leucoxene.

Geochemically, and unlike primary mantle-derived melts, the dyke has a relatively evolved compositions (SiO_2 53–56 wt%, ≤ 200 ppm Cr, ≤ 100 ppm Ni). Its affinity is transitional between tholeiitic and calc-alkaline. Key geochemical features include, moderately high TiO_2 contents (1.3–1.4 wt%); relatively high concentrations of Zr (111–144 ppm); a very high $^{147}Sm/^{144}Nd$ ratio between 0.13 and 0.16; model ages between 2523 and 3638 Ma; a high La/Sm ratio (3.7–4.8); high Th/Nb ratio (0.3–0.5); and a distinct negative Ti anomaly ($Ti/Ti^* < 0.7$), features that either resulted from the assimilation of large amounts of crustal material, or alternatively, were inherited from a mantle source containing a recycled crustal component. The above field, petrographic and geochemical features clearly distinguish the dyke from other Palaeoproterozoic diabase dykes of the present and of forgoing studies within the Huronian Basin, including igneous rocks of the 2.22 Ga Nipissing Suite, but also impact melt rocks of the 1.85 Ga Sudbury Igneous Complex.

Based on relative age relations, orientation, lithology, and geochemistry, the dyke is suggested to be a member of the regional 2.17 Ga Biscotasing Dyke Swarm emanating from the Ungava Bay region, northern Quebec. Dykes of this swarm were not previously known to occur this far from the inferred plume centre. The new data demonstrate that dykes of the Biscotasing Dyke Swarm had also intruded into the Huronian Basin and were initially present within the area subsequently struck by the Sudbury impact. Thus, these new observations provide evidence of yet another, hitherto unrecognised, mafic lithology in the target area of one of the largest impact structures known on Earth.

8.2 Local Geology

Mackelcan Township is centred around 46°50N 80°37W some 45 km northeast of the City of Sudbury, and 10 km northeast of Wanapitei Lake. It borders McConnell Township to the north, McCarthy Township to the east, Rathbun Township to the south, and Aylmer Township to the west. Mackelcan Township covers approximately 90 km^2 and extents across the eastern portion of the Temagami geophysical anomaly. The magnetic peak of the Temagami Anomaly occurs 20 km, the gravity peak 15 km, northeast. Access is provided by the Kukagami Road which joins the Trans-Canada Highway about 10 km east of the town Wahnapitae. After following the Kukagami Road for 25 km north, the Bushy Bay Road and then several unnamed logging and drill roads lead to the area of interest. Water access is provided by the north arm of Matagamasi Lake. Field work by the author and the company involved was preceded by reconnaissance mapping of Ontario Geological Survey (Dressler 1982; Gates 1991). For detailed insights into the local geology, the reader is referred to these publications; a generalised overview is given in **Figure 8.1** and in the text below.

The entire Mackelcan Township is underlain by Palaeoproterozoic sedimentary rocks of the Cobalt Group (upper Huronian Supergroup). Sandstone of the Lorrain Formation predominates in the western half of the township, pelitic sedimentary rocks of the Gowganda Formation in the east. Although the contact between the two units is not directly exposed in the study area, it is thought to strike approximately N-S based on geophysical evidence (Easton et al. 2020) and a significant change in outcrop abundance and relief across the supposed contact. No igneous rocks of the 2.22 Ga Nipissing Suite or the 1.23 Ga Sudbury Dyke Swarm are present, at least not at surface.

The Lorrain Formation is a very thick and relative monotonous unit of fluviatile arenite. Dressler (1982) estimated its total preserved thickness at 3,400 m; drilling in the Wolf Lake area revealed an apparent thickness of 670 m and a gradual transition to the underlying Gowganda Formation (Schandl 2002). In the study area, the Lorrain Formation encompasses quartzofeldspathic rocks ranging from quartzite, (sub-)arkose, arkosic arenite and arkosic wacke. A thickly bedded massive sub-arkose is by far the most common lithology, and wacke becomes more abundant in the lowermost parts of the formation (e.g. Schandl 2002). Sedimentary structures are only really apparent at the outcrop scale and include thick planar bedding, through-cross stratification, and layers of quartz pebbles. Colours range in outcrop from dull white, light grey to different shades of green, beige, pink and brick red, all of which reflects different styles of post-depositional alteration and the presence of different secondary minerals such as hematite, chlorite, carbonate, or albite. Prograde metamorphism is evident by so-called bulging recrystallisation (Stipp et al. 2002) of quartz grains that occur in mutual contact with each other, and by the replacement of detrital felspar with sericite and saussurite. Lack of biotite, however, indicates that the upper greenschist facies (biotite zone) was either not attained or that biotite was replaced by retrograde chlorite. These observations constrain the temperature of the regional metamorphic overprint to ca. 280–390°C (e.g. Stipp et al. 2002), which is consistent with Card (1978). Rocks of the Lorrain Formation are typically cemented with chlorite and quartz, locally also with albite and carbonate. Silicified lithotypes, especially the quartzite from Wolf Mountain and Cobalt Hill, are very resistant to weathering and erosions, resulting locally in a significant relief (> 100 m).

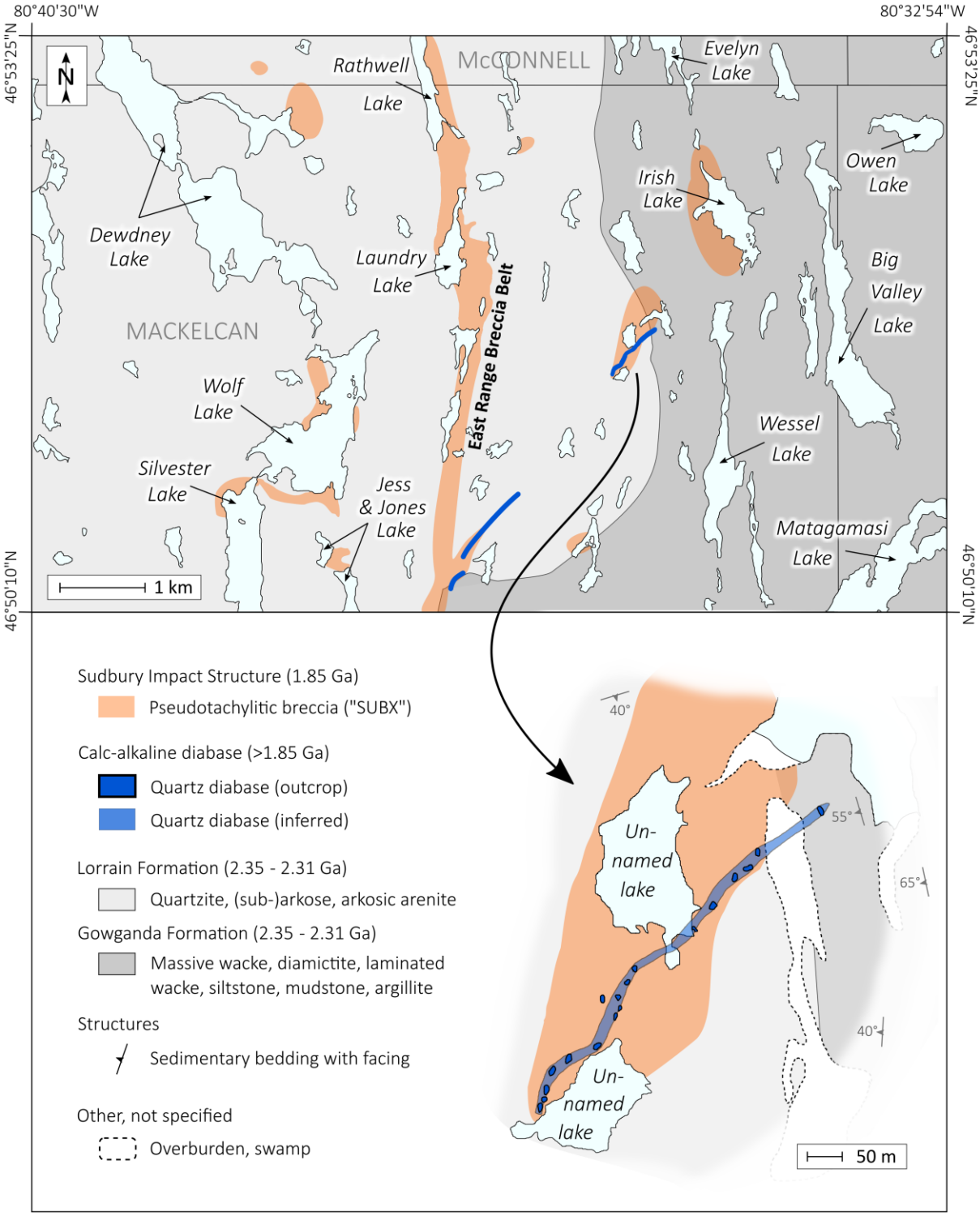

Figure 8.1 Geological map of Mackelcan Township showing the regional geological and lithostratigraphic context of the calc-alkaline diabase dyke; based on Dressler (1981a) and Whymark (2019) and additional mapping by the author in the course of this study.

The Gowganda Formation is likewise thick and extensive but less well exposed due to a higher susceptibility to erosion. In most general terms, the formation is a heterogeneous sequence of wacke, siltstone, and mudstone. The rocks were deposited between ~2.35 and 2.31 Ga in a glaciogenic to pro-deltaic environment (e.g. Young et al. 2001). A two-fold division of the Gowganda Formation in the Cobalt Embayment has been proposed (e.g. Rainbird & Donaldson 1988). The Coleman Member, which is abundant in the east of the study area, at McCarthy Township, comprises massive non-stratified greenish wacke with an occasional matrix-supported conglomerate facies (diamictite). Clasts are highly variable in size and shape and they lack any sorting. The most common clast lithology is pink granite, which gives the Coleman Formation a very distinctive appearance in the field. The Firstbrook Member, which conformably overlies the Coleman Member, comprises (from bottom to top) thinly and rhythmically bedded siltstone, mudstone, and eventually sandstone; dropstones are absent (e.g. Rainbird & Donaldson 1988). Argillaceous units of the Firstbrook Member display a diagnostic varve-like bedding of alternating light- and dark grey laminae and may be organic-rich or magnetite-bearing in places. Unfortunately, these relatively soft rocks are rarely exposed within the study area. The Firstbrook Member is more commonly observed in the eastern part of Mackelcan Township, near the contact to the overlying Lorrain Formation, which confirms an overall younging direction of the Huronian strata from east to west. Rocks of the Gowganda Formation were metamorphosed under lower greenschist-facies conditions as evident by the ubiquitous presence of chlorite, sericite, and the replacement of detrital plagioclase by epidote. Quartz-carbonate-chlorite veining can be intense and may locally be associated with Cu-Au mineralisation. Deformation is restricted to gentle folding and faulting.

Breccias related to the Sudbury impact event ("Sudbury Breccia") are widespread, but their identification strongly depends on the outcrop quality. Sudbury Breccia is typically found as irregular masses and dykes in all types of country rock, where it appears preferentially developed along contacts between host rocks of varying competence (e.g. arkose–mudstone) or utilising planes of prior weakness such as faults, joints, and bedding plains. Veinlets of ultracataclasite and recrystallised pseudotachylite revealed to be ubiquitous in the region but may be macroscopically mistaken for hydrothermal chlorite veins. A massive (megaclastic) type of Sudbury Breccia (**Fig. 4.2A**) is more easily recognised in the field, with continuous exposure over 14 km along a N-trending lineament from Matagamasi as far as Chiniguchi Lake, with an additional 15 km of discontinuous exposure further north and south. Interestingly, this belt strikes concentrically around the Sudbury Igneous Complex. By analogy to the South Range Breccia Belt (Scott & Spray 1999), it will be referred to as the *East Range Breccia Belt*. Sudbury Breccia shows significant petrographic diversity. Mono-, bi- and heterolithic, matrix- and clast supported varieties exist; clasts range in diameter from a few mm to at least 12 m and have a fractal grain size distribution. They are typically sub-rounded with aspect ratios < 2. Most clasts are of very local derivation and underwent little displacement or rotation. Some exceptions of allochthonous or even exotic clasts do, however, occur in the centre of the breccia belt. These could not be linked to any lithology in the vicinity, or in some cases, are entirely exotic (e.g. **Fig. 4.2B**). The texture of the breccia matrix ranges from homogeneous (**Fig. 4.2A**) to flow-banded (**Fig. 4.2C**), cataclastic, devitrified, intersertal, to vesicular and amygdaloidal. Injection dykes of breccia matrix into dilational sites within the ambient host rock were also observed (**Fig. 4.2C**). Locally, these may resemble isoclinal or sheath folds.

8.3 Field Relations

Another mafic dyke, here and in the following referred to as the calc-alkaline (quartz-) diabase, was discovered in Mackelcan Township in 2019. The dyke occurs in a remote area between two unnamed lakes (46°51 41N 80°35 34W) ca. 1.7 km southwest of Irish Lake. The dyke extends for 700 m, is non-magnetic, predominantly found in contact with brecciated ± albitised Lorrain Formation arkose and only its northeastern-most outcrop (near Bonesteel Lake) in contact with Firstbrook Member (Gowganda Formation). As it is rarely exposed, however, its thickness, dip and exact contact relation to the host rocks remain uncertain, its orientation can only be inferred (**Fig. 8.1**). The overall strike is N40°E, i.e., parallel to the tholeiitic dyke (**Chapter 6**) and perpendicular to the alkaline diabase (**Chapter 7**), but no intersection between the different intrusion could be found. A southern extension of the calc-alkaline diabase was discovered in 2020 north of Island Lake, striking for another 800 m continuously N40°E. There, the dyke stands out from its surroundings as a distinct morphological feature, forming ridges and linear valleys. Outcrop conditions are more insightful than in the north, revealing sharp vertically dipping (≥ 80° ESE) chilled contacts against the Lorrain Formation, which are in places (e.g. 46°50 33N 80°36 53W; 46°60 42N 80°36 41W) intensively sheared, brecciated, altered, and mineralised (< 3 vol% Py + Ccp + Mal ± Po). The dyke itself, however, is mostly free of sulphide; in no place is it visibly sheared. Where the dyke enters the East Range Breccia Belt (**Fig. 8.1**), it is offset ca. 100 m to the south while maintaining its original strike. No outcrop of the dyke could be found west of the breccia belt. The exact relation between Sudbury Breccia and the dyke is equivocal in the field, but as will be shown below, the calc-alkaline diabase shows clear signs of impact-related brecciation as well.

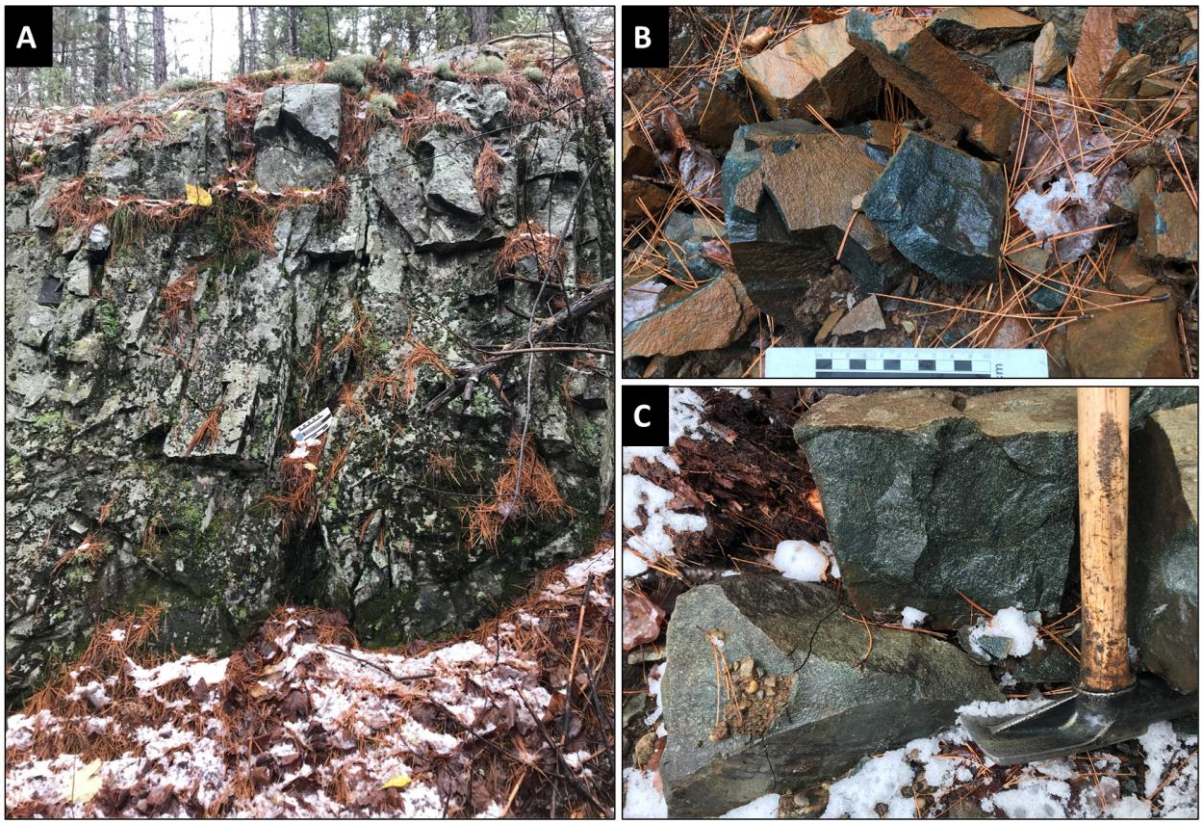

Figure 8.2 Photographs of the calc-alkaline quartz diabase dyke in outcrop; **A:** outcrop of the diabase showing columnar jointing parallel to the dyke's margin (46°50 34N 80°36 52W); **B–C:** freshly broken chunks; 10 cm-card for scale; photographs were kindly provided by Jacob VanderWal and Renan Silva.

8.4 Petrography

Macroscopically, the dyke bears all hallmarks of a typical diabase, which makes an in-situ distinction from the alkaline diabase (**Chapter 7**) or the regional Nipissing Suite gabbro almost impossible. It is a medium grained (< 3 mm), massive, non-foliated, melanocratic rock (colour index 50–60) of dark green colour. Its texture is remarkably uniform along strike and within a given outcrop except for aphantic, likely chilled, margins. No xenoliths were observed throughout, either because of their complete digestion or because of their absence in the first place. A photograph of a representative hand specimen of the calc-alkaline quartz diabase is shown in **Figure 8.3A**.

In thin section (and in stark contrast to its macroscopic appearance) the dyke barely resembles what one would call an igneous rock: Epidote (10–25 vol%), chlorite (10–15 vol%), quartz (10–30 vol%) and amphibole (20–40 vol%) – all anhedral – are the major rock-forming minerals, and the original texture has been altered beyond recognition. In addition, extensive "opaque veining" was observed in every thin section even though this is not apparent in hand specimen. These veins are variable in thickness, ranging from a few µm to several cm, with sharp and well-defined margins. They are colourless or green under plane polarised light, micro- to cryptocrystalline and thus almost opaque under crossed polars, all of which gives them the appearance of tectonic shear bands. In contrast to tectonic (i.e., endogenetic) shears, however, these veins lack a preferred orientation; they form anastomosing (braded), in places orthogonal, mesh-like stockworks. Based on analogues features described before (**Chapters 6.4** and **7.5**) and elsewhere in the literature (e.g. Chubb et al. 1994; Kovaleva et al. 2018a), these veins are interpreted as recrystallised pseudotachylite or ultracataclasite, and by implication, as Sudbury Breccia. An example that clearly demonstrates the brecciated nature of these features is shown in **Figure 8.2B**. In other places, Sudbury Breccia is in sharp contact to the host rock, devoid of refractory clasts, mineralogically indistinct from the host rock and thus only identified by its very small grain size (**Fig. 8.3C**).

Notwithstanding the pervasive alteration and brecciation, the original magmatic texture of the diabase is in very rare instances, though pseudomorphically, preserved (**Fig. 8.3D**). It may be described as holocrystalline, (sub-)equigranular and aphyric. Contours of tabular 1.5 mm-large plagioclase are recognised here and there, and occasionally, even relict polysynthetic twinning and rims of albite can be observed. Undeformed monocrystalline quartz occurs as a ubiquitous mineral, anhedral and interstitial between former plagioclase and mafic minerals. It is typically 0.25 mm large and considered a primary constituent of the rock as well. Quartz is often vermicular-textured (**Fig. 8.3E**) which is interpreted as relict granophyric intergrowths with feldspar. No pyroxene is present, and pale green fibrous amphibole is the most abundant mafic mineral in all samples. Amphibole occurs as 0.5 mm large aggregates possibly secondary after pyroxene; most amphibole is, in turn, replaced by Fe-rich (purple) chlorite. Angular, up to 0.15 mm large, non-magnetic leucoxene occurs disseminated throughout; apatite was never observed. This, together with the abundance of quartz, provides a petrographic criterion to distinguish the rock from the apatite-rich quartz-free alkaline diabase dykes introduced in the previous chapter (**Chapter 7**).

Hydrous alteration in form of a pervasive chloritisation and epidotisation is omnipresent, and domains of > 50 vol% granular epidote are not uncommon (**Fig. 8.3F**). Cross-cutting relations indicate that the epidote alteration must have occurred prior to 1.85 Ga. Texturally late quartz-carbonate-hematite veining similar to that near Laundry Lake was also observed (**Fig. 8.2A,B**).

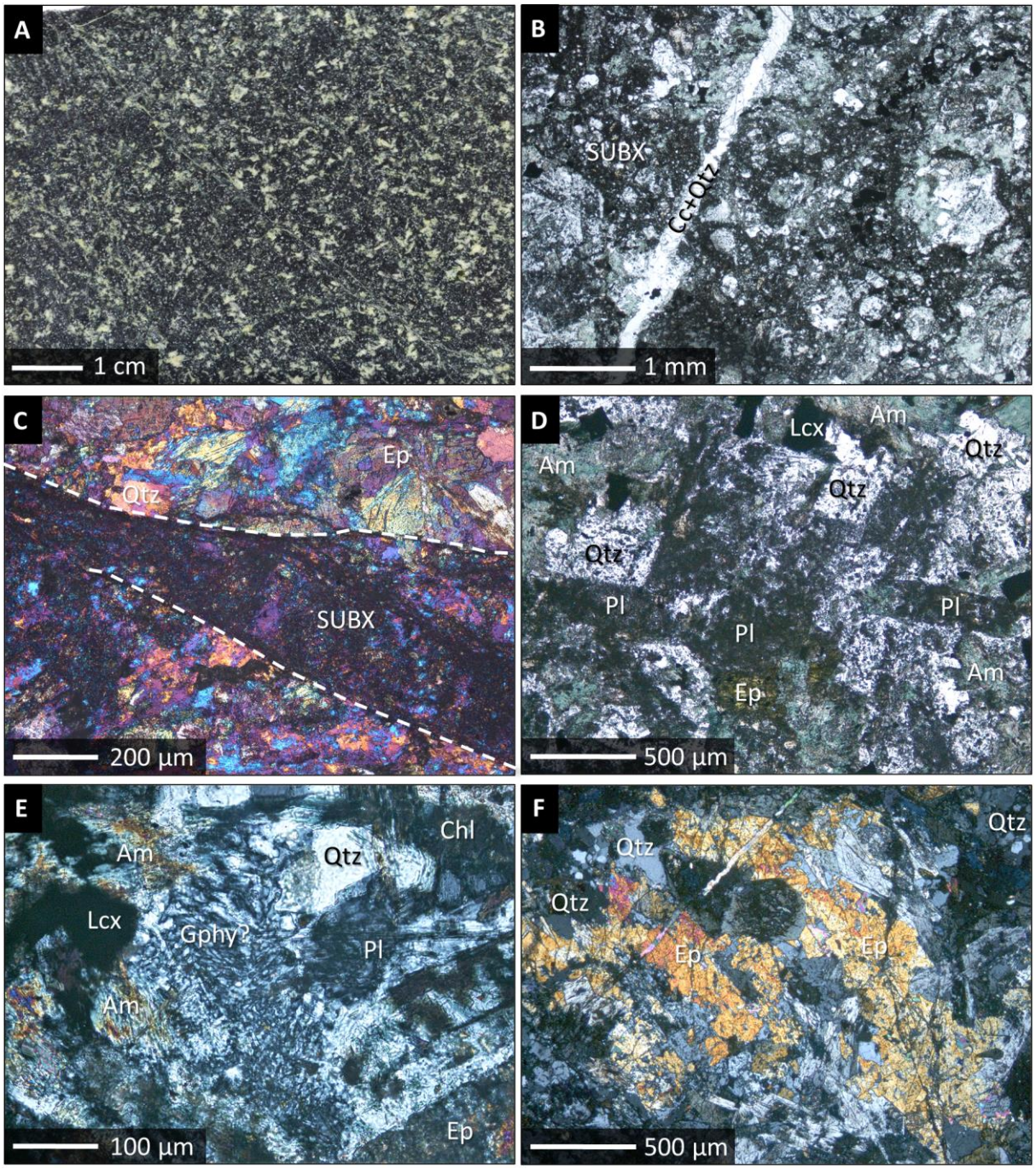

Figure 8.3 Photograph and microphotographs of the calc-alkaline quartz diabase dyke from Mackelcan Township; **A:** polished hand specimen representative of the entire dyke; **B:** thin section under transmitted light and plane polars (sample AK19-21), showing pseudotachylitic breccia (Sudbury Breccia) developed within the quartz diabase and with abundant refractory quartz-rich clasts; the breccia is crosscut by a later calcite-quartz vein; **C:** same thin section but different spot under crossed polars and with gypsum compensator; note the truncation of the epidote grains by the pseudotachylitic vein; **D:** thin section under transmitted light and plane polars (sample AK19-29), showing a rare sample in which the original texture of the diabase seems remotely preserved; **E:** thin section under transmitted light and crossed polars (sample AK19-24), showing vermicular-textured quartz and plagioclase, possibly representing an altered granophyric intergrowth; **D:** thin section under transmitted light and crossed polars (sample AK19-21), showing large anhedral epidote grains replacing the quartz diabase. Abbreviations: SUBX = Sudbury Breccia; Cc = calcite; Qtz = quartz; Ep = epidote; Am = amphibole; Pl = plagioclase; Lcx = leucoxene; Gphy = granophyric intergrowth; Chl = chlorite.

8.5 Geochemistry

General characteristics

Quartz diabase from eastern Mackelcan Township has a uniform, subaluminous, subalkaline, and in terms of SiO_2 (53–56 wt%) intermediate composition (**Tab. 8.1**). Fe_2O_3 ranges from 13 to 15 wt%, and MgO from 4 to 6 wt%, corresponding to a Mg# (=100×molar MgO/[MgO+FeO]) between 43 and 48. As already expected from its hydrothermally altered appearance, the rock is rich in volatiles (2–6 wt% LOI). Concentrations of TiO_2 are typically between 1.3 and 1.4 wt% and P_2O_5 is below 0.1 wt%. The rock is furthermore characterised by moderate to high concentrations of Cr (60–194 ppm) and Ni (33–100 ppm), and somewhat elevated concentrations of incompatible lithophile elements such as, Zr (111–144 ppm), Nb (8–13 ppm), Th (3.9–5.5 ppm), U (1.0–1.3 ppm), and ΣREE+Y (120–162 ppm). Its average CIPW normative mineralogy is as follows: 45 vol% plagioclase, 21 vol% hypersthene, 14 vol% quartz, 9 vol% diopside, 5 vol% orthoclase, and 3 vol% ilmenite/magnetite, corresponding to a hypothetical rock density of 3.0 g/cm^3.

Igneous rock classification

The quartz diabase's composition conforms to basaltic andesite (intrusive equivalent: gabbroic diorite) according to the TAS diagram (**Fig. 8.4B**). A tholeiitic magmatic affinity is indicated by the AFM plot (**Fig. 8.4C**). Although the isocon method demonstrates little secondary mobility of most major elements (**Fig. 8.4A**), classification plots using typically immobile trace elements (Ti, Nb, Y, Zr, Th) are generally preferred. In such diagrams (e.g. **Fig. 8.4D**), the samples also plot within the field of basalt/gabbro. Most classification schemes, including **Figure 8.4E** and others not shown here (e.g. Jensen 1976; Hastie et al. 2007; Ross & Bédard 2009), suggest a calc-alkaline magmatic affinity. This classification agrees with mantle-normalised trace element patterns of the rock (**Fig. 8.4F**), which exhibit the diagnostic features of (calc-alkaline) arc magmatism namely, the decoupling and enrichment of LILE from and over HFSE. This is evident from pronounced negative anomalies of Ti, Nb and Ta, and variably positive anomalies of Rb, Ba, Sr and especially of Pb, relative to the primitive mantle and relative to other elements of similar incompatibility (**Fig. 8.4F**). Potassium is highly variable and produces both negative and positive anomalies. A peculiar feature of the quartz diabase is its lack of HREE depletion compared to any other rock analysed in this study. A negative Eu anomaly, expressed as $Eu_N/(Sm_N \times Gd_N)^{0.5}$, also exists (0.5–0.6).

Nd-Sr-Pb isotopes

A summary of whole-rock radioisotope data obtained for the quartz diabase is presented in **Table 8.2**. The rock is characterised by a very narrow, within the analytical uncertainty almost identical, range in $^{143}Nd/^{144}Nd$ equivalent to an εNd between –18.51 and –17.23. The $^{147}Sm/^{144}Nd$ ratio is relatively high for a mafic dyke, and ranges from 0.13 to 0.16. Accordingly, one-stage Nd model ages are unrealistically old (2523–3638 Ma), indicating the involvement of older crust in the magmatic evolution of the dyke. The $^{206}Pb/^{204}Pb$ ratio ranges from 17.88 to 18.58, $^{207}Pb/^{204}Pb$ from 15.54 to 15.59, and $^{208}Pb/^{204}Pb$ from 37.34 to 38.00. These values fall on the orogen/upper crustal Pb isotope evolution curves according to Zartman & Doe (1981) indicative of magma-crust interaction. The modelled initial $^{207}Pb/^{204}Pb$ ratio at 1850 Ma is 15.22–15.30. The $^{87}Sr/^{86}Sr$ ratio is very radiogenic and exhibits a considerable range, from 0.717 to 0.735. The $^{87}Rb/^{86}Sr$ ratio ranges from 0.267 to 0.746. None of the above isotope ratios is of any age significance.

Table 8.1 Major element oxide concentrations (wt%) and trace element concentrations (ppm) in calc-alkaline quartz diabase, Mackelcan Township

	AK19 21	AK19 22	AK19 23	AK19 24	AK19 25	AK19 26	AK19 27	AK19 29	AK19 30	ILN20 01	ILN20 2A	ILN20 2B	ILN20 3A	ILN20 3B	ILN20 4A	ILN20 05	ILN20 06	ILN20 07	ILN20 08	ILN20 9A	ILN20 9B	ILN20 9C
Lat.	46°51 38	46°51 40	46°51 41	46°51 41	46°51 41	46°51 44	46°51 34	46°51 32	46°51 30	46°50 41	46°50 38	46°50 38	46°50 34	46°50 34	46°50 33	46°50 29	46°50 23	46°50 21	46°50 42	46°50 42	46°50 42	46°50 42
Long.	80°35 32	80°35 30	80°35 29	80°35 29	80°35 29	80°35 22	80°35 38	80°35 42	80°35 45	80°36 45	80°36 48	80°36 48	80°36 52	80°36 52	80°36 53	80°36 57	80°36 58	80°37 01	80°36 42	80°36 41	80°36 41	80°36 41
SiO_2	54.5	53.4	53.2	53.7	52.3	53.9	53.7	54.2	52.2	53.0	52.0	53.0	52.6	51.3	52.4	52.9	52.9	53.1	53.1	52.0	51.9	51.9
TiO_2	1.34	1.35	1.34	1.33	1.35	1.36	1.37	1.35	1.30	1.38	1.28	1.36	1.37	1.31	1.39	1.37	1.29	1.36	1.36	1.35	1.38	1.31
Al_2O_3	13.5	13.6	13.4	13.4	13.4	13.5	13.6	13.3	13.4	13.4	13.3	13.5	13.4	12.8	13.4	13.4	13.4	13.5	13.3	12.8	13.5	13.1
Fe_2O_3	13.2	14.0	13.9	14.2	13.2	13.9	13.2	13.3	13.9	14.0	14.1	14.0	14.3	13.7	14.3	14.2	13.7	14.4	13.4	14.5	14.3	13.8
MgO	5.0	4.8	4.9	4.8	4.5	4.8	5.3	4.9	5.1	4.9	5.2	4.9	4.8	4.7	5.4	4.8	4.9	4.8	5.1	6.3	4.8	4.9
CaO	8.0	8.0	8.2	8.1	8.5	7.8	7.2	7.2	7.5	7.5	8.4	7.4	7.2	7.6	6.5	7.8	8.2	7.5	7.6	2.42	7.8	8.1
MnO	0.17	0.18	0.18	0.19	0.14	0.17	0.16	0.16	0.18	0.18	0.17	0.18	0.24	0.23	0.24	0.20	0.18	0.19	0.17	0.14	0.17	0.16
Na_2O	1.81	1.97	1.53	1.75	1.15	1.44	2.26	2.04	1.52	2.45	2.14	2.20	2.29	1.79	2.05	1.83	1.90	2.03	2.39	2.17	1.93	2.11
K_2O	0.30	0.32	1.17	0.53	1.07	0.40	0.63	0.81	0.48	0.59	0.33	0.35	0.65	0.90	0.77	0.54	0.97	0.42	0.29	3.42	0.38	0.66
P_2O_5	0.07	0.06	0.07	0.04	0.08	0.05	0.07	0.05	0.02	0.02	0.01	0.01	< 0.01	0.03	< 0.01	0.03	0.03	0.02	0.04	< 0.01	0.04	0.04
LOI	3.3	2.4	2.8	2.1	5.4	3.1	2.6	2.5	4.9	2.4	2.6	2.7	2.4	5.8	2.9	2.6	2.3	2.4	2.6	4.6	2.6	4.3
Total	101.14	100.06	100.66	100.17	101.08	100.41	99.95	99.76	100.58	99.77	99.50	99.59	99.27	100.17	99.38	99.65	99.80	99.69	99.44	99.72	98.65	100.34
V	309.1	310.7	308.2	308.5	308.5	306.0	314.3	303.8	302.2	307.3	310.3	321.5	310.6	303.9	319.1	321.7	309.1	313.3	314.7	313.5	332.2	340.5
Cr	193.8	109.2	84.86	105.0	81.59	95.75	64.72	151.7	70.82	131.4	83.20	122.6	104.3	60.44	69.86	102.0	88.86	99.35	68.55	66.73	108.0	78.74
Ni	99.47	59.15	47.49	56.98	52.87	53.63	42.98	83.94	38.71	68.68	54.56	65.09	55.32	33.54	42.22	51.06	44.20	52.13	37.43	32.66	54.88	46.90
Cu	59.05	42.00	41.29	53.24	90.76	31.37	64.34	67.24	64.16	54.83	36.40	61.20	42.43	42.96	58.43	47.07	33.82	35.22	52.60	18.41	28.62	47.84
Rb	7.179	19.61	53.95	12.03	39.07	9.438	30.96	28.87	27.11	28.77	6.709	7.293	18.86	44.10	28.26	13.45	41.90	20.57	5.569	178.9	11.16	41.21
Sr	435.8	540.0	430.5	347.5	499.2	549.8	270.2	387.4	248.7	285.7	283.2	299.0	299.9	221.0	334.8	331.1	508.1	668.9	296.8	57.45	392.6	286.4
Y	28.37	34.20	27.61	28.41	27.71	27.84	29.39	30.52	27.06	31.86	27.16	29.49	35.53	30.65	32.10	30.57	29.61	33.85	30.46	17.15	30.39	31.23
Zr	123.9	128.8	141.4	125.1	139.8	143.5	126.2	128.9	137.4	126.7	110.7	122.6	127.3	130.5	130.2	127.1	123.4	129.3	127.9	127.8	127.3	129.9
Nb	12.30	11.51	9.398	11.30	9.306	9.805	9.786	13.13	8.480	12.13	8.777	12.30	11.09	9.859	10.96	11.99	10.50	11.03	10.56	10.46	11.93	10.66
Ba	78.46	75.76	315.5	152.8	365.8	181.8	145.6	181.1	109.9	135.3	81.25	139.4	209.4	188.5	213.0	158.7	253.7	137.9	221.5	344.5	91.80	110.5
La	18.11	21.86	17.06	18.50	17.36	17.12	19.85	19.24	16.79	21.93	16.59	20.63	23.86	20.69	20.38	20.37	20.26	22.16	19.78	20.02	22.93	20.25
Ce	37.94	43.53	36.53	40.72	36.50	35.70	42.72	41.36	35.20	44.24	36.20	43.10	44.01	43.74	42.68	43.98	41.93	45.23	42.89	40.50	47.43	42.38
Pr	4.705	5.456	4.540	4.907	4.563	4.505	5.125	5.007	4.395	5.660	4.594	5.453	6.046	5.461	5.507	5.802	5.344	5.753	5.699	5.092	5.861	5.312
Nd	18.10	22.52	17.57	20.53	17.63	17.35	21.30	20.68	17.09	20.99	16.87	20.22	22.16	20.01	20.80	21.49	20.07	21.49	21.19	18.34	21.19	19.97
Sm	4.390	4.997	4.346	4.600	4.352	4.286	4.690	4.567	4.215	5.270	4.322	5.120	5.530	5.022	5.390	5.458	5.150	5.438	5.393	4.211	5.304	5.022
Eu	1.338	1.479	1.314	1.400	1.358	1.278	1.520	1.434	1.205	1.501	1.409	1.526	1.613	1.475	1.549	1.494	1.457	1.553	1.554	1.002	1.644	1.519
Tb	0.765	0.871	0.772	0.811	0.757	0.756	0.823	0.831	0.745	0.939	0.814	0.917	1.010	0.927	0.938	0.949	0.878	0.993	0.947	0.576	0.951	0.904
Gd	4.845	5.647	4.840	5.267	4.742	4.731	5.372	5.360	4.626	5.701	4.848	5.554	6.198	5.545	5.711	5.726	5.369	6.073	5.705	3.743	5.738	5.640
Dy	4.740	5.768	4.677	5.264	4.681	4.673	5.372	5.461	4.628	5.652	4.856	5.432	6.060	5.505	5.764	5.618	5.320	5.990	5.596	3.256	5.655	5.496
Ho	0.974	1.153	0.963	1.049	0.965	0.969	1.072	1.088	0.947	1.207	1.053	1.175	1.298	1.194	1.215	1.218	1.129	1.284	1.213	0.696	1.228	1.152
Er	2.887	3.549	2.898	3.201	2.872	2.848	3.258	3.338	2.810	3.511	2.982	3.369	3.756	3.351	3.553	3.479	3.301	3.713	3.456	2.179	3.510	3.387
Tm	0.412	0.501	0.413	0.442	0.412	0.413	0.454	0.467	0.405	0.517	0.445	0.503	0.560	0.507	0.516	0.516	0.477	0.554	0.515	0.363	0.529	0.493
Yb	2.756	3.394	2.800	2.994	2.743	2.757	3.045	3.161	2.697	3.322	2.863	3.195	3.553	3.191	3.340	3.213	3.106	3.544	3.246	2.533	3.288	3.181
Lu	0.434	0.520	0.438	0.454	0.437	0.437	0.469	0.480	0.427	0.538	0.428	0.481	0.565	0.477	0.520	0.487	0.488	0.564	0.489	0.410	0.486	0.494
Hf	3.491	3.528	3.553	3.489	3.554	3.558	3.429	3.500	3.443	3.418	2.858	3.355	3.425	3.351	3.833	3.486	3.648	3.523	3.504	3.490	3.487	3.493
Ta	0.584	0.660	0.588	0.611	0.582	0.581	0.608	0.628	0.557	0.703	0.607	0.678	0.666	0.692	1.014	0.700	1.274	0.692	0.681	0.677	0.683	0.625
Pb	7.406	7.956	10.07	7.837	8.414	9.478	6.362	6.031	6.235	6.517	4.375	7.138	10.51	5.766	12.29	28.40	12.55	73.44	5.444	4.567	10.56	4.764
Th	3.873	5.125	3.971	4.226	3.909	3.900	4.198	4.619	3.883	4.901	3.892	4.631	5.509	4.610	4.727	4.930	4.402	5.171	4.814	4.800	4.949	4.728
U	1.054	1.045	1.008	1.045	0.968	0.994	1.016	1.107	0.955	1.131	0.978	1.083	1.175	1.144	1.127	1.146	1.079	1.154	1.132	1.243	1.268	1.043

Table 8.2 Summary of whole-rock Nd-Sr-Pb isotope data for calc-alkaline quartz diabase, Mackelcan Township

	$\frac{^{143}Nd}{^{144}Nd}$	±2σ	$\frac{^{147}Sm}{^{144}Nd}$	εNd present	εNd 2220 Ma	1-stage t_{DM}	2-stage t_{DM}	$\frac{^{87}Sr}{^{86}Sr}$	±2σ	$\frac{^{87}Rb}{^{86}Sr}$	$\frac{^{87}Sr}{^{86}Sr_{2220}}$	$\frac{^{208}Pb}{^{204}Pb}$	±2σ	$\frac{^{207}Pb}{^{204}Pb}$	±2σ	$\frac{^{206}Pb}{^{204}Pb}$	±2σ	$\frac{^{207}Pb}{^{204}Pb_{1850}}$
Northeast dyke segment																		
AK19-22	0.511695	12	0.134	−18.39	−0.5	2583	2228	0.727794	13	0.304	0.71805	37.3448	22	15.5356	8	17.8841	8	15.26
AK19-24	0.511712	15	0.135	−18.06	−0.5	2594	2231	0.723650	11	0.298	0.71409	37.4776	25	15.5879	8	17.9856	8	15.30
AK19-27	0.511706	10	0.133	−18.19	0.0	2528	2194	0.726259	14	0.514	0.70977	37.3569	25	15.5428	8	18.1387	9	15.24
AK19-29	0.511714	11	0.133	−18.02	+0.1	2523	2190	0.731035	12	0.408	0.71797	37.9927	23	15.5743	8	18.5836	8	15.22
AK19-30	0.511699	12	0.149	−18.31	−4.71	3222	2868	0.728987	13	0.500	0.71296	38.0837	27	15.6038	9	18.4746	9	15.26
Southwest dyke segment																		
ILN20-1	0.511719	17	0.152	−17.92	−5.09	3324	2898	0.728383	12	0.478	0.71308	37.4300	29	15.6236	9	18.2317	9	15.31
ILN20-2A	0.511755	13	0.155	−17.23	−5.28	3417	2912	0.717355	15	0.267	0.70880	38.0230	29	15.7103	11	19.1429	8	15.29
ILN20-3A	0.511729	13	0.151	−17.73	−4.63	3242	2863	0.726056	12	0.375	0.71404	36.6068	20	15.5603	7	17.4102	7	15.34
ILN20-3B	0.511694	10	0.152	−18.42	−5.56	3388	2934	0.735689	14	0.746	0.71178	38.1461	34	15.7249	12	18.9592	12	15.33
ILN20-4A	0.511723	10	0.156	−17.85	−6.41	3638	3000	0.731868	13	0.435	0.71794	37.7048	30	15.6592	10	18.1185	9	15.36
ILN20-6	0.511689	10	0.155	−18.51	−6.63	3628	3020	0.725163	10	0.428	0.71146	36.5746	26	15.6682	10	17.3784	9	15.45
ILN20-7	0.511721	9	0.153	−17.88	−5.38	3389	2920	0.723086	12	0.288	0.71387	35.6459	5	15.5586	8	16.2962	8	15.46
ILN20-9C	0.511713	11	0.152	−18.05	−5.29	3357	2913	0.726886	12	0.594	0.70786	38.4050	27	15.7557	9	19.2750	9	15.33

$^{147}Sm/^{144}Nd$ and $^{87}Rb/^{86}Sr$ ratios were calculated using measured Sm, Nd, Rb and Sr concentrations, which are given in Table 8.1;
2σ uncertainties of $^{147}Sm/^{144}Nd$ and $^{87}Rb/^{86}Sr$ are < 3% based on the propagated analytical error of Sm, Nd, Rb and Sr concentration data;
$^{143}Nd/^{144}Nd$ ratios are normalised to $^{146}Nd/^{144}Nd = 0.72190$;
2σ uncertainties of $^{143}Nd/^{144}Nd$ are < 0.004% based on the long-term in-house reproducibility of BHVO-2;
2σ uncertainties of $^{87}Sr/^{86}Sr$ are < 0.007% based on the long-term in-house reproducibility of BHVO-2;
2σ uncertainties of $^{208}Pb/^{204}Pb$, $^{207}Pb/^{204}Pb$ and $^{206}Pb/^{204}Pb$ are < 0.18%, < 0.09% and < 0.5%, respectively, based on the long-term in-house reproducibility of BHVO-2;
For sake of readability, all listed 2σ absolute errors only refer to the last significant decimal digits of the measured isotope ratios;
εNd values were calculated relative to CHUR with $^{147}Sm/^{144}Nd = 0.1967$ and $^{143}Nd/^{144}Nd = 0.512638$;
One-stage Nd model ages (t_{DM}) were calculated according to DePaolo (1981a,b);
Two-stage Nd model ages (t_{DM}) were calculated according to Liew & Hofmann (1988) using a $^{147}Sm/^{144}Nd = 0.106$ for the contaminant, which is the regional average crustal composition as approximated by the composition of the Sudbury Igneous Complex (e.g. Prevec et al. 2000)
$^{207}Pb/^{206}Pb_{1850}$ was calculated according to Darling et al. (2010a)

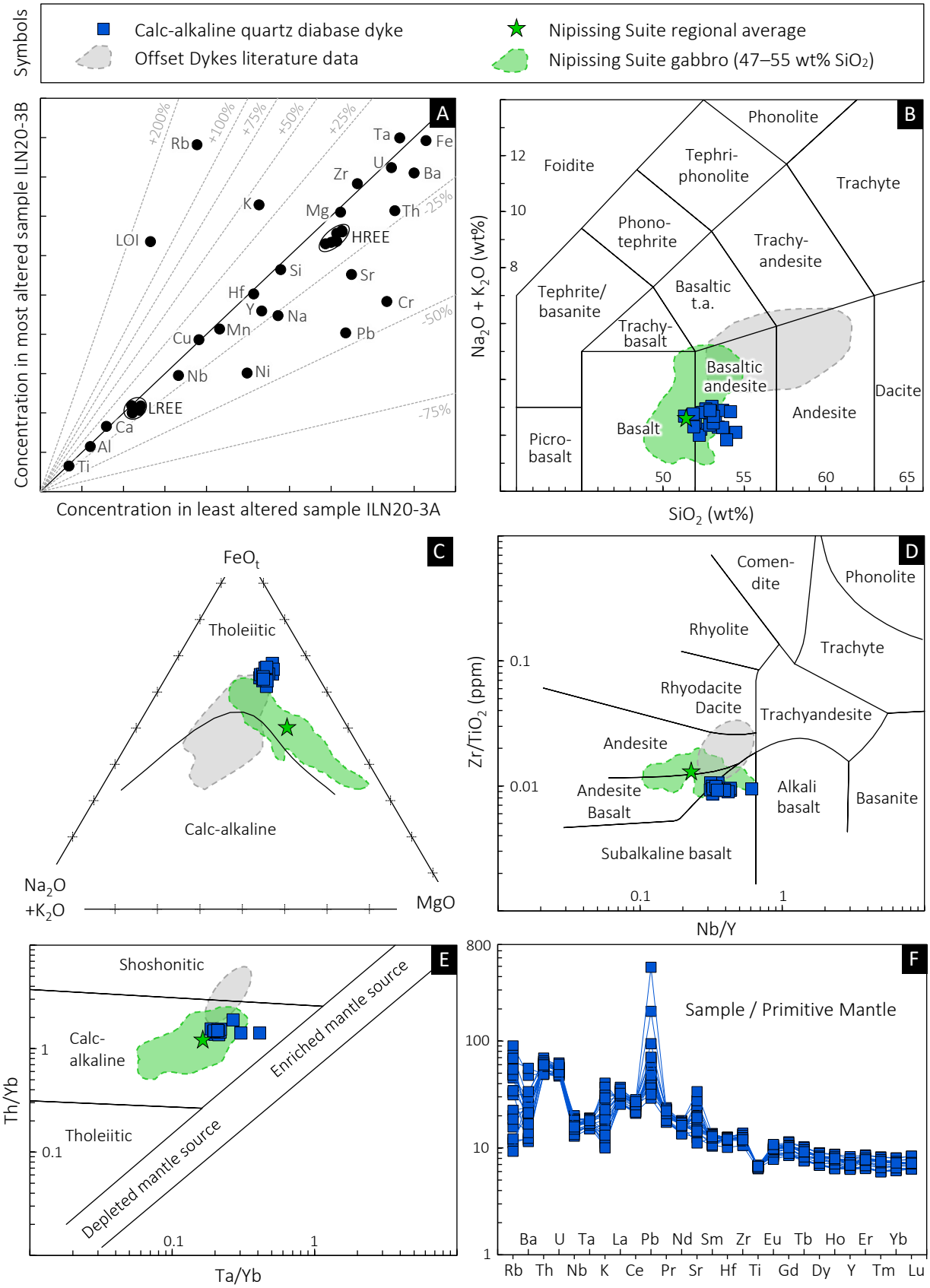

Figure 8.4 A selection of plots used to illustrate the effects of metasomatism on, and the geochemical classification and magmatic affinity of, the calc-alkaline quartz diabase from Mackelcan Township; **A:** isocon diagram after Grant (1986); **B:** TAS classification after Le Bas et al. (1986); **C:** AFM plot after Irvine & Baragar (1971); **D:** discrimination plot after Winchester & Floyd (1977); **E:** discrimination plot after Pearce (1983); **F:** spidergram with normalisation values after McDonough & Sun (1995); Offset Dyke data (excluding outliers) are mainly from Lightfoot et al. (1997c); data for the Nipissing Suite are from Lightfoot & Naldrett (1996b) and Jobin-Bevans (2016); propagated 2σ error bars are smaller than the symbol size.

8.6 Interpretation

Assessment of post-depositional alteration

Quartz diabase from Mackelcan Township underwent extensive sub-solidus alteration as evident from a lack of preservation of primary igneous minerals and textures (e.g. **Fig. 8.3**), and a preponderance of carbonates and hydrous silicates. Some of these changes are likely related to regional greenschist-facies metamorphism and expected to have occurred under isochemical conditions (simple hydration), whereas others (e.g. sericitisation, carbonatisation) are more erratic or seem to be related to later crosscutting hydrothermal veining and imply an open system behaviour of certain elements. Thus, it is first necessary to assess the extent of secondary element mobility, and to identify those immobile elements that are representative of the protolith's composition.

The isocon method after Grant (1986) offers a straightforward approach to element mobility: Contrasting the composition of the freshest sample available (ILN-3A) with that of the most intensely altered sample from the same outcrop (ILN-3B) reveals that most elements (esp. HFSE) remained constant within the analytical uncertainty, because they plot on, or close to, a straight line (an isocon) through the origin (**Fig. 8.4A**). The slope of this regression line is close to one, indicating that – despite volatile gain (LOI +140%) – volume change was negligible. Interestingly, Ca, Al, and Si seemingly remained constant as well, indicating that epidotisation and chloritisation were isochemical processes, and are merely a consequence of retrograde metamorphism. Only Sr (–26%), Na (–22%), and Pb (–45%) appear mobile possibly due to local metal redistribution following the breakdown of magmatic feldspar, and their overall higher solubility. Interestingly, the isocon method also implies mobility of Cr (–42%) and Ni (–40%), although it cannot be ruled out that this reflects primary inhomogeneities. Sericitisation could explain the apparent gain of K (+39%) and Rb (+134%) as well as the large scatter in the TAS diagram (**Fig. 8.4B**). Relatively low element mobility, at least for HFSE, is further supported by constant inter-element ratios (**Fig. 8.4D,E**), uniform trace element patterns (**Fig. 8.4F**), and optimal alteration indices (not shown).

The discussion of fluid mobility also applies to radiogenic isotope ratios. Due to the low capacity of most fluids to carry trivalent REE (e.g. Bau 1991), it is not expected that either Sm or Nd were significantly mobilised during low/medium-grade metamorphism or mild metasomatism, nor should have Sm/Nd elemental fractionation taken place unless the fluid:rock ratio was exceptionally high (e.g. DePaolo & Wasserburg 1979). Immobility of these elements and their isotopes is supported by constant Sm/Nd, $^{143}Nd/^{144}Nd$, and $^{147}Sm/^{144}Nd$ ratios. There is no correlation at all between the measured $^{143}Nd/^{144}Nd$ ratio and the whole-rock volatile content, the latter serving as an alteration proxy (**Fig. 8.5A**). Lead isotope ratios are weakly positively correlated with the volatile content ($R^2 = 0.30$), but a significant scatter exists even among the least altered samples. It is therefore questionable whether Pb isotope ratios bear any petrogenetic information at all. Furthermore, a decoupling between the U-Pb and Th-Pb decay systems is implied in **Figure 8.5F**,**G**, because thorogenic Pb defines a linear array typical of a closed system evolution, whereas uranogenic Pb shows a wide scatter. A large variably also exists with respect to the measured $^{87}Sr/^{86}Sr$ isotope ratios, even though these are not well correlated with the whole-rock volatile content. This scatter persists even when Rb/Sr ratios are used to calculate the initial $^{87}Sr/^{86}Sr$ ratios for any arbitrary datum in the Palaeoproterozoic. The observed decoupling of Sr isotope ratios from Nd isotope ratios indicates fluid-induced disturbance, at least of the Rb-Sr isotope system.

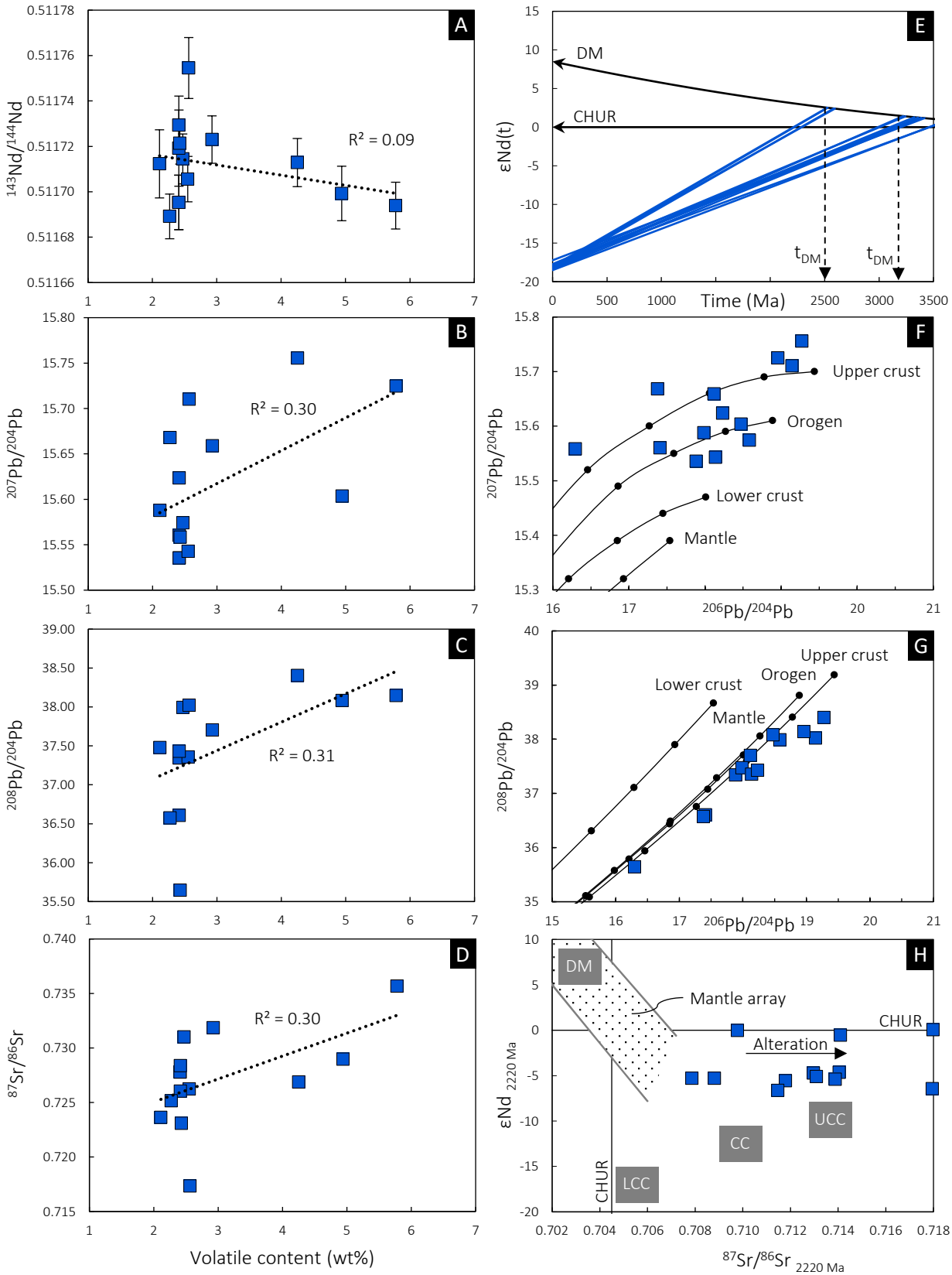

Figure 8.5 Bivariate plots of whole-rock Nd, Pb and Sr isotope ratios for calc-alkaline quartz diabase, Mackelcan Township; **A–D:** measured isotope ratios vs. whole-rock volatile content, illustrating the effects of fluid-rock interaction on the isotopic composition; **E:** neodymium isotope evolution diagram with εNd displayed as a function of time; depleted mantle curve (DM) after DePaolo (1981a,b); **F–G:** lead isotope ratio plots with growth curves after Zartman & Doe (1981) for different reservoirs, with 400 Ma-increments until present; **H:** plot of the initial εNd vs. the initial $^{87}Sr/^{86}Sr$; crustal reservoirs after Faure (1986); error bars represent 2σ internal errors but are smaller than the symbol size in most of the panels.

Distinction from Sudbury Offset Dykes and the Nipissing Suite

Although the quartz diabase from Mackelcan Township petrographically resembles the quartz diorite from Afton Township (**Chapter 3**) or Laura Creek (**Chapter 4**), the dyke cannot be another Offset Dyke of the Sudbury Igneous Complex. Aside from the fact that the dyke is crosscut by pseudotachylitic breccia (Sudbury Breccia) (**Fig. 8.3B,C**), and therefore definitely older than the 1.85 Ga Sudbury impact event, it also has a distinct trace element signature. This can be seen in **Figure 8.6**, where the trace element pattern of the quartz diabase is contrasted against the average composition of the Offset Dykes. The graph reveals a large discrepancy that is particular evident in the slope and the absolute abundance of the REE. Apart from that, the Offset Dykes have invariably lower concentrations of TiO_2, Nb and Ta compared to the quartz diabase dyke, but higher concentrations of Zr, Hf, Th, and alkali metals. Moreover, the quartz diabase has a more radiogenic Nd isotope signature relative to the Sudbury Offset Dykes. It follows that the quartz diabase dyke from Mackelcan Township, though being similar in modal quartz content, SiO_2 concentration, and calc-alkaline affinity, cannot be genetically related to the Sudbury impact event.

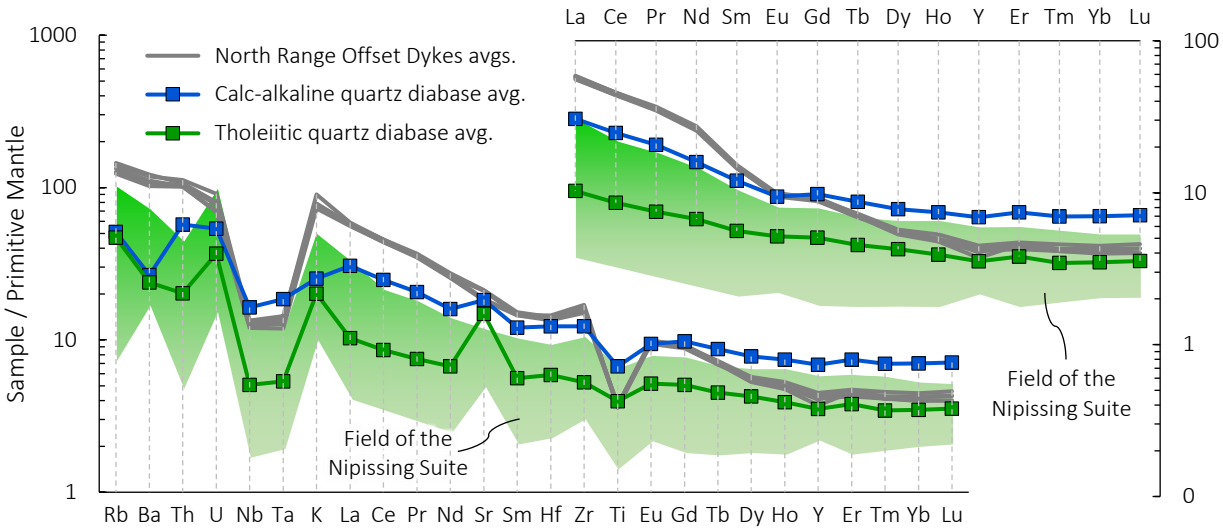

Figure 8.6 Primitive mantle-normalised trace element abundances for the calc-alkaline quartz diabase dyke from Mackelcan Township and, for comparison, selected Offset Dyke averages of the Sudbury Igneous Complex, and the average composition of the tholeiitic quartz diabase dyke found in the same township as well as the compositional field as defined by mafic rocks of the Nipissing Suite; normalisation values from Sun & McDonough (1989); Offset Dyke literature data are from Lightfoot et al. (1997c); data for the Nipissing Suite are from Lightfoot & Naldrett (1996b), Jobin-Bevans (2016), Hagen (2020) and this study (Appendix_1).

In terms of orientation and whole-rock Nd isotope composition, the quartz diabase is more akin to the mafic rocks of the 2.22 Ga Nipissing Suite and the tholeiitic (also Nipissing Suite-related) dyke of **Chapter 6**. All of these have an εNd between –20 and –10, a very high $^{147}Sm/^{144}Nd$ of > 0.13, and a t_{DM} > 3 Ga, which, in conjunction with weakly negative Nb-Ta-Ti-P anomalies, suggests derivation from a subduction-modified Ti-poor and/or rutile-bearing mantle source (e.g. Lightfoot et al. 1993; Lightfoot & Naldrett 1989, 1996a). However, as evident from **Figure 8.6**, the quartz diabase cannot be genetically related to the Nipissing Suite either, for there exists no overlap in trace element composition. Although the quartz diabase and the Nipissing Suite exhibit parallel REE patterns, these are outside the compositional range defined by the Nipissing Suite. A mismatch also exists in terms of Nb, Ta, Ti, Zr, Th and U concentrations and ratios thereof. Such evolved composition is not expected for dykes related to the Nipissing Suite, and it is uncommon even in the most differentiated (SiO_2-rich) portions of larger sills (Lightfoot & Naldrett 1996a,b).

Correlation with the 2.17 Ga Biscotasing Dyke Swarm

In light of the above considerations and non-correlations, the calc-alkaline quartz diabase dyke from Mackelcan Township is most likely related the 2.17 Ga Biscotasing Dyke Swarm (**Fig. 8.7).** Arguments for this will be present below, following a brief overview of this particular dyke swarm.

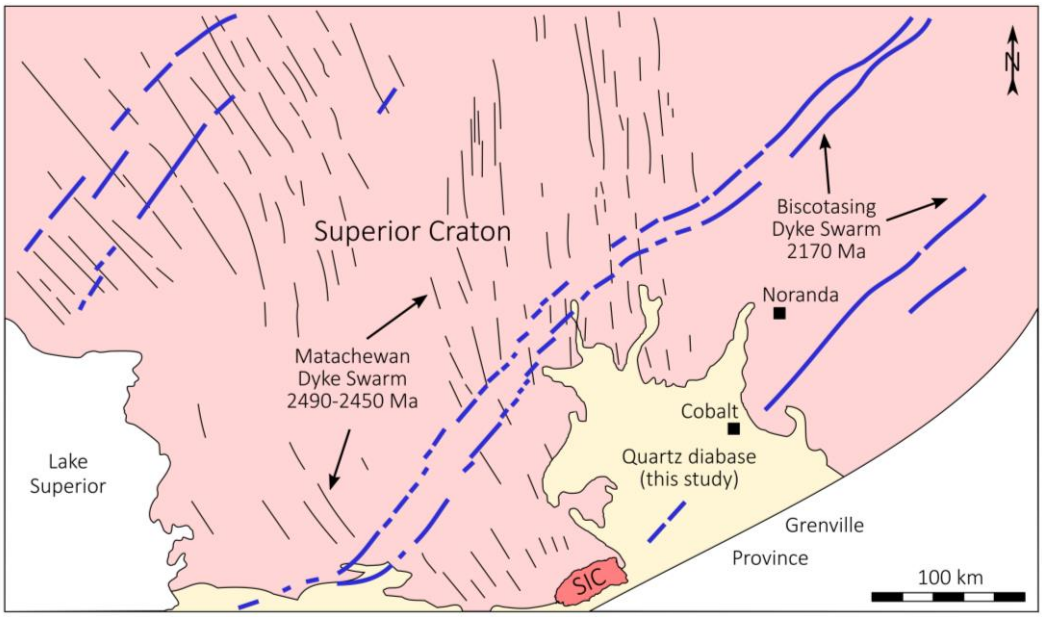

Figure 8.7 Geological sketch map of the southeast Superior Craton, showing the location of dykes assigned to the 2.17 Ga Biscotasing Dyke Swarm; after Halls & Davis (2004); note that the calc-alkaline quartz diabase of the present study lies on the same trend as the Biscotasing Dyke Swarm.

Expect for a few geochronological and palaeomagnetic studies, little work has been done on the so-called Biscotasing Dyke Swarm. The dykes have first been recognised as part of distinct swarm by Buchan et al. (1993) and Halls & Davis (2004), who obtained U-Pb baddeleyite ages of 2166.7 ± 1.4 Ma, 2167.8 ± 2.2 Ma, 2171.6 ± 1.2 Ma for a number of different localities, including one dyke near Cobalt and Noranda (**Fig. 8.7**). Individual dykes are typically tens of meters wide (e.g. Ernst & Buchan 2010) and can be traced for hundreds of kilometres across the Superior Craton, along a consistent strike northeast. The dykes seem to be part of a parallel swarm emanating from the Ungava Bay region, and have lately been correlated with gabbroic sills of the Otish Basin, and with the Payne River Dykes in northern Quebec (Hamilton & Buchan 2016; Milidragovic et al. 2016).

The hypothesis that the quartz diabase is correlative with the Biscotasing Dyke Swarm is mainly based on two arguments. First, the quartz diabase lies exactly on the projected trend of the Biscotasing Dyke Swarm, and it appears to be an extension of one of the dykes that has been mapped northeast of the Cobalt Embayment (**Fig. 8.7**). Second, the quartz diabase has the same trace element signature as other members of the Biscotasing Dyke Swarm, as evident from **Figure 8.8**. Minor mismatches exist with respect to Th, U, and Sr, but these are explicable by the dyke of having experienced secondary element mobility and/or assimilation of Th-U rich Huronian Supergroup sedimentary rocks. The extremely low Nb/Ta ratio reported previously for the Biscotasing Dyke Swarm (Ernst & Buchan 2010, and references therein) is likely an analytical artifact. Apart from that, there exists a good overlap in terms of major element concentrations (cf. Ernst & Buchan 2010). Unfortunately, no whole-rock Sm-Nd isotope data have been published for the Biscotasing Dyke Swarm therefore preventing correlation on the basis of Nd isotope systematics.

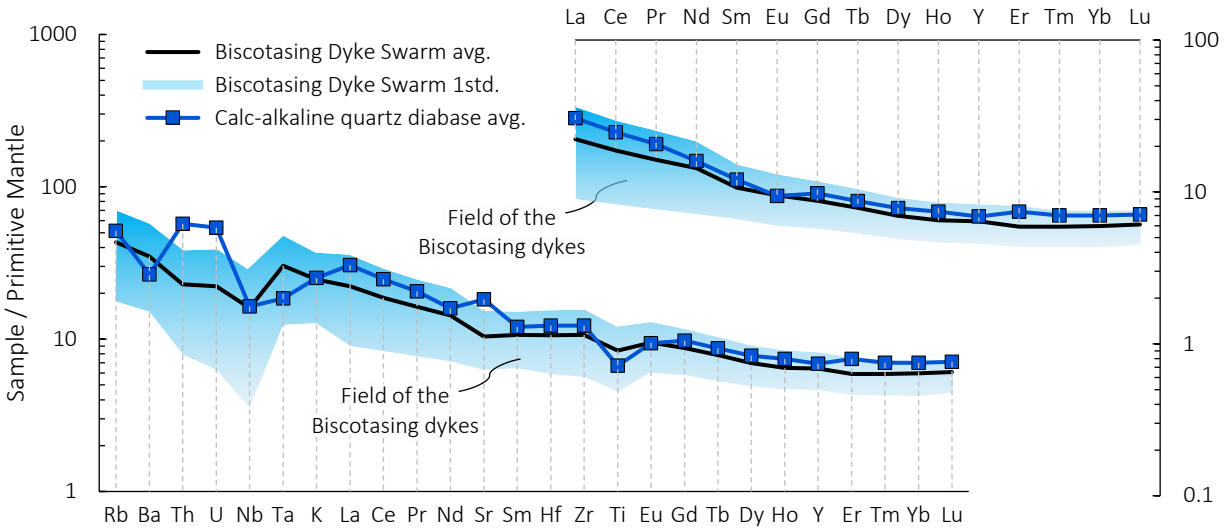

Figure 8.8 Primitive mantle-normalised trace element abundances for the calc-alkaline quartz diabase dyke from Mackelcan Township and, for comparison, the Biscotasing Dyke Swarm; normalisation values are from Sun & McDonough (1989); literature data from Halls & Davis (2004), Hamilton & Stott (2008) and Buchan & Ernst (2010).

If the above hypothesis turns out to be correct, and the quartz diabase dyke does correlate with the 2.17 Ga Biscotasing Dyke Swarm, it would be indication of yet another, hitherto unrecognised, mafic magmatic event having affected the Huronian Basin and the target area of the 1.85 Ga Sudbury impact. Together with the recognition of 1.88–1.86 Ga alkaline ultrabasic dykes in the area (**Chapter 7**), the picture emerges of a more complex, divers, and protracted magmatic history of the Huronian Basin than previously assumed. The economic significance of the Biscotasing magmatic event, for example with respect to potential Ni-Cu-PGE sulphide mineralisation, remains to be demonstrated.

Felsic Dykes

9.1 Summary

Hornblende syenite occurs on an island at Matagamasi Lake, Rathbun Township. The “dyke” has a roughly lenticular shape, is about 20–50 cm wide, strikes N20°W, and cuts across gabbro of the Nipissing Suite, which seems to have undergone intense metasomatism along the intrusive contact. The syenite is composed primarily of albite (Ab_{98}–Ab_{99}) and Ti-rich magnesio hornblende. Albite occurs as fine grains in a polygonal texture, or as larger tabular grains with a distinct chessboard pattern. All albite, regardless of morphology, contains exsolutions of K-rich feldspar, suggesting crystallisation above the solvus. Hornblende thermobarometry and hornblende-albite exchange thermometry reveal a pressure of 0.9–1.7 kbar and a temperature of 600–710°C. All of this points to a magmatic origin of the rock, not to metasomatic replacement in the sense of an episyenite. The best age constraint available is a three-point mineral-rock Sm-Nd isochron, which yielded, however, only an ambiguous date of or 1842 ± 170 Ma. Therefore, the syenite could either be genetically related to the 1872 ± 3 Ma alkaline ultrabasic magmatism documented above, including the 1881 Ma Spanish River Carbonatite, or the 1750–1700 Ma Killarney Magmatic Belt. Whether the syenite pre- or post-dated the 1850 Ma Sudbury impact event is, for a lack of cross-cutting relations, not known. A genetic relationship to regional Na-metasomatism (albitisation) and hydrothermal Cu-Au mineralisation previously documented in the area is possible.

In addition, aplitic (tonalitic) dykes of random orientation cut across gabbro of the Nipissing Suite and across wacke of the Gowganda Formation at Matagamasi Lake, Rathbun Township. The dykes are ≤ 2 m wide, ≤ 20 m long, dip subvertical, and occur in sharp, non-chilled, contact with their host rocks. One of the aplitic dykes is cut by pseudotachylitic breccia, thus, dyke emplacement is constrained between 2220 Ma and 1850 Ma. Petrographically, the aplitic rocks have a fine-grained equigranular aphyric texture and are composed of quartz, albite-rich plagioclase, microcline, and minor chlorite + ilmenite likely after biotite or amphibole. In terms of lithogeochemistry, the aplitic rocks are very siliceous (77 wt% SiO_2), sodium-rich, peraluminous, and ambiguously classified as either I-type or S-type granitoids. They are further characterised by very low REE concentrations (0.4–22 ppm La), low P_2O_5 (≤ 0.01 wt%), and a significant depletion LREE relative to HREE suggesting fractionation by allanite, monazite and/or apatite; elevated contents of Cr (34–456 ppm) and Ni (5–243 ppm) may indicate interaction with, or deviation from, mafic magma. Geochemically, the aplitic dykes defy most tectonic/genetic granite classification schemes; whole-rock Sm-Nd and Pb isotope systematics were likely affected by monazite fractionation and, therefore, provide no reliable petrogenetic information either. Based on the shapes and the distribution of the aplitic dykes, their aphyric nature and lack of chilled margins, and their pronounced depletion in Sr (12–71 ppm) coupled with distinct negative Eu anomalies, it is proposed that the aplitic dykes represent residual, highly fractionated felsic melt extracted from a mafic (plagioclase-pyroxene ± apatite ±monazite-bearing) crystal mush, for example, through gas-driven filter pressing. Thus, the aplitic dykes are interpreted as syn-magmatic with, and genetically related to, the 2.22 Ga Nipissing Suite.

9.2 Local Geology

Rathbun Township is located 10–15 km northeast of the City of Sudbury. It extends across the 10 km-large Wanapitei Lake and covers the southwest part of the Temagami Anomaly. It borders the 1.85 Ga Sudbury Igneous Complex and Norman Township in the west, Aylmer and Mackelcan townships to the north, Kelly Township to the east, and Scadding and MacLennan townships to the south. Access is provided via Highway 17 coming from Sudbury, then turning into Kukagami Road and heading for 30 km north along the Bushy Bay Road until Portage Bay, which is situated at the isthmus between Wanapitei Lake and Matagamasi Lake. Some outcrops around Portage Bay may be accessed by boat only. In contrast to much of the eastern part of the Temagami Anomaly, outcrops in the Portage Bay area are abundant, especially along the shoreline, at roads, and other manmade excavations. Black smelter coatings are mostly absent. Relief is significant, in places.

The oldest rocks in the Matagamasi Lake area are siliciclastic sedimentary rocks of the Cobalt Group (upper Huronian Supergroup), deposited between 2.35 and 2.31 Ga in a glaciogenic to fluviatile environment. Wacke, silt- and mudstone of the Gowganda Formation prevail; arenites of the overlying Lorrain Formation are only exposed in a narrow corridor in the northeast corner of the study area, and within an enclave around Bassfin Lake (**Fig. 9.1**). A greenish grey massive and wacke (Coleman Member) is the aerially most extensive lithology of the Gowganda Formation; laminated argillite (Firstbrook Member) is locally found north of Rathbun Lake and near Bassfin Lake. Typical features observed in the Gowganda Formation include Archaean dropstones (mostly pink granitoid), rhythmical bedding and, occasionally, conglomeratic layers. Sedimentary features typically observed in the Lorrain Formation include thin layers of quartz pebbles, planar and through cross-stratification. The thickness of the Cobalt Group in the area is not reliably known.

Rocks of the Cobalt Group were, in many places, intruded by tholeiitic magmas of the 2.22 Ga Nipissing Suite, forming typically sills of up to 1 km in thickness, which are concordant with the Gowganda-Lorrain contact, rarely dykes. An exceptionally well-studied member of the Nipissing Suite is exposed at Portage Bay, stretching across Matagamasi and Kukagami Lake, and extending as far as Scadding Bay to the south. The so-called Wanapitei Intrusion (not to be confused with the 1.75 Ga Wanapitei *Complex* in the Grenville Province; Prevec 1995) is a lopolith-like body that received considerable attention throughout the past as a Cu-Ni-PGE prospect. Dated at 2109 ± 40 Ma using the K-Ar method (Edgar 1986) it was confirmed as being a member of the Nipissing Suite (see also: Dressler 1982; Lightfoot & Naldrett 1996a). The lopolith could have originally exceeded 8 km in diameter and 800 m in thickness (Edgar 1986); the three separate lobes of the intrusion measure 3 x 1 km in plain view each. Their basal intrusive contacts dip steeply and face a common centre at Bassfin Lake (**Fig. 9.1**). Thermal metamorphism of the country rock is restricted to < 2 m of baking. A basal unit of fine-grained quartz diabase (< 5 vol% quartz) is typically present, but more than 98 vol% of the Wanapitei Intrusion consists of massive, medium-grained, equigranular and relatively fresh Nipissing Suite-typical orthopyroxene gabbro without macroscopic evidence of igneous layering (see however: Finn et al. 1982; Finn & Edgar 1986). Pegmatoidal segregations (with cm-sized augite and/or hornblende crystals) occur here and there, but always > 100 m above the basal intrusive contact. Deformation is very limited; chloritic shears may be occasionally observed. The Wanapitei Intrusions hosts, in places, subeconomic Cu-Ni-PGE mineralisation in form of disseminated (< 3 vol%) patchy to globular chalcopyrite, pyrrhotite ± pentlandite of orthomagmatic origin (Lightfoot & Naldrett 1996a; Jobin-Bevans 2000; Lightfoot 2016, p. 91).

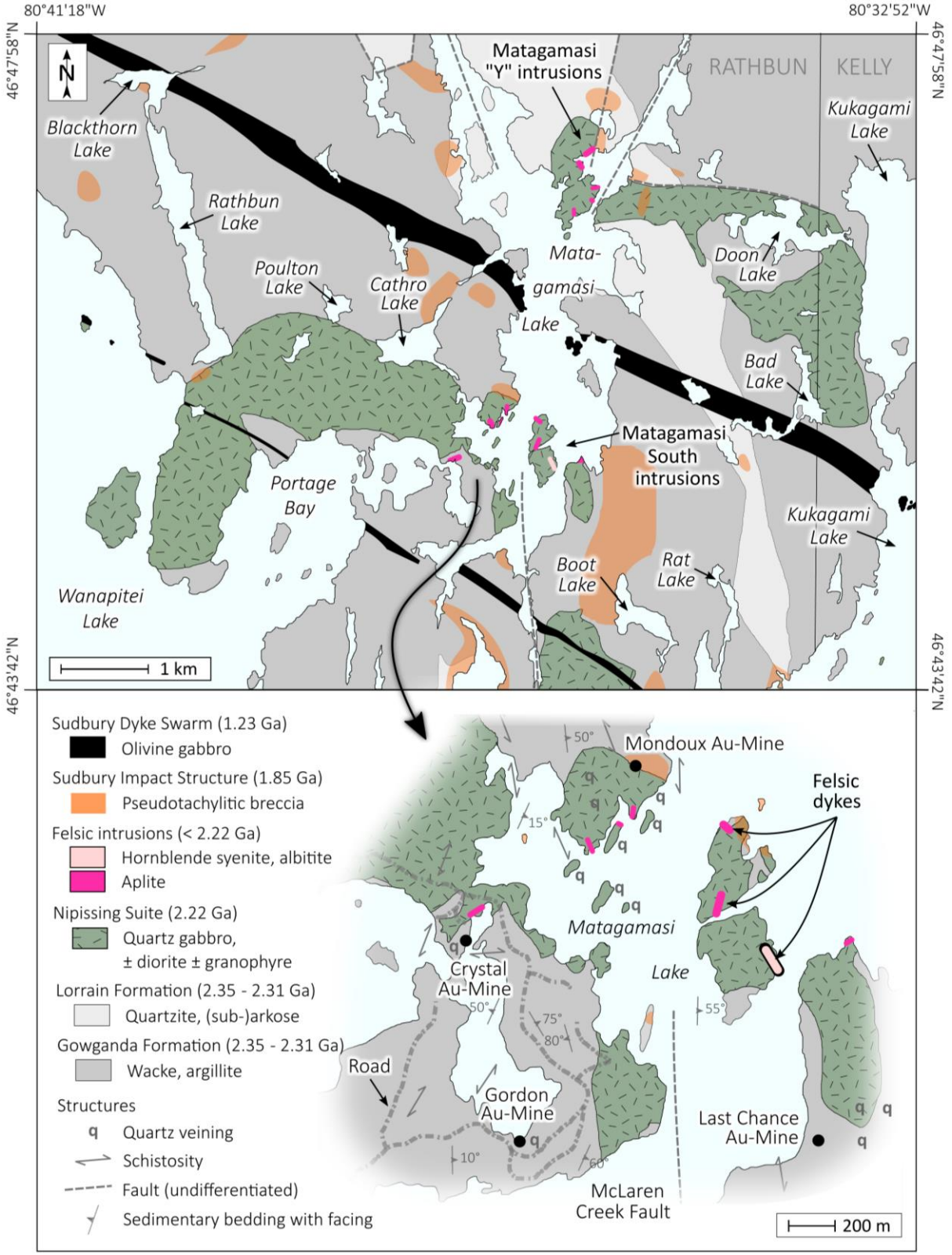

Figure 9.1 Geological map of Matagamasi Lake, Rathbun Township, showing the regional geological and lithostratigraphic context of the felsic intrusions and their suspicious proximity to hydrothermal gold occurrences; based on maps of Dressler (1981a,b, 1982) and Goad & Rowell (1985).

The youngest rocks in the area are, once again, dykes of alkaline olivine gabbro related to the 1.23 Ga Sudbury Dyke Swarm. The dykes are very continuous in suboutcrop and can be – thanks to their high magnetite content – traced for many tens of kilometres in aeromagnetic maps. The thickest dyke trends across Kukagami Lake and Matagamasi Lake. It is up to 300 m wide and exhibits steeply dipping and chilled contacts (Dressler 1982; Shellnutt & MacRae 2012). The dyke is clearly visible in satellite imagery as a sparsely vegetated lineament, and in the field as a prominent ridge. A number of parallel dykes of likely the same age occur to the north and south, for instance, around Portage Bay (**Fig. 9.1**). Olivine gabbro is also found all over Scadding Township, including the Scadding Au-Mine. A grab sample collected from there revealed the rock to be composed of fresh plagioclase, augite, olivine, and opaques. Olivine is remarkbely pristine, and only surficial weathered to iddingsite. Considering the ease at which olivine would have been altered to serpentine, magnesite or chlorite, the fresh mineralogy of the dyke indicates that it must have escaped regional metamorphism and alteration, and this provides important constraints as to the relative timing of regional deformation, metamorphism, and hydrothermal activity in the area. Evidently, the effects of the nearby 1.1–1.0 Ga Grenville Orogen must have been very limited.

The area around Wanapitei Lake is characterised by a high density of gold occurrences ("Wahnapitae Gold Region"; Gates 1991, p. 3). Most of these were discovered in the 1890s and intermittently mined for short periods. A detailed account on their history and geology was given by Dressler (1982) and Gates (1991). Four gold occurrences are found within a small area of less than 2 km^2 at southern Matagamasi Lake (**Fig. 9.1**), the most famous of which being the Crystal/Comstock property. The name referrers to large grains of native gold associated with extensive quartz veining (Coleman 1898). Exceptional high Au grades (ca. 300 g/t) for this occurrence were previously reported by Blue (1896, as cited in Gates 1991, p. 179), but subsequent exploration failed to reproduce these impressive values (e.g. Goad & Rowell 1985; Gates 1991). All the Au occurrences in the Wanapitei Lake area share similar characteristics suggesting they could have formed by the same process, perhaps even during the same event: They are all hosted by massive, up to 15 m thick quartz veins, quartz stockworks and/or hydrothermal breccias, with quartz, chlorite, albite, carbonate (calcite, ankerite, dolomite ± rhodochrosite), pyrite, chalcopyrite ± galena ± arsenopyrite ± bornite ± fuchsite being the typical gangue (Gates 1991); tourmaline was only reported by Goad & Rowell (1985); actinolite roses were locally observed by the author. The host rocks can be quite variable. Many occurrences are found in the Gowganda and Lorrain formations, some in sedimentary rocks of the lower Huronian Supergroup, or in gabbro of the Nipissing Suite. A common theme, however, is the proximity (< 1 km) of each occurrence to mafic rocks of the Nipissing Suite. This close spatial association could point to a genetic relationship. On a very local scale, the distribution of the mineralisation and the orientation of the ore-hosting veins seems random and without an obvious structural control. On a regional scale, however, all occurrences lie on a structural trend coincident with the orientation of the Onaping Fault System. The so-called Garbage Dump zone (Gates 1991), for example, is found at the south end of the McLaren Creek Fault, and the Crystal, Gordon, Mondoux, Last Chance and Crystal North showings are found on the northern extension of the same structure (**Fig. 9.1**). The Rainy/Telteck occurrences (Aylmer Township) – two extensive hydrothermal breccia bodies with marginal Cu-Au sulphide mineralisation and of potential use as dimension stone (Gates 1991) – are found directly adjacent to the upper Wanapitei River Fault. The Cobalt Hill and Wolf Lake showings are yet another example of Cu-Au mineralisation spatially linked to these N-trending structures (i.e., the Laundry Lake structure/fault; Dressler 1982; **Chapter 6**).

9.3 Field Relations

Recent field work by Inventus Mining Corp. identified a number of felsic dykes in and around Matagamasi Lake, Rathbun Township. Some of these dykes were already recognised by Dressler (1982) and Goad & Rowell (1985) but have not been investigated in any detail since. Dressler (1982), who tentatively mapped the dykes as part of the Nipissing Suite, distinguished between three types: tonalite-granodiorite, fine-grained granitic dykes, and a monzodioritic pegmatite. For each lithology, Dressler (1982) provided a very brief description, and whole-rock major element analyses obtained on one or two samples, although he did not provide coordinates of the sample locations. Due to their exotic nature and suspicious proximity to several hydrothermal gold occurrences (**Fig. 9.1**), the felsic dykes from Matagamasi Lake have been revisited for this study.

Certainly the most interesting dyke, a pegmatitic hornblende quartz syenite, was observed on an island in southern Matagamasi Lake (**Fig. 9.2A**; corresponding sample MAT20-2B). The syenite at this location (i.e., the pegmatite of Dressler 1982, p. 31) is a very irregular-textured, non-magnetic lenticular or dyke-like feature, at least 20–50 cm wide, and in sharp contact with gabbro of the Nipissing Suite. No decrease in grain size of the syenite was observed near the contact. The syenite extends for about 3 m striking N20°W and likely continuous for a few more metres southeast into the lake; its exact orientation remains, due to the two-dimensional nature of the outcrop, uncertain. As seen in **Figure 9.2A**, the syenite is either pegmatoidal or compositionally zoned with an inner mafic part (dominated by hornblende) and an outer felsic part (pink feldspar, white quartz). The country rock at the syenite-gabbro contact underwent extensive metasomatism as evident by an irregular bleaching of the gabbro and its pervasive texturally destructive replacement by epidote, amphibole, and beige, cream-coloured, locally red, feldspar-looking mineral(s) (scapolite?). Sharp-walled apophyses and curvy vein-like alteration features, apparently composed of massive albite extend from the main syenite dyke outward into the country rock. Some of these apophyses show a similar zonation as the syenite; they consist of stretched amphibole fibres, rimmed with, what appears to be, albite ± quartz. Although Sudbury Breccia does occur in the area (**Fig. 9.1**), the relationship between syenite, alteration, and the brecciation is not known. Unfortunately, channel sampling of the outcrop was not permitted at the time of visiting, thus limiting the number of available samples of the hornblende syenite to a few small hand specimens and rock chips.

All the other felsic dykes from Matagamasi Lake are, as it seems, of the same category: They are aplitic, texturally uniform weather light grey, beige, or brick red, and are, without exception, non-magnetic. The aplitic dykes are relatively resistant and massive, exhibit either rectangular or no type of jointing at all, and typically create a positive relief against their soft host rocks. The dykes are between 5 cm and 3 m thick, randomly oriented, and can be traced continuously in outcrop for as much as 15 m along strike (**Fig. 9.2B**) or possibly beyond. Where the outcrop conditions permit to obtain structural data, the dykes dip (sub-)vertically (**Fig. 9.2C**). Sharp contacts against the country rock (gabbro, wacke) are the norm. One of the aplitic dykes (**Fig. 9.2B**) was found to cut discordantly at a low angle (35°) across the bedding-parallel intrusive contact between fine- to medium grained Nipissing Suite gabbro and Gowganda Formation wacke. In contrast to the syenite above, the aplitic dykes are not associated with extensive zones of metasomatism, but they are themselves locally cut by quartz-chlorite-carbonate-hematite veins. Field relations between Sudbury Breccia and the aplitic dykes are equivocal. However, as will be shown below, there is clear textural evidence of the aplitic dykes being older than the 1.85 Ga Sudbury Breccia.

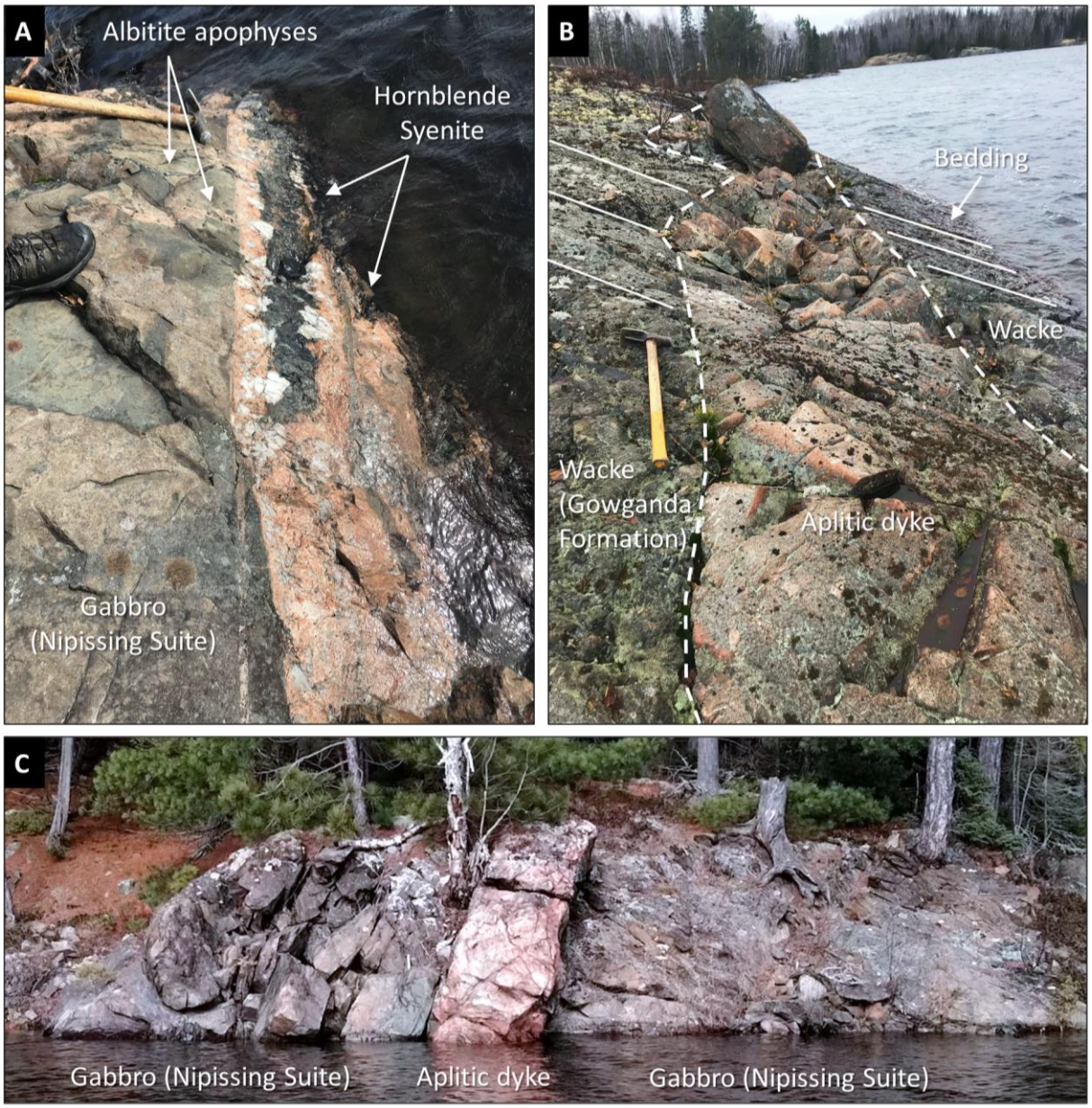

Figure 9.2 Photographs of felsic dykes from Matagamasi Lake, Rathbun Township; **A:** pegmatitic hornblende syenite cutting metasomatised Nipissing Suite gabbro, Matagamasi south islands (46°45 06N 80°36 21W; sample MAT20-2B); **B:** aplitic dyke cutting Gowganda Formation wacke at the "Matagamasi Y" peninsula (46°47 04N 80°36 06W; sample MAT20-4); **C:** aplitic dyke cutting Nipissing Suite gabbro at "Matagamasi Y" peninsula (46°47 07N 80°36 01W; sample MAT20-8); length of the hammer = 50 cm; photographs were kindly provided by Jacob VanderWal and Renan Silva.

A third type of felsic rock was observed at the "Matagamasi Y" peninsula, although not in outcrop. At this location (46°46 55N 80°35 57W), subangular boulders of feldspar porphyry were noted, several decimetres in size. The rock is composed of ca. 75 vol% euhedral alkali feldspar phenocrysts (2–4 cm grain size), set in an aphantic dark green groundmass; phenocrysts exhibit compositional zoning and are crudely aligned. The shape and high population of these boulders is inconsistent with a glacial and/or fluviatile transport, and instead points to a very local origin. However, as their source outcrop could not be identified, the feldspar porphyry will not be considered further in this study. It is, nevertheless, interesting to note that a similar type of porphyric dyke was mentioned by Dressler (1982, p. 31) for two locations in northwest Rathbun Township, cutting across gabbro of the Nipissing Suite. Unfortunately, Dressler (1982) did not give any details.

9.4 Petrography

Hornblende syenite

Syenite from southern Matagamasi Lake is salmon pink on freshly broken surfaces and weathers beige to grey. The available samples are non-magnetic, leucocratic with irregular dispersed mafic clots, and of granitic to locally pseudo pegmatoidal texture (**Fig. 9.3A**). The rock exhibits a considerable variation of grain size, even within a single thin section. Examination of thin sections reveal a relatively simple mineralogical composition, with hornblende (5–10 vol%) and albite (90–95 vol%) being identified. Neither nepheline nor quartz was observed in thin section. Accordingly, the rock is classified as hornblende alkali feldspar syenite/albitite sensu Streckeisen (1976).

Albite occurs as two different morphological types. It is predominantly found as 50–300 µm large, mostly un-twinned, homogeneous, anhedral grains within monomineralic domains. These domains are characterised by an equigranular polygonal texture and appear cherty due to the relatively fresh and fine-grained nature of the albite they are composed of (**Fig. 9.3B**). Monomineralic albite domains may be easily mistaken for large anhedral flesh-coloured alkali feldspar crystals in hand specimen (**Fig. 9.3A**). Albite is also found within coarse-grained patches together with hornblende, forming subhedral angular grains of up to 1.5 mm in size. Coarse-grained albite may be with or without polysynthetic twinning and typically exhibits an irregular extinction (**Fig. 9.3C**). Some of the albite (< 10%) also exhibits grid-like "chessboard" twinning (**Fig. 9.3D,E**) – a specific form of albite widely documented but poorly understood (e.g. Becke 1906; Exner 1949; Starkey 1959; Siemiatkowska & Martin 1975; Schandl 2004). The chessboard pattern of albite can be, on first sight, easily mistaken for tartan twinning of microcline, and it required XRD and EMP analyses to identify the mineral as almost pure albite (see **Chapter 9.5**).

Hornblende occurs as subhedral to anhedral prismatic or rhombic grains of up to 1 mm in size within mafic patches (**Fig. 9.3B,C**), but also within the more felsic domains together with polygonal albite (**Fig. 9.3D–F**). The amphibole, whose chemical composition conforms to that of titaniferous magnesio hornblende, displays pleochroism from greyish green to brownish green, second-order interference colours, and shows no optical zonation. In BSE images, however, almost all grains exhibit a pronounced yet patchy distributed compositional zonation, from bright cores (higher average atomic number) to dark rims (lower average atomic number). Preliminary microprobe analyses indicate that this zonation is, at least in part, due to variations in the Fe/Mg ratio.

Another interesting feature of the rock is the presence of accessory (< 0.01 vol%) calcite without any obvious link to hydrothermal alteration. Although one sample does contain calcite-zoisite veins of arguably secondary origin, calcite was also observed within entirely fresh samples, where it occurs as an anhedral interstitial mineral between amphibole and albite (**Fig. 9.3E,F**). Thus, there is a certain possibility that some of the observed calcite is a primary magmatic phase. Other accessory minerals comprise leucoxene and monazite. Ilmenite occurs as amoeboid, vermicular or rice grain-shaped opaque grains surrounded by cryptocrystalline semi opaque selvages. Monazite is found as < 50 µm large anhedral grains enclosed in amphibole, and typically surrounded by metamict (brown to entirely opaque) halos.

No pseudotachylitic breccia was observed in any of the available samples. The age of the hornblende syenite relative to the 1.85 Ga Sudbury impact event, therefore, remains equivocal.

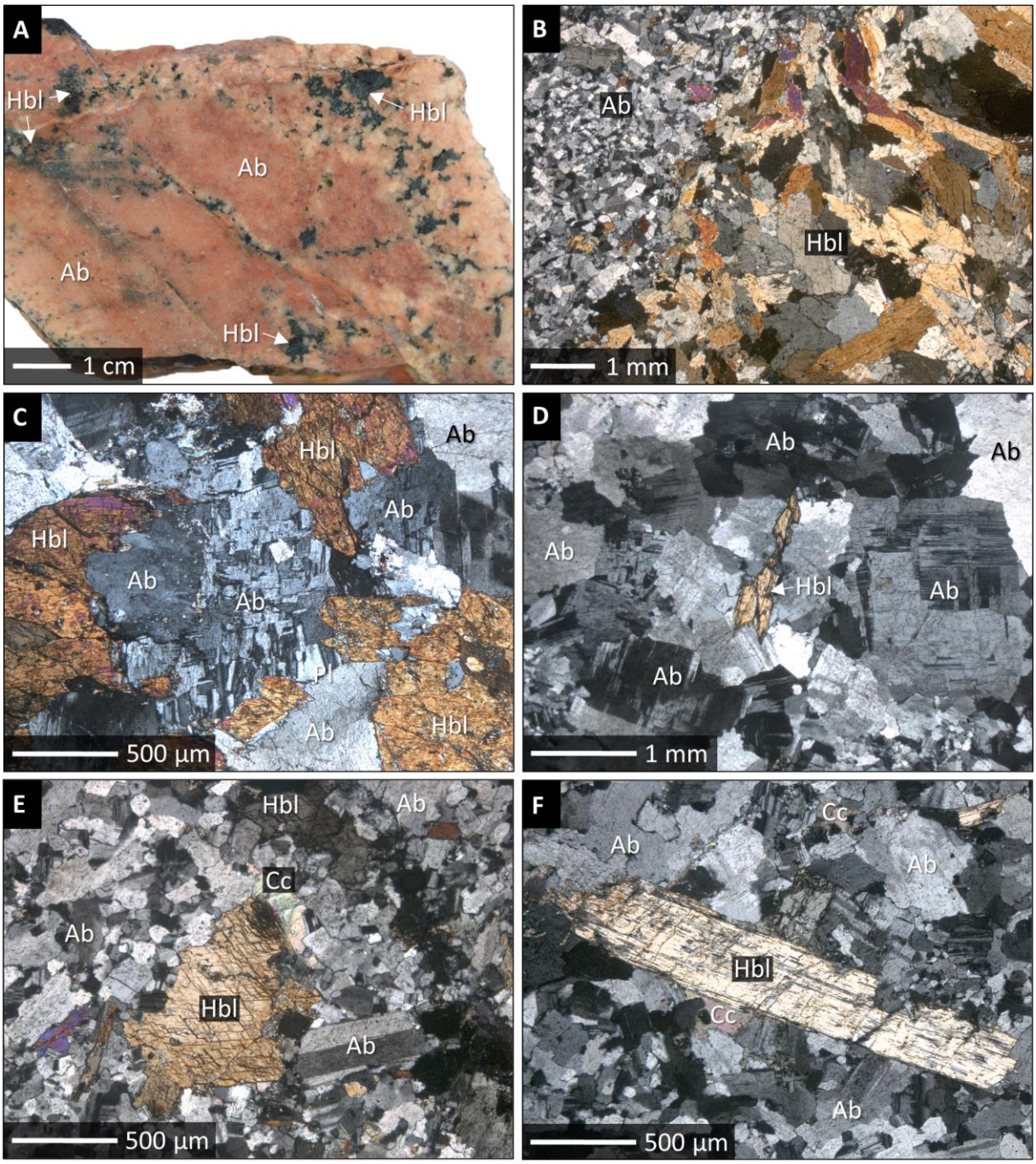

Figure 9.3 Photograph and microphotographs of hornblende syenite from southern Matagamasi Lake, Rathbun Township; **A:** polished hand specimen (sample MAT20-2B); **B:** thin section of the same specimen under transmitted light and crossed polars, showing patches of hornblende together with patches of massive albite; **C–D:** thin section under transmitted light and crossed polars, showing "chessboard" albite intergrown with hornblende; **E:** thin section under transmitted light and crossed polars, showing a hornblende crystal with a well-developed diagnostic cleavage, set in a groundmass of fine-grained polygonal albite; note the calcite interstitial between hornblende and albite; **F:** thin section under transmitted light and crossed polars, showing another example of calcite interstitial between prismatic hornblende and granular polygonal albite. Abbreviations: Ab = albite; Hbl = hornblende; Cc = calcite.

Aplitic dykes

Aplitic rocks from Matagamasi Lake weather beige, white to brick red (**Fig. 9.4A,B**). The rocks are massive, non-magnetic, (holo-)leucocratic, equigranular and texturally uniform at the outcrop scale. Textures range from sugary aphantic to phaneritic fine-grained (≤ 1 mm). Mafic minerals, which account for less than 5 vol% of the rock, can be occasionally observed, though not identified, in hand specimen. In spite of the wide range in colour that is observed in outcrop and in hand specimens, thin section microscopy reveals a remarkable uniform mineralogical composition and texture. The texture can be described as holocrystalline, aphyric, equigranular and polygonal; the principal rock-forming minerals are quartz (35–50 vol%), plagioclase (40–60 vol%), microcline (5–10 vol%), chlorite (1–5 vol%), and traces of leucoxene, zircon, and possibly monazite. These modal abundances classify the rock as tonalite or granodiorite according to Streckeisen (1976).

Quartz occurs as clear subangular anhedral and equant grains of < 1.5 mm in size (**Fig. 9.4C**). Brittle deformation prevails; no undulose extinction was observed. Sutured and bulging grain boundaries are common where multiple quartz grains are in mutual contact. Granophyric textures are absent. Plagioclase occurs as subhedral tabular grains (aspect ratio 1:2 to 1:4). The mineral exhibits polysynthetic twinning of the albite law and, in many places, a pronounced core-rim zonation. Plagioclase, while being mostly pristine, is locally replaced by relatively coarse-grained sericite fibres (**Fig. 9.4D**). The cores of plagioclase appear to have been preferentially affected by this replacement process. Replacement by epidote, on the other hand, was only observed at one locality. K-feldspar is found as angular subhedral grains < 1 mm, forming triple junctions with plagioclase and quartz. K-feldspar, like plagioclase, is of dusty appearance under plane polars; alteration to sericite or clay is the norm. The mineral is distinguished form plagioclase by its diagnostic tartan twinning (**Fig. 9.4E,F**) and the absence of an optical zonation. Chlorite was found as a minor constituent in every sample, interstitial between quartz and feldspar (**Fig. 9.4E**). Chlorite is anhedral or forms bundles, exhibits olive to grey interference colours and abundant metamict rims around inclusions of granular monazite (< 50 μm) and zircon (< 20 μm). It appears that chlorite is secondary after primary ferromagnesian minerals, either biotite or amphibole. Another ubiquitous mineral is leucoxene, which occurs in accessory amounts (~0.01 vol%) interstitial between quartz and feldspar, and frequently intergrown with chlorite. Leucoxene is beige, brown, grey, or entirely opaque in plane polarised light; the mineral aggregate is most likely another replacement product of primary Ti-rich biotite or hornblende.

Barren veins of quartz > carbonate > chlorite can be observed at most sample localities. With exception of these hydrothermal veins and minor sericitisation of feldspar, the aplitic rocks are fresh. One sample, however, had been affected by pervasive carbonatisation and the alteration of feldspar by iron oxide (and possibly clay) along fractures, grain boundaries, twin- and cleavage plains. The latter is likely responsible for the brick red staining of the rock (**Fig. 9.4B**).

Most of the aplitic rocks, especially from southern Matagamasi Lake, contain microfractures that are only apparent in thin section (**Fig. 9.4F**). The origin of these fractures is unclear, but they could represent a variety of Sudbury Breccia, similar to the features documented before in mafic lithotypes (**Chapters 5–7**). One outcrop provides unequivocal evidence of the aplite being older than the 1.85 Ga Sudbury impact, as the aplite there is cut by, and has been reworked as clasts into, pseudotachylitic breccia (**Fig. 9.5**). This breccia sample bears all hallmarks of the typical granite-hosted Sudbury Breccia elsewhere and, therefore, does not require further elaboration.

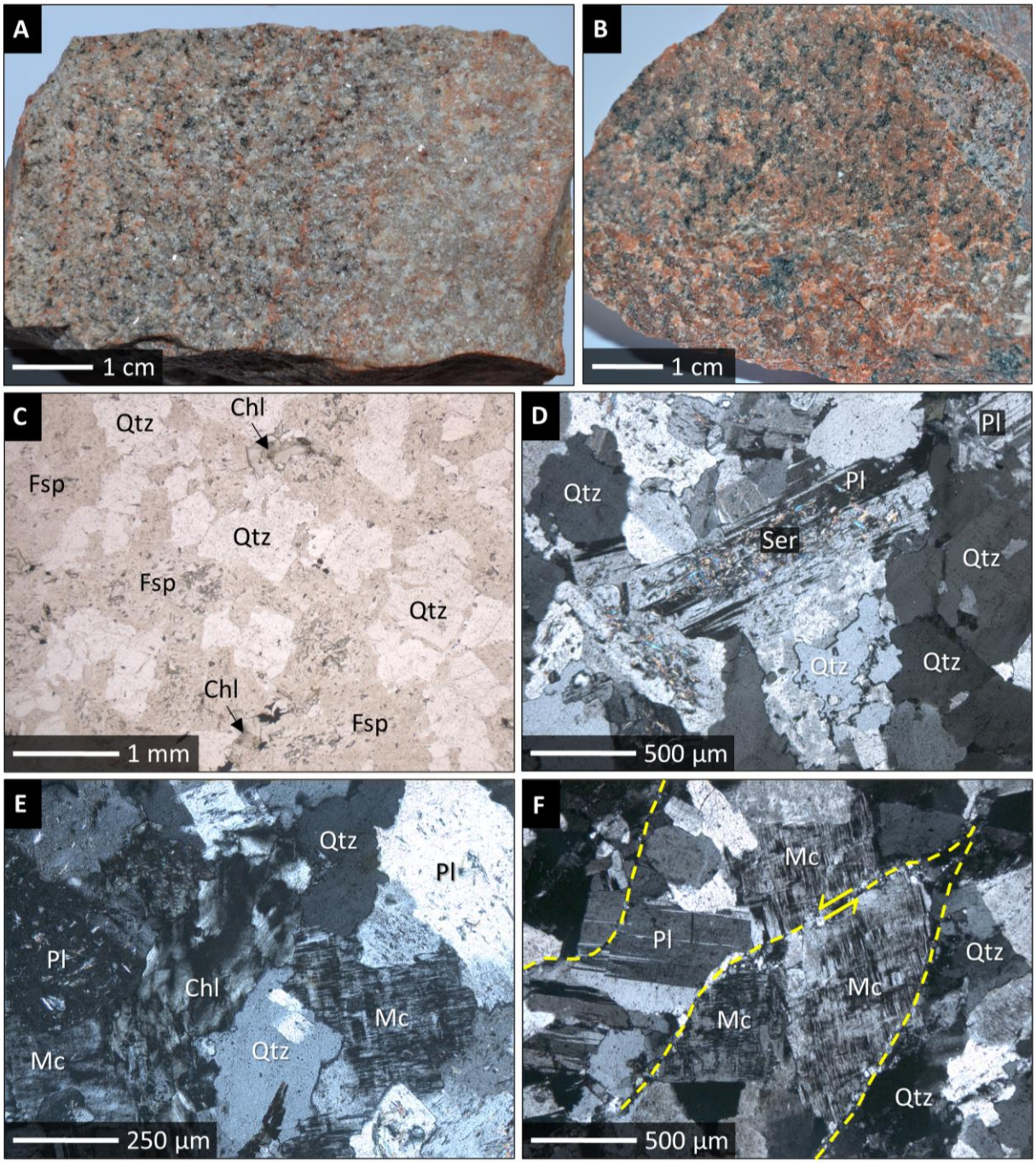

Figure 9.4 Photographs and microphotographs of aplitic rocks from Matagamasi Lake, Rathbun Township; **A:** hand specimen of a relatively fresh aplite (sample MAT20-5); **B:** hand specimen of an altered aplite (sample MAT20-4); the brick red staining is seemingly due to alteration of feldspar associated with a pervasive carbonatisation; **C:** thin section (sample MAT20-6A) under transmitted light and plane polars, showing quartz and feldspar in an equigranular texture; **D:** thin section (sample MAT20-6A) under transmitted light and crossed polars, showing slightly altered plagioclase together with quartz; **E:** thin section (sample MAT20-8A) under transmitted light and crossed polars, showing chlorite interstitial to plagioclase, microcline, and quartz; **F:** thin section (sample MAT20-8B) under transmitted light and crossed polars, showing relatively fresh but microfractured microcline, plagioclase, and quartz. Abbreviations: Qtz = quartz; Fsp = feldspar; Ser = sericite; Pl = plagioclase; Chl = chlorite; Mc = microcline.

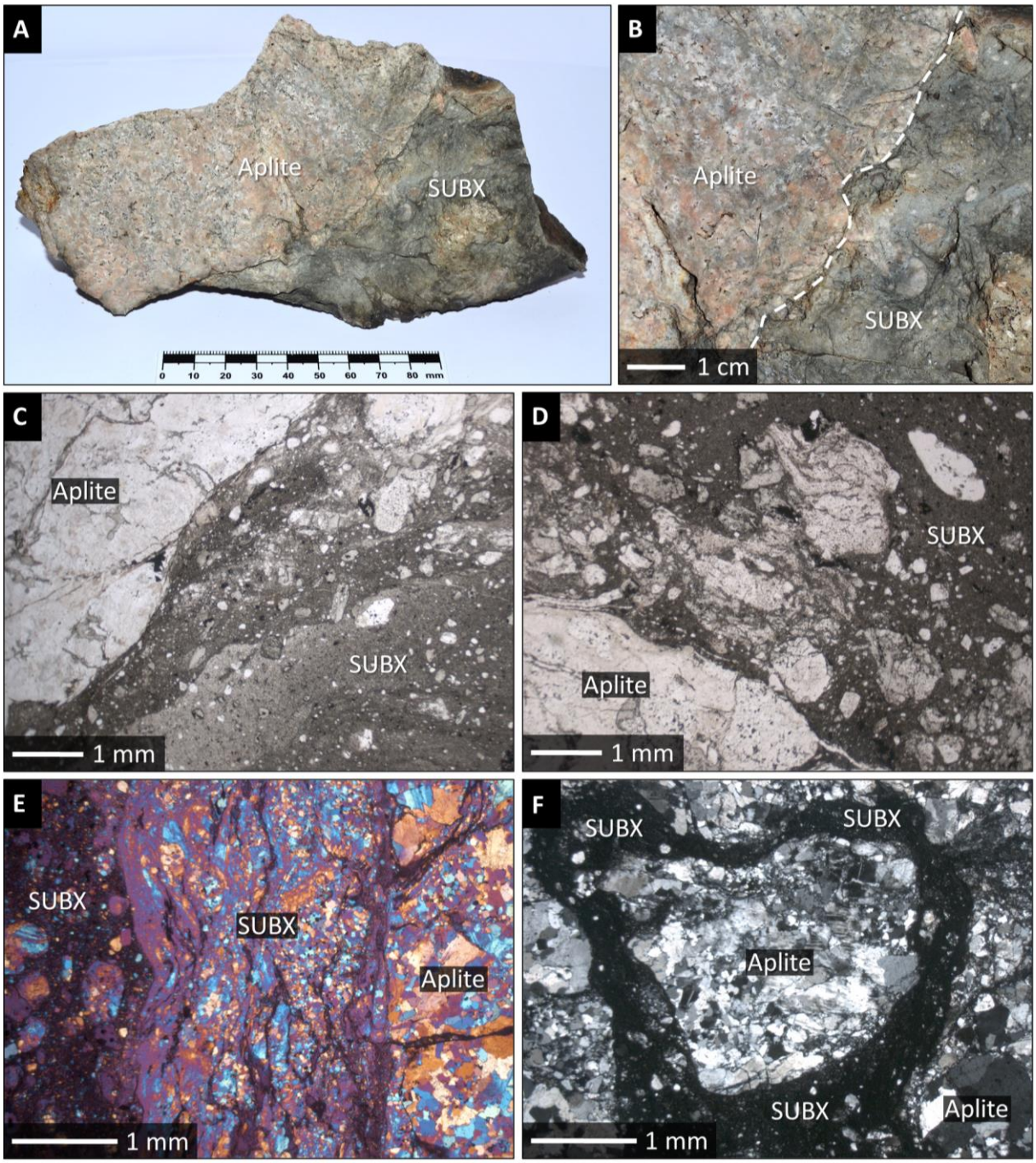

Figure 9.5 Photographs and microphotographs of Sudbury Breccia cutting an aplitic dyke from southern Matagamasi Lake, Rathbun Township; **A:** hand specimen (sample MAT20-1A) of pseudotachylitic breccia developed in aplite; **B:** close-up image of the same specimen; **C–D:** thin section under transmitted light and plane polars, showing pseudotachylitic breccia (cryptocrystalline rock flour) with abundant clasts of the aplitic host rock; **E:** thin section under transmitted light, crossed polars, and with gypsum compensator, showing the transition between aplite and massive matrix-supported pseudotachylitic breccia; note the off-shoots of breccia matrix (injection veins) into the aplite, perpendicular to the main zone of brecciation; **F:** thin section under transmitted light and crossed polars, showing a lithic clast of aplite surrounded by a cryptocrystalline, almost opaque (glass-bearing?), matrix. Abbreviations: SUBX = Sudbury Breccia.

9.5 Mineral Chemistry

Amphibole

Representative compositional data for amphibole from the hornblende syenite from Matagamasi Lake are presented in **Table 9.1** together with structural formulae calculated on the basis of 13 cations per formula unit (excluding Na, Ka, Ca), and with a stochiometric Fe^{3+}/Fe^{2+} determination following Holland & Blundy (1994). The amphibole grains have a fairly homogeneous composition, although incipient alteration of the amphibole to chlorite (and Fe-oxide?) occasionally resulted in mixed analyses with totals of less than 97 wt%; these analyses were discarded. Electron microprobe analyses further revealed that the amphibole is intergrown, at the micron-level, with accessory ilmenite. The SiO_2 content of the amphibole is between 50 and 54 wt%, CaO has a narrow range between 10 and 11 wt%, and all analyses are low in Al_2O_3 (2–4 wt%) and alkali metals (≤ 1 wt%). This composition classifies the amphibole as calcic, and more specifically, as magnesio hornblende according to the nomenclature of Leake et al. (1997). The hornblende has a Mg# (= 100×Mg/[Mg+Fe]) between 57 and 74, and it exhibits a wide range in the $Fe^{3+}/(Fe^{3+}+Fe^{2+})$ ratio, between 0.20 and 0.98, although most samples are between 0.25 and 0.70. The relatively low $Fe^{3+}/(Fe^{3+}+Fe^{2+})$ ratio encountered in most of the analyses is indicative of a low oxygen fugacity (ΔNNO –1; Ridolfi & Renzulli 2012), which is commenced with the presence of ilmenite in the sample (magnetite or titanite would indicate oxidised conditions). Of note, the hornblende has elevated TiO_2 contents between 0.5 and 1.2 wt% (0.81 wt% on average).

Application of the various thermometric and barometric equations listed in **Chapter 2.2.4** revealed a low-pressure high-temperature origin of the magnesio hornblende. For instance, the thermometer of Ridolfi & Renzulli (2012) gave an average temperature (± 1 std.) of 604 ± 116°C (*n*=69); the thermometer of Ridolfi et al. (2010) gave 708 ± 20°C. These values are in good agreement with the temperature derived from the Ti-in-amphibole thermometer of Liao et al. (2021), which yielded an average of 654 ± 33°C. Using the amphibole data in concert with chemical analyses of the presumably co-genetic albite (**Tab. 9.2**), the plagioclase-amphibole thermometer of Holland & Blundy (1994) gave an average temperature of 601 ± 35°C. Note that all these temperatures are within the uncertainty of the different methods and the quoted standard deviations almost identical; also note that these temperatures far exceed the peak metamorphic conditions previously established for the region (Card 1978; Dressler 1982; Easton 2000).

None of the linear Al-in-amphibole barometers (e.g. Hammarstrom & Zen 1986; Hollister et al. 1987; Johnson & Rutherford 1989; Schmidt 1992) gave meaningful results because of the low Al_2O_3 content of the hornblende in question. The equation of Mutch et al. (2016), in combination with the results of the thermometry above, yielded an average pressure of 0.93 ± 0.12 kbar equating to a depth of 3.6 ± 0.5 km at an average overburden density of 2,600 kg/m³. A pressure of 1.73 ± 0.10 kbar equivalent to a crustal depth of 6.8 ± 0.4 km was obtained via Anderson & Smith (1995) – excluding (as recommended) those analyses with a $Fe^{3+}/(Fe^{3+}+Fe^{2+})$ ratio ≥ 0.25 and Fe# ≤ 0.65. An unrealistically low pressure, 0.34 ± 0.09 kbar, was obtained using the barometer of Ridolfi & Renzulli (2012). This pressure is below the lower stability limit of amphibole (e.g. Mutch et al. 2016) and therefore considered geologically meaningless. The other pressure estimates, however, seem reasonable and are consistent with emplacement of the rock and the crystallisation of the amphibole at a paleodepth of 3–7 km, i.e., at the base of the ~5 km thick Cobalt Group.

Table 9.1 Representative electron microprobe data and structural formulae for amphibole in the hornblende syenite from Matagamasi Lake, Rathbun Township

SiO_2	TiO_2	Al_2O_3	Cr_2O_3	FeO	MgO	CaO	MnO	Na_2O	K_2O	Sum	Tetrahedral site				M1, M2, M3 sites								M4 site				A site		
wt%	wt%	wt%	wt%	wt%	wt%	wt%	wt%	wt%	wt%	wt%	Si	Al(IV)	Ti(IV)	Σ	Al(VI)	Ti	Cr	Fe3+	Mg	Fe2+	Mn	Σ	Fe2+	Ca	Na	Σ	Na	K	Σ
53.0	1.24	3.27	0.07	11.9	16.5	10.8	0.12	0.85	0.16	97.79	7.45	0.54	0.01	8.00	0.00	0.12	0.01	0.77	3.46	0.63	0.01	5.00	0.00	1.63	0.23	1.86	0.00	0.03	0.03
52.9	1.20	3.10	0.03	11.2	17.2	11.1	0.12	0.67	0.14	97.66	7.43	0.51	0.06	8.00	0.00	0.07	0.00	0.83	3.60	0.49	0.01	5.00	0.00	1.67	0.18	1.85	0.00	0.03	0.03
52.7	1.19	3.05	0.07	11.3	16.6	11.3	0.11	0.78	0.16	97.30	7.48	0.51	0.01	8.00	0.00	0.11	0.01	0.60	3.52	0.75	0.01	5.00	0.00	1.72	0.22	1.93	0.00	0.03	0.03
53.1	1.18	3.11	0.08	11.0	17.3	11.2	0.09	0.75	0.15	97.94	7.44	0.51	0.04	8.00	0.00	0.08	0.01	0.74	3.61	0.55	0.01	5.00	0.00	1.69	0.20	1.89	0.00	0.03	0.03
53.6	1.11	3.00	0.14	11.1	16.2	11.3	0.10	0.67	0.15	97.34	7.61	0.39	0.00	8.00	0.11	0.12	0.02	0.39	3.42	0.93	0.01	5.00	0.00	1.71	0.18	1.90	0.00	0.03	0.03
53.1	1.09	2.76	0.01	11.5	16.6	11.5	0.12	0.64	0.13	97.47	7.53	0.46	0.01	8.00	0.00	0.11	0.00	0.55	3.52	0.81	0.01	5.00	0.00	1.75	0.18	1.93	0.00	0.02	0.02
50.1	1.06	4.03	0.05	15.7	13.9	10.8	0.23	0.99	0.20	97.06	7.26	0.69	0.05	8.00	0.00	0.07	0.01	0.86	3.00	1.03	0.03	5.00	0.00	1.68	0.28	1.96	0.00	0.04	0.04
52.9	1.05	2.82	0.06	11.3	17.1	10.9	0.13	0.73	0.12	97.19	7.46	0.47	0.07	8.00	0.00	0.04	0.01	0.86	3.60	0.47	0.02	5.00	0.00	1.65	0.20	1.85	0.00	0.02	0.02
52.7	1.05	3.10	0.05	12.0	16.7	10.6	0.11	0.87	0.16	97.35	7.43	0.52	0.06	8.00	0.00	0.05	0.01	0.92	3.51	0.50	0.01	5.00	0.00	1.61	0.24	1.85	0.00	0.03	0.03
52.2	1.04	3.39	0.18	12.2	16.3	11.2	0.16	0.86	0.17	97.66	7.40	0.57	0.04	8.00	0.00	0.07	0.02	0.73	3.45	0.71	0.02	5.00	0.00	1.70	0.24	1.94	0.00	0.03	0.03
50.4	1.02	4.02	0.09	15.3	13.8	11.1	0.24	0.84	0.19	97.06	7.32	0.68	0.00	8.00	0.00	0.11	0.01	0.71	2.99	1.14	0.03	5.00	0.00	1.73	0.24	1.97	0.00	0.04	0.04
50.3	0.99	3.94	0.11	16.7	13.3	11.2	0.21	0.95	0.20	97.89	7.29	0.67	0.04	8.00	0.00	0.07	0.01	0.74	2.87	1.28	0.03	5.00	0.00	1.74	0.26	2.00	0.01	0.04	0.04
53.1	0.93	2.61	0.03	11.4	17.3	11.4	0.10	0.81	0.14	97.87	7.48	0.43	0.09	8.00	0.00	0.01	0.00	0.74	3.63	0.60	0.01	5.00	0.00	1.71	0.22	1.94	0.00	0.02	0.02
52.0	0.93	3.18	0.17	13.5	15.5	11.0	0.14	0.66	0.17	97.26	7.41	0.53	0.05	8.00	0.00	0.05	0.02	0.84	3.31	0.77	0.02	5.00	0.00	1.68	0.18	1.87	0.00	0.03	0.03
52.7	0.93	2.99	0.15	11.2	17.0	11.2	0.09	0.71	0.13	97.02	7.46	0.50	0.04	8.00	0.00	0.06	0.02	0.74	3.58	0.59	0.01	5.00	0.00	1.70	0.19	1.89	0.00	0.02	0.02
51.0	0.93	3.57	0.12	15.1	14.2	11.5	0.22	0.74	0.20	97.61	7.37	0.61	0.02	8.00	0.00	0.08	0.01	0.63	3.06	1.20	0.03	5.00	0.00	1.78	0.21	1.99	0.00	0.04	0.04
51.6	0.91	3.36	0.15	15.8	13.9	11.0	0.29	0.79	0.18	97.95	7.41	0.57	0.02	8.00	0.00	0.08	0.02	0.76	2.97	1.14	0.04	5.00	0.00	1.69	0.22	1.91	0.00	0.03	0.03
50.9	0.91	3.59	0.08	15.6	13.8	11.3	0.21	0.78	0.17	97.41	7.38	0.61	0.00	8.00	0.00	0.10	0.01	0.64	2.97	1.25	0.03	5.00	0.00	1.76	0.22	1.98	0.00	0.03	0.03
53.3	0.90	2.58	0.03	11.6	17.1	11.4	0.11	0.64	0.13	97.86	7.50	0.43	0.07	8.00	0.00	0.02	0.00	0.75	3.60	0.61	0.01	5.00	0.00	1.71	0.18	1.89	0.00	0.02	0.02
53.0	0.89	2.90	0.04	11.8	16.8	10.8	0.12	0.62	0.12	97.09	7.47	0.48	0.04	8.00	0.00	0.05	0.00	0.91	3.54	0.48	0.01	5.00	0.00	1.64	0.17	1.80	0.00	0.02	0.02
51.5	0.87	2.95	0.04	16.0	14.2	11.3	0.29	0.77	0.15	97.99	7.53	0.47	0.00	8.00	0.04	0.10	0.00	0.79	3.10	0.97	0.04	5.04	0.20	1.77	0.04	2.00	0.18	0.03	0.21
53.8	0.86	2.57	0.07	11.0	17.1	11.3	0.10	0.66	0.15	97.57	7.58	0.42	0.00	8.00	0.01	0.09	0.01	0.59	3.58	0.70	0.01	5.00	0.00	1.71	0.18	1.89	0.00	0.03	0.03
53.1	0.85	2.07	0.03	12.6	16.4	11.4	0.19	0.71	0.13	97.48	7.69	0.31	0.00	8.00	0.04	0.09	0.00	0.67	3.54	0.65	0.02	5.02	0.21	1.77	0.02	2.00	0.17	0.02	0.20
51.5	0.84	4.01	0.04	15.7	13.4	10.8	0.28	0.86	0.17	97.64	7.41	0.59	0.00	8.00	0.09	0.09	0.00	0.70	2.88	1.20	0.03	5.00	0.00	1.67	0.24	1.91	0.00	0.03	0.03
52.7	0.84	2.69	0.18	13.0	15.9	11.6	0.12	0.58	0.15	97.77	7.50	0.45	0.05	8.00	0.00	0.04	0.02	0.61	3.37	0.94	0.01	5.00	0.00	1.77	0.16	1.93	0.00	0.03	0.03
50.9	0.84	3.82	0.14	16.2	13.2	10.8	0.22	0.96	0.16	97.35	7.39	0.61	0.00	8.00	0.04	0.09	0.02	0.71	2.86	1.25	0.03	5.00	0.00	1.68	0.27	1.95	0.00	0.03	0.03
51.1	0.82	3.24	0.13	15.6	14.0	11.1	0.26	0.82	0.15	97.24	7.41	0.55	0.04	8.00	0.00	0.05	0.02	0.73	3.02	1.15	0.03	5.00	0.00	1.73	0.23	1.96	0.00	0.03	0.03
51.2	0.82	3.22	0.04	16.1	13.8	11.1	0.27	0.72	0.16	97.47	7.41	0.55	0.04	8.00	0.00	0.05	0.00	0.77	2.98	1.18	0.03	5.00	0.00	1.73	0.20	1.93	0.00	0.03	0.03
51.7	0.81	3.02	0.05	15.1	14.3	11.4	0.17	0.67	0.17	97.49	7.47	0.51	0.02	8.00	0.00	0.07	0.01	0.62	3.08	1.21	0.02	5.00	0.00	1.77	0.19	1.95	0.00	0.03	0.03
51.6	0.81	3.41	0.17	16.2	13.2	11.2	0.24	0.69	0.17	97.71	7.47	0.53	0.00	8.00	0.05	0.09	0.02	0.59	2.85	1.37	0.03	5.00	0.00	1.73	0.19	1.93	0.00	0.03	0.03
51.8	0.81	3.15	0.05	15.4	14.5	11.1	0.23	0.70	0.15	97.80	7.42	0.53	0.05	8.00	0.00	0.04	0.01	0.84	3.09	1.01	0.03	5.00	0.00	1.70	0.19	1.89	0.00	0.03	0.03
50.7	0.81	3.65	0.06	16.6	13.5	10.5	0.32	0.82	0.14	97.23	7.33	0.62	0.05	8.00	0.00	0.03	0.01	1.03	2.91	0.98	0.04	5.00	0.00	1.63	0.23	1.86	0.00	0.03	0.03
54.4	0.80	2.17	0.02	10.9	17.5	11.2	0.14	0.53	0.09	97.74	7.61	0.36	0.03	8.00	0.00	0.06	0.00	0.72	3.65	0.56	0.02	5.00	0.00	1.68	0.15	1.83	0.00	0.02	0.02
51.7	0.79	3.25	0.12	15.1	14.1	11.4	0.23	0.79	0.16	97.64	7.46	0.54	0.00	8.00	0.01	0.09	0.01	0.59	3.04	1.24	0.03	5.00	0.00	1.76	0.22	1.98	0.00	0.03	0.03
52.1	0.78	2.97	0.14	15.4	14.4	10.7	0.27	0.79	0.12	97.56	7.46	0.50	0.04	8.00	0.00	0.04	0.02	0.89	3.06	0.95	0.03	5.00	0.00	1.63	0.22	1.85	0.00	0.02	0.02
51.0	0.78	3.86	0.05	17.2	12.9	10.6	0.25	0.69	0.18	97.56	7.36	0.64	0.00	8.00	0.02	0.08	0.01	0.93	2.78	1.14	0.03	5.00	0.00	1.64	0.19	1.84	0.00	0.03	0.03
50.9	0.77	3.78	0.04	16.7	12.9	11.0	0.26	0.78	0.14	97.27	7.40	0.60	0.00	8.00	0.05	0.08	0.00	0.70	2.80	1.33	0.03	5.00	0.00	1.72	0.22	1.93	0.00	0.03	0.03
53.3	0.77	2.34	0.06	12.1	16.1	11.5	0.14	0.58	0.12	97.03	7.62	0.38	0.00	8.00	0.02	0.08	0.01	0.48	3.43	0.97	0.02	5.00	0.00	1.76	0.16	1.92	0.00	0.02	0.02
53.5	0.77	2.53	0.11	11.7	17.1	11.1	0.17	0.71	0.10	97.75	7.52	0.42	0.07	8.00	0.00	0.02	0.01	0.82	3.58	0.55	0.02	5.00	0.00	1.67	0.19	1.86	0.00	0.02	0.02

Feldspar

Representative mineral chemical analyses of feldspar from the hornblende syenite are reported in **Table 9.2** together with structural formulae calculated on the basis of eight oxygen atoms and five cations per formula unit. As can be seen from this table, the composition of the feldspar is relatively uniform and conforms to almost pure albite ($NaAlSi_3O_8$); the orthoclase component ($KAlSi_3O_8$) is typically below 6 mol%, and the anorthite component ($CaAl_2Si_2O_8$) is below 1 mol%. The celsian component ($BaAl_2Si_2O_8$) was found to be close to or below the detection limit of the electron microprobe, as were the concentrations of Sr, Mg, Fe, and Ti. Accordingly, the composition of the feldspar can be described to range from $Ab_{100}Or_0An_0$ to $Ab_{93}Or_6An_1$, although most analyses have a much tighter compositional range, between $Ab_{99}Or_{0.5}An_{0.5}$ and $Ab_{98}Or_1An_1$. No compositional difference was noted between the large grains of chessboard albite (**Fig. 9.3C**) and the fine-grained mosaic-like granular type of albite (**Fig. 9.3B,E**). There was also no core-rim-zonation observed, nor did the feldspar exhibit any alteration to, for example, sericite or saussurite.

Of note, all albite grains, while appearing optical homogeneous, contain irregular-shaped yet regular spaced crudely oriented patches of K-rich feldspar (**Fig. 9.6**). These lamellae constitute ca. 1–2 area% of their host mineral and are mostly < 5 µm in width. This texture implies initial crystallisation above the alkali feldspar solvus, i.e., above ~400°C at 1 kbar PH_2O and at a Na/(Na+K) ratio of 0.98 (e.g. Smith & Parsons 1974), and subsequent exsolution of an initially homogeneous feldspar solid solution into albite ± K-rich feldspar upon cooling (also referred to as antiperthite).

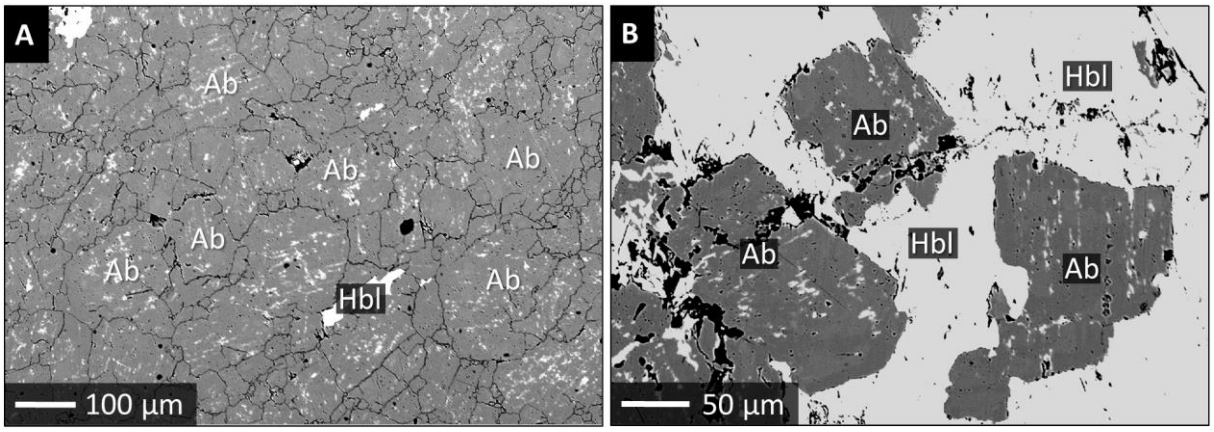

Figure 9.6 Representative backscattered electron images of albite (antiperthite, dark grey) in the hornblende syenite, with exsolution lamellae of K-feldspar (bright). Abbreviations: Ab = albite; Hbl = hornblende.

Accessory minerals

Ilmenite was found as a ubiquitous accessory constituent of the rock, preferentially intergrown with and enclosed within hornblende. Ilmenite occurs as spherical to amoeboid grains, typically 5–15 µm in size. An interesting feature of the ilmenite is its invariably high Mn content, ranging from 2.0 to 3.5 wt% MnO. Manganese-rich ilmenite appears to be typical, although not exclusively restricted to, alkaline rocks including carbonatites, kimberlites, lamprophyres, and nepheline syenites (e.g. Mitchell 1978; Wolff 1987; Kaminsky & Belousova 2009). The composition of the carbonate that was locally observed in thin section (**Fig. 9.3E,F**), interstitial between albite and hornblende, corresponds to calcite. Its MgO content ranges from 0.1 to 0.2 wt%, FeO from 0.2 to 0.7 wt%, and MnO from 0.1 to 0.4 wt%. No zircon or baddeleyite was detected using the EMP.

Table 9.2 Representative electron microprobe data and structural formulae for albite in the hornblende syenite from Matagamasi Lake, Rathbun Township

SiO_2	Al_2O_3	FeO	CaO	Na_2O	K_2O	Sum	Si	Al	Fe	Ca	Na	K	Σ	%Or	%An	%Ab
wt%	wt%	wt%	wt%	wt%	wt%	wt%	apfu	apfu	apfu	apfu	apfu	apfu	apfu			
68.6	19.3	0.02	0.01	11.7	0.03	99.65	3.00	1.00	0.00	0.00	0.99	0.00	4.99	0.18	0.06	99.76
67.8	19.5	0.03	0.05	11.6	0.06	99.05	2.99	1.01	0.00	0.00	0.99	0.00	5.00	0.33	0.26	99.41
69.2	19.4	0.00	0.06	11.3	0.07	99.96	3.01	1.00	0.00	0.00	0.95	0.00	4.97	0.39	0.28	99.33
68.5	19.6	0.00	0.09	11.4	0.04	99.59	3.00	1.01	0.00	0.00	0.97	0.00	4.98	0.25	0.44	99.31
68.9	19.5	0.01	0.05	11.3	0.08	99.82	3.01	1.00	0.00	0.00	0.96	0.00	4.97	0.45	0.24	99.31
68.5	19.0	0.02	0.06	11.4	0.10	99.19	3.01	0.99	0.00	0.00	0.97	0.01	4.98	0.56	0.29	99.15
68.4	19.4	0.00	0.13	11.4	0.05	99.30	3.00	1.00	0.00	0.01	0.97	0.00	4.98	0.29	0.60	99.11
68.4	19.4	0.01	0.12	11.6	0.06	99.52	3.00	1.00	0.00	0.01	0.98	0.00	4.99	0.33	0.57	99.10
68.4	19.7	0.01	0.10	11.0	0.07	99.37	3.00	1.02	0.00	0.00	0.94	0.00	4.96	0.41	0.51	99.08
68.4	19.5	0.02	0.11	11.7	0.09	99.80	2.99	1.01	0.00	0.01	0.99	0.01	5.00	0.50	0.51	98.99
68.4	19.1	0.39	0.11	11.3	0.09	99.49	3.00	0.99	0.01	0.01	0.97	0.01	4.99	0.53	0.55	98.93
68.8	19.5	0.01	0.16	11.3	0.06	99.81	3.00	1.00	0.00	0.01	0.96	0.00	4.98	0.37	0.76	98.88
68.5	19.7	0.02	0.15	11.3	0.07	99.66	3.00	1.02	0.00	0.01	0.95	0.00	4.98	0.40	0.74	98.86
68.2	19.4	0.02	0.17	11.2	0.05	99.04	3.00	1.01	0.00	0.01	0.96	0.00	4.97	0.30	0.84	98.86
68.4	19.6	0.05	0.16	11.3	0.06	99.52	3.00	1.01	0.00	0.01	0.96	0.00	4.98	0.35	0.79	98.86
68.3	19.5	0.00	0.13	11.0	0.09	99.12	3.00	1.01	0.00	0.01	0.94	0.01	4.96	0.54	0.62	98.84
68.6	19.3	0.02	0.16	11.6	0.07	99.72	3.00	1.00	0.00	0.01	0.98	0.00	4.99	0.40	0.77	98.83
68.5	19.4	0.02	0.17	11.5	0.07	99.75	3.00	1.00	0.00	0.01	0.98	0.00	4.99	0.38	0.80	98.82
69.4	18.6	0.00	0.13	11.5	0.11	99.70	3.03	0.96	0.00	0.01	0.97	0.01	4.98	0.60	0.61	98.79
68.6	19.2	0.01	0.13	11.5	0.11	99.55	3.01	0.99	0.00	0.01	0.97	0.01	4.99	0.62	0.60	98.79
68.6	19.4	0.12	0.19	11.2	0.07	99.66	3.00	1.00	0.00	0.01	0.95	0.00	4.98	0.40	0.91	98.69
68.8	19.7	0.05	0.20	11.1	0.06	99.87	3.00	1.01	0.00	0.01	0.94	0.00	4.96	0.34	0.99	98.67
68.3	19.3	0.03	0.08	11.2	0.17	99.02	3.01	1.00	0.00	0.00	0.95	0.01	4.97	0.96	0.41	98.63
68.5	19.1	0.03	0.15	11.3	0.12	99.22	3.01	0.99	0.00	0.01	0.96	0.01	4.98	0.70	0.74	98.56
68.5	19.6	0.08	0.14	11.2	0.14	99.64	3.00	1.01	0.00	0.01	0.95	0.01	4.98	0.79	0.66	98.55
69.0	19.6	0.05	0.22	11.0	0.06	99.94	3.01	1.01	0.00	0.01	0.93	0.00	4.95	0.37	1.11	98.52
68.8	19.4	0.03	0.15	11.2	0.14	99.71	3.01	1.00	0.00	0.01	0.95	0.01	4.97	0.82	0.73	98.45
68.1	19.4	0.05	0.20	11.2	0.10	99.10	3.00	1.01	0.00	0.01	0.96	0.01	4.98	0.60	0.98	98.42
68.3	20.4	0.02	0.27	10.6	0.05	99.67	2.98	1.05	0.00	0.01	0.90	0.00	4.95	0.29	1.38	98.33
68.5	19.7	0.01	0.23	11.3	0.10	99.83	2.99	1.02	0.00	0.01	0.95	0.01	4.98	0.60	1.12	98.28
68.2	19.3	0.04	0.08	11.3	0.24	99.10	3.00	1.00	0.00	0.00	0.96	0.01	4.98	1.40	0.38	98.22
68.1	19.3	0.17	0.22	11.2	0.12	99.21	3.00	1.00	0.01	0.01	0.96	0.01	4.98	0.70	1.08	98.22
68.4	19.6	0.09	0.19	11.4	0.16	99.92	2.99	1.01	0.00	0.01	0.97	0.01	4.99	0.90	0.89	98.21
68.4	19.1	0.04	0.19	11.2	0.16	99.15	3.01	0.99	0.00	0.01	0.96	0.01	4.98	0.89	0.93	98.18
68.4	19.7	0.04	0.28	11.1	0.08	99.57	2.99	1.02	0.00	0.01	0.94	0.00	4.97	0.48	1.36	98.16
68.8	19.4	0.03	0.08	11.3	0.26	99.92	3.01	1.00	0.00	0.00	0.95	0.01	4.98	1.47	0.40	98.14
68.1	19.6	0.11	0.30	11.2	0.08	99.33	2.99	1.01	0.00	0.01	0.95	0.00	4.98	0.45	1.44	98.11
68.0	19.8	0.14	0.24	11.0	0.13	99.31	2.99	1.02	0.01	0.01	0.94	0.01	4.97	0.76	1.16	98.07
68.2	19.6	0.03	0.11	11.4	0.26	99.62	2.99	1.01	0.00	0.01	0.97	0.01	4.99	1.45	0.51	98.03
68.0	19.4	0.08	0.17	11.4	0.23	99.25	2.99	1.01	0.00	0.01	0.97	0.01	5.00	1.29	0.83	97.89
68.4	19.7	0.08	0.29	11.0	0.14	99.56	3.00	1.02	0.00	0.01	0.93	0.01	4.97	0.84	1.41	97.75
68.0	19.9	0.04	0.37	11.0	0.08	99.46	2.98	1.03	0.00	0.02	0.94	0.00	4.97	0.46	1.81	97.73
68.5	19.3	0.05	0.09	11.2	0.34	99.55	3.00	1.00	0.00	0.00	0.96	0.02	4.98	1.92	0.44	97.65
68.6	19.6	0.05	0.17	11.1	0.27	99.73	3.00	1.01	0.00	0.01	0.94	0.01	4.97	1.55	0.82	97.63
69.0	19.3	0.01	0.16	11.1	0.32	99.88	3.01	0.99	0.00	0.01	0.94	0.02	4.97	1.85	0.76	97.39
68.3	19.2	0.18	0.27	11.2	0.25	99.41	3.00	1.00	0.01	0.01	0.95	0.01	4.98	1.42	1.29	97.29
68.6	19.5	0.02	0.16	11.3	0.38	99.89	3.00	1.00	0.00	0.01	0.95	0.02	4.99	2.17	0.76	97.07
68.4	19.1	0.02	0.12	11.0	0.41	99.10	3.01	0.99	0.00	0.01	0.94	0.02	4.98	2.35	0.59	97.06
68.2	19.4	0.15	0.19	11.1	0.37	99.42	3.00	1.01	0.01	0.01	0.95	0.02	4.98	2.10	0.90	97.00
68.9	19.2	0.02	0.05	11.2	0.55	99.88	3.01	0.99	0.00	0.00	0.95	0.03	4.98	3.13	0.24	96.63
68.7	19.9	0.08	0.37	10.5	0.29	99.81	3.00	1.02	0.00	0.02	0.89	0.02	4.95	1.76	1.89	96.35
68.4	19.5	0.03	0.04	11.0	0.61	99.52	3.00	1.01	0.00	0.00	0.93	0.03	4.98	3.53	0.18	96.29
68.3	19.4	0.10	0.11	11.0	0.82	99.64	3.00	1.00	0.00	0.01	0.93	0.05	4.99	4.64	0.53	94.83
68.6	19.6	0.14	0.33	10.6	0.63	99.88	3.00	1.01	0.01	0.02	0.90	0.03	4.96	3.67	1.62	94.71
67.8	19.7	0.10	0.33	11.0	0.87	99.80	2.98	1.02	0.00	0.02	0.94	0.05	5.00	4.87	1.56	93.57
68.6	19.3	0.05	0.27	10.6	0.94	99.77	3.01	1.00	0.00	0.01	0.90	0.05	4.97	5.43	1.31	93.26
68.0	19.1	0.01	0.22	10.8	1.04	99.16	3.00	0.99	0.00	0.01	0.93	0.06	4.99	5.87	1.04	93.08

Concentrations of Sr, Ba, Ti and Mg were very close to, or below, the detection limit (< 0.01 wt%) and therefore not reported; abbreviations: apfu = atoms per formula unit; %Or = percentage of the orthoclase component in the feldspar analyses; %An = percentage of the anorthite component; %Ab = percentage of the albite component.

9.6 Geochemistry

General characteristics

Major- and trace element data of representative grab samples of the aplitic dykes from Matagamasi Lake, Rathbun Township, are presented in **Table 9.3**, and reveal a subalkaline, peraluminous and in terms of SiO_2 (69–79 wt%) acidic composition. Concentrations of Fe_2O_3 and MgO are with 0.2–2.6 wt% and 0.4–3.1 wt%, respectively, relatively low and uniform; the corresponding Mg# ranges from 63 to 79. In agreement with microscopic observations which revealed a high modal proportion of albite, the Na_2O concentrations are high (5.4–6.8 wt%), whereas K_2O is typically below 1 wt%. The aplitic dykes are quite poor in TiO_2 (0.2–0.5 wt%) and have P_2O_5 values close to, or even below, the detection limit of the EDS-XRF (< 0.01 wt%). The volatile content (expressed as LOI) is < 1.5 wt%, which is consistent with the observed lack of hydrous silicates or carbonates; exception being a carbonate-bearing sample with 3.1 wt% LOI. Interestingly, all the aplitic dykes have variable but high concentrations of Cr (34–456 ppm) and Ni (5–243 ppm). While Zr values are comparable to those found in the mafic dykes discussed in previous chapters (79–126 ppm), the ΣREE+Y concentrations for the aplitic rocks are extremely low (7–75 ppm) – much lower than in any of the mafic rocks analysed in this study. The CIPW normative mineralogy is 50–60 vol% plagioclase (mostly albite), 35–40 vol% quartz, 1–6 vol% orthoclase, and 2–7 vol%. Further, all the aplitic dykes have 1–2 vol% corundum in their norm. The hypothetical density is ca. 2.7 g/cm^3.

Table 9.3 also includes three analyses of the hornblende syenite found at southern Matagamasi Lake. One of these analyses is thought to reflect the whole-rock composition of the dyke, whereas the other two analyses were obtained on a feldspar- and a hornblende-rich mineral separate. The hornblende syenite can be readily distinguished from the aplitic dykes by its lower SiO_2 content (63 wt%). The syenite is also characterised by extraordinary high concentrations of Na_2O (7.7 – 10.6 wt%), whereas K_2O is below 1 wt%. The hornblende syenite is relatively rich in Zr (213 ppm) and Nb (9 ppm). Also note the elevated concentrations of Cr (117 ppm) and Ni (64 ppm). Conversely, the ΣREE+Y concentrations are around 100 ppm, which is higher than in the aplitic dykes, but still lower than expected for an alkaline felsic igneous rock. The CIPW normative mineralogy is as follows: 87 vol% plagioclase (83 vol% albite), 4 vol% K-feldspar, 7 vol% diopside, 1 vol% olivine, and 1 vol% nepheline, equating a rock density of 2.7 g/cm^3.

Igneous rock classification

The aplitic dykes are classified as subalkaline and rhyolitic/granitic in terms of their total alkali vs. silica content (**Fig. 9.7B**); the hornblende syenite as alkaline and trachytic/syenitic. In terms of aluminium saturation (**Fig. 9.7C**), the aplitic dykes are peraluminous throughout (typical of S-type granitoids); the syenite is metaluminous (typical of I- and A-type granitoids). Using trace elements that are generally regarded as fluid immobile during weathering, low-temperature alteration, and low-/medium grade metamorphism (e.g. Zr, Ti, Nb, Th, REE, Y), the composition of the aplitic dykes conforms to rhyodacite (**Fig. 9.7D**), and that of the syenite conforms to trachyandesite, which is broadly consistent with the major element classifications. Both the aplitic dykes and the syenite are classified as either I-type or S-type according to Whalen et al. (1987) due to their low contents of Zr, Nb, Ce, and Y (**Fig. 9.7E**). Using the Y+Nb vs. Rb classification scheme of Pearce et al. (1984) (not shown), both the aplitic dykes and the hornblende syenite are ambiguously classified as either VAG (volcanic arc granite) or synCOLG (syn-collision granite).

Trace element patterns

Primitive mantle-normalised trace element abundances for the felsic dykes are presented in **Figure 9.7F**. The aplitic samples exhibit a wide range of subparallel trace element pattens that are characterised by a pronounced enrichment of Th, U, K and especially Pb, and negative anomalies of Sr, Nb, Ta, and Ti. An interesting feature of almost all the aplitic dykes is a distinct depletion in LREE and MREE relative to HREE, and relative to the primitive mantle. A Eu anomaly is observed in most samples but ranges widely from strongly negative (Eu/Eu* = 0.5) to slightly positive (Eu/Eu* = 1.3). Another notable feature is the wide range in Nb/Ta_N (0.5–1.7). The hornblende syenite shows a similar trace element pattern, but it lacks the pronounced LREE-MREE depletion that characterises most of the aplitic samples. The syenite further shows a near-chondritic Zr/Hf, a sub-chondritic Nb/Ta_N (0.5) ratio, and very distinct negative Eu, Sr, and Ti anomalies.

Nd-Sr-Pb isotopes

A summary of whole-rock radioisotope data for the two groups of felsic dykes from Matagamasi Lake is presented in **Table 9.4**. The aplitic dykes exhibit a wide range in $^{143}Nd/^{144}Nd$ corresponding to a present-day εNd between –25.60 and –11.34 which is, besides, negatively correlated with the whole-rock Nd concentration. The $^{147}Sm/^{144}Nd$ ratios are very high, between 0.138 and 0.226, and do not permit the calculation of a realistic model age. The $^{147}Sm/^{144}Nd$ ratio is positively correlated with the $^{143}Nd/^{144}Nd$ ratio (R^2 = 0.85), but without age significance. The $^{87}Sr/^{86}Sr$ isotope ratio varies greatly, from 0.717 to 0.782, and this wide range also persists in the initial $^{87}Sr/^{86}Sr$ ratio (calculated for any arbitrary point in time). The calculated $^{87}Rb/^{86}Sr$ ratio ranges from 0.4 to 3.3 and it is highly correlated (R^2 = 0.93) with the $^{87}Sr/^{86}Sr$ ratio (**Fig. 9.8H**). A York-regression (using *IsoplotR*; Vermeesch 2018) passing through all twelve analyses gave a Rb-Sr errorchron date of 1806.5 ± 14 Ma (MSWD = 170) and an initial $^{87}Sr/^{86}Sr$ of 0.70850 ± 0.00017. Other statistical approaches (e.g. ordinary least square regression) gave comparable results. There is no correlation (R^2 = 0.17) between the $^{206}Pb/^{204}Pb$ and the $^{208}Pb/^{204}Pb$ isotope ratio; there is, however, a very strong correlation (R^2 = 0.95) between $^{206}Pb/^{204}Pb$ and $^{207}Pb/^{204}Pb$. This permits the calculation of an errorchron date (for *n*=11, excluding one outlier). A York regression gave a datum of 2010 ± 0.7 Ma (MSWD = 31,000); an ordinary least square regression gave 1945 ± 128 Ma. These dates are broadly consistent with the above Rb-Sr errorchron date, and they are consistent with the relative age relations established in the field – that the aplitic dykes must be younger than the 2.22 Ga Nipissing Suite (**Fig. 9.2C**), but older than the 1.85 Ga Sudbury impact event (**Fig. 9.5**).

Table 9.4 additionally includes three analyses obtained on the hornblende syenite. The whole-rock sample MAT20-2B has a $^{143}Nd/^{144}Nd$ ratio corresponding to an εNd of –14.3; the $^{147}Sm/^{144}Nd$ ratio of the sample is 0.180. The measured $^{87}Sr/^{86}Sr$ ratio is 0.721, and the calculated $^{87}Rb/^{86}Sr$ ratio is 0.632. The whole-rock sample in combination with the feldspar- and hornblende-rich mineral separates define a three-point Pb-Pb errorchron of 1697 ± 29 Ma (MSWD = 18) or 1938 ± 74 Ma, depending on the statistical approach (again *IsoplotR*, Vermeesch 2018). These dates compare relatively well with a Sm-Nd isochron date of 1845 ± 300 Ma (MSWD = 0.31), or 1842 ± 170 Ma, obtained on the same three samples (whole-rock plus minerals), by assuming a 2σ-error of 3% for $^{147}Sm/^{144}Nd$ based on the maximum analytical error of the ICP-MS trace element analyses for Sm and Nd. Unfortunately, these dates do not permit to distinguish whether the hornblende syenite is older or younger than the 1.85 Ga Sudbury impact event, but the approach at least provides an estimate for the initial $^{207}Pb/^{206}Pb$ ratio (ca. 0.11) and the initial $^{143}Nd/^{144}Nd$ ratio (0.51122).

Table 9.3 Major element oxide concentrations (wt%) and trace element concentrations (ppm) in felsic dykes, Matagamasi Lake, Rathbun Township

	Aplitic dykes												Hornblende syenite		
	MAT201A	**MAT201B**	**MAT201C**	**MAT203**	**MAT204**	**MAT205**	**MAT206A**	**MAT206B**	**MAT207A**	**MAT207B**	**MAT208A**	**MAT208B**	**MAT202B**	**2B-FSP**	**2B-AM**
Lat.	46°45 15	46°45 15	46°45 15	46°45 06	46°47 04	46°46 44	46°46 55	46°46 55	46°47 04	46°47 04	46°47 07	46°47 07	46°45 08	46°45 08	46°45 08
Long.	80°36 32	80°36 32	80°36 32	80°36 21	80°36 06	80°36 09	80°35 57	80°35 57	80°36 06	80°36 06	80°36 01	80°36 01	80°36 21	80°36 21	80°36 21
SiO_2	77.6	74.0	73.9	69.7	69.0	75.0	77.7	76.0	72.1	76.8	74.4	78.9	63.4	65.7	61.9
TiO_2	0.19	0.38	0.41	0.46	0.48	0.34	0.25	0.32	0.43	0.38	0.40	0.34	0.66	0.53	0.81
Al_2O_3	12.8	13.5	13.3	12.9	13.0	12.4	12.1	13.3	14.4	12.1	13.1	11.8	17.5	19.3	15.3
Fe_2O_3	1.40	2.34	2.41	2.55	2.15	1.70	0.78	0.92	1.66	0.96	1.33	0.22	2.01	0.66	4.83
MgO	1.53	2.49	2.49	1.99	3.14	1.70	0.70	0.78	2.18	1.09	2.16	0.35	1.63	0.50	3.41
CaO	0.41	0.51	0.47	3.30	1.54	0.19	0.26	0.25	0.18	0.19	0.22	0.17	2.76	1.30	4.26
MnO	< 0.01	0.01	0.01	0.05	0.02	0.01	0.01	0.01	0.01	0.01	0.01	0.01	0.04	0.02	0.07
Na_2O	5.8	5.9	5.6	6.2	5.7	5.4	6.0	6.8	6.7	5.6	6.0	6.3	9.5	10.6	7.7
K_2O	0.20	0.24	0.37	0.36	1.66	0.91	0.67	0.91	0.89	0.89	0.98	0.61	0.60	0.57	0.53
P_2O_5	< 0.01	< 0.01	< 0.01	0.12	0.07	< 0.01	< 0.01	< 0.01	< 0.01	< 0.01	< 0.01	< 0.01	0.01	< 0.01	< 0.01
LOI	0.92	1.33	1.41	1.71	3.12	1.01	0.51	0.56	1.38	0.96	1.19	0.40	1.58	1.07	1.49
Total	100.81	100.67	100.35	99.40	99.80	98.67	99.02	99.80	99.86	98.96	99.72	99.03	99.73	100.14	100.32
Cr	61.17	109.5	320.9	93.65	455.7	46.16	71.74	196.6	65.49	56.93	151.0	33.87	116.7	25.39	88.02
Ni	35.16	59.45	173.8	41.54	242.5	30.19	32.43	98.67	34.23	26.57	84.65	5.164	63.61	6.025	38.92
Cu	6.954	6.266	6.924	7.175	11.89	6.429	6.666	7.379	8.889	4.269	5.492	6.652	6.304	6.589	4.591
Rb	1.597	2.091	3.602	5.176	9.888	27.78	8.833	9.209	18.11	17.96	15.68	6.488	8.334	6.691	5.706
Sr	17.72	12.05	13.88	70.79	22.80	24.06	17.33	18.59	29.10	21.20	37.47	26.16	52.53	45.08	46.96
Y	6.404	13.33	9.080	26.30	11.09	7.183	4.056	2.706	2.768	2.561	4.620	3.259	29.24	17.85	35.88
Zr	79.40	104.5	91.11	125.6	117.7	102.2	88.27	104.3	93.13	100.8	105.0	102.5	213.1	248.8	173.3
Nb	5.029	7.299	15.40	7.862	20.28	5.085	4.998	9.158	5.125	4.952	8.691	3.830	8.816	4.430	6.425
Ba	10.25	9.833	15.92	97.50	44.65	56.02	38.19	38.41	44.31	47.47	42.95	22.29	63.90	59.83	56.15
La	3.437	10.82	6.682	22.33	10.95	1.941	1.018	0.441	1.840	0.487	0.904	0.856	10.11	7.293	8.955
Ce	7.546	25.26	16.89	53.88	24.20	4.712	2.583	2.012	4.047	1.272	2.169	1.943	21.17	14.83	24.34
Pr	0.911	3.219	2.000	7.334	2.942	0.598	0.320	0.152	0.451	0.156	0.273	0.226	3.064	1.861	3.907
Nd	3.239	11.39	7.160	27.15	10.56	2.191	1.225	0.599	1.508	0.607	1.079	0.838	12.88	7.604	16.75
Sm	0.851	2.730	1.771	6.183	2.418	0.683	0.420	0.213	0.364	0.226	0.404	0.277	3.848	2.074	5.245
Eu	0.216	0.648	0.424	1.237	0.410	0.178	0.190	0.101	0.158	0.083	0.144	0.117	0.749	0.563	0.786
Tb	0.173	0.395	0.266	0.878	0.348	0.153	0.104	0.058	0.064	0.055	0.105	0.076	0.780	0.455	1.054
Gd	0.970	2.537	1.638	5.675	2.261	0.847	0.606	0.320	0.391	0.299	0.565	0.407	4.595	2.671	6.019
Dy	1.124	2.308	1.591	5.036	2.043	1.009	0.650	0.380	0.396	0.381	0.711	0.515	4.951	2.845	6.377
Ho	0.243	0.488	0.337	1.011	0.431	0.236	0.143	0.094	0.092	0.093	0.160	0.121	1.046	0.628	1.377
Er	0.757	1.441	1.027	2.910	1.320	0.800	0.457	0.321	0.330	0.315	0.525	0.398	2.996	1.790	3.836
Tm	0.122	0.215	0.155	0.412	0.207	0.137	0.074	0.060	0.059	0.054	0.087	0.066	0.430	0.259	0.558
Yb	0.840	1.394	1.054	2.569	1.438	1.046	0.554	0.462	0.476	0.425	0.650	0.489	2.725	1.771	3.456
Lu	0.141	0.223	0.172	0.387	0.238	0.192	0.099	0.085	0.095	0.079	0.116	0.087	0.421	0.270	0.508
Hf	2.522	2.952	2.685	3.607	3.322	2.694	2.489	2.478	2.541	2.681	2.651	2.647	5.334	6.223	4.273
Ta	0.546	0.513	0.569	0.659	0.666	0.571	0.448	0.436	0.586	0.492	0.533	0.435	0.932	0.826	1.003
Pb	1.507	2.603	2.390	7.232	3.120	4.400	5.388	5.347	6.755	1.587	2.255	3.101	3.428	3.690	2.658
Th	6.469	7.380	7.665	10.45	5.765	13.00	3.955	1.417	6.146	3.557	7.909	4.274	5.401	4.415	5.674
U	2.052	1.884	2.029	1.463	1.600	3.040	3.970	1.536	3.762	1.585	1.840	1.293	1.574	1.781	1.711

Table 9.4 Summary of whole-rock Nd-Sr-Pb isotope data for felsic dykes from Matagamasi Lake, Rathbun Township

	$\frac{^{143}Nd}{^{144}Nd}$	±2σ	$\frac{^{147}Sm}{^{144}Nd}$	εNd present	Assumed age	εNd initial	$\frac{^{87}Sr}{^{86}Sr}$	±2σ	$\frac{^{87}Rb}{^{86}Sr}$	$^{87}Sr/^{86}Sr(i)$	$\frac{^{208}Pb}{^{204}Pb}$	±2σ	$\frac{^{207}Pb}{^{204}Pb}$	±2σ	$\frac{^{206}Pb}{^{204}Pb}$	±2σ	$\frac{^{208}Pb}{^{204}Pb(i)}$	$\frac{^{207}Pb}{^{204}Pb(i)}$	$\frac{^{206}Pb}{^{204}Pb(i)}$
Aplitic dykes																			
MAT 20-1A	0.511390	15	0.159	–24.34	2220 Ma	–13.56	0.724070	18	0.448	0.70972	43.3011	37	16.8128	12	29.6131	18	43.30	16.81	29.61
MAT 20-1B	0.511441	12	0.145	–23.35	2220 Ma	–8.57	0.725100	47	0.673	0.70354	40.2481	35	16.3310	10	24.1230	13	40.25	16.33	24.12
MAT 20-1C	0.511436	10	0.149	–23.45	2220 Ma	–10.01	0.730254	17	0.906	0.70121	40.9416	39	16.4255	13	25.0845	16	40.94	16.43	25.08
MAT 20-3	0.511353	13	0.138	–25.06	2220 Ma	–8.22	0.716911	14	0.400	0.70409	44.3336	32	16.1582	10	22.0932	11	44.33	16.16	22.09
MAT 20-4	0.511326	12	0.138	–25.60	2220 Ma	–8.99	0.729827	18	1.375	0.68576	41.0124	25	16.3796	9	23.9901	11	41.01	16.38	23.99
MAT 20-5	0.511828	22	0.188	–15.81	2220 Ma	–13.48	0.781896	23	3.332	0.67512	38.4535	26	16.9784	10	21.5329	10	38.45	16.98	21.53
MAT 20-6A	0.512057	23	0.207	–11.34	2220 Ma	–14.38	0.748319	13	1.585	0.69751	36.6117	21	16.0780	7	22.6297	8	36.61	16.08	22.63
MAT 20-6B	0.511841	25	0.215	–15.55	2220 Ma	–20.81	0.749459	13	1.547	0.69989	35.9158	26	15.8713	9	20.2373	10	35.92	15.87	20.24
MAT 20-7A	0.511467	38	0.146	–22.84	2220 Ma	–8.36	0.748925	26	1.888	0.68841	38.9086	26	16.0317	9	21.4956	10	38.91	16.03	21.50
MAT 20-7B	0.511777	46	0.225	–16.80	2220 Ma	–24.97	0.775815	18	2.502	0.69562	39.5812	31	17.2845	10	30.8600	18	39.58	17.28	30.86
MAT 20-8A	0.512039	27	0.226	–11.68	2220 Ma	–20.19	0.746194	16	1.338	0.70330	40.5778	28	16.6621	10	26.2101	13	40.58	16.66	26.21
MAT 20-8B	0.511873	20	0.200	–14.92	2220 Ma	–15.84	0.732240	13	0.876	0.70418	40.7209	28	16.3232	9	23.4632	10	40.72	16.32	23.46
Hornblende syenite																			
MAT 20-2B AM	0.512038	12	0.189	–11.71	1842 Ma	–9.96	0.720861	11	0.531	0.70674	40.7710	34	16.3698	98	23.9084	12	40.77	16.37	23.91
MAT 20-2B FSP	0.511744	10	0.165	–17.43	1842 Ma	–9.90	0.719790	12	0.604	0.70375	39.9696	30	16.2094	8	22.5455	9	39.97	16.21	22.54
MAT 20-2B WR	0.511904	9	0.180	–14.33	1842 Ma	–10.53	0.721557	13	0.632	0.70478	40.2239	30	16.2463	10	22.9107	11	40.22	16.25	22.91

$^{147}Sm/^{144}Nd$ and $^{87}Rb/^{86}Sr$ ratios were calculated using measured Sm, Nd, Rb and Sr concentrations, which are given in Table 9.3;
2σ uncertainties of $^{147}Sm/^{144}Nd$ and $^{87}Rb/^{86}Sr$ are < 3% based on the propagated analytical error of Sm, Nd, Rb and Sr concentration data;
$^{143}Nd/^{144}Nd$ ratios are normalised to $^{146}Nd/^{144}Nd = 0.72190$;
2σ uncertainties of $^{143}Nd/^{144}Nd$ are < 0.004% based on the long-term in-house reproducibility of BHVO-2;
2σ uncertainties of $^{87}Sr/^{86}Sr$ are < 0.007% based on the long-term in-house reproducibility of BHVO-2;
2σ uncertainties of $^{208}Pb/^{204}Pb$, $^{207}Pb/^{204}Pb$ and $^{206}Pb/^{204}Pb$ are < 0.18%, < 0.09% and < 0.5%, respectively, based on the long-term in-house reproducibility of BHVO-2;
For sake of readability, all listed 2σ absolute errors only refer to the last significant decimal digits of the measured isotope ratios;
εNd values were calculated relative to CHUR with $^{147}Sm/^{144}Nd = 0.1967$ and $^{143}Nd/^{144}Nd = 0.512638$;
Initial isotope ratios were calculated using measured Sm, Nd, Rb, Sr, U, Th and Pb concentrations, which are given in Table 9.3;

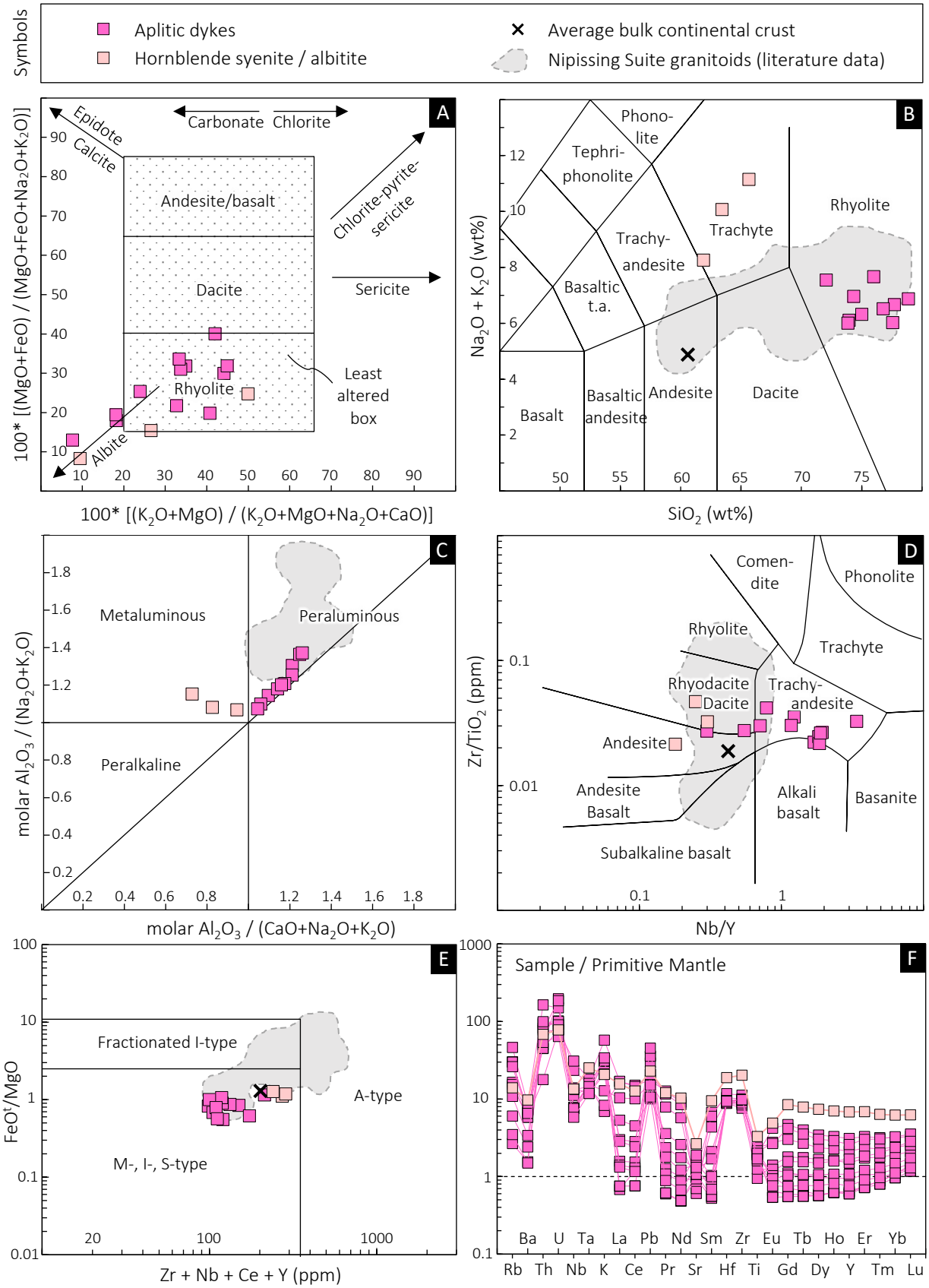

Figure 9.7 A selection of plots used to illustrate the effects of metasomatism on, and the geochemical classification and magmatic affinity of, the felsic dykes from Matagamasi Lake, Rathbun Township; **A:** alteration box plot after Large et al. (2001); **B:** TAS classification after Le Bas et al. (1986); **C:** discrimination plot after Maniar & Piccoli (1989); **D:** discrimination plot after Winchester & Floyd (1977); **E:** discrimination plot after Whalen et al. (1987); **F:** spidergram with normalisation values after McDonough & Sun (1995); literature data for granitoid rocks that have previously been genetically assigned to the Nipissing Suite are from Lightfoot & Naldrett (1996b); 2σ-error bars are typically smaller than the symbol size.

9.7 Interpretation

Assessment of post-depositional alteration

Microscopic studies of the felsic dykes from Matagamasi Lake revealed the preservation of relatively pristine minerals and rock textures in almost all the samples, with the exception of minor sericitisation, chloritisation, and carbonatisation. Although alteration appears marginal in comparison to the strongly altered mafic rocks discussed before, it is nonetheless inevitable to consider whether the felsic dykes have remained a closed system with respect to their chemical composition. One way of testing for secondary element mobility is the so-called isocon method of Grant (1986). This approach is, however, not applicable to the samples in questions for the following reasons. First, the samples are mineralogically and texturally very uniform at the outcrop scale, so that it was not possible to obtain or define altered and fresh endmember pairs. Second, there is a considerable geochemical heterogeneity among the aplitic dykes from different locations, which is more likely the result of primary variations, rather than metasomatism.

Alternatively, the degree to which the felsic dykes were affected by metasomatism can be addressed semi-quantitatively by plotting the analyses into the so-called alteration box plot after Large et al. (2001). The approach has several advantages over the isocon method, including that it has been specifically calibrated for igneous rocks, that it includes alteration vectors, and that is allows to compare a larger set of samples; a major disadvantage is that trace element concentrations are not considered. Application of the alteration box plot to the felsic dykes from Matagamasi Lake reveals that most samples fall into the field of fresh rhyolite/granite, with only a few outliers plotting toward normative albite. This is not only in accordance with the petrographic observations, but it also indicates that elements such as Al, Fe, Mg, Na, K and Ca had not been significantly mobilised during whatever post-magmatic process. By association, it may be inferred that those elements with a similar geochemical affinity (e.g. Ba, Rb, Sr, Mn) remained relatively immobile as well. This can be further evaluated by comparing inter-element ratios (e.g. Rb/Sr, K/Rb, Th/U, Ni/Cr) between the different aplitic samples, which revealed to be constant. Little overall element mobility is also supported by relatively consistent geochemical classifications (e.g. **Fig. 9.7B–E**), and especially by the parallelism of normalised trace element patterns (**Fig. 9.7F**). These demonstrate that the normalised ratios of Rb/Sr, Rb/Ba, Th/U etc. are relatively constant in spite of the geochemical heterogeneity recorded by the various samples. It is concluded that the obtained geochemical data are representative of the protolith' composition, and that alteration was merely an isochemical process (except for H_2O and CO_2). Unfortunately, only one whole-rock sample of the hornblende syenite was available. From its relatively pristine mineralogy and texture, however, little alteration and secondary element mobility is inferred, although the possibility remains that at least Na (and by association, K and Rb) was locally re-redistributed at the outcrop scale.

At issue is whether the large dispersion in measured isotope ratios reflects primary heterogeneities or later disturbance. However, as most elements, including Rb, Sr, U, Pb, Sm and Nd seemingly behaved immobile, it is reasonable to assume that the Nd, Sr and Pb isotopes did as well. There is no correlation between the measured isotope ratios and the whole-rock volatile content (**Fig. 9.8A–D**), suggesting that hydration and carbonatisation, limited as they were, had no bearing on the Sm-Nd, Rb-Sr, or U-Th-Pb isotope systematics. The whole-rock errorchron dates (**Fig. 9.8E,F**) could therefore approximate the initial crystallisation ages of the dykes.

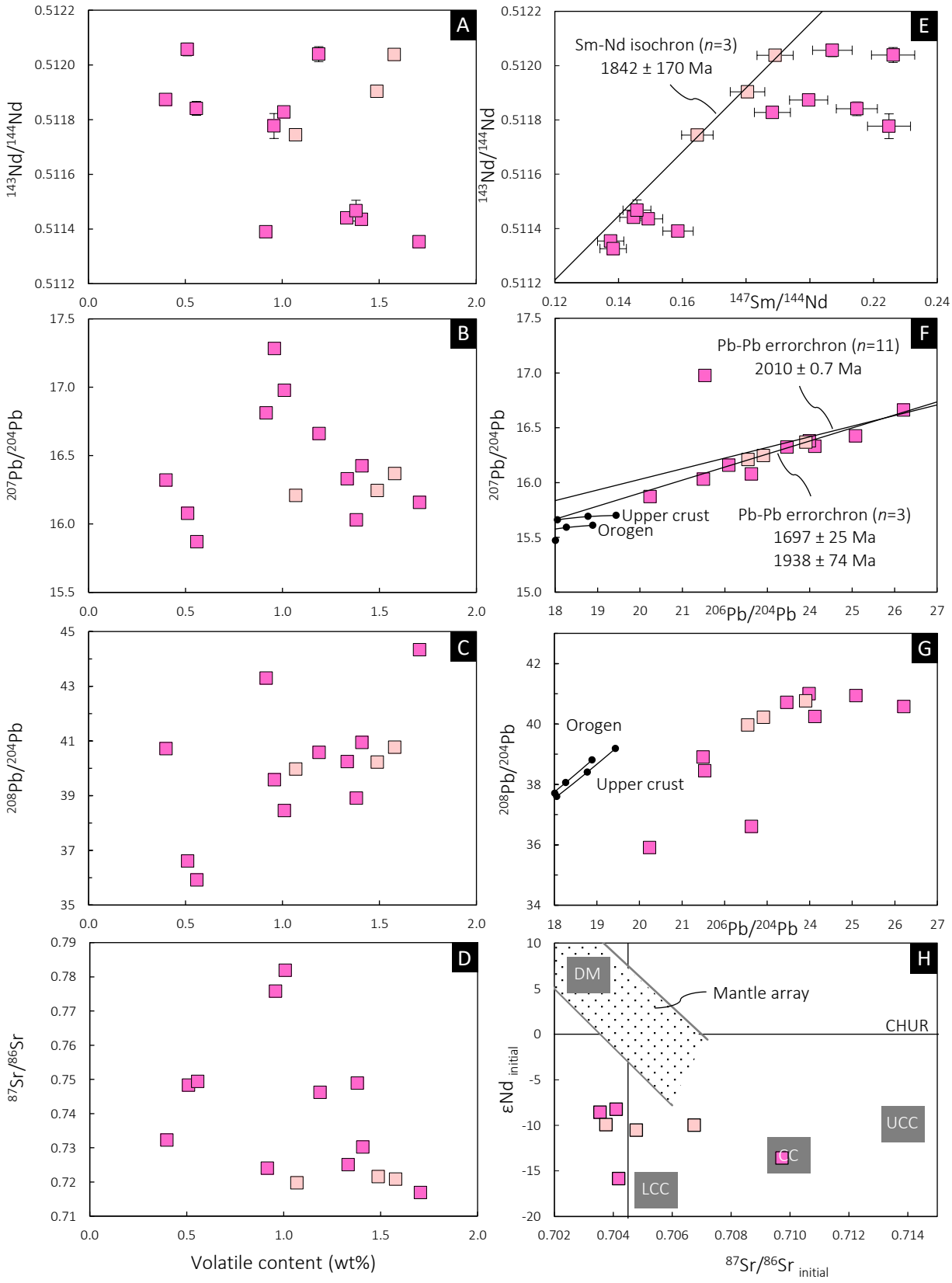

Figure 9.8 Bivariate plots of whole-rock Nd, Pb and Sr isotope ratios for the felsic dykes from Matagamasi Lake; **A–D:** measured isotope ratios vs. whole-rock volatile content, illustrating the effects of fluid-rock interaction on the isotopic composition; **E:** samarium- and Nd isotope correlation plot; **F–G:** lead isotope ratio plots with growth curves after Zartman & Doe (1981) for different reservoirs, with 400 Ma-increments until present; **H:** plot of the initial εNd vs. the initial $^{87}Sr/^{86}Sr$; upper (UCC) and lower continental crust (LCC) after Faure (1986); error bars represent 2σ internal errors but are smaller than the symbol size in most of the panels.

Hornblende syenite – magmatic or metasomatic?

The hornblende syenite from Matagamasi Lake differs strongly, in terms of texture, mineralogy, and geochemistry, from any lithology documented so far within the Huronian Basin, including igneous or metasomatic rocks of the Nipissing and East Bull Lake suites, the Matachewan, Sudbury and Grenville dyke swarms, and from various types of rocks related to the Sudbury impact event. The age of the hornblende syenite could be loosely constrained to 1842 ± 170 Ma based on a three-point Sm-Nd isochron (**Fig. 9.8E**). Unfortunately, the large error associated with this date, together with the absence of pseudotachylitic breccia or shock features in the outcrop, do not permit to distinguish whether the hornblende syenite is older or younger than, or coeval with, the 1850 Ma Sudbury impact event. Theoretically, the rock could be genetically related to the 1883–1864 Ma alkaline magmatism documented in **Chapter 7**. Syenitic rocks were, for example, described before at the 1881 Spanish River Carbonatite, 70 km west of Matagamasi Lake (Sage 1987; Rukhlov & Bell 2010). It is also possible that the hornblende syenite is genetically related to the regional albitisation dated by Schandl et al. (1994) between 1916–1700 Ma, or to the 1750–1700 Ma Killarney Magmatic Belt south of Sudbury. A ~1.7 Ga emplacement age would be consistent with the Pb-Pb errorchron date obtained from the hornblende syenite (**Fig. 9.8F**). However, studies by Roscoe et al. (1992), Fedo et al. (1997), McLennan et al. (2000), Potter & Taylor (2009) and Ono & Fayek (2011) indicated regional isotopic disturbance, especially of the Rb-Sr and U-Pb systems, in all kinds of Palaeoproterozoic rocks within the Huronian Basin, at sometime between 1.9 and 1.7 Ga. Similar observations of unreasonably young whole-rock Pb-Pb and Rb-Sr errorchron dates were also made throughout the present study (**Chapters 3.5**, **4.5** and **6.5**). Therefore, any Rb-Sr and Pb-Pb errorchron obtained on the hornblende syenite must be treated with great suspicion; more likely does it reflect later isotopic disturbance rather than the true emplacement age of the rock. Theoretically, a genetic relationship between the hornblende syenite and the 1.85 Ga Sudbury impact event is also possible, though inconceivable, given that an analogues lithology has not been documented before within the Sudbury Impact Structure. Additional geochronological work (U-Pb on monazite, Ar-Ar on hornblende) is, therefore, highly desirable.

At issue is – apart from the emplacement age – whether the hornblende syenite from Matagamasi Lake is a magmatic rock at all, or instead a product of regional albitisation. Syenite-like rocks formed by alkali metasomatism are also known as episyenite[1] (the prefix "epi" stands here for epigenetic). In a recent review, Suikkanen & Rämö (2019, p. 861) defined episyenite as a small and relatively rare yet economically important type of "*sub-solidus quartz-depleted, alkali-feldspar-rich rock*" that is formed by the metasomatic replacement of granitic, gneissic or migmatitic rocks through the dissolution of quartz and the addition of Na ± K. Typical rock-forming minerals of episyenite are albite, microcline, chlorite ± epidote; transitions to almost monomineralic albitites do exist. Other features of episyenite include, but are not limited to, (i) a dyke-like or podiform geometry; (ii) a close spatial association with sub-vertical faults; (iii) an often vuggy appearance in outcrop; (iv) a common genetic association with Au-, U-, W-, and Sn mineralisation. Suikkanen & Rämö (2019) concluded that episyenite forms above the brittle-ductile-transition in shallow crustal environments at < 1.3 kbar and < 500°C (typically 300–450°C) along dilational sites from weakly saline fluids (magmatic, meteoric, metamorphic, connate, or mixtures thereof) in the presence of magmatic heat and at a high fluid:rock ratio.

[1] "an igneous-looking rock of syenite composition, displaying rounded cavities produced by hydrothermal dissolution of quartz crystals" (Le Maitre et al. 2002, p. 76).

The hornblende syenite from Matagamasi Lake shows indeed some features characteristic of an episyenite, including (i) a mono- or bimineralic modal composition; (ii) the absence of typical igneous textures; (iii) the considerable variation in grain size, even within a single thin section (**Fig. 9.3B**); (iv) microscopic features (**Fig. 9.3E,F**) and large quartz aggregates, both resembling infilled vuggs; (v) a vein-like appearance in outcrop (**Fig. 9.2B**); (vi) a location amidst regional albitisation and multiple hydrothermal Au occurrences; (vii) a crude spatial relation to faults (e.g. the McLaren Creek Fault). Besides, the rock lacks minerals that would be expected in a typical igneous syenite, such as, nepheline, cancrinite, leucite, sodalite, pyroxene, biotite, apatite, or zircon (e.g. Mitchell & Platt 1981; Sage 1987; Okrusch & Frimmel 2020, p. 268). Another conspicuous feature of the rock is the presence of so-called chessboard albite (**Fig. 9.3C**). The literature seems to indicate that this type of albite is widely regarded as a replacement phenomenon resulting from Na-metasomatism of quartzofeldspathic rocks (Goldschmidt 1922; Moore & Liou 1979; Hildebrand 1986; Morad 1988; Morad et al. 1990; Schandl et al. 1994; Engvik et al. 2008; Kaur et al. 2014); it has been described within fenite aureoles (e.g. Siemiatkowska & Martin 1975; Kresten & Morogan 1986), and in episyenite itself as a replacement product of primary K-rich feldspar (e.g. Charoy & Pollard 1989; Hecht et al. 1999; Suikkanen & Rämö 2017). Chessboard albite does, however, also occur as a primary magmatic mineral without any obvious link to metasomatism (e.g. de Kock et al. 2000; Kaur & Mehta 2005). The whole-rock geochemistry of the hornblende syenite is less conclusive of its origin since episyenite has no specific composition and differs, by necessity, geochemically from its host rocks due to extensive element mobility and authigenic mineral growth (Suikkanen & Rämö 2019). In fact, compositional differences between an episyenite and its photolith (e.g. **Fig. 9.9**) are to be expected, especially when formed under a high fluid:rock ratio. It is, nevertheless, interesting to note that the hornblende syenite has a similar $^{147}Sm/^{144}Nd$ ratio and Nd as the typical gabbro of the Nipissing Suite (cf. Lightfoot & Naldrett 1996a; Davey et al. 2019).

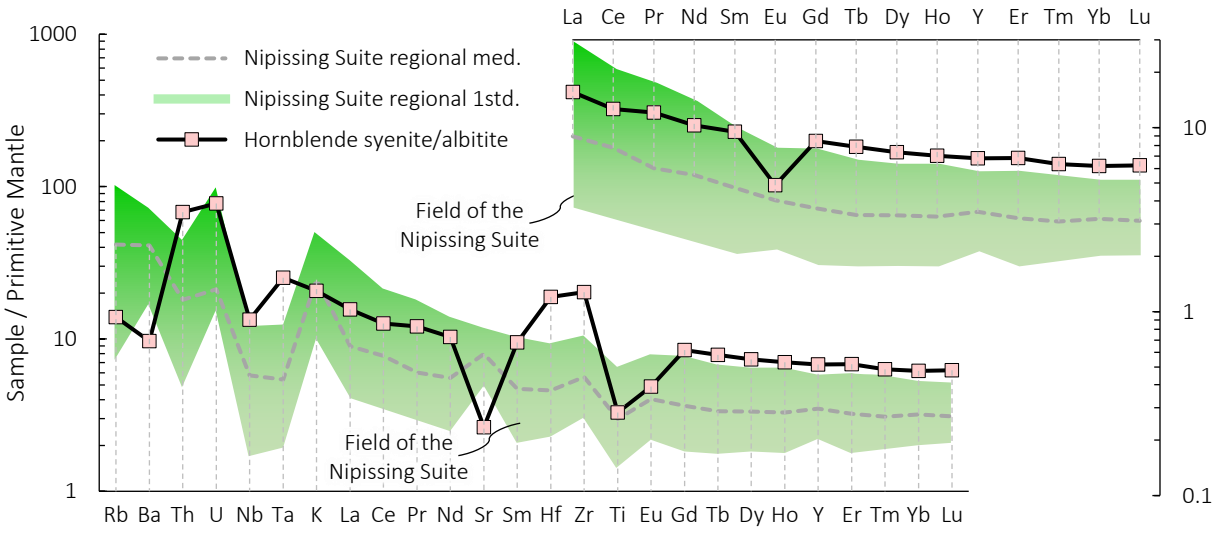

Figure 9.9 Primitive mantle-normalised trace element diagrams for the hornblende syenite from Matagamasi Lake, Rathbun Township, in comparison to gabbroic rocks of the Nipissing Suite; normalisation values are from Sun & McDonough (1989); data for the Nipissing Suite are from Lightfoot & Naldrett (1996b), Jobin-Bevans (2016), Hagen (2020) and this study (Appendix_1); regional median and standard deviation were calculated based on more than 500 analyses excluding altered and mineralised outliers with < 47 wt% SiO_2 as well as differentiated and contaminated outliers with > 55 wt% SiO_2.

Many other features, on the other hand, argue against a metasomatic origin of the hornblende syenite. For instance, the hornblende syenite is hosted by gabbro, whereas *all* known episyenites have either granitoid or gneiss as a protolith (Suikkanen & Rämö 2019). Furthermore, the hornblende syenite shows no evidence of replacing pre-existing minerals, and it does not exhibit inherited textures from the magmatic host rock. Partial preservation of relict textures is, however, typical of most episyenites (e.g. López-Moro et al. 2019). There is also no petrographic evidence of the albite replacing primary K-feldspar; albitisation of K-feldspar is, however, the main process behind the formation of episyenites. Apart from that, the hornblende syenite differs mineralogically from almost all known episyenite occurrences in that it contains quartz but completely lacks chlorite and epidote; hornblende is the only ferromagnesian mineral. As all episyenites are formed below 500°C (Suikkanen & Rämö 2019), (anti-)perthitic alkali feldspar has not been documented before in most episyenites (with one notable exception: Suikkanen & Rämö 2017). The presence of cryptoperthitic K-feldspar exsolutions in the samples implies feldspar crystallisation above the alkali feldspar solvus, i.e., at temperatures exceeding those of typical episyenite formation. In addition, the whole-rock geochemistry reveals a typical magmatic behaviour of all trace elements, as evident from near-chondritic Zr/Hf and Y/Ho ratios (Bau 1996), a Nb/Ta ratio ≥ 5 (Ballouard et al. 2016), an enrichment of the most incompatible lithophile elements relative to the less incompatible lithophile elements (**Fig. 9.9**), overall smooth REE patterns, including a lack of decoupling of fluid-mobile LREE relative to immobile HREE, no oxidative decoupling of Ce^{3+}/Ce^{4+}, as well as lack of decoupling of La-Ce-Pr-Nd, Pm-Sm-Eu-Gd, Gd-Tb-Dy-Ho, and Er-Tb-Yb-Lu (referred to as the *tetrad effect*, which, if observed, would be indicative of a high fluid:rock ratio, REE complexation, and/or REE adsorption; Bau 1996; Censi et al. 2007) (**Fig. 9.10**). The most convincing argument for a magmatic and against a metasomatic origin, however, is the abundance of Ti-rich magnesio hornblende. As mentioned above, mineral thermometry has shown that this hornblende must have crystallised at temperatures as high as 600–650°C, which far exceeds the temperature range in which episyenite is generally believed to form (300–450°C) (Suikkanen & Rämö 2019). Together with a low crystallisation pressure of 0.9–1.7 kbar (still within the typical range of episyenite formation), an extremely high geothermal gradient (~100°C/km) would be required to explain the origin of the hornblende syenite simply by fluid-rock interaction. The high temperature and relatively low pressure are strong indicators of a magmatic origin of the rock.

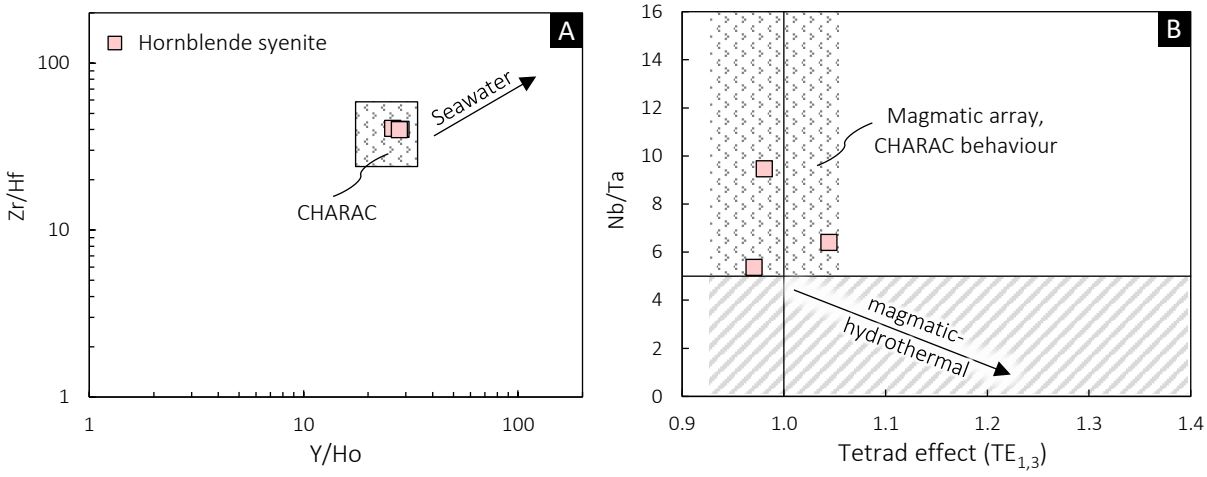

Figure 9.10 Plots used to distinguish between magmatic and hydrothermal influence on selected trace element ratios; **A:** Y/Ho vs. Zr/Hf; after Bau (1996); **B:** the extent of the REE tetrad effect vs. Nb/Ta; after Ballouard et al. (2016); $TE_{1,3}$ calculated after Irber (1999); deviation from the CHARAC (charge-and-radius-controlled) array may indicate element fractionation by hydrothermal processes (Bau 1996; Irber 1999).

Possible origin of the aplitic dykes

Aplitic dykes are not an unusual, though volumetrically minor, and genetically not very well understood, occurrence within the Nipissing Suite. Aplitic units occur typically within the upper parts of mafic intrusions of the Nipissing Suite, forming narrow veins, dykes, and pods of random orientation, 5–100 cm thickness, and up to 50 m length (Miller 1913; Simony 1964; Hriskevich 1968; Lightfoot & Naldrett 1989; Jobin-Bevans 2004). The contact between aplite and gabbro is typically described as sharp and irregular, and only in rare instances, as gradual. According to all cited studies, such aplitic rocks seem to be confined exclusively to mafic intrusions of the Nipissing Suite and are therefore considered syngenetic with this 2.22 Ga magmatic event. According to Miller (1913, p. 104), they "*are believed to represent residual, acidic segregations of the diabase magma*", whereas Lightfoot & Naldrett (1989) argued, based on trace element and a limited set of Nd isotope data, that the aplitic rocks represent anatectic melts generated by in-situ partial melting of the roof sedimentary rocks above large Nipissing Suite sills. Note, however, that no study has ever provided a radiometric age of these aplitic units, thus leaving the (although unlikely) possibility of the aplitic dykes being completely unrelated to the Nipissing Suite.

The observations made in the present study together with the new trace element and isotope data invite to test the different hypothesis of aplite formation as well as their supposed genetic relationship to the Nipissing Suite. First, however, it its necessary to compare the aplitic dykes from Matagamasi Lake to those described before in the literature from other locations in the Huronian Basin. A mutual characteristic between the aplites from Matagamasi Lake and other places, apart from their similar texture, modal mineralogy, and overall mode of appearance, is their high SiO_2 content, high Na_2O/K_2O ratio, and their peraluminous geochemical affinity (cf. Hriskevich 1968; Jobin-Bevans 2016; Lightfoot & Naldrett 1989, 1996b). In stark contrast to the aplitic masses described in previous studies, however, the aplitic dykes from Matagamasi Lake are not restricted to any stratigraphic level within a given Nipissing Suite sill; they occur near the upper intrusive Nipissing-Lorrain contact, close to the basal intrusive Nipissing-Gowganda contact, and apparently also in the central portions of a sill. More significantly, however, the aplitic dykes described here differ in their trace element composition significantly from the data provided by Lightfoot & Naldrett (1989, 1996b). For example, the aplitic dykes from Matagamasi Lake have extremely low concentrations of La and Ce compared to the aplitic units from the literature (unfortunately, Lightfoot & Naldrett (1989, 1996b) only obtained the concentrations of selected trace elements, therefore, it is not possible to directly compare REE patterns). Extreme depletion in LREE, as evidenced by low a La in combination with a low La/Yb ratio, indicates fractionation by some cryptic phase, most likely allanite, monazite, and/or apatite (e.g. Miller & Mittlefehldt 1982; Bea 1996), which would also explain the very low P_2O_5 contents below the detection limit of 0.01 wt% in almost all aplitic dyke samples. Fractionation of zircon cannot be excluded at this point and would, in fact, explain the low Zr (79–126 ppm) of the aplites. The LREE depletion, however, suggests monazite/apatite fractionation still outweigh any possible zircon (i.e., MREE-, HREE-) fractionation.

The apparent involvement of LREE-fractionating phases (monazite, allanite, apatite) in the magmatic evolution of the aplitic dykes poses a serious problem and compromises the use of whole-rock Sm-Nd isotope systematics (e.g. McDaniel et al. 1994b; Ayres & Harris 1997). This is because Nd is more compatible in these accessory minerals than Sm, thus strongly increasing (in contrast to most other rock-forming minerals) the time integrated Sm/Nd of the residual melt. In light of this obvious disturbance of whole-rock Sm-Nd isotope systematics (as evidenced by a wide range

in Sm/Nd ratios and initial εNd values, and irrational old model ages), the obtained data (**Fig. 9.11**) bear, unfortunately, no reliable petrogenetic information. The same discussion also applies to the whole-rock Pb isotope systematics, as the above mentioned LREE-fractioning phases will influence the U/Th/Pb ratios of the magmatic system (e.g. Bea 1996).

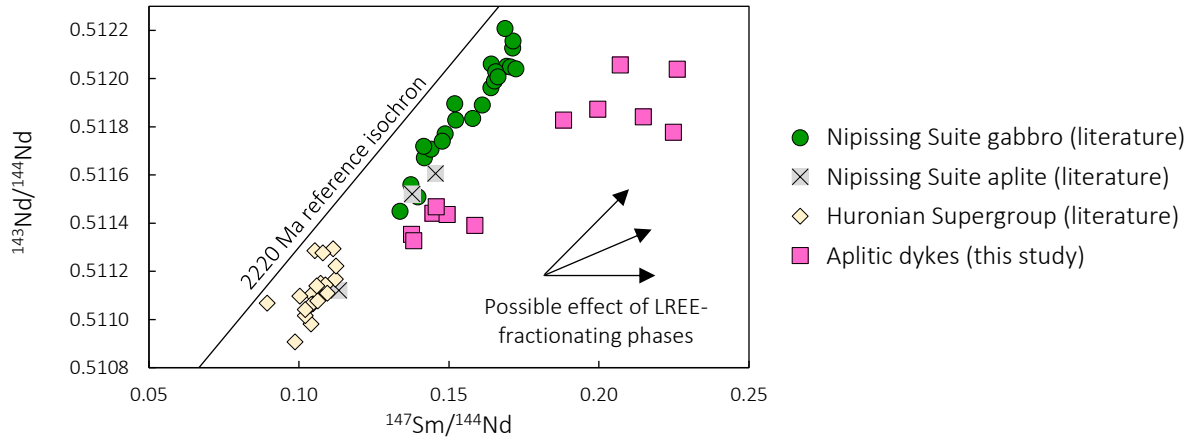

Figure 9.11 Plot of the $^{147}Sm/^{144}Nd$ ratio vs. the measured present-day $^{143}Nd/^{144}Nd$ ratio of aplitic dykes from Matagamasi Lake compared to previously published data of gabbroic and aplitic rocks of the Nipissing Suite, and of siliciclastic sedimentary rocks of the Huronian Supergroup; data for the Nipissing Suite are from Lightfoot & Naldrett (1996a); data for the Huronian Supergroup are from McLennan et al. (2000).

In consideration of the problems discussed above, the data do unfortunately not permit to test the widely accepted hypothesis of Lightfoot & Naldrett (1989) according to which aplitic units associated with the Nipissing Suite were formed by a combination of assimilation and fractional crystallisation. It is, nevertheless, tempting to point out some weaknesses of this hypothesis and its applicability to the aplitic dykes from Matagamasi Lake. For instance, the aplitic dykes of the present study as well as those documented before throughout the Huronian Basin have an unusually high K_2O/Na_2O ratio, much higher than expected for melts generated by partial melting of quartzofeldspathic rocks (e.g. Holness 1999; Péntek et al. 2011). Whereas differences in LILE, HFSE, and Nd-Pb isotope characteristics between these aplites and the Huronian Supergroup could theoretically be explained disequilibrium partial melting (e.g. Ayres & Harris 1997), the aplitic units also have suspiciously high Cr and Ni concentrations compared to the locally exposed sedimentary rocks (Dressler 1982), which is difficult to reconcile with these aplites representing pure crustal melts. That said, igneous rocks formed by crustal anatexis would likely contain primary Al-rich minerals (sillimanite, muscovite, cordierite). The aplitic dykes of the present study, although peraluminous and corundum-normative, do not contain such minerals. Moreover, the aplitic dykes described here are not confined to intrusive contacts. If these aplites were indeed generated by partial melting of the roof (Lightfoot & Naldrett 1989), how can this be reconciled with their occurrence throughout the magmatic stratigraphy of the Nipissing Suite? Given the very small *T*-interval of < 50°C between liquidus and solidus of such high-silica melts, coupled with their high viscosity (Waters & Lange 2017; Pistone et al. 2020), it seems rather unlikely that they would have migrated over larger distances. As a matter of fact, partial melting around even the largest mafic intrusions rarely resulted in massive granitic dykes like those at Matagamasi Lake. A case study from the Rum Igneous Complex, for example, has shown that partial melting, though extensive, occurred mainly in situ and static (Holness & Isherwood 2003). Even in the most extreme case, the aureole of the Sudbury Igneous Complex, partial melt features are distinctly different in texture, mode of occurrence, and volume, compared to the aplitic dykes described here

(cf. Péntek et al. 2011). The most significant problem, however, is the complete absence of restite material in form of xenoliths, schlieren, or xenocrysts of the sedimentary wall rocks (Clemens 2003, for a review) from which the aplitic melts were supposed to have emanated. None of such features have been observed within or in vicinity to the aplitic dykes from Matagamasi Lake.

What other process, then, could possibly explain the origin of the aplitic dykes, their aphantic texture, their lack of chilled margins, and their close spatial association with mafic rocks of the Nipissing Suite? By analogy to aplitic dykes found within granodioritic batholites (Eichelberger et al. 2006; Glazner et al. 2020), and by analogy to crystal-poor high-silica rhyolites (Bachmann & Bergantz 2004, 2008), it is proposed that the aplitic dykes from Matagamasi Lake represent near-eutectic melts extracted from a crystal mush, that is, a rigid network of crystals and silicate liquid. The so-called mush model summarises as follows: Once an intermediate magma reaches a crystal content of 50–60 vol%, the system (i.e., the mush) will rheologically lock up, thereby preventing chamber-wide convection and crystal settling. The interstitial melt between this rigid semicrystalline network will then become increasingly more siliceous, even rhyolitic, upon approaching the eutectic as crystallisation progresses at low pressure (e.g. Gualda & Ghiorso 2013). This highly evolved interstitial melt may then crystallise to form intercumulus minerals (quartz and feldspar, or micrographic intergrowths thereof). Under certain conditions, however, the interstitial melt may escape the mush through porous- and channelled flow (Eichelberger et al. 2006), eventually forming aplitic pods and dykes, or erupting to form rhyolitic crystal-poor ignimbrites. Although initially developed for intermediate and felsic systems, residual melt escape features have also been reported in mafic-ultramafic systems (e.g. the Bushveld Complex, Hayes et al. 2018).

In most of the rocks of the Nipissing Suite, interstitial quartz and granophyric intergrowths between quartz and feldspar are common (e.g. Hriskevich 1968; **Fig. 9.13A**), thus lending support that the trapped interstitial melt, following the crystallisation of plagioclase and pyroxene, will indeed approach leucogranitic/tonalitic composition, possibly in the presence of a volatile phase (e.g. Therriault et al. 2002; Morgan & London 2012). This interstitial melt will most likely be depleted in Mg, Fe, V and Ti (all sequestered by pyroxene) as well as depleted in Ca, Sr, Pb and Eu (sequestered by plagioclase) – exactly as observed in the aplitic dykes from Matagamasi Lake. In detail, fractionation models of Lightfoot & Naldrett (1996a) predict that after 70% of solidification of the typical Nipissing Suite magma (as defined by Lightfoot et al. 1993) the Sr concentration of the residual melt will drop below 50 ppm (the typical Sr concentration of the aplitic dykes); K-feldspar and apatite will appear on the liquidus after 75% of crystallisation (Lightfoot & Naldrett 1996a). The concentrations of REE and HFSE in the interstitial melt, on the other hand, will strongly depend on when and which accessory phases enter the sequence. In calc-alkaline systems, for which the mush model was initially developed, fractionation of titanite has shown to result in a strong depletion of MREE in the residual melt/aplitic dykes (e.g. Bachmann & Bergantz 2008; Glazner et al. 2020). In the Nipissing Suite, titanite is not part of the primary mineral assemblage, and other phases like apatite, monazite, or allanite (Hriskevich 1968; Jambor 1971) will instead sequester LREE relative to the MREE and HREE. As discussed above, this would explain the low LREE and P_2O_5 of the aplitic dykes as well as their high $^{147}Sm/^{144}Nd$ ratios (see also: Miller & Mittlefehldt 1982); those aplitic dykes without LREE depletion were simply extracted from the mush prior to apatite saturation. Thus, the composition of the aplitic dykes is fully consistent with a syngenetic origin with the Nipissing Suite, and their origin from a highly evolved interstitial melt, expelled from a plagioclase-pyroxene ±apatite ±monazite-bearing residual cumulate.

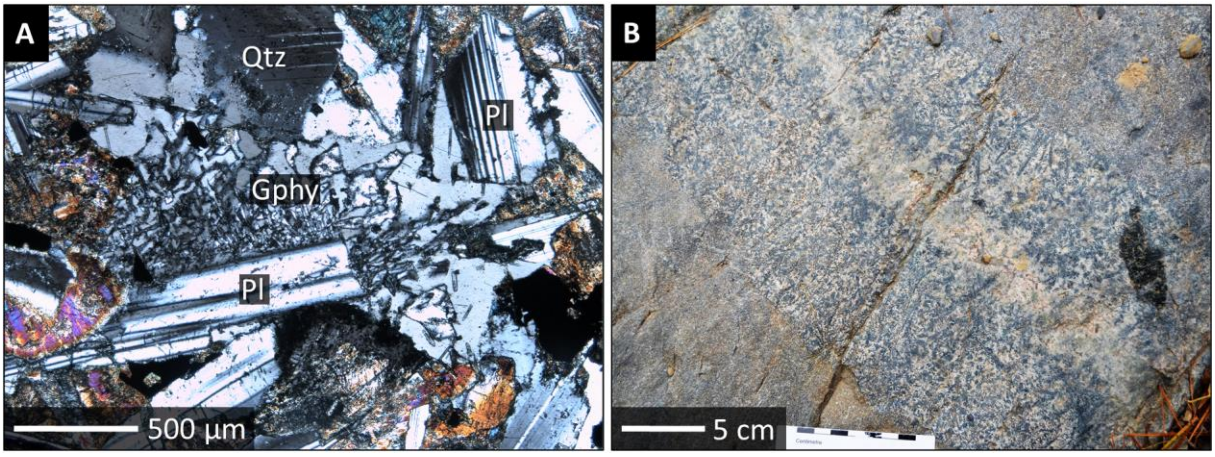

Figure 9.12 Photographs highlighting certain features associated with mafic rocks of the Nipissing Suite; **A:** microphotograph of a thin section of a typical quartz gabbro of the Nipissing Suite under transmitted light and crossed polars, showing quartz- and feldspar-rich granophyric intergrowths interstitial between plagioclase and altered pyroxene; **B:** photograph of a comb-textured syn-magmatic pegmatoidal feature, possibly related to escaping volatiles, within Nipissing Suite gabbro (46°42 39.12N 80°38 45.32W, Scadding Township). Abbreviations: Pl = plagioclase; Qtz = quartz; Gphy = granophyric intergrowths.

The question remains what process exactly caused the interstitial silica-rich melt (**Fig. 9.12A**) to migrate and to coalesce, eventually forming larger aplitic pods and dykes like those observed at Matagamasi Lake. Considering the high degree of solidification (70–75%) required to explain the depletion in P_2O_5, Sr, Eu, and LREE, and all the rheological limitations that come along with this, it is unlikely that the interstitial melt would have simply escaped from the mush due to buoyancy, gravity-driven settling and -compaction (e.g. McKenzie 1984; Bachmann & Bergantz 2004; Holness 2018). Alternative mechanism of melt extraction may include the following (Holness 2018):

- Mush rejuvenation by magma replenishment. Some workers have suggested that the heat resulting from new batches of hot, more primitive, magma could lead to an increase in melt pressure and thermal expansion of the mush, thus favouring the escape of interstitial melt along dilational fractures (e.g. Huber et al. 2011). However, there is currently little evidence that the Nipissing Suite was fed by multiple injections or voluminous magma recharges.
- External forces. Syn-magmatic compressional deformation has been suggested to promote crystal-melt separation (tectonic filter pressing/shear pumping, e.g. Berger et al. 2017). New age constraints on the Blezardian Orogeny, previously believed to have occurred at 2.4–2.2 Ga (Stockwell 1982; Riller & Schwerdtner 1997), indicate that compressional deformation ceased already at about 2.34 Ga (Raharimahefa et al. 2014), i.e., long before the emplacement of the 2.22 Ga Nipissing Suite, plus, there is no reported evidence of syn-magmatic deformation.
- Gas-driven filter pressing. According to Sisson & Bacon (1999), crystallisation of anhydrous minerals could release vapor from the residual melt (also known as second boiling). The associated increase in pore (melt) pressure would generate a hydraulic gradient within the mush or cumulate pile, thereby forcing melt upwards, vertical to the solidification front. The process of second boiling is restricted to shallow crustal levels (< 10 km), which is consistent with the emplacement depth of the Nipissing Suite of presumably less than 5 km below palaeosurface. Gas-driven filter pressing would also explain the very low volatile content of the aplitic dykes (< 1.5 wt% LOI) and, meanwhile, their close spatial association with features possibly representing volatile escape structures (e.g. vertical degassing pipes, miarolitic cavities, comb-textured pegmatoidal segregations; **Fig. 9.12B**, see also: Hartung et al. 2017; Pistone et al. 2020).

Synthesis

10.1 Impact-Related Features

10.1.1 Allochthonous impactites (Offset Dykes)

One of the principal goals of this study, as outlined in **Chapter 1.3**, has been to assess the relationship between the recently discovered igneous dykes above the Temagami Anomaly and the 1.85 Ga Sudbury impact event. By means of petrographic criteria as well as geochemical and isotopic fingerprinting it was possible to identify three dykes, each geographically separated by ca. 15 km, as genetically related to the Sudbury impact event. These new so-called Offset Dyke are:

- The *Afton Offset Dyke* (Afton Township), intersected at the bottom of a 2,200 m deep diamond drill hole into the Temagami Anomaly, 45 km northeast of the outer margin of the Main Mass of the Sudbury Igneous Complex (**Chapter 3**).
- The *Laura Offset Dyke* (Mackelcan Township), discovered and mapped along 4 km in outcrop, some 25–30 km northeast of the Main Mass of the Sudbury Igneous Complex (**Chapter 4**).
- The *Rathbun Offset Dyke* (Rathbun Township), discovered in a single outcrop 15 km east of the Main Mass of the Sudbury Igneous Complex (**Chapter 5**).

The following criteria have, in combination, been used to argue for an impact origin of the dykes, and helped to distinguish them from other magmatic (i.e., endogenic) dyke swarms in the region:

- A high content of lithic clasts, together with textural/chemical evidence of their assimilation.
- A quartz-rich modal composition and the abundance of granophyric intergrowths.
- An arc-like trace element signature and a pronounced crustal affinity, identical to previously published data on other Offset Dykes (Lightfoot et al. 1997c) and matching the global average composition of the middle/upper continental crust (Rudnick & Gao 2013).
- A Sm-Nd isotope signature matching both the regional average continental crust at Sudbury and the isotope signature of the Sudbury Complex (McLennan et al. 2000; Prevec et al. 2000).
- Whole-rock Sm-Nd, Rb-Sr, and Pb-Pb errorchron dates approximating the absolute U-Pb age of the 1850 ± 1 Ma Sudbury impact event (Krogh et al. 1984; Davis 2008; Bleeker et al. 2015).

The most important features of these new Offset Dykes are summarised in **Table 10.1**. Although these dykes have, like all the 17 other previously known Offset Dykes within the Sudbury Impact Structure (Lightfoot 2016, for a review), a uniform and almost identical major- and trace element geochemistry, they differ in terms of petrography, mode of appearance, metal endowment and economic potential, quite significantly from each other, and in part from most of the previously described Offset Dykes, which is here attributed to be the result of variable degrees of undercooling, assimilation, post-depositional alteration/ metamorphism, different emplacement levels and different current levels of erosion, a function of the proximity to the Main Mass, but also in part a reflection of the poor quality of the available outcrops, or in some cases, the complete lack thereof. Below follows a more comprehensive summary of the new findings, a discussion of their wider implications, and a brief outline of topics for future research.

Petrographic characteristics

Despite having apparently been formed by the same event from the same pool of homogeneous impact melt, the Offset Dyke discovered here, in conjunction with the 17 previously known Offset Dykes, exhibit a significant petrographic diversity. Compare, for example, the Afton Offset Dyke with the Laura Offset Dyke (**Tab. 10.1**). While the Afton Offset Dyke has a very fine grained aphantic texture, exhibits little grain size variation throughout, and is mostly free of lithic clasts, the more proximal Laura Offset Dyke is characterised by a large grain size variation and an abundance of lithic clasts; it is also rich in granophyric intergrowths. The Rathbun Offset Dyke, in turn, is relatively coarse-grained and phaneritic, rich in mafic xenoliths, and rich in quartz, yet it is free of granophyric intergrowths, and it is the only of the three new Offset Dykes that contains appreciable amounts of base metal sulphide. In contrast to the other two Offset Dykes, secondary carbonates were not observed in the Rathbun Offset Dyke (except for rare malachite coatings).

Significant variations in grain size and texture have been documented before, even along within, or along the strike of, a single Offset Dyke (Lightfoot 2016, p. 116ff.), and may be a function of local temperature fluctuations, the proximity of an Offset Dyke to the ultimate heat source (i.e., the melt sheet) or the incorporation of cold lithic clasts and thus may be a mere consequence of undercooling to variable degrees. Granophyric intergrowths, for example, are widely regarded as a product of magmatic undercooling (Morgan & London 2012), a notion that is fully consistent with the presence of granophyric intergrowths in the distal, fine-grained, and apparently rapidly cooled Afton and Laura Offset Dykes, but their absence in the more proximal, relatively coarse-grained (i.e., slowly cooled) Rathbun Offset. Alternatively the variations in grain size and texture might reflect different emplacement levels and, by implication, different levels of erosion; the fine-grained granophyre-bearing Offset Dykes could have been emplaced into colder rock, closer to surface, whereas the more coarse-grained granophyre-free varieties were emplaced at greater depth.

In contrast to most other Offset Dykes (e.g. Grant & Bite 1984; French 1998; Pattison 2009; Coulter 2015), spherulitic textures and well-developed chilled margins have not been observed in either the Rathbun, Laura or Afton Offset Dyke. Their absence could have several reasons. For example, glassy margins (or other types of quench textures) could have originally been present, but subsequently overprinted by sub-solidus alteration. As noted above, all the dykes had been affected by regional metamorphism reaching at least the lower greenschist facies, and locally affected by pervasive, texturally destructive, metasomatism. Alternatively, the absence of quench textures could be the result of a minimal thermal gradient between the impact melt and the host rock, which could again be explained by a greater depth of emplacement. Finally, the lack of discrete chilled margins could be a direct consequence of the intrusion mechanism of the Offset Dykes. For basaltic dykes it is well known that laminar flow favours the development and preservation of marginal chills, whereas in thick and/or turbulently flowing dykes a chilled margin may initially form but will be subsequently remelted as the thermal front moves outward into the country rock (Huppert & Sparks 1989). Interestingly, Huppert & Sparks (1989) further noted that incomplete meltback of chilled margins can result in sharp internal contacts within igneous bodies, which are then not necessarily the product of multiple magma replenishments. Maybe this would explain the nature of the contact between the IQD and the marginal tQD noted within the Laura Offset Dyke as well as schlieren observed in the latter facies (**Chapter 4**) ("cryptic banding" in the sense of Grant & Bite 1984, p. 280). In case of the Rathbun Offset Dyke, meltback of a chilled margin (if initially present) would have been complete, and the heat supply sufficient to melt the local wall rock.

Table 10.1 Summary of the key features of the new Offset Dykes discovered northeast of Sudbury

	Afton Offset Dyke	**Laura Offset Dyke**	**Rathbun Offset Dyke**
Township	Afton	Mackelcan	Rathbun
Discovery site	46°56 31N 80°21 08W	46°49 56.03N 80°34 25.84W	46°45 50.80N 80°39 21.17W
Mapped surface extent	Drill core intersection (AT-14-01)	4,300 m	Single outcrop
Thickness/width	~50 m (apparent thickness)	10 – 15 m (true thickness)	~5 m (apparent thickness)
Strike	Unknown	N/S	Unknown
Dip	Unknown	Subvertical, dip-direction unclear	Unknown
Vertical extent	2,100 m (assuming surface connection)	> 80 m	Unknown
Distance to Main Mass	45 km	25 – 30 km	15 km
Host rock	Neoarchaean banded iron formation, Neoarchaean feldspar-quartz porphyry	Gowganda Formation argillite	Nipissing Suite gabbro, Gowganda Formation wacke
Nature of contact	Brecciated, sharp but sheared and altered	Brecciated and gradual, indistinct	Indistinct, diffuse, obscured by gossan
Hosted by SUBX?	Maybe (brecciated iron formation)	Yes (brecciated argillite)	Maybe (thermally overprinted?)
Mineralogy	Pl–Bt–Ep ±Qtz ±Act ±Chl ±Cc ±Mag ±Py	Qtz–Fsp–Chl–Ser–Cc ±Ep ±Lcx ±Py	Qtz–Pl–Hbl ±Bt ±Lcx ±Chl ±Ep ±Ap
Texture	Interstitial	Granophyric, interstitial	Ophitic
Grain size	Fine-grained	Fine- to medium-grained	Medium-grained
Inclusions, enclaves	Xenoliths of BIF and chlorite schist (rare)	Argillite and diabase xenoliths (abundant); possibly autoliths (?); miarolitic cavities	Gabbroic xenoliths (very abundant); Hornfelsed siltstone xenoliths (rare)
Magnetic properties	Strongly magnetic where containing inclusions of BIF, otherwise weakly magnetic	Weakly to non-magnetic	Strongly magnetic (massive sulphide) to weakly/non-magnetic (quartz diorite)
Deformation	Sheared contacts	Weak foliation in some places	Locally sheared
Alteration, metamorphism	Greenschist facies + carbonate-chlorite-stilpnomelane alteration along sheared contacts	Greenschist facies + intense quartz-carbonate veining, locally pervasive and texturally destructive	Greenschist facies + intense quartz-epidote-chlorite alteration in proximity to sulphide + supergene alteration of sulphides
Mineralisation	None	Auriferous quartz-carbonate veins	Semi-massive Ccp–Py± Pn ±Mag ±PGM + disseminated PGM–Qtz–Ep
Economic potential	Low	Moderate	Very high
Geochemical affinity	North Range	South Range	Indistinct (obscured by contamination)
Interpretation, comments	Offset Dyke (geometry unknown); rapidly chilled; emplaced along lithological contact acting as a plain of weakness; most distant Offset Dyke known so far; maybe impact melt outflow/pond outside the crater rim	Concentric Offset Dyke; strikes parallel to the East Range Breccia Belt; orientation likely defined by bedding planes and/or pre-existing structures; possibly defines a second and more distant ring feature	Lowermost termination of a deeply eroded Offset Dyke (geometry unknown) beneath a thick part (3–5 km) of the impact melt sheet; host of footwall mineralisation; strongly contaminated by local wall rocks; slowly cooled
Possible equivalent(s)/ closest analogue(s)	Whistle/Parkin, Foy/Tyrone, Cascaden, Ministic, Trill	Manchester, Hess (based on geometry); Copper Cliff, Worthington (geochemistry)	Frood-Stobie, Vermillion, Worthington (New Victoria-Totten Segment)

Single- vs. multiphase dyke emplacement

Most of the Offset Dykes within the Sudbury Impact Structure exhibit at least two distinct lithofacies, traditionally referred to as inclusion-rich ("IQD") and inclusion-free ("QD") quartz diorite (Lightfoot 2016, and references therein). The fact that inclusions (anteliths?) of both QD and IQD within IQD can be locally observed in other Offset Dykes (Lightfoot & Farrow 2002; Tuchscherer & Spray 2002; Lafrance et al. 2014; Lightfoot 2016; Pilles et al. 2017, 2018b), together with transitional to sharp contacts between QD and IQD, has prompted a lively debate over the last decades as to whether the Offset Dykes were emplaced in one single pulse – through flow differentiation (Grant & Bite 1984; Pattison 2009; Pilles et al. 2018b) – or instead by two injections (QD followed by IQD), each separated in time by a few days to perhaps thousands of years (Lightfoot & Farrow 2002; Murphy & Spray 2002; Hecht et al. 2008; Prevec & Büttner 2018). Some workers have even alluded to the idea of a three-phase dyke emplacement (e.g. Morris 1982; Klimesch et al. 2008).

Unfortunately, the limited field data available on the new Offset Dykes in the East Range coupled with an omnipresent, locally texturally destructive, metamorphic and/or hydrothermal overprint, do not permit to support either emplacement model. Contact relationships between the Offset Dykes and their host rocks are equivocal, and the distinction between QD and IQD is arbitrary at best. The Afton Offset Dyke, for example, seems to consist solely of QD, although local xenoliths are present. The Laura Offset Dyke, by contrast, does contain a variety of different inclusions (including strange "ghost clasts" that look like QD but show evidence of contact metasomatism) throughout the dyke and along its entire strike length, but these make up less than 1 vol% of the rock, raising the question whether it should be classified as IQD or QD. The Rathbun Offset Dyke contains very abundant, locally derived, xenoliths, but it lacks inclusions of either QD and IQD, and it seems to occur in direct contact with the host rock, i.e., without a marginal QD facies. The observations on the Rathbun, Laura and Afton Offset Dykes seem confusing at first but they are in keeping with more recent studies (e.g. Pilles et al. 2018a,b; Mathieu et al. 2021; VanderWal 2021) indicating that the relationship between QD and IQD is more complex, and the distinction less absolute, than previously thought (or perhaps acknowledged?). The long-lasting debate as to whether the Offset Dykes, and comparable impact melt dykes at Vredefort, South Africa (Huber et al. 2021), were formed by a single catastrophic event, or by multiple pulses, will likely continue.

Geochemical variations across the Offset Dykes

A secondary but nonetheless interesting observation of the present study is the existence of subtle geochemical and isotopic variations between Offset Dykes from different settings around the Main Mass, different host rocks, and different dyke geometries. This was first recognised by Lightfoot et al. (1997a), who noted that Offset Dykes in the North Range of the Main Mass (all hosted by Archaean footwall rocks), have a slightly and yet systematically higher LREE/HREE ratio and higher Sr concentrations than those Offset Dykes in the South Range of the Main Mass (all hosted by the Huronian Supergroup), which tend to have lower LREE/HREE ratios and lower Sr concentrations. The same dichotomy between North Range and South Range was subsequently recognised in terms of Pb isotopes, with North Range Offset Dykes being characterised by a lower μ and higher κ, and South Range Offset Dykes being characterised by a higher μ and lower κ (Darling et al. 2010b). A similar N/S divide in geochemistry, Pb isotopes, and modal mineralogy, has long been known to exist within the Main Mass (Naldrett & Hewins 1984; Lightfoot 2016; McNamara et al. 2017). Two hypotheses have been brought forward to explain these regional differences:

Either the impact melt sheet from which the Main Mass and the Offset Dykes crystallised was never completely homogenised (e.g. Dickin et al. 1996; Darling et al. 2010b; Dickin 2010), or the melt sheet was initially homogeneous but subsequently assimilated isotopically distinct footwall rocks (e.g. Lightfoot et al. 1997a; Darling et al. 2010a; Kenny et al. 2017; McNamara et al. 2017).

The new observations made in the present study could provide clarification to this outstanding problem. Both the Afton Offset Dyke and Laura Offset Dykes occur in close proximity to each other suggesting they were most likely fed by the same pool of impact melt, yet they differ in their Pb isotope and trace element composition from each other. The Afton Offset Dyke, which is hosted by Archaean basement rocks, has a high Ce/Yb ratio, high Sr, low μ, and high κ (**Chapter 3.6**), whereas the Laura Offset Dyke, which is hosted by sedimentary rocks of the Huronian Supergroup, has a lower Ce/Yb ratio, lower Sr, higher μ, and lower κ (**Chapter 4.6**). These local variations seem to mimic the broader, regional differences between North Range and South Range lithologies. This, in turn, would imply that the observed compositional variations are not primarily a function of the relative position of a dyke to the impact site, but rather a reflection of the different types of country rock that locally interacted with the impact melts after the dyke's emplacement, therefore, supporting the hypothesis of an initially homogeneous melt sheet (e.g. Kenny et al. 2017).

Variable contamination of an initially homogeneous impact melt does, however, not explain why there are apparently systematic differences in trace element ratios between radial and concentric Offset Dykes that are hosted by the same type of country rock (Lightfoot et al. 1997a,c; Lightfoot 2016; Pilles et al. 2018a). It also fails to explain why, for example, the concentric Hess Offset Dyke in the North Range is geochemically equivalent to the radial South Range Offset Dykes, or why the Creighton Offset Dyke is so fundamentally different in composition compared to all the other Offset Dykes (Lightfoot et al. 1997a,c). Evidently, some other factor(s) must have influenced the composition of the Offset Dyke, in addition to assimilation. A possible solution to this problem was offered by Pilles et al. (2017, 2018a), who argued for an episodic emplacement of the Offset Dykes, that is, some of the dykes were tapped sooner from the evolving melt sheet than other dykes, thus allowing for variable degrees of fractional crystallisation to manifest. The hypothesis, however, needs additional testing, ideally through a more comprehensive comparative study that should take all Offset Dykes, including those discovered in the distal East Range, into account.

Evidence of in-situ assimilation of local wall rocks

Additional insights into the physical and chemical interaction between the Sudbury impact melts and their target rocks were given in **Chapter 5** for the case of the Rathbun Offset Dyke. The quartz there has shown textural and geochemical evidence of assimilation of the local gabbroic wall rocks by the arguably superheated impact melt, with geochemical and isotopic mixing calculations pointing to a significant extent of in-situ assimilation, but without evidence of significant clast transport. These observations conflict with previous studies, having found little or no evidence of chemical interaction between the Offset Dykes and their immediate host rocks post emplacement (e.g. Hecht et al. 2008). More recent field studies, on the other hand, indicate that the Offset Dykes were very well capable of ripping off or even assimilating their local wall rocks, at least in places, although not along the entire strike length (e.g. Pilles et al. 2018b; Mathieu et al. 2021; VanderWal 2021). A possible implication of this is that the emplacement of the Offset Dykes was not a purely passive, gravity-driven mechanism involving downward draining of impact into the fractured crater floor, but it was facilitated (at least to some extent) through thermomechanical erosion.

In general, the capacity of a melt to erode its local wall rock strongly depends on the temperature contrast between assimilant and contaminant, and the type of flow regime, with turbulent flow favouring assimilation over a laminar flow regime (Huppert & Sparks 1985). In the concrete case of the strongly contaminated Rathbun Offset Dyke, this could point to a turbulent flow regime, although additional work is needed to backup this conclusion. Alternatively, the extensive assimilation of wall rocks in some places (e.g. at Rathbun), and the development of chilled (or at least fine-grained) margins in other places (Afton), could be the result of local temperature fluctuations of either the impact melt or the contaminant, variations in the thickness of the Offset Dyke and the overlying melt sheet, and/or a function of the local availability of volatiles. Zones of Sudbury Breccia (i.e., local thermal anomalies in the crater footwall) would have been especially prone to assimilation and, as a matter of fact, such breccia zones seem to have frequently acted as favourable sites for the intrusion of Offset Dykes; the Laura Offset Dyke (**Chapter 4**) being a good example of this. According to Thompson & Spray (1996), the friction heat involved in the formation Sudbury Breccia may have reached 800–900°C; even greater temperatures (~1,450°C) have been inferred for tectonic (endogenic) pseudotachylite elsewhere (Di Toro & Pennacchioni 2004). It is only reasonable to assume that, where the Offset Dykes intruded into such preheated semi-consolidated substrate, the temperature contrast was negligible, thus enabling thermomechanical erosion, assimilation, or giving rise to complex mingling relationships between quartz diorite and Sudbury Breccia as documented elsewhere (e.g. Grant & Bite 1984; Mathieu et al. 2021; VanderWal 2021).

Furthermore, the observations made in this study help to constrain the emplacement temperature of the impact melt, thereby providing additional ground truth for what has been predicted before in numerical simulations of the impact process (e.g. Ivanov & Deutsch 1999; Prevec & Cawthorn 2002). Based on the apparent corrosion and assimilation of gabbroic xenoliths at Rathbun Offset Dyke (as evidenced by textural features and geochemical mixing considerations), the initial melt temperature must have significantly exceeded 1,200°C. Note, however, that this is just a minimum estimate; the true temperature must have been far greater in order to facilitate effective resorption and to sustain a high temperature in spite of all the energy that was consumed for heating and melting the cold xenoliths. Incomplete assimilation of quartzite-, chert- and BIF xenoliths in the Laura and Afton Offset Dykes, respectively, would in turn place the upper temperature limit to ca. 1,700°C (e.g. Swamy et al. 1994). These temperature estimates are in good agreement with previous petrological studies (Coulter et al. 2014; Prevec & Büttner 2018, for a review).

Footwall-type mineralisation in distal Offset Dykes

Of the three new Offset Dykes, the one at Rathbun Lake is the only one affected by sulphide mineralisation, and this to a significant extent, with grab samples reaching up to 23 wt% Cu, 63 g/t Pd, and 33 g/t Pt. While a close association between mafic inclusion-bearing quartz diorite and Ni-Cu-PGE mineralisation is well known among local geologists and therefore not particularly surprising, the Rathbun Offset Dyke is unusual insofar as it occurs 15 km east of the Main Mass – much further away than any other mineralised segment of an Offset Dyke. Offset Dykes at the same distance to the Main Mass were previously regarded as barren, and no deposit, whether breccia- or Offset Dyke-hosted, was known to occur at a distance greater than 6–7 km from the Main Mass (Lightfoot 2016). Consequently, the discovery of high-grade PGE-Cu±Ni sulphide mineralisation associated with the Rathbun Offset Dyke (**Chapter 5**) expands the sphere of potentially mineralised Offset Dykes outward, up to 15 km, thus opening entirely new perspectives in the search for unconventional ore deposits within the Sudbury Impact Structure.

The reason for the exceptional PGE- and Cu-enrichment at Rathbun is currently not clear. As discussed earlier in **Chapter 5.8**, local enrichment within the Rathbun Offset Dyke could be explained by structural traps for dense sulphide liquid within a highly dynamic flow regime (e.g. branches, bifurcations, kinks, lithological contacts, wall-rock relief, rheological changes, changes in wetting properties in response to xenolith incorporation and -assimilation, local S-saturation due to assimilation of pre-existing sulphide, etc.). Alternatively, and by analogy to footwall embayments beneath the Main Mass, the Rathbun Offset Dyke could have been located within a topographic low on the undulating crater floor, beneath a relatively thick portion of the impact melt sheet. Studies by Morrison (1984), Dreuse et al. (2010), Ripley et al. (2015) and Lightfoot (2016) have indicated that such physical depressions (= areas of thicker melt sheet) acted as favourable sites to concentrate large masses of Ni-Cu-PGE sulphide. A thick melt sheet above the currently exposed Rathbun Offset Dyke is additionally supported by (i) amphibole geobarometry; (ii) the lack of chilled margins and lack of granophyric intergrowths, pointing to a limited temperature contrast between impact melt and host rock (i.e., greater emplacement depth); and (iii) the mere association of the Rathbun Offset Dyke with typical *footwall*-style Cu-PGE mineralisation, the occurrence of which is, by definition, restricted to the deep footwall beneath the SIC (Farrow et al. 2005).

Constraints on the melt sheet thickness

Relating to the above notion of crater floor topography, a novelty of this study lies in the first successful application of conventional mineral geobarometry in order to reconstruct the depth of emplacement (and thus, the level of erosion) of an impact melt rock (**Chapter 5.5**). To the author's knowledge, this has not been done before on either terrestrial or extra-terrestrial impactite, evidently because of a lack of pressure-sensitive minerals and mineral assemblages. In the present study, however, single-phase amphibole barometry (Ridolfi & Renzulli 2012; Mutch et al. 2016) could be successfully applied to igneous Ti-rich hornblende occurring in textural equilibrium with ilmenite, feldspar, quartz, and biotite in quartz diorite from the Rathbun Offset Dyke. Mineral barometry revealed a crystallisation pressure of 0.8–1.3 kbar, which equates to an emplacement depth of 3–5 km by assuming a magmastatic pressure and average upper crustal density (Card et al. 1984) or the average density of a dioritic impact melt (Warren et al. 1996). This depth corresponds surprisingly well to the combined average true thickness of the Main Mass plus Onaping Formation (Naldrett & Hewins 1984; Ames et al. 2009) and seems to confirm the deep injection hypothesis according to which the Offset Dykes were emplaced at the base of the impact melt sheet by draining of undifferentiated melt into the fractured crater floor (e.g. Wichman & Schultz 1993; Therriault et al. 1996; Tuchscherer & Spray 2002; Kovaleva et al. 2019; Mathieu et al. 2021).

Primary amphibole is in fact quite abundant in other areas and lithologies of the Sudbury Impact Structure, including other Offset Dykes, the Main Mass, and its thermal aureole (e.g. Fleet & Barnett 1978; Lafrance et al. 2014; Lightfoot 2016; Jørgensen et al. 2018), which holds significant potential for further studies, and additional work is already in progress to establish the initial thickness of the now eroded melt sheet in other areas of the Sudbury Impact Structure. Geobarometry also holds the potential of being applied to other, deeply eroded, terrestrial impact structures in which the confining pressure was sufficient to stabilise primary amphibole. For instance, Kovaleva et al. (2018b) reported on presumably igneous amphibole in one of the Granophyre Dykes from the Vredefort Impact Structure, South Africa. Accepting that these Granophyre Dykes are genetically equivalent to the Offset Dykes at Sudbury (e.g. Huber et al. 2020), amphibole barometry could be used to reconstruct the thickness of the now eroded impact melt sheet at Vredefort.

Quantifying the volatile content of the impact melt

The preservation of primary igneous hornblende in the Rathbun Offset Dyke (**Chapter 5**) not only provides a means of calculating a crystallisation pressure, but it also makes it possible to quantify the equilibrium H_2O content of the impact melt from which the hornblende had crystallised, for example, by using the mineral chemical approach ("geohygrometer") of Ridolfi & Renzulli (2012):

$$\ln H_2O_{melt}\ [\pm 0.78\ wt\%] = -65.907 + 5.0981Si + 3.1308Ti + 4.9211Al + 4.9744Fe + 4.6536Mg + 1.0018Ca - 0.789Na - 0.539K + 0.4642\ln P \quad \textbf{(10.1)}$$

Application of the equation above to hornblende from the Rathbun Offset Dykes reveals an equilibrium H_2O melt content of, on average, 5.6 ± 0.5 wt% (n=74). These values seem unusually high for a terrestrial impact melt rock (e.g. Koeberl 2013), although limited data are available on the *primary* volatile content of terrestrial, holocrystalline, impact melt rocks other than obviously dry tektites and impact glasses (Koeberl 2013, and references therein). Theoretically, the abundance of hornblende in the Rathbun Offset Dyke, and the high H_2O content of the melt deduced from this, could be a very local phenomenon, having resulted from the assimilation and devolatilisation of H_2O-rich wall rocks and xenoliths (siltstone, hydrated gabbro) by the intrusion of the impact melt at a relatively high confining pressure (≥ 0.8 kbar). However, primary hydrous minerals (biotite, amphibole) have been reported before in many other lithologies and areas of the Sudbury Igneous Complex (e.g. Therriault et al. 2002; Lightfoot 2016), including presumably primary biotite in the Afton Offset Dyke (**Chapter 3**), and granophyric intergrowths in essentially all lithologies, which are generally attributed to magmatic undercooling either due to conductive heat loss or volatile exsolution (Therriault et al. 2002; Morgan & London 2012). In addition, supporting evidence of a volatile-rich impact melt comes from an elevated LOI (1.8–2.4 wt%) previously obtained on vitric samples of quartz diorite from the Trill Offset Dyke (O'Sullivan et al. 2016); a high LOI (≥ 2 wt%) reported in distal ejecta related to the Sudbury impact event (Huber et al. 2014); the presence miarolitic cavities in the Sudbury Igneous Complex (including the Laura Offset Dyke, **Chapter 4**), the latter suggesting crystallisation at or close to volatile saturation (e.g. Hanley et al. 2011; Stewart 2017; Candela 1997); textural, geochronological and isotopic evidence of extensive fluid-melt-rock interaction within the Main Mass and in the Whitewater Group immediately following the impact (e.g. Ames et al. 1998, 2002; Hanley et al. 2011; Stewart 2017; Ubide et al. 2017).

Altogether, the new observations contribute supporting evidence that H_2O-rich conditions persisted throughout the formation and evolution of the Sudbury impact melt system. The new data also demonstrate that terrestrial impact melt rocks are not necessarily as dry as they are often perceived (e.g. Morgan & London 2012, p. 1260). The big question that emerges from this: Where did the volatiles come from? Are they a consequence of the impact having occurred in a shallow marine environment, or ingress of seawater afterwards? Devolatilisation of mixed sedimentary-crystalline target rocks? Perhaps a contribution from the impactor itself (Daly & Schultz 2018), for which some workers (e.g. Darling et al. 2010b; Petrus et al. 2015) have suggested it was a comet? Also, why are the Granophyre Dykes at Vredefort, South Africa, which have so frequently been compared to the Offset Dykes, very low in volatiles (< 0.01–0.83 wt% LOI; Huber et al. 2020), and what does this mean for petrologic/thermal modelling and our understanding of late-stage devolatilisation and fluid-rock interaction at Sudbury in general? The study of primary volatiles in the Sudbury Igneous Complex certainly holds some promising potential for future research.

Implications for the multi-ring hypothesis

Uncertainty still exists regarding the initial diameter of the Sudbury Impact Structure and whether it was a peak-ring (e.g. Scott & Benn 2001; Ames et al. 2002; Grieve & Osinski 2020) or a multi-ring basin (e.g. Deutsch et al. 1995; Spray et al. 2004). The debate is largely based on whether a singular or multiple concentric zones of impact-related features existed around the supposed impact centre, currently estimated to have been located just west of the City of Sudbury (e.g. Grieve et al. 2008). Specifically Spray et al. (2004), following earlier observations of Butler (1994) and Spray & Thompson (1995), have claimed to found evidence of multiple concentric features around the Main Mass, outlining four, although not perfectly circular, rings (Spray et al. 2004; **Fig. 10.1B**):

- **Ring 1** (~90 km diameter) was defined by Spray et al. (2004) by the maximum outer extent of shock metamorphic features (shatter cones, PDFs) around the Main Mass; the pervasive distribution of pseudotachylitic breccia; the strike of the concentric Hess and Manchester Offset Dykes; and the preservation of down-faulted Huronian Supergroup outliers in the North Range.
- **Ring 2** (~130 km diameter) corresponds to an enhanced zone of pseudotachylitic breccia development and the sphere of thermal demagnetisation of the basement rocks. It also coincides with the orientation of roughly circumferential lineaments, and it corresponds the maximum radial (lateral) extent of the previously known Offset Dykes. Ring 2 was interpreted as the original pre-erosional extent of the coherent impact melt sheet (now preserved as the Main Mass).
- **Ring 3** (~180 km diameter) was defined by another zone of enhanced pseudotachylitic breccia development in the North Range of the Main Mass. This zone is equidistant to the impact breccias found at Whitefish Falls and East Bull Lake, and it was interpreted as a blind superfault.
- **Ring 4** (~260 km) was defined by the outermost confirmed occurrence of pseudotachylitic breccia at Temagami Lake; it was interpreted as the manifestation of another concentric superfault and as the final rim-to-rim diameter of the so-defined Sudbury multi-ring basin.

Spray & Thompson (1995), drawing comparison to multi-ring basins on the Moon (**Fig. 10.1A**), recognised that the spacing of the above rings (especially the breccia belts in the undeformed North Range) follows a surprisingly accurate square root-relation (Pike & Spudis 1987) between inferred crater diameter and ring spacing, that is, $\sqrt{260\ \text{km}} = 16$ km, which was taken as further confirmation of the multi-ring hypothesis. Grieve et al. (2008), however, called the existence of the circumferential lineaments of Butler (1994) and their interpretation as concentric fault traces into question, and instead proposed that the Hess and Manchester Offset Dykes represent a singular annular through typical of a peak-ring basin. Grieve et al. (2008) further revised the estimated final rim diameter at 130–180 km, although they did agree with Spray et al. (2004) that the maximum lateral extent of the Foy Offset Dyke and the sphere of thermal basement demagnetisation likely defines the maximum pre-erosional extent of an initially coherent impact melt sheet.

How do the recently discovered Rathbun, Laura, and Afton Offset Dykes fit into this debate? For one, they occur far east of the Main Mass, in an area not previously known for Offset Dykes, and in case of Afton, much further away from the impact site than previously considered possible, suggesting that the melt sheet was once laterally much more extensive. Moreover, the Rathbun Offset occurs 15 km east of the Main Mass; it seems to coincide with the postulated inner ring of Spray et al. (2004) (**Fig. 10.1B**) yet it is not clear whether this Offset Dyke was concentric or radial. Interestingly, the Laura Offset Dyke lies exactly on the second ring, and the Afton Offset Dyke

broadly coincides with the third ring structure. Even more interesting, the lateral spacing between these Offset Dykes measures ~15 km, which is consistent with the above square-root-relation and thus reinforces the idea of Sudbury representing a former multi-ring basin. By the same token, the apparent spacing of the new Offset Dykes would imply a final crater diameter of 15^2 km = 225 km, which is intermediate between previous, independent, estimates (Grieve et al. 2008, for a review).

Obviously, these observations must be treated with caution; geological information for the distal East Range are still very limited, and the structural geology, specifically with respect to post-impact deformation, is not well understood. Besides, it cannot be fully excluded at this point that the orientation of the Laura Offset Dyke, even though it seems to define another concentric Offset Dyke, was instead controlled by pre-existing structures (e.g. bedding planes, faults), and after all, the possibility still exists to discover additional Offset Dykes in the East Range that defy the above square-root-relation. For future research it is therefore recommended to search of additional concentric Offset Dykes along the postulated Ring 2 (~130 km) in the North Range (**Fig. 10.1B**).

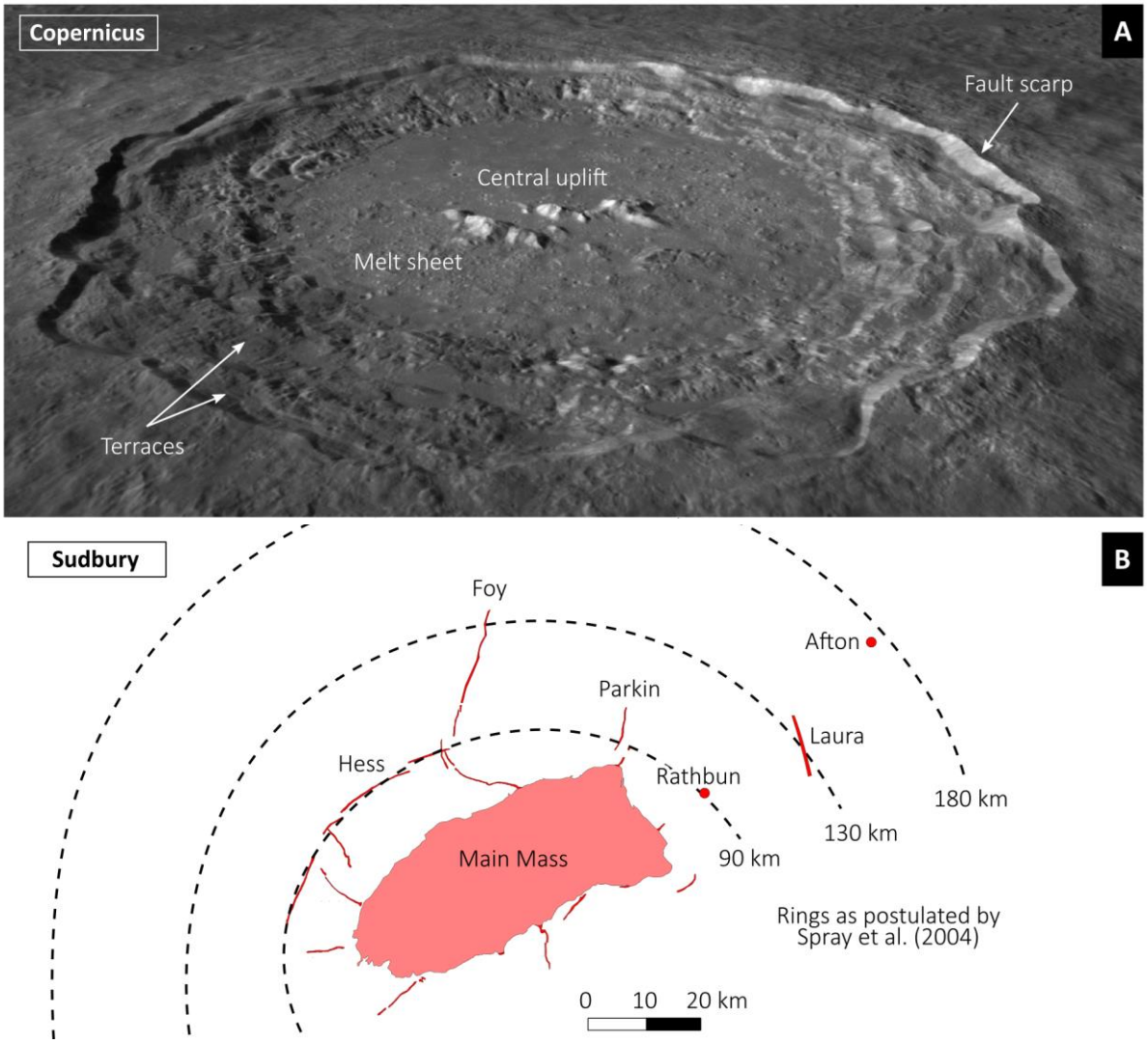

Figure 10.1 The Offset Dykes of the 1.85 Ga Sudbury Igneous Complex in context of the multi-ring hypothesis; **A:** image of the lunar impact structure Copernicus (~93 km diameter) as an extra-terrestrial analogue to Sudbury multi-ring basin (image source: National Aeronautics and Space Administration (NASA) 2021); **B:** map of the present-day configuration of the Sudbury Igneous Complex (= Main Mass and Offset Dykes), highlighting the distribution of the Offset Dykes (including the recently discovered Rathbun, Laura and Afton Offset Dykes) and the previously postulated ring features; redrawn after Spray et al. (2004).

10.1.2 Autochthonous impactites (Sudbury Breccia)

Apart from the discovery of impact melt dykes (= allochthonous impactites), this study has shown that pseudotachylitic breccia (= autochthonous impactites) east of the Sudbury Igneous Complex is far more abundant than previously perceived. In fact, pseudotachylitic breccia (locally termed Sudbury Breccia) revealed to be nearly ubiquitous in the study area, both in outcrop and in drill cores. The breccia covers an entire spectrum, from mm-sized hair-like fracture systems that can be easily mistaken for hydrothermal veinlets and that are only identifiable in thin section, to megaclastic breccia that is readily identifiable in the field. The perceived abundance of Sudbury Breccia overall seems to decline from Wanapitei Lake in the west to Temagami Lake in the east – the most distant confirmed occurrence of Sudbury Breccia (Simony 1964; Rousell et al. 2003).

As mentioned earlier, Sudbury Breccia east of the Main Mass does not differ from Sudbury Breccia described elsewhere within the Sudbury Impact Structure, and, therefore, needs no further elaboration; the reader is instead referred to the studies of Parmenter et al. (2002), Rousell et al. (2003) or Fedorowich et al. (2009). There are, however, a few aspects that deserve comment:

- Megaclastic Sudbury Breccia, with clasts of up to 12 m in size, revealed to be continuously exposed within a 14 km accurate N-S trending zone or "belt", referred to here as the *East Range Breccia Belt* (ERBB). This megastructure bears strong resemblance to the well-known *South Range Breccia Belt* (SRBB) (Scott & Spray 1999, 2000). Like the SRBB, the ERBB is a relatively linear, well-defined, mappable zone of megaclastic Sudbury Breccia, tens to hundreds of meters wide. Unlike the SRBB, however, the ERBB experienced little tectonic deformation, it was emplaced into relatively uniform host rocks, its breccias are mono- or bilithic, the belt occurs at a greater distance to the Main Mass (25 km) than the SRBB (0–5 km), and pods of quartz diorite (discontinuous Offset Dykes in the sense of Grant & Bite 1984) have yet to be discovered in the ERBB. Like the SRBB parallels pre-existing lithological contacts and faults (Murray Fault), the ERBB trends parallel to the N/NW-striking Onaping Fault System. By analogy to the SRBB (Spray 1997; Scott & Spray 1999, 2000), the ERBB could have been a listric normal circumferential crater fault that formed during the crater modification stage.
- Sudbury Breccia exhibits a very well-developed flow-banding. This resembles the "clastic type" of Sudbury Breccia as defined by Rousell et al. (2003), and it was only observed within, or at the contact to, sedimentary host rocks (argillite, wacke). In contrast, a black aphantic type of Sudbury Breccia was predominantly, though not exclusively, observed within crystalline/igneous host rocks (both mafic and felsic). Paradoxically, some of the best examples of flow-banding were observed in breccias developed in massive (unstratified) quartzite and arkose (**Chapter 6.2**). The origin of the flow-banding and its lithological controls remain enigmatic.
- Foreign lithic clasts were observed within exceptionally wide zones of brecciation. The exotic clasts comprise gabbro (likely Nipissing Suite), laminated sandy siltstone (uppermost Gowganda Formation), and, in one place, massive pyrite (**Chapter 4.2**). None of these lithologies are exposed in vicinity to the breccia site, suggesting clast transport over 10s to 100s of meters and thus calling upon a parautochthonous origin of the breccia, at least in some places.
- This study has possibly identified Sudbury Breccia within Archaean banded iron formation (**Chapter 3.3**). To the author's knowledge, pseudotachylitic breccia (or endogenic pseudotachylite for that matter) has not been described before in this kind of protolith.

10.1.3 Thermal effects related to the impact event

Although most of the foregoing discussion has concentrated on the discovery of new Offset Dykes, the Sudbury impact event does not only manifest in form of discrete, mappable, breccias and melt rocks above the Temagami Anomaly, but also as subtle thermal effects imposed upon the target rocks. Uranium-Pb geochronology of one of the pre-impact mafic dykes, 25 km northeast of the Main Mass, yielded a titanite date of 1872 ± 3 Ma, which is interpreted as the magmatic crystallisation age of the host rock, whereas apatite from the same outcrop yielded 1851 ± 3 Ma, which is interpreted to reflect later isotopic re-equilibration during the 1850 ±1 Ma Sudbury impact event (**Chapter 7.7**). Apatite has a higher Pb diffusivity and thus a lower closure temperature than titanite (Cherniak 2010) and it is consequently more susceptible to isotopic disturbance, whether through impact-related processes (e.g. McGregor et al. 2019, 2020b), or hydrothermal processes (e.g. Corfu & Stone 1998). So, while the observed age discrepancy between apatite and titanite makes perfectly sense from a thermodynamic perspective, the exact mineralogical-geological process responsible for the resetting is not clear, as the sampled outcrop did not show any signs of thermal metamorphism, brecciation, interaction with impact melts, not even of micro fracturing.

Shock metamorphism as a cause of age resetting (Deutsch & Schärer 1990; Moser et al. 2011) can be excluded a priori, because the sample location occurs more than 15 km outside the zone of shatter cones and planar deformation features (Ames et al. 2005; Grieve et al. 2008); none of these features have been observed in the study area. More likely, age resetting of apatite occurred through protracted heating above the apatite closure temperature (but still below the titanite closure temperature) allowing for volume-diffusion to take place, with conductive heat transfer from the overlying (now eroded) impact melt sheet into the underlying footwall (e.g. Ivanov & Deutsch 1999). A similar conclusion was reached by Spray et al. (2004), who observed that the 2.45 Ga Matachewan Dyke Swarm had apparently lost its remnant magnetic signature within a ~30 km radius around the Main Mass, possibly because of heating above the respective Curie temperature. This led Spray et al. (2004) to propose that the Main Mass (= the impact melt sheet) was originally much more extensive than the currently exposed 60 x 30 km, possibly up to 130 km in diameter. A 130 km-diameter impact melt sheet would also explain why Offset Dykes – assuming the downward injection hypothesis is correct – occur as much as 45 km away from the currently exposed Main Mass (**Chapter 3**). Alternatively, isotopic resetting in the outcrop of question could have been caused by convective heat transfer through fluid-rock interaction initiated by the impact, or through fluid-mediated dissolution-reprecipitation. Evidence of long-lived regional hydrothermal activity has been suggested for the Chicxulub, among other, impact structures (e.g. Osinski et al. 2013; Kring et al. 2020). At Sudbury, no study has so far focused on potential impact-induced hydrothermal activity outside the actual Sudbury Basin, in more distal areas of the crater.

Regardless of the exact mechanism behind the isotopic resetting, the recovery of impact ages from distal footwall units alone implies that the Sudbury impact event must have had much more profound and far-reaching effects on the target rocks than the mere outcrop situation and the distribution of macroscopic impact-related features suggests. This demonstrates that U-Pb mineral dates of ~1850 Ma obtained on rocks even in the wider Sudbury area cannot be used as a reliable, and certainly not as the sole, evidence of an impact origin (see also: Corfu & Lightfoot 1996; Lightfoot et al. 2001; Prevec & Baadsgaard 2005), which underlines the importance of an integrated petrographic, lithogeochemical and isotopic approach as adopted in the present study.

10.2 Pre-Impact Magmatism

Apart from the recognition of impact related features east of the Sudbury Igneous Complex, this study provided new insights into the magmatic history of the Huronian Basin prior the 1.85 Ga Sudbury impact event. Among the known igneous rocks in this area there are mafic metavolcanic of the 2.7 Ga Abitibi Subprovince, which are locally exposed as erosional windows or have been intersected in deep drill holes into the Temagami Anomaly; and very widespread gabbroic sills of the 2.22 Ga Nipissing Suite, which have been encountered in almost every single of the studied townships, both in outcrop and drill cores. New igneous rock discoveries include:

- An almost 10 km long NE-striking tholeiitic quartz diabase dyke, likely related to the 2.22 Ga Nipissing Suite/Senneterre Dyke Swarm (**Chapter 6**).
- A more discontinuous, also NE-striking, calc-alkaline quartz diabase dyke, correlative with the regional 2.17 Ga Biscotasing Dyke Swarm (**Chapter 8**).
- NW-striking alkaline ultrabasic dykes, dated at 1872 ± 3 Ma, and correlated with the 1.88–1.86 Ga Circum-Superior LIP and the 1.88 Ga Spanish River Carbonatite (**Chapter 7**).

A pre-impact intrusion age of all the above listed dykes is evident by cross-cutting field relations, since all of them are either pervaded by, or have been reworked as megaclasts into, impact-generated pseudotachylitic breccia (Sudbury Breccia). Maximum emplacement ages are, in turn, constrained by the depositional age of host rock, the ~2.3 Ga Cobalt Group (Hill et al. 2018).

As such, this study not only adds to the existing geochronological record of the Sudbury District (**Fig. 10.2**), but it also provided insights into the target rock diversity and -stratigraphy of one of the largest and oldest impact structures known on Earth. Specifically, these mafic rocks could have been yet another source of the exceptional Ni-Cu-PGE-enrichment in the Sudbury Igneous Complex, thus maybe providing the missing link between pre-enrichment target rocks (Keays & Lightfoot 2020) and the formation of one of the world's largest ore provinces. Perhaps the unique metal endowment of the Sudbury Complex only became possible because the impacting bolide hit a portion of continental crust in which coincidentally three large igneous provinces overlapped in space. Apart from the known rocks of the ore-hosting 2490–2445 Ma *Matachewan LIP*, and of the 2229–2199 Ma *Ungava LIP* (locally represented by sills and dykes of the Nipissing Suite), rocks of a third LIP, the ore-hosting 1883–1864 Ma *Circum-Superior LIP*, are now indicated by this study. Furthermore, this study provided first evidence that mafic rocks of another event, the 2173–2166 Ma *Biscotasing Dyke Swarm*, were emplaced into the Huronian Basin prior to the impact.

An interesting follow-up study would be a more detailed comparison of these newly discovered dykes with the exotic xenoliths that are found within the Sudbury Igneous Complex. For instance, are the exotic (ultra-)mafic xenoliths, specifically the Group IIB and Group III inclusions of Wang et al. (2020), perhaps sourced from an unexposed 1.88 Ga ultramafic complex, or from a 2.17 Ga Biscotasing Dyke? Dupuis et al. (1982, 1990) reported on exotic clasts of supposedly alkaline gabbro in Sudbury Breccia near Ramsey Lake. Could these clasts be related to any of the new discoveries? Does the U-Pb zircon date of 1859 ± 13 Ma obtained on the ultramafic Drury Township Intrusion (εNdi –4.3 to +2.0) in the footwall of the Sudbury Igneous Complex really reflect isotopic resetting, as suggested by Prevec & Baadsgaard (2005), or does the intrusion represent yet another member of the ~1.88 Ga Circum-Superior LIP? Keays & Lightfoot (2020) recently obtained

a 2168 ± 11 Ma U-Pb zircon age for the so-called Sudbury Gabbro at Totten, adjacent to the Worthington Offset Dyke (south of the Main Mass), and based on this, they suggested the gabbro to represent "*simply a more mafic variant of the Nipissing Diabase*" (Keays & Lightfoot 2020, p. 103435). In light of the new observations (**Chapter 8**), could the Sudbury Gabbro at Totten instead be genetically related to the 2170 Ma Biscotasing magmatic event?

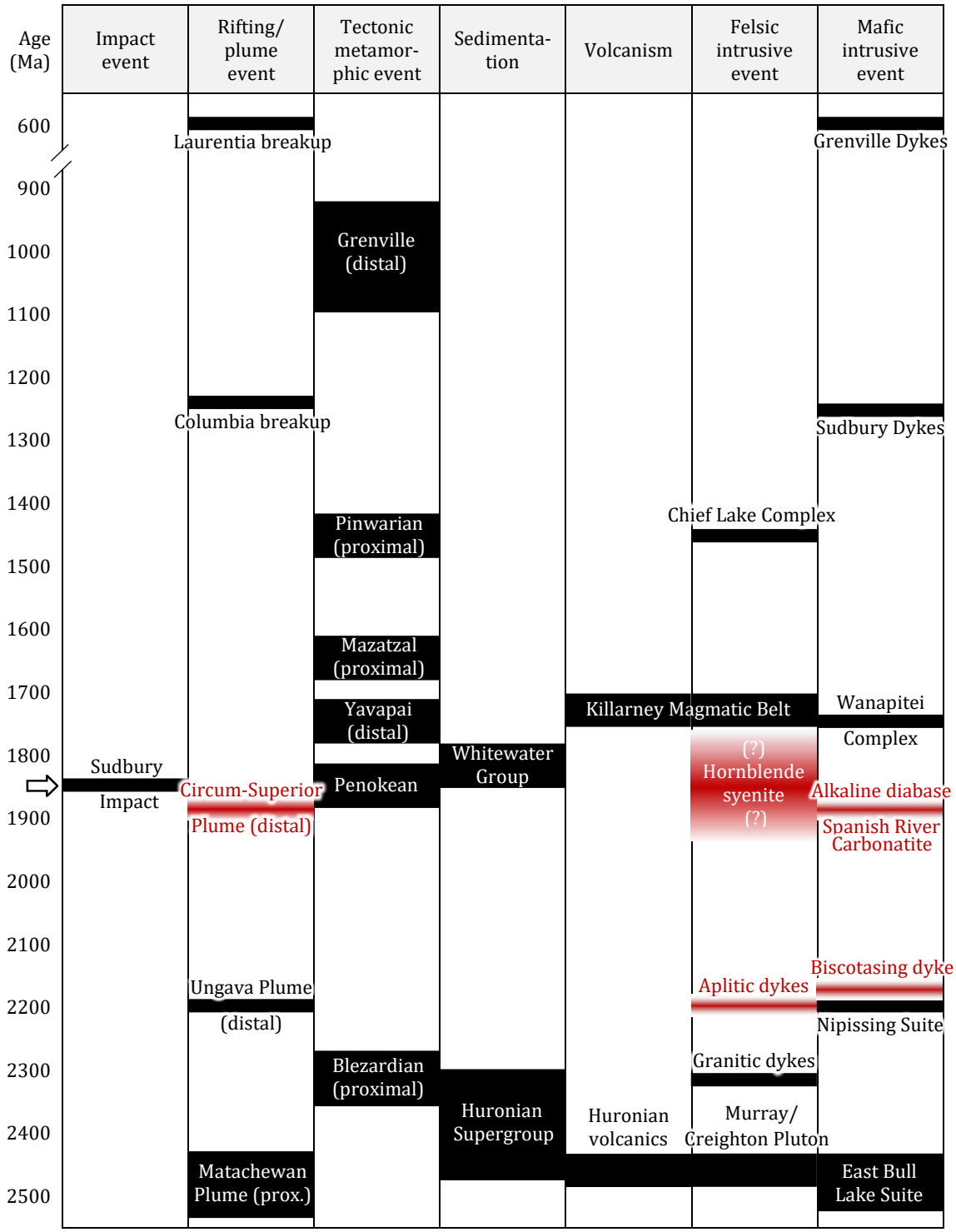

Figure 10.2 Stratigraphic chart for the Sudbury District, showing the newly discovered magmatic rocks in a regional geological context.; previously known rocks or events are displayed in black; hitherto unrecognised events are displayed in red; figure is in part based on Ames et al. (2008) and Lightfoot (2016); for age references see Chapter 2.1.

10.3 Temagami Anomaly

Although not primarily aimed at resolving the deep-seated and thus inaccessible geological cause of the Temagami Anomaly, this thesis should not close without at least some qualitative geophysical discussion because the new geological information made available through this study invites to reassess the various hypothesis brought forward to explain the Temagami Anomaly and its potential relationship to the Sudbury impact event; for a quantitative and more comprehensive treatise of the topic, the reader is referred to the recent publication by Adetunji et al. (2021).

Banded iron formation

As predicted by the geophysical models of Card et al. (1984), drilling into the magnetic peak of the Temagami Anomaly at Afton Township (**Chapter 3**) revealed the presence of a thick succession of Neoarchaean Algoma-type banded iron formation (BIF). There is little doubt that the intersected BIF unit is the same as the one cropping out near Emerald Lake, which is in turn an extension of the well-known BIF of the Temagami Greenstone Belt (Bennett 1978). The BIF recovered in drill hole AT-14-01 has a total apparent thickness of ca. 500 m and matches the assumed proportion of 18 vol% magnetite used in the model of Card et al. (1984). It surely contributes to the Temagami Anomaly to some degree and could explain why the anomaly is more magnetic and shallower in the eastern part than is in the western part. The locally high graphite content of the BIF, and the presence of interconnected magnetite and sulphide (pyrite), likely explains some of the resistive/conductive features noted in previous magnetotelluric surveys (Craven et al. 1998; Adetunji et al. 2021). However, the intersected BIF does not differ in thickness, structural position, or mineralogy, from the BIF in the Temagami or Emerald Lake greenstone belts, where it occurs as a distinct linear near-surface feature on aeromagnetic maps without an associated regional gravity anomaly (Card et al. 1984; Pilkington 1997). It is also unlikely that structural repetition of the intersected BIF, for example through isoclinal folding (John Ayer, pers. comm. 2019), is responsible for the Temagami Anomaly, because the BIF (and the entire greenstone succession) in drill core AT-14-01 and in the Emerald Lake and Temagami greenstone belts appears to be relatively undeformed (e.g. Meyn 1977; Bennett 1978). According to Adetunji et al. (2021), a threefold stacking of this 500 m-thick BIF would be required to explain the magnetic features of the Temagami Anomaly. Besides, BIF alone can presumably not account for the up to +20 mGal gravity feature that is associated with the western part of the Temagami Anomaly (Card et al. 1984).

Gowganda Formation

Similarly, sedimentary rocks of the Huronian Supergroup cannot explain the Temagami Anomaly because their petrophysical properties are insufficient to explain a magnetic and gravity anomaly of such size, scale, and magnitude (e.g. Card et al. 1984). Although locally, disseminated, probably syn-depositional, magnetite can be concentrated within the Gowganda Formation (e.g. Easton et al. 2020), such magnetite-rich facies are volumetrically by far not sufficient to explain the Temagami Anomaly as a whole, not to mention the overall thin thickness of intersected Gowganda Formation at Afton Township (< 300 m; **Chapter 3**) or Sheppard Township (< 1,000 m; **Chapter 7**). It also appears unlikely for the regional and aerially extensive Gowganda Formation (or the Huronian Supergroup in general) to result in a 11,000 nT anomaly only in this part of the Huronian Basin. The low average density of the Huronian Supergroup sedimentary rocks (2.65 g/cm^3; Card et al. 1984) further precludes a causative relationship with the Temagami Anomaly.

Sudbury Impact Structure

Ever since the discovery of the Temagami Anomaly and the recognition of the Sudbury Igneous Complex as being impact-related, there have been speculations about a link between the two structures (e.g. Card et al. 1984). A genetic connection between the two is, however, neither borne out by the evidence, nor in light of our current understanding of the impact crater formation, a particularly realistic hypothesis. First, there is no evidence whatsoever for the Temagami Anomaly representing a twin crater. Second, there is no reason for such a highly asymmetric geophysical signature resulting from an impact. Instead, plenty of evidence exists for the Sudbury Impact Structure having originally been circular (e.g. Hirt et al. 1993; Golightly 1994; Roest & Pilkington 1994), and even in the case of an oblique impact, the structure and the melt sheet (not the ejecta) would have still been more or less circular (Melosh 1989; Pierazzo & Melosh 2000a,b), as would be any geophysical anomaly resulting from such oblique impact (cf. Schultz & D'Hondt 1996; Collins et al. 2020). It is also difficult to explain the anomaly by the lateral intrusion of impact melt into the middle/lower crust, especially considering that the volume of such injection must have exceeded that of the current Main Mass. Third, with the availability of high-quality geophysical data (Olaniyan et al. 2015; Adetunji et al. 2021) it becomes increasingly evident that the potential field anomaly associated with the Sudbury Igneous Complex is, in fact, not that intense, and that it differs in many respects from the Temagami Anomaly, including magnitude, susceptibility contrast, density contrast, shape and depth of the causative body. For example, the density of the Main Mass ranges from 2.70 g/cm^3 (granophyre) to 2.88 g/cm^3 (gabbro, norite), corresponding to a weighted mean of 2.78 g/cm^3, which is almost indiscernible from the average density of the target rocks (2.65–2.88 g/cm^3) (Gupta et al. 1984; McGrath & Broome 1994; Lightfoot & Zotov 2005). According to Adetunji et al. (2021), however, a large body with an average density of at least 2.90 g/cm^3 would be required to explain the +20 mGal Temagami Anomaly. The Sudbury Complex has, furthermore, a relatively low magnetic susceptibility between 0.001 SI (granophyre) and 0.035 SI (norite, gabbro) (Hearst et al. 1994; Lightfoot & Zotov 2005). These values are far lower than the 0.1–0.2 SI required to explain the deeper source of the Temagami Anomaly (Adetunji et al. 2021). It is also important to stress that the main cause of the Temagami Anomaly occurs at a depth of 5–15 km or beyond, whereas the Sudbury Igneous Complex is a shallow upper-crustal feature that does not extend for more than 10 km into subsurface (e.g. Wu et al. 1995; Olaniyan et al. 2014).

The present study has identified new Offset Dykes and extensive zones of Sudbury Breccia right above the Temagami Anomaly. Although it might be tempting to speculate about a genetic relationship between these new discoveries and the Temagami Anomaly, it should be born in mind that all these impact-related features also occur elsewhere around the Sudbury Igneous Complex, where they are not associated with any larger geophysical anomaly. The quartz dioritic dykes and the pseudotachylitic breccias are, here and elsewhere, weakly magnetic, they are not much denser than their surroundings, and they are relatively narrow features of typically less than 100 m in width (Lightfoot 2016, p. 524; Mahmoodi et al. 2017). In detail, Offset Dykes have a very low magnetic susceptibility of < 0.0005 SI and density of 2.75–2.85 g/cm^3 (Mueller et al. 1998; Giroux 2005; Mahmoodi & Smith 2015; Mahmoodi et al. 2017; Gordon et al. 2018). The density and magnetic susceptibility of Sudbury Breccia might be more variable (Scott & Spray 1999; Nakamura & Iyeda 2005; Szabó & Halls 2006; Gordon et al. 2018), but by necessity, it cannot diverge too much from its host rock (cf. Henkel & Reimold 2002). Consequently, neither dykes nor breccias can be a major contributor to the Temagami Anomaly. The author suspects that the discovery of new Offset Dykes and impact-generated breccias above the Temagami Anomaly is purely coincidental.

Archaean mafic-ultramafic intrusions

The above considerations only leave the option of a mafic-ultramafic intrusion unrelated to the 1850 Ma Sudbury impact event as an explanation for the Temagami Anomaly, a conclusion that was also arrived in previous studies (Adetunji et al. 2021, and references therein). Theoretically, such ultramafic complex could be of Neoarchaean age. While small ultramafic intrusions do occur in this part of the Abitibi Subprovince (e.g. Ontario Geological Survey 2011), including in the Temagami Greenstone Belt (James & Hawke 1984), these are volumetrically far not sufficient to explain a regional geophysical anomaly of the size of the Temagami Anomaly. The fact that Archaean basement rocks in this part of the Superior Craton are not associated with any broad-scale gravity and magnetic anomalies (e.g. Coles et al. 1981; Card et al. 1984; Buchan & Ernst 1994; Ludden & Hynes 2000) implies that the cause of the Temagami Anomaly is most likely of post-Archaean age.

Nipissing Suite

Mafic rocks of the 2220 Ma Nipissing Suite, although widespread, are an unlikely cause of the Temagami Anomaly either, because they are, in general and in the studied drill cores and outcrops, weakly magnetic. They are also free of olivine, which means that an increase in magnetic susceptibility due to serpentinisation can be ruled out. Although some sections exhibit higher susceptibility owing to large leucoxene grains (1–5 vol%), and an elevated conductivity due to disseminated sulphide, the Nipissing Suite gabbro in bore holes AT-14-01 (300 m) and M-SH-2 (150 m) is too thin and too shallow to be a major contributor to the Temagami Anomaly. Easton et al. (2020) and Adetunji et al. (2021) discussed the possibility of metamorphism, hydrothermal alteration and shearing increasing their magnetic susceptibility and electric conductivity. However, these affects are considered miniscule and very local. Also, there is no reason why the Nipissing Suite, extending over some 100,000 km^2 throughout the entire Huronian Basin, should result only in one place in such extreme geophysical signal. According to Lightfoot et al. (1993), gabbroic rocks of the Nipissing Suite were emplaced as second-stage melts into the Huronian Supergroup; the parental magma underwent fractionation of olivine prior to emplacement. Theoretically, this would raise the possibility of genetically related ultramafic cumulates at depth causing the Temagami Anomaly. However, as indicated by Buchan et al. (1993, 1998) and Palmer et al. (2007), the Nipissing Suite was likely fed laterally (horizontally) from NE to SW into the Huronian Basin through the Senneterre Dyke Swarm, emanating from a plume centre in northern Quebec (e.g. Davey et al. 2019). If correct, this emplacement mechanism would preclude the existence of deep-seated ultramafic cumulates *beneath* the currently outcropping sills of the Nipissing Suite. Also, if ultramafic Nipissing Suite-related cumulates existed, these would be expected to occur throughout the entire Huronian Basin, and not just in the area of the Temagami Anomaly. Thus, a genetic relationship between the Nipissing Suite and the Temagami Anomaly seems inconceivable.

Regional mafic dyke swarms

Likewise, quartz diabase of the regional 2170 Ma Biscotasing Dyke Swarm (**Chapter 8**) is volumetrically and petrophysically inadequate to explain the Temagami Anomaly. Neither are the known dykes of this swarm themselves associated with distinctively positive magnetic and gravity features, nor is the Biscotasing Dyke Swarm linked to any larger mafic-ultramafic complex of sufficient size and physical properties to result in a regional geophysical feature at the scale and magnitude of the 1,200 km^2 Temagami Anomaly. The same holds true for the regional ca. 1238 Ma Sudbury Dyke Swarm and the ca. 590 Ma Grenville Dyke Swarm. Even though members of the

Sudbury Dyke Swarm do occur in the study area, where they show as strongly magnetic linear features, these are very distinct from the Temagami Anomaly and, in fact, seem to cut across (i.e., are younger than) the Temagami Anomaly (Easton et al. 2020); they are not associated with any gravity feature either. There is currently little evidence that the Sudbury Dyke Swarm was once connected to large deep-seated mafic-ultramafic magma chambers (cf. Easton 2002), and even if this were the case, such voluminous chambers would be expected to occur more proximal to the plume centre near the point of dyke convergence (Ernst et al. 2019), wherever this point might have been in light of the conflicting nature of existing data (Ernst 1994; Hou et al. 2010).

East Bull Lake Suite

A possible candidate to explain the Temagami Anomaly could be a layered mafic-ultramafic complex of the early Proterozoic (2496–2450 Ma) East Bull Lake Suite. Members of this suite are exposed all around Sudbury, and one of these – the River Valley Intrusion – crops out just 25 km south of the Temagami Anomaly. These mafic-ultramafic complexes are not only thick (> 1,000 m), voluminous and dense, but they also contain abundant titanomagnetite to produce significant magnetic anomalies elsewhere (e.g. Mueller et al. 1996). In detail, however, and as correctly pointed out by Adetunji et al. (2021), petrophysical properties established for the East Bull Lake Suite (Kurtz et al. 1986; Mueller et al. 1996; Legault et al. 2011) do not even closely match the requirements to explain the Temagami Anomaly. For instance, even the most primitive portions of these intrusions (troctolite units) have a low magnetic susceptibility (≤ 0.045 SI; Mueller et al. 1996); they lack pervasive serpentinisation; and they contain only sparse disseminated (not interconnected) magnetite (< 5 vol%) and rather erratic disseminated contact-style sulphide mineralisation (e.g. Easton et al. 2010; Holwell et al. 2014) – all of which is insufficient to account for the magnetic and especially the conductive features of the Temagami Anomaly (Adetunji et al. 2021). Another complication arises from the exceptionally large size of the Temagami Anomaly (1,200 km^2), which contrasts the relatively small size of all known members of the East Bull Lake Suite. Even the largest member, the 50 km^2-large and 2 km-thick Agnew Intrusion west of Sudbury (Vogel et al. 1998a), produces a geophysical feature distinctly different from the Temagami Anomaly in terms of shape, structure, and magnitude. This notwithstanding, Adetunji et al. (2021) suggested – for lack of an alternative explanation – that the Temagami Anomaly might be caused by an intrusive ultramafic complex of the East Bull Lake Suite at the base of the Huronian Supergroup. Although this hypothesis may account for some of the observed geophysical features, it is solely based on circumstantial argumentation, and it remains almost impossible to test.

Circum-Superior Large Igneous Province

A discovery that has the potential of casting the Temagami Anomaly in a completely new light is that of 1872 ± 3 Ma alkaline ultrabasic dykes both in outcrop and in a deep exploration drill hole. As discussed in **Chapter 7**, the dykes are likely related to a mantle plume because of their OIB-like trace element signature; they are interpreted as part of a regional magmatic event, the 1883–1864 Ma Circum-Superior Large Igneous Province (LIP). Other well-known members of this LIP include the Thompson Nickel Belt, the Fox River Sill, the Raglan Formation/Cape Smith Belt, and a range of carbonatite complexes, many of which are themselves associated with large-scale geophysical anomalies (e.g. Zurbrigg 1963; Dowsett 1970; Sage 1987; McRitchie 1995; Ferguson et al. 2015).

Obviously, the alkaline ultrabasic dykes alone cannot explain the Temagami Anomaly. Their close spatial association with one of the largest unexplained potential field anomalies on the Canadian

Shield (Pilkington 1997) is, however, unlikely to be a pure coincidence; it could well be that there is some sort of causative relationship. Such relationship could exist in form of a magmatic plumbing system (e.g. Ernst et al. 2019), in which the dykes represent but a high-level manifestation of a larger and more primitive mafic-ultramafic magma chamber – the actual cause of the Temagami Anomaly. In this context it might be interesting to point out that a large-scale magmatic plumbing system has been suggested for the ~1.88 Ga Cape Smith Belt (Mungall 2007; McKevitt et al. 2019).

Granted, the above hypothesis is based on a range of assumptions and needs to be tested trough additional field work and drilling, but indirect support comes from the following: First, the alkaline ultrabasic dykes discovered in this study are apparently, and unlike the Matachewan, Biscotasing, Sudbury or Grenville dykes, not part of a regional dyke swarm. This, in turn, excludes lateral dyke emplacement over larger distances and instead points to a more local magma source (Ernst et al. 2019). Second, the alkaline diabase dykes have a relatively evolved composition, compared to primary mantle derived melts, suggesting fractional crystallisation occurred before or during their emplacement (at depth?). Third, amphibole phenocrysts in one of the dykes record crystallisation pressures of 3.7–4.4 kbar equivalent to a current depth of 10–15 km. This corresponds to the same depth as the supposed cause of the Temagami Anomaly (Adetunji et al. 2021). Fourth, the petrophysical properties established for (other) members of the Circum-Superior LIP do match the requirements better than any other lithology known in the Huronian Basin. The Fox River Sill, for example, a layered complex comprising strongly serpentinised peridotite, has an average magnetic susceptibility of 0.1–0.2 SI (Ferguson et al. 2015), which is exactly the required value for the Temagami Anomaly. Apart from that, the size of the interpreted "*Temagami Igneous Complex*" (~600 km^2) compares well with the size of (other) members of the Circum-Superior LIP. The Fox River Sill, for example, extends across ~500 km^2; ultramafic rocks of the Thompson Nickel Belt, although strongly deformed, for at least 1,000 km^2; the Expo Intrusive Suite (Cape Smith Belt) measures ~100 km^2; the Sutton Inlier ~500 km^2; the Winnipegosis Komatiite Belt ~4.500 km^2. Each is associated with a regional gravity and magnetic high of about comparable scale and magnitude as the Temagami Anomaly (e.g. Eaton & Darbyshire 2010). As a matter of fact, some of these members and associated ore deposits have only been discovered because of their extreme geophysical signature (e.g. Zurbrigg 1963; McRitchie 1995; Hamilton & Stott 2008). A more detailed comparison is, unfortunately, beyond the scope of this study and the publicly available data, but it is recommended that future work should particularly focus on the geophysical similarities between the Temagami Anomaly and known members of the of the Circum-Superior LIP.

Summary

In summary, it is tentatively suggested, based on the observations made in the present study, that the Temagami Anomaly might be caused by a combination of shallow (< 2 km), locally exposed, Archaean banded iron formation, and a deep-seated (> 5 km) ultramafic (± serpentinised) intrusive complex genetically related to the 1883–1864 Ma Circum-Superior LIP. The interpreted intrusive complex would have a dimension of 60 x 10 x 10 km, an average susceptibility of 0.2 SI equivalent to a magnetite content of 5 vol%, and it seems to become increasingly denser with depth (Adetunji et al. 2021) possibly reflecting internal magmatic differentiation. The complex was likely emplaced along the ~1.9 Ga Onaping Fault System (Buchan & Ernst 1994) and along the boundary between Archaean basement and Huronian Supergroup having acted as density barrier, causing the intruding magma to stagnate and differentiate. The hypothesis of a genetic relationship between the Temagami Anomaly and the Sudbury impact event should be discarded.

10.4 Recommendations for Mineral Exploration

Sudbury-type PGE-Au-Cu-Ni sulphide

Irrespective of what the cause of the Temagami Anomaly might be, the discovery of new Offset Dykes – one of the principal ore-hosting lithologies of the world-class Sudbury Mining Camp – has significant implications for the future Ni-Cu-PGE prospectivity of the area east/northeast of the Sudbury Igneous Complex. Below are some suggestions that one might consider when exploring these new Offset Dykes for potential Sudbury-type ore deposits.

The highest economic potential arises from the so-called Rathbun Lake occurrence, a small but high-grade Pd-showing that has been known for at least 130 years, and that has previously been genetically ascribed to the regional 2.22 Ga Nipissing Suite. Prior studies have reported exceptionally high grades of Pd (≤ 53 g/t), Pt (≤ 33 g/t), Au (≤ 6.4 g/t), and Cu (≤ 19.9 wt%) in grab samples *at surface* (Koulomzine 1955; Rowell & Edgar 1986; Lightfoot et al. 1991), which could be confirmed in the present study (**Chapter 5.7**). In fact, new assays returned even greater values of Au (≤ 9.6 g/t), Pd (≤ 62.5 g/t), and Cu (≤ 22.8 wt%). Most significantly, however, this study indicated that PGE grades at Rathbun do not necessarily correlate with measured sulphur nor visible sulphide content; Pd values of up to 13 g/t were found even in sulphide-free samples. This style of mineralisation shares many similarities with the so-called *low-sulphide high-precious metal mineralisation* (LSHPM) known from elsewhere within the Sudbury Mining Camp; the semi massive Cu-rich style resembles the *sharp-walled footwall vein mineralisation* (cf. Farrow et al. 2005).

In spite of these highly encouraging metal grades and a considerable amount of foregoing studies at Rathbun, the origin of this occurrence has remained controversial and has been proposed to be either epigenetic/hydrothermal (Rowell & Edgar 1986) or syngenetic with the emplacement of the Nipissing Suite (Lightfoot & Naldrett 1996a). Subsequent prospectors that have subscribed to either model have, however, completely failed to identify any extension of the Rathbun Lake occurrence, nor have they discovered comparable high-grade occurrences elsewhere in the Huronian outcrop belt associated with the Nipissing Suite (Davey et al. 2019, for a review).

The present study reported on the discovery of a quartz dioritic Offset Dyke at Rathbun Lake and made a strong case for the Rathbun Lake occurrence also being impact related (**Chapter 5**). This drastically changes the view on the occurrence and how further exploration should be approached, that is, Rathbun Lake should be treated as, an explored like, an Offset Dyke/breccia-hosted mineral system similar to the Frood-Stobie, Totten, Kelly Lake, Vermillion or New Victoria deposits. Highest priority should have the tracing of any extension or branch of the Rathbun Offset Dyke in (sub-)outcrop as well as an accurate determination of its strike, width, dip, and down-dip continuity. Crucial will also be to build a 3D-model of the occurrence, its lateral distribution, and its continuation at depth. This should include mechanical stripping, detailed outcrop mapping, channel sampling, assaying even of sulphide-poor samples, and diamond drilling. Geophysical exploration should follow the case studies of other Offset Dykes (e.g. Mueller et al. 1998; Polzer 2000; Bellefleur & Chouteau 2001; Spicer 2016; Mahmoodi et al. 2017; Smith 2017). For instance, quartz diorite could be identified as a local relative gravity low within the Nipissing Suite gabbro, or as a relative gravity high within the Gowganda Formation. Ground electric resistivity tomography, ground-penetrating radar, borehole vector magnetics, and airborne LiDAR have previously

proofed successful in locating Sudbury-type massive sulphide bodies, and in delineating lithological contacts (see also: Fourie et al. 2019). Furthermore, historic drill cores from Rathbun Lake should be re-examined for previously unnoticed impact-related features (quartz diorite, Sudbury Breccia, metabreccia) and LSHPM mineralisation. Owing to the S-poor nature of the latter, similar occurrences could have been easily overlooked in the past. Therefore, a reassessment of known base metal sulphide occurrences in the wider Rathbun Lake/Portage Bay area, especially of those occurrences initially and perhaps erroneously attributed to the Nipissing Suite, is suggested.

Aside from the immediate Rathbun Lake area, focus should be directed towards the wider Wanapitei Lake region, especially the under-explored Aylmer Township northwest of Rathbun Lake – some 100 km^2 of supposedly flat lying Gowganda Formation. Chances are good of finding additional Offset Dykes (and related mineralisation) not only there but also within Scadding Township and elsewhere within Rathbun Township. Recent work by Inventus Mining (VanderWal 2021), for example, indicates widespread brecciation and additional quartz diorite exposures in the southern part of Rathbun Township, around Bassfin Lake. If and how these new discoveries are related to the Rathbun Offset Dyke (e.g. in form of a parallel dyke or a branch), and whether these are as equally endowed, is part of ongoing investigations. Also, given that Offset Dykes and related mineral systems tend to be relatively narrow and small-scale geological features, they might have well been overlooked in earlier reconnaissance mapping by the OGS, especially in the more poorly exposed areas along the Wanapitei River. The revisiting and geochemical sampling of mafic dyke-, granophyre-, and quartz diorite occurrences that have previously (and perhaps erroneously) been mapped as members (or differentiated portions) of the Nipissing Suite is, therefore, recommended. A manual on how to identify new Offset Dykes based of geochemical fingerprinting has already been outlined in **Chapter 3.6**. Till geochemistry and indicator mineralogy has lately demonstrated to be a valuable greenfield exploration tool in and around the Sudbury Mining Camp (e.g. McClenaghan al. 2019; Hashmi et al. 2021) and could help to locate additional occurrences.

In contrast to the well-endowed Rathbun Offset Dyke (**Chapter 5**), the two other Offset Dykes at Afton Township (**Chapter 3**) and Mackelcan Township (**Chapter 4**) are considered being of less economic significance, first, because of their distant position relative to the impact site, and second, because of their barren appearance, the latter being corroborated by a lack of an anomalous Cu, Ni, or PGE enrichment. Their potential should, however, not be entirely dismissed. As work by Wallbridge Mining (Smith 2017) has demonstrated, small subeconomic Cu- and PGE-rich sulphide occurrences can still be found even in the more distant Offset Dykes (e.g. Trill, Hess, Parkin). Therefore, at least some field work should be devoted to (i) trace the Laura Offset Dyke in (sub-)outcrop further north and south, (ii) find potential splays or branches of the Laura Offset Dyke, (iii) locate the surface expression of the Afton Offset Dyke. According to Lightfoot (2016), structural traps (branches, steps, pre-impact lithological boundaries and faults) likely played an important role in the formation of Offset Dyke-hosted ore deposits (e.g. the Totten and New Victoria deposits associated with the Worthington Offset Dyke). Such structural traps are something that should be specifically looked out for when tracing the Afton, Laura, and Rathbun Offset Dykes. Another possible scenario that could have potentially led to a local enrichment of Ni-Cu-PGE sulphide, even in the more distant Offset Dykes, is the assimilation of S-rich country rock (pyritic shale, sulphidic BIF, pyritiferous Mississagi and Matinenda formations, sulphide-bearing Nipissing Suite gabbro) by the impact melt. Thus, an elevated potential to discover Ni-Cu-PGE sulphide occurrences might be expected in areas where Offset Dykes had intruded and interacted with

those kinds of country rock. Also, the Au potential, the spatial extent, and the structural-lithological controls of the quartz-carbonate veins that crosscut the Laura Offset Dyke should be assessed.

Intrusion-related Ni-Cu-PGE sulphide

An elevated economic potential does, however, not only arise from the discovery of new Offset Dykes, but from some of the pre-impact lithologies as well. In fact, one of the most important findings of the present study is the discovery of 1872 ± 3 Ma alkaline ultrabasic dykes (**Chapter 7**), even though these do not carry any sulphide mineralisation themselves. As demonstrated here through age dating and geochemistry, the dykes are part of the same regional magmatic event that also formed some of the world's largest Ni deposits at Thompson, Manitoba, and Raglan, Cape Smith (e.g. Bleeker & Kamo 2018). The mere fact that dykes of this 1.88–1.86 Ga magmatic event happen to occur right above one of the largest unexplained geophysical anomalies of the Canadian Shield sheds completely new light on the Temagami Anomaly and whatever its geological cause might be, and it creates a hitherto unknown potential for mafic intrusion-hosted Ni-Cu-PGE sulphide mineralisation within the Huronian Basin. Additional drilling and the extension of existing bore holes into the Temagami Anomaly is, therefore, probably warranted.

With the recognition of the Rathbun Lake occurrence being impact related (**Chapter 5**), the 2220 Ma Nipissing Suite loses significantly in economic appeal. Although there are many other Cu-Ni-PGE sulphide occurrences unequivocally genetically related to the Nipissing Suite, these magmatic occurrences are (with only one exception) currently regarded as subeconomic (Davey et al. 2019). Their genetic and spatial controls are still not well understood. The author considers the probability of making significant new Cu-Ni-PGE discoveries related to the Nipissing Suite relatively low.

Hydrothermal Cu-Co-Au sulphide/arsenide

Further studies should be carried out to understand the timing and cause of the regional Na metasomatism (albitisation) that affected large areas of the Scadding, Rathbun, Mackelcan and Aylmer townships above the eastern part of the Temagami Anomaly. As already noted by Gates (1991), a number of past-producing Au mines and Cu-Co-Au occurrences can be linked to this metasomatic event. A particular close spatial connection seems to exist between hydrothermal Cu-Co-Au mineralisation, mafic rocks of the Nipissing Suite, and N-trending structures of the Onaping Fault System (**Chapter 6** and **Chapter 9**). Areas that meet those criteria should be prospected for additional base- and precious metal occurrences. Extensive stream and lake sediment geochemical data provided by the OGS (e.g. Dyer et al. 2004) could further help to identify previously unrecognised zones of albitisation and mineralisation by searching for local anomalies of Na, Cu, Co, Au and As. Massive hydraulic breccias, like those at Scadding, Aylmer, Cobalt Hill, and Wolf Lake, have the best potential to host economic Cu-Co-Au concentrations. Such breccias, together with accessory fuchsite (Cr-rich mica) and authigenic LREE minerals (e.g. Schandl et al. 1994), seem to indicate a high fluid flux and could serve as an exploration vector. Whether a genetic relationship exists between the albitisation, the Au mineralisation, and the exotic felsic intrusive rocks (aplitic dykes, hornblende syenite, albitite) at Matagamasi Lake (**Chapter 9**) needs be tested, ideally through additional field work and radiometric age dating. Finally, and with the availability of more field data, the initial classification of this regional metasomatic event as a "modified IOCG-system" (Schandl & Gorton 2007) should be reconsidered in light of the more recent definition of the IOCG clan (e.g. Groves et al. 2010; Barton 2013).

10.5 Concluding Remarks

The Temagami Anomaly is, and likely continues to be, one of the largest unexplained potential field anomalies on the Canadian Shield. Its relationship to the 1.85 Ga impact-generated Sudbury Igneous Complex in its immediate vicinity has remained enigmatic, its origin elusive. In an attempt to explore the origin of the anomaly and to test for a genetic relationship between impact and anomaly, field work and deep drilling has lately provided new insights into the poorly understood surface geological makeup of this under-explored area by having revealed the existence of numerous igneous dykes of unknown age and origin above the Temagami Anomaly. These dykes, which have not previously been documented in the wider area, range broadly in composition, magmatic affinity, potential field characteristics, orientation, the style of mineralisation and alteration or the lack thereof. Accordingly, the main objectives of this study were to:

- Provide a first and systematic lithological and lithogeochemical characterisation of the dykes.
- Test if and how the dykes are genetically related to the 1.85 Ga Sudbury impact event.
- Investigate whether the dykes can be correlated with known magmatic units/events within the immediate study area or within the wider region.
- Establish their petrogenesis, mode and timing of emplacement, and post-magmatic evolution.
- Test whether the dykes could be a surface manifestation of a deep-seated ultramafic complex.
- Reconstruct their mineralisation history (if applicable) / evaluate their economic potential.
- Gain a better understanding of the geology and magmatic evolution of the area in general.

Most of the above objectives could be achieved through an integrated approach of field work, petrographic studies, lithogeochemical and Nd-Sr-Pb isotope analyses, and (where possible) U-Pb mineral dating, making it possible to draw the following conclusions: Some of the dykes are indeed genetically related to the 1.85 Ga Sudbury impact event and identified as so-called Offset Dykes; some pre-date the impact event by 20–370 Ma; some are highly prospective targets for PGE-Cu-Ni exploration; some are entirely exotic and could not be assigned to any known magmatic event in the wider area. Therefore, this study has not only provided unexpected insights into one of the least understood parts of the Sudbury Impact Structure, but also into the pre-impact magmatic history of the area, which reveals to be much more complex, diverse, and protracted than initially thought. The actual cause of the Temagami Anomaly remains open to debate.

Due to the nature of this project and this being the first comprehensive geological study on the Temagami Anomaly and the more remote parts of Sudbury's East Range, there are many topics of interest for future studies emerging, and several outstanding problems that should be addressed in order to gain a better understanding of regional geology, magmatic history, metallogeny, and perhaps even the cause of the Temagami Anomaly itself. Topics for future work may include:

- To precisely date the felsic dykes from Matagamasi Lake, and to explore their spatial and perhaps genetic relationship to hydrothermal Au-mineralisation in this area.
- To establish the age and origin of the regional and pervasive albitisation, and to test for a genetic link between alkali metasomatism and the newly discovered alkaline magmatic rocks.
- To test whether any of the dykes, and the alkaline ultrabasic dykes in particular, are part of a regional swarm, or rather the surface manifestation of a deep-seated ultramafic complex.
- To trace the new Offset Dykes further in outcrop and to establish their mode of emplacement.
- To drill deeper into the Temagami Anomaly and to conduct additional geophysical studies.

References

Adam, J., & Green, T. (2006). Trace element partitioning between mica- and amphibole-bearing garnet lherzolite and hydrous basanitic melt: 1. Experimental results and the investigation of controls on partitioning behaviour. Contributions to Mineralogy and Petrology, 152(1), 1-17.

Adetunji, A. Q., Ferguson, I. J., Vayavur, R., Cheraghi, S., Naghizadeh, M., Whymark, W. E., ... & Craven, J. A. (2021). Evidence of magmatism and rifting in the southern superior craton from the Temagami geophysical anomaly. Precambrian Research, 362, 106310.

Albarède, F., Albalat, E., & Télouk, P. (2015). Instrumental isotope fractionation in multiple-collector icp-ms. Journal of Analytical Atomic Spectrometry, 30(8), 1736-1742.

Aleinikoff, J. N., Wintsch, R. P., Fanning, C. M., & Dorais, M. J. (2002). U-Pb geochronology of zircon and polygenetic titanite from the Glastonbury Complex, Connecticut, USA: an integrated SEM, EMPA, TIMS, and SHRIMP study. Chemical Geology, 188(1-2), 125-147.

Ames, D. E., Buckle, J., Davidson, A., & Card, K. D. (2005). Sudbury bedrock compilation: Geological Survey of Canada, Open File 4570, geology, color map, and digital tables, scale 1:50000.

Ames, D. E., Davidson, A., & Wodicka, N. (2008). Geology of the giant Sudbury polymetallic mining camp, Ontario, Canada. Economic Geology, 103(5), 1057-1077.

Ames, D. E., Golightly, J. P., Lightfoot, P. C., & Gibson, H. L. (2002). Vitric compositions in the Onaping Formation and their relationship to the Sudbury Igneous Complex, Sudbury structure. Economic Geology, 97(7), 1541-1562.

Ames, D. E., Stoness, J. A., & Rousell, D. H. (2009). Whitewater Group. In: Rousell, D. H., Brown, G. H. (eds.), A Field Guide to the Geology of Sudbury, Ontario. Ontario Geological Survey, Open File Report 6243, 37-44.

Ames, D. E., Watkinson, D. H., & Parrish, R. R. (1998). Dating of a regional hydrothermal system induced by the 1850 Ma Sudbury impact event. Geology, 26(5), 447-450.

Anders, D. (2016). The Sudbury Impact Structure - New Insights into the Origin and Emplacement of the Basal Onaping Intrusion and the Parkin, Trill and Foy Offset Dykes of the North Range. Unpublished PhD thesis, The University of Western Ontario, London, Ontario, Canada, 261p., Electronic Thesis and Dissertation Repository 4223, https://ir.lib.uwo.ca/etd/4223

Anders, D., Osinski, G. R., Grieve, R. A. F., & Brillinger, D. T. (2015). The basal Onaping intrusion in the north range: roof rocks of the Sudbury igneous complex. Meteoritics & Planetary Science, 50(9), 1577-1594.

Anderson, J. L. (1996). Status of thermobarometry in granitic batholiths. Earth and Environmental Science Transactions of the Royal Society of Edinburgh, 87(1-2), 125-138.

Anderson, J. L., & Smith, D. R. (1995). The effects of temperature and fO_2 on the Al-in-hornblende

barometer. American Mineralogist, 80(5-6), 549-559.

Anderson, J. L., Barth, A. P., Wooden, J. L., & Mazdab, F. (2008). Thermometers and thermobarometers in granitic systems. Reviews in Mineralogy and Geochemistry, 69(1), 121-142.

Ariskin, A. A., & Barmina, G. S. (1999). An empirical model for the calculation of spinel-melt equilibria in mafic igneous systems at atmospheric pressure: 2. Fe-Ti oxides. Contributions to Mineralogy and Petrology, 134(2-3), 251-263.

Arndt, N. T., Lesher, C. M., & Czamanske, G. K. (2005). Mantle-derived magmas and magmatic Ni-Cu-(PGE) deposits. In: Hedenquist, J. W., Thompson, J. F. H., Goldfarb, R. J., Richards, J. P. (eds.), Economic Geology 100th Anniversary Volume, 5-24.

Aulbach, S., Griffin, W. L., Pearson, N. J., & O'Reilly, S. Y. (2013). Nature and timing of metasomatism in the stratified mantle lithosphere beneath the central Slave craton (Canada). Chemical Geology, 352, 153-169.

Ayer, J. A., Chartrand, J. E., Grabowski, G. P. D, Josey, S., Rainsford, D., & Trowell, N. F. (2006). Geological compilation of the Cobalt– Temagami area, Abitibi greenstone belt. Ontario Geological Survey, Preliminary Map P.3581, scale 1:100000.

Ayres, M., & Harris, N. (1997). REE fractionation and Nd-isotope disequilibrium during crustal anatexis: constraints from Himalayan leucogranites. Chemical Geology, 139(1-4), 249-269.

Bachmann, O., & Bergantz, G. W. (2004). On the origin of crystal-poor rhyolites: extracted from batholithic crystal mushes. Journal of Petrology, 45(8), 1565-1582.

Bachmann, O., & Bergantz, G. W. (2008). Rhyolites and their source mushes across tectonic settings. Journal of Petrology, 49(12), 2277-2285.

Bachmann, O., & Dungan, M. A. (2002). Temperature-induced Al-zoning in hornblendes of the Fish Canyon magma, Colorado. American Mineralogist, 87(8-9), 1062-1076.

Bai, L., Barnes, S. J., & Baker, D. R. (2017). Sperrylite saturation in magmatic sulfide melts: Implications for formation of PGE-bearing arsenides and sulfarsenides. American Mineralogist, 102(5), 966-974.

Bailey, J. M., Lafrance, B., McDonald, A. M., Fedorowich, J. S., Kamo, S. L., & Archibald, D. A. (2004). Mazatzal Labradorian-age (1.7–1.6 Ga) ductile deformation of the South Range Sudbury impact structure at the Thayer Lindsley mine, Ontario. Canadian Journal of Earth Sciences, 41(12), 1491-1505.

Baker, J. A., Menzies, M. A., Thirlwall, M. F., & Macpherson, C. G. (1997). Petrogenesis of Quaternary intraplate volcanism, Sana'a, Yemen: implications for plume-lithosphere interaction and polybaric melt hybridization. Journal of Petrology, 38(10), 1359-1390.

Baker, M. B., & Wyllie, P. J. (1992). High-pressure apatite solubility in carbonate-rich liquids: implications for mantle metasomatism. Geochimica et Cosmochimica Acta, 56(9), 3409-3422.

Ballhaus, C. G., & Stumpfl, E. F. (1986). Sulfide and platinum mineralization in the Merensky Reef:

evidence from hydrous silicates and fluid inclusions. Contributions to Mineralogy and Petrology, 94(2), 193-204.

Ballouard, C., Poujol, M., Boulvais, P., Branquet, Y., Tartèse, R., & Vigneresse, J. L. (2016). Nb-Ta fractionation in peraluminous granites: A marker of the magmatic-hydrothermal transition. Geology, 44(3), 231-234.

Barnes, H. L., & Seward, T. M. (1997). Geothermal Systems and Mercury Deposits. In: Barnes, H. L. (ed.), Geochemistry of Hydrothermal Ore Deposits. 3rd edition, John Wiley & Sons, New York, 699-736.

Barnes, S. J., & Lightfoot, P. C. (2005). Formation of magmatic nickel-sulfide ore deposits and processes affecting their copper and platinum-group element contents. In: Hedenquist, J. W., Thompson, J. F. H., Goldfarb, R. J., Richards, J. P. (eds.), Economic Geology 100th Anniversary Volume, 179-213.

Barnes, S. J., & Liu, W. (2012). Pt and Pd mobility in hydrothermal fluids: evidence from komatiites and from thermodynamic modelling. Ore Geology Reviews, 44, 49-58.

Barnes, S. J., & Ripley, E. M. (2016). Highly siderophile and strongly chalcophile elements in magmatic ore deposits. Reviews in Mineralogy and Geochemistry, 81(1), 725-774.

Barnes, S. J., Taranovic, V., Miller, J. M., Boyce, G., & Beresford, S. (2020a). Sulfide emplacement and migration in the Nova-Bollinger Ni-Cu-Co deposit, Albany-Fraser orogen, Western Australia. Economic Geology, 115(8), 1749-1776.

Barnes, S. J., Taranovic, V., Schoneveld, L. E., Mansur, E. T., Le Vaillant, M., Dare, S., ... & Blanks, D. (2020b). The occurrence and origin of pentlandite-chalcopyrite-pyrrhotite loop textures in magmatic Ni-Cu sulfide ores. Economic Geology, 115(8), 1777-1798.

Barth, M. G., McDonough, W. F., & Rudnick, R. L. (2000). Tracking the budget of Nb and Ta in the continental crust. Chemical Geology, 165(3-4), 197-213.

Barton, M. D. (2013). Iron oxide (-Cu-Au-REE-P-Ag-U-Co) systems. In: Turekian, K. K., Holland, H. D. (eds.), Treatise on Geochemistry. 2nd edition, Elsevier Science, Volume 13, 515-541.

Bates, M. P., & Halls, H. C. (1991). Broad-scale Proterozoic deformation of the central Superior Province revealed by paleomagnetism of the 2.45 Ga Matachewan dyke swarm. Canadian Journal of Earth Sciences, 28(11), 1780-1796.

Bau, M. (1991). Rare-earth element mobility during hydrothermal and metamorphic fluid-rock interaction and the significance of the oxidation state of europium. Chemical Geology, 93(3-4), 219-230.

Bau, M. (1996). Controls on the fractionation of isovalent trace elements in magmatic and aqueous systems: evidence from Y/Ho, Zr/Hf, and lanthanide tetrad effect. Contributions to Mineralogy and Petrology, 123(3), 323-333.

Bea, F. (1996). Residence of REE, Y, Th and U in granites and crustal protoliths; implications for the chemistry of crustal melts. Journal of Petrology, 37(3), 521-552.

Beakhouse, G. P. (2011). The Abitibi Subprovince plutonic record: Tectonic and metallogenic implications. Ontario Geological Survey, Open File Report 6268, 161p.

Beard, B. L., & Johnson, C. M. (1993). Hf isotope composition of late Cenozoic basaltic rocks from northwestern Colorado, USA: new constraints on mantle enrichment processes. Earth and Planetary Science Letters, 119(4), 495-509.

Beaudoin, G., Laurent, R., & Ohnenstetter, D. (1990). First report of platinum-group minerals at Blue Lake, Labrador Trough, Quebec. The Canadian Mineralogist, 28(3), 409-418.

Becke, F. (1906). Zur Physiography der Gemengteile der Krystallinen Schiefer. Denkschriften der Kaiserlichen Akademie der Wissenschaften, mathematisch-naturwissenschaftliche Klasse, xxv, 97-152.

Becker, L., Bada, J. L., Winans, R. E., Hunt, J. E., Bunch, T. E., & French, B. M. (1994). Fullerenes in the 1.85-billion-year-old Sudbury impact structure. Science, 265(5172), 642-645.

Becker, L., Poreda, R. J., & Bada, J. L. (1996). Extraterrestrial helium trapped in fullerenes in the Sudbury impact structure. Science, 272(5259), 249-252.

Bekker, A., Kaufman, A. J., Karhu, J. A., & Eriksson, K. A. (2005). Evidence for Paleoproterozoic cap carbonates in North America. Precambrian Research, 137(3-4), 167-206.

Bellefleur, G., & Chouteau, M. (2001). Massive sulphide delineation using borehole radar: Tests at the McConnell nickel deposit, Sudbury, Ontario. Journal of Applied Geophysics, 47(1), 45-61.

Bennett, G. (1978). Geology of the Northeast Temagami Area, District of Nipissing. Ontario Geological Survey, Report 163, 128p.

Bennett, G., Dressler, B. O., & Robertson, J. A. (1991). The Huronian Supergroup and associated intrusive rocks. In: Thurston, P. C., Williams, H. R., Sutcliffe, R. H., Stott, G. M. (eds.), Geology of Ontario Part 1. Ontario Geological Survey, Special Volume 4, 549-591.

Berger, J., Lo, K., Diot, H., Triantafyllou, A., Plissart, G., & Féménias, O. (2017). Deformation-driven Differentiation during in situ Crystallization of the 2.7 Ga Iguilid Mafic Intrusion (West African Craton, Mauritania). Journal of Petrology, 58(4), 819-840.

Berlenbach, J. W., & Roering, C. (1992). Sheath-fold-like structures in pseudotachylytes. Journal of Structural Geology, 14(7), 847-856.

Bernstein, L., & Young, G. M. (1990). Depositional environments of the Early Proterozoic Espanola Formation, Ontario, Canada. Canadian Journal of Earth Sciences, 27(4), 539-551.

Best, M. G. (1974). Mantle-derived amphibole within inclusions in alkalic-basaltic lavas. Journal of Geophysical Research, 79(14), 2107-2113.

Bethune, K. M. (1997). The Sudbury dyke swarm and its bearing on the tectonic development of the Grenville Front, Ontario, Canada. Precambrian Research, 85(3-4), 117-146.

Bickford, M. E., Van Schmus, W. R., & Zietz, I. (1986). Proterozoic history of the midcontinent region of North America. Geology, 14(6), 492-496.

Bickford, M. E., Van Schmus, W. R., Karlstrom, K. E., Mueller, P. A., & Kamenov, G. D. (2015). Mesoproterozoic-trans-Laurentian magmatism: A synthesis of continent-wide age distributions, new SIMS U–Pb ages, zircon saturation temperatures, and Hf and Nd isotopic compositions. Precambrian Research, 265, 286-312.

Bizimis, M., Salters, V. J., & Dawson, J. B. (2003). The brevity of carbonatite sources in the mantle: evidence from Hf isotopes. Contributions to Mineralogy and Petrology, 145(3), 281-300.

Blanks, D. E., Holwell, D. A., Fiorentini, M. L., Moroni, M., Giuliani, A., Tassara, S., ... & Ferrari, E. (2020). Fluxing of mantle carbon as a physical agent for metallogenic fertilization of the crust. Nature Communications, 11, 4342.

Bleeker, W., & Ernst, R. E. (2006). Short-lived mantle generated magmatic events and their dyke swarms: the key unlocking Earth's paleogeographic record back to 2.6 Ga. In: Hanski, E., Mertanen, S., Rämö, T., Vuollo, J. (eds.), Dyke Swarms – Time Markers of Crustal Evolution. Taylor and Francis/ Balkema, London, 3-26.

Bleeker, W., & Kamo, S. L. (2018). Extent, origin, and deposit-scale controls of the 1883 Ma Circum-Superior large igneous province, northern Manitoba, Ontario, Quebec, Nunavut and Labrador. In: Rogers, N. (ed.), Targeted Geoscience Initiative: 2017 report of activities. Geological Survey of Canada, Open File 8373, 5-14.

Bleeker, W., Kamo, S. L., Ames, D. E., & Davis, D. W. (2015). New field observations and U-Pb ages in the Sudbury area: toward a detailed cross-section through the deformed Sudbury Structure. In: Ames, D. E., Houlé, M. G. (eds.), Targeted Geoscience Initiative 4: Canadian Nickel-Copper-Platinum Group Elements-Chromium Ore Systems – Fertility, Pathfinders, New and Revised Models. Geological Survey of Canada, Open File 7856, 151-166.

Blichert-Toft, J., & Arndt, N. T. (1999). Hf isotope compositions of komatiites. Earth and Planetary Science Letters, 171(3), 439-451.

Boast, M., & Spray, J. G. (2006). Superimposition of a Thrust-Transfer Fault System on a Large Impact Structure: Implications for Ni-Cu-PGE Exploration at Sudbury. Economic Geology, 101(8), 1583-1594.

Bodinier, J. L., Fabriès, J., Lorand, J. P., Dostal, J., & Dupuy, C. (1987). Geochemistry of amphibole pyroxenite veins from the Lherz and Freychinede ultramafic bodies (Ariege, French Pyrenees). Bulletin de minéralogie, 110(4), 345-358.

Böhlke, J. K., De Laeter, J. R., De Bievre, P., Hidaka, H., Peiser, H. S., Rosman, K. J. R., & Taylor, P. D. P. (2005). Isotopic compositions of the elements, 2001. Journal of Physical and Chemical Reference Data, 34(1), 57-67.

Bohor, B. F., Betterton, W. J., & Krogh, T. E. (1993). Impact-shocked zircons: discovery of shock-induced textures reflecting increasing degrees of shock metamorphism. Earth and Planetary Science Letters, 119(3), 419-424.

Bolikhovskaya, S. V., Vasil'yeva, M. O., & Koptev-Dvornikov, Y. V. (1996). Simulating Low-Calcium Pyroxene Crystallization in Basite Systems: New Geothermometer Versions. Geochemistry International, 33(12), 1-19.

Borisov, A. A., & Shapkin, A. I. (1990). A new empirical equation rating Fe^{3+}/Fe^{2+} in magmas to their composition, oxygen fugacity, and temperature. Geochemistry International, 27(1), 111-116.

Boudreau, A. E., Mathez, E. A., & McCallum, I. S. (1986). Halogen geochemistry of the Stillwater and Bushveld Complexes: evidence for transport of the platinum-group elements by Cl-rich fluids. Journal of Petrology, 27(4), 967-986.

Bowen, N. L. (1910). Diabase and granophyre of the Gowganda Lake district, Ontario. The Journal of Geology, 18(7), 658-674.

Bowins, R. J., & Crocket, J. H. (1994). Sulfur and carbon isotopes in Archean banded iron formations: implications for sulfur sources. Chemical Geology, 111(1-4), 307-323.

Bowins, R. J., & Heaman, L. M. (1991). Age and timing of igneous activity in the Temagami greenstone belt, Ontario: a preliminary report. Canadian Journal of Earth Sciences, 28(11), 1873-1876.

Bruand, E., Storey, C., & Fowler, M. (2014). Accessory Mineral Chemistry of High Ba-Sr Granites from Northern Scotland: Constraints on the Petrogenesis and Records of Whole-rock Signature. Journal of Petrology, 55(8), 1619-1651.

Buchan, K. L., & Ernst, R. E. (1994). Onaping fault system: age constraints on deformation of the Kapuskasing structural zone and units underlying the Sudbury Structure. Canadian Journal of Earth Sciences, 31(7), 1197-1205.

Buchan, K. L., & Ernst, R. E. (2018). A giant circumferential dyke swarm associated with the High Arctic Large Igneous Province (HALIP). Gondwana Research, 58, 39-57.

Buchan, K. L., & Ernst, R. E. (2021). Plumbing systems of large igneous provinces (LIPs) on Earth and Venus: Investigating the role of giant circumferential and radiating dyke swarms, coronae and novae, and mid-crustal intrusive complexes. Gondwana Research, 100, 25-43.

Buchan, K. L., Card, K. D., & Chandler, F. W. (1989). Multiple ages of Nipissing Diabase intrusion: paleomagnetic evidence from the Englehart area, Ontario. Canadian Journal of Earth Sciences, 26(3), 427-445.

Buchan, K. L., Goutier, J., Hamilton, M. A., Ernst, R. E., & Matthews, W. A. (2007). Paleomagnetism, U–Pb geochronology, and geochemistry of Lac Esprit and other dyke swarms, James Bay area, Quebec, and implications for Paleoproterozoic deformation of the Superior Province. Canadian Journal of Earth Sciences, 44(5), 643-664.

Buchan, K. L., Harris, B. A., Ernst, R. E., & Hanes, J. A. (2003). Ar–Ar dating of the Pickle Crow diabase dyke in the western Superior craton of the Canadian Shield of Ontario and implications for a possible plume centre associated with ca. 1880 Ma Molson magmatism of Manitoba. In: Abstracts Volume 28. Annual meeting of the Geological Association of Canada–Mineralogical Association of Canada–Society of Economic Geologists, 25-28 Mai 2003, Vancouver, British Columbia, 17.

Buchan, K. L., Mortensen, J. K., & Card, K. D. (1993). Northeast-trending Early Proterozoic dykes

of southern Superior Province: multiple episodes of emplacement recognized from integrated paleomagnetism and U–Pb geochronology. Canadian Journal of Earth Sciences, 30(6), 1286-1296.

Buchan, K. L., Mortensen, J. K., Card, K. D., & Percival, J. A. (1998). Paleomagnetism and U-Pb geochronology of diabase dyke swarms of Minto block, Superior Province, Quebec, Canada. Canadian Journal of Earth Sciences, 35(9), 1054-1069.

Bucher, K., & Frey, M. (2002). Petrogenesis of Metamorphic Rocks. 7th edition, Springer Verlag, Heidelberg and Berlin, 341p.

Bursztyn, N. E., & Olivo, G. R. (2010). PGE-rich Ni-Cu sulfide mineralization in the Flin Flon greenstone belt, Manitoba, Canada: Implications for hydrothermal remobilization of platinum group elements in basic-ultrabasic sequences. Economic Geology, 105(8), 1469-1490.

Butler, H. R. (1994). Lineament analysis of the Sudbury multiring impact structure. In: Dressler, B. O., Grieve, R. A. F., Sharpton, V. L. (eds.), Large Meteorite Impacts and Planetary Evolution. Geological Society of America, Special Paper 293, 319-330.

Cabri, L. J. (2002). The platinum-group minerals. In: Cabri, L. J. (ed.), The geology, geochemistry, mineralogy and mineral beneficiation of platinum-group elements. Canadian Institute of Mining, Metallurgy and Petroleum, Special Volume 54, 13-130.

Cabri, L. J., & Laflamme, J. G. (1976). The mineralogy of the platinum-group elements from some copper-nickel deposits of the Sudbury area, Ontario. Economic Geology, 71(7), 1159-1195.

Cabri, L. J., Laflamme, J. G., & Stewart, J. M. (1973). Temagamite, a new palladium-mercury telluride from the Temagami copper deposit, Ontario, Canada. The Canadian Mineralogist, 12(3), 193-198.

Campbell, I. H. (1985). The difference between oceanic and continental tholeiites: a fluid dynamic explanation. Contributions to Mineralogy and Petrology, 91(1), 37-43.

Campbell, I. H. (2007). Testing the plume theory. Chemical Geology, 241(3-4), 153-176.

Campbell, I. H., Lesher, C. M., Coad, P., Franklin, J. M., Gorton, M. P., & Thurston, P. C. (1984). Rare-earth element mobility in alteration pipes below massive Cu-Zn-sulfide deposits. Chemical Geology, 45(3-4), 181-202.

Candela, P. A. (1997). A Review of Shallow, Ore-related Granites: Textures, Volatiles, and Ore Metals. Journal of Petrology, 38(12), 1619-1633.

Caquineau, T., Paquette, J. L., & Philippot, P. (2018). U-Pb detrital zircon geochronology of the Turee Creek Group, Hamersley Basin, Western Australia: timing and correlation of the Paleoproterozoic glaciations. Precambrian Research, 307, 34-50.

Card, K. D. (1965). The Croker Island complex. Ontario Department of Mines, Geological Circular No. 14, 11p.

Card, K. D. (1978). Metamorphism of the Middle Precambrian (Aphebian) rocks of the eastern Southern Province. In: Fraser, J. A., Heywood, W. W. (eds.), Metamorphism in the Canadian

Shield. Geological Survey of Canada, Paper 78-10, 269-282.

Card, K. D. (1979). Regional geological synthesis, central Superior Province. Current Research, part A. Geological Survey of Canada, Paper 79-1A, 87-90.

Card, K. D. (1990). A review of the Superior Province of the Canadian Shield, a product of Archean accretion. Precambrian Research, 48(1-2), 99-156.

Card, K. D., & Innes, D. G. (1991). Geology of the Benny area, District of Sudbury. Ontario Geological Survey, Report 206, 117p.

Card, K. D., & Pattison, E. F. (1973). Nipissing diabase of the Southern Province, Ontario. In: Young, G. M. (ed.), Huronian Stratigraphy and Sedimentation. Geological Association of Canada, Special Paper 12, 7-30.

Card, K. D., Gupta, V. K., McGrath, P. H., & Grant, F. S. (1984). The Sudbury structure: Its regional geological and geophysical setting. In: Pye, E. G., Naldrett, A. J., Giblin, P. E. (eds.), The Geology and Ore Deposits of the Sudbury Structure. Ontario Geological Survey, Special Volume 1, 25-43.

Censi, P., Sprovieri, M., Saiano, F., Di Geronimo, S. I., Larocca, D., & Placenti, F. (2007). The behaviour of REEs in Thailand's Mae Klong estuary: Suggestions from the Y/Ho ratios and lanthanide tetrad effects. Estuarine, Coastal and Shelf Science, 71(3-4), 569-579.

Chamberlain, K. R., & Bowring, S. A. (2001). Apatite–feldspar U–Pb thermochronometer: a reliable, mid-range (~450°C), diffusion-controlled system. Chemical Geology, 172(1-2), 173-200.

Charoy, B., & Pollard, P. J. (1989). Albite-rich, silica-depleted metasomatic rocks at Emuford, Northeast Queensland; mineralogical, geochemical, and fluid inclusion constraints on hydrothermal evolution and tin mineralization. Economic Geology, 84(7), 1850-1874.

Cherniak, D. J. (1993). Lead diffusion in titanite and preliminary results on the effects of radiation damage on Pb transport. Chemical Geology, 110(1-3), 177-194.

Cherniak, D. J. (2010). Diffusion in accessory minerals: zircon, titanite, apatite, monazite and xenotime. Reviews in Mineralogy and Geochemistry, 72(1), 827-869.

Cherniak, D. J., & Watson, E. B. (2001). Pb diffusion in zircon. Chemical Geology, 172(1-2), 5-24.

Cherniak, D. J., Lanford, W. A., & Ryerson, F. J. (1991). Lead diffusion in apatite and zircon using ion implantation and Rutherford backscattering techniques. Geochimica et Cosmochimica Acta, 55(6), 1663-1673.

Chew, D. M., Petrus, J. A., & Kamber, B. S. (2014). U–Pb LA–ICPMS dating using accessory mineral standards with variable common Pb. Chemical Geology, 363, 185-199.

Chew, D. M., Sylvester, P. J., & Tubrett, M. N. (2011). U–Pb and Th–Pb dating of apatite by LA-ICPMS. Chemical Geology, 280(1-2), 200-216.

Christoffersen, P. (2017). Stable Cu, Fe, and Ni isotopic systematics of the Sudbury offset dikes and associated rocks. Unpublished MSc thesis, The University of Western Ontario, London, Ontario, Canada, 111p., Electronic Thesis and Dissertation Repository 5179,

https://ir.lib.uwo.ca/etd/5179

Christopher, A. (1992). Assessment Report on the Exploration Program on the Emerald Lake Property, Sheppard and McCarthy Townships, Ontario. Unpublished report, prepared for Teck Exploration Ltd., 106p., Ontario Assessment File Database record number 41I16NW0061.

Chubb, P. T., Vogel, D. C., Peck, D. C., James, R. S., & Keays, R. R. (1994). Occurrences of pseudotachylyte at the East Bull Lake and Shakespeare-Dunlop intrusions, Ontario, Canada. Canadian Journal of Earth Sciences, 31(12), 1744-1748.

Ciborowski, T. J. R. (2013). The geochemistry and petrogenesis of the early Proterozoic Matachewan Large Igneous Province. Unpublished PhD thesis, Cardiff University, United Kingdom, 461p., http://orca.cardiff.ac.uk/id/eprint/51146

Ciborowski, T. J. R., Kerr, A. C., Ernst, R. E., McDonald, I., Minifie, M. J., Harlan, S. S., & Millar, I. L. (2015). The Early Proterozoic Matachewan large igneous province: geochemistry, petrogenesis, and implications for Earth evolution. Journal of Petrology, 56(8), 1459-1494.

Ciborowski, T. J. R., Minifie, M. J., Kerr, A. C., Ernst, R. E., Baragar, B., & Millar, I. L. (2017). A mantle plume origin for the Palaeoproterozoic Circum-Superior Large Igneous Province. Precambrian Research, 294, 189-213.

Clark, F. W., & Catlett, C. (1889). A platinoferrous nickel ore from Canada, Laspeyres's (sic) polydymite. American Journal of Science, 37, 372-374.

Class, C., & Goldstein, S. L. (1997). Plume-lithosphere interactions in the ocean basins: constraints from the source mineralogy. Earth and Planetary Science Letters, 150(3-4), 245-260.

Clemens, J. D. (2003). S-type granitic magmas – petrogenetic issues, models and evidence. Earth-Science Reviews, 61(1-2), 1-18.

Clendenen, W. S., Kligfield, R., Hirt, A. M., & Lowrie, W. (1988). Strain studies of cleavage development in the Chelmsford Formation, Sudbury Basin, Ontario. Tectonophysics, 145(3-4), 191-211.

Cochrane, L. B. (1984). Ore deposits of the Copper Cliff offset. In: Pye, E. G., Naldrett, A. J., Giblin, P. E. (eds.), The Geology and Ore Deposits of the Sudbury Structure. Ontario Geological Survey, Special Volume 1, 347-361.

Cochrane, R., Spikings, R. A., Chew, D., Wotzlaw, J. F., Chiaradia, M., Tyrrell, S., ... & Van der Lelij, R. (2014). High temperature (> 350 °C) thermochronology and mechanisms of Pb loss in apatite. Geochimica et Cosmochimica Acta, 127, 39-56.

Cohen, A. S., Burnham, O. M., Hawkesworth, C. J., & Lightfoot, P. C. (2000). Pre-emplacement Re–Os ages from ultramafic inclusions in the sublayer of the Sudbury Igneous Complex, Ontario. Chemical Geology, 165(1-2), 37-46.

Coleman, A. P. (1889). Notes on the petrology of Ontario. Ontario Bureau of Mines, Annual Report No. 7, part 2, 107-145.

Coleman, A. P. (1903). The Sudbury nickel deposits. Ontario Bureau of Mines Report for 1902, 235-303.

Coleman, A. P. (1908). The lower Huronian ice age. The Journal of Geology, 16(2), 149-158.

Coles, R. L., Haines, G. V., & Hannaford, W. (1981). Broad-scale magnetic anomalies over central and eastern Canada: a discussion. Canadian Journal of Earth Sciences, 18(3), 657-661.

Collins, G. S., Patel, N., Davidson, T. M., Rae, A. S., Morgan, J. V., Gulick, S. P., IODP-ICDP Expedition 364 Science Party, & Third-Party Scientists (2020). A steeply-inclined trajectory for the Chicxulub impact. Nature Communications, 11, 1480.

Coltorti, M., Bonadiman, C., Hinton, R. W., Siena, F., & Upton, B. G. J. (1999). Carbonatite metasomatism of the oceanic upper mantle: evidence from clinopyroxenes and glasses in ultramafic xenoliths of Grande Comore, Indian Ocean. Journal of Petrology, 40(1), 133-165.

Condie, K. C., Bobrow, D. J., & Card, K. D. (1987). Geochemistry of Precambrian mafic dykes from the southern Superior Province of the Canadian Shield. In: Halls, H. C., Fahrig, W. F. (eds.), Mafic Dyke Swarms. Geological Association of Canada, Special Paper, 34, 95-108.

Conrod, D. M. (1989). The petrology and geochemistry of the Duncan Lake, Beaton Bay, Milner Lake, and Miller Lake Nipissing intrusions within the Gowganda area, District of Timiskaming. Ontario Geological Survey, Open File Report 5701, 210p.

Corfu, F., & Andrews, A. J. (1986). A U–Pb age for mineralized Nipissing diabase, Gowganda, Ontario. Canadian Journal of Earth Sciences, 23(1), 107-109.

Corfu, F., & Easton, R. M. (2001). U–Pb evidence for polymetamorphic history of Huronian rocks within the Grenville front tectonic zone east of Sudbury, Ontario, Canada. Chemical Geology, 172(1-2), 149-171.

Corfu, F., & Lightfoot, P. C. (1996). U-Pb geochronology of the sublayer environment, Sudbury Igneous Complex, Ontario. Economic Geology, 91(7), 1263-1269.

Corfu, F., & Stone, D. (1998). The significance of titanite and apatite U-Pb ages: constraints for the post-magmatic thermal-hydrothermal evolution of a batholithic complex, Berens River area, northwestern Superior Province, Canada. Geochimica et Cosmochimica Acta, 62(17), 2979-2995.

Coulter, A. B. (2015). Recent discoveries in the Ni-Cu-PGE bearing Trill and Parkin offset dykes, Sudbury impact structure, Canada. Unpublished MSc thesis, The University of Western Ontario, London, Ontario, Canada, 152p., Electronic Thesis and Dissertation Repository 3473, https://ir.lib.uwo.ca/etd/3473

Coulter, A. B., Osinski, G. R., Bailey, J. M., Péntek, A., & Smith, D. A. (2014). Temperature constraints during emplacement of the Parkin Offset Dyke, Sudbury impact structure, Ontario. In: GCA-MAC/AGC-AMC Joint Annual Meeting, 21-23 May 2014, Fredericton, New Brunswick, Canada, Abstracts Volume 37, 65-66.

Craddock, J. P., Anziano, J., Wirth, K., Vervoort, J. D., Singer, B., & Zhang, X. (2007). Structure, geo-

chemistry and geochronology of a penokean lamprophyre dike swarm, Archean Wawa Terrane, Little Presque Isle, Michigan, USA. Precambrian Research, 157(1-4), 50-70.

Craig, J. R. (1971). Violarite stability relations. American Mineralogist, 56(7-8), 1303-1311.

Craig, J. R., & Kullerud, G. (1969). Phase relations in the Cu-Fe-Ni-S system and their application to magmatic ore deposits. Economic Geology Monograph, 4, 344-358.

Craven, J. A., Boerner, D. E., Kurtz, R. D., Stevens, K., & Watts, A. (1998). Magnetotelluric and 2-D seismic investigation over the Temagami Lake magnetic anomaly. In: SEG Technical Program Expanded Abstracts (1998). 68th Annual Meeting of the Society of Exploration Geophysicists, 13-18 September 1998, New Orleans, Louisiana, USA, 764-767, https://doi.org/10.1190/1.1820586

Dai, L. Q., Zhao, Z. F., Zheng, Y. F., An, Y. J., & Zheng, F. (2017). Geochemical distinction between carbonate and silicate metasomatism in generating the mantle sources of alkali basalts. Journal of Petrology, 58(5), 863-884.

Daly, T. R., & Schultz, P. H. (2018). The delivery of water by impacts from planetary accretion to present. Science Advances, 4(4), eaar2632.

Danyushevsky, L. V. (2001). The effect of small amounts of H_2O on crystallisation of mid-ocean ridge and backarc basin magmas. Journal of Volcanology and Geothermal Research, 110(3-4), 265-280.

Danyushevsky, L. V., & Plechov, P. (2011). Petrolog3: Integrated software for modeling crystallization processes. Geochemistry, Geophysics, Geosystems, 12(7), Q07021.

Dare, S. A., Barnes, S. J., & Beaudoin, G. (2012). Variation in trace element content of magnetite crystallized from a fractionating sulfide liquid, Sudbury, Canada: Implications for provenance discrimination. Geochimica et Cosmochimica Acta, 88, 27-50.

Dare, S. A., Barnes, S. J., Prichard, H. M., & Fisher, P. C. (2014). Mineralogy and geochemistry of Cu-rich ores from the McCreedy East Ni-Cu-PGE deposit (Sudbury, Canada): Implications for the behavior of platinum group and chalcophile elements at the end of crystallization of a sulfide liquid. Economic Geology, 109(2), 343-366.

Darling, J. R., Hawkesworth, C. J., Lightfoot, P. C., Storey, C. D., & Tremblay, E. (2010a). Isotopic heterogeneity in the Sudbury impact melt sheet. Earth and Planetary Science Letters, 289(3-4), 347-356.

Darling, J. R., Hawkesworth, C. J., Storey, C. D., & Lightfoot, P. C. (2010b). Shallow impact: Isotopic insights into crustal contributions to the Sudbury impact melt sheet. Geochimica et Cosmochimica Acta, 74(19), 5680-5696.

Dasgupta, R., Hirschmann, M. M., & Smith, N. D. (2007). Partial melting experiments of peridotite+ CO_2 at 3 GPa and genesis of alkalic ocean island basalts. Journal of Petrology, 48(11), 2093-2124.

Dasti, I. (2014). The geochemistry and petrogenesis of the Ni-Cu-PGE Shakespeare deposit, Ontario, Canada. Unpublished MSc thesis, Lakehead University, Thunder Bay, Ontario, Canada,

233p., http://knowledgecommons.lakeheadu.ca/handle/2453/659

Davey, S., Bleeker, W., Kamo, S. L., Davis, D. W., Easton, R. M., & Sutcliffe, R. H. (2019). Ni-Cu-PGE potential of the Nipissing sills as part of the ca. 2.2 Ga Ungava large igneous province. In: Rogers, N. (ed.), Targeted Geoscience Initiative: 2018 report of activities. Geological Survey of Canada, Open File Report 8549, 403-419.

Davidson, A. (1986). Grenville front relationships near Killarney, Ontario. In: Moore, J. M., Davidson, A., Baer, A. J. (eds.), The Grenville Province. Geological Association of Canada, Special Paper 31, 107-117.

Davidson, A., & Van Breemen, O. (1994). U-Pb ages of granites near the Grenville Front, Ontario. Radiogenic Age and Isotope Studies: Report 8. Geological Survey of Canada, Current Research 1994-F, 107-114.

Davidson, A., Van Breemen, O., & Sullivan, R. W. (1992). Circa 1.75 Ga ages for plutonic rocks from the Southern Province and adjacent Grenville Province: what is the expression of the Penokean orogeny? In: Radiogenic Age and Isotopic Studies, Report 6. Geological Survey of Canada, Paper 92-2, 107-118.

Davis, D. W. (2008). Sub-million-year age resolution of Precambrian igneous events by thermal extraction–thermal ionization mass spectrometer Pb dating of zircon: Application to crystallization of the Sudbury impact melt sheet. Geology, 36(5), 383-386.

Dawson, J. B., & Smith, J. V. (1982). Upper-mantle amphiboles: a review. Mineralogical Magazine, 45(337), 35-46.

Dawson, J. B., & Smith, J. V. (1988). Metasomatised and veined upper-mantle xenoliths from Pello Hill, Tanzania: evidence for anomalously-light mantle beneath the Tanzanian sector of the East African Rift Valley. Contributions to Mineralogy and Petrology, 100(4), 510-527.

de Kock, G. S., Eglington, B., Armstrong, R. A., Harmer, R. E., & Walraven, F. (2000). U–Pb and Pb–Pb ages of the Naauwpoort rhyolite, Kawakeup leptite and Okongava Diorite: implications for the onset of rifting and of orogenesis in the Damara belt, Namibia. Communications of the Geological Survey of Namibia, 12, 81-88.

DePaolo, D. J. (1981a). Neodymium isotopes in the Colorado Front Range and crust–mantle evolution in the Proterozoic. Nature, 291(5812), 193-196.

DePaolo, D. J. (1981b). A neodymium and strontium isotopic study of the Mesozoic calc-alkaline granitic batholiths of the Sierra Nevada and Peninsular Ranges, California. Journal of Geophysical Research: Solid Earth, 86(B11), 10470-10488.

DePaolo, D. J. (1981c). Trace element and isotopic effects of combined wallrock assimilation and fractional crystallization. Earth and Planetary Science Letters, 53(2), 189-202.

DePaolo, D. J. (1988). Age dependence of the composition of continental crust: evidence from Nd isotopic variations in granitic rocks. Earth and Planetary Science Letters, 90(3), 263-271.

DePaolo, D. J., & Wasserburg, G. J. (1976a). Inferences about magma sources and mantle structure from variations of $^{143}Nd/^{144}Nd$. Geophysical Research Letters, 3(12), 743-746.

DePaolo, D. J., & Wasserburg, G. J. (1976b). Nd isotopic variations and petrogenetic models. Geophysical Research Letters, 3(5), 249-252.

DePaolo, D. J., & Wasserburg, G. J. (1979). Sm-Nd age of the Stillwater Complex and the mantle evolution curve for neodymium. Geochimica et Cosmochimica Acta, 43(7), 999-1008.

Desharnais, G. (2005). Geochemical and Isotopic Investigation of Magmatism in the Fox River Belt: Tectonic and Economic Implications. Unpublished PhD thesis, University of Manitoba, Winnipeg, Manitoba, Canada, 207p., http://hdl.handle.net/1993/8597

Desharnais, G., Peck, D. C., Theyer, P., Potter, L., Huminicki, M., Scoates, R. F. J., ... & Kohut, G. (2000). Geology and mineral occurrences of the Fox River sill in the Great Falls area, Fox River Belt (part of NTS 53M/16). In: Report of Activities 2000, Manitoba Industry, Trade and Mines. Manitoba Geological Survey, 42-48.

Deutsch, A. (1994). Isotope systematics support the impact origin of the Sudbury structure (Ontario, Canada). In: Dressler, B. O., Grieve, R. A. F., Sharpton, V. L. (eds.), Large Meteorite Impacts and Planetary Evolution. Geological Society of America, Special Paper 293, 289-302.

Deutsch, A., & Schärer, U. (1990). Isotope systematics and shock-wave metamorphism: I. U-Pb in zircon, titanite and monazite, shocked experimentally up to 59 GPa. Geochimica et Cosmochimica Acta, 54(12), 3427-3434.

Deutsch, A., Grieve, R. A. F., Avermann, M., Bischoff, L., Brockmeyer, P., Buhl, D., ... & Stöffler, D. (1995). The Sudbury structure (Ontario, Canada): A tectonically deformed multi-ring impact basin. Geologische Rundschau, 84(4), 697-709.

Dickin, A. P. (2010). Scientific comment on “Isotopic heterogeneity in the Sudbury impact melt sheet” [EPSL 289 (2010) 347-356]. Earth and Planetary Science Letters, 299(3-4), 434-435.

Dickin, A. P., Artan, M. A., & Crocket, J. H. (1996). Isotopic evidence for distinct crustal sources of North and South Range ores, Sudbury Igneous Complex. Geochimica et Cosmochimica Acta, 60(9), 1605-1613.

Dickin, A. P., Nguyen, T., & Crocket, J. H. (1999). Isotopic evidence for a single impact melting origin of the Sudbury Igneous Complex. In: Dressler, B. O., Sharpton, V. L. (eds.), Large Meteorite Impacts and Planetary Evolution II. Geological Society of America, 339, 361-371.

Dickin, A. P., Richardson, J. M., Crocket, J. H., McNutt, R. H., & Peredery, W. V. (1992). Osmium isotope evidence for a crustal origin of platinum group elements in the Sudbury nickel ore, Ontario, Canada. Geochimica et Cosmochimica Acta, 56(9), 3531-3537.

Dietz, R. S. (1964). Sudbury structure as an astrobleme. The Journal of Geology, 72(4), 412-434.

Di Toro, G., & Pennacchioni, G. (2004). Superheated friction-induced melts in zones pseudotachylytes within the Adamello tonalites (Italian Southern Alps). Journal of Structural Geology, 26(10), 1783-1801.

Dixon, J., Clague, D. A., Cousens, B., Monsalve, M. L., & Uhl, J. (2008). Carbonatite and silicate melt metasomatism of the mantle surrounding the Hawaiian plume: Evidence from volatiles,

trace elements, and radiogenic isotopes in rejuvenated-stage lavas from Niihau, Hawaii. Geochemistry, Geophysics, Geosystems, 9(9).

Djon, M. L. N., & Barnes, S. J. (2012). Changes in sulfides and platinum-group minerals with the degree of alteration in the Roby, Twilight, and High Grade Zones of the Lac des Iles Complex, Ontario, Canada. Mineralium Deposita, 47(8), 875-896.

Dobson, D. P., Crichton, W. A., Vocădlo, L., Jones, A. P., Wang, Y., Uchida, T., Rivers, M., Sutton, S., & Brodholt, J. P. (2000). In situ measurement of viscosity of liquids in the Fe-FeS system at high pressures and temperatures. American Mineralogist, 85(11-12), 1838-1842.

Dodson, M. H. (1973). Closure temperature in cooling geochronological and petrological systems. Contributions to Mineralogy and Petrology, 40(3), 259-274.

Donaldson, C. H. (1976). An experimental investigation of olivine morphology. Contributions to mineralogy and Petrology, 57(2), 187-213.

Doucelance, R., Hammouda, T., Moreira, M., & Martins, J. C. (2010). Geochemical constraints on depth of origin of oceanic carbonatites: the Cape Verde case. Geochimica et Cosmochimica Acta, 74(24), 7261-7282.

Downes, H. (2001). Formation and modification of the shallow sub-continental lithospheric mantle: a review of geochemical evidence from ultramafic xenolith suites and tectonically emplaced ultramafic massifs of western and central Europe. Journal of Petrology, 42(1), 233-250.

Dowsett, J. S. (1970). Geophysical exploration methods for nickel. In: Morley, L. W. (ed.), Mining and Groundwater Geophysics/1967. Geological Survey of Canada, Economic Geology Report 26, 310-321.

Dressler, B. O. (1981a). Otter Lake, Sudbury District. Ontario Geological Survey, Precambrian Geology Series, Map 2450, scale 1:31680.

Dressler, B. O. (1981b). Massey Bay, Sudbury District. Ontario Geological Survey, Precambrian Geology Series, Map 2451, scale 1:31680.

Dressler, B. O. (1982). Geology of the Wanapitei Lake Area, District of Sudbury. Ontario Geological Survey, Report 213, 131p.

Dressler, B. O. (1984). The Effects of the Sudbury Event and the Intrusion of the Sudbury Igneous Complex on the Footwall Rocks of the Sudbury Structure. In: Pye, E. G., Naldrett, A. J., Giblin, P. E. (eds.), The Geology and Ore Deposits of the Sudbury Structure. Ontario Geological Survey, Special Volume 1, 97-138.

Dressler, B. O. (1986). Geology of the Chiniguchi Lake area, District of Sudbury. Ontario Geological Survey, Report 242, 19p.

Dressler, B. O., & Reimold, W. U. (2001). Terrestrial impact melt rocks and glasses. Earth-Science Reviews, 56(1-4), 205-284.

Dreuse, R., Doman, D., Santimano, T., & Riller, U. (2010). Crater floor topography and impact melt

sheet geometry of the Sudbury impact structure, Canada. Terra Nova, 22(6), 463-469.

Dudàs, F. O., Davidson, A., & Bethune, K. M. (1994). Age of the Sudbury diabase dykes and their metamorphism in the Grenville Province, Ontario. Radiogenic Age and Isotopic Studies: Report 8. Geological Survey of Canada, Current Research 1994-F, 97-106.

Dupuis, L., Whitehead, R. E. S., & Davies, J. F. (1982). Evidence for a genetic link between Sudbury breccias and fenite breccias. Canadian Journal of Earth Sciences, 19(6), 1174-1184.

Dupuis, L., Whitehead, R. E. S., & Davies, J. F. (1990). Alkali gabbro fragments in Sudbury breccia. Canadian Journal of Earth Sciences, 27(6), 784-786.

Dupuy, C., Liotard, J. M., & Dostal, J. (1992). Zr/Hf fractionation in intraplate basaltic rocks: carbonate metasomatism in the mantle source. Geochimica et Cosmochimica Acta, 56(6), 2417-2423.

Duran, C. J., Barnes, S. J., & Corkery, J. T. (2016). Geology, petrography, geochemistry, and genesis of sulfide-rich pods in the Lac des Iles palladium deposits, western Ontario, Canada. Mineralium Deposita, 51(4), 509-532.

Duran, C. J., Barnes, S. J., Pleše, P., Prašek, M. K., Zientek, M. L., & Pagé, P. (2017). Fractional crystallization-induced variations in sulfides from the Noril'sk-Talnakh mining district (polar Siberia, Russia). Ore Geology Reviews, 90, 326-351.

Dyer, R. D., Takats, P. A., & Felix, V. E. (2004). Sudbury area lake sediment geochemical survey. Ontario Geological Survey, Open File Report 6216, 106p.

Easton, R. M. (1992). The Grenville Province and the Proterozoic history of central and southern Ontario. In: Thurston, P. C., Williams, H. R., Sutcliffe, R. H., Stott, G. M. (eds.), Geology of Ontario Part 2. Ontario Geological Survey, Special Volume 4, 715-904.

Easton, R. M. (2000). Metamorphism of the Canadian shield, Ontario, Canada. II. Proterozoic metamorphic history. The Canadian Mineralogist, 38(2), 319-344.

Easton, R. M. (2002). Geology of mafic intrusions of Flett and Angus townships, Grenville Province. Ontario Geological Survey, Open File Report 6090, 70p.

Easton, R. M., James, R. S., & Jobin-Bevans, L. S. (2010). Geological guidebook to the Paleoproterozoic East Bull Lake intrusive suite plutons at East Bull Lake, Agnew Lake and River Valley: a field trip for the 11th International Platinum Symposium. Ontario Geological Survey, Open File Report 6253, 108p.

Easton, R. M., Rainsford, D. R. B., & Préfontaine, S. (2020). Preliminary Interpretation of the Sturgeon River Aeromagnetic Survey, Northeastern Ontario. In: Easton, R. M., Préfontaine, S., Hamilton, S. M., Rainsford, D. R. B., Burnham, O. M., Duguet, M., Hechler, J. H., Dyer, R. D. (eds.), Summary of Field Work and Other Activities, 2020. Ontario Geological Survey, 6370, 6-1 to 6-15.

Eaton, D. W., & Darbyshire, F. (2010). Lithospheric architecture and tectonic evolution of the Hudson Bay region. Tectonophysics, 480(1-4), 1-22.

Edgar, A. D. (1986). Petrology, Geochemistry and Economic Potential of the Nipissing Diabase. Ontario Geological Survey, Open File Report 5573, 42p.

Eichelberger, J. C., Izbekov, P. E., & Browne, B. L. (2006). Bulk chemical trends at arc volcanoes are not liquid lines of descent. Lithos, 87(1-2), 135-154.

Engvik, A. K., Putnis, A., Fitz Gerald, J. D., & Austrheim, H. (2008). Albitization of granitic rocks: the mechanism of replacement of oligoclase by albite. The Canadian Mineralogist, 46(6), 1401-1415.

Ernst, R. E. (1994). Mapping the magma flow pattern in the Sudbury dyke swarm in Ontario using magnetic fabric analysis. Geological Survey of Canada, Current Research 1994-E, 183-192.

Ernst, R. E. (2014). Large Igneous Provinces. 1st edition, Cambridge University Press, Cambridge, UK, 666p.

Ernst, R. E., & Bell, K. (2010). Large igneous provinces (LIPs) and carbonatites. Mineralogy and Petrology, 98(1), 55-76.

Ernst, R. E., & Bleeker, W. (2010). Large igneous provinces (LIPs), giant dyke swarms, and mantle plumes: significance for breakup events within Canada and adjacent regions from 2.5 Ga to the Present. Canadian Journal of Earth Sciences, 47(5), 695-739.

Ernst, R. E., & Buchan, K. L. (2010). Geochemical database of Proterozoic intraplate mafic magmatism in Canada. Geological Survey of Canada, Open File 6016, 1 CD-ROM.

Ernst, R. E., Liikane, D. A., Jowitt, S. M., Buchan, K. L., & Blanchard, J. A. (2019). A new plumbing system framework for mantle plume-related continental Large Igneous Provinces and their mafic-ultramafic intrusions. Journal of Volcanology and Geothermal Research, 384, 75-84.

Exner, C. (1949). Tektonik, Feldspatausbildung und deren gegenseitige Beziehungen in den östlichen Hohen Tauern. Tschermak's Mineralogische und Petrographische Mitteilungen, xxx, 197-284.

Faggart, B. E., Basu, A. R., & Tatsumoto, M. (1985). Origin of the Sudbury Complex by meteoritic impact: Neodymium isotopic evidence. Science, 230(4724), 436-439.

Fahrig, W. F., & Wanless, R. K. (1963). Age and significance of diabase dyke swarms of the Canadian Shield. Nature, 200(4910), 934-937.

Farmer, G. L. (2013). Continental Basaltic Rocks. In: Turekian, K. K., Holland, H. D. (eds.), Treatise on Geochemistry. 2nd edition, Elsevier Science, Volume 4, 75-110.

Farrow, C. E., & Watkinson, D. H. (1997). Diversity of precious-metal mineralization in footwall Cu-Ni-PGE deposits, Sudbury, Ontario; implications for hydrothermal models of formation. The Canadian Mineralogist, 35(4), 817-839.

Farrow, C. E., Everest, J. O., King, D. M., & Jolette, C. (2005). Sudbury Cu-(Ni)-PGE systems: Refining the classification using McCreedy West mine and Podolsky project case studies. In:

Mungall, J. E. (ed.), Accelerating the world's research. Exploration for Platinum-Group Elements Deposits, 6-7 August 2005, Oulu, Finland, Mineralogical Association of Canada, Short Course Series Volume 35, 163-180.

Faure, G. (1986). Principles of Isotope Geology. 2nd edition, John Wiley & Sons, New York, 589p.

Fedo, C. M., Young, G. M., Nesbitt, H. W., & Hanchar, J. M. (1997). Potassic and sodic metasomatism in the southern province of the Canadian Shield: evidence from the Paleoproterozoic Serpent Formation, Huronian Supergroup, Canada. Precambrian Research, 84(1-2), 17-36.

Fedorowich, J. S., Golightly, J. P., & Rousell, D. H. (2009). Breccias in the Footwall. In: Rousell, D. H., Brown, G. H. (eds.), A Field Guide to the Geology of Sudbury, Ontario. Ontario Geological Survey, Open File Report 6243, 45-55.

Fedorowich, J. S., Parrish, R. R., & Sager-Kinsman, A. (2006). U-Pb dating of a diabase dike resolves the problem of mutually crosscutting relationships within the Fraser-Strathcona Deep Copper vein system, Sudbury basin. Economic Geology, 101(8), 1595-1603.

Ferguson, I., Epp, D., Saturnino, T., Orellana, M., Craven, J. A., & Jones, A. (2015). Interpretation of resistivity and magnetic anomalies from the Fox River Sill, Trans Hudson Orogen, Canada. In: ASEG Extended Abstracts (2015). 24th International Geophysical Conference and Exhibition – Geophysics and Geology Together for Discovery, 15-18 February 2015, Perth, Australia, volume 1, 1-5, https://doi.org/10.1071/ASEG2015ab066

Finn, G. C., & Edgar, A. D. (1986). The Wanapitei intrusion, northeastern Ontario: an Example of a Mafic Intrusion with Cycles of Reverse Differentiation. Neues Jahrbuch für Mineralogie Abhandlungen, 154(1), 75-91.

Finn, G. C., Edgar, A. D., & Rowell, W. F. (1982). Petrology, Geochemistry, and Economic Potential of the Nipissing Diabase; Grant 100. In: Pye, E. G. (ed.), Geoscience Research Grant Program, Summary of Research 1981-1982. Ontario Geological Survey, Miscellaneous Paper 103, 43-57.

Fitton, J. G., & Dunlop, H. M. (1985). The Cameroon line, West Africa, and its bearing on the origin of oceanic and continental alkali basalt. Earth and Planetary Science Letters, 72(1), 23-38.

Fleet, M. E. (1979). Tectonic origin for Sudbury, Ontario, shatter cones. Geological Society of America Bulletin, 90(12), 1177-1182.

Fleet, M. E., & Barnett, R. L. (1978). Al iv/Al vi partitioning in calciferous amphiboles from the Frood Mine, Sudbury, Ontario. The Canadian Mineralogist, 16(4), 527-532.

Fleet, M. E., Barnett, R. L., & Morris, W. A. (1987). Prograde metamorphism of the Sudbury igneous complex. The Canadian Mineralogist, 25(3), 499-514.

Floyd, P. A., & Winchester, J. A. (1975). Magma type and tectonic setting discrimination using immobile elements. Earth and Planetary Science Letters, 27(2), 211-218.

Foley, S. F. (1991). High-pressure stability of the fluor-and hydroxy-endmembers of pargasite and K-richterite. Geochimica et Cosmochimica Acta, 55(9), 2689-2694.

Foley, S. F. (1992). Vein-plus-wall-rock melting mechanisms in the lithosphere and the origin of potassic alkaline magmas. Lithos, 28(3-6), 435-453.

Foley, S. F. (2008). Rejuvenation and erosion of the cratonic lithosphere. Nature Geoscience, 1(8), 503-510.

Foley, S. F., & Fischer, T. P. (2017). An essential role for continental rifts and lithosphere in the deep carbon cycle. Nature Geoscience, 10(12), 897-902.

Fölling, P. G., Zartman, R. E., & Frimmel, H. E. (2000). A novel approach to double-spike Pb–Pb dating of carbonate rocks: examples from Neoproterozoic sequences in southern Africa. Chemical Geology, 171(1-2), 97-122.

Fonseca, R. O., Campbell, I. H., O'Neill, H. S. C., & Fitzgerald, J. D. (2008). Oxygen solubility and speciation in sulphide-rich mattes. Geochimica et Cosmochimica Acta, 72(11), 2619-2635.

Fourie, F. D., Huber, M. S., & Kovaleva, E. (2019). Geophysical characterization of the Daskop granophyre dyke and surrounding host rocks, Vredefort impact structure, South Africa. Meteoritics & Planetary Science, 54(7), 1579-1593.

French, B. M. (1967). Sudbury structure, Ontario: Some petrographic evidence for origin by meteorite impact. Science, 156(3778), 1094-1098.

French, B. M. (1998). Traces of Catastrophe: A Handbook of Shock-Metamorphic Effects in Terrestrial Meteorite Impact Structures. 1st edition, Lunar and Planetary Institute, Houston, Texas, 120p. (LPI Contribution No. 954).

French, J. E., Heaman, L. M., Chacko, T., & Srivastava, R. K. (2008). 1891–1883 Ma Southern Bastar–Cuddapah mafic igneous events, India: A newly recognized large igneous province. Precambrian Research, 160(3-4), 308-322.

Frey, F. A., Garcia, M. O., Wise, W. S., Kennedy, A., Gurriet, P., & Albarède, F. (1991). The evolution of Mauna Kea volcano, Hawaii: petrogenesis of tholeiitic and alkalic basalts. Journal of Geophysical Research: Solid Earth, 96(B9), 14347-14375.

Frey, F. A., Green, D. H., & Roy, S. D. (1978). Integrated models of basalt petrogenesis: a study of quartz tholeiites to olivine melilitites from south eastern Australia utilizing geochemical and experimental petrological data. Journal of Petrology, 19(3), 463-513.

Frimmel, H. E., & Gartz, V. H. (1997). Witwatersrand gold particle chemistry matches model of metamorphosed, hydrothermally altered placer deposits. Mineralium Deposita, 32(6), 523-530.

Fueten, F., & Redmond, D. J. (1997). Documentation of a 1450 Ma contractional orogeny preserved between the 1850 Ma Sudbury impact structure and the 1 Ga Grenville orogenic front, Ontario, Canada. Geological Society of America Bulletin, 109(3), 268-279.

Fyon, J. A., & Crocket, J. H. (1986). Exploration potential for base and precious metal mineralization in part of Strathy Township, Temagami area. Ontario Geological Survey, Open File Report 5591, 46p.

Galer, S. J. G., & Abouchami, W. (1998). Practical application of lead triple spiking for correction of instrumental mass discrimination. Mineralogical Magazine, 62, 491-492.

Gao, X. Y., Zheng, Y. F., Chen, Y. X., & Guo, J. (2012). Geochemical and U–Pb age constraints on the occurrence of polygenetic titanites in UHP metagranite in the Dabie orogen. Lithos, 136, 93-108.

Garde, A. A., & Klausen, M. B. (2016). A centennial reappraisal of the Vredefort pseudotachylytes: shaken, not stirred by meteorite impact. Journal of the Geological Society, 173(6), 954-965.

Garde, A. A., & Klausen, M. B. (2018). Comments on "The impact pseudotachylitic breccia controversy: Insights from first isotope analysis of Vredefort impact-generated melt rocks" by Reimold et al. 2017 (GCA 214, 266–282). Geochimica et Cosmochimica Acta, 233, 187-190.

Gasparrini, E., & Naldrett, A. J. (1972). Magnetite and ilmenite in the Sudbury nickel irruptive. Economic Geology, 67(5), 605-621.

Gates, B. I. (1991). Sudbury Mineral Occurrence Study. Ontario Geological Survey, Open File Report 5771, 235p.

Gerdes, A., & Zeh, A. (2006). Combined U–Pb and Hf isotope LA-(MC-) ICP-MS analyses of detrital zircons: comparison with SHRIMP and new constraints for the provenance and age of an Armorican metasediment in Central Germany. Earth and Planetary Science Letters, 249(1-2), 47-61.

Gerdes, A., & Zeh, A. (2009). Zircon formation versus zircon alteration – new insights from combined U–Pb and Lu–Hf in-situ LA-ICP-MS analyses, and consequences for the interpretation of Archean zircon from the Central Zone of the Limpopo Belt. Chemical Geology, 261(3-4), 230-243.

Giblin, P. E. (1984). History of exploration and development, of geological studies and development of geological concepts. In: Pye, E. G., Naldrett, A. J., Giblin, P. E. (eds.), The Geology and Ore Deposits of the Sudbury Structure. Ontario Geological Survey, Special Volume 1, 3-23.

Giroux, L. A. (2005). Magnetic subfabrics of the Whistle Offset dyke and embayment, Sudbury Impact Structure, Sudbury, Ontario. Unpublished MSc thesis, University of Ottawa, Canada, 171p., http://hdl.handle.net/10393/26913 http://dx.doi.org/10.20381/ruor-11826

Giroux, L. A., & Benn, K. (2005). Emplacement of the Whistle dike, the Whistle embayment and hosted sulfides, Sudbury impact structure, based on anisotropies of magnetic susceptibility and magnetic remanence. Economic Geology, 100(6), 1207-1227.

Glazner, A. F., Bartley, J. M., Coleman, D. S., & Lindgren, K. (2020). Aplite diking and infiltration: a differentiation mechanism restricted to plutonic rocks. Contributions to Mineralogy and Petrology, 175(4), 1-17.

Goad, R. E., & Rowell, W. F. (1985). Report on the Geology and Exploration of Selected Claims and Related Properties in Rathbun, Scadding and Mackelcan Townships, Sudbury Mining District, Ontario. Unpublished company report, prepared for Flag Resources Ltd., 248p., Ontario Assessment File Database record number 41I15NE0015.

Godel, B., & Barnes, S. J. (2008). Image analysis and composition of platinum-group minerals in the JM Reef, Stillwater Complex. Economic Geology, 103(3), 637-651.

Godel, B., Barnes, S. J., Barnes, S. J., & Maier, W. D. (2010). Platinum ore in three dimensions: Insights from high-resolution X-ray computed tomography. Geology, 38(12), 1127-1130.

Goldschmidt, V. M. (1922). On the metasomatic processes in silicate rocks. Economic Geology, 17(2), 105-123.

Goldstein, S. L., O'Nions, R. K., & Hamilton, P. J. (1984). A Sm-Nd isotopic study of atmospheric dusts and particulates from major river systems. Earth and Planetary Science Letters, 70(2), 221-236.

Golightly, J. P. (1994). The Sudbury Igneous Complex as an impact melt: Evolution and ore genesis. In: Lightfoot, P. C., Naldrett, A. J. (eds.), Proceedings of the Sudbury-Noril'sk Symposium. Ontario Geological Survey, Special Volume 5, 105-118.

Göllner, P. L., Wüstemann, T., Bendschneider, L., Reimers, S., Clark, M. D., Gibson, L., ... & Riller, U. (2019). Thermo-mechanical interaction of a large impact melt sheet with adjacent target rock, Sudbury impact structure, Canada. Meteoritics & Planetary Science, 54(6), 1228-1245.

Gómez-Ulla, A., Sigmarsson, O., Huertas, M. J., Devidal, J. L., & Ancochea, E. (2018). The historical basanite-alkali basalt-tholeiite suite at Lanzarote, Canary Islands: Carbonated melts of heterogeneous mantle source?. Chemical Geology, 494, 56-68.

Gordon, C. A. (2016). Geological, geochemical, geophysical, and geochronological data from the Morin and Otter townships bedrock geology mapping project, Southern and Superior provinces. Ontario Geological Survey, Miscellaneous Release – Data 332.

Gordon, C. A., Simard, R. L., & Généreux, C. A. (2018). Geological, geochemical and geophysical data for Drury Township, southwest Sudbury Structure. Ontario Geological Survey, Miscellaneous Release – Data 369.

Gore, T. E. (2020). A study of millerite from Cu-Ni-PGE footwall veins, Sudbury, ON: crystal-chemistry, morphology, & geological implications. Unpublished MSc thesis, Laurentian University, Sudbury, Ontario, Canada, 124p., https://zone.biblio.laurentian.ca/handle/10219/3581

Gorring, M. L., & Kay, S. M. (2000). Carbonatite metasomatized peridotite xenoliths from southern Patagonia: implications for lithospheric processes and Neogene plateau magmatism. Contributions to Mineralogy and Petrology, 140(1), 55-72.

Govindaraju, K. (1989). 1989 compilation of working values and sample description for 272 geostandards. Geostandards Newsletter, 13, 1-113.

Graham, S. D., Holwell, D. A., McDonald, I., Jenkin, G. R. T., Hill, N. J., Boyce, A. J., ... & Sangster, C. (2017). Magmatic Cu-Ni-PGE-Au sulfide mineralisation in alkaline igneous systems: An example from the Sron Garbh intrusion, Tyndrum, Scotland. Ore Geology Reviews, 80, 961-984.

Grant, J. A. (1986). The isocon diagram; a simple solution to Gresens' equation for metasomatic

alteration. Economic Geology, 81(8), 1976-1982.

Grant, R. W., & Bite, A. (1984). Sudbury quartz diorite offset dikes. In: Pye, E. G., Naldrett, A. J., Giblin, P. E. (eds.), The Geology and Ore Deposits of the Sudbury Structure. Ontario Geological Survey, Special Volume 1, 275-301.

Green, D. H., Hibberson, W. O., Kovács, I., & Rosenthal, A. (2010). Water and its influence on the lithosphere–asthenosphere boundary. Nature, 467(7314), 448-451.

Green, D. H., & Ringwood, A. E. (1967). The genesis of basaltic magmas. Contributions to Mineralogy and Petrology, 15(2), 103-190.

Green, T. H., Blundy, J. D., Adam, J., & Yaxley, G. M. (2000). SIMS determination of trace element partition coefficients between garnet, clinopyroxene and hydrous basaltic liquids at 2–7.5 GPa and 1080–1200°C. Lithos, 53(3-4), 165-187.

Grieve, R. A. F., & Osinski, G. R. (2020). The Upper Contact Unit of the Sudbury Igneous Complex in the Garson region: Constraints on the depth of origin of a peak ring at the Sudbury impact structure. Meteoritics & Planetary Science, 55(8), in press, doi.org/10.1111/maps.13542

Grieve, R. A. F., Ames, D. E., Morgan, J. V., & Artemieva, N. (2010). The evolution of the Onaping Formation at the Sudbury impact structure. Meteoritics & Planetary Science, 45(5), 759-782.

Grieve, R. A. F., Reimold, W. U., Morgan, J., Riller, U., & Pilkington, M. (2008). Observations and interpretations at Vredefort, Sudbury, and Chicxulub: Towards an empirical model of terrestrial impact basin formation. Meteoritics & Planetary Science, 43(5), 855-882.

Grieve, R. A. F., Stöffler, D., & Deutsch, A. (1991). The Sudbury structure: Controversial or misunderstood?. Journal of Geophysical Research: Planets, 96(E5), 22753-22764.

Gross, G. A. F. (1980). A classification of iron formations based on depositional environments. The Canadian Mineralogist, 18(2), 215-222.

Groves, D. I., Bierlein, F. P., Meinert, L. D., & Hitzman, M. W. (2010). Iron oxide copper-gold (IOCG) deposits through Earth history: Implications for origin, lithospheric setting, and distinction from other epigenetic iron oxide deposits. Economic Geology, 105(3), 641-654.

Gualda, G. A., & Ghiorso, M. S. (2013). Low-pressure origin of high-silica rhyolites and granites. The Journal of Geology, 121(5), 537-545.

Gualda, G. A., & Ghiorso, M. S. (2015). MELTS _Excel: A Microsoft Excel-based MELTS interface for research and teaching of magma properties and evolution. Geochemistry, Geophysics, Geosystems, 16(1), 315-324.

Gudfinnsson, G. H., & Presnall, D. C. (2005). Continuous gradations among primary carbonatitic, kimberlitic, melilititic, basaltic, picritic, and komatiitic melts in equilibrium with garnet lherzolite at 3–8 GPa. Journal of Petrology, 46(8), 1645-1659.

Gupta, V. K., Grant, F. S., & Card, K. D. (1984). Gravity and magnetic characteristics of the Sudbury Structure. In: Pye, E. G., Naldrett, A. J., Giblin, P. E. (eds.), The Geology and Ore Deposits of

the Sudbury Structure. Ontario Geological Survey, Special Volume 1, 381-410.

Gurov, Y. P., French, B. M., & Permiakov, V. V. (2020). Carbon-rich microfossils preserved in the Proterozoic crater-filling breccias of the Sudbury impact structure, Canada. Meteoritics & Planetary Science, 55(12), 2727-2740.

Guy-Bray, J. V., & Geological Staff (1966). Shatter cones at Sudbury. The Journal of Geology, 74(2), 243-245.

Haase, K. M., Goldschmidt, B., & Garbe-Schönberg, C. D. (2004). Petrogenesis of Tertiary continental intra-plate lavas from the Westerwald region, Germany. Journal of Petrology, 45(5), 883-905.

Hagen, K. (2020). Petrological and geochemical characterization of the Nipissing Gabbro northeast of Sudbury. Unpublished MSc thesis, University of Würzburg, Germany, 144p.

Hall, M. F., Lafrance, B., & Gibson, H. L. (2020). Emplacement of sharp-walled sulfide veins during the formation and reactivation of impact-related structures at the Broken Hammer Mine, Sudbury, Ontario. Canadian Journal of Earth Sciences, 57(10), 1149-1166.

Halls, H. C. (1991). The Matachewan dyke swarm, Canada: an early Proterozoic magnetic field reversal. Earth and Planetary Science Letters, 105(1-3), 279-292.

Halls, H. C., & Davis, D. W. (2004). Paleomagnetism and U Pb geochronology of the 2.17 Ga Biscotasing dyke swarm, Ontario, Canada: evidence for vertical-axis crustal rotation across the Kapuskasing Zone. Canadian Journal of Earth Sciences, 41(3), 255-269.

Halls, H. C., Lovette, A., Hamilton, M. A., & Söderlund, U. (2015). A paleomagnetic and U–Pb geochronology study of the western end of the Grenville dyke swarm: Rapid changes in paleomagnetic field direction at ca. 585 Ma related to polarity reversals?. Precambrian Research, 257, 137-166.

Halls, H. C., Stott, G. M., & Davis, D. W. (2005). Paleomagnetism, geochronology and geochemistry of several Proterozoic mafic dike swarms in northwestern Ontario. Ontario Geological Survey, Open File Report 6171, 59p.

Hamilton, M. A., & Buchan, K. L. (2016). A 2169 Ma U–Pb baddeleyite age for the Otish Gabbro, Quebec: implications for correlation of Proterozoic magmatic events and sedimentary sequences in the eastern Superior Province. Canadian Journal of Earth Sciences, 53(2), 119-128.

Hamilton, M. A., & Stott, G. M. (2008). The significance of new U/Pb baddeleyite ages from two Paleoproterozoic diabase dikes in Northern Ontario. In: Baker, C. L., Debicki, E. J., Kelly, R. I., Ayer, J. A., Stott, G. M. (eds.), Summary of Field Work and Other Activities 2008. Ontario Geological Survey, Open File Report 6226, p.17-1 to 17-10.

Hamilton, P. J., O'Nions, R. K., Bridgwater, D., & Nutman, A. (1983). Sm-Nd studies of Archaean metasediments and metavolcanics from West Greenland and their implications for the Earth's early history. Earth and Planetary Science Letters, 62(2), 263-272.

Hammarstrom, J. M., & Zen, E. A. (1986). Aluminum in hornblende: an empirical igneous geobarometer. American Mineralogist, 71(11-12), 1297-1313.

Hammouda, T., & Laporte, D. (2000). Ultrafast mantle impregnation by carbonatite melts. Geology, 28(3), 283-285.

Hanley, J. J., Ames, D. E., Barnes, J., Sharp, Z., & Guillong, M. (2011). Interaction of magmatic fluids and silicate melt residues with saline groundwater in the footwall of the Sudbury Igneous Complex, Ontario, Canada: New evidence from bulk rock geochemistry, fluid inclusions and stable isotopes. Chemical Geology, 281(1-2), 1-25.

Harris, C., Fourie, D. S., & Fagereng, A. (2013). Stable isotope evidence for impact-related pseudotachylite formation at Vredefort by local melting of dry rocks. South African Journal of Geology, 116(1), 101-118.

Harris, C., Le Roux, P., Cochrane, R., Martin, L., Duncan, A. R., Marsh, J. S., ... & Class, C. (2015). The oxygen isotope composition of Karoo and Etendeka picrites: high $\delta^{18}O$ mantle or crustal contamination?. Contributions to Mineralogy and Petrology, 170(1), 1-24.

Hart, S. R., & Davis, K. E. (1978). Nickel partitioning between olivine and silicate melt. Earth and Planetary Science Letters, 40(2), 203-219.

Harte, B., Hunter, R. H., & Kinny, P. D. (1993). Melt geometry, movement and crystallization, in relation to mantle dykes, veins and metasomatism. Philosophical Transactions of the Royal Society of London. Series A: Physical and Engineering Sciences, 342(1663), 1-21.

Hartmann, G., & Wedepohl, K. H. (1990). Metasomatically altered peridotite xenoliths from the Hessian Depression (Northwest Germany). Geochimica et Cosmochimica Acta, 54(1), 71-86.

Hartnady, M. I., Kirkland, C. L., Clark, C., Spaggiari, C. V., Smithies, R. H., Evans, N. J., & McDonald, B. J. (2019). Titanite dates crystallization: Slow Pb diffusion during super-solidus re-equilibration. Journal of Metamorphic Geology, 37(6), 823-838.

Hartung, E., Caricchi, L., Floess, D., Wallis, S., Harayama, S., Kouzmanov, K., & Chiaradia, M. (2017). Evidence for residual melt extraction in the Takidani Pluton, Central Japan. Journal of Petrology, 58(4), 763-788.

Hashmi, S., Leybourne, M. I., Layton-Matthews, D., Hamilton, S., McClenaghan, M. B., & Voinot, A. (2021). Surficial geochemical and mineralogical signatures of Ni-Cu-PGE deposits in glaciated terrain: examples from the South Range of the Sudbury Igneous Complex, Ontario, Canada. Ore Geology Reviews, 137, 104301, doi.org/10.1016/j.oregeorev.2021.104301

Hastie, A. R., Kerr, A. C., Pearce, J. A., & Mitchell, S. F. (2007). Classification of altered volcanic island arc rocks using immobile trace elements: development of the Th–Co discrimination diagram. Journal of Petrology, 48(12), 2341-2357.

Hauri, E. H. (2002). SIMS analysis of volatiles in silicate glasses, 2: isotopes and abundances in Hawaiian melt inclusions. Chemical Geology, 183(1-4), 115-141.

Hauri, E. H., Shimizu, N., Dieu, J. J., & Hart, S. R. (1993). Evidence for hotspot-related carbonatite metasomatism in the oceanic upper mantle. Nature, 365(6443), 221-227.

Hawkesworth, C. J., & Kemp, A. I. S. (2006). Evolution of the continental crust. Nature, 443(7113), 811-817.

Hawley, J. E. (1962). The Sudbury ores, their mineralogy and origin; Part 1, The geological setting. The Canadian Mineralogist, 7(1), 1-29.

Hawley, J. E. (1965). Upside-down zoning at Frood, Sudbury, Ontario. Economic Geology, 60(3), 529-575.

Hayes, B., Bybee, G. M., Mawela, M., Nex, P. A., & van Niekerk, D. (2018). Residual melt extraction and out-of-sequence differentiation in the Bushveld Complex, South Africa. Journal of Petrology, 59(12), 2413-2434.

Heaman, L. M. (1997). Global mafic magmatism at 2.45 Ga: Remnants of an ancient large igneous province?. Geology, 25(4), 299-302.

Heaman, L. M., Peck, D., & Toope, K. (2009). Timing and geochemistry of 1.88 Ga Molson Igneous Events, Manitoba: insights into the formation of a craton-scale magmatic and metallogenic province. Precambrian Research, 172(1-2), 143-162.

Hearst, R., Morris, W., & Thomas, M. (1994). Magnetic interpretation along the Sudbury Structure Lithoprobe transect. Geophysical Research Letters, 21(10), 951-954.

Hecht, L., Thuro, K., Plinninger, R., & Cuney, M. (1999). Mineralogical and geochemical characteristics of hydrothermal alteration and episyenitization in the Königshain granites, northern Bohemian Massif, Germany. International Journal of Earth Sciences, 88(2), 236-252.

Hecht, L., Wittek, A., Riller, U., Mohr, T., Schmitt, R. T., & Grieve, R. A. F. (2008). Differentiation and emplacement of the Worthington Offset Dike of the Sudbury impact structure, Ontario. Meteoritics & Planetary Science, 43(10), 1659-1679.

Henkel, H., & Reimold, W. U. (2002). Magnetic model of the central uplift of the Vredefort impact structure, South Africa. Journal of Applied Geophysics, 51(1), 43-62.

Hess, P. C. (1992). Phase Equilibria Constraints on the Origin of Ocean Floor Basalts. In: Morgan, J. P., Blackman, D. K., Sinton, J. M. (eds.), Mantle Flow and Melt Generation at Mid-Ocean Ridges. American Geophysical Union, Geophysical Monograph 72, 67-102.

Hiess, J., Condon, D. J., McLean, N., & Noble, S. R. (2012). $^{238}U/^{235}U$ systematics in terrestrial uranium-bearing minerals. Science, 335(6076), 1610-1614.

Higgins, M. D., Hankard, F., Ganerød, M., & Van der Voo, R. (2018). The vesicular Sainte-Sophie dykes: a chemically distinct, near-surface facies of the Grenville Dyke Swarm?. Canadian Journal of Earth Sciences, 55(3), 241-251.

Hildebrand, R. S. (1986). Kiruna-type deposits; their origin and relationship to intermediate subvolcanic plutons in the Great Bear magmatic zone, Northwest Canada. Economic Geology, 81(3), 640-659.

Hill, C. M. (2019). Sedimentology, Lithostratigraphy and Geochronology of the Paleoproterozoic Gordon Lake Formation, Huronian Supergroup, Ontario, Canada. Unpublished PhD thesis,

The University of Western Ontario, London, Ontario, Canada, 256p., Electronic Thesis and Dissertation Repository 6084, https://ir.lib.uwo.ca/etd/6084

Hill, C. M., Davis, D. W., & Corcoran, P. L. (2018). New U-Pb geochronology evidence for 2.3 Ga detrital zircon grains in the youngest Huronian Supergroup formations, Canada. Precambrian Research, 314, 428-433.

Hirose, K. (1997). Melting experiments on lherzolite KLB-1 under hydrous conditions and generation of high-magnesian andesitic melts. Geology, 25(1), 42-44.

Hirschmann, M. M., Kogiso, T., Baker, M. B., & Stolper, E. M. (2003). Alkalic magmas generated by partial melting of garnet pyroxenite. Geology, 31(6), 481-484.

Hirt, A. M., Lowrie, W., Clendenen, W. S., & Kligfield, R. (1993). Correlation of strain and the anisotropy of magnetic susceptibility in the Onaping Formation: evidence for a near-circular origin of the Sudbury Basin. Tectonophysics, 225(4), 231-254.

Hoernle, K., Tilton, G., Le Bas, M. J., Duggen, S., & Garbe-Schönberg, D. (2002). Geochemistry of oceanic carbonatites compared with continental carbonatites: mantle recycling of oceanic crustal carbonate. Contributions to Mineralogy and Petrology, 142(5), 520-542.

Hofmann, A. W. (1997). Mantle geochemistry: the message from oceanic volcanism. Nature, 385(6613), 219-229.

Hofmann, A. W., Jochum, K. P., Seufert, M., & White, W. M. (1986). Nb and Pb in oceanic basalts: new constraints on mantle evolution. Earth and Planetary Science Letters, 79(1-2), 33-45.

Hofmann, H. J., Pearson, D. A. B., & Wilson, B. H. (1980). Stromatolites and fenestral fabric in early Proterozoic Huronian Supergroup, Ontario. Canadian Journal of Earth Sciences, 17(10), 1351-1357.

Holder, R. M., Hacker, B. R., Seward, G. G., & Kylander-Clark, A. R. (2019). Interpreting titanite U–Pb dates and Zr thermobarometry in high-grade rocks: empirical constraints on elemental diffusivities of Pb, Al, Fe, Zr, Nb, and Ce. Contributions to Mineralogy and Petrology, 174(5), 1-19.

Holland, H. D. (2002). Volcanic gases, black smokers, and the Great Oxidation Event. Geochimica et Cosmochimica Acta, 66(21), 3811-3826.

Holland, T., & Blundy, J. (1994). Non-ideal interactions in calcic amphiboles and their bearing on amphibole-plagioclase thermometry. Contributions to Mineralogy and Petrology, 116(4), 433-447.

Hollister, L. S., Grissom, G. C., Peters, E. K., Stowell, H. H., & Sisson, V. B. (1987). Confirmation of the empirical correlation of Al in hornblende with pressure of solidification of calc-alkaline plutons. American Mineralogist, 72(3-4), 231-239.

Holness, M. B. (1999). Contact metamorphism and anatexis of Torridonian arkose by minor intrusions of the Rum Igneous Complex, Inner Hebrides, Scotland. Geological Magazine, 136(5), 527-542.

Holness, M. B. (2018). Melt segregation from silicic crystal mushes: a critical appraisal of possible mechanisms and their microstructural record. Contributions to Mineralogy and Petrology, 173(6), 1-17.

Holness, M. B., & Isherwood, C. E. (2003). The aureole of the Rum Tertiary igneous complex, Scotland. Journal of the Geological Society, 160(1), 15-27.

Holness, M. B., Richardson, C., & Helz, R. T. (2012). Disequilibrium dihedral angles in dolerite sills: a new proxy for cooling rate. Geology, 40(9), 795-798.

Holtz, F., & Johannes, W. (1994). Maximum and minimum water contents of granitic melts: implications for chemical and physical properties of ascending magmas. Lithos, 32(1), 149-159.

Holwell, D. A., & Blanks, D. E. (2021). Emplacement of magmatic Cu-Au-Te (-Ni-PGE) sulfide blebs in alkaline mafic rocks of the Mordor Complex, Northern Territory, Australia. Mineralium Deposita, 56(4), 789-803.

Holwell, D. A., & McDonald, I. (2010). A review of the behaviour of platinum group elements within natural magmatic sulfide ore systems. Platinum Metals Review, 54(1), 26-36.

Holwell, D. A., Adeyemi, Z., Ward, L. A., Smith, D. J., Graham, S. D., McDonald, I., & Smith, J. W. (2017). Low temperature alteration of magmatic Ni-Cu-PGE sulfides as a source for hydrothermal Ni and PGE ores: A quantitative approach using automated mineralogy. Ore Geology Reviews, 91, 718-740.

Holwell, D. A., Keays, R. R., Firth, E. A., & Findlay, J. (2014). Geochemistry and mineralogy of platinum group element mineralization in the River Valley intrusion, Ontario, Canada: A model for early-stage sulfur saturation and multistage emplacement and the implications for "Contact-Type" Ni-Cu-PGE sulfide mineralization. Economic Geology, 109(3), 689-712.

Holwell, D. A., Keays, R. R., McDonald, I., & Williams, M. R. (2015). Extreme enrichment of Se, Te, PGE and Au in Cu sulfide microdroplets: evidence from LA-ICP-MS analysis of sulfides in the Skaergaard Intrusion, east Greenland. Contributions to Mineralogy and Petrology, 170(5), 1-26.

Hou, G., Kusky, T. M., Wang, C., & Wang, Y. (2010). Mechanics of the giant radiating Mackenzie dyke swarm: a paleostress field modeling. Journal of Geophysical Research: Solid Earth, 115(B2).

Hou, G., Santosh, M., Qian, X., Lister, G. S., & Li, J. (2008). Tectonic constraints on 1.3~1.2 Ga final breakup of Columbia supercontinent from a giant radiating dyke swarm. Gondwana Research, 14(3), 561-566.

Howarth, G. H., Moore, A. E., Harris, C., van der Meer, Q. H., & Le Roux, P. (2019). Crustal versus mantle origin of carbonate xenoliths from Kimberley region kimberlites using CO-Sr-Nd-Pb isotopes and trace element abundances. Geochimica et Cosmochimica Acta, 266, 258-273.

Hriskevich, M. E. (1968). Petrology of the Nipissing diabase sill of the Cobalt area, Ontario, Canada. Geological Society of America Bulletin, 79(10), 1387-1404.

Hu, Q., Evensen, N. M., Smith, P. E., & York, D. (1998). A world in a grain of sand: regional metamorphic history from $^{40}Ar/^{39}Ar$ laser probe analyses of Proterozoic sediments from the Canadian Shield. Precambrian Research, 91(3-4), 287-294.

Huber, C., Bachmann, O., & Dufek, J. (2011). Thermo-mechanical reactivation of locked crystal mushes: Melting-induced internal fracturing and assimilation processes in magmas. Earth and Planetary Science Letters, 304(3-4), 443-454.

Huber, M. S., Kovaleva, E., Clark, M. D., & Prevec, S. A. (2021). Inhomogeneous distribution of lithic clasts within the Daskop granophyre dike, Vredefort impact structure: Implications for emplacement of impact melt in large impact structures. In: Reimold, W. U., Koeberl, C. (eds.), Large Meteorite Impacts and Planetary Evolution VI. Geological Society of America, Special Paper 550, 255-267.

Huber, M. S., Kovaleva, E., & Riller, U. (2020). Modeling the geochemical evolution of impact melts in terrestrial impact basins: Vredefort granophyre dikes and Sudbury offset dikes. Meteoritics & Planetary Science, 55(10), 2320-2337.

Huber, M. S., McDonald, I., & Koeberl, C. (2014). Petrography and geochemistry of ejecta from the Sudbury impact event. Meteoritics & Planetary Science, 49(10), 1749-1768.

Huminicki, M. A. E., Sylvester, P. J., Cabri, L. J., Lesher, C. M., & Tubrett, M. (2005). Quantitative mass balance of platinum group elements in the Kelly Lake Ni-Cu-PGE deposit, Copper Cliff offset, Sudbury. Economic Geology, 100(8), 1631-1646.

Humphris, S. E., & Thompson, G. (1978). Trace element mobility during hydrothermal alteration of oceanic basalts. Geochimica et Cosmochimica Acta, 42(1), 127-136.

Hunt, L., Stachel, T., Grütter, H., Armstrong, J., McCandless, T. E., Simonetti, A., & Tappe, S. (2012). Small mantle fragments from the Renard kimberlites, Quebec: powerful recorders of mantle lithosphere formation and modification beneath the Eastern Superior Craton. Journal of Petrology, 53(8), 1597-1635.

Huppert, H. E., & Sparks, R. S. J. (1989). Chilled margins in igneous rocks. Earth and Planetary Science Letters, 92(3-4), 397-405.

Huppert, H. E., & Sparks, R. S. J. (1985). Cooling and contamination of mafic and ultramafic magmas during ascent through continental crust. Earth and Planetary Science Letters, 74(4), 371-386.

Hurley, T. D. (1985). Petrology and geochemistry of the volcanic host rocks to the west and north pits of the Sherman Mine iron formation, Temagami, Ontario. Unpublished MSc thesis, McMaster University, Hamilton, Ontario, Canada, 154p., http://hdl.handle.net/11375/19835

Hutchinson, D., & Kinnaird, J. A. (2005). Complex multistage genesis for the Ni–Cu–PGE mineralisation in the southern region of the Platreef, Bushveld Complex, South Africa. Applied Earth Science, 114(4), 208-224.

Innes, D. G. (1984). Emerald Lake Resources Golden Rose Project 1984 Exploration Summary.

Unpublished report, 274p., Ontario Assessment File Database record number 41I16NW0013.

Ionov, D. A., Chazot, G., Chauvel, C., Merlet, C., & Bodinier, J. L. (2006). Trace element distribution in peridotite xenoliths from Tok, SE Siberian craton: a record of pervasive, multi-stage metasomatism in shallow refractory mantle. Geochimica et Cosmochimica Acta, 70(5), 1231-1260.

Ionov, D. A., Dupuy, C., O'Reilly, S. Y., Kopylova, M. G., & Genshaft, Y. S. (1993). Carbonated peridotite xenoliths from Spitsbergen: implications for trace element signature of mantle carbonate metasomatism. Earth and Planetary Science Letters, 119(3), 283-297.

Irber, W. (1999). The lanthanide tetrad effect and its correlation with K/Rb, Eu/Eu*, Sr/Eu, Y/Ho, and Zr/Hf of evolving peraluminous granite suites. Geochimica et Cosmochimica Acta, 63(3-4), 489-508.

Irvine, T. N., & Baragar, W. R. A. (1971). A guide to the chemical classification of the common volcanic rocks. Canadian Journal of Earth Sciences, 8(5), 523-548.

Ivanov, B. A., & Deutsch, A. (1999). Sudbury impact event: Cratering mechanics and thermal history. In: Dressler, B. O., Sharpton, V. L. (eds.), Large Meteorite Impacts and Planetary Evolution II. Geological Society of America, Special Paper 339, 389-397.

Jackson, S. E., Pearson, N. J., Griffin, W. L., & Belousova, E. A. (2004). The application of laser ablation-inductively coupled plasma-mass spectrometry to in situ U–Pb zircon geochronology. Chemical Geology, 211(1-2), 47-69.

Jackson, S. J., & Fyon, J. A. (1991). The western Abitibi Subprovince in Ontario. In: Thurston, P. C., Williams, H. R., Sutcliffe, R. H., Stott, G.M. (eds.), Geology of Ontario Part 1. Ontario Geological Survey, Special Volume 4, 405-482.

Jackson, S. L., & Cruden, A. R. (1995). Formation of the Abitibi greenstone belt by arc-trench migration. Geology, 23(5), 471-474.

Jacobsen, S. B., & Wasserburg, G. J. (1980). Sm-Nd isotopic evolution of chondrites. Earth and Planetary Science Letters, 50(1), 139-155.

Jaffey, A. H., Flynn, K. F., Glendenin, L. E., Bentley, W. C., & Essling, A. M. (1971). Precision measurement of half-lives and specific activities of ^{235}U and ^{238}U. Physical Review C, 4(5), 1889.

Jambor, J. L. (1971). The Nipissing diabase. The Canadian Mineralogist, 11(1), 34-75.

James, R. S., & Hawke, D. (1984). Geology and petrogenesis of the Kanichee layered complex, Ontario. The Canadian Mineralogist, 22(1), 93-109.

James, R. S., Easton, R. M., Peck, D. C., & Hrominchuk, J. L. (2002). The East Bull Lake intrusive suite: Remnants of a ~2.48 Ga large igneous and metallogenic province in the Sudbury area of the Canadian Shield. Economic Geology, 97(7), 1577-1606.

Janoušek, V., Moyen, J. F., Martin, H., Erban, V., & Farrow, C. (2016). Geochemical modelling of igneous processes: principles and recipes in R language. 1st edition, Springer-Verlag, Berlin

and Heidelberg, 346p.

Jensen, L. S. (1976). A new plot for classifying subalkalic volcanic rocks. Ontario Division of Mines, Miscellaneous Paper 66, 22p.

Jobin-Bevans, L. S. (2000). Wanapitei Lake area, Scadding Township, Sudbury Mining Division. OPAP Project (OP99-273), Final Report, 90p., Ontario Assessment File Database record number 41I10NE2016.

Jobin-Bevans, L. S. (2004). Platinum-group element mineralization in Nipissing gabbro intrusions and the River Valley intrusion, Sudbury region, Ontario. Unpublished PhD thesis, The University of Western Ontario, London, Ontario, Canada, 572p.

Jobin-Bevans, L. S. (2009). Nipissing Gabbro. In: Rousell, D. H., Brown, G. H. (eds.), A Field Guide to the Geology of Sudbury, Ontario. Ontario Geological Survey, Open File Report 6243, 31-36.

Jobin-Bevans, L. S. (2016). Geochemical data related to a study of platinum group element mineralization in Nipissing gabbro intrusions and the River Valley intrusion, Sudbury region, Southern Province. Ontario Geological Survey, Miscellaneous Release–Data 336.

Jobin-Bevans, L. S., Keays, R. R., & MacRae, N. D. (1997). Metallogenic potential of the Nipissing diabase: New approaches to ascertaining the mineral potential. In: Ayer, J. A., Baker, C. L., Laderoute, D. G., Thurston, P. C. (eds.), Summary of Field Work and Other Activities 1997. Ontario Geological Survey, Miscellaneous Paper 168, 93-95.

Jochum, K. P., Nohl, U., Herwig, K., Lammel, E., Stoll, B., & Hofmann, A. W. (2005). GeoReM: a new geochemical database for reference materials and isotopic standards. Geostandards and Geoanalytical Research, 29(3), 333-338.

Johnson, M. C., & Rutherford, M. J. (1989). Experimental calibration of the aluminum-in-hornblende geobarometer with application to Long Valley caldera (California) volcanic rocks. Geology, 17(9), 837-841.

Joreau, P., French, B. M., & Doukhan, J. C. (1996). A TEM investigation of shock metamorphism in quartz from the Sudbury impact structure (Canada). Earth and Planetary Science Letters, 138(1-4), 137-143.

Jørgensen, T. R., Tinkham, D. K., & Lesher, C. M. (2019). Low-P and high-T metamorphism of basalts: Insights from the Sudbury impact melt sheet aureole and thermodynamic modelling. Journal of Metamorphic Geology, 37(2), 271-313.

Jørgensen, T. R., Tinkham, D. K., Lesher, C. M., & Petrus, J. A. (2018). Decoupling of Zr-Hf during contact metamorphic anatexis of metabasalts and timing of zircon growth, Sudbury, Canada. Geology, 46(2), 159-162.

Jourdan, F., Féraud, G., Bertrand, H., Watkeys, M. K., Kampunzu, A. B., & Le Gall, B. (2006). Basement control on dyke distribution in Large Igneous Provinces: case study of the Karoo triple junction. Earth and Planetary Science Letters, 241(1-2), 307-322.

Jowitt, S. M., & Ernst, R. E. (2013). Geochemical assessment of the metallogenic potential of Proterozoic LIPs of Canada. Lithos, 174, 291-307.

Jung, S., & Hellebrand, E. (2007). Textural, geochronological and chemical constraints from polygenetic titanite and monogenetic apatite from a mid-crustal shear zone: an integrated EPMA, SIMS, and TIMS study. Chemical Geology, 241(1-2), 88-107.

Jung, S., & Hoernes, S. (2000). The major-and trace-element and isotope (Sr, Nd, O) geochemistry of Cenozoic alkaline rift-type volcanic rocks from the Rhön area (central Germany): petrology, mantle source characteristics and implications for asthenosphere–lithosphere interactions. Journal of Volcanology and Geothermal Research, 99(1-4), 27-53.

Jung, S., & Masberg, P. (1998). Major-and trace-element systematics and isotope geochemistry of Cenozoic mafic volcanic rocks from the Vogelsberg (central Germany): constraints on the origin of continental alkaline and tholeiitic basalts and their mantle sources. Journal of Volcanology and Geothermal Research, 86(1-4), 151-177.

Jung, S., Vieten, K., Romer, R. L., Mezger, K., Hoernes, S., & Satir, M. (2012). Petrogenesis of Tertiary alkaline magmas in the Siebengebirge, Germany. Journal of Petrology, 53(11), 2381-2409.

Junge, M., Oberthür, T., Kraemer, D., Melcher, F., Piña, R., Derrey, I. T., ... & Strauss, H. (2019). Distribution of platinum-group elements in pristine and near-surface oxidized Platreef ore and the variation along strike, northern Bushveld Complex, South Africa. Mineralium Deposita, 54(6), 885-912.

Kamber, B. S., & Schönberg, R. (2020). Evaporative loss of moderately volatile metals from the superheated 1849 Ma Sudbury impact melt sheet inferred from stable Zn isotopes. Earth and Planetary Science Letters, 544, 116356.

Kaminsky, F. V., & Belousova, E. A. (2009). Manganoan ilmenite as kimberlite/diamond indicator mineral. Russian Geology and Geophysics, 50(12), 1212-1220.

Kamo, S. L., Krogh, T. E., & Kumarapeli, P. S. (1995). Age of the Grenville dyke swarm, Ontario–Quebec: implications for the timing of lapetan rifting. Canadian Journal of Earth Sciences, 32(3), 273-280.

Kastek, N. (2019). 2.0 to 1.9 Ga large igneous province magmatism in northern Quebec – U-Pb geochronology and geochemistry. Unpublished PhD thesis, Carleton University, Ottawa, Canada, 360p., Library Catalogue Record https://doi.org/10.22215/etd/2019-13791

Kaur, G., & Mehta, P. K. (2005). The Gothara plagiogranite: evidence for oceanic magmatism in a non-ophiolitic association, North Khetri Copper Belt, Rajasthan, India?. Journal of Asian Earth Sciences, 25(5), 805-819.

Kaur, P., Chaudhri, N., Hofmann, A. W., Raczek, I., Okrusch, M., Skora, S., & Koepke, J. (2014). Metasomatism of ferroan granites in the northern Aravalli orogen, NW India: geochemical and isotopic constraints, and its metallogenic significance. International Journal of Earth Sciences, 103(4), 1083-1112.

Kawohl, A., & Frimmel, H. E. (2016). Isoferroplatinum-pyrrhotite-troilite intergrowth as evidence of desulfurization in the Merensky Reef at Rustenburg (western Bushveld Complex, South Africa). Mineralogical Magazine, 80(6), 1041-1053.

Keays, R. R. (1995). The role of komatiitic and picritic magmatism and S-saturation in the formation of ore deposits. Lithos, 34(1-3), 1-18.

Keays, R. R., & Crocket, J. H. (1970). A study of precious metals in the Sudbury nickel irruptive ores. Economic Geology, 65(4), 438-450.

Keays, R. R., & Lightfoot, P. C. (2004). Formation of Ni–Cu–platinum group element sulfide mineralization in the Sudbury impact melt sheet. Mineralogy and Petrology, 82(3), 217-258.

Keays, R. R., & Lightfoot, P. C. (2007). Siderophile and chalcophile metal variations in Tertiary picrites and basalts from West Greenland with implications for the sulphide saturation history of continental flood basalt magmas. Mineralium Deposita, 42(4), 319-336.

Keays, R. R., & Lightfoot, P. C. (2020). Mafic intrusions in the footwall of the Sudbury Igneous Complex: Origin of the Sudbury impact melt sheet and its associated ore deposits. Ore Geology Reviews, 120, 103435.

Keays, R. R., Nickel, E. H., Groves, D. I., & McGoldrick, P. J. (1982). Iridium and palladium as discriminants of volcanic-exhalative, hydrothermal, and magmatic nickel sulfide mineralization. Economic Geology, 77(6), 1535-1547.

Keays, R. R., Vogel, D. C., James, R. S., Peck, D. C., Lightfoot, P. C., & Prevec, S. A. (1995). Metallogenic potential of the Huronian-Nipissing magmatic province. The Canadian Mineralogist, 33(4), 932-933.

Keevil, N. B. (2017). Never Rest on Your Ores: Building a Mining Company, one Stone at a Time. 1st edition, McGill-Queen's University Press, Volume 26, 496p.

Keevil, N. B., Parsons, G. E., & Westrick, E. W. (1948). Interpretation of aeromagnetic survey of central Afton Claims. Unpublished report, prepared for the Dominion Gulf Company, 73p., Ontario Assessment File Database record number 41I16NW0057.

Kenkmann, T., Hornemann, U., & Stöffler, D. (2000). Experimental generation of shock-induced pseudotachylites along lithological interfaces. Meteoritics & Planetary Science, 35(6), 1275-1290.

Kenny, G. G., Petrus, J. A., Whitehouse, M. J., Daly, J. S., & Kamber, B. S. (2017). Hf isotope evidence for effective impact melt homogenisation at the Sudbury impact crater, Ontario, Canada. Geochimica et Cosmochimica Acta, 215, 317-336.

Ketchum, J. W. F., & Davidson, A. (2000). Crustal architecture and tectonic assembly of the Central Gneiss Belt, southwestern Grenville Province, Canada: a new interpretation. Canadian Journal of Earth Sciences, 37(2-3), 217-234.

Ketchum, K. Y., Heaman, L. M., Bennett, G., & Hughes, D. J. (2013). Age, petrogenesis and tectonic setting of the Thessalon volcanic rocks, Huronian Supergroup, Canada. Precambrian Research, 233, 144-172.

Kirkland, C. L., Hollis, J., Danišík, M., Petersen, J., Evans, N. J., & McDonald, B. J. (2017). Apatite and titanite from the Karrat Group, Greenland; implications for charting the thermal evolution of crust from the U-Pb geochronology of common Pb bearing phases. Precambrian Research, 300, 107-120.

Kirkland, C. L., Yakymchuk, C., Gardiner, N. J., Szilas, K., Hollis, J., Olierook, H., & Steenfelt, A. (2020). Titanite petrochronology linked to phase equilibrium modelling constrains tectono-thermal events in the Akia Terrane, West Greenland. Chemical Geology, 536, 119467.

Kleinboeck, J. (2015). Phase 1 diamond drilling program: TeckMag1 project, Canadian Continental Exploration Corp. Unpublished report, 203p., Ontario Assessment File Database record number 20000014558.

Klimesch, L. M., Hecht, L., & Riller, U. (2008). Petrology of the Trill Offset Dike, Sudbury, Canada. Abstract presented to the 86. Annual DMG Meeting, 15-17 September 2008, Berlin, Germany, 545, https://www.dmg-home.org./fileadmin/user_upload/Konferenzen/DMG-CD/filedir/545_abstract.pdf

Koeberl, C. (2013). The Geochemistry and Cosmochemistry of Impacts. In: Turekian, K. K., Holland, H. D. (eds.), Treatise on Geochemistry. 2nd edition, Elsevier Science, Volume 2, 73-118.

Kohn, M. J. (2017). Titanite petrochronology. Reviews in Mineralogy and Geochemistry, 83(1), 419-441.

Kono, Y., Kenney-Benson, C., Hummer, D., Ohfuji, H., Park, C., Shen, G., ... & Manning, C. E. (2014). Ultralow viscosity of carbonate melts at high pressures. Nature Communications, 5, 5091.

Konzett, J., Armstrong, R. A., & Günther, D. (2000). Modal metasomatism in the Kaapvaal craton lithosphere: constraints on timing and genesis from U–Pb zircon dating of metasomatized peridotites and MARID-type xenoliths. Contributions to Mineralogy and Petrology, 139(6), 704-719.

Koulomzine, T. H. (1955). Unpublished report on Dolmac Mines Limited property, Rathbun Township, District of Sudbury. Ontario Assessment File Database record number 41I15SE0090.

Kovaleva, E., Huber, M. S., & Zaccarini, F. (2018b). Petrography and geochemistry of coarse-crystalline veins within Vredefort Granophyre, Vredefort impact structure, South Africa. South African Journal of Geology, 121(4), 383-402.

Kovaleva, E., Huber, M. S., Fourie, F., & Pittarello, L. (2018a). Comparative study of pseudotachylite microstructures in felsic and mafic rocks from the Vredefort impact structure, South Africa. Implications for the experimental studies. South African Journal of Geology, 121(4), 403-420.

Kovaleva, E., Zamyatin, D. A., & Habler, G. (2019). Granular zircon from Vredefort granophyre (South Africa) confirms the deep injection model for impact melt in large impact structures. Geology, 47(8), 691-694.

Kresten, P., & Morogan, V. (1986). Fenitization at the Fen complex, southern Norway. Lithos,

19(1), 27-42.

Kretz, R., Hartree, R., Garrett, D., & Cermignani, C. (1985). Petrology of the Grenville swarm of gabbro dikes, Canadian Precambrian Shield. Canadian Journal of Earth Sciences, 22(1), 53-71.

Kring, D. A., Tikoo, S. M., Schmieder, M., Riller, U., Rebolledo-Vieyra, M., Simpson, S. L., ... & Yamaguchi, K. E. (2020). Probing the hydrothermal system of the Chicxulub impact crater. Science Advances, 6(22), eaaz3053.

Krogh, T. E., Corfu, F., Davis, D. W., Dunning, G. R., Heaman, L. M., Kamo, S. L., Machado, N., Greenough, J. D., & Nakamura, E. (1987). Precise U-Pb isotopic ages of diabase dykes and mafic to ultramafic rocks using trace amounts of baddeleyite and zircon. In: Halls, H. C., Fahrig, W. F. (eds), Mafic Dyke Swarms. Geological Association of Canada, Special Paper 34, 147-152.

Krogh, T. E., Davis, D. W., & Corfu, F. (1984). Precise U–Pb zircon and baddeleyite ages for the Sudbury Structure. In: Pye, E. G., Naldrett, A. J., Giblin, P. E. (eds.), The Geology and Ore Deposits of the Sudbury Structure. Ontario Geological Survey, Special Volume 1, 431-446.

Krogh, T. E., Kamo, S. L., Bohor, B. F., Basu, A., & Hart, S. (1996). Shock metamorphosed zircons with correlated U-Pb discordance and melt rocks with concordant protolith ages indicate an impact origin for the Sudbury structure. American Geophysical Union, Geophysical Monograph 95, 343-354.

Kullerud, G. (1963). Thermal stability of pentlandite. The Canadian Mineralogist, 7(3), 353-366.

Kurtz, R. D., Ostrowski, J. A., & Niblett, E. R. (1986). A magnetotelluric survey over the East Bull Lake gabbro-anorthosite complex. Journal of Geophysical Research: Solid Earth, 91(B7), 7403-7416.

Lafrance, B., & Kamber, B. S. (2010). Geochemical and microstructural evidence for in situ formation of pseudotachylitic Sudbury breccia by shock-induced compression and cataclasis. Precambrian Research, 180(3-4), 237-250.

Lafrance, B., Bygnes, L. C., & McDonald, A. M. (2014). Emplacement of metabreccia along the Whistle offset dike, Sudbury: implications for post-impact modification of the Sudbury impact structure. Canadian Journal of Earth Sciences, 51(5), 466-484.

Lafrance, B., Legault, D., & Ames, D. E. (2008). The formation of the Sudbury breccia in the North Range of the Sudbury impact structure. Precambrian Research, 165(3-4), 107-119.

Lahaye, Y., Arndt, N. T., Byerly, G., Chauvel, C., Fourcade, S., & Gruau, G. (1995). The influence of alteration on the trace-element and Nd isotopic compositions of komatiites. Chemical Geology, 126(1), 43-64.

Lambert, I. B., & Wyllie, P. J. (1974). Melting of tonalite and crystallization of andesite liquid with excess water to 30 kilobars. The Journal of Geology, 82(1), 88-97.

Langmuir, D. (1978). Uranium solution-mineral equilibria at low temperatures with applications to sedimentary ore-deposits. Geochimica et Cosmochimica Acta, 42, 547-569.

Large, R. R., Gemmell, J. B., Paulick, H., & Huston, D. L. (2001). The alteration box plot: A simple approach to understanding the relationship between alteration mineralogy and lithogeochemistry associated with volcanic-hosted massive sulfide deposits. Economic Geology, 96(5), 957-971.

Latypov, R., Chistyakova, S., Grieve, R. A. F., & Huhma, H. (2019). Evidence for igneous differentiation in Sudbury Igneous Complex and impact-driven evolution of terrestrial planet protocrusts. Nature Communications, 10, 508.

Laurora, A., Mazzucchelli, M., Rivalenti, G., Vannucci, R., Zanetti, A., Barbieri, M. A., & Cingolani, C. A. (2001). Metasomatism and melting in carbonated peridotite xenoliths from the mantle wedge: the Gobernador Gregores case (Southern Patagonia). Journal of Petrology, 42(1), 69-87.

Layton-Matthews, D., Lesher, C. M., Burnham, O. M., Liwanag, J., Halden, N. M., Hulbert, L. J., ... & Goodfellow, W. D. (2007). Magmatic Ni-Cu-platinum-group element deposits of the Thompson Nickel Belt. In: Goodfellow, W. D. (ed.), Mineral deposits of Canada: a synthesis of major deposit types, district metallogeny, the evolution of geological provinces, and exploration methods. Geological Association of Canada, Mineral Deposits Division, Special Publication 5, 409-432.

Lazar, O. R., Bohacs, K. M., Macquaker, J. H., Schieber, J., & Demko, T. M. (2015). Capturing key attributes of fine-grained sedimentary rocks in outcrops, cores, and thin sections: nomenclature and description guidelines. Journal of Sedimentary Research, 85(3), 230-246.

Le Bas, M. J., Le Maitre, R. W., Streckeisen, A., Zanettin, B., & IUGS Subcommission on the Systematics of Igneous Rocks (1986). A chemical classification of volcanic rocks based on the total alkali-silica diagram. Journal of Petrology, 27(3), 745-750.

Le Maitre, R. W., Streckeisen, A., Zanettin, B., Le Bas, M. J., Bonin, B., Bateman, P., ... & Woolley, A. R. (2002). Igneous rocks. A Classification and Glossary of Terms: Recommendations of the International Union of Geological Sciences Subcommission on the Systematics of Igneous Rocks. 2nd edition, Cambridge University Press, Cambridge, UK, 252p.

Le Vaillant, M., Barnes, S. J., Fiorentini, M. L., Santaguida, F., & Törmänen, T. (2016). Effects of hydrous alteration on the distribution of base metals and platinum group elements within the Kevitsa magmatic nickel sulphide deposit. Ore Geology Reviews, 72, 128-148.

Leake, B. E., Woolley, A. R., Arps, C. E., Birch, W. D., Gilbert, M. C., Grice, J. D., ... & Youzhi, G. (1997). Nomenclature of amphiboles; report of the Subcommittee on Amphiboles of the International Mineralogical Association Commission on new minerals and mineral names. Mineralogical Magazine, 61(405), 295-310.

Lechler, P. J., & Desilets, M. O. (1987). A review of the use of loss on ignition as a measurement of total volatiles in whole-rock analysis. Chemical Geology, 63(3-4), 341-344.

Legault, F., Francis, D., Hynes, A., & Budkewitsch, P. (1994). Proterozoic continental volcanism in the Belcher Islands: implications for the evolution of the Circum Ungava Fold Belt. Canadian Journal of Earth Sciences, 31(10), 1536-1549.

Legault, J. M., Orta, M., Kumar, H., & Zhao, S. (2011). ZTEM and VTEM airborne EM survey results over PGM-Cu-Ni targets at East Bull Lake anorthositic complex, Massey, Ontario. In: SEG Technical Program Expanded Abstracts (2011). Annual Meeting of the Society of Exploration Geophysicists, 18-23 September 2011, San Antonio, Texas, USA, 629-634, https://doi.org/10.1190/1.3628158

Lenauer, I., & Riller, U. (2017). A trishear model for the deformation of the Sudbury Igneous Complex, Canada. Journal of Structural Geology, 97, 212-224.

Lesher, C. M. (2007). Ni-Cu-PGE Deposits in the Raglan Area, Cape Smith Belt, New Quebec. In: Goodfellow, W. D. (ed.), Mineral deposits of Canada: a synthesis of major deposit types, district metallogeny, the evolution of geological provinces, and exploration methods. Geological Association of Canada, Mineral Deposits Division, Special Publication 5, 351-386.

Lesher, C. M. (2017). Roles of xenomelts, xenoliths, xenocrysts, xenovolatiles, residues, and skarns in the genesis, transport, and localization of magmatic Fe-Ni-Cu-PGE sulfides and chromite. Ore Geology Reviews, 90, 465-484.

Lesher, C. M., & Arndt, N. T. (1995). REE and Nd isotope geochemistry, petrogenesis and volcanic evolution of contaminated komatiites at Kambalda, Western Australia. Lithos, 34(1-3), 127-157.

Li, C., & Naldrett, A. J. (1993). Sulfide capacity of magma; a quantitative model and its application to the formation of sulfide ores at Sudbury, Ontario. Economic Geology, 88(5), 1253-1260.

Li, C., Naldrett, A. J., Coats, C. J. A., & Johannessen, P. (1992). Platinum, palladium, gold, copper-rich stringers at the Strathcona Mine, Sudbury; their enrichment by fractionation of a sulfide liquid. Economic Geology, 87(6), 1584-1598.

Li, C., Ripley, E. M., Merino, E., & Maier, W. D. (2004). Replacement of base metal sulfides by actinolite, epidote, calcite, and magnetite in the UG2 and Merensky Reef of the Bushveld Complex, South Africa. Economic Geology, 99(1), 0173-0184.

Li, C., Ripley, E. M., Oberthür, T., Miller, J. D., & Joslin, G. D. (2008). Textural, mineralogical and stable isotope studies of hydrothermal alteration in the main sulfide zone of the Great Dyke, Zimbabwe and the precious metals zone of the Sonju Lake Intrusion, Minnesota, USA. Mineralium Deposita, 43(1), 97-110.

Li, L., Shi, Y., Anderson, J. L., Ubide, T., Nemchin, A. A., Caulfield, J., ... & Zhao, J. X. (2021). Dating mafic magmatism by integrating baddeleyite, zircon and apatite U–Pb geochronology: A case study of Proterozoic mafic dykes/sills in the North China Craton. Lithos, 380, 105820.

Liao, Y., Wei, C., & Rehman, H. U. (2021). Titanium in calcium amphibole: Behavior and thermometry. American Mineralogist, 106(2), 180-191.

Lieger, D., Riller, U., & Gibson, R. L. (2009). Generation of fragment-rich pseudotachylite bodies during central uplift formation in the Vredefort impact structure, South Africa. Earth and Planetary Science Letters, 279(1-2), 53-64.

Liew, T. C., & Hofmann, A. W. (1988). Precambrian crustal components, plutonic associations,

plate environment of the Hercynian Fold Belt of central Europe: indications from a Nd and Sr isotopic study. Contributions to Mineralogy and Petrology, 98(2), 129-138.

Lightfoot P. C., & Zotov I. A. (2005). Geology and Geochemistry of the Sudbury Igneous Complex, Ontario, Canada: Origin of Nickel Sulfide Mineralization Associated with an Impact-Generated Melt Sheet. Geology of Ore Deposits, 47(5), 349-381.

Lightfoot, P. C. (2016). Nickel Sulfide Ores and Impact Melts: Origin of the Sudbury Igneous Complex. 1st edition, Elsevier, Amsterdam, 680p.

Lightfoot, P. C., & Farrow, C. E. (2002). Geology, geochemistry, and mineralogy of the Worthington offset dike: A genetic model for offset dike mineralization in the Sudbury Igneous Complex. Economic Geology, 97(7), 1419-1446.

Lightfoot, P. C., & Naldrett, A. J. (1989). Assimilation and crystallization in basic magma chambers: trace-element and Nd-isotopic variations in the Kerns sill, Nipissing diabase province, Ontario. Canadian Journal of Earth Sciences, 26(4), 737-754.

Lightfoot, P. C., & Naldrett, A. J. (1996a). Petrology and geochemistry of the Nipissing gabbro: Exploration strategies for Ni, Cu and PGE in a large igneous province. Ontario Geological Survey, Study 58, 80p.

Lightfoot, P. C., & Naldrett, A. J. (1996b). Analytical data for Nipissing Intrusions. Ontario Geological Survey, Miscellaneous Release – Data 19.

Lightfoot, P. C., de Souza, H., & Doherty, W. (1991). Mineral potential of the Nipissing Diabase: Some geochemical considerations. Ontario Geological Survey, Miscellaneous Paper 157, 237-246.

Lightfoot, P. C., de Souza, H., & Doherty, W. (1993). Differentiation and source of the Nipissing Diabase intrusions, Ontario, Canada. Canadian Journal of Earth Sciences, 30(6), 1123-1140.

Lightfoot, P. C., Doherty, W., Farrell, K. P., Keays, R. R., Moore, M., & Pekeski, D. (1997c). Analytical Data for Geochemistry of the Main Mass, Sublayer, Offsets and Inclusions from the Sudbury Igneous Complex, Table 5, 6 and 7. Ontario Geological Survey, Open File Report 5959, Miscellaneous Release–Data 30.

Lightfoot, P. C., Keays, R. R., & Doherty, W. (2001). Chemical Evolution and Origin of Nickel Sulfide Mineralization in the Sudbury Igneous Complex, Ontario, Canada. Economic Geology, 96(8), 1855-1875.

Lightfoot, P. C., Keays, R. R., Morrison, G. G., Bite, A., & Farrell, K. P. (1997a). Geochemical relationships in the Sudbury igneous complex; origin of the main mass and offset dikes. Economic Geology, 92(3), 289-307.

Lightfoot, P. C., Keays, R. R., Morrison, G. G., Bite, A., & Farrell, K. P. (1997b). Geologic and geochemical relationships between the contact sublayer, inclusions, and the main mass of the Sudbury Igneous Complex; a case study of the Whistle Mine Embayment. Economic Geology, 92(6), 647-673.

Liu, Y., & Brenan, J. (2015). Partitioning of platinum-group elements (PGE) and chalcogens (Se,

Te, As, Sb, Bi) between monosulfide-solid solution (MSS), intermediate solid solution (ISS) and sulfide liquid at controlled fO_2–fS_2 conditions. Geochimica et Cosmochimica Acta, 159, 139-161.

Liu, Z., Shea, J. J., Foley, S. F., Bussweiler, Y., Rohrbach, A., Klemme, S., & Berndt, J. (2021). Clarifying source assemblages and metasomatic agents for basaltic rocks in eastern Australia using olivine phenocryst compositions. Lithos, 390, 106122.

Lofgren, G. (1971). Spherulitic textures in glassy and crystalline rocks. Journal of Geophysical Research, 76(23), 5635-5648.

Long, D. G. F. (2004). The tectonostatigraphic evolution of the Huronian basement and the subsequent basin fill: geological constraints on impact models of the Sudbury event. Precambrian Research, 129(3-4), 203-223.

Long, D. G. F. (2009). The Huronian Supergroup. In: Rousell, D. H., Brown, G. H. (eds.), A Field Guide to the Geology of Sudbury, Ontario. Ontario Geological Survey, Open File Report 6243, 14-30.

Longerich, H. P., Fryer, B. J., & Strong, D. F. (1987). Determination of lead isotope ratios by inductively coupled plasma-mass spectrometry (ICP-MS). Spectrochimica Acta Part B: Atomic Spectroscopy, 42(1-2), 39-48.

López-Moro, F. J., Romer, R. L., Rhede, D., Fernández, A., Timon-Sanchez, S. M., & Moro, M. C. (2019). Early uranium mobilization in late Variscan strike-slip shear zones affecting leucogranites of central western Spain. Journal of Iberian Geology, 45(1), 223-243.

Lorand, J. P., & Luguet, A. (2016). Chalcophile and siderophile elements in mantle rocks: Trace elements controlled by trace minerals. Reviews in Mineralogy and Geochemistry, 81(1), 441-488.

Ludden, J., & Hynes, A. (2000). The Lithoprobe Abitibi-Grenville transect: two billion years of crust formation and recycling in the Precambrian Shield of Canada. Canadian Journal of Earth Sciences, 37(2-3), 459-476.

Ludwig, K. R. (2003). User's manual for Isoplot 3.00, a geochronlogical toolkit for Microsoft Excel. Berkeley Geochronological Center, Special Publication 4, 25-32.

Lugmair, G. W., & Marti, K. (1978). Lunar initial $^{143}Nd/^{144}Nd$: differential evolution of the lunar crust and mantle. Earth and Planetary Science Letters, 39(3), 349-357.

Lumbers, S. B., & Card, K. D. (1977). Sudbury-Cobalt, geological compilation series, Algoma, Manitoulin, Nipissing, Parry Sound, Sudbury and Timiskaming districts. Ontario Geological Survey, Map 2361, scale 1:253440.

MacLean, W. H. (1988). Rare earth element mobility at constant inter-REE ratios in the alteration zone at the Phelps Dodge massive sulphide deposit, Matagami, Quebec. Mineralium Deposita, 23(4), 231-238.

Mahmoodi, O., & Smith, R. S. (2015). Clustering of downhole physical property measurements at the Victoria property, Sudbury for the purpose of extracting lithological information. Journal

of Applied Geophysics, 118, 145-154.

Mahmoodi, O., Smith, R. S., & Spicer, B. (2017). Using constrained inversion of gravity and magnetic field to produce a 3D litho-prediction model. Geophysical Prospecting, 65(6), 1662-1679.

Maier, W. D. (2005). Platinum-group element (PGE) deposits and occurrences: Mineralization styles, genetic concepts, and exploration criteria. Journal of African Earth Sciences, 41(3), 165-191.

Maier, W. D., Andreoli, M. A., McDonald, I., Higgins, M. D., Boyce, A. J., Shukolyukov, A., ... & Hart, R. J. (2006). Discovery of a 25-cm asteroid clast in the giant Morokweng impact crater, South Africa. Nature, 441(7090), 203-206.

Maniar, P. D., & Piccoli, P. M. (1989). Tectonic discrimination of granitoids. Geological Society of America Bulletin, 101(5), 635-643.

Masaitis, V. L., Shafranovsky, G. I., Balmasov, E. L., Fedorova, I. G., Grieve, R. A. F., Therriault, A. M., ... & Peredery, W. V. (1999). Impact diamonds in the Suevitic Breccias of the Black Member of the Onaping Formation, Sudbury Structure, Ontario, Canada. In: Dressler, B. O., Sharpton, V. L. (eds.), Large Meteorite Impacts and Planetary Evolution II. Geological Society of America, Special Paper 339, 317-321.

Mathieu, L., Riller, U., Gibson, L., & Lightfoot, P. C. (2021). Structural controls on the localization of the mineralized Copper Cliff embayment and the Copper Cliff offset dyke, Sudbury Igneous Complex, Canada. Ore Geology Reviews, 113, 104071.

McClenaghan, M. B., Ames, D. E., & Cabri, L. J. (2019). Indicator mineral and till geochemical signatures of the Broken Hammer Cu-Ni-PGE-Au deposit, North Range, Sudbury Structure, Ontario, Canada. Geochemistry: Exploration, Environment, Analysis, 20(3), 337-356.

McCulloch, M. T., & Black, L. P. (1984). Sm-Nd isotopic systematics of Enderby Land granulites and evidence for the redistribution of Sm and Nd during metamorphism. Earth and Planetary Science Letters, 71(1), 46-58.

McDaniel, D. K., Hemming, S. R., McLennan, S. M., & Hanson, G. N. (1994a). Petrographic, geochemical, and isotopic constraints on the provenance of the early Proterozoic Chelmsford Formation, Sudbury Basin, Ontario. Journal of Sedimentary Research, 64(2a), 362-372.

McDaniel, D. K., Hemming, S. R., McLennan, S. M., & Hanson, G. N. (1994b). Resetting of neodymium isotopes and redistribution of REEs during sedimentary processes: The Early Proterozoic Chelmsford Formation, Sudbury Basin, Ontario, Canada. Geochimica et Cosmochimica Acta, 58(2), 931-941.

McDonough, W. F. (1990). Constraints on the composition of the continental lithospheric mantle. Earth and Planetary Science Letters, 101(1), 1-18.

McDonough, W. F., & Sun, S. S. (1995). The composition of the Earth. Chemical Geology, 120(3-4), 223-253.

McDowell, F. W., McIntosh, W. C., & Farley, K. A. (2005). A precise ^{40}Ar–^{39}Ar reference age for the

Durango apatite (U–Th)/He and fission-track dating standard. Chemical Geology, 214(3-4), 249-263.

McGrath, P. H., & Broome, H. J. (1994). A gravity model for the Sudbury Structure along the Lithoprobe seismic line. Geophysical Research Letters, 21(10), 955-958.

McGrath, P. H., Hood, P. J., & Darnley, A. G. (1977). Magnetic anomaly map of Canada. Geological Survey of Canada, Map 1255A, scale 1:5000000.

McGregor, M., Dence, M. R., McFarlane, C. R., & Spray, J. G. (2020a). U–Pb geochronology of apatite and zircon from the Brent impact structure, Canada: a Late Ordovician Sandbian–Katian boundary event associated with L-Chondrite parent body disruption. Contributions to Mineralogy and Petrology, 175(7), 1-21.

McGregor, M., Erickson, T. M., Spray, J. G., & Whitehouse, M. J. (2021). High-resolution EBSD and SIMS U–Pb geochronology of zircon, titanite, and apatite: insights from the Lac La Moinerie impact structure, Canada. Contributions to Mineralogy and Petrology, 176(10), 1-25.

McGregor, M., McFarlane, C. R., & Spray, J. G. (2018). In situ LA-ICP-MS apatite and zircon U–Pb geochronology of the Nicholson Lake impact structure, Canada: shock and related thermal effects. Earth and Planetary Science Letters, 504, 185-197.

McGregor, M., McFarlane, C. R., & Spray, J. G. (2019). In situ multiphase U–Pb geochronology and shock analysis of apatite, titanite and zircon from the Lac La Moinerie impact structure, Canada. Contributions to Mineralogy and Petrology, 174(7), 1-20.

McGregor, M., Walton, E. L., McFarlane, C. R., & Spray, J. G. (2020b). Multiphase U-Pb geochronology of sintered breccias from the Steen River impact structure, Canada: Mixed target considerations for a Jurassic-Cretaceous boundary event. Geochimica et Cosmochimica Acta, 274, 136-156.

McKenzie, D. (1984). The Generation and Compaction of Partially Molten Rock. Journal of Petrology, 25(3), 713-765.

McKenzie, D. (1989). Some remarks on the movement of small melt fractions in the mantle. Earth and Planetary Science Letters, 95(1-2), 53-72.

McKenzie, D., & O'Nions, R. K. (1991). Partial melt distributions from inversion of rare earth element concentrations. Journal of Petrology, 32(5), 1021-1091.

McKevitt, D. J., Lesher, C. M., & Houlé, M. G. (2019). Geology, geochemistry and petrogenesis of the Expo-Ungava–Raglan dike, sill and lava-channel system in the Paleoproterozoic Cape Smith Belt, Northern Nunavik, Quebec. In: Rogers, N. (ed.), Targeted Geoscience Initiative 5: 2018 report of activities. Geological Survey of Canada, Open File 8549, 393-401.

McKinstry, H. E. (1959). Mineral assemblages in sulfide ores; the system Cu-Fe-SO. Economic Geology, 54(6), 975-1001.

McLennan, S. M., Simonetti, A., & Goldstein, S. L. (2000). Nd and Pb isotopic evidence for provenance and post-depositional alteration of the Paleoproterozoic Huronian Supergroup, Canada. Precambrian Research, 102(3-4), 263-278.

McLeod, G. W., Dempster, T. J., & Faithfull, J. W. (2011). Deciphering magma-mixing processes using zoned titanite from the Ross of Mull Granite, Scotland. Journal of Petrology, 52(1), 55-82.

McNamara, G. S., Lesher, C. M., & Kamber, B. S. (2017). New feldspar lead isotope and trace element evidence from the Sudbury Igneous Complex indicate a complex origin of associated Ni-Cu-PGE mineralization involving underlying country rocks. Economic Geology, 112(3), 569-590.

McRitchie, W. D. (1995). Mineral development potential in Manitoba - Nickel in the Southwest Extension of the Thompson Nickel Belt: Manitoba Energy and Mines, Geological Services, Economic Geology Report ER95-2, 29p.

Meecham, R., & Truscott, D. (1992). M-SH-02 Drill Hole Record, Sheppard Township. Ontario Assessment File Database record number 41I16NW0065.

Meldrum, A., Abdel-Rahman, A. F., Martin, R. F., & Wodicka, N. (1997). The nature, age and petrogenesis of the Cartier Batholith, northern flank of the Sudbury Structure, Ontario, Canada. Precambrian Research, 82(3-4), 265-285.

Melezhik, V. A., Young, G. M., Eriksson, P. G., Altermann, W., Kump, L. R., & Lepland, A. (2013). Huronian-Age Glaciation. In: Melezhik, V. A., Young, G. M., Eriksson, P. G., Altermann, W., Kump, L. R., Lepland, A. (eds.), Reading the Archive of Earth's Oxygenation. Springer, Berlin and Heidelberg, 1059-1109.

Melosh, H. J. (1989). Impact cratering: A geologic process. 1st edition, Oxford University Press, New York, 245p.

Meschede, M. (1986). A method of discriminating between different types of mid-ocean ridge basalts and continental tholeiites with the Nb-Zr-Y diagram. Chemical Geology, 56(3-4), 207-218.

Meyer, W., Campbell, R. W., & Toews, F. H. (1987). Sudbury Resident Geologist's Area, Northeastern Region. In: Kustra, C. R. (ed.), Report of Activities, 1986 Regional and Resident Geologists. Ontario Geological Survey, Miscellaneous Paper 134, 256-257.

Meyn, H. D. (1970). Geology of Hutton and Parkin Townships. Ontario Department of Mines, Geological Report 80, 78p.

Meyn, H. D. (1977). Geology of Afton, Scholes, Macbeth, and Clement Townships, Districts of Sudbury and Nipissing. Ontario Geological Survey, Report 170, 77p.

Michener, C. E., & Yates, A. B. (1944). Oxidation of primary nickel sulphides [Canada]. Economic Geology, 39(7), 506-514.

Míková, J., & Denková, P. (2007). Modified chromatographic separation scheme for Sr and Nd isotope analysis in geological silicate samples. Journal of Geosciences, 52(3-4), 221-226.

Milidragovic, D., Beaudoin, G., Hamilton, M. A., & King, J. J. (2016). The Paleoproterozoic Otish Gabbro suite and coeval dyke swarms of the Superior Province: Probing the ca. 2.17 Ga mantle. Precambrian Research, 278, 126-144.

Milkereit, B., & Wu, J. (1996). Seismic image of an early Proterozoic rift basin. Tectonophysics, 264(1-4), 89-100.

Miller, C. F., & Mittlefehldt, D. W. (1982). Depletion of light rare-earth elements in felsic magmas. Geology, 10(3), 129-133.

Miller, W. G. (1913). The cobalt-nickel arsenides and silver deposits of Timiskaming. Ontario Bureau of Mines, Annual Report 19, part 2, 729p.

Millonig, L. J., Gerdes, A., & Groat, L. A. (2012). U–Th–Pb geochronology of meta-carbonatites and meta-alkaline rocks in the southern Canadian Cordillera: a geodynamic perspective. Lithos, 152, 202-217.

Minifie, M. J. (2010). Nature and origin of the ~1880 ma circum-superior large igneous province. Unpublished PhD thesis, Cardiff University, United Kingdom, 575p., http://orca.cardiff.ac.uk/id/eprint/54142

Minifie, M. J., Kerr, A. C., Ernst, R. E., Hastie, A. R., Ciborowski, T. J. R., Desharnais, G., & Millar, I. L. (2013). The northern and southern sections of the western ca. 1880 Ma circum-Superior large igneous province, North America: The Pickle Crow dyke connection?. Lithos, 174, 217-235.

Misra, K. C., & Fleet, M. E. (1974). Chemical composition and stability of violarite. Economic Geology, 69(3), 391-403.

Mitchell, R. H. (1978). Manganoan magnesian ilmenite and titanian clinohumite from the Jacupiranga carbonatite, Sao Paulo, Brazil. American Mineralogist, 63(5-6), 544-547.

Mitchell, R. H., & Platt, R. G. (1982). Mineralogy and petrology of nepheline syenites from the Coldwell alkaline complex, Ontario, Canada. Journal of Petrology, 23(2), 186-214.

Mohr-Westheide, T., & Reimold, W. U. (2011). Formation of pseudotachylitic breccias in the central uplifts of very large impact structures: Scaling the melt formation. Meteoritics & Planetary Science, 46(4), 543-555.

Mole, D. R., Thurston, P. C., Marsh, J. H., Stern, R. A., Ayer, J. A., Martin, L. A. J., & Lu, Y. J. (2021). The formation of Neoarchean continental crust in the south-east Superior Craton by two distinct geodynamic processes. Precambrian Research, 356, 106104.

Moore, D. E., & Liou, J. G. (1979). Chessboard-twinned albite from Franciscan metaconglomerates of the Diablo Range, California. American Mineralogist, 64(3-4), 329-336.

Morad, S. (1988). Albitized microcline grains of post-depositional and probable detrital origins in Brøttum Formation sandstones (Upper Proterozoic), Sparagmite Region of southern Norway. Geological Magazine, 125(3), 229-239.

Morad, S., Bergan, M., Knarud, R., & Nystuen, J. P. (1990). Albitization of detrital plagioclase in Triassic reservoir sandstones from the Snorre Field, Norwegian North Sea. Journal of Sedimentary Research, 60(3), 411-425.

Morgan, G. B., & London, D. (2012). Process of granophyre crystallization in the Long Mountain

Granite, southern Oklahoma. Geological Society of America Bulletin, 124(7-8), 1251-1261.

Morley, L. W., McLaren, A. S., & Charbonneau, B. W. (1968). Magnetic anomaly map of Canada. Geological Survey of Canada, Map 1255A, scale 1:5000000.

Morrison, G. G. (1984). Morphological features of the Sudbury structure in relation to an impact origin. In: Pye, E. G., Naldrett, A. J., Giblin, P. E. (eds.), The Geology and Ore Deposits of the Sudbury Structure. Ontario Geological Survey, Special Volume 1, 513-522.

Morris, W. A. (1982). A paleomagnetic investigation of the Sudbury basin offsets, Ontario, Canada. Tectonophysics, 85(3-4), 291-312.

Moser, D. E., Cupelli, C. L., Barker, I. R., Flowers, R. M., Bowman, J. R., Wooden, J., & Hart, J. R. (2011). New zircon shock phenomena and their use for dating and reconstruction of large impact structures revealed by electron nanobeam (EBSD, CL, EDS) and isotopic U–Pb and (U–Th)/He analysis of the Vredefort dome. Canadian Journal of Earth Sciences, 48(2), 117-139.

Mossman, D., Eigendorf, G., Tokaryk, D., Gauthier-Lafaye, F., Guckert, K. D., Melezhik, V., & Farrow, C. E. (2003). Testing for fullerenes in geologic materials: Oklo carbonaceous substances, Karelian shungites, Sudbury Black Tuff. Geology, 31(3), 255-258.

Mougel, B., Moynier, F., Göpel, C., & Koeberl, C. (2017). Chromium isotope evidence in ejecta deposits for the nature of Paleoproterozoic impactors. Earth and Planetary Science Letters, 460, 105-111.

Mountain, B. W., & Wood, S. A. (1988). Chemical controls on the solubility, transport and deposition of platinum and palladium in hydrothermal solutions; a thermodynamic approach. Economic Geology, 83(3), 492-510.

Mourão, C., Mata, J., Doucelance, R., Madeira, J., da Silveira, A. B., Silva, L. C., & Moreira, M. (2010). Quaternary extrusive calciocarbonatite volcanism on Brava Island (Cape Verde): A nephelinite-carbonatite immiscibility product. Journal of African Earth Sciences, 56(2-3), 59-74.

Mudd, G. M. (2010). Global trends and environmental issues in nickel mining: Sulfides versus laterites. Ore Geology Reviews, 38(1-2), 9-26.

Mueller, E. L., Morris, W. A., & Jewell, T. (1996). A 3-D geological and potential field model of the East Bull Lake Pluton. In: SEG Technical Program Expanded Abstracts (1996). 66th Annual Meeting of the Society of Exploration Geophysicists, 10-15 November 1996, Denver, Colorado, USA, 1387-1390, https://doi.org/10.1190/1.1826367

Mueller, E. L., Morris, W. A., Killeen, P. G., & Balch, S. (1998). Combined 3-D interpretation of airborne, surface, and borehole vector magnetics at the McConnell nickel deposit. Journal of Environmental and Engineering Geophysics, 3(4), 203-214.

Muir, T. L. (1984). The Sudbury Structure: Consideration and models for an endogenic origin. In: Pye, E. G., Naldrett, A. J., Giblin, P. E. (eds.), The Geology and Ore Deposits of the Sudbury Structure. Ontario Geological Survey, Special Volume 1, 449-489.

Muir, T. L., & Peredery, W. V. (1984). The Onaping Formation. In: Pye, E. G., Naldrett, A. J., Giblin,

P. E. (eds.), The Geology and Ore Deposits of the Sudbury Structure. Ontario Geological Survey, Special Volume 1, 139-210.

Muir, T. L., Buse, S., Trowell, N. F., & Duguet, M. (2016). A library of standards for rock names, rock modifiers and terms related to structure, alteration, mineralization and minerals for Precambrian rocks in Ontario. Ontario Geological Survey, Open File Report 6289, 204p.

Mukwakwami, J., Lafrance, B., & Lesher, C. M. (2012). Back-thrusting and overturning of the southern margin of the 1.85 Ga Sudbury Igneous Complex at the Garson mine, Sudbury, Ontario. Precambrian Research, 196, 81-105.

Mukwakwami, J., Lafrance, B., Lesher, C. M., Tinkham, D. K., Rayner, N. M., & Ames, D. E. (2014). Deformation, metamorphism, and mobilization of Ni–Cu–PGE sulfide ores at Garson Mine, Sudbury. Mineralium Deposita, 49(2), 175-198.

Müller, S., Dziggel, A., Sindern, S., Kokfelt, T. F., Gerdes, A., & Kolb, J. (2018). Age and temperature-time evolution of retrogressed eclogite-facies rocks in the Paleoproterozoic Nagssugtoqidian Orogen, South-East Greenland: Constrained from U-Pb dating of zircon, monazite, titanite and rutile. Precambrian Research, 314, 468-486.

Mungall, J. E. (2007). Crustal contamination of picritic magmas during transport through dikes: the Expo Intrusive Suite, Cape Smith fold belt, New Quebec. Journal of Petrology, 48(5), 1021-1039.

Mungall, J. E., & Su, S. (2005). Interfacial tension between magmatic sulfide and silicate liquids: Constraints on kinetics of sulfide liquation and sulfide migration through silicate rocks. Earth and Planetary Science Letters, 234(1-2), 135-149.

Mungall, J. E., Ames, D. E., & Hanley, J. J. (2004). Geochemical evidence from the Sudbury structure for crustal redistribution by large bolide impacts. Nature, 429(6991), 546-548.

Mungall, J. E., Hanley, J. J., Arndt, N. T., & Debecdelievre, A. (2006). Evidence from meimechites and other low-degree mantle melts for redox controls on mantle-crust fractionation of platinum-group elements. Proceedings of the National Academy of Sciences, 103(34), 12695-12700.

Mutch, E. J. F., Blundy, J. D., Tattitch, B. C., Cooper, F. J., & Brooker, R. A. (2016). An experimental study of amphibole stability in low-pressure granitic magmas and a revised Al-in-hornblende geobarometer. Contributions to Mineralogy and Petrology, 171(10), 1-27.

Nakamura, N., & Iyeda, Y. (2005). Magnetic properties and paleointensity of pseudotachylytes from the Sudbury structure, Canada: Petrologic control. Tectonophysics, 402(1-4), 141-152.

Naldrett, A. J. (1969). A portion of the system Fe–S–O between 900 and 1080 °C and its application to sulfide ore magmas. Journal of Petrology, 10(2), 171-201.

Naldrett, A. J. (2004). Magmatic Sulfide Deposits. Geology, Geochemistry, and Exploration. 1st edition, Springer-Verlag, Berlin and Heidelberg, 728p.

Naldrett, A. J., & Hewins, R. H. (1984). The Main Mass of the Sudbury Igneous Complex. In: Pye, E. G., Naldrett, A. J., Giblin, P. E. (eds.), The Geology and Ore Deposits of the Sudbury Structure.

Ontario Geological Survey, Special Volume 1, 235-252.

Naldrett, A. J., Asif, M., Schandl, E. S., Searcy, T., Morrison, G. G., Binney, W. P., & Moore, C. (1999). Platinum-group elements in the Sudbury ores; significance with respect to the origin of different ore zones and to the exploration for footwall orebodies. Economic Geology, 94(2), 185-210.

Naldrett, A. J., Rao, B. V., & Evensen, N. M. (1986). Contamination at Sudbury and its role in ore formation. In: Gallagher, M. J., Ixer, R. A., Neary, C. R., Prichard, H. M. (eds.), Metallogeny of basic and ultrabasic rocks. Institute of Mining and Metallogeny, London, 75-91.

Nelson, D. O., Morrison, D. A., & Phinney, W. C. (1990). Open-system evolution versus source control in basaltic magmas: Matachewan–Hearst dike swarm, Superior Province, Canada. Canadian Journal of Earth Sciences, 27(6), 767-783.

Nemchin, A. A., Pidgeon, R. T., Healy, D., Grange, M. L., Whitehouse, M. J., & Vaughan, J. (2009). The comparative behavior of apatite-zircon U-Pb systems in Apollo 14 breccias: Implications for the thermal history of the Fra Mauro Formation. Meteoritics & Planetary Science, 44(11), 1717-1734.

Nesbitt, H., & Young, G. M. (1982). Early Proterozoic climates and plate motions inferred from major element chemistry of lutites. Nature, 299(5885), 715-717.

Neumann, E. R., Wulff-Pedersen, E., Pearson, N. J., & Spencer, E. A. (2002). Mantle xenoliths from Tenerife (Canary Islands): evidence for reactions between mantle peridotites and silicic carbonatite melts inducing Ca metasomatism. Journal of Petrology, 43(5), 825-857.

Nickel, E. H., Ross, J. R., & Thornber, M. R. (1974). The supergene alteration of pyrrhotite-pentlandite ore at Kambalda, Western Australia. Economic Geology, 69(1), 93-107.

Nielsen, R. L. (1985). EQUIL: a program for the modeling of low-pressure differentiation processes in natural mafic magma bodies. Computers & Geosciences, 11(5), 531-546.

Nielson, J. E., & Noller, J. S. (1987). Processes of mantle metasomatism; constraints from observations of composite peridotite xenoliths. In: Morris, E. M., Pasteris, J. D. (eds.), Mantle Metasomatism and Alkaline Magmatism. Geological Society of America, Special Paper 215, 61-76.

Nielson, J. E., & Wilshire, H. G. (1993). Magma transport and metasomatism in the mantle: a critical review of current geochemical models. American Mineralogist, 78(11-12), 1117-1134.

Noble, S. R., & Lightfoot, P. C. (1992). U–Pb baddeleyite ages of the Kerns and Triangle Mountain intrusions, Nipissing diabase, Ontario. Canadian Journal of Earth Sciences, 29(7), 1424-1429.

Norrish, K., & Hutton, J. T. (1969). An accurate X-ray spectrographic method for the analysis of a wide range of geological samples. Geochimica et Cosmochimica Acta, 33(4), 431-453.

O'Callaghan, J. W., Osinski, G. R., Lightfoot, P. C., Linnen, R. L., & Weirich, J. R. (2016). Reconstructing the geochemical signature of Sudbury Breccia, Ontario, Canada: implications for its formation and trace metal content. Economic Geology, 111(7), 1705-1729.

O'Driscoll, B., & González-Jiménez, J. M. (2016). Petrogenesis of the platinum-group minerals. Reviews in Mineralogy and Geochemistry, 81(1), 489-578.

O'Sullivan, E. M., Goodhue, R., Ames, D. E., & Kamber, B. S. (2016). Chemostratigraphy of the Sudbury impact basin fill: Volatile metal loss and post-impact evolution of a submarine impact basin. Geochimica et Cosmochimica Acta, 183, 198-233.

Ogden, M. (1957). Dolmac Mines Limited, Report of the Geological Survey on the Sudbury Area Property. Unpublished report, 30p., Ontario Assessment File Database record number 41I15SE0096.

Ogden, M. (1958). Dolmac Mines Limited, Sudbury Property, Diamond Drilling Programme. Unpublished report, Ontario Assessment File Database record number 41I15SE0102.

Okrusch, M., & Frimmel, H. E. (2020). Mineralogy: An Introduction to Minerals, Rocks, and Mineral Deposits. 1st edition, Springer Nature, Heidelberg and Berlin, 730p.

Olaniyan, O., Smith, R. S., & Lafrance, B. (2014). A constrained potential field data interpretation of the deep geometry of the Sudbury structure. Canadian Journal of Earth Sciences, 51(7), 715-729.

Olaniyan, O., Smith, R. S., & Lafrance, B. (2015). Regional 3D geophysical investigation of the Sudbury Structure. Interpretation, 3(2), SL63-SL81.

Olaniyan, O., Smith, R. S., & Morris, B. (2013). Qualitative geophysical interpretation of the Sudbury Structure. Interpretation, 1(1), T25-T43.

Ono, S., & Fayek, M. (2011). Decoupling of O and Pb isotope systems of uraninite in the early Proterozoic conglomerates in the Elliot Lake district. Chemical Geology, 288(1-2), 1-13.

Ontario Geological Survey (2011). 1:250000 scale bedrock geology of Ontario. Ontario Geological Survey, Miscellaneous Release–Data 126–Revision 1.

Osinski, G. R., & Pierazzo, E. (2012). Impact Cratering: Processes and Products. 1st edition, Wiley-Blackwell, 336p.

Osinski, G. R., Grieve, R. A. F., Bleacher, J. E., Neish, C. D., Pilles, E. A., & Tornabene, L. L. (2018). Igneous rocks formed by hypervelocity impact. Journal of Volcanology and Geothermal Research, 353, 25-54.

Osinski, G. R., Tornabene, L. L., Banerjee, N. R., Cockell, C. S., Flemming, R., Izawa, M. R., ... & Southam, G. (2013). Impact-generated hydrothermal systems on Earth and Mars. Icarus, 224(2), 347-363.

Ostermann, M., Schärer, U., & Deutsch, A. (1996). Impact melt dikes in the Sudbury multi-ring basin (Canada): Implications from uranium-lead geochronology on the Foy Offset Dike. Meteoritics & Planetary Science, 31(4), 494-501.

Özdemir, Y., & Güleç, N. (2014). Geological and geochemical evolution of the Quaternary Süphan Stratovolcano, Eastern Anatolia, Turkey: evidence for the lithosphere–asthenosphere interaction in post-collisional volcanism. Journal of Petrology, 55(1), 37-62.

Palme, H., & O'Neill, H. S. C. (2013). Cosmochemical Estimates of Mantle Composition. In: Turekian, K. K., Holland, H. D. (eds.), Treatise on Geochemistry. 2nd edition, Elsevier Science, Volume 3, 1-39.

Palmer, H. C., Ernst, R. E., & Buchan, K. L. (2007). Magnetic fabric studies of the Nipissing sill province and Senneterre dykes, Canadian Shield, and implications for emplacement. Canadian Journal of Earth Sciences, 44(4), 507-528.

Papanastassiou, D. A., & Wasserburg, G. J. (1970). Rb–Sr ages from the ocean of storms. Earth and Planetary Science Letters, 8(4), 269-278.

Papapavlou, K., Darling, J. R., Lightfoot, P. C., Lasalle, S., Gibson, L., Storey, C. D., & Moser, D. (2018a). Polyorogenic reworking of ore-controlling shear zones at the South Range of the Sudbury impact structure: A telltale story from in situ U–Pb titanite geochronology. Terra Nova, 30(3), 254-261.

Papapavlou, K., Darling, J. R., Moser, D. E., Barker, I. R., White, L. F., Lightfoot, P. C., ... & Dunlop, J. (2018b). U–Pb isotopic dating of titanite microstructures: potential implications for the chronology and identification of large impact structures. Contributions to Mineralogy and Petrology, 173(10), 1-15.

Papapavlou, K., Darling, J. R., Storey, C. D., Lightfoot, P. C., Moser, D. E., & Lasalle, S. (2017). Dating shear zones with plastically deformed titanite: New insights into the orogenic evolution of the Sudbury impact structure (Ontario, Canada). Precambrian Research, 291, 220-235.

Parmenter, A. C., Lee, C. B., & Coniglio, M. (2002). "Sudbury Breccia" at Whitefish Falls, Ontario: evidence for an impact origin. Canadian Journal of Earth Sciences, 39(6), 971-982.

Paterson, B. A., & Stephens, W. E. (1992). Kinetically induced compositional zoning in titanite: implications for accessory-phase/melt partitioning of trace elements. Contributions to Mineralogy and Petrology, 109(3), 373-385.

Pattison, E. F. (1979). The Sudbury sublayer. The Canadian Mineralogist, 17(2), 257-274.

Pattison, E. F. (1980). Tectonic origin for Sudbury, Ontario, shatter cones: Discussion and reply: Discussion. Geological Society of America Bulletin, 91(12), 754-754.

Pattison, E. F. (2009). Sudbury Igneous Complex. In: Rousell, D. H., Brown, G. H. (eds.), A Field Guide to the Geology of Sudbury, Ontario. Ontario Geological Survey, Open File Report 6243, 56-74.

Pearce, J. A. (1983). Trace element characteristics of lavas from destructive plate boundaries. In: Thorpe, R. S. (ed.), Orogenic andesites and related rocks. John Wiley and Sons, Chichester, England, 528-548.

Pearce, J. A. (1996). A user's guide to basalt discrimination diagrams. In: Wyman, D. A. (ed.), Trace element geochemistry of volcanic rocks: applications for massive sulphide exploration. Geological Association of Canada, Short Course Notes 12, 79-113.

Pearce, J. A. (2008). Geochemical fingerprinting of oceanic basalts with applications to ophiolite classification and the search for Archean oceanic crust. Lithos, 100(1-4), 14-48.

Pearce, J. A., Harris, N. B., & Tindle, A. G. (1984). Trace element discrimination diagrams for the tectonic interpretation of granitic rocks. Journal of Petrology, 25(4), 956-983.

Pearson, D. G., & Nowell, G. M. (2002). The continental lithospheric mantle: characteristics and significance as a mantle reservoir. Philosophical Transactions of the Royal Society of London. Series A: Mathematical, Physical and Engineering Sciences, 360(1800), 2383-2410.

Peck, D. C., Keays, R. R., James, R. S., Chubb, P. T., & Reeves, S. J. (2001). Controls on the formation of contact-type platinum-group element mineralization in the East Bull Lake intrusion. Economic Geology, 96(3), 559-581.

Péntek, A., Molnár, F., Tuba, G., Watkinson, D. H., & Jones, P. C. (2013). The significance of partial melting processes in hydrothermal low sulfide Cu-Ni-PGE mineralization within the footwall of the Sudbury Igneous Complex, Ontario, Canada. Economic Geology, 108(1), 59-78.

Péntek, A., Molnár, F., Watkinson, D. H., Jones, P. C., & Mogessie, A. (2011). Partial melting and melt segregation in footwall units within the contact aureole of the Sudbury Igneous Complex (North and East Ranges, Sudbury structure), with implications for their relationship to footwall Cu–Ni–PGE mineralization. International Geology Review, 53(2), 291-325.

Peredery, W. V. (2010). Report on Post Creek Property in Norman and Parkin Townships. Unpublished report, prepared for North American Nickel Inc., 53p., Ontario Assessment File Database record number 20000006524.

Peredery, W. V., & Geological Staff (1982). Geology and nickel sulphide deposits of the Thompson Belt, Manitoba. Precambrian Sulphide Deposits, HS Robinson Memorial Volume. In: Hutchinson, R. W., Spence, C. D., Franklin, J. M. (eds.), Precambrian sulphide deposits. H.S. Robinson Memorial Volume. Geological Association of Canada, Special Paper 25, 165-209.

Peredery, W. V., & Naldrett, A. J. (1975). Petrology of the upper irruptive rocks, Sudbury, Ontario. Economic Geology, 70(1), 164-175.

Peters, T. J., Menzies, M., Thirlwall, M. F, & Kyle, P. R. (2008). Zuni–Bandera volcanism, Rio Grande, USA–Melt formation in garnet-and spinel-facies mantle straddling the asthenosphere–lithosphere boundary. Lithos, 102(1-2), 295-315.

Petrus, J. A., Ames, D. E., & Kamber, B. S. (2015). On the track of the elusive Sudbury impact: geochemical evidence for a chondrite or comet bolide. Terra Nova, 27(1), 9-20.

Petrus, J. A., Kenny, G. G., Ayer, J. A., Lightfoot, P. C., & Kamber, B. S. (2016). Uranium–lead zircon systematics in the Sudbury impact crater-fill: implications for target lithologies and crater evolution. Journal of the Geological Society, 173(1), 59-75.

Pettijohn, F. J. (1975). Sedimentary Rocks. 3rd edition, Harper & Row, New York, 628p.

Pfänder, J. A., Jung, S., Münker, C., Stracke, A., & Mezger, K. (2012). A possible high Nb/Ta reservoir in the continental lithospheric mantle and consequences on the global Nb budget–Evidence from continental basalts from Central Germany. Geochimica et Cosmochimica Acta, 77, 232-251.

Philibert, J., & Tixier, R. (1968). Electron penetration and the atomic number correction in electron probe microanalysis. Journal of Physics D: Applied Physics, 1(6), 685.

Phinney, W. C., & Halls, H. C. (2001). Petrogenesis of the Early Proterozoic Matachewan dyke swarm, Canada, and implications for magma emplacement and subsequent deformation. Canadian Journal of Earth Sciences, 38(11), 1541-1563.

Picard, C., Lamothe, D., Piboule, M., & Oliver, R. (1990). Magmatic and geotectonic evolution of a Proterozoic oceanic basin system: The Cape Smith thrust-fold belt (New-Quebec). Precambrian Research, 47(3-4), 223-249.

Pierazzo, E., & Melosh, H. J. (2000a). Melt production in oblique impacts. Icarus, 145(1), 252-261.

Pierazzo, E., & Melosh, H. J. (2000b). Understanding oblique impacts from experiments, observations, and modeling. Annual Review of Earth and Planetary Sciences, 28(1), 141-167.

Piercey, P., Schneider, D. A., & Holm, D. K. (2007). Geochronology of Proterozoic metamorphism in the deformed Southern Province, northern Lake Huron region, Canada. Precambrian Research, 157(1-4), 127-143.

Pike, R. J., & Spudis, P. D. (1987). Basin-ring spacing on the moon, Mercury, and Mars. Earth, Moon, and Planets, 39(2), 129-194.

Pilet, S. (2015). Generation of low-silica alkaline lavas: Petrological constraints, models, and thermal implications. The interdisciplinary Earth. In: Foulger, G. R., Lustrino, M., King, S. D. (eds.), The Interdisciplinary Earth: A Volume in Honor of Don L. Anderson. Geological Society of America, Special Paper 514, and American Geophysical Union Special Publication 71, 281-304.

Pilet, S., Baker, M. B., & Stolper, E. M. (2008). Metasomatized lithosphere and the origin of alkaline lavas. Science, 320(5878), 916-919.

Pilet, S., Baker, M. B., Müntener, O., & Stolper, E. M. (2011). Monte Carlo simulations of metasomatic enrichment in the lithosphere and implications for the source of alkaline basalts. Journal of Petrology, 52(7-8), 1415-1442.

Pilkington, M. (1997). 3-D magnetic imaging using conjugate gradients. Geophysics, 62(4), 1132-1142.

Pilles, E. A. (2016). Emplacement of the Foy, Hess and Pele Offset Dykes at the Sudbury impact structure, Canada. Unpublished PhD thesis, The University of Western Ontario, London, Ontario, Canada, 184p., Electronic Thesis and Dissertation Repository 4158, https://ir.lib.uwo.ca/etd/4158

Pilles, E. A., Osinski, G. R., Grieve, R. A. F., Coulter, A. B., Smith, D. A., & Bailey, J. M. (2018a). The Pele offset dykes, Sudbury impact structure, Canada. Canadian Journal of Earth Sciences, 55(3), 230-240.

Pilles, E. A., Osinski, G. R., Grieve, R. A. F., Smith, D. A., & Bailey, J. M. (2017). Chemical variations and genetic relationships between the Hess and Foy offset dikes at the Sudbury impact structure. Meteoritics & Planetary Science, 52(12), 2647-2671.

Pilles, E. A., Osinski, G. R., Grieve, R. A. F., Smith, D. A., & Bailey, J. M. (2018b). Formation of large-scale impact melt dikes: A case study of the Foy Offset Dike at the Sudbury impact structure, Canada. Earth and Planetary Science Letters, 495, 224-233.

Pin, C., & Zalduegui, J. S. (1997). Sequential separation of light rare-earth elements, thorium and uranium by miniaturized extraction chromatography: application to isotopic analyses of silicate rocks. Analytica Chimica Acta, 339(1-2), 79-89.

Pin, C., Briot, D., Bassin, C., & Poitrasson, F. (1994). Concomitant separation of strontium and samarium-neodymium for isotopic analysis in silicate samples, based on specific extraction chromatography. Analytica Chimica Acta, 298(2), 209-217.

Pin, C., Gannoun, A., & Dupont, A. (2014). Rapid, simultaneous separation of Sr, Pb, and Nd by extraction chromatography prior to isotope ratios determination by TIMS and MC-ICP-MS. Journal of Analytical Atomic Spectrometry, 29(10), 1858-1870.

Piña, R., Gervilla, F., Barnes, S. J., Oberthür, T., & Lunar, R. (2016). Platinum-group element concentrations in pyrite from the Main Sulfide Zone of the Great Dyke of Zimbabwe. Mineralium Deposita, 51(7), 853-872.

Piña, R., Gervilla, F., Barnes, S. J., Ortega, L., & Lunar, R. (2015). Liquid immiscibility between arsenide and sulfide melts: evidence from a LA-ICP-MS study in magmatic deposits at Serranía de Ronda (Spain). Mineralium Deposita, 50(3), 265-279.

Piña, R., Gervilla, F., Helmy, H., Fonseca, R. O., & Ballhaus, C. (2020). Partition behavior of platinum-group elements during the segregation of arsenide melts from sulfide magma. American Mineralogist: Journal of Earth and Planetary Materials, 105(12), 1889-1897.

Pistone, M., Baumgartner, L. P., Bégué, F., Jarvis, P. A., Bloch, E., Robyr, M., ... & Blundy, J. D. (2020). Felsic melt and gas mobilization during magma solidification: An experimental study at 1.1 kbar. Frontiers in Earth Science, 8, article 175.

Pochon, A., Poujol, M., Gloaguen, E., Branquet, Y., Cagnard, F., Gumiaux, C., & Gapais, D. (2016). U-Pb LA-ICP-MS dating of apatite in mafic rocks: Evidence for a major magmatic event at the Devonian-Carboniferous boundary in the Armorican Massif (France). American Mineralogist, 101(11), 2430-2442.

Polzer, B. (2000). The role of borehole EM in the discovery and definition of the Kelly Lake Ni-Cu deposit, Sudbury, Canada. In: SEG Technical Program Expanded Abstracts (2000). 70th Annual Meeting of the Society of Exploration Geophysicists, 6-11 August 2000, Calgary, Alberta, Canada, 1063-1066, https://doi.org/10.1190/1.1815568

Potter, E. G., & Taylor, R. P. (2009). The lead isotope composition of ore minerals from precious metal-bearing, polymetallic vein systems in the Cobalt Embayment, northern Ontario: metallogenetic implications. Economic Geology, 104(6), 869-879.

Prevec, S. A. (1995). Sm–Nd isotopic evidence for crustal contamination in the ca. 1750 Ma Wanapitei Complex, western Grenville Province, Ontario. Canadian Journal of Earth Sciences, 32(4), 486-495.

Prevec, S. A., & Baadsgaard, H. (2005). Evolution of Palaeoproterozoic mafic intrusions located within the thermal aureole of the Sudbury Igneous Complex, Canada: Isotopic, geochronological and geochemical evidence. Geochimica et Cosmochimica Acta, 69(14), 3653-3669.

Prevec, S. A., & Büttner, S. H. (2018). Multiphase emplacement of impact melt sheet into the footwall: Offset dykes of the Sudbury Igneous Complex, Canada. Meteoritics & Planetary Science, 53(7), 1301-1322.

Prevec, S. A., & Cawthorn, R. G. (2002). Thermal evolution and interaction between impact melt sheet and footwall: A genetic model for the contact sublayer of the Sudbury Igneous Complex, Canada. Journal of Geophysical Research: Solid Earth, 107(B8), ECV-5.

Prevec, S. A., Cowan, D. R., & Cooper, G. R. (2005). Geophysical evidence for a pre-impact Sudbury dome, southern Superior Province, Canada. Canadian Journal of Earth Sciences, 42(1), 1-9.

Prevec, S. A., Lightfoot, P. C., & Keays, R. R. (2000). Evolution of the sublayer of the Sudbury Igneous Complex: geochemical, Sm–Nd isotopic and petrologic evidence. Lithos, 51(4), 271-292.

Prichard, H. M., Hutchinson, D., & Fisher, P. C. (2004). Petrology and crystallization history of multiphase sulfide droplets in a mafic dike from Uruguay: implications for the origin of Cu-Ni-PGE sulfide deposits. Economic Geology, 99(2), 365-376.

Prytulak, J., & Elliott, T. (2007). TiO_2 enrichment in ocean island basalts. Earth and Planetary Science Letters, 263(3-4), 388-403.

Pye, E. G., Naldrett, A. J., & Giblin, P. E. (eds.) (1984). The Geology and Ore Deposits of the Sudbury Structure. Ontario Geological Survey, Special Volume 1, 603p.

Raharimahefa, T., Lafrance, B., & Tinkham, D. K. (2014). New structural, metamorphic, and U–Pb geochronological constraints on the Blezardian Orogeny and Yavapai Orogeny in the Southern Province, Sudbury, Canada. Canadian Journal of Earth Sciences, 51(8), 750-774.

Rainbird, R. H., & Donaldson, J. A. (1988). Nonglaciogenic deltaic deposits in the early Proterozoic Gowganda Formation, Cobalt Basin, Ontario. Canadian Journal of Earth Sciences, 25(5), 710-724.

Rajesh, H. M., Chisonga, B. C., Shindo, K., Beukes, N. J., & Armstrong, R. A. (2013). Petrographic, geochemical and SHRIMP U–Pb titanite age characterization of the Thabazimbi mafic sills: extended time frame and a unifying petrogenetic model for the Bushveld Large Igneous Province. Precambrian Research, 230, 79-102.

Rasmussen, B., Bekker, A., & Fletcher, I. R. (2013). Correlation of Paleoproterozoic glaciations based on U–Pb zircon ages for tuff beds in the Transvaal and Huronian Supergroups. Earth and Planetary Science Letters, 382, 173-180.

Rehkämper, M., Halliday, A. N., Fitton, J. G., Lee, D. C., Wieneke, M., & Arndt, N. T. (1999). Ir, Ru, Pt, and Pd in basalts and komatiites: new constraints for the geochemical behavior of the platinum-group elements in the mantle. Geochimica et Cosmochimica Acta, 63(22), 3915-3934.

Reimold, W. U. (1998). Exogenic and endogenic breccias: a discussion of major problematics. Earth-Science Reviews, 43(1-2), 25-47.

Reimold, W. U., & Gibson, R. L. (2005). “Pseudotachylites” in large impact structures. In: Koeberl, C., Henkel, H. (eds.), Impact Tectonics. Springer-Verlag, Berlin and Heidelberg, 1-53.

Reimold, W. U., Hauser, N., Hansen, B. T., Thirlwall, M. F., & Hoffmann, M. (2017). The impact pseudotachylitic breccia controversy: Insights from first isotope analysis of Vredefort impact-generated melt rocks. Geochimica et Cosmochimica Acta, 214, 266-281.

Reimold, W. U., Hauser, N., Hansen, B. T., Thirlwall, M. F., & Hoffmann, M. (2018). Reply to “Comments on “The impact pseudotachylitic breccia controversy: Insights from first isotope analysis of Vredefort impact-generated melt rocks” by Reimold et al. 2017 (GCA 214, 266–282)” by AA Garde and MB Klausen (GCA 233, 187–190)”. Geochimica et Cosmochimica Acta, 240, 331-332.

Reimold, W. U., Hoffmann, M., Hauser, N., Schmitt, R. T., Zaag, P. T., & Mohr-Westheide, T. (2016). A geochemical contribution to the discussion about the genesis of impact-related pseudotachylitic breccias: Studies of PTB in the Otavi and Kudu Quarries of the Vredefort Dome support the “In Situ Formation” hypothesis. South African Journal of Geology 2016, 119(3), 453-472.

Ridolfi, F., & Renzulli, A. (2012). Calcic amphiboles in calc-alkaline and alkaline magmas: thermobarometric and chemometric empirical equations valid up to 1,130° C and 2.2 GPa. Contributions to Mineralogy and Petrology, 163(5), 877-895.

Ridolfi, F., Puerini, M., Renzulli, A., Menna, M., & Toulkeridis, T. (2008). The magmatic feeding system of El Reventador volcano (Sub-Andean zone, Ecuador) constrained by texture, mineralogy and thermobarometry of the 2002 erupted products. Journal of Volcanology and Geothermal Research, 176(1), 94-106.

Ridolfi, F., Renzulli, A., & Puerini, M. (2010). Stability and chemical equilibrium of amphibole in calc-alkaline magmas: an overview, new thermobarometric formulations and application to subduction-related volcanoes. Contributions to Mineralogy and Petrology, 160(1), 45-66.

Riller, U. (2005). Structural characteristics of the Sudbury impact structure, Canada: Impact-induced versus orogenic deformation – a review. Meteoritics & Planetary Science, 40(11), 1723-1740.

Riller, U., Lieger, D., Gibson, R. L., Grieve, R. A. F., & Stöffler, D. (2010). Origin of large-volume pseudotachylite in terrestrial impact structures. Geology, 38(7), 619-622.

Riller, U., & Schwerdtner, W. M. (1997). Mid-crustal deformation at the southern flank of the Sudbury Basin, central Ontario, Canada. Geological Society of America Bulletin, 109(7), 841-854.

Ripley, E. M., Lightfoot, P. C., Stifter, E. C., Underwood, B., Taranovic, V., Dunlop III, M., & Donoghue, K. A. (2015). Heterogeneity of S isotope compositions recorded in the Sudbury Igneous Complex, Canada: significance to formation of Ni-Cu sulfide ores and the host rocks. Economic Geology, 110(4), 1125-1135.

Robertson, J. A., Frarey, M. J., & Card, K. D. (1969). The Federal–Provincial Committee on Huronian Stratigraphy: Progress report. Canadian Journal of Earth Sciences, 6(2), 335-336.

Robinson, J. A. C., & Wood, B. J. (1998). The depth of the spinel to garnet transition at the peridotite solidus. Earth and Planetary Science Letters, 164(1-2), 277-284.

Roest, W. R., & Pilkington, M. (1994). Restoring post-impact deformation at Sudbury: A circular argument. Geophysical Research Letters, 21(10), 959-962.

Rollinson, H. R. (1993). Using Geochemical Data. Evaluation, Presentation, Interpretation. 1st edition, Routledge, London and New York, 384p.

Rooney, T. O., Nelson, W. R., Ayalew, D., Hanan, B., Yirgu, G., & Kappelman, J. (2017). Melting the lithosphere: Metasomes as a source for mantle-derived magmas. Earth and Planetary Science Letters, 461, 105-118.

Rosatelli, G., Wall, F., & Stoppa, F. (2007). Calcio-carbonatite melts and metasomatism in the mantle beneath Mt. Vulture (Southern Italy). Lithos, 99(3-4), 229-248.

Roscoe, S. M. (1973). The Huronian Supergroup, a Paleoaphebian succession showing evidence of atmospheric evolution. In: Young, G. M. (ed.), Huronian Stratigraphy and Sedimentation. Geological Association of Canada, Special Paper 12, 31-47.

Roscoe, S. M., Theriault, R. J., & Prasad, N. (1992). Circa 1.7 Ga Rb-Sr re-setting in two Huronian paleosols. Elliot Lake, Ontario and Ville Marie, Quebec. Geological Survey of Canada, Paper 92-2, 119-124.

Rosman, K. J. R., & Taylor, P. D. P. (1998). Isotopic compositions of the elements 1997 (Technical Report). Pure and Applied Chemistry, 70(1), 217-235.

Ross, P. S., & Bédard, J. H. (2009). Magmatic affinity of modern and ancient subalkaline volcanic rocks determined from trace-element discriminant diagrams. Canadian Journal of Earth Sciences, 46(11), 823-839.

Rousell, D. H. (1984). Onwatin and Chelmsford formations. In: Pye, E. G., Naldrett, A. J., Giblin, P. E. (eds.), The Geology and Ore Deposits of the Sudbury Structure. Ontario Geological Survey, Special Volume 1, 211-218.

Rousell, D. H., & Brown G. H. (eds.) (2009). A Field Guide to the Geology of Sudbury, Ontario. Ontario Geological Survey, Open File Report 6243, 233p.

Rousell, D. H., Fedorowich, J. S., & Dressler, B. O. (2003). Sudbury Breccia (Canada): a product of the 1850 Ma Sudbury Event and host to footwall Cu–Ni–PGE deposits. Earth-Science Reviews, 60(3-4), 147-174.

Rowell, W. F., & Edgar, A. D. (1986). Platinum-group element mineralization in a hydrothermal Cu-Ni sulfide occurrence, Rathbun Lake, northeastern Ontario. Economic Geology, 81(5), 1272-1277.

Rudnick, R. L., & Gao, S. (2013). Composition of the Continental Crust. In: Turekian, K. K., Holland, H. D. (eds.), Treatise on Geochemistry. 2nd edition, Elsevier Science, Volume 4, 1-51.

Rudnick, R. L., McDonough, W. F., & Chappell, B. W. (1993). Carbonatite metasomatism in the

northern Tanzanian mantle: petrographic and geochemical characteristics. Earth and Planetary Science Letters, 114(4), 463-475.

Rukhlov, A. S., & Bell, K. (2010). Geochronology of carbonatites from the Canadian and Baltic Shields, and the Canadian Cordillera: clues to mantle evolution. Mineralogy and Petrology, 98(1-4), 11-54.

Sage, R. P. (1987). Geology of the carbonatite-alkalic complexes in Ontario, Spanish River carbonatite complex, District of Sudbury. Ontario Geological Survey, Study 30, 62p.

Salters, V. J., Longhi, J. E., & Bizimis, M. (2002). Near mantle solidus trace element partitioning at pressures up to 3.4 GPa. Geochemistry, Geophysics, Geosystems, 3(7), 1-23.

Saumur, B. M., & Cruden, A. R. (2017). Ingress of magmatic Ni-Cu sulphide liquid into surrounding brittle rocks: Physical & structural controls. Ore Geology Reviews, 90, 439-445.

Schandl, E. S. (2002). An integrated study, based on reinterpretation of drill logs, assays, and previous mineralogical and fluid inclusion studies on Cobalt Hill. Unpublished report, prepared for Flag Resources Ltd., 42p., Ontario Assessment File Database record number 41I15SE2032.

Schandl, E. S. (2004). The role of saline fluids base-metal and gold mineralization at the Cobalt Hill prospect northeast of the Sudbury Igneous Complex, Ontario: A fluid-inclusion and mineralogical study. The Canadian Mineralogist, 42(5), 1541-1562.

Schandl, E. S., & Gorton, M. P. (1991). Postore mobilization of rare earth elements at Kidd Creek and other Archean massive sulfide deposits. Economic Geology, 86(7), 1546-1553.

Schandl, E. S., & Gorton, M. P. (2007). The Scadding gold mine, east of the Sudbury igneous complex, Ontario: An IOCG-type deposit?. The Canadian Mineralogist, 45(6), 1415-1441.

Schandl, E. S., Gorton, M. P., & Davis, D. W. (1994). Albitization at 1700±2 Ma in the Sudbury–Wanapitei Lake area, Ontario: implications for deep-seated alkalic magmatism in the Southern Province. Canadian Journal of Earth Sciences, 31(3), 597-607.

Schmidt, M. W. (1992). Amphibole composition in tonalite as a function of pressure: an experimental calibration of the Al-in-hornblende barometer. Contributions to Mineralogy and Petrology, 110(2), 304-310.

Schoene, B., & Bowring, S. A. (2007). Determining accurate temperature–time paths from U–Pb thermochronology: An example from the Kaapvaal craton, southern Africa. Geochimica et Cosmochimica Acta, 71(1), 165-185.

Scholten, L., Watenphul, A., Beermann, O., Testemale, D., Ames, D. E., & Schmidt, C. (2018). Nickel and platinum in high-temperature H_2O+ HCl fluids: Implications for hydrothermal mobilization. Geochimica et Cosmochimica Acta, 224, 187-199.

Schultz, P. H., & D'Hondt, S. (1996). Cretaceous-Tertiary (Chicxulub) impact angle and its consequences. Geology, 24(11), 963-967.

Scott, D. J., & St-Onge, M. R. (1995). Constraints on Pb closure temperature in titanite based on

rocks from the Ungava orogen, Canada: Implications for U-Pb geochronology and PTt path determinations. Geology, 23(12), 1123-1126.

Scott, R. G., & Benn, K. (2001). Peak-ring rim collapse accommodated by impact melt-filled transfer faults, Sudbury impact structure, Canada. Geology, 29(8), 747-750.

Scott, R. G., & Benn, K. (2002). Emplacement of sulfide deposits in the Copper Cliff offset dike during collapse of the Sudbury crater rim: Evidence from magnetic fabric studies. Economic Geology, 97(7), 1447-1458.

Scott, R. G., & Spray, J. G. (1999). Magnetic fabric constraints on friction melt flow regimes and ore emplacement direction within the South Range breccia belt, Sudbury impact structure. Tectonophysics, 307(1-2), 163-189.

Scott, R. G., & Spray, J. G. (2000). The South Range breccia belt of the Sudbury impact structure: A possible terrace collapse feature. Meteoritics & Planetary Science, 35(3), 505-520.

Scribbins, B. T., Rae, D. R., & Naldrett, A. J. (1984). Mafic and ultramafic inclusions in the sublayer of the Sudbury igneous complex. The Canadian Mineralogist, 22(1), 67-75.

Seabrook, C. L., Prichard, H. M., & Fisher, P. C. (2004). Platinum-group minerals in the Raglan Ni–Cu–(PGE) sulfide deposit, Cape Smith, Quebec, Canada. The Canadian Mineralogist, 42(2), 485-497.

Seifert, W., & Kramer, W. (2003). Accessory titanite: an important carrier of zirconium in lamprophyres. Lithos, 71(1), 81-98.

Sekine, Y., Tajika, E., Tada, R., Hirai, T., Goto, K. T., Kuwatani, T., ... & Kirschvink, J. L. (2011). Manganese enrichment in the Gowganda Formation of the Huronian Supergroup: A highly oxidizing shallow-marine environment after the last Huronian glaciation. Earth and Planetary Science Letters, 307(1-2), 201-210.

Seymour, K. S., & Kumarapeli, P. S. (1995). Geochemistry of the Grenville Dyke Swarm: role of plume-source mantle in magma genesis. Contributions to Mineralogy and Petrology, 120(1), 29-41.

Shand, S. J. (1916). The pseudotachylyte of Parijs (Orange Free State), and its relation to “trapshotten gneiss” and “flinty crush rock”. Quarterly Journal of the Geological Society of London, 72, 198-221.

Shaw, D. M. (1970). Trace element fractionation during anatexis. Geochimica et Cosmochimica Acta, 34(2), 237-243.

Shaw, J. E., Baker, J. A., Menzies, M. A., Thirlwall, M. F., & Ibrahim, K. M. (2003). Petrogenesis of the largest intraplate volcanic field on the Arabian Plate (Jordan): a mixed lithosphere–asthenosphere source activated by lithospheric extension. Journal of Petrology, 44(9), 1657-1679.

Shea, J. J., & Foley, S. F. (2019). Evidence for a carbonatite-influenced source assemblage for intraplate basalts from the Buckland Volcanic Province, Queensland, Australia. Minerals, 9(9), 546.

Shellnutt, J. G., & MacRae, N. D. (2012). Petrogenesis of the Mesoproterozoic (1.23 Ga) Sudbury dyke swarm and its questionable relationship to plate separation. International Journal of Earth Sciences, 101(1), 3-23.

Shervais, J. W. (1982). Ti-V plots and the petrogenesis of modern and ophiolitic lavas. Earth and Planetary Science Letters, 59(1), 101-118.

Siemiatkowska, K. M., & Martin, R. F. (1975). Fenitization of Mississagi quartzite, Sudbury area, Ontario. Geological Society of America Bulletin, 86(8), 1109-1122.

Sillitoe, R. H., & Clark, A. H. (1969). Copper and copper-iron sulfides as the initial products of supergene oxidation, Copiapó mining district, northern Chile. American Mineralogist, 54(11-12), 1684-1710.

Simonetti, A., Heaman, L. M., Chacko, T., & Banerjee, N. R. (2006). In situ petrographic thin section U–Pb dating of zircon, monazite, and titanite using laser ablation–MC–ICP-MS. International Journal of Mass Spectrometry, 253(1-2), 87-97.

Simony, P. S. (1964). Northwestern Timagami area. Ontario Department of Mines, Geological Report 28, 30p.

Sisson, T. W., & Bacon, C. R. (1999). Gas-driven filter pressing in magmas. Geology, 27(7), 613-616.

Smit, K. V., Stachel, T., Creaser, R. A., Ickert, R. B., DuFrane, S. A., Stern, R. A., & Seller, M. (2014). Origin of eclogite and pyroxenite xenoliths from the Victor kimberlite, Canada, and implications for Superior craton formation. Geochimica et Cosmochimica Acta, 125, 308-337.

Smith, D. A. (2017). Technical Report on Wallbridge's Sudbury Area Properties, Ontario (Canada). Unpublished report, 167p., https://wallbridgemining.com/site/assets/files/2741/2017_technical_report_final_draft.pdf (last accessed: 19.09.2021).

Smith, D. A., Bailey, J. M., & Pattison, E. F. (2013). Discovery of new offset dykes and insights into the Sudbury Impact Structure. In: Large Meteorite Impacts and Planetary Evolution V. 5-8 August 2013, Sudbury, Canada, Lunar and Planetary Institute, LPI Contribution No. 1737, Abstract 3090.

Smith, J. W., Holwell, D. A., & McDonald, I. (2014). Precious and base metal geochemistry and mineralogy of the Grasvally Norite–Pyroxenite–Anorthosite (GNPA) member, northern Bushveld Complex, South Africa: implications for a multistage emplacement. Mineralium Deposita, 49(6), 667-692.

Smith, P., & Parsons, I. (1974). The alkali-feldspar solvus at 1 kilobar water-vapour pressure. Mineralogical Magazine, 39(307), 747-767.

Snyder, D. B., Savard, G., Kjarsgaard, B. A., Vaillancourt, A., Thurston, P. C., Ayer, J. A., & Roots, E. (2021). Multidisciplinary Modeling of Mantle Lithosphere Structure Within the Superior Craton, North America. Geochemistry, Geophysics, Geosystems, 22(4), e2020GC009566.

Souch, B. E., Podolsky, T., & the Inco Ltd. geological staff (1969). The sulfide ores at Sudbury.

Their particular relation to inclusion-bearing facies of the nickel irruptive. Economic Geology Monograph, 4, 252-261.

Sparks, R. S. J. (1986). The role of crustal contamination in magma evolution through geological time. Earth and Planetary Science Letters, 78(2-3), 211-223.

Spear, F. S. (1981). An experimental study of hornblende stability and compositional variability in amphibolite. American Journal of Science, 281(6), 697-734.

Speers, E. C. (1957). The age relation and origin of common Sudbury Breccia. The Journal of Geology, 65(5), 497-514.

Spencer, C. J., Kirkland, C. L., & Taylor, R. J. (2016). Strategies towards statistically robust interpretations of in situ U–Pb zircon geochronology. Geoscience Frontiers, 7(4), 581-589.

Spicer, B. (2016). Geophysical signature of the Victoria property, vectoring toward deep mineralization in the Sudbury Basin. Interpretation, 4(3), T281-T290.

Spray, J. G. (1995). Pseudotachylyte controversy: Fact or friction?. Geology, 23(12), 1119-1122.

Spray, J. G. (1997). Superfaults. Geology, 25(7), 579-582.

Spray, J. G. (2010). Frictional melting processes in planetary materials: From hypervelocity impact to earthquakes. Annual Review of Earth and Planetary Sciences, 38, 221-254.

Spray, J. G. (2016). Experimental vibration melting without offset: Post-shock materials behaviour. In: 79th Annual Meeting of the Meteoritical Society, 7-12 August 2016, Berlin, Germany. LPI Contribution No. 1921. Meteoritics & Planetary Science, 51, No. S1, abstract 6118.

Spray, J. G., & Thompson, L. M. (1995). Friction melt distribution in a multi-ring basin. Nature, 373(6510), 130-132.

Spray, J. G., Butler, H. R., & Thompson, L. M. (2004). Tectonic influences on the morphometry of the Sudbury impact structure: Implications for terrestrial cratering and modeling. Meteoritics & Planetary Science, 39(2), 287-301.

Spray, J. G., Murphy, A. J., Shaw, C. S., & Tuchscherer, M. G. (2003). Chilling Evidence for the Bulk Composition of the Impact Melt Sheet at Sudbury: Evidence from Offset Dykes. In: Dressler, B. O. et al. (eds.), Third International Conference on Large Meteorite Impacts, 5-7 August 2003, Nördlingen, Germany, Abstract 4101.

Sproule, R. A., Sutcliffe, R., Tracanelli, H., & Lesher, C. M. (2007). Palaeoproterozoic Ni–Cu–PGE mineralisation in the Shakespeare intrusion, Ontario, Canada: a new style of Nipissing gabbro-hosted mineralisation. Applied Earth Science, 116(4), 188-200.

Stacey, J. T., & Kramers, J. D. (1975). Approximation of terrestrial lead isotope evolution by a two-stage model. Earth and Planetary Science Letters, 26(2), 207-221.

Starkey, J. (1959). Chess-board albite from New Brunswick, Canada. Geological Magazine, 96(2), 141-145.

Staude, S., Barnes, S. J., & Le Vaillant, M. (2017). Thermomechanical erosion of ore-hosting embayments beneath komatiite lava channels: textural evidence from Kambalda, Western Australia. Ore Geology Reviews, 90, 446-464.

Steiger, R. H., & Jäger, E. (1977). Subcommission on geochronology: convention on the use of decay constants in geo-and cosmochronology. Earth and Planetary Science Letters, 36(3), 359-362.

Stein, E., & Dietl, C. (2001). Hornblende thermobarometry of granitoids from the Central Odenwald (Germany) and their implications for the geotectonic development of the Odenwald. Mineralogy and Petrology, 72(1-3), 185-207.

Stewart, R. C. (2017). Characterization of barren and mineralized hydrothermal systems in an impact structure: the granophyre unit and footwall of the Sudbury Igneous Complex, Ontario, Canada. Unpublished PhD thesis, Laurentian University, Sudbury, Ontario, Canada, 362p., https://zone.biblio.laurentian.ca/handle/10219/2756

Stevenson, J. S. (1963). The upper contact phase of the Sudbury micropegmatite. The Canadian Mineralogist, 7(3), 413-419.

Stevenson, J. S., & Stevenson, L. S. (1980). Sudbury, Ontario, and the meteorite theory. Geoscience Canada, 7(3), 103-108.

Stipp, M., Stünitz, H., Heilbronner, R., & Schmid, S. M. (2002). The eastern Tonale fault zone: a 'natural laboratory' for crystal plastic deformation of quartz over a temperature range from 250 to 700°C. Journal of Structural Geology, 24(12), 1861-1884.

Stockwell, C. H. (1982). Proposals for the time classification and correlation of Precambrian rocks and events in Canada and adjacent areas of the Canadian Shield. Geological Survey of Canada, Paper 80-19, 135p.

Stöffler, D., & Grieve, R. A. F. (2007). Impactites. In: Fettes, D., Desmons, J. (eds.), Metamorphic Rocks: A Classification and Glossary of Terms, Recommendations of the International Union of Geological Sciences. Cambridge University Press, Cambridge, UK, 82-92, 111-125, and 126-242.

Stone, D. (2000). Temperature and pressure variations in suites of Archean felsic plutonic rocks, Berens River area, northwest Superior Province, Ontario, Canada. The Canadian Mineralogist, 38(2), 455-470.

St-Onge, M. R., Henderson, I., & Ford, A. (2007). Digital geoscience atlas of Baffin Island (south of 70°N and east of 80°W), Nunavut. Geological Survey of Canada, Open File 5117.

Storey, C. D., Smith, M. P., & Jeffries, T. E. (2007). In situ LA-ICP-MS U–Pb dating of metavolcanics of Norrbotten, Sweden: Records of extended geological histories in complex titanite grains. Chemical Geology, 240(1-2), 163-181.

Stosch, H. G., & Seck, H. A. (1980). Geochemistry and mineralogy of two spinel peridotite suites from Dreiser Weiher, West Germany. Geochimica et Cosmochimica Acta, 44(3), 457-470.

Streckeisen, A. (1976). To each plutonic rock its proper name. Earth-Science Reviews, 12(1), 1-

33.

Suikkanen, E., & Rämö, O. T. (2017). Metasomatic alkali-feldspar syenites (episyenites) of the Proterozoic Suomenniemi rapakivi granite complex, southeastern Finland. Lithos, 294, 1-19.

Suikkanen, E., & Rämö, O. T. (2019). Episyenites – characteristics, genetic constraints, and mineral potential. Mining, Metallurgy & Exploration, 36(5), 861-878.

Sullivan, R. W., & Davidson, A. (1993). Monazite age of 1747 Ma confirms post-Penokean age of the Eden Lake Complex, Southern Province, Ontario. In: Radiogenic Age and Isotopic Studies, Report 7. Geological Survey of Canada, Paper 93-2, 45-48.

Sun, S. S., & McDonough, W. F. (1989). Chemical and isotopic systematics of oceanic basalts: implications for mantle composition and processes. In: Saunders, A. D., Norry, M. J. (eds.), Magmatism in the Ocean Basins. Geological Society, London, Special Publications, 42(1), 313-345.

Sutcliffe, R. H., Barrie, C. T., Burrows, D. R., & Beakhouse, G. P. (1993). Plutonism in the southern Abitibi Subprovince; a tectonic and petrogenetic framework. Economic Geology, 88(6), 1359-1375.

Szabó, E., & Halls, H. C. (2006). Deformation of the Sudbury Structure: Paleomagnetic evidence from the Sudbury breccia. Precambrian Research, 150(1-2), 27-48.

Szentpéteri, K., Molnár, F., Watkinson, D. H., & Jones, P. C. (2003). Geology and high grade hydrothermal PGE mineralization of the Vermilion quartz diorite offset dike, Sudbury, Canada. In: Eliopoulos, D. G. et al. (eds.), Mineral Exploration and Sustainable Development, Proceedings of the 7th Biennial SGA Meeting, Athens, Greece, 24-28 August 2003, Millpress, Rotterdam, Netherlands, 643-646.

Szentpéteri, K., Watkinson, D. H., Molnár, F., & Jones, P. C. (2002). Platinum-group elements-Co-Ni-Fe sulfarsenides and mineral paragenesis in Cu-Ni-platinum-group element deposits, Copper Cliff North area, Sudbury, Canada. Economic Geology, 97(7), 1459-1470.

Swamy, V., Saxena, S. K., Sundman, B., & Zhang, J. (1994). A thermodynamic assessment of silica phase diagram. Journal of Geophysical Research, 99(B6), 11787-11794.

Tanaka, T., Togashi, S., Kamioka, H., Amakawa, H., Kagami, H., Hamamoto, T., ... & Dragusanu, C. (2000). JNdi-1: a neodymium isotopic reference in consistency with LaJolla neodymium. Chemical Geology, 168(3-4), 279-281.

Tang, H., & Chen, Y. (2013). Global glaciations and atmospheric change at ca. 2.3 Ga. Geoscience Frontiers, 4(5), 583-596.

Taylor, S. R., & McLennan, S. M. (1985). The continental crust: its composition and evolution. 1st edition, Blackwell Scientific, Oxford, 312p.

Tenailleau, C., Pring, A., Etschmann, B., Brugger, J., Grguric, B., & Putnis, A. (2006). Transformation of pentlandite to violarite under mild hydrothermal conditions. American Mineralogist, 91(4), 706-709.

Tera, F., & Wasserburg, G. J. (1972). U-Th-Pb systematics in three Apollo 14 basalts and the problem of initial Pb in lunar rocks. Earth and Planetary Science Letters, 14(3), 281-304.

Therriault, A. M., Fowler, A. D., & Grieve, R. A. F. (2002). The Sudbury Igneous Complex: A differentiated impact melt sheet. Economic Geology, 97(7), 1521-1540.

Therriault, A. M., Reimold, W. U., & Reid, A. M. (1996). Field relations and petrography of the Vredefort Granophyre. South African Journal of Geology, 99(1), 1-21.

Thirlwall, M. F. (2002). Multicollector ICP-MS analysis of Pb isotopes using a ^{207}pb-^{204}pb double spike demonstrates up to 400 ppm/amu systematic errors in Tl-normalization. Chemical Geology, 184(3-4), 255-279.

Thirlwall, M. F., Upton, B. G. J., & Jenkins, C. (1994). Interaction between continental lithosphere and the Iceland plume – Sr-Nd-Pb isotope geochemistry of Tertiary basalts, NE Greenland. Journal of Petrology, 35(3), 839-879.

Thomas, W. M, & Ernst, W. G. (1990). The aluminium content of hornblende in calc-alkaline granitic rocks: a mineralogic barometer calibrated experimentally to 12 kbar. In: Spencer, R. J., Chou, I. M. (eds.), Fluid-mineral interactions: a tribute to H.P. Eugster. Geochemical Society, Special Publication 2, 56-63.

Thompson, L. M., & Spray, J. G. (1994). Pseudotachylytic rock distribution and genesis within the Sudbury impact structure. In: Dressler, B. O., Grieve, R. A. F., Sharpton, V. L. (eds.), Large Meteorite Impacts and Planetary Evolution. Geological Society of America, Special Paper 293, 275-275.

Thompson, L. M., & Spray, J. G. (1996). Pseudotachylyte petrogenesis: constraints from the Sudbury impact structure. Contributions to Mineralogy and Petrology, 125(4), 359-374.

Thompson, L. M., Spray, J. G., & Kelley, S. P. (1998). Laser probe argon-40/argon-39 dating of pseudotachylyte from the Sudbury Structure: Evidence for postimpact thermal overprinting in the North Range. Meteoritics & Planetary Science, 33(6), 1259-1269.

Thomson, M. L., Barnett, R. L., Fleet, M. E., & Kerrich, R. (1985). Metamorphic assemblages in the South-Range norite and footwall mafic rocks near the Kirkwood mine, Sudbury, Ontario. The Canadian Mineralogist, 23(2), 173-186.

Thomson, O. A., Cavosie, A. J., Moser, D. E., Barker, I., Radovan, H. A., & French, B. M. (2014). Preservation of detrital shocked minerals derived from the 1.85 Ga Sudbury impact structure in modern alluvium and Holocene glacial deposits. Geological Society of America Bulletin, 126(5-6), 720-737.

Thornber, C. R., & Huebner, J. S. (1985). Dissolution of olivine in basaltic liquids: experimental observations and applications. American Mineralogist, 70(9-10), 934-945.

Thurston, P. C., Kamber, B. S., & Whitehouse, M. (2012). Archean cherts in banded iron formation: insight into Neoarchean ocean chemistry and depositional processes. Precambrian Research, 214, 227-257.

Timms, N. E., Erickson, T. M., Zanetti, M. R., Pearce, M. A., Cayron, C., Cavosie, A. J., ... & Carpenter,

P. K. (2017). Cubic zirconia in > 2370° C impact melt records Earth's hottest crust. Earth and Planetary Science Letters, 477, 52-58.

Timms, N. E., Kirkland, C. L., Cavosie, A. J., Rae, A. S., Rickard, W. D., Evans, N. J., ... & Gulick, S. P. (2020). Shocked titanite records Chicxulub hydrothermal alteration and impact age. Geochimica et Cosmochimica Acta, 281, 12-30.

Tomkins, A. G. (2010). Wetting facilitates late-stage segregation of precious metal–enriched sulfosalt melt in magmatic sulfide systems. Geology, 38(10), 951-954.

Tschirhart, P., & Morris, B. (2012). Grenville age deformation of the Sudbury impact structure: evidence from magnetic modelling of the Sudbury diabase dyke swarm. Terra Nova, 24(3), 213-220.

Tuba, G., Molnár, F., Ames, D. E., Péntek, A., Watkinson, D. H., & Jones, P. C. (2014). Multi-stage hydrothermal processes involved in "low-sulfide" Cu (–Ni)–PGE mineralization in the footwall of the Sudbury Igneous Complex (Canada): Amy Lake PGE zone, East Range. Mineralium Deposita, 49(1), 7-47.

Tuchscherer, M. G., & Spray, J. G. (2002). Geology, mineralization, and emplacement of the Foy Offset Dike, Sudbury impact structure. Economic Geology, 97(7), 1377-1397.

Ubide, T., Guyett, P. C., Kenny, G. G., O'Sullivan, E. M., Ames, D. E., Petrus, J. A., ... & Kamber, B. S. (2017). Protracted volcanism after large impacts: Evidence from the Sudbury impact basin. Journal of Geophysical Research: Planets, 122(4), 701-728.

Vaillancourt, C., Sproule, R. A., MacDonald, C. A., & Hulbert, L. J. (2001). Potential for Platinum Group Elements Mineralization in Mafic-Ultramafic Intrusions in Ontario. In: Baker, C. L., Kelly, R. I., Parker, J. R. (eds.), Summary of Field Work and Other Activities 2001. Ontario Geological Survey, Open File Report 6070, 38-1 to 38-10.

Valsami, E., & Cann, J. R. (1992). Mobility of rare earth elements in zones of intense hydrothermal alteration in the Pindos ophiolite, Greece. In: Parson, L. M., Murton, B. J., Browning, P. (eds.), Ophiolites and their Modern Oceanic Analogues. Geological Society, London, Special Publications 60(1), 219-232.

Van Baalen, M. R. (1993). Titanium mobility in metamorphic systems: a review. Chemical Geology, 110(1-3), 233-249.

Van Breemen, O., & Davidson, A. (1988). Northeast extension of Proterozoic terranes of mid-continental North America. Geological Society of America Bulletin, 100(5), 630-638.

Van Schmus, W. R. (1965). The Geochronology of the Blind River-Bruce Mines Area Ontario, Canada. The Journal of Geology, 73(5), 755-780.

Van Schmus, W. R. (1971). Ages of lamprophyre dikes and of the Mongowin Pluton, north shore of Lake Huron, Ontario, Canada. Canadian Journal of Earth Sciences, 8(10), 1203-1209.

Van Schmus, W. R., Card, K. D., & Harrower, K. L. (1975). Geology and ages of buried Precambrian basement rocks, Manitoulin Island, Ontario. Canadian Journal of Earth Sciences, 12(7), 1175-1189.

VanderWal, J. (2020a). LC20-01 Drillhole Log, Mackelcan Township. Ontario Assessment File Database record number 20000019196.

VanderWal, J. (2020b). LC20-03 Drillhole Log, Mackelcan Township. Ontario Assessment File Database record number 20000019196.

VanderWal, J. (2020c). LC20-04 Drillhole Log, Mackelcan Township. Ontario Assessment File Database record number 20000019196.

VanderWal, J. (2020d). LC20-04 Drillhole Log, Mackelcan Township. Ontario Assessment File Database record number 20000019196.

VanderWal, J. (2021). Geology and Geochemistry of the Bassfin Offset Dyke East of the Sudbury Igneous Complex, Ontario, Canada. Unpublished MSc thesis, Laurentian University, Sudbury, Ontario, Canada, 76p.

Vermeesch, P. (2018). IsoplotR: A free and open toolbox for geochronology. Geoscience Frontiers, 9(5), 1479-1493.

Vervoort, J. D., & Blichert-Toft, J. (1999). Evolution of the depleted mantle: Hf isotope evidence from juvenile rocks through time. Geochimica et Cosmochimica Acta, 63(3-4), 533-556.

Viehmann, S., Hoffmann, J. E., Münker, C., & Bau, M. (2014). Decoupled Hf-Nd isotopes in Neoarchean seawater reveal weathering of emerged continents. Geology, 42(2), 115-118.

Villemant, B., Jaffrezic, H., Joron, J. L., & Treuil, M. (1981). Distribution coefficients of major and trace elements; fractional crystallization in the alkali basalt series of Chaine des Puys (Massif Central, France). Geochimica et Cosmochimica Acta, 45(11), 1997-2016.

Vogel, D. C., James, R. S., & Keays, R. R. (1998a). The early tectono-magmatic evolution of the Southern Province: implications from the Agnew Intrusion, central Ontario, Canada. Canadian Journal of Earth Sciences, 35(7), 854-870.

Vogel, D. C., Keays, R. R., James, R. S., & Reeves, S. J. (1999). The geochemistry and petrogenesis of the Agnew intrusion, Canada: A product of S-undersaturated, high-Al and low-Ti tholeiitic magmas. Journal of Petrology, 40(3), 423-450.

Vogel, D. C., Vuollo, J. I., Alapieti, T. T., & James, R. S. (1998b). Tectonic, stratigraphic, and geochemical comparisons between ca. 2500–2440 Ma mafic igneous events in the Canadian and Fennoscandian Shields. Precambrian Research, 92(2), 89-116.

Walker, R. J., Morgan, J. W., Naldrett, A. J., Li, C., & Fassett, J. D. (1991). Re-Os isotope systematics of Ni-Cu sulfide ores, Sudbury Igneous Complex, Ontario: evidence for a major crustal component. Earth and Planetary Science Letters, 105(4), 416-429.

Walter, M. J. (1998). Melting of garnet peridotite and the origin of komatiite and depleted lithosphere. Journal of Petrology, 39(1), 29-60.

Wang, K., Plank, T., Walker, J. D., & Smith, E. I. (2002). A mantle melting profile across the Basin and Range, SW USA. Journal of Geophysical Research: Solid Earth, 107(B1), ECV-5.

Wang, Y., Lesher, C. M., Lightfoot, P. C., Pattison, E. F., & Golightly, J. P. (2020). Geochemistry and

petrogenesis of mafic and ultramafic inclusions in Sublayer and Offset dikes, Sudbury Igneous Complex, Canada. Journal of Petrology, 61(6), egaa059.

Wang, Y., Lesher, C. M., Lightfoot, P. C., Pattison, E. F., & Golightly, J. P. (2018). Shock metamorphic features in mafic and ultramafic inclusions in the Sudbury Igneous Complex: Implications for their origin and impact excavation. Geology, 46(5), 443-446.

Warren, M. R., Hanley, J. J., Ames, D. E., & Jackson, S. E. (2015). The Ni–Cr–Cu content of biotite as pathfinder elements for magmatic sulfide exploration associated with mafic units of the Sudbury Igneous Complex, Ontario, Canada. Journal of Geochemical Exploration, 153, 11-29.

Warren, P. H., Claeys, P., & Cedillo-Pardo, E. (1996). Mega-impact melt petrology (Chicxulub, Sudbury, and the Moon): Effects of scale and other factors on potential for fractional crystallization and development of cumulates. In: Ryder, G., Fastovsky, D., Gartner, S. (eds.), The Cretaceous–Tertiary Event and Other Catastrophes in Earth History. Geological Society of America, Special Paper 307, 105-124.

Wass, S. Y., & Rogers, N. W. (1980). Mantle metasomatism – precursor to continental alkaline volcanism. Geochimica et Cosmochimica Acta, 44(11), 1811-1823.

Waters, L. E., & Lange, R. A. (2017). Why aplites freeze and rhyolites erupt: controls on the accumulation and eruption of high-SiO_2 (eutectic) melts. Geology, 45(11), 1019-1022.

Waterton, P., Pearson, D. G., Kjarsgaard, B., Hulbert, L., Locock, A., Parman, S., & Davis, B. (2017). Age, origin, and thermal evolution of the ultra-fresh ~1.9 Ga Winnipegosis Komatiites, Manitoba, Canada. Lithos, 268, 114-130.

Watkinson, D. H., & Melling, D. R. (1992). Hydrothermal origin of platinum-group mineralization in low-temperature copper sulfide-rich assemblages, Salt Chuck intrusion, Alaska. Economic Geology, 87(1), 175-184.

Watts, K. M. (2014). A melt inclusion study of the Sudbury Igneous Complex (Ontario, Canada): evidence for two-liquid immiscibility and constraints on trace element distribution. Unpublished MSc thesis, Saint Mary's University, Halifax, Nova Scotia, Canada, 129p., https://library2.smu.ca/handle/01/25841

Weatherston, A. J. (1996). OGS Editorial Guide. Ontario Geological Survey, Miscellaneous Paper 165, 132p.

Wehrle, E. A., & McDonald, A. M. (2019). Cathodoluminescence and trace-element chemistry of quartz from Sudbury offset dikes: Observations, interpretations, and genetic implications. The Canadian Mineralogist, 57(6), 947-963.

Weis, D., Kieffer, B., Maerschalk, C., Pretorius, W., & Barling, J. (2005). High-precision Pb-Sr-Nd-Hf isotopic characterization of USGS BHVO-1 and BHVO-2 reference materials. Geochemistry, Geophysics, Geosystems, 6(2).

West, G. F., & Ernst, R. E. (1991). Evidence from aeromagnetics on the configuration of Matachewan dykes and the tectonic evolution of the Kapuskasing Structural Zone, Ontario, Canada. Canadian Journal of Earth Sciences, 28(11), 1797-1811.

Whalen, J. B., Currie, K. L., & Chappell, B. W. (1987). A-type granites: geochemical characteristics, discrimination and petrogenesis. Contributions to Mineralogy and Petrology, 95(4), 407-419.

Whitmeyer, S. J., & Karlstrom, K. E. (2007). Tectonic model for the Proterozoic growth of North America. Geosphere, 3(4), 220-259.

Whitney, D. L., & Evans, B. W. (2010). Abbreviations for names of rock-forming minerals. American Mineralogist, 95(1), 185-187.

Whymark, W. A. (2018). Assessment Report: 2018 Field Mapping, Prospecting, Stripping, Trenching and Channel Sampling in Mackelcan, Sheppard and McCarthy Townships. Unpublished report, 300p., Ontario Assessment File Database record number 20000019191.

Whymark, W. A. (2019). Assessment Report: 2019 Mapping, Prospecting, Stripping, Trenching and Channel Sampling in Mackelcan, Rathbun, Sheppard and McCarthy Townships. Unpublished report, 388p., Ontario Assessment File Database record number 20000018008.

Whymark, W. A. (2020). Assessment Report: 2020 Diamond Drilling and I.P. Survey; Mackelcan and McCarthy Township, Ontario. Unpublished report, 286p., Ontario Assessment File Database record number 20000019196.

Whymark, W. E., & Frimmel, H. E. (2018). Regional gold-enrichment of conglomerates in Paleoproterozoic supergroups formed during the 2.45 Ga rifting of Kenorland. Ore Geology Reviews, 101, 985-996.

Whymark, W. E., & VanderWal, J. (2020). LC20-02 Drillhole Log, Mackelcan Township. Ontario Assessment File Database record number 20000019196.

Wichman, R. W., & Schultz, P. H. (1993). Floor-fractured crater models of the Sudbury Structure, Canada: Implications for initial crater size and crater modification. Meteoritics, 28(2), 222-231.

Wieser, M. E. (2006). Atomic weights of the elements 2005 (IUPAC Technical Report). Pure and Applied Chemistry, 78(11), 2051-2066.

Will, T. M., & Frimmel, H. E. (2013). The influence of inherited structures on dike emplacement during Gondwana breakup in southwestern Africa. The Journal of Geology, 121(5), 455-474.

Will, T. M., Frimmel, H. E., Gaucher, C., & Bossi, J. (2014). Geochemical and isotopic composition of Pan-African metabasalts from southwestern Gondwana: Evidence of Cretaceous South Atlantic opening along a Neoproterozoic back-arc. Lithos, 202, 363-381.

Willbold, M., & Stracke, A. (2006). Trace element composition of mantle end-members: Implications for recycling of oceanic and upper and lower continental crust. Geochemistry, Geophysics, Geosystems, 7(4).

Wilshire, H. G. (1987). A model of mantle metasomatism. In: Morris, E. M., Pasteris, J. D. (eds.), Mantle Metasomatism and Alkaline Magmatism. Geological Society of America, Special Paper 215, 47-60.

Wilson, J. T. (1968). Static or mobile earth: the current scientific revolution. Proceedings of the American Philosophical Society, 112(5), 309-320.

Winchester, J. A., & Floyd, P. A. (1977). Geochemical discrimination of different magma series and their differentiation products using immobile elements. Chemical Geology, 20, 325-343.

Wolff, J. A. (1987). Crystallisation of nepheline syenite in a subvolcanic magma system: Tenerife, Canary Islands. Lithos, 20(3), 207-223.

Wood, C. R., & Spray, J. G. (1998). Origin and emplacement of offset dykes in the Sudbury impact structure: Constraints from Hess. Meteoritics & Planetary Science, 33(2), 337-347.

Wood, D. A. (1980). The application of a Th–Hf–Ta diagram to problems of tectonomagmatic classification and to establishing the nature of crustal contamination of basaltic lavas of the British Tertiary Volcanic Province. Earth and Planetary Science Letters, 50(1), 11-30.

Workman, R. K., & Hart, S. R. (2005). Major and trace element composition of the depleted MORB mantle (DMM). Earth and Planetary Science Letters, 231(1-2), 53-72.

Wu, J., Milkereit, B., & Boerner, D. E. (1995). Seismic imaging of the enigmatic Sudbury Structure. Journal of Geophysical Research: Solid Earth, 100(B3), 4117-4130.

Wyman, D. A., Hollings, P., & Conceição, R. V. (2015). Geochemistry and radiogenic isotope characteristics of xenoliths in Archean diamondiferous lamprophyres: Implications for the Superior Province cratonic keel. Lithos, 233, 111-130.

Wyman, D. A., Kerrich, R., & Polat, A. (2002). Assembly of Archean cratonic mantle lithosphere and crust: plume–arc interaction in the Abitibi–Wawa subduction–accretion complex. Precambrian Research, 115(1-4), 37-62.

Yaxley, G. M., Crawford, A. J., & Green, D. H. (1991). Evidence for carbonatite metasomatism in spinel peridotite xenoliths from western Victoria, Australia. Earth and Planetary Science Letters, 107(2), 305-317.

Yaxley, G. M., Green, D. H., & Kamenetsky, V. (1998). Carbonatite metasomatism in the southeastern Australian lithosphere. Journal of Petrology, 39(11-12), 1917-1930.

York, D., Evensen, N. M., Martinez, M. L., & De Basabe Delgado, J. (2004). Unified equations for the slope, intercept, and standard errors of the best straight line. American Journal of Physics, 72(3), 367-375.

Young, G. M. (1969). Geochemistry of early Proterozoic tillites and argillites of the Gowganda Formation, Ontario, Canada. Geochimica et Cosmochimica Acta, 33(4), 483-492.

Young, G. M. (1970). An extensive early Proterozoic glaciation in North America?. Palaeogeography, Palaeoclimatology, Palaeoecology, 7(2), 85-101.

Young, G. M. (2001). Comparative geochemistry of Pleistocene and Paleoproterozoic (Huronian) glaciogenic laminated deposits: relevance to crustal and atmospheric composition in the last 2.3 Ga. The Journal of Geology, 109(4), 463-477.

Young, G. M. (2013). Precambrian supercontinents, glaciations, atmospheric oxygenation, metazoan evolution and an impact that may have changed the second half of Earth history. Geoscience Frontiers, 4(3), 247-261.

Young, G. M. (2018). Precambrian Glacial Deposits: Their Origin, Tectonic Setting, and Key Role in Earth Evolution. In: Menzies, J., van der Meer, J. J. M. (eds.), Past Glacial Environments. 2nd edition, Elsevier, 17-45.

Young, G. M. (2019). Aspects of the Archean-Proterozoic transition: How the great Huronian Glacial Event was initiated by rift-related uplift and terminated at the rift-drift transition during break-up of Lauroscandia. Earth-Science Reviews, 190, 171-189.

Young, G. M., Long, D. G. F., Fedo, C. M., & Nesbitt, H. W. (2001). Paleoproterozoic Huronian basin: product of a Wilson cycle punctuated by glaciations and a meteorite impact. Sedimentary Geology, 141, 233-254.

Zack, T., & Brumm, R. (1999). Ilmenite/liquid partition coefficients of 26 trace elements determined through ilmenite/clinopyroxene partitioning in garnet pyroxenites. In: Gurney, J. J. et al. (eds.), Extended Abstracts, 7th International Kimberlite Conference, 11-17 April 1998, Cape Town, South Africa, 986-988.

Zanetti, A., Vannucci, R., Bottazzi, P., Oberti, R., & Ottolini, L. (1996). Infiltration metasomatism at Lherz as monitored by systematic ion-microprobe investigations close to a hornblendite vein. Chemical Geology, 134(1-3), 113-133.

Zartman, R. E., & Doe, B. R. (1981). Plumbotectonics – the model. Tectonophysics, 75(1-2), 135-162.

Zeng, G., Chen, L. H., Xu, X. S., Jiang, S. Y., & Hofmann, A. W. (2010). Carbonated mantle sources for Cenozoic intra-plate alkaline basalts in Shandong, North China. Chemical Geology, 273(1-2), 35-45.

Zhang, G. L., Chen, L. H., Jackson, M. G., & Hofmann, A. W. (2017). Evolution of carbonated melt to alkali basalt in the South China Sea. Nature Geoscience, 10(3), 229-235.

Zieg, M. J., & Marsh, B. D. (2005). The Sudbury Igneous Complex: Viscous emulsion differentiation of a superheated impact melt sheet. Geological Society of America Bulletin, 117(11-12), 1427-1450.

Zou, H., & Reid, M. R. (2001). Quantitative modeling of trace element fractionation during incongruent dynamic melting. Geochimica et Cosmochimica Acta, 65(1), 153-162.

Zulauf, G., Gerdes, A., Hattingen, E., Hoefer, H. E., Loeckle, F., Marschall, H. R., ... & Zulauf, J. (2021). Development of a synorogenic composite sill at deep structural levels of a continental arc (Odenwald, Germany). Part 1: Sederholm-type emplacement portrayed by contact melt in shrinkage cracks. Tectonophysics, 805, 228774.

Zurbrigg, H. F. (1963). Thompson mine geology. Canadian Institute of Mining and Metallurgy Bulletin, 56(614), 227-236.

Internet sources

Earth Impact Database (2021). http://passc.net/EarthImpactDatabase/New%20website_05-2018/Index.html (last accessed: 29.11.2021).

Natural Resources Canada (2021a). Geoscience Data Repository for Geophysical Data. http://gdrdap.agg.nrcan.gc.ca (last accessed: 29.11.2021).

Natural Resources Canada (2021b). Minerals and Metal Facts. https://www.nrcan.gc.ca/our-natural-resources/minerals-mining/minerals-metals-facts/20507 (last accessed: 29.11.2021)

National Aeronautics and Space Administration (NASA) (2021). Moon Trek, Version 3.5.2, September 2021. https://trek.nasa.gov/moon/ (last accessed: 29.11.2021).

Appendix

This thesis contains electronic supplementary material (attached to this pdf file), which may also be accessed through the Online Publication Service (OPUS) of the University of Würzburg (https://opus.bibiolthek.uni-wuerzburg.de/home). The supplementary material is also available on request (alexander.kawohl@uni-wuerzburg.de, hartwig.frimmel@uni-wuerzburg.de).

Appendix_1 Whole-rock geochemical data.xls

A Microsoft Excel spreadsheet presenting major, minor and trace element concentration data of whole-rock samples collected during this study. It also includes information about the sample type, the geographic location (coordinates), and the laboratory that carried out the analyses.

Appendix_2 Whole-rock Nd-Sr-Pb isotope data.xls

A Microsoft Excel spreadsheet that contains whole-rock Nd-Sr-Pb isotope data.

Appendix_3 U-Pb isotope data.xls

A Microsoft Excel spreadsheet containing U-Pb isotope data for titanite, apatite and zircon.

Appendix_4 Mineral chemical data.xls

A Microsoft Excel spreadsheet containing electron microprobe-based mineral chemical analyses for amphibole and feldspar for a number of different locations and rock types.

Declaration of Authorship

I, Alexander Kawohl, born on 16th August 1993 in Schweinfurt, affirm on oath in lieu by my signature that I have authored the above presented thesis titled '*The Petrology and Geochemistry of Igneous Dykes above the Temagami Anomaly (Ontario, Canada) and their Relationship to the 1.85 Ga Sudbury Impac*t' independently and without the help of others, all passages that I have made literally or in the sense of publications, marked as such, and that I have not used any publications, sources and resources other than listed. I affirm in lieu of oath by my signature that I have read and understood the guidelines of the University of Würzburg on good scientific practice, in particular that my opportunity to undertake this doctoral project has not been commercially mediated and that no person or organisation which, for a fee, provides a supervisor for this dissertation. I affirm in lieu of oath that I have given the above information to the best of my knowledge and belief and that the information is true and that I have not concealed anything. I am aware of the criminal liability of a false affidavit, namely penalty threat according to §156 StGB of up to three years imprisonment or fine in case of wilful commission of the offence or, pursuant to §161 para. 1 StGB, imprisonment for up to one year or fine for negligent commission.

Ich, Alexander Kawohl, geboren am 16. August 1993 in Schweinfurt, versichere an Eides Statt durch meine Unterschrift, dass ich diese Dissertation mit dem Titel '*The Petrology and Geochemistry of Igneous Dykes above the Temagami Anomaly (Ontario, Canada) and their Relationship to the 1.85 Ga Sudbury Impac*t' selbständig und ohne fremde Hilfe angefertigt, alle Stellen, die ich wörtlich oder dem Sinne nach aus Veröffentlichungen entnommen habe, als solche kenntlich gemacht und ich auch keine anderen als die von mir angegebenen Quellen und Hilfsmittel benutzt habe. Ich versichere an Eides Statt durch meine Unterschrift, dass ich die Regeln der Universität Würzburg über gute wissenschaftliche Praxis eingehalten habe, insbesondere, dass ich die Gelegenheit zum Promotionsvorhaben nicht kommerziell vermittelt bekommen und insbesondere nicht eine Person oder Organisation eingeschaltet habe, die gegen Entgelt Betreuer bzw. Betreuerinnen für die Anfertigung von Dissertationen sucht. Ich versichere an Eides Statt, dass ich die vorgenannten Angaben nach bestem Wissen und Gewissen gemacht habe und dass die Angaben der Wahrheit entsprechen und ich nichts verschwiegen habe. Die Strafbarkeit einer falschen eidesstattlichen Versicherung ist mir bekannt, namentlich die Strafandrohung gemäß § 156 StGB bis zu drei Jahren Freiheitsstrafe oder Geldstrafe bei vorsätzlicher Begehung der Tat bzw. gemäß § 161 Abs. 1 StGB bis zu einem Jahr Freiheitsstrafe oder Geldstrafe bei fahrlässiger Begehung.

Ort, Datum Unterschrift